Institut für Physik und Astronomie
Astrophysik I

Massive star evolution, star formation, and feedback at low metallicity

Quantitative spectroscopy of OB stars in the Magellanic Clouds

---

Kumulative Dissertation
zur Erlangung des akademischen Grades
“doctor rerum naturalium”
(Dr. rer. nat.)
in der Wissenschaftsdisziplin Astrophysik

eingereicht an der
Mathematisch-Naturwissenschaftlichen Fakultät
der Universität Potsdam

von
Varsha Ramachandran
varsha@astro.physik.uni-potsdam.de

Disputation: Potsdam, den 06.08.2019

Published online at the
Institutional Repository of the University of Potsdam:
https://doi.org/10.25932/publishup-43245
https://nbn-resolving.org/urn:nbn:de:kobv:517-opus4-432455

CONTENTS

Chapter 1.

Introduction

1.1. Massive stars

A star is called "massive" if it formed with a high enough initial mass so that it can ignite carbon burning in its core during its final evolutionary stages. They represent the most luminous stars ($10^4 - 10^6\,L_\odot$), which allows to observe them even far away at large cosmic distances. Massive stars are the main sources of ionizing radiation in star-forming galaxies, and are often surrounded by bright H II regions of ionized gas. Their high mass determines their final fate. A star with similar mass to the Sun will ultimately end up as a white dwarf, but a more violent ending awaits for massive counterpart. Since they go further into nucleosynthesis stages than stars like the Sun, massive stars play a key role in the chemical enrichment of galaxies. Such stars start their lives with spectral types O and early-B and are the progenitors of core-collapse supernovae, long gamma-ray bursts, neutron stars, and black holes. Through strong radiation, winds and their exotic fate, massive stars play a significant role in galaxy evolution.

Understanding massive stars, from their birth to death, is still in its on-going phase. They are born predominantly in clusters or part of associations. Massive stars are rare, even less than one percent of the young stellar population in galaxies, as given by the slope of Salpeter initial mass function (IMF). Their formation process, accretion, and upper stellar mass limit remains unsolved. Despite having enormous fuel, massive stars evolve fast, lifetimes are only up to a few tens of million years. So, these stars generally do not get enough time to 'run' or 'walk' far away from their birthplace and mostly occur in groups. Only a few isolated objects happened to be formed in a cluster and then ejected later on, because of dynamical few-body interactions or the kick due to binary-supernova explosions. As a result, massive stars often belong to crowded clusters or in their early phases, are embedded deep inside the parental cloud, making it difficult to observe. Their evolutionary path is still poorly understood, because of this short lifetime, scarcity and location. The vital role of massive stars in various fields of astrophysics invoke us to investigate formation, evolution, and feedback of massive stars in detail.

Massive stars have profound influence to their surrounding environment. They are one of the main sources of stellar feedback in star-forming galaxies even at high red-shift. They can dynamically change the surrounding interstellar medium (ISM) at different scales by protostellar outflows (e.g. Matzner 2007; Frank et al. 2014), radiation pressure (e.g. Krumholz & Matzner 2009; Murray et al. 2010), UV radiation (e.g. Dale et al. 2012; Walch et al. 2012; Walch et al. 2013), stellar winds (e.g. Toalá & Arthur 2011; Rogers & Pittard 2013), and supernova explosions (e.g. Mac Low et al. 2005; Walch & Naab 2015).

For a better understanding of massive stars, their properties, evolution, and feedback, conducting a comprehensive census of massive star population is ideal rather than focusing on individual stars. There are many on-going studies on young stellar populations, clusters, OB associations to probe populations of massive stars within and outside Galaxy. Widely used observation techniques to

study massive stars and their associated ISM are imaging, photometry, and spectroscopy. It is well known from photometric studies that early-type stars, far from the peak of their energy output, are largely degenerate. Therefore, spectroscopic techniques are required for the reliable determination of physical properties. Spectroscopy is a key tool which provides detailed knowledge of stellar and wind parameters of the massive star and its chemical composition, and kinematics. This also provides information on ages of stars, star-formation history of the region, and ISM evolution.

Quantitative analyses of massive stars are required to understand how their feedback creates and shapes large scale structures of the ISM. A single massive star can produce a hot bubble, ring shell, or a nebula of few tens of parsec in diameter. The combined action of stars in clusters can create huge structures called superbubbles or supergiant shells, with a size of hundreds of parsec. Three main agents of feedback are ionizing radiation, stellar winds, and supernova. Massive stars are responsible for a large fraction of the ultraviolet radiation in galaxies, thereby ionize the ISM and heat the dust. Their winds and final explosion as supernova provide a significant input of mechanical and radiative energy into the ISM together with the injection of nuclear-processed material. This input shapes the multi-phase ISM and affects the star formation, consequently the evolution of stellar clusters and galaxies (e.g. Kudritzki 2002; Springel & Hernquist 2003; de Avillez & Breitschwerdt 2005). Understanding how massive stars interact and shape the ISM is essential to comprehend the Universe we see.

Bright massive stars can be studied individually at nearby galaxies, demonstrating how different metallicity environments can impact on stellar evolution and feedback. The impact of metal-poor massive stars on chemistry, dynamics, and evolution of the ISM also need to be investigated. In fact, going to low metallicity is a window to understand the past or early universe, where the first massive stars are expected to be responsible for re-ionization. However, when we go very far away, the individual stars cannot be resolved. Therefore, we rely on relatively nearby metal-poor massive stars, particularly in the Magellanic Clouds, to form the basis of our understanding for other massive stars in the distant universe. Together, the spectroscopic studies of representative samples of OB and Wolf-Rayet (WR) stars in the Small Magellanic Cloud (SMC) and Large Magellanic Cloud (LMC) allow us to test massive star evolution, their feedback, and star-formation at low metallicity.

1.1.1. OB stars: classification, properties

A star's spectrum presents information about its mass, temperature, luminosity, radius and chemical composition, and can also be used to identify and measure rotational velocity, magnetic fields, stellar winds, etc. Spectral classification is a method to organize this wealth of information around the fundamental properties of temperature and luminosity. Massive stars start their life on the zero age main sequence (ZAMS) with spectral types O and B. They spend most of their time in this young phase by burning hydrogen in their core with CNO catalysts. So, most of the observed massive stars belong to the spectral classes O and B.

The overall shape of a star's emergent spectral energy distribution (SED) is related to the temperature of its photosphere – from the 'blue' type O and B stars that peak in the ultraviolet to Sun-like stars peaking in the visual. The spectral type corresponds to the effective temperature of a star. As photons from the interior of the star pass through a relatively cooler and less dense atmosphere, they get absorbed at specific wavelengths corresponding to transitions between excitation energy levels in an atom. Depending on the temperature and density of the atmosphere, characteristic absorption or emission features or lines get imprinted on the continuum. The spectral classification is based on finding a closest match to the defined prototypes; gradiations in the types

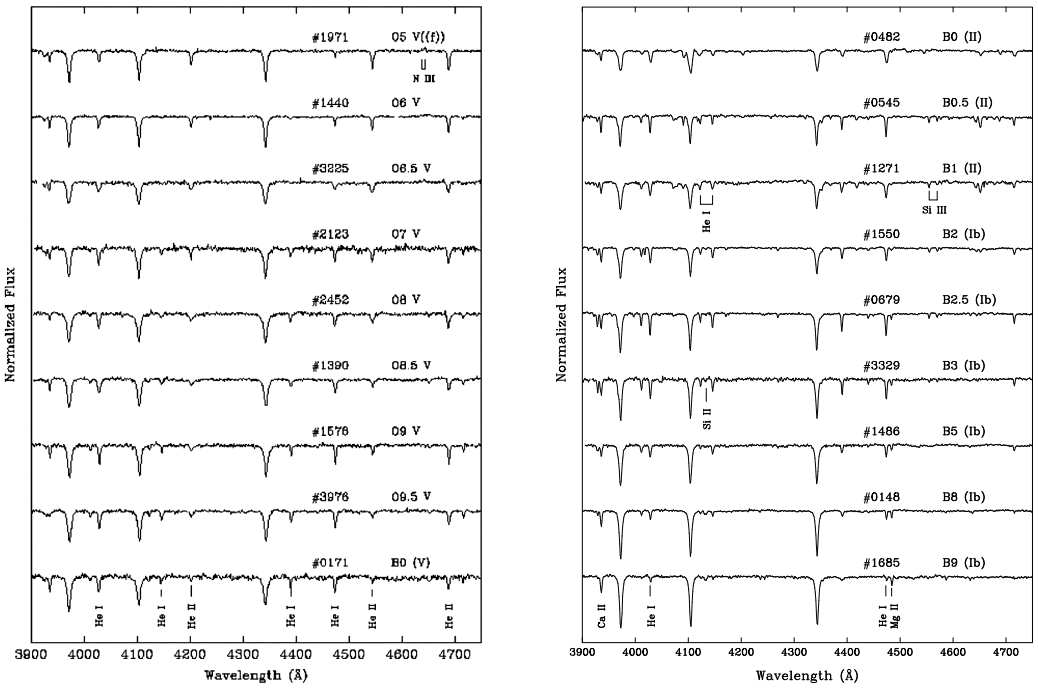

Figure 1.1.: Sample optical spectra of OB stars marked with respective diagnostic lines, taken from Evans et al. (2004)

are reflected by Arabic numbers by subtypes, e.g. O6. A spectral atlas of OB subtypes is shown in Fig. 1.1. Generally, the ratio between the strength of specific absorption lines is used to define the subtype. The initial metallicity of a star also affects the strength of spectral lines.

The spectral classification can be done using the strength and width of spectral lines, separately or as ratios between pairs of lines. Lines used in these comparisons are different across the different spectral types. In the case of O stars, primary lines are of helium and nitrogen whereas for B stars helium, silicon and magnesium lines are useful to classify. The typical range of temperatures spanned by O stars is around 50,000 K at the earliest subtypes (O2) up to $T_{\rm eff} \sim 30{,}000$ K in the case of late O (O9) or early B-type (B0) stars. Temperature of late B-type (B9) stars can go down to $\sim 10{,}000$ K. Previous studies have established temperature-spectral type calibrations through spectroscopic analysis (e.g. Martins et al. 2012, 2005a).

Differences in luminosity classes are a result of the evolution of the star. Starting from the main sequence (V), stars move on to larger and brighter phases such as subgiants (IV), giants (III/II), and supergiants (Ia/b). Luminosity classes are determined using the width of the most prominent spectral lines and from the intensity of emission or absorption lines.

1.1.2. Wolf-Rayet stars

WR stars generally refer to stars which show prominent broad emission lines of ionized helium and highly ionized nitrogen or carbon. The spectra show indications of strong stellar winds and enhancement of heavy elements. WR stars are very hot, their surface temperatures range from 30,000 K up to 200,000 K. Classical WR stars represent the late evolutionary stages of very massive ($\gtrsim 25\,M_{\odot}$) O stars before their final fate. During evolution, massive stars lose a significant

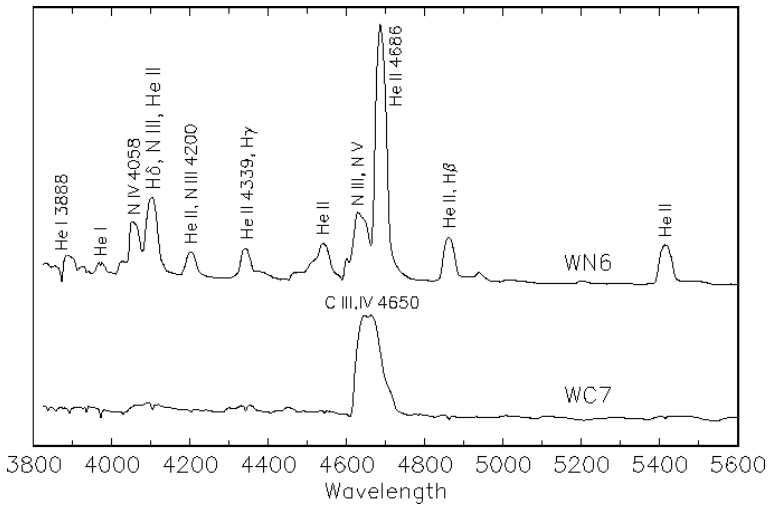

Figure 1.2.: Sample optical spectra of WN and WC stars

amount of their initial mass due to energetic stellar winds or binary interaction, and finally removes their outer envelope.

WR stars have very strong, optically thick stellar winds, with mass-loss rates of $\dot{M} \sim 10^{-5} - 10^{-4}\, M_\odot\, \mathrm{yr}^{-1}$ at speeds of up to 3,000 km/s, leading to the characteristic broad emission lines in the spectra. They are often surrounded by circumstellar nebulae of ejected material, known as WR nebula. Similar to O stars, their winds are driven by radiation pressure, but multiple photon scattering in the optically thick outflow can increase the mass-loss rate to well above the single-scattering limit.

The spectra of WR stars show hydrogen deficiency, and enrichment of nuclear burning products. On the basis of the surface abundances and ratios of line strengths of ionized nitrogen, carbon, and oxygen, they are classified into several subtypes (see Fig. 1.2). WN stars have increased He and N abundances, consistent with equilibrium values from the CNO-cycle. Based on the hydrogen abundance, WN stars can be of 'late' (with $X_\mathrm{H} < 0.4$) or 'early' ($X_\mathrm{H} = 0$) subtype. WC stars have no hydrogen, little or no N, and increased He, C, and O abundances (consistent with partial He-burning). WO stars are similar to WC stars with significantly increased O abundances (as expected for nearly complete He burning). This apparently represents an evolutionary stage at which the envelope of a massive star is peeled off to a larger extent by mass loss.

The numbers and properties of WR stars vary with the chemical composition of their progenitor stars. This is mainly due to the change in the mass-loss rate at different levels of metallicity. Higher metallicity leads to high mass loss, which affects the evolution of massive stars and also the properties of WR stars.

1.1.3. Stellar winds

Hot star winds are driven by the scattering of UV photons by metal lines (e.g. Castor et al. 1975b; Gräfener & Hamann 2005). Winds are able to modify the ionizing radiation of hot stars (Gabler et al. 1992; Najarro et al. 1996). Their momenta and energies contribute substantially to the dynamics and energetics of the ISM by creating structures like wind-blown bubbles.

Winds of hot stars are characterized by two main parameters, the terminal velocity v_∞ and the rate of mass-loss $\dot{M}$. A typical value of the terminal velocity is about three times the escape

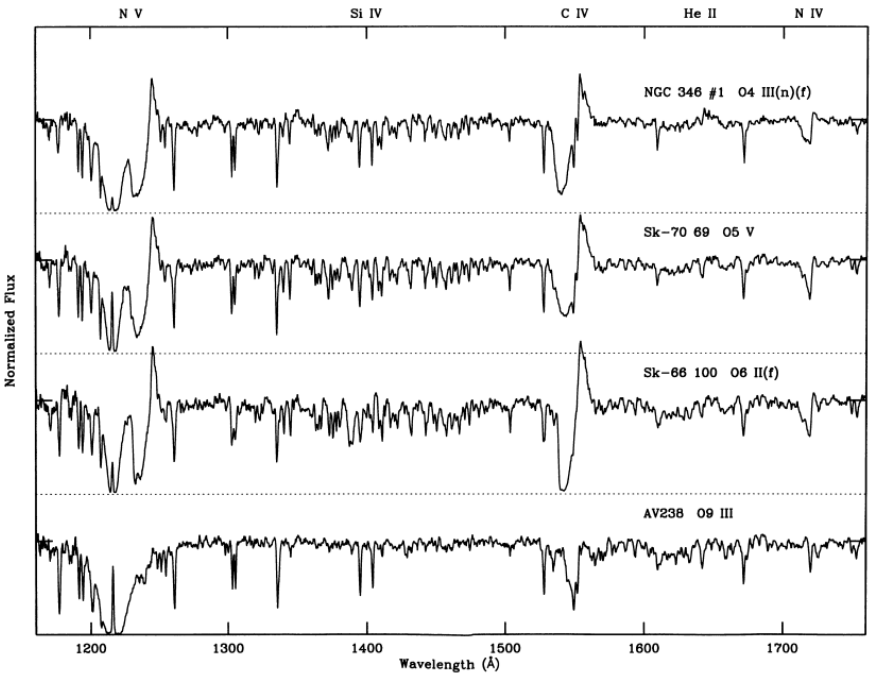

Figure 1.3.: Sample UV spectra of massive OB stars, taken from Walborn et al. (1995). The P-Cygni profiles N v$\lambda\lambda$1238–1242 and C iv$\lambda\lambda$1548–1550 are typical diagnostic lines to measure the terminal wind velocities and mass-loss rates.

velocity from the stellar surface, $v_\infty \approx 3v_{\rm esc}$. Typically, OB star winds have mass loss rates of $\dot{M} \lesssim 10^{-6}\,M_\odot{\rm yr}^{-1}$ and velocities $v_\infty \approx 2000\,$km/s. We see direct evidence of mass-loss in the UV spectral line profiles of highly ionized species such as C iv, Si iv, and N v (see Fig. 1.3). Post-main-sequence stars often eject large quantities of mass in strong ($\dot{M} \gtrsim 10^{-4}\,M_\odot{\rm yr}^{-1}$) but slow ($v_\infty \sim 100\,$km/s) winds. These include luminous blue variables (LBVs) and blue supergiants (BSGs), and red supergiants (RSGs). WR stars have fast winds with large mass-loss rates, typically a factor of ten larger than O-stars with the same luminosity. However, in the case of very massive O stars, the mass loss can be very strong even on the main sequence. Shedding a large percentage of a star's initial mass via wind clearly has a significant impact on its evolution and final fate.

One of the areas of active research is to constrain mass-loss rates in different evolutionary stages of massive stars. Mass-loss rates derived from Hα, UV wind lines or radio fluxes have been available since the 1970s. These empirical results can be compared with theoretical recipes of mass-loss rates (Vink et al. 2000, 2001). However, theoretical values are often considered to overestimate $\dot{M}$ by a factor of 2-3 (Smith 2014). One factor which makes uncertainties in $\dot{M}$ measurements is the inhomogeneity present in the wind ('clumping').

Previous studies of massive star winds found that below a certain luminosity $\log(L/L_\odot) \sim 5.2$ (late O and early B-type dwarfs), the observed wind momenta and mass-loss rates are much lower than theoretically predicted. This is commonly referred to as the "weak-wind problem" and observed in our Galaxy as well as in the Magellanic Clouds (Martins et al. 2004; Puls et al. 2008). The physical mechanism leading to weak wind phenomena remains unknown.

The winds from hot, massive stars are described by the radiative line-driven wind theory (Castor et al. 1975b). Radiation-driven mass-loss dependents on the metallicity Z because the lines of

heavier elements mostly contribute to the line driving. The winds are weaker at lower metallicity, hence remove less mass and angular momentum. Thus, metal-poor stars are expected to undergo core collapses at higher (final) masses. Since the angular momentum loss is less they are expected to be fast rotators than the stars at higher metallicities. A dependence of $\dot{M} \propto Z^{0.7}$ has been inferred theoretically, as well as from observations (Vink et al. 2001; Mokiem et al. 2007b) for OB stars. However, Hainich et al. (2017) found a significantly steeper dependence of $\dot{M} \propto Z^{1.2}$ for WR star winds. Constraining mass-loss rates and its relation with metallicity is essential to understand the formation of massive black holes detected by LIGO.

1.1.4. Stellar evolution

Similar to the formation of massive stars, their subsequent evolution and death remain unclear, especially at lower metallicity. Detection of gravitational waves from coalescing black holes further highlighted a need for better understanding of massive stars. Evolution of a star is mainly decided by its mass, mass-loss history, composition, rotation rate, and binary status.

The Hertzsprung-Russell diagram (HRD, Fig. 1.4) connects two main stellar properties, temperature, and luminosity. The narrow diagonal band on the H-R diagram marks the 'main sequence' where stars fuse H in their cores. Being luminous and initially hot, massive stars predominantly occupy the extreme upper left region of the HRD. Typical locations of OB stars and their evolved phases such as supergiants and WR stars are illustrated in the Fig. 1.4.

The evolutionary path of a massive star on the HRD is way different from that of low mass stars. An O star on the main sequence become cooler and larger after it runs out of hydrogen in its core. During the evolution, its position in the HRD will move almost horizontally towards the RSG phase. As seen in Fig. 1.4, the upper right region is comparatively sparsely populated. Only a few LBVs occasionally cross into this area, while BSGs and RSGs observationally appear to have a strict luminosity limit. By studying the Galactic massive star population, Humphreys & Davidson (1979a) has established this limit, known as HD limit. On the other hand, we see WR stars close to the ZAMS or even left part it, spreading to very hot temperatures. Only relatively massive stars can reach this stage, $M > 25\,M_{\odot}$ with $L > 10^5\,L_{\odot}$.

The most popular evolution scenario of massive stars is the so-called "Conti-scenario" (Conti 1975): massive stars follow the path O→X→WN→WC. Here, X is a phase that depends on the mass of the star, i.e. an RSG phase if the star has $M < 40\,M_{\odot}$ and an LBV stage otherwise (Maeder & Meynet 2005). For example a star with initial mass $M \sim 25\,M_{\odot}$ (see Fig. 1.4) settles on the main sequence as an O-star. The star then evolves towards the right part of the HRD and becomes BSG, YSG, followed by the RSG stage. Stars with $M < 40\,M_{\odot}$ spend a large fraction of their core He-burning phase as RSG (Ekström et al. 2013). During this RSG phase, a large part or even the entire envelope can be shed by the wind, partially exposing the helium core of the star, and transferring it to the WR phase. In the case of relatively lower mass stars, for example, a star with $M \sim 15\,M_{\odot}$, mass loss is strong during the RSG phase, but not strong enough to remove the whole H-rich envelope. In this case, the star explodes as SN-II in the RSG phase.

It is believed that stars with initial masses above $\gtrsim 40\,M_{\odot}$ pass through a short ($\sim 10^5$ yr) LBV phase. High mass-loss rates and violent eruptions are common during this phase, which eventually blows off the envelope before the RSG phase can be reached and the star instead become a WR. The most massive stars with initial masses $> 60\,M_{\odot}$ are expected to lose enough mass at the main-sequence so that they directly evolve to the WR stage. The cooler WNLs usually contain a fraction of hydrogen in their atmospheres, while the hotter, early subtypes (WNE) are hydrogen free (Hamann et al. 1991). The WN phase may be followed by a WC stage when the

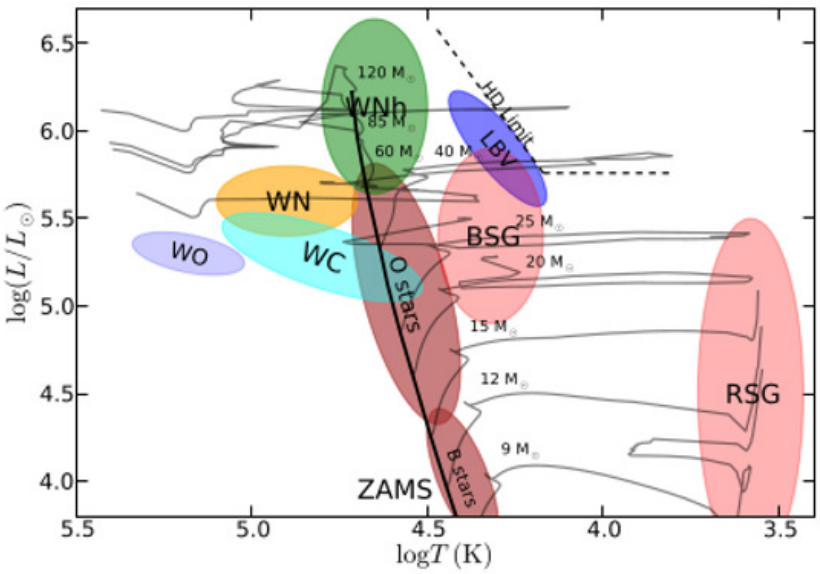

Figure 1.4.: HR diagram illustration showing position of OB stars, supergiants and WR stars (credit:F. Tramper)

products of helium burning appear in the stellar atmosphere. At its last evolutionary stage prior to core-collapse, a massive star displays a WO-type spectrum.

Mass loss has an extremely important influence on the evolution affecting evolutionary timescales, rotation, chemical profiles, surface abundances, and luminosities (Maeder & Meynet 1988). During the main-sequence lifetime, it is responsible for steadily decreasing the mass of a star, typically at a rate of about $10^{-7} - 10^{-6}\,M_{\odot}\,\mathrm{yr}^{-1}$ (for exceptions, see weak winds in Chapter 4). The mass-loss rates further increases during the later stages of the evolution: the mass-loss rate of typical Wolf-Rayet stars is $10^{-5} - 10^{-4}\,M_{\odot}\,\mathrm{yr}^{-1}$. Gigantic mass ejections can even take place during the RSG or LBV phases. The separation between the photosphere and the very thick wind is thus less and less clear as the star evolves and material that was once in the convective core of the star, where the nuclear reactions happen, becomes exposed at the stellar surface. This explains the anomalous abundances observed in the spectrum of these stars: for example, WN stars show the products of hydrogen burning through the CNO process at the surface, whereas WC stars expose layers that were originally deep inside the star and partially undergone helium burning.

Finally, it is supposed that massive stars end their life in a supernova explosion. However, it is still under debate whether they end up as supernovae or undergo a more or less silent collapse. The supernova observations indicate a possible threshold around $20\,M_{\odot}$, where RSGs with larger initial masses directly collapse to form black holes with no visible supernova (Smartt 2015; Sukhbold et al. 2016). Massive progenitors have even been proposed for the powerful gamma-ray bursts. However, all these scenarios can change as we consider lower metallicities. Metal-poor massive stars are expected to be fast rotators and to have weak winds, strongly affecting their evolutionary paths.

The scenarios discussed above are only applicable to single stars. The presence of a companion can drastically alter the evolutionary path of a massive star. This is crucial because about 70% of all massive stars are expected to interact with a companion during their lifetime (Sana et al. 2012). Out of this, a large fraction of systems are close enough to transfer mass between the components

by Roche-lobe overflow, which can change the structures of both stars and their subsequent evolution. In close binary systems, the primary can be stripped of its entire envelope, losing much of its original mass and becoming a WR star. The secondary might gain mass and angular momentum, resulting in strong mixing of the stellar interior and a corresponding modification of its evolutionary path (Brott et al. 2011). A fraction of massive stars is expected to merge after forming a common-envelope.

Rotation and mixing can also have an impact on the evolution of massive stars. Stellar evolution models predict rotationally induced chemical mixing in massive main-sequence stars following homogeneous evolution channels, predominantly at low metallicity. If a star rotates fast enough, the mixing timescale becomes shorter than the nuclear timescale so that the material produced in the stellar core immediately get mixed with the outer layers (Maeder 1987; Langer 1992). In this case, the star is (quasi) chemically homogeneous (QCHE). Chemically homogeneous stars evolve very differently from normal massive stars. When the chemical gradient between the envelope and core becomes small, the efficiently transported large fraction of helium in the outer layers reduces the opacity, causing the star to become hotter. Consequently, chemically homogeneous stars evolve directly to the blue part of the HR diagram from the main sequence. If the star is very well mixed, there is no distinction between the core and the envelope, and the whole star contracts. This leads to a star that is smaller, hotter, and more luminous than normally evolved stars (de Mink & Mandel 2016). We expect more such stars in metal-poor environments, because lower mass loss implies also lower loss of angular momentum.

1.1.5. Stellar feedback

Stellar feedback is one of the largest uncertainties in star and galaxy formation. Massive stars are of great interest because of their far-reaching feedback effects that alter the surrounding environment on local, global, and cosmic scales. Massive stars can dynamically shape their surrounding ISM on timescales of a few Myr. The stellar winds and supernova explosions are important sources of mechanical power causing ISM turbulence and the formation of shells and cavities. The dynamics of these regions, or at least of their remaining gas content, seem to be dominated by feedback from massive stars in the form of giant or multiple H II regions, wind-blown bubbles, and supernova shells.

The winds participate in the dissemination of the chemical elements built in the star as well as the transfer large amounts of mechanical momentum to the ISM. We may note in this context that the total amount of mechanical energy released through the wind during the entire lifetime of a massive star is comparable to the mechanical energy of one supernova explosion: the wind contribution can thus not be neglected. In general, wind power depends on the evolutionary status of a star. It is strongest in the supergiant and WR phases. For example, during a short timescale of $\sim 10^5$ yr, a single WO star can provide the ISM with $\sim 10^{51}$ erg of mechanical energy and about $1\,M_\odot$ of matter composed of 40% carbon, 30% oxygen, and 30% helium (by mass).

On the galactic scale, O stars dominate the radiative input to the ISM and supply nearly all of the ionizing photons. Once a star with $M > 8\,M_\odot$ reaches the end of its lifetime, it might explode as a Type II supernova (but see Chapter 4 for an updated discussion). A typical supernova releases mechanical energy of 10^{51} erg. SNe inject momentum into the ISM and drive turbulence; typical value of momentum released from a supernova explosion is $\sim 10^{43}\,\mathrm{g\,cm\,s^{-1}}$ (Geen et al. 2016; Martizzi et al. 2015). Nevertheless, radiation, winds, and SNe provide comparable amounts of energy to the ISM because of the lower efficiency of radiative heating compared to winds and SNe. Comparing input sources for the energy budget of the ISM, the radiation from O stars dominates

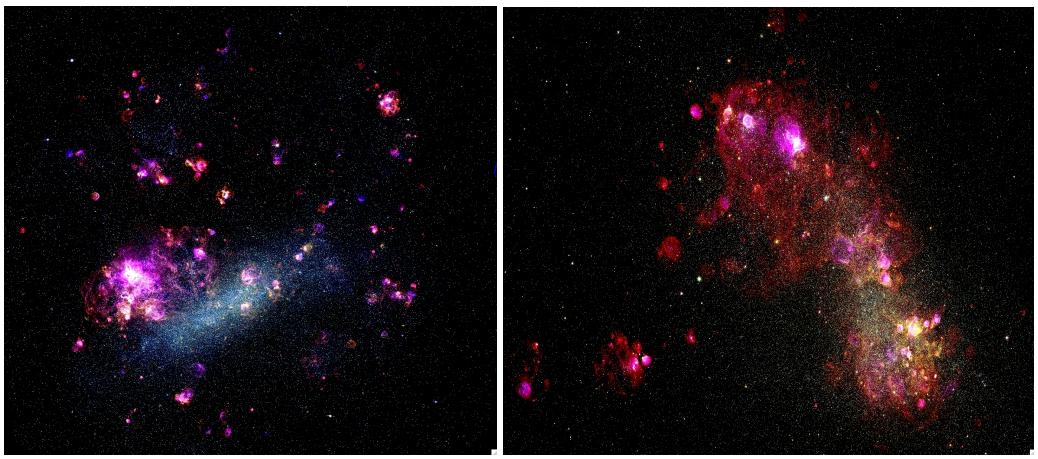

Figure 1.5.: False-color composite images of the LMC (left) and SMC (right), made from mosaics of MCELS data. Red is Hα, green is [S II], and blue is [O III].

the heating of the warm ionized medium, SNe and stellar radiation play almost equal roles in heating the neutral phase of the ISM, while the hot phase ($\gtrsim 10^6$ K) is predominately powered by WR winds and SNe. B, A, and late spectral types contribute only little to the energy budget. However, these conclusions are significantly depending on the metallicity of the ISM.

1.2. The interstellar medium in the Magellanic Clouds

Dwarf galaxies are considered as active sites of star formation in the metal-poor early universe. The Magellanic Clouds offer an outstanding opportunity to investigate star formation and feedback under conditions typical for the vast majority of dwarf galaxies. With a distance of only $\sim$50 kpc, the LMC is one of the closest and the best-studied galaxies in the Local Group. The SMC has a distance of $\sim$60 kpc from the Milky Way and $\sim$20 kpc from the LMC. Both LMC and SMC are metal-deficient, $Z \sim 1/2$ and 1/7 solar, respectively (Larsen et al. 2000; Trundle et al. 2007), and may be considered as unfavorable for star formation. However, these galaxies show prominent young stellar populations as traced by H II regions (see Fig. 1.5). The Magellanic Clouds provide an ideal site for observational studies of the ISM – being at high Galactic latitude, they offer unobscured views due to the small foreground and internal extinctions (typically $A_V < 0.5$ mag). Their proximity allows high spatial resolution.

1.2.1. Bubbles, superbubbles, and supergiant shells

The large energy output of massive stars has a huge impact on their environment. The interaction of a star via winds and ionizing radiation with its surroundings usually lead to an interstellar bubble (Castor et al. 1975a; Weaver et al. 1977). These bubbles have typical sizes of about ten parsec when blown by a single star, but can reach few kpc if several of these stars act collectively (they are then called superbubbles or supershells).

One of the first attempts to model these structures was presented by Weaver et al. (1977); a schematic representation is given in Fig. 3.1. A massive star will first form an H II region around itself. When the stellar winds are strong enough, they interact with the surrounding ionized gas. Here, the fast (typically 2000 km/s) stellar wind is hypersonic with respect to the ambient medium

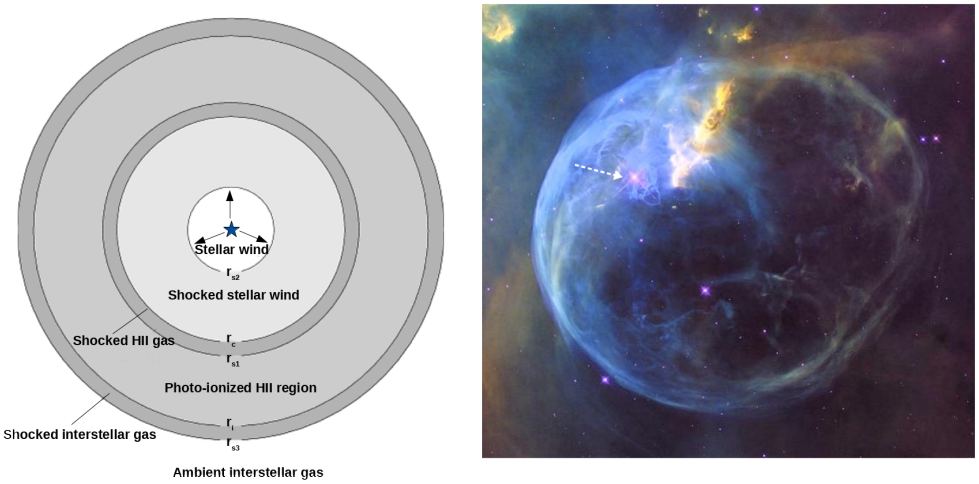

Figure 1.6.: (Left) Schematic structure of a wind blown bubble based on Weaver et al. (1977). Here r_{s1}, r_c, r_{s2}, r_i, and r_{s3} represent the radii of the reverse shock, contact discontinuity, forward shock of the bubble, ionization front, and the forward shock of the H II region expansion, respectively. (Right) HST image of a wind blown bubble – the Bubble Nebula, being blown into this shape by a bright O star SAO20575, which is de-centered and marked by an arrow (image credit: NASA/ESA/Hubble Heritage Team).

(sound speed ~ 10 km/s in photoionized gas of 10 kK) which leads to two-shock flow patterns: the forward shock (r_{s2}) sweeps up the ambient medium, accelerating, compressing and heating it, while the reverse shock (r_{s1}) decelerates the stellar wind, heating and compressing it.

The evolution of a typical wind-blown bubble proceeds through three main stages (Dyson & de Vries 1972; Weaver et al. 1977; Lamers & Cassinelli 1999). In the initial so-called 'adiabatic phase', the bubble expands so fast that the radiative cooling does not have enough time to affect its evolution. The shock velocity decreases as there is an increasing amount of swept-up matter which makes the cooling of the shell of shocked ISM becoming important. As a result, the gas is compressed into a very thin and dense shell. During this phase, the shocked wind becomes hotter but has not enough time to cool. The pressure of this hot, shocked wind is so high that it drives the expansion of the bubble, moving on to an 'energy-driven' phase. During this phase the bubbles are detectable through (nearly) the whole electromagnetic spectrum; most observed bubbles are in this phase. The expansion of the bubble can trigger the formation of new stars.

The stellar wind flows first at thousands of km/s, but it nearly stops at the reverse shock that expands with velocities of only a few tens of km/s. Thus the entire kinetic energy is converted into thermal energy, heating up the shocked wind to millions of degrees, emitting X-rays. Subsequently, the hot wind cools down and collapses into a dense shell. At this point, the wind impacts into the shell, and directly transfers momentum to it: 'momentum-conserving bubble'. Even though the thin shell of shocked ISM has cooled but it remains typically at a temperature of $\sim 10^4$ K, since it is still ionized by the stellar radiation. It is detectable by the usual nebular emission lines (eg. Hα, [O III]).

Spanning across a wide range of spatial scales, bubbles, superbubbles, and supergiant shells are shaped and powered by the energy of massive stars. While few ten-parsec size bubbles are powered by the stellar winds of an individual massive star, superbubbles with hundreds of parsec

diameter are created by the cumulative contribution from a cluster or OB association, possibly aided by multiple supernovae. The dynamic age of superbubbles is in the order of million years, thus requiring only one episode of star formation. Supergiant shells (SGSs) are even bigger; their sizes can reach a kiloparsec scale, and their dynamic age is about 100 million years, typically, suggesting that they experienced multiple generations or episodes of star formation. It is believed that these gigantic bubbles or shells are filled with hot gas. Soft X-ray emission has been detected in many objects, for e.g, SGSs such as LMC 2 (Points et al. 2000) and LMC 4 (Bomans et al. 1994), superbubbles like N 11 (Mac Low et al. 1998), M 17 (Dunne et al. 2003), and 30 Dor (Smith & Wang 2004). However, some objects are not bright in X-rays (Chu et al. 1995), but rather commonly detected in Hα (Meaburn 1980) or radio (Staveley-Smith et al. 1997). This lack of X-ray emission could mean that the hot gas already escaped or cooled down.

Superbubbles and supergiant shells have a huge impact on the evolution of galaxies; they can break out of the galactic disk, releasing their energy into the galactic halo or even into the intergalactic medium. They are a lot more complex than wind-blown bubbles in terms of their formation and evolution. It remains unclear whether stellar feedback can account for the large kinetic energy required to drive an SGS (Rhode et al. 1999). Alternative mechanisms for creating SGSs were proposed such as the distortion of the ISM by γ-ray bursts (Efremov et al. 1999) or instabilities in turbulent galactic disks (Wada et al. 2000).

1.3. Motivation for the thesis

Due to their importance, massive stars are a central topic of astrophysics. There are many past and ongoing studies of individual massive stars and populations in massive star-forming regions and clusters in our Galaxy (Cygnus OB2, Carina, arches, etc). The large scale Tarantula survey in the LMC (Evans et al. 2011; Schneider et al. 2018a) brings new perspectives on our understanding of massive stars and star formation. The SMC has been the target to study massive stars at low metallicity (Mokiem et al. 2006; Bouret et al. 2013). Massive stars in distant low metallicity galaxies like IC 1613, Sextans A, LeoP are recently subject to research. However, most of the massive star studies are focusing on specific aspects such as their physical properties, winds, or in some cases evolution. Feedback from massive stars is relevant for understanding star formation as well as ISM evolution. There were some feedback studies in the past based on massive star content (Smith 2006; Doran et al. 2013) and nebula/gas content (Lopez et al. 2014; McLeod et al. 2018). Feedback simulations starting from small to large scales are also an active area at the moment. At this point, we found that the information in these various research areas are not interconnected. Here we make an attempt to get a comprehensive picture of massive stars, their evolution, star formation, and feedback.

Not many studies have been performed on quantitative spectroscopy of a large population of OB stars, especially at low metallicity. The role of the metallicity of the environment on massive star's physical properties, winds, evolution, and feedback is still puzzling. This is a clear motivation for selecting the massive star population at two different metallicities and compare them in many aspects.

The groundbreaking discovery of gravitational waves by the LIGO from relatively massive merging black holes questions our understanding of massive star evolution. This prompts us to investigate the evolution of low metallicity massive stars and the mechanisms that affect the evolution, such as stellar winds and rotation. To understand the role of radiatively driven winds in creating such massive black hole progenitors, we need to study the winds of young massive

stars and compare with theoretical predictions. Evolved stages of massive stars in the SMC have been previously analyzed, e.g. WR stars (Hainich et al. 2015; Shenar et al. 2016), and red supergiants (Levesque et al. 2006). Here we bridge the gap by quantitative analyses of young OB stars. At low metallicity, we expect faster rotating massive stars, and hence stars that might evolve chemically homogeneously due to rotationally induced mixing. WR stars in the SMC are known to be strikingly different from those at higher metallicity environments (Martins et al. 2009; Hainich et al. 2015). All these indications demand a systematic analysis of OB stars.

Although huge structures like superbubbles and supergiant shells in the ISM are fascinating, their formation mechanisms are still debated. The impact of stellar feedback on these structures, their evolution, and their contribution to galactic halos and fountains are open and need to be explored. We find two perfect candidates to test and understand these questions.

1. The N 206 superbubble in the LMC

2. The supergiant shell SMC-SGS 1 in the Wing of the SMC

The first region, N 206, is filled with hot gas, emitting X-rays and hosting a young massive cluster (Chapters 2 and 3). The second region, SMC-SGS 1, is a kiloparsec scale ionized shell with no signs of enclosed hot gas, but active star formation at the rim, and hosting a relatively small cluster (Chapter 4). The SGS in the Wing of the SMC has a lower content of gas, dust, and stars, and resembles typical conditions for low-metallicity dwarf irregular galaxies, while the LMC N 206 region is very bright, dense and young, encompassing many massive stars. These regions are interesting test-beds to establish their star formation history, and to probe how star formation proceeds as a result of feedback.

The open questions which motivate us to invest in this thesis include:

- Evolution of stars at low metallicity, and implications on their final fate
- What are main factors of evolution – mass, mass-loss rates, rotation?
- Winds of OB stars at low metallicity
- SFR and modes of star formation in different environments
- Quantitative stellar feedback: ionizing photon flux, mechanical energy, and momentum injected by massive stars into the ISM
- Role of OB stars in the feedback process
- How superbubbles and supergiant shells are formed? How their evolution affects the ISM; induces or suppresses star-formation?
- Which are the key feedback agents? Stellar winds vs. supernovae
- Energy budget: matching with observation or excess or lacking energy?
- How does feedback depend on metallicity?

All these questions motivate us to compare the stellar populations in the two star-forming regions in the Magellanic Clouds, bringing far-reaching implications on massive stars, stellar winds, star formation, evolution, and feedback, in different environments.

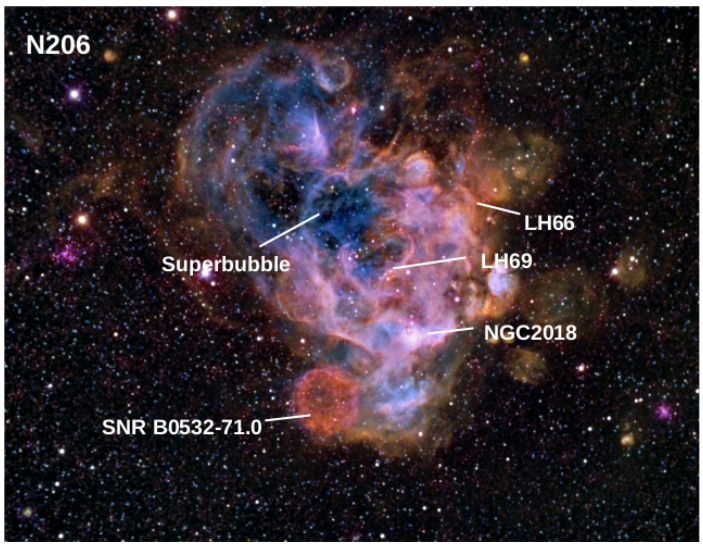

Figure 1.7.: False-color composite image of the N 206 complex in the LMC. Red is Hα, green is [S II], and blue is [O III] (image credit: Fred Vanderhaven)

1.4. A brief introduction to our target regions

1.4.1. Superbubble N 206 in the LMC

The energetic star-forming region N 206 (alias Henize 206, LHA120-N206) is located near the southern edge of the LMC. The optical image of the region is shown in Fig. 1.7. The complex encompasses a superbubble at the center, filled with hot gas. The current star formation in N 206 is taking place at the rim of the X-ray superbubble (Gruendl & Chu 2009). The well studied supernova remnant SNR B0532-71.0 is located ~75 pc away from N 206 (Williams et al. 2005). The superbubble N 206 is apparently powered by the young massive cluster NGC 2018 and the OB associations LH 66 and 69. Gorjian et al. (2004) estimate the star formation rate (SFR) in that region as $\sim 10^{-3}\ M_{\odot}\mathrm{yr}^{-1}$ i.e. very high.

It is generally believed that superbubbles are powered by massive stars. A parental OB association supplies the energy via massive-star winds and, later on, SNe, blowing a superbubble encompassed by an H I shell (Chu 2008). The hot gas filling the bubble cools at the interface. As a consequence, the expanding shell becomes gravitationally unstable and fragments. The input of energy from the parental star cluster may induce the formation of a second generation of stars. It is apparent that N 206 provides an excellent laboratory to test this scenario. The X-rays analysis of the superbubble and the parameters of its hot gas are provided in Kavanagh et al. (2012) and Dunne et al. (2001). However, to establish the energy budget of the superbubble, detailed knowledge on the massive star population is essential. Our aim is to close this gap and perform a comprehensive multiwavelength study of the interaction between the massive stars, the hot superbubble, and star formation.

1.4.2. Supergiant shell SGS 1 in the Wing of the SMC

The tidal tail ('Wing') of the SMC, is an ideal nearby laboratory to study stellar evolution and feedback in a low-density low-metallicity environment. The only Hα supergiant shell in the SMC

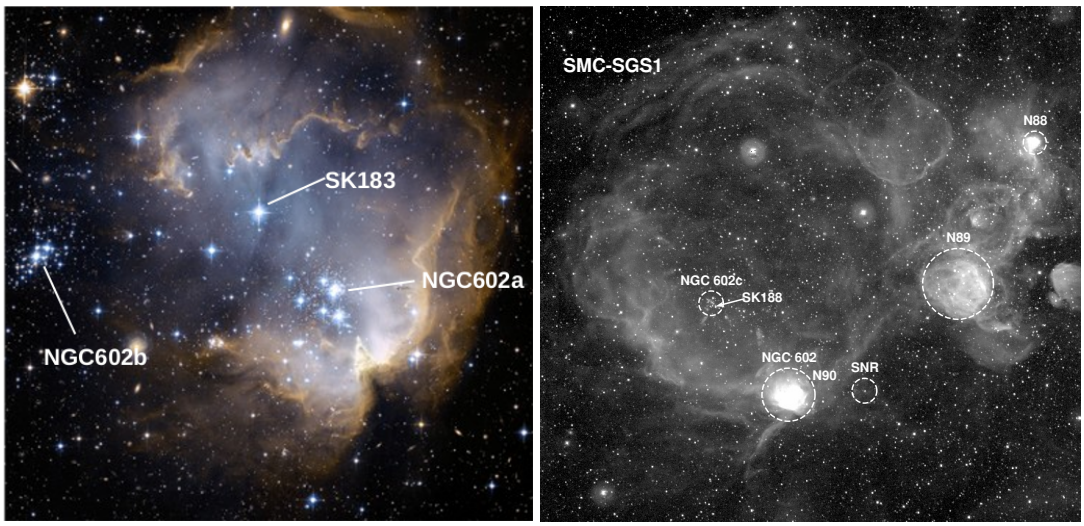

Figure 1.8.: (Left) HST color composite image of NGC 602 (Credit: HST/NASA/ESA). The O3 stars Sk 183 is just above center, NGC 602a just below and left of center, and NGC 602b towards the left edge. (Right) MCELS Hα image of the SMC-SGS 1 marking prominent clusters and nebular regions.

(Meaburn 1980) is located in the Wing (Fig. 1.8, right). The Wing has a lower content of gas, dust, and stars than the main body of the SMC. The environment of the Wing is considered as unfavorable to star formation. Yet the young stellar cluster NGC 602 (Fig. 1.8 left) associated with the SGS, presents spectacular evidence for the contrary, with a SFR comparable to Galactic star-forming regions (Cignoni et al. 2009).

The X-ray surveys of *Chandra*, *XMM-Newton* and ROSAT revealed two high mass X-ray binaries (HMXBs) in the eastern region of the Wing, namely SXP 1062 (Hénault-Brunet et al. 2012) and RX J0123.4-7321 (Sturm et al. 2013). SXP 1062 is associated with the supernova remnant MCSNR J0127-7332. A candidate HMXB [YIT2003] 104 in the shell is also reported by Liu et al. (2005). These HMXBs are closely related to the recent star-formation in the complex (Shtykovskiy & Gilfanov 2005).

The nebular complexes of the region were first identified by Davies et al. (1976) and classified into eight different emission regions DEM 160-167. Three H II regions, N 88, N 89, and N 90, are located at the rim of the shell (see Fig. 1.8, right). The H II region N 88 comprise the high-excitation blob N 88A (Heydari-Malayeri et al. 1999). Its high extinction (average $A_V \sim 1.5$ mag) indicates early stages of massive star formation.

The main cluster NGC 602a and the adjacent cluster NGC 602b is immersed in the emission nebula N 90, while NGC 602c is located at about $\sim 11'$ to the northeast (Westerlund 1964). According to Nigra et al. (2008), the NGC 602 cluster might have formed by the compression and turbulence associated with the interaction of two expanding H I shells, started ~ 7 Myr ago. Optical and infra-red studies of NGC 602a indicate that it is a relatively low-mass cluster, with a stellar mass of about 2000 $M_\odot$ (Cignoni et al. 2009; Carlson et al. 2011). NGC 602 contains many OB stars, including a rare pre-SN star of WO type (Sk 188) in NGC 602c and an early type O3 star (Sk 183) in NGC 602a (Evans et al. 2012). Carlson et al. (2007) found that stars in NGC 602a belong to three distinct age groups: extremely metal-poor field stars as old as 6 Gyr; hot massive stars, pre-main sequence and low-mass stars of age ~ 4 Myr; 10 Kyr young stellar

objects embedded in the dusty pillars.

In a standard scenario, the evolution of a large OB association formed a few Myrs ago might have resulted in the creation of SGS-SMC 1. The expansion of the SGS might have triggered a violent starburst that produced the young OB stars of NGC 602, and induced star formation at the rim. Our census of massive stars in SGS-SMC 1 can test this scenario (Chapter 4). SGS-SMC 1 provides a unique chance to learn about the fundamental processes which shape the ISM at such huge scale. The information on the massive-star population of SGS-SMC 1 is essential to address the fundamental question on the process and sources that drive the evolution of such ISM structures at low metallicity.

1.5. Overview of the manuscripts

We present three manuscripts in the upcoming chapters, which describe the results of stellar population studies (Chapters 2, 3, 4). These three scientific papers are already published (or in press) in a refereed journal. A final comprehensive discussion is presented in Chapter 5, and a summary in Chapter 6. The three scientific papers are already published (or in press) in a refereed journal. I performed the spectral analyses of all stars discussed in these papers (altogether more than five hundred objects), and for that I have calculated several stellar atmosphere models. As the first author, the results presented in these works were obtained by myself, and the manuscripts were fully written by myself.

Manuscript I

Status: published in Astronomy & Astrophysics, Volume 609, A7, 26 pp. (2018)
DOI: 10.1051/0004-6361/201731093

Title: Stellar population of the superbubble N 206 in the LMC I. Analysis of the Of-type stars

Authors: Ramachandran, Varsha; Hainich, R.; Hamann, W. -R.; Oskinova, L. M.; Shenar, T.; Sander, A. A. C.; Todt, H.; Gallagher, J. S.

Objective: We aim to estimate stellar and wind parameters of all OB stars in N 206 by means of quantitative spectroscopic analyses. In this first paper, we focus on the nine Of-type stars located in this region. We determine their ionizing flux and wind mechanical energy. The analysis of nitrogen abundances in our sample probes rotational mixing.

Manuscript II

Status: published in Astronomy & Astrophysics, Volume 615, A40, 72 pp. (2018)
DOI: 10.1051/0004-6361/201832816

Title: Stellar population of the superbubble N 206 in the LMC II. Parameters of the OB and WR stars, and the total massive star feedback

Authors: Ramachandran, V.; Hamann, W. -R.; Hainich, R.; Oskinova, L. M.; Shenar, T.; Sander, A. A. C.; Todt, H.; Gallagher, J. S.

Objective: We aim to perform quantitative spectral analyses of all massive stars associated with the N 206 superbubble, in order to provide their stellar and wind parameters. We compare the superbubble energy budget to the stellar energy input and discuss the star formation history of the region.

Manuscript III

Status: published in Astronomy & Astrophysics, Volume 625, A104, 20 pp. (2019)
DOI: 10.1051/0004-6361/201935365

Title: Testing massive star evolution, star formation history, and feedback at low metallicity: Spectroscopic analysis of OB stars in the SMC Wing

Authors: Ramachandran, Varsha; Hamann, W. -R.; Oskinova, L. M.; Gallagher, J. S.; Hainich, R.; Shenar, T.; Sander, A. A. C.; Todt, H.; Fulmer, L.

Objective: At low metallicities, the properties of massive stars and their evolution are not yet fully explored. Our goal is to perform spectral analyses of OB stars associated with SMC-SGS 1 in the Wing of the SMC. Using the derived stellar and wind parameters, we discuss massive star evolution, star-formation history, and feedback in this low-density, low-metallicity region.

Chapter 2.

Stellar population of the superbubble N 206 in the LMC I. Analysis of the Of-type stars (Manuscript I)

Varsha Ramachandran, R. Hainich, W.-R. Hamann, L. M. Oskinova, T. Shenar, A. A. C. Sander, H. Todt, and J. S. Gallagher

*A*stronomy & Astrophysics, 2018, Volume 609

Abstract

Massive stars severely influence their environment by their strong ionizing radiation and by the momentum and kinetic energy input provided by their stellar winds and supernovae. Quantitative analyses of massive stars are required to understand how their feedback creates and shapes large scale structures of the interstellar medium. The giant H II region N 206 in the Large Magellanic Cloud contains an OB association that powers a superbubble filled with hot X-ray emitting gas, serving as an ideal laboratory in this context.

We aim to estimate stellar and wind parameters of all OB stars in N 206 by means of quantitative spectroscopic analyses. In this first paper, we focus on the nine Of-type stars located in this region. We determine their ionizing flux and wind mechanical energy. The analysis of nitrogen abundances in our sample probes rotational mixing.

We obtained optical spectra with the multi-object spectrograph FLAMES at the ESO-VLT. When possible, the optical spectroscopy was complemented by UV spectra from the HST, IUE, and FUSE archives. Detailed spectral classifications are presented for our sample Of-type stars. For the quantitative spectroscopic analysis we used the Potsdam Wolf-Rayet (PoWR) model atmosphere code. We determined the physical parameters and nitrogen abundances of our sample stars by fitting synthetic spectra to the observations.

The stellar and wind parameters of nine Of-type stars, which are largely derived from spectral analysis are used to construct wind momentum – luminosity relationship. We find that our sample follows a relation close to the theoretical prediction, assuming clumped winds. The most massive star in the N 206 association is an Of supergiant that has a very high mass-loss rate. Two objects in our sample reveal composite spectra, showing that the Of primaries have companions of late O subtype. All stars in our sample have an evolutionary age of less than 4 million years, with the O2-type star being the youngest. All these stars show a systematic discrepancy between evolutionary and spectroscopic masses. All stars in our sample are nitrogen enriched. Nitrogen enrichment shows a clear correlation with increasing projected rotational velocities.

The mechanical energy input from the Of stars alone is comparable to the energy stored in the N 206 superbubble as measured from the observed X-ray and Hα emission.

2.1. Introduction

Superbubbles filled by hot, $\sim$ 1 MK, gas are the large scale structures with characteristic size $\sim$ 100 pc in the interstellar medium (ISM) (Mac Low & McCray 1988). Superbubbles provide direct evidence for the energy feedback from massive star clusters or OB associations to the ISM. With a distance modulus of only $DM = 18.5$ mag (Madore & Freedman 1998; Pietrzyński et al. 2013), the Large Magellanic Cloud (LMC) provides a good platform for detailed spectroscopy of massive stars in superbubbles. Additionally, its face-on aspect and low interstellar extinction make it an excellent laboratory to study feedback. With an observed metallicity of approximately [Fe/H] = -0.31 ± 0.04 or 0.5 $Z_\odot$ (Rolleston et al. 2002), the LMC exhibits a very different history of star formation compared to the Milky Way. Several massive star-forming regions in the LMC, especially 30 Doradus and the associated stellar populations have been extensively studied by many authors (e.g., Evans et al. 2011; Ramírez-Agudelo et al. 2017). In this paper we present the study of the Of-type stars in the massive star-forming region N 206.

N 206 (alias LHA 120-N 206 or DEM L 221) is a giant H II region in the south-east of the LMC that is energized by the young cluster NGC 2018 (see Fig. 1) and two OB associations, LH 66 and LH 69. Imaging studies with *HST*, *Spitzer*, and *WISE* in the optical and infrared (IR) have already unveiled the spatial structure of the NGC 2018/N 206 region (Gorjian et al. 2004; Romita et al. 2010). This complex contains a superbubble observed as a source of diffuse X-rays, and a supernova remnant. The current star formation in N 206 is taking place at the rim of the X-ray superbubble (Gruendl & Chu 2009). The X-ray emission in N 206 region has been studied by Kavanagh et al. (2012) using observations obtained by the *XMM-Newton* X-ray telescope. However, the study of feedback was constrained by the lack of detailed knowledge on its massive star population.

To obtain a census of young massive stars in N 206 complex and study their feedback we conducted a spectroscopic survey of all blue stars with $m_V < 16$ mag with the FLAMES multi-object spectrograph at ESO's Very Large Telescope (VLT). Our total sample comprises 164 OB-type stars. The inspection and classification of the spectra revealed that nine objects belong to the Of subclass (Walborn et al. 2002) and comprise the hottest stars in our whole sample. The present paper focuses on the spectral analysis of these Of-type stars, while the subsequent paper (Paper II) will cover the detailed analyses of the entire OB star population, along with a detailed investigation of the energy feedback in this region.

The spectroscopic observations and spectral classifications are presented in Sect. 4.2. Section 4.3 describes the quantitative analyses of these stellar spectra using Potsdam Wolf-Rayet (PoWR) atmosphere models. Section 3.7 presents the results and discussions. The final Sect. 3.8 provides a summary and general conclusions. The appendices encompass comments on the individual objects (Appendix A) and the spectral fits of the analyzed Of stars (Appendix B).

2.2. Spectroscopy

We observed the complete massive star population associated with the N 206 superbubble on 2015 December 19-20 with VLT-FLAMES. In the Medusa-fiber mode, FLAMES (Pasquini et al. 2002) can simultaneously record the spectra of up to 132 targets. Each fiber has an aperture of 1.2″ radius.

The nine Of stars are a subsample of this larger survey. The observation was carried out using three of the standard settings of the Giraffe spectrograph LR02 (resolving power $R = 6000$, 3960–4567 Å), LR03 ($R = 7500$, 4501–5071 Å), and HR15N ($R = 19200$, 6442–6817 Å), respectively. We took three to six exposures (30 minutes each) for each pointing in three spectrograph setting to improve the S/N. The higher resolution at Hα is utilized to determine stellar wind parameters and to distinguish nebular emission from the stellar lines.

The ESO Common Pipeline Library[1] FLAMES reduction routines were executed for the standard processing stages such as bias subtraction, flat fielding, and wavelength calibration. We used the ESO data file organizer GASGANO[2] for organizing and inspecting the VLT data and to execute the data reduction tasks. The obtained spectra are not flux calibrated. Multi-exposures were normalized and median combined to get the final spectra without cosmic rays in each settings. The spectra were rectified by fitting the stellar continuum with a piece-wise linear function. Finally, for each star, the LR02 and LR03 spectra were merged to form the medium resolution blue spectra from 3960 to 5071 Å. The sky background was negligibly small compared to the stellar spectra. The spectral data reduction was carried out without nebular background subtraction. Therefore, stars with a bright background might show nebular emission lines such as Hα, [O III], [N II] and [S II] superimposed on the stellar spectra.

We obtained a total of 234 spectra with good signal-to-noise (S/N> 50). The whole sample encompasses the spectra of 164 OB stars. Additional fibers were placed on the H II region, X-ray bubble, and supernova remnant. We assigned a naming convention for all the objects with N206-FS (N 206 FLAMES Survey) and a number corresponding to ascending order of their right-ascension (1–234). Paper II (Ramachandran et al. in prep.) will publish the catalog in detail. We identified and analyzed nine Of-type stars among this sample. Their positions are marked on the color composite image of N 206 in Fig. 2.1.

Ultraviolet (UV) spectra are available for three Of stars in our sample, and we retrieved these from the Mikulski Archive for Space Telescopes (MAST[3]). For N206-FS 187, a HST/Space Telescope Imaging Spectrograph (STIS) spectrum (ID: O63521010) exists. This was taken with the E140M grating (aperture $0.2'' \times 0.2''$), covering the wavelength interval 1150–1700 Å, with an effective resolving power of $R = 46000$. An International Ultraviolet Explorer (IUE) short-wavelength spectrum taken in high dispersion mode is available for N206-FS 180 (ID: SWP14022). This spectrum was taken with a large aperture ($21'' \times 9''$) in the wavelength range 1150–2000 Å. A far-UV Far Ultraviolet Spectroscopic Explorer (FUSE) spectrum is available for N206-FS 214 (ID: d0980601) in the wavelength range 905–1187 Å, taken with a medium aperture ($4'' \times 20''$).

In addition to the spectra, we used various photometric data from the VizieR archive to construct the spectral energy distribution (SED). Ultraviolet and optical (U, B, V, and I) photometry were taken from Zaritsky et al. (2004). The infrared magnitudes (JHK_s and *Spitzer-IRAC*) of the sources are based on the catalog by Bonanos et al. (2009).

Spectral classification

The spectral classification of the stars is primarily based on the spectral lines in the range 3960–5071 Å. We mainly followed the classification schemes proposed in Sota et al. (2011), Sota et al. (2014), and Walborn et al. (2014).

[1] http://www.eso.org/observing/cpl

[2] VLT-PRO-ESO-19000-1930/1.0/27-Sep-99 VLT Data Flow System, Gasgano DFS File Organizer Design Document

[3] http://archive.stsci.edu/

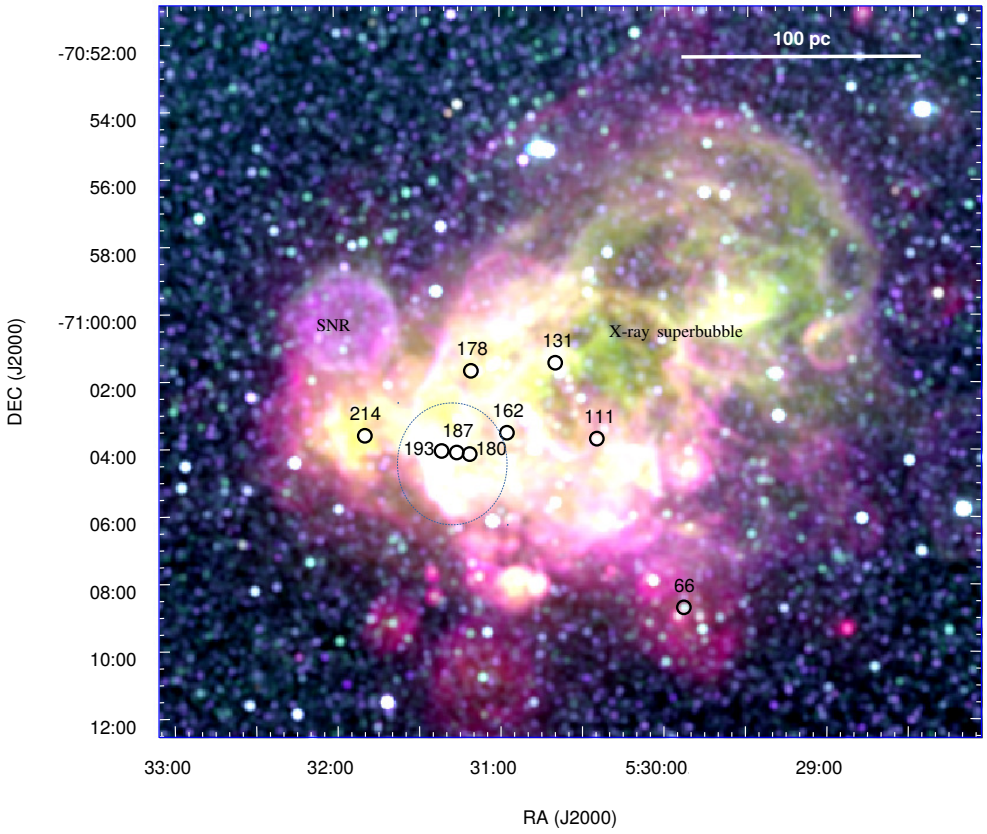

Figure 2.1.: Location of the Of-type stars in the N 206 H II region. Three color composite image (Hα (red) + [O III] (green) + [S II] (blue)) shown in the background is from the Magellanic Cloud Emission-Line Survey (MCELS; Smith et al. 2005). The Of stars studied here are marked with the N206-FS number corresponding to Table 2.1. The dotted circle (blue) shows the rough locuuus of young cluster NGC 2018. The superbubble is located north-west and the SNR is at north-east of NGC 2018.

The main criterion for spectral classification is the He I/He II ionization equilibrium. The diagnostic lines used for this purpose are He I lines at 4471 Å, 4713 Å, and 4387 Å compared to the He II lines at 4200 Å and 4541 Å. However, this criterion leaves uncertainties in the subtype of the earliest O stars because of their weak or negligible He I lines.

Moreover, the strength and morphology of the optical nitrogen lines N III $\lambda\lambda$4634–4640–4642 (hereafter N III), N IV λ4058 (hereafter N IV) and N V $\lambda\lambda$4604–4620 (hereafter N V) are the fundamental classification criteria of the different Of spectral subtypes (Walborn 1971). As suggested by Walborn et al. (2002), we used the N IV λ4058/N III λ4640 (here after N IV/N III) and N IV λ4058/N V λ4620 (hereafter N IV/N V) emission line ratio as the primary criterion for the Of subtypes, instead of He I/He II. The luminosity-class criteria of early O stars are mainly based on the strength of He II 4686 and N III lines.

The spectral type and coordinates of the nine Of-type stars are given in Table 2.1, together with their most prominent aliases. The corresponding normalized spectra are shown in Fig. 2.3. In the following, we comment on the individual Of stars.

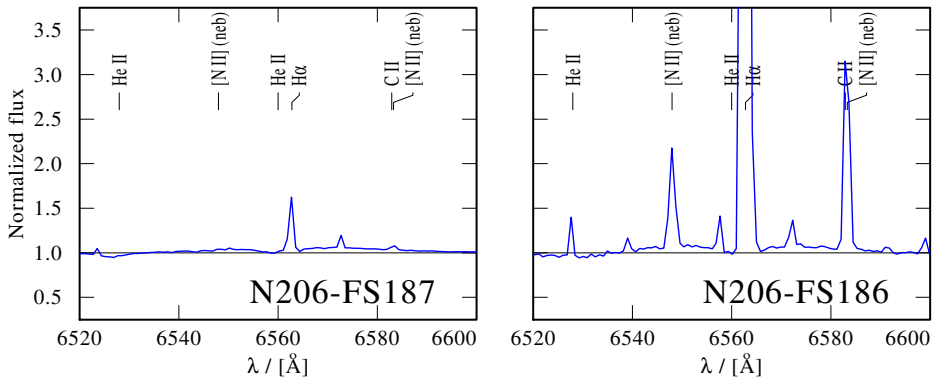

Figure 2.2.: Comparison of Hα lines of N206-FS 187 (O4 If) and neighboring star N206-FS 186 (O8.5 (V)e).

Our sample contains one star of very early spectral subtype O2 (N206-FS 180), which was classified as an O5 V by Kavanagh et al. (2012). It is located in the bright cluster NGC 2018. The characteristic features of the O2 class in the blue spectra are strong N v absorption lines and the N IV emission significantly stronger than the N III emission. This subtype was introduced by Walborn et al. (2002), also discussed in Rivero González et al. (2012a) and Walborn et al. (2014). The presence of strong He II 4686 absorption shows that N206-FS 180 is a young main sequence star. According to the definition by Walborn et al. (2002), the primary characteristic of the spectral type O2 V((f*)) in comparison to O3 V((f*)) is weak or absent N III emission. The spectrum of N206-FS 180 clearly complies with this. The presence of He I absorption lines in this very early O2 spectrum indicates a secondary component (see Sect. 2.3.2).

Two Of-type supergiants are present in the sample, N206-FS 187 and 214. N206-FS 187 was identified as binary/ multiple system (Of + emission line star) in Hutchings (1980). Hutchings (1982) denoted this object as an emission line star. Kavanagh et al. (2012) classified this star as an O4-5 giant. We reclassified this spectrum as O4 If (see Table 3 and Section 3.1.3 of Sota et al. (2011) for more details of this classification scheme). This star is situated in the crowded region of the young cluster NGC 2018. We took the spectrum of N206-FS 186 (O8.5 (V)e), that is $\approx$ 2.5″ away from N206-FS 187. This emission line (late Oe type) star could have been wrongly identified as a companion in previous papers (see their Hα lines in Fig. 2.2). Given the spacial proximity of the two stars, they were erroneously considered as a single source in several past studies.

In both supergiants N206-FS 187 and 214, the N IV emission is much weaker than the N III emission, and the N v absorption is negligible, which indicates an O4 spectral type. Also, the He I absorption lines are almost absent or negligible in the spectra. The significant He II 4686 emission confirms its supergiant nature. In addition to this, narrow Si IV λ4089–4116 emission features are also present in both spectra.

Compared to this, N206-FS 131 has no or very weak He II 4686 absorption and is therefore classified as bright giant (luminosity class II). The spectrum of this star shows a strong N III emission line, but with no N v and Si IV emission lines, implying this star is cooler than previous stars (O6.5). This star is also suspected as a binary from the strength of the He I lines. Another giant with strong N III emission is N206-FS 178 but with comparatively strong He II 4686 absorption (luminosity class III).

We discovered two stars that exhibit special characteristics typical for the Vz class, namely, N206-FS 193 and N206-FS 111. According to Walborn (2006), these objects may be near or on the

Table 2.1.: Spectral type and coordinates of the nine Of-type stars in the N 206 superbubble

N206-FS[(2)] #	RA (J2000) (h:m:s)	DEC (J2000) (°: ′: ″)	Alias names[(1)]	Spectral type
66	5:29:52.750	−71:08:44.70	2MASS J05295273-7108446, [MLD95] LMC 1-263	O8 IV((f))
111	5:30:24.680	−71:03:44.50	2MASS J05302469-7103445, [MLD95] LMC 1-584	O7 V((f))z
131	5:30:39.870	−71:01:29.30	HDE 269656, Sk −71 39	O6.5 II(f) + O8-9
162	5:30:57.560	−71:03:33.70	BI 189, [L63] 275, [MLD95] LMC 1-598	O8 IV((f))e
178	5:31:10.670	−71:01:43.30	2MASS J05311070-7101433, [MLD95] LMC 1-716	O7.5 III((f))
180	5:31:11.780	−71:04:10.10	2MASS J05311185-7104101, [MLD95] LMC 1-550	O2 V((f*)) + O8-9
187	5:31:15.650	−71:04:10.00	HDE 269676, Sk −71 45	O4 If
193	5:31:21.470	−71:04:05.80	2MASS J05312153-7104057, [MLD95] LMC 1-556	O7 V((f))z
214	5:31:49.510	−71:03:38.0	Sk −71 46, 2MASS J05314960-7103381	O4 If

Notes. [(1)] Taken from http://simbad.u-strasbg.fr/simbad/ [(2)] The number refers to the whole catalog of objects in the N 206 superbubble (Ramachandran et al. in prep.) based out of FLAMES survey (N206-FS). This contains 234 fiber positions in ascending order of their RA (N206-FS 1–234).

zero-age main sequence (ZAMS). As described in Walborn et al. (2014), the main characteristic of the Vz class is the prominent He II 4686 absorption feature that is stronger than any other He line in the blue-violet region. Strong absorption in He II 4686 corresponds to lower luminosity and a very young age (i.e., the inverse Of effect). These spectral features can be easily contaminated with strong nebular contribution, however.

Another interesting spectrum in the sample belongs to an Oef star, N206-FS 162. The Hα line is in broad emission while other Balmer lines are partially filled with disk emission, which is a feature of a classical Oe/Be star. A very small N III emission indicates the 'Of nature'. The star N206-FS 66 is classified as a subgiant. It shows weak N III emission lines and a significant He II 4686 absorption line.

2.3. The analysis

Our immediate objective is to determine the physical parameters of the individual stars. In order to analyze the FLAMES spectra, we calculated synthetic spectra using the Potsdam Wolf-Rayet (PoWR) model atmosphere code, and then fitted those to the observed spectra.

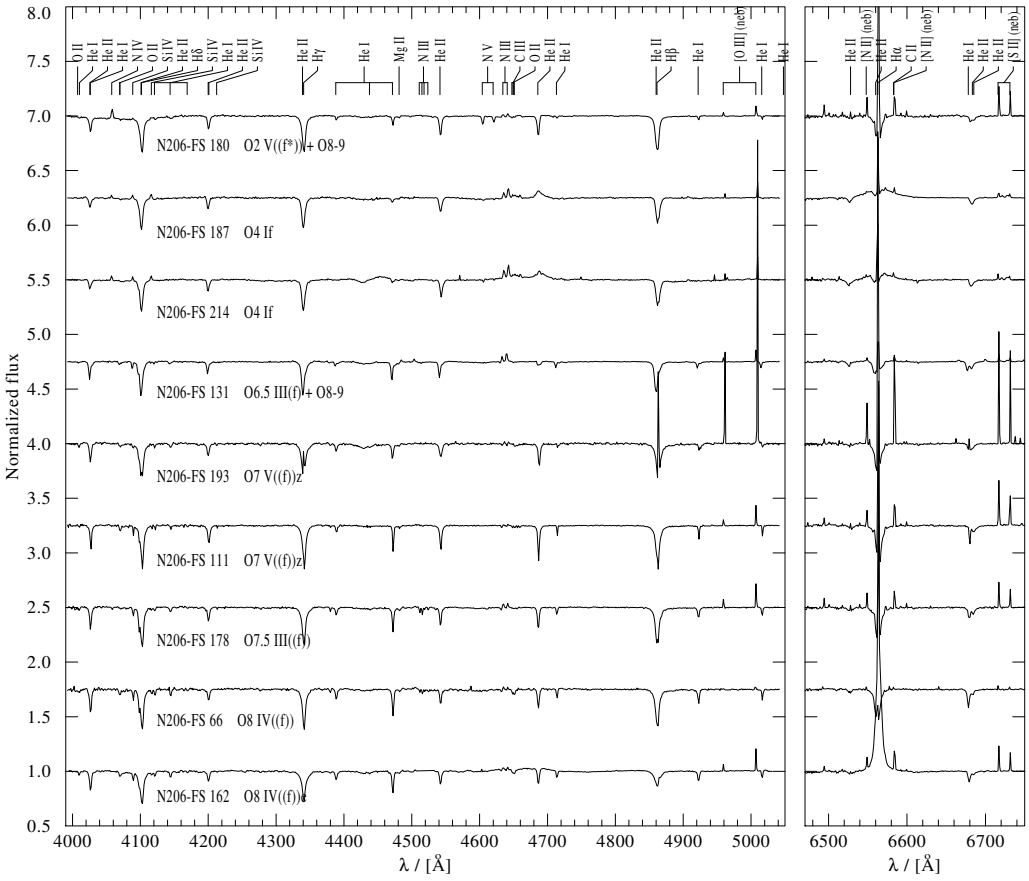

Figure 2.3.: Normalized spectra of the nine Of-type stars. The left panel depicts the medium resolution spectra in the blue (setting: LR02 and LR03). The high resolution spectra in the red (setting: HR15N) are shown in the right panel which includes Hα line. The central emission in Hα and the [O III], [N II], and [S II] lines are from nebular emission (neb).

2.3.1. The models

The PoWR code solves the radiative transfer equation for a spherically expanding atmosphere and the statistical equilibrium equations simultaneously, while accounting for energy conservation and allowing for deviations from local thermodynamic equilibrium (i.e., non-LTE). Stellar parameters were determined iteratively. Since the hydrostatic and wind regimes of the atmosphere are solved consistently in the PoWR model (Sander et al. 2015), this code can be used for the spectroscopic analysis of any type of hot stars with winds, across a broad range of metallicities (Hainich et al. 2014, 2015; Oskinova et al. 2011; Shenar et al. 2015). More details of the PoWR code are described in Gräfener et al. (2002) and Hamann & Gräfener (2004).

A PoWR model is specified by its luminosity L, the stellar temperature T_*, the surface gravity g_*, and the mass-loss rate $\dot{M}$ as main parameters. PoWR defines the "stellar temperature" T_* as the effective temperature referring to the stellar radius R_* where, again by definition, the Rosseland optical depth reaches 20. In the standard definition, the "effective temperature" $T_{\rm eff}$ refers to the radius $R_{2/3}$ where the Rosseland optical depth is 2/3,

$$L = 4\pi\sigma_{\rm SB}\, R_*^2\, T_*^4 \;\; = \; 4\pi\sigma_{\rm SB}\, R_{2/3}^2 \;\; T_{\rm eff}^4 \tag{2.1}$$

In the case of our program stars, the winds are optically thin and the differences between T_* and $T_{\rm eff}$ are negligible. Since model spectra are most sensitive to T_*, $\log g_*$, $\dot{M}$, and L these parameters are varied to find the best-fit model systematically.

In the non-LTE iteration, the line opacity and emissivity profiles are Gaussian with a constant Doppler width $v_{\rm Dop}$. This parameter is set to 30 km s^{-1} for our 'Of' sample. For the energy spectra, the Doppler velocity is split into the depth-dependent thermal velocity and a "microturbulence velocity" $\xi(r)$. We adopt $\xi(r) = max(\xi_{min}, 0.1v(r))$ for O-star models, where $\xi_{min} = 20\,{\rm km\,s^{-1}}$ (Shenar et al. 2016).

Optically thin inhomogeneities in the model iterations are prescribed by the "clumping factor" D by which the density in the clumps is enhanced compared to a homogeneous wind of the same $\dot{M}$ (Hamann & Koesterke 1998). In the current study, we account for depth-dependent clumping assuming that the clumping starts at the sonic point, increases outward, and reaches a density contrast of $D = 10$ at a radius of $R_{\rm D} = 10\,R_*$. Note that the empirical mass-loss rates when derived from Hα emission scale with $D^{-1/2}$, since this line is mainly fed via recombination. We also varied the values of D and $R_{\rm D}$, when necessary. Higher D values and lower $R_{\rm D}$ values lead to a decrease in the mass-loss rates derived from Hα.

The detailed form of the velocity field in the wind domain can affect spectral features originating in the wind. In the subsonic region, the velocity field is defined such that a hydrostatic density stratification is approached (Sander et al. 2015). In the supersonic region, the pre-specified wind velocity field $v(r)$ is assumed to follow the so-called β -law (Castor et al. 1975b)

$$v(r) = v_\infty \left(1 - \frac{r_0}{r}\right)^\beta . \tag{2.2}$$

In this work, we adopt β=0.8, which is a typical value for O-type stars (Kudritzki et al. 1989).

The models are calculated using complex model atoms for H, He, C, N, O, Si, Mg, S, and P. The iron group elements (e.g., Fe, Ni) are treated with the so-called "superlevel approach" as described in Gräfener et al. (2002).

2.3.2. Spectral fitting

The spectral analysis is based on systematic fitting of observed spectra with grids of stellar atmosphere models. We constructed OB-star grids for LMC metallicity with the stellar temperature T_* and the surface gravity $\log g_*$ as parameters varied in the grid. Additional parameters such as stellar mass M and luminosity L in the grid models are chosen according to the evolutionary tracks calculated by Brott et al. (2011). The other parameters, namely the chemical composition and terminal wind velocity, are kept constant within one model grid. We also calculated some models with adjusted C, N, O, and Si abundance, when necessary. The LMC OB star grid[4] spans from $T_* = 13$ kK to 54 kK with a spacing of 1 kK, and $\log g_* = 2.2$ to 4.4 with a spacing of 0.2 dex.

We proceeded as follows to derive the stellar and wind parameters. The main method to identify the stellar temperature is to fit the He I/He II line ratio. For the present Of-type sample we also made use of N III/ N IV/ N V line ratios. The uncertainty in temperature determination according to the grid resolution is ±1 kK. Since for hotter stars, the temperature determination mainly depends on the nitrogen ionization equilibrium, and the He I lines are very weak, the uncertainty becomes larger (±2-3 kK). The surface gravity $\log g_*$ was mainly determined from the wings of the Balmer

[4] www.astro.physik.uni-potsdam.de/PoWR.html

lines, which are broadened by the Stark effect. Since the Hα line is often affected by wind emission, we mainly used Hγ and Hδ for this purpose. The typical uncertainty for $\log g_*$ is ±0.2 dex. The uncertainty in $\log g_*$ also propagates to the temperature and gives a total uncertainty of $\sim$ ±2 kK.

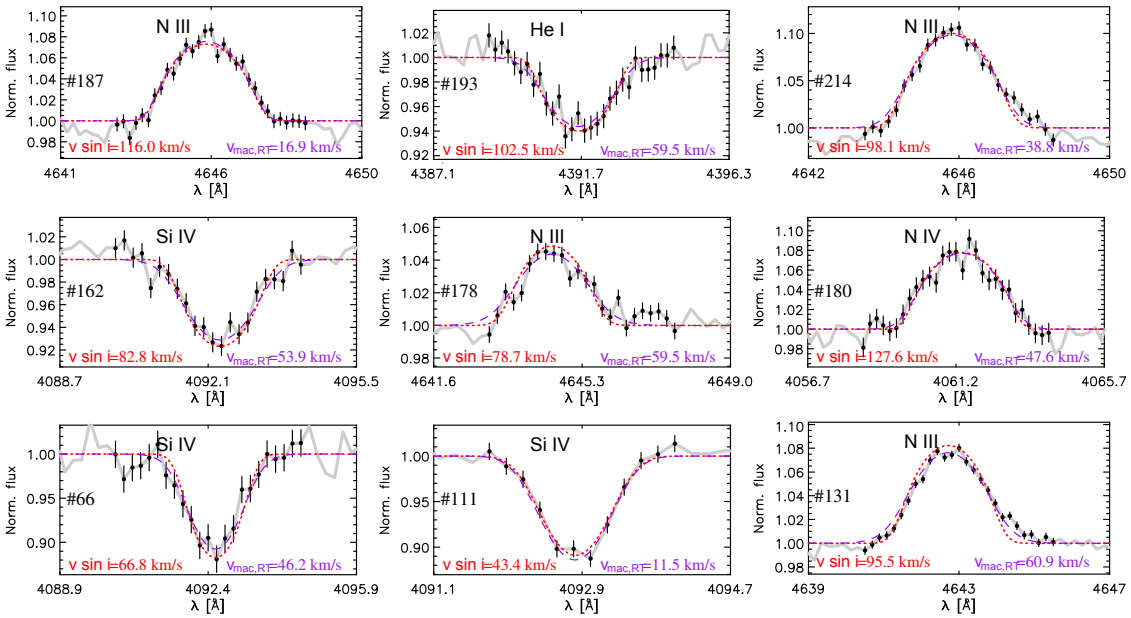

Figure 2.4.: Rotation velocity ($v \sin i$) from the line profile fitting of Of-type stars using the `iacob-broad` tool. The gray curves show the observed line profile. The $v \sin i$ is calculated from line profile fitting based on Fourier transform method (red dotted line) and goodness-of-fit analysis (violet dashed line). See text for more details.

We calculated two model grids; one with a mass-loss rate of 10^{-7} $M_\odot\,\mathrm{yr}^{-1}$ and another with 10^{-8} $M_\odot\,\mathrm{yr}^{-1}$. The mass-loss rate is scaled proportional to $L^{3/4}$ to preserve the emission of recombination lines such as Hα and He II 4686. In order to best fit the UV P-Cygni profiles and Hα line, we also calculated models with different mass-loss rates for individual stars when necessary. The primary diagnostic lines used for the mass-loss rate determination in the UV are the resonance doublets N V $\lambda\lambda$1238–1242 and C IV $\lambda\lambda$1548–1551 (HST/ IUE range). To reproduce the N V $\lambda\lambda$1238–1242 lines, we accounted for shock generated X-ray emission in the model. For objects that were observed by FUSE, we made use of P V $\lambda\lambda$1118–1128, C IV at 1169 Å, and C III at 1176 Å. For stars with available UV spectra (N206-FS 180, 187 and 214), the error in $\log \dot{M}$ is approximately 0.1 dex. For the remaining stars, we derived the mass-loss rates solely on the basis of Hα and He II 4686. If Hα is in strong absorption (no wind contamination), the mass-loss rates are based on nitrogen emission (N III and N IV) lines with a large uncertainty. The UV P-Cygni profiles P V $\lambda\lambda$1118–1128, N IV λ1718, and O V λ1371 provide diagnostics for stellar wind clumping in early-type O stars (Bouret et al. 2003; Martins 2011; Šurlan et al. 2013). We constrained the values of clumping parameters D and R_D (also clumping onset) by consistently fitting these lines in comparison to optical lines.

The terminal velocity v_∞ defines the absorption trough of P-Cygni profiles in the UV. In contrast to the optical, UV P Cygni lines are rather insensitive to temperature and abundance variations if saturated (Crowther et al. 2002). For stars with UV spectra, we inferred the terminal velocities from these P-Cygni profiles and recalculated the models accordingly. The main diagnostic lines

used are P-Cygni N v $\lambda\lambda$1238–1242 and C iv $\lambda\lambda$1548–1551, P v $\lambda\lambda$1118–1128, and S v $\lambda\lambda$1122–1134 profiles. The terminal velocity has been measured from the blue edge of the absorption component. The typical uncertainty for v_∞ is $\pm$ 100 km s^{-1}. We calculated the terminal velocities theoretically from the escape velocity $v_{\rm esc}$ for those stars for which we only have optical spectra. For Galactic stars, the ratio of the terminal and escape velocity has been obtained from both theory and observations. For stars with $T_* \geq 21$ kK, the ratio is $v_\infty/v_{\rm esc} \simeq 2.6$, and for stars with $T_* < 21$ kK the ratio is $\approx$1.3 (Lamers et al. 1995; Vink et al. 2001). The terminal velocity also depends on metallicity, $v_\infty \propto (Z/Z_\odot)^q$, where $q = 0.13$ (Leitherer et al. 1992). We used this scaling to account for the LMC metallicity.

We calculated our models with typical LMC abundances (Trundle et al. 2007). The mass fractions of C, N, and O are varied for individual objects when necessary to best fit their observed spectra. The abundances of these elements were determined from the overall strengths of their lines with uncertainties of ~20–50 %. The carbon and oxygen abundance were primarily based on C iii and O ii absorption lines. For the determination of nitrogen abundance, we particularly used the N iii absorption lines at λ4510–4525 and N v absorption lines.

Table 2.2.: Main diagnostics used in our spectral fitting process.

Parameter	UV lines	Optical lines
T_*		He i/He ii, N iii/ N iv/ N v line ratios.
$\log g_*$		Hγ and Hδ line wings
$\dot{M}$	N v 1238–1242, C iv 1548–1551 N iv 1718, O iv 1338–1343, He ii 1640 P v 1118–1128, C iv 1169, C iii 1176	Hα, He ii 4686 emission
v_∞	N v 1238–1242, C iv 1548–1551 Si iv 1393–1403, N iv 1718 P v 1118–1128, C iv 1169, C iii 1176 blue edge	Hα line width
D	P v 1118–1128, N iv 1718, O v 1371	Hα
$v \sin i$		N iii 4640–4642, N iv 4058 Si iv 4089–4116, He i 4388
Abundances		C iii 4647–4650–4651, Si iv 4089–4116 O ii 4649, O ii 4070, N iii 4510–4525, N v 4620

Finally, the projected rotation velocity $v \sin i$ is constrained from the line profile shapes. We used the `iacob-broad` tool implemented in IDL, which was developed by Simón-Díaz & Herrero (2014). This tool provides $v \sin i$ values based on a combined Fourier transform (FT) and goodness-of-fit (GOF) analysis. We used two of the methods described in Simón-Díaz & Herrero (2014). In the first method, the $v \sin i$ comes from the first zero of the FT method. In this case the assumption is that macroturbulence is negligible, i.e., the additional broadening is by rotation.

The second fitting method is a combination of FT and GOF analysis, where the line profile is additionally convolved with a macroturbulent profile. The macroturbulent velocity ($v_{\rm mac}$) is calculated from the GOF when $v \sin i$ is fixed to the value corresponding to the first zero of the FT.

We selected He I, Si IV absorption lines and N III and N IV emission lines for determining $v \sin i$ using these methods. In some cases, absorption lines which are not pressure broadened (e.g., He I and metal lines) are very weak or completely absent in the spectra. In this case, we used the `iacob-broad` tool on emission lines that form close to the photosphere, such as N IV 4058 and N III 4510–4525. To ensure that the inferred values of $v \sin i$ from these emission lines are reliable, we calculated the synthetic spectrum via a 3D integration algorithm that accounts for rotation and that is appropriate for nonphotospheric lines (Shenar et al. 2014). These calculations resulted in spectra which are similar to the convolved ones. Hence, the `iacob-broad` tool is valid for these emission lines. For binaries, we selected those lines which have only contribution from either a primary or secondary. The fitted line profiles for individual stars are given in Fig 2.4. The formal uncertainty in $v \sin i$ is ~ 3–$8\,{\rm km\,s^{-1}}$. Corresponding to these velocities, the model spectra are convolved with rotational and macroturbulent profiles. This yields consistent fits with the observations.

The main diagnostic lines for stellar and wind parameters used in our spectral fitting process are summarized in Table 2.2.

The luminosity and the color excess E_{B-V} of individual objects were determined by fitting the model SED to the photometry. The model flux is scaled with the LMC distance modulus of 18.5 mag, which corresponds to a distance of 50 kpc (Pietrzyński et al. 2013). The uncertainty in the luminosity determination is an error propagation from color excess (relatively small for LMC stars), temperature, and observed photometry. All these uncertainties give a final accuracy of about 0.2 in $\log L/L_\odot$. For stars with available flux-calibrated UV spectra (HST, IUE, or FUSE), the model SED is iteratively fitted to this calibrated spectra and normalized consistently by dividing the reddened model continuum. The uncertainty in luminosity is smaller in these cases ($\approx$0.1 dex).

Subsequently, individual models with refined stellar parameters and abundances are calculated for each Of-type star in our sample. All these fitting processes were performed iteratively until no further improvement of the fit was possible.

Single star model

As an example, the fit for N206-FS 187 is given in Fig. 2.5. The upper panel of the figure shows the theoretical SED fitted to multiband photometry and calibrated UV spectra. We appropriately varied the reddening and luminosity for fitting the observed data with the model SED. Reddening includes the contribution from the Galactic foreground ($E_{B-V} = 0.04$ mag) adopting the reddening law from Seaton (1979), and from the LMC using the reddening law described in Howarth (1983) with $R_V = 3.2$. The total E_{B-V} is a fitting parameter. Since flux calibrated HST/STIS and IUE spectra are available for this star, reddening and luminosity are well constrained.

The second panel shows the normalized high resolution HST/STIS UV spectrum fitted to the model. This spectrum was consistently normalized with the reddened model continuum. The last three panels show the normalized VLT-FLAMES spectrum (normalized by eye) in comparison to the PoWR spectrum.

This star is best fitted with a model of $T_* = 38$ kK, based on the N III/ N IV line ratio. The Balmer absorption lines in the observation are weaker compared to the model, because they are partially filled with nebular emission. The broad emission in Hα and He II 4686 is formed in the stellar wind, which provides a constraint to the mass-loss rate.

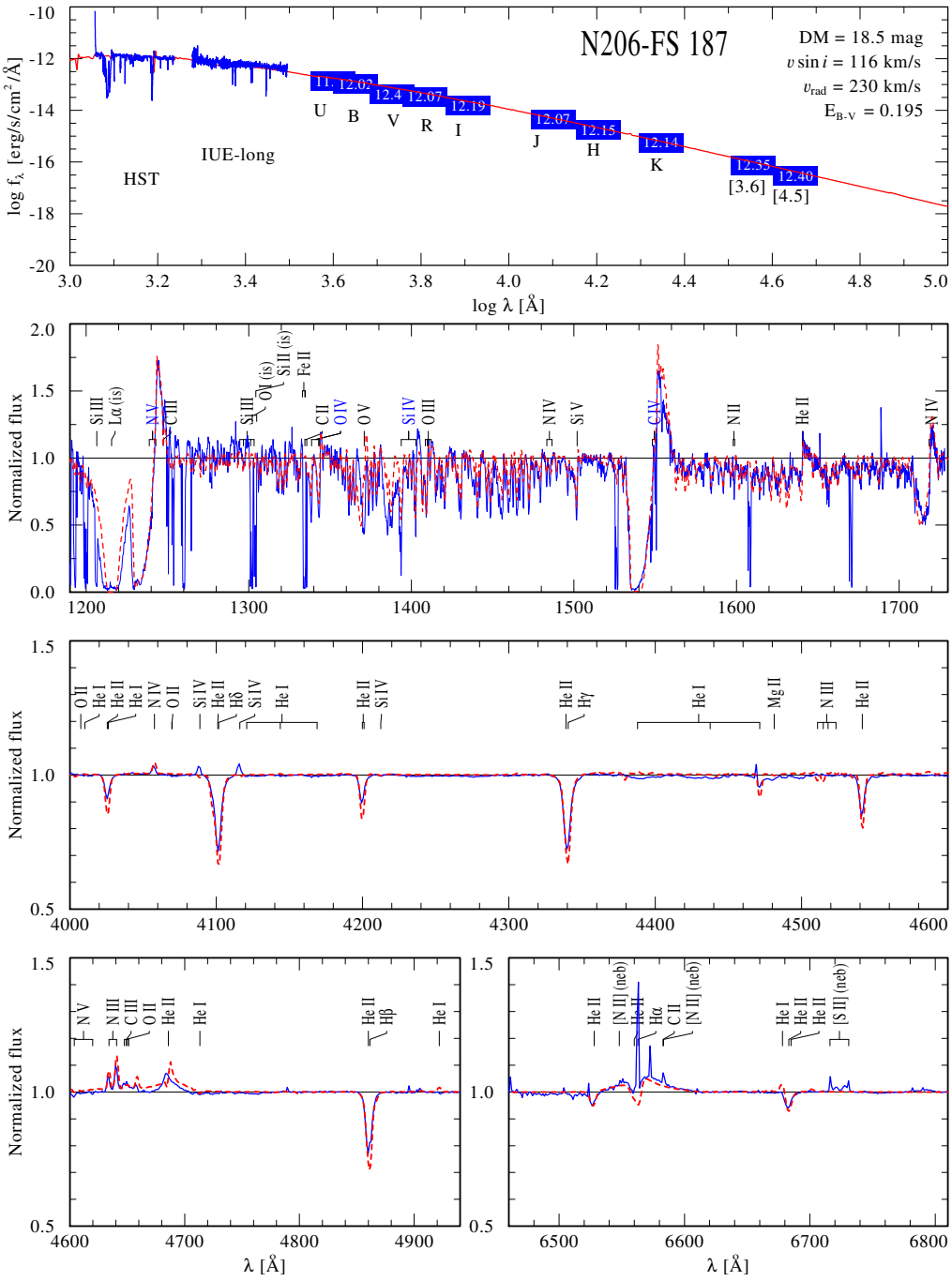

Figure 2.5.: Spectral fit for N206-FS 187. The upper panel shows the model SED (red) fitted to the available photometry from optical (UBV and I) and infrared (JHK_s and $IRAC$ 3.6 & 4.5 μm) bands (blue boxes) as well as the calibrated UV spectra from HST and IUE. The lower panels show the normalized HST and VLT-FLAMES spectra (blue solid line), overplotted with the PoWR model (red dashed line). The parameters of this best-fit model are given in Table 2.3. The observed spectrum also contains nebular emission lines (neb) and interstellar absorption lines (is).

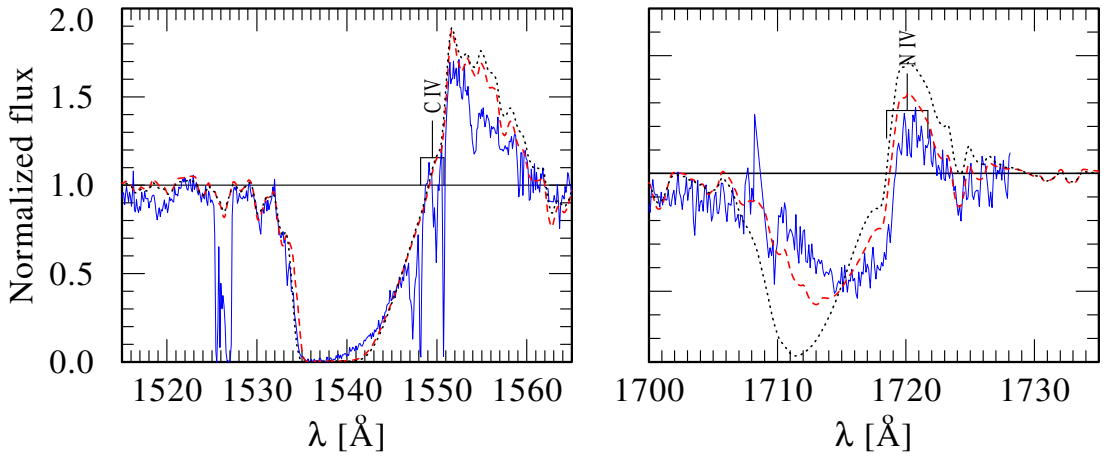

Figure 2.6.: Models with different clumping parameters are compared to the P-Cygni profiles C IV $\lambda\lambda$1548–1551 and N IV λ1718 of N206-FS 187 (blue solid line). Dashed lines (red) are for the model with $\dot{M} = 2.6 \times 10^{-6}\, M_\odot\,\mathrm{yr}^{-1}$, $D = 20$, and $R_\mathrm{D} = 0.05\, R_*$. The dotted lines (black) show the model with $\dot{M} = 1 \times 10^{-5}\, M_\odot\,\mathrm{yr}^{-1}$, $D = 10$, and $R_\mathrm{D} = 10\, R_*$.

The wind parameters of this star are better estimated by fitting the strong P-Cygni N V and C IV profiles. The N V $\lambda\lambda$1238–1242 line is better reproduced by incorporating the X-ray field in the model, with X-ray luminosity $L_\mathrm{X} = 4.7 \times 10^{33}\,\mathrm{erg\,s^{-1}}$. The X-ray field influences the ionization structure and especially strengthen this N V line (Cassinelli & Olson 1979; Baum et al. 1992). Moreover, this star is detected as a X-ray point source in *XMM-Newton* observation of Kavanagh et al. (2012). Its strong X-ray luminosity might be due to binarity (see Sect. 2.4.3), but we do not see any sign of secondary component in the spectra. Therefore, the star is here fitted as a single star.

The left panel of Fig. 2.6 shows the C IV $\lambda\lambda$1548–1551 resonance doublet. We measured v_∞ from its blue edge as $2300 \pm 50\,\mathrm{km\,s^{-1}}$. Since this line is saturated, it is not sensitive to clumping. But the N IV λ1718 line shown in the right panel is unsaturated, and found to be weaker in the observed spectrum than in the model. This could be an indication of strongly clumped wind. Figure 2.6 compares two models with different clumping parameters as described in Sect. 3.5.1. In order to decrease the strength of the N IV λ1718 P-Cygni profile in the model, clumping should start before the sonic point and reach its maximum value D already at a very low radius. The model with a density contrast $D = 20$ and the clumping starts at a radius of $0.025\, R_*$ and reaches the maximum value of D at $R_\mathrm{D} = 0.05\, R_*$, best reproduces the observation (see right panel of Fig. 2.6). Since clumping enhances the emission of Hα, we decreased the mass-loss rate by a factor of 4 compared to the model with the default clumping. The O V λ1371 line is similarly affected by wind clumping. However, the strong X-ray luminosity and possible binarity (see Sect. 2.4.3) of this source might be related to the strength of these lines.

Composite model

The spectrum of N206-FS 187 shown in Fig. 2.5 is satisfactorily fitted by a single-star model. However, there are two objects in our sample (N206-FS 180, N206-FS 131) for which the observed spectra cannot be reproduced by a single synthetic spectrum.

The spectrum of N206-FS 180 is shown in Fig. A.7. The weakness of the N III lines, N IV lines in emission, and the presence of strong N V absorption lines indicate a very high stellar temperature.

We selected the temperature of the model so that the synthetic spectrum reproduces the observed N IV/N V and N III/N IV line ratios. The best fit is achieved for $T_* = 50$ kK and $\log g_* = 4.2$. Since the temperature of this model is very high, it does not predict any He I lines to show up. Hence, the small He I absorption lines in the observed spectrum can be attributed to a companion, which must be an O star of late subtype (later than O6 to produce He I absorption lines, but earlier than B0 since Si, C, O, and Mg absorption lines are absent).

The observed spectrum is fully reproduced with a composite model (see Fig A.8). The final model spectrum is the sum of an early-type Of star O2 V((f*)) and an O8-9 star. The light ratio of the components is constrained by the diluted strength of absorption features which are attributed to the secondary component (Shenar et al. 2016). These absorption features should be insensitive to the remaining stellar parameters. In our case of N206-FS 180, the He I lines at 4388Å, 4472Å, and 4922Å are available for this purpose. Here our main assumption is that the primary component is more luminous and hotter than the secondary. We also ensured that the primary model perfectly reproduces the N V and N IV lines, assuming that they have no contribution from the secondary component (late O-type). The individual and the composite SEDs are depicted in the upper panel of Fig A.8.

The luminosity and reddening derived from fitting IUE-short spectrum and photometric data are different. The UV spectrum fit best with a model SED of high luminosity $\log L/L_\odot = 6.47$, while the photometry is best fitted with a SED having $\log L/L_\odot = 6.11$ (primary). Both the high resolution and low resolution IUE spectrum (flux calibrated) show deviation from the photometry. Since the aperture of the IUE is large ($\approx 21'' \times 9''$) and the star belongs to the crowded region of the cluster, the observed spectrum is likely to be contaminated from nearby stars. So, we have adapted the luminosity corresponding to photometry.

For those stars which show Hα in absorption, the mass-loss rate and terminal velocity can be solely derived from UV spectra. For N206-FS 180, the normalized IUE spectrum is shown in the second panel of Fig. A.7. The P-Cygni O V line at 1371Å is stronger in the model than in the observation, which usually indicates strong wind clumping. But according to Massey et al. (2005) if Hα is in absorption, the only wind contribution is from layers very close to the sonic point, so absorption-type profiles are hardly affected by clumping. Apart from this, we could not fit the observed spectrum using a model with stronger clumping prescriptions. Hence, we consider only the default clumping with $D = 10$ in the model (see Sect. 3.5.1).

Since this star is still in the hydrogen burning phase, the increase in nitrogen abundance would result in a lower oxygen abundance (CNO balance). Models with three different oxygen mass fractions (varied by a factor of 10) are compared to the O V line in Fig. 2.7. We can only reproduce this line with a model with 100 times lower oxygen abundance compared to the typical LMC value. However, the total CNO abundance of this model is inconsistent with the typical LMC values.

The nitrogen lines of N V and N IV in the optical are also found to be affected by changing the mass-loss rate and terminal velocity in the model. We estimate $\dot{M} = 7 \times 10^{-6}\, M_\odot\, \mathrm{yr}^{-1}$ for the primary from the best fit. The terminal velocity measured from the blue edge of C IV $\lambda\lambda$1548–1551 is 2800 km s^{-1}. In the cases where UV spectra are not available and Hα is in absorption, $\dot{M}$ has a large uncertainty and v_∞ is theoretically determined as described in Sect. 4.3.2.

We suspect the star N206-FS 131 also to be a binary. The remaining Of stars are well fitted with single star models. Individual descriptions and spectral fits of all stars of our sample are given in Appendix A and Appendix B, respectively.

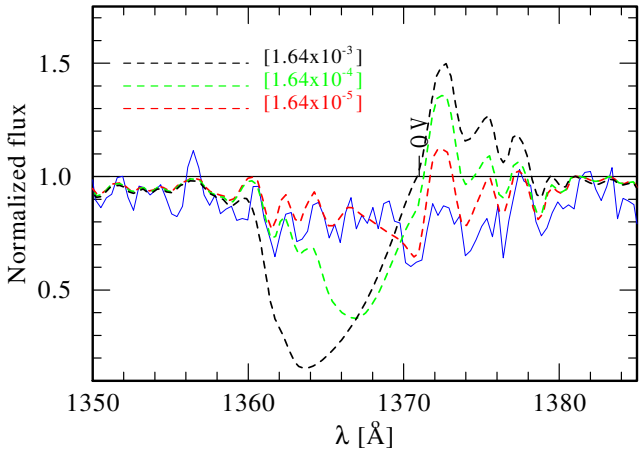

Figure 2.7.: The O v P-Cygni line profile of N206-FS 180 (blue solid line). Three models with different oxygen mass fractions (see labels) are shown for comparison.

2.4. Results and discussions

2.4.1. Stellar parameters

The fundamental parameters for the individual stars are given in Table 2.3. The rate of hydrogen ionizing photons (log Q) and the mechanical luminosity of the stellar winds ($L_{\rm mec} = 0.5\,\dot{M}\,v_\infty^2$) are also tabulated. All these models are calculated with default clumping parameters as described in Sect. 3.5.1.

The gravities shown here are not corrected for rotation. The effect is insignificant and much less than the uncertainty values, even for the fastest rotating star in our sample ($\log(g_* + (v \sin i)^2/R_*) - \log g_* < 0.03$). The reddening of our sample stars is only $0.1 - 0.3$ mag (see Table 2.3). The absolute visual magnitudes ($M_{\rm V}$) in the table are also derived from the respective models. The spectroscopic masses, calculated from $\log g_*$ and R_* (using relation $g_* = G\,M_*\,R_*^{-2}$), are in the range $30 - 150\,M_\odot$.

For the binary candidates N206-FS 180 and N206-FS 131, the stellar parameters for the individual components ('a' denotes the primary and 'b' the secondary component) are given in the table as well. Only the primaries of these binary systems are considered in the following discussions.

Figure 4.11 shows how the effective temperature correlates with the spectral subtypes of our sample. Different luminosity classes are denoted using squares, triangles, and circles for luminosity class V-IV, III-II, and I, respectively. The O2 subtype shows an outstandingly high effective temperature, $T_* = 50$ kK, which is comparable to the temperatures of other O2 stars (e.g., Rivero González et al. 2012a,b; Walborn et al. 2004). This supports the results of Mokiem et al. (2007a) and Rivero González et al. (2012b,a), who suggest a steeper slope in the temperature - spectral type relation for the earliest subtypes (O2-O3).

2.4.2. Wind parameters

In addition to the stellar parameters, the spectra provide information on the stellar winds of our sample. The primary stellar wind parameters are wind terminal velocities (v_∞) and mass-loss rates ($\dot{M}$). The mass-loss rate has great influence on the evolution of massive stars. The $\dot{M}$ scales

Table 2.3.: Stellar parameters of nine Of-type stars in N 206 superbubble.

N206-FS #	T_* [kK]	$\log L$ [$L_\odot$]	$\log g_*$ [cm s^{-2}]	$\log \dot{M}$ [$M_\odot$ yr^{-1}]	E_{B-V} [mag]	M_V [mag]	R_* [$R_\odot$]	v_∞ [km s^{-1}]	$v \sin i$ [km s^{-1}]	M_*[(1)] [$M_\odot$]	$\log Q$ [s^{-1}]	$\log L_{mec}$[(4)] [$L_\odot$]	Spectral type
66	35.0	5.22	4.0	−6.38	0.17	-4.61	11.1	2200	67	45	48.7	2.22	O8 IV((f))
111	37.0	5.03	4.2	−6.85	0.10	-4.20	8.0	2500	43	37	48.6	1.86	O7 V((f))z
131a[(2)]	36.0	5.80	3.6	−5.50	0.11	-6.23	20.5	1500	96	61	49.4	2.77	O6.5 II(f)
131b[(3)]	30.0	5.04	3.8	−6.57	0.12	-5.00	12.3	1900	79	35	48.0	1.91	O9.7 IV
162	34.0	5.60	3.8	−6.03	0.20	-5.67	18.2	2100	83	77	49.1	2.53	O8 IV((f))e
178	35.0	5.22	4.0	−6.38	0.14	-4.55	11.1	2200	79	45	48.7	2.22	O7.5 III((f))
180a[(2)]	50.0	6.11	4.2	−5.32	0.16	-5.77	15.2	2800[(7)]	128	133	50.0	3.49	O2 V((f*))
180b[(3)]	32.0	4.91	4.2	−6.62	0.18	-4.50	9.3	2900	42	50	48.0	2.21	O8 IV
187[(5)]	38.0	6.28	3.6	−4.80	0.19	-6.70	31.9	2300[(7)]	116	148	50.0	3.86	O4 If
193	36.0	5.20	4.2	−6.36	0.20	-4.44	10.3	2900	103	61	48.7	2.48	O7 V((f))z
214[(6)]	38.0	6.10	3.6	−4.93	0.33	-6.26	26.0	2300[(7)]	98	98	49.8	3.71	O4 If

Notes. [(1)] Spectroscopic masses [(2)] Primary component [(3)] Secondary component [(4)] The mechanical luminosity $0.5\dot{M}v_\infty^2$ [(5)] When strong clumping ($D = 20$ and $R_D = 0.05\,R_*$) is adopted then $\log \dot{M} = -5.59\,M_\odot\,\mathrm{yr}^{-1}$ and $\log L_{mec} = 3.05\,L_\odot$. The X-ray field is included in this model, with X-ray luminosity $L_X = 4.7 \times 10^{33}$ erg s^{-1}. [(6)] When strong clumping ($D = 20$ and $R_D = 0.05\,R_*$) is adopted then $\log \dot{M} = -5.72\,M_\odot\,\mathrm{yr}^{-1}$ and $\log L_{mec} = 2.92\,L_\odot$. The X-ray field is included in this model, with X-ray luminosity $L_X = 1.7 \times 10^{33}$ erg s^{-1}. [(7)] v_∞ is determined from UV P-Cygni profiles. Other values are theoretically calculated from v_{esc}.

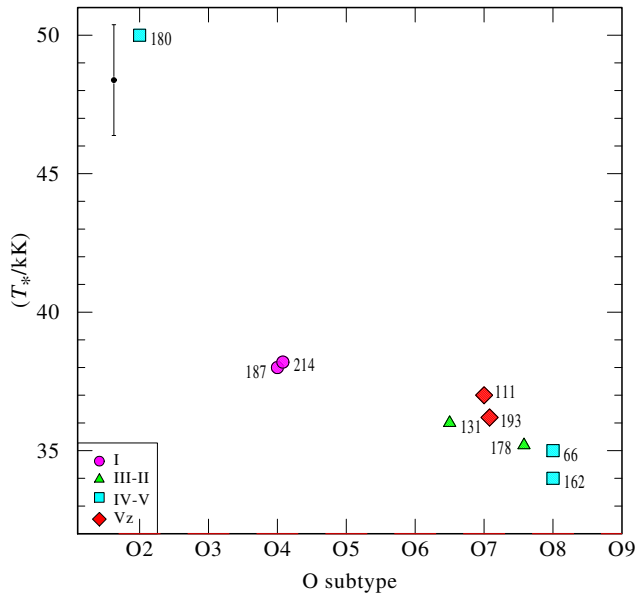

Figure 2.8.: Effective temperature as a function of spectral type. Squares, triangles, and circles denote the luminosity classes Vz, V-IV, III-II and I, respectively. Typical uncertainties are indicated by the error bar in the upper left corner.

with the metallicity of stars (Leitherer et al. 1992; Vink et al. 2001). The lower LMC metallicity results in less efficient wind driving in comparison to the Galactic environment, and consequently in lower mass-loss rates (Vink et al. 2000).

For stars with available UV spectra (N206-FS 180, N206-FS 187, and N206-FS 214), the mass-loss rate is obtained from P Cygni lines as explained in Sect. 4.3.2. For N206-FS 131, Hα is partially filled with wind emission, and the corresponding spectral fit yields $\dot{M}$. The rest of the sample shows Hα in pure absorption, so the $\dot{M}$ values are estimated from the nitrogen emission lines. Since these nitrogen lines are also affected by the nitrogen abundance, these mass-loss rates have an additional uncertainty. The derived mass-loss rates of our Of samples are in the range from $10^{-6.9}$ to $10^{-4.8}$ $M_\odot\,\mathrm{yr}^{-1}$.

Mass-loss rate and luminosity exhibit a clear correlation in Fig. 2.9. Here the supergiants are in the upper right corner with high luminosity and $\dot{M}$. This relation can be fitted as a power-law with an exponent ≈ 1.5 (uncertainties are considered in the fit). The models of two supergiants with alternative clumping prescriptions (see Sect.2.3.2) would yield a lower mass-loss rate by a factor 5 (open circles). The supergiant N206-FS 187 has a very high luminosity and mass-loss rate, even compared to the Galactic stars with the same spectral type. A star (VFTS 1021) with similar high values of L and $\dot{M}$ has been found by Bestenlehner et al. (2014).

Wind-momentum luminosity relationship

To investigate the winds of Of stars in the LMC quantitatively, we plotted the modified wind momentum - luminosity relation (WLR) in Fig. 2.10. This diagram depicts the modified stellar wind momentum $D_{\mathrm{mom}} \equiv \dot{M} v_\infty R_*^{0.5}$ (Kudritzki & Puls 2000), as a function of the stellar luminosity.

For the WLR, a relation in the form

$$\log D_{\mathrm{mom}} = x \log(L_*/L_\odot) + \log D_0 \tag{2.3}$$

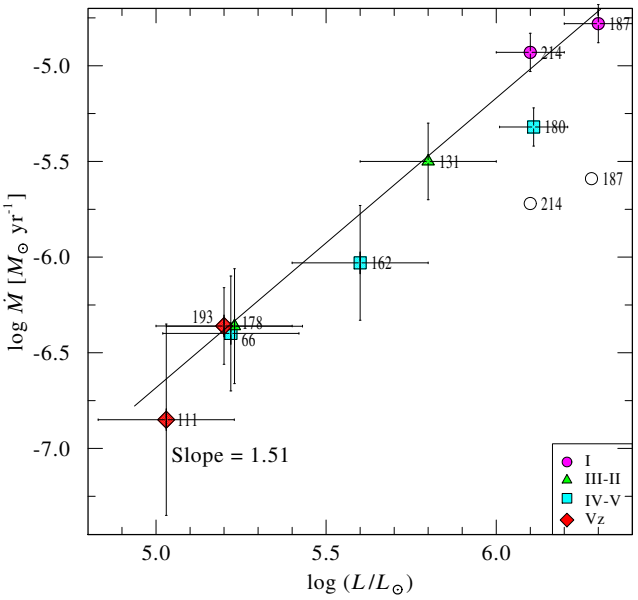

Figure 2.9.: Mass-loss rates vs. luminosity for the Of stars in the N 206 superbubble in the LMC. Open circles denote alternative values for the two supergiants obtained with stronger clumping (see Sect. 2.3.2). A power law is fitted to the data points. Symbols have the same meaning as in Fig 4.11. The error bars are shown for each source.

is expected, where x corresponds to the inverse of the slope of the line-strength distribution function, and D_0 is related to the effective number of lines contributing to stellar wind acceleration (Puls et al. 2000). The distribution of line strengths is important to compare the observed wind strengths to the predictions of line driven wind theory. A linear regression to the logarithmic values of the modified wind momenta obtained in this work (see Fig. 2.10) yields the relation

$$\log D_{\rm mom} \;=\; (1.8 \pm 0.12)\log(L_*/L_\odot) \;+\; (-11.94 \pm 0.71) \tag{2.4}$$

Figure 2.10 also shows the relation for the LMC stars (x = 1.83) as predicted by Vink et al. (2000). The dotted lines represent the empirical WLR for LMC OB stars (x = 1.81) as determined by Mokiem et al. (2007a). Bestenlehner et al. (2014) also found an empirical WLR for O stars in the 30 Doradus region of the LMC with x = 1.45. The Of stars in the superbubble N 206 shows a good correlation with both empirical and theoretical WLR. It should be noted that for the wind momentum calculation of some of the sources, we adopted theoretical v_∞ values in the absence of available the UV spectrum. The uncertainties of parameters are also estimated and included in the linear regression.

The wind momenta of the supergiants would be much lower if strong clumping is adopted (open circles). Figure 2.10 shows the WLR with default clumping as described in Sect. 2.3.2 for all the stars. This is close to the theoretical relation (x ∼1.8). The alternative clumping prescriptions for two supergiants (strong clumping) would result a less steeper WLR relation. Mokiem et al. (2007a) also tested clumping corrections for one supergiant and obtained a less steep relation (x ∼1.43). Note that the theoretical WLR is based on unclumped winds. In our analysis, a depth dependent clumping was accounted for all stars.

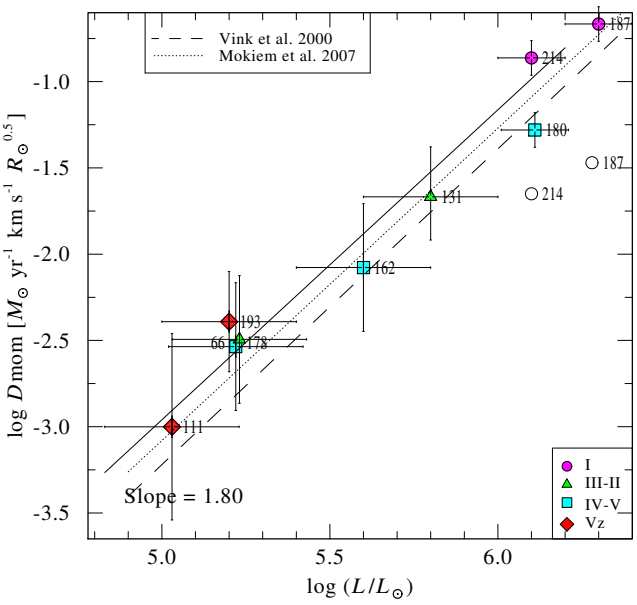

Figure 2.10.: Modified wind momentum ($D_{\rm mom}$) in units of $M_\odot\,{\rm yr}^{-1}\,{\rm km\,s}^{-1}\,R_\odot^{0.5}$ as a function of the stellar luminosity for the analyzed LMC Of stars. The alternative values for the two supergiants adapting strong clumping (see Sect. 2.3.2) are indicated in open circles. The data are fitted by a power law (solid line). The theoretical WLR from Vink et al. (2000) (dashed line) and empirical WLR from Mokiem et al. (2007a) for LMC stars are also plotted. Luminosity classes are distinguished by different symbols. Individual error bars are given in the plot.

2.4.3. Outstanding X-ray luminosity of N206-FS 187 points to its binarity

The supergiant N206-FS 187 was detected in X-rays with the *XMM-Newton* telescope (Kavanagh et al. 2012). Since no X-ray spectral information was presented by Kavanagh et al. (2012), we adopted the X-ray flux from "The third XMM-Newton serendipitous source catalog" (Rosen et al. 2016). Correcting for interstellar absorption, $N_{\rm H} = 9 \times 10^{21}\,{\rm cm}^{-2}$ (Kavanagh et al. 2012), the estimated X-ray luminosity of N206-FS 187 is $L_{\rm X} \approx 4 \times 10^{34}\,{\rm erg\,s}^{-1}$ in the 0.2-12.0 keV band. Hence, the ratio between X-ray and bolometric luminosity is $\log L_{\rm X}/L_{bol} \approx -5$.

This is an outstandingly high X-ray luminosity for an O-type star. Single O-type stars in the Galaxy have significantly lower X-ray luminosities (e.g., Oskinova 2005). The high X-ray luminosity of N206-FS 187 might indicate that this object is a binary. In a massive binary, the bulk of X-ray emission might be produced either by collision of stellar winds from binary components, or by accretion of stellar wind if the companion is a compact object.

Some colliding wind binaries consisting of a WR and an O-type component have comparably high X-ray luminosities (Portegies Zwart et al. 2002; Guerrero & Chu 2008). However our spectral analysis of N206-FS 187 rules out a WR component. Most likely, the binary component in N206-FS 187 is an O-type star of similar spectral type. Even in this case, it is outstandingly X-ray luminous. For example, the X-ray luminosity of the O3.5If* + O3.5If* binary LS III+46 11 is an order of magnitude lower than that of N206-FS 187 (Maíz Apellániz et al. 2015, and references therein). Some wind-wind colliding (WWC) feature may be present in the lines such as Hα (Moffat 1989). However, as the WWC effects are usually of the order of a few percentage (Hill et al. 2000),

that are not expected to highly influence the spectral features.

On the other hand, the X-ray luminosity of N206-FS 187 is not in the correct range to suspect that it harbors a compact companion. The latter systems are either usually significantly more X-ray luminous (in case of persistent sources), or significantly less X-ray luminous in quiescence (in case of transients) (Martínez-Núñez et al. 2017).

Therefore, on the basis of the high X-ray luminosity of N206-FS 187 and taking into account the uncertainties on its X-ray spectral properties, we believe that N206-FS 187 is one of the X-ray brightest colliding wind binaries consisting of stars with similar spectral types. Interestingly the other Of supergiant N206-FS 214 does not show any X-ray emission, even though it is an eclipsing binary of similar spectral types (see Sect. C.1 for more details).

Note that the X-ray luminosity derived from our model using UV spectral line fit ($L_{\rm X} \approx 4.7\times10^{33}$ erg s^{-1}) is an order of magnitude less than this observed X-ray luminosity (see Sec. 2.3.2). One reason could be the variability of X-ray emission if it is a WWC binary. Another possibility is that the observed X-ray luminosity might be overestimated from the interstellar absorption values.

2.4.4. The Hertzsprung-Russell diagram

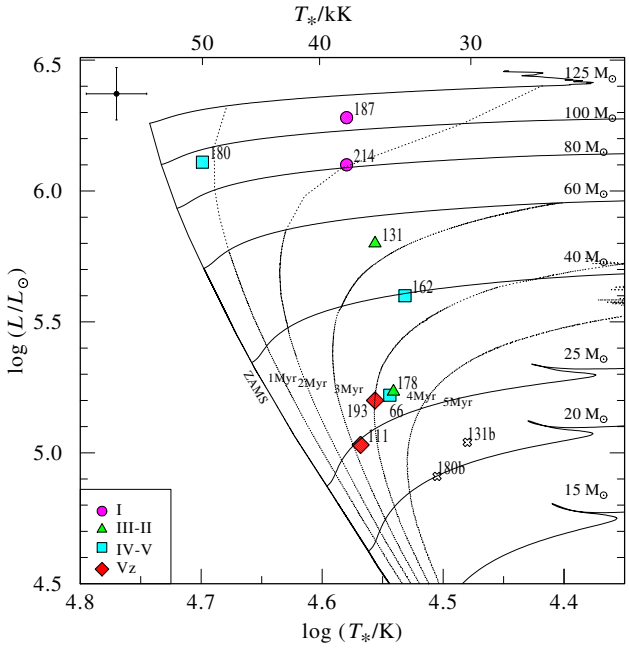

Figure 2.11.: Hertzsprung-Russell diagram for the nine Of stars in the N 206 superbubble in the LMC. The evolutionary tracks and isochrones are based on rotating ($V_{\rm rot,init} \sim 100$ km s^{-1}) evolutionary models presented in Brott et al. (2011) and Köhler et al. (2015). Different luminosity classes are denoted using rhombus, squares, triangles, and circles for luminosity class Vz, V-IV, III-II, and I, respectively. The position of the secondary components of N206-FS 131 and N206-FS 180 are also marked in the diagram with a cross symbol.

The Hertzsprung-Russell diagram (HRD) for the Of stars in the N 206 superbubble, constructed from the temperature and luminosity estimates (see Table 2.3), is given in Fig. 2.11. The evolutionary tracks and isochrones are adapted from Brott et al. (2011) and Köhler et al. (2015), accounting

for an initial rotational velocity of ~ 100 km s^{-1}. The evolutionary tracks are shown for stars with initial masses of $15 - 125\ M_{\odot}$, while the isochrones span from the zero age main sequence (ZAMS) to 5 Myr in 1 Myr intervals. Stars are represented by respective luminosity class symbols as in Fig. 2.11.

The isochrones suggest that the O2((f*)) star N206-FS 180 (primary) is very young and close to the ZAMS (assuming single-star evolution). The evolutionary mass predicted from the tracks is $\approx 93\ M_{\odot}$ for the primary component of this binary system. The other Of stars are younger than ≈ 4 Myr and more massive than $\approx 25\ M_{\odot}$. The supergiants in our sample are nearly 2 Myr old with masses in the range 70 to 100 $M_{\odot}$.

The evolutionary masses from the HRD are compared in Fig. 2.12 to the spectroscopic masses derived (see Table 2.3). Here, the evolutionary mass refers to the current stellar mass as predicted by the corresponding evolutionary track. It is evident from Fig. 2.12 that the spectroscopic masses of the objects are systematically larger than their evolutionary masses. However we have to acknowledge that, the errors in our spectroscopic mass estimates are large (at least a factor 2). The wind contamination in the Balmer wings also affects the log g determination, and we adopt theoretical values for v_{∞} in some cases.

This mass discrepancy problem was extensively investigated for Galactic and extragalactic star clusters by many authors (Herrero et al. 1992; Vacca et al. 1996; Repolust et al. 2004). This mass difference is strongly affected by the mass-loss recipe used in the evolutionary calculations (McEvoy et al. 2015). According to Hunter et al. (2008a), the observed mass discrepancy of main-sequence stars could be due to binarity, errors in the distance estimate, bolometric corrections, reddening, or the derived surface gravities. However, the systematic trend in the discrepancy may not be due to the uncertainties in our parameter measurements, but could originate from the evolutionary masses.

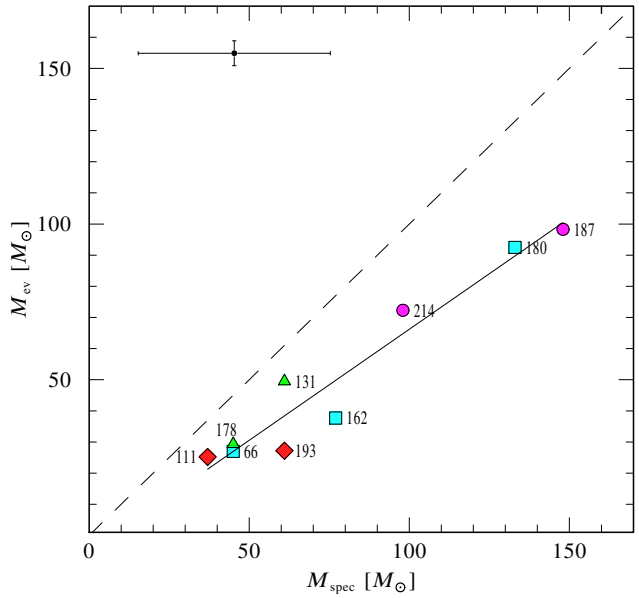

Figure 2.12.: Evolutionary masses compared to the spectroscopic masses. The discrepancy grows roughly linearly with the mass (see linear fit). The one-to-one correlation of spectroscopic and evolutionary masses is indicated by the dashed line.

Table 2.4.: Chemical abundance for the nine Of-type stars in the N 206 superbubble derived from spectral fitting. The abundances are given in mass fractions.

N206-FS #	X_N [10^{-3}]	X_C [10^{-3}]	X_O [10^{-3}]
66	0.28	0.57	1.64
111	<0.08	0.47	2.64
131	0.72	0.23	1.04
162	0.28	0.38	1.64
178	0.7	0.18	1.64
180	2.2	0.18	0.02
187	0.72	0.23	3.04
193	0.48	0.28	2.64
214	0.72	0.23	3.04
Typical LMC[(1)] values	0.08	0.47	2.64

Notes. [(1)] taken from Trundle et al. (2007)

2.4.5. Chemical abundance

The chemical abundances of our Of sample derived in terms of mass fraction are given in Table 2.4. These have been obtained by fitting the observed spectra with PoWR models calculated for different C, N, and O mass fractions (see Table 2.2 for more details). Since the nitrogen lines are formed by complex NLTE processes, changes in the N abundance can have a large impact on the strength of the lines (Rivero González et al. 2012b). The P, Mg, Si, and S abundances are fixed for all the models. We could not reproduce the Si IV emission lines in supergiants N206-FS 187 and N206-FS 214 with our models.

The distribution of nitrogen abundances with effective temperature is illustrated in Fig 2.13. We can see a direct correlation in our sample (except N206-FS 111). In addition, all these stars show lower abundance in either oxygen or carbon (compared to typical LMC values) due to the CNO process. The O2 spectral type shows a very high nitrogen abundance in comparison to the other Of stars (but less than the total CNO mass fraction). In turn, its oxygen abundance measured from the O V line at 1371Å is much lower by a factor of 100 than the typical LMC values.

One of the key questions of massive star evolution is rotational mixing and its impact on the nitrogen abundance. Evolutionary models accounting for rotation (Hunter et al. 2008a; Brott et al. 2011; Rivero González et al. 2012b,a) predict that the faster a star rotates, the more mixing will occur, and the larger the nitrogen surface abundance that should be observed. Figure 2.14 shows a so-called "Hunter-diagram", depicting the variation of the nitrogen enrichment with the projected rotational velocity. Our Of sample shows projected rotational velocities in the range of ~40–130 km s^{-1} and nitrogen abundances (log (N/H) +12) from 8 to 9.6. This diagram shows a relative increase in nitrogen abundance with rotation. It should be noted that the projected rotational velocity and the true rotational velocity differ by a factor $\sin i$. However, Maeder et al. (2009) suggests that chemical enrichment is not only a function of projected rotational velocity, but also

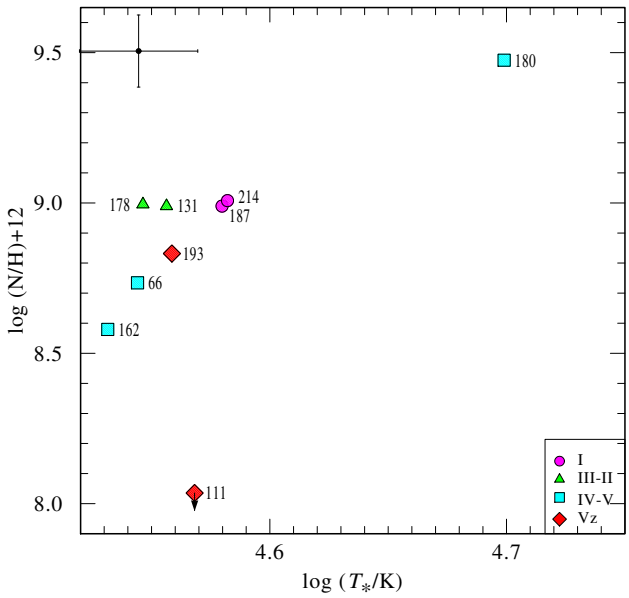

Figure 2.13.: Surface nitrogen abundances as a function of the effective temperature. The downward arrow indicates an upper limit to the nitrogen abundance of N206-FS 111.

depends on ages, masses, and metallicities. The nitrogen enriched stars are very massive in our case.

The following conclusions can be made from the diagram:

- The O2 dwarf N206-FS 180 shows a exceptionally high nitrogen abundance, and its projected rotational velocity is highest among the sample.
- Evolved stars (giants and supergiants) are more nitrogen enriched than dwarfs of the same effective temperature.
- The slowest rotator in our sample (also least massive), N206-FS 111 ($v \sin i = 43$ km s^{-1}), shows very little enrichment. Although N206-FS 111 and N206-FS 193 are ZAMS candidates (Vz), N206-FS 193 ($v \sin i = 103$ km s^{-1}) shows nitrogen enhancement.
- The two binary candidates (N206-FS 180a and N206-FS 131a) are more nitrogen enriched than other stars with similar rotational velocities.

According to Kohler et al. (2015), a strong nitrogen surface enhancement can be obtained even in models with initial rotational velocities well below the threshold value. All our sample stars are nitrogen enriched with rotational velocities below 200 km/s. Because of the strong mass loss and large convective core masses, their evolutionary models above 100 $M_\odot$ shows nitrogen-enrichment irrespective of their rotation rate. The large nitrogen enhancement in our sample star N206-FS 180 is very similar(M≈100 $M_\odot$, $v \sin$ i≈150 km/s, age≈1Myr) to their model predictions. Moreover, this source is a part of binary system, which may also have influence in the enrichment.

2.4.6. Stellar feedback

The main contribution to the stellar feedback in the N 206 superbubble is expected to come from stars in our Of sample. The number of ionizing photons and the mechanical luminosity of

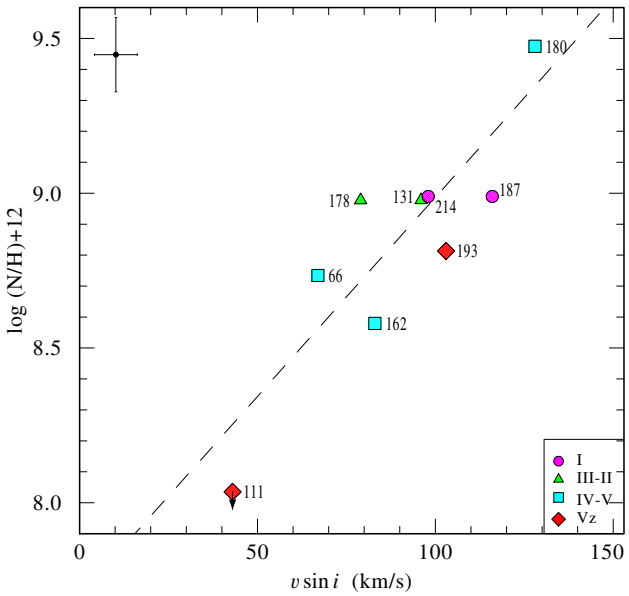

Figure 2.14.: Surface nitrogen abundances as a function of the projected rotation velocity $v \sin i$. The dashed line is a linear regression to the data. The downward arrow indicates an upper limit to the nitrogen abundance of N206-FS 111.

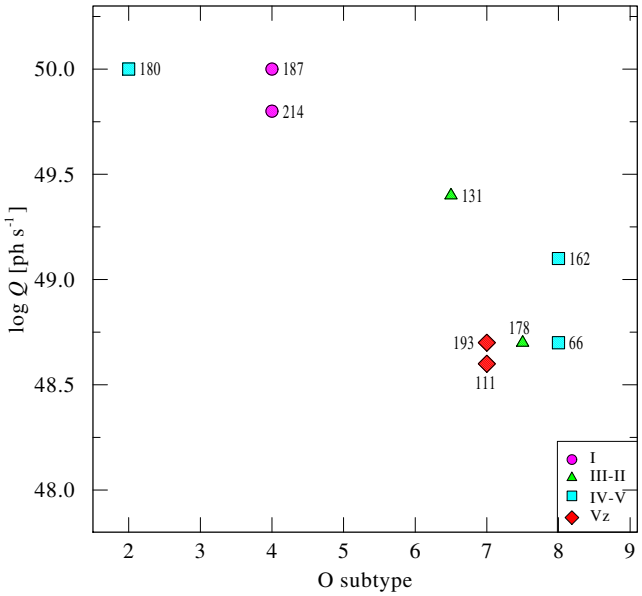

Figure 2.15.: Rate of ionizing photons as a function of the O subtype.

the stellar winds as a function of O subtypes are shown in Figs. 2.15 and 2.16. Both of these energy feedback mechanisms show a correlation with spectral subtype, where the O2((f*)) star and the two supergiants dominate. The combined ionizing photon flux from the nine Of stars is approximately $Q_0 \approx 3 \times 10^{50}\,\mathrm{s}^{-1}$. The total mechanical feedback from these Of stars is $L_{mec} = 0.5\dot{M}v_\infty^2 \approx 1.7 \times 10^4\,L_\odot\,(\equiv 6.5 \times 10^{37}\mathrm{erg\,s}^{-1})$. We stress that the v_∞ was adopted for majority of the sample. The uncertainties in these estimates are propagated from mass-loss rate

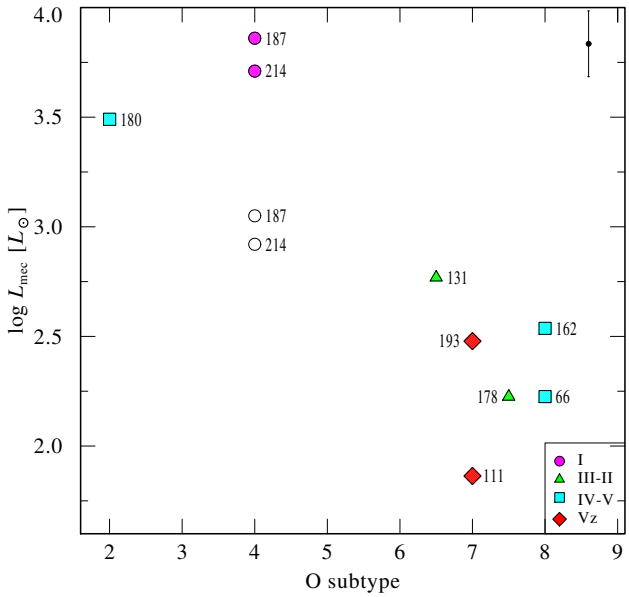

Figure 2.16.: Mechanical luminosity of stellar winds as a function of the O subtype. The open circles for the two supergiants refers to the models with alternative solution with higher clumping. Typical uncertainties are indicated with error bar in the upper right corner.

and terminal velocity. As now discussed, the total mechanical luminosity is dominated by the three Of stars, for which an uncertainty of approximately 30% is estimated. Assuming stronger clumping in models would lower this total feedback by a factor of two.

Kavanagh et al. (2012) analyzed the X-ray superbubble in N 206 using XMM-*Newton* data. The thermal energy stored in the superbubble was estimated using the X-ray emitting gas, the kinetic energy of the Hα shells, and the kinetic energy of the surrounding H I gas. Using spectral fits Kavanagh et al. (2012) derived the physical properties of the hot gas and hence estimated the thermal energy content of the X-ray superbubble. Along with this, they calculated the kinetic energy of the expansion of the shell in the surrounding neutral gas using MCELS and 21 cm line emission line data from the ATCA-Parkes survey of the Magellanic Clouds (Kim et al. 1998). They estimated the total energy to be $(4.7 \pm 1.3) \times 10^{51}$ erg.

This thermal energy could be supplied by the stars in the N206 superbubble via stellar winds and the supernova occurred in this region (SNR B0532-71.0). We calculated the current mechanical energy supply from these Of stars. In order to provide the total energy estimate of these Of-type stars, we must derive their current ages. So, we adopted the ages of individual stars from the HRD (see Sect. 4.5) using isochrone fitting. The total mechanical energy supplied by these stars throughout their lifetimes is $(5.8 \pm 1.8) \times 10^{51}$ erg. As in Kavanagh et al. (2012), we also assumed that these stars provide same amount of mechanical energy throughout their lifetime, since they are very young. Also, the time duration is short for a significant contribution from radiative and other cooling processes, and can be neglected for this rough estimate. The energy estimates are consistent with Kavanagh et al. (2012), even though we consider only the mechanical feedback from stellar winds. The total momentum provided from these stars over time is $\approx 1.86 \times 10^{43}$ g *cm* s^{-1}.

This shows that the Of stars in our sample provide a significant contribution to the energy feedback. The total feedback in the superbubble including the entire OB population, Wolf-Rayet

stars (BAT99 53, BAT99 49), and supernova will be discussed in Paper II.

2.5. Summary and conclusions

We have obtained and analyzed FLAMES spectra of nine massive Of-type stars in the N 206 giant H II complex located in the LMC. On the basis of these data complemented by archival UV spectra, we determined precise spectral types and performed a thorough spectral analysis. We used sophisticated PoWR model atmospheres to derive the physical and wind parameters of the individual stars. Our main conclusions are as follows.

- All stars have an age less than 4 Myr. The earliest O2 star appears to be less than 1 Myr old, while the two supergiants are 2 Myr old.
- The wind-momentum luminosity relation of our sample are comparable to that of theoretically predicted, with the assumption of a depth dependent clumping in all models.
- The star N206-FS 187 shows very high mass-loss rate and luminosity. Its large X-ray luminosity suggests that this object is one of the X-ray brightest colliding wind binaries consisting of stars with similar spectral types.
- Most of the Of stars are nitrogen enriched. A clear trend toward more enrichment with rotation as well as with temperature is found. The binary stars and more evolved stars show nitrogen enrichment compared to others.
- The O2 star N206-FS 180 shows a very high nitrogen mass fraction, while oxygen is strongly depleted compared to the typical LMC values.
- The evolutionary masses are systematically lower than the corresponding spectroscopic masses obtained from our analysis.
- The total ionizing photon flux and stellar wind mechanical luminosity of the Of stars are estimated to 3×10^{50} s^{-1} and $1.7 \times 10^4\ L_\odot$, respectively. This leads us to conclude that the program stars play a significant role in the evolution of the N 206 superbubble.

The subsequent paper (Ramachandran et al. in prep.) will provide the detailed analysis and discussion of complete OB star population in the N 206 superbubble.

2.6. Acknowledgements

V.R. is grateful for financial support from Deutscher Akademischer Austauschdienst (DAAD), as a part of Graduate School Scholarship Program. LMO acknowledges support by the DLR grant 50 OR 1508. A.S. is supported by the Deutsche Forschungsgemeinschaft (DFG) under grant HA 1455/26. T.S. acknowledges support from the German "Verbundforschung" (DLR) grant 50 OR 1612. We thank C. J. Evans for helpful discussions. This research made use of the VizieR catalog access tool, CDS, Strasbourg, France. The original description of the VizieR service was published in A&AS 143, 23. Some data presented in this paper were obtained from the Mikulski Archive for Space Telescopes (MAST). STScI is operated by the Association of Universities for Research in Astronomy, Inc., under NASA contract NAS5-26555. Support for MAST for non-HST data is provided by the NASA Office of Space Science via grant NNX09AF08G and by other grants and contracts.

2.7. Comments on the individual stars

N206-FS 66: This O8 subgiant is located at the periphery of the superbubble N 206, far away from the young cluster NGC 2018. The noticeable spectral features are the N III emission line (weak), the C III & O II absorption blend near 4560 Å, and strong Si IV absorption lines. The model with T_* = 36 kK is fitted to this spectrum based on the He I/He II line ratios. The nitrogen abundance is mainly constrained through the N III absorption lines in the range 4510−4525 Å. Since the Hα line is fully in absorption and no UV spectrum is available, we estimated the wind parameters with large uncertainties.

N206-FS 111: This is one of the ZAMS type Of stars in the sample with spectral type O7 V((f))z. The most prominent feature in the spectrum is a very strong He II absorption line at 4686 Å. The model with T_* = 37 kK is fitted to the spectrum based on the He I/He II line ratios. This star is also described by Kavanagh et al. (2012) using the Magellanic Cloud Emission Line Survey (MCELS) observations. They determined its spectral type as O7 V and derived a similar mass-loss rate (using theoretical relations) as in our analysis. The terminal velocity and the mass-loss rate have large errors, since Hα is in absorption. This is the slowest rotating star in the sample. The nitrogen lines are very weak, hence the determined abundance is an upper limit.

N206-FS 131: This is one of the binary candidates in the sample. The presence of weak He I absorption lines in the spectrum gives a clue about the secondary component. The strong N III emission lines and the very weak He II 4686 confirm that the primary is an Of giant. The temperature of the primary Of is determined to be T_* = 38 kK. The secondary component is an O star with late subtype and best fitted with a model of T_* = 30 kK. This star was mentioned as a single O8 II star in Bonanos et al. (2009). The Hα absorption in the spectrum is partially filled with wind emission and is best fitted with a mass-loss rate of 3.1 $\times 10^{-6} M_\odot$ yr^{-1}. The radial velocity of this star is measured to be 185 km s^{-1}, which is significantly less than the systematic velocity of the LMC ($\approx$ 260 km s^{-1}).

N206-FS 162: This object was identified as an emission line star in previous papers (Howarth 2013; Lindsay 1963). The weak N III emission lines in the spectrum confirm its 'Of nature'. Based on the broad and very strong Hα emission, we conclude that it is the only Oef-type star in the N 206 superbubble. Based on the He I/He II line ratios, we estimate a stellar temperature of T_* = 34 kK. The spectrum also shows prominent Si IV and O II absorption lines, which are used to constrain the abundance. Although we tried to fit the wings of Hα emission (also nitrogen emission lines), the estimated wind parameters are highly uncertain due to the superimposed disk emission. The projected rotational velocity of this star ($v \sin i \sim 83$ km s^{-1}) seems to be exceptionally low compared to typical Oe/Be stars. However, the morphology of the Hα line also suggests a nearly "pole-on" observer aspect.

N206-FS 178: This object is one of the giants in the sample. The spectrum is best fitted with a model with T_* = 35 kK and $\log g_*$ = 4.0. We mainly used the He I/He II line ratio and the strong N III emission lines for determining the stellar temperature. Since Hα is in absorption, we tried to measure the wind parameters by adjusting the nitrogen emission line fits. For this star, we varied the abundance N in the model to best fit the N III absorption lines.

N206-FS 193: This is one of the stars located at the center of the cluster NGC 2018. This star is also tabulated in Kavanagh et al. (2012), but with spectral type O8 V. We classified this star as O7 Vz. The spectrum with weak N III emission lines and a very strong He II 4686 absorption

line is best fitted with a model that has a temperature of $T_* = 36\,\mathrm{kK}$. This spectrum is highly contaminated with nebular emission.

N206-FS 214: An Of supergiant in the sample. Massey et al. (1995) catalogued this star as an O4 If spectral type. Graczyk et al. (2011) identified this object as an eclipsing binary (OGLE-LMC-ECL-18366) with a period of 64.9 days based on the data from Optical Gravitational Lensing Experiment (OGLE). Their light curve suggests that both components have similar temperatures (from the depth) and the primary has a much larger radius (from the width). We identified this spectrum as an O4 If supergiant, with no trace of a secondary component in the optical spectrum. This could be an indication of a very faint secondary (dwarf/giant).

The spectral features of this object are similar to N206-FS 187, and both are best fitted with the same model. A FUSE spectrum is available for this object, which is shown in the second panel of Fig. A.10. The prominent UV P-Cygni profiles P v $\lambda\lambda$1118–1128 and S v $\lambda\lambda$1122–1134 are used to measure the wind parameters along with Hα. In order to best fit the P v lines, we used a model with stronger clumping ($D = 20$ and $R_\mathrm{D} = 0.05\,R_*$) and lower mass-loss rate, i.e., a factor of 4 lower than a model with default clumping, similar to N206-FS 187. The carbon lines C IV at 1169 Å and C III at 1176 Å show strong absorption. The calibrated UV spectrum is normalized and fitted consistently with the model SED, and hence constrained the luminosity and reddening values of this star at high precision.

Chapter 3.

Stellar population of the superbubble N 206 in the LMC II. Parameters of the OB and WR stars, and the total massive star feedback (Manuscript II)

Varsha Ramachandran, W.-R. Hamann, R. Hainich, L. M. Oskinova, T. Shenar, A. A. C. Sander, H. Todt, and J. S. Gallagher

*A*stronomy & Astrophysics, 2018, Volume 615

Abstract

Clusters or associations of early-type stars are often associated with a 'superbubble' of hot gas. The formation of such superbubbles is caused by the feedback from massive stars. The complex N 206 in the Large Magellanic Cloud exhibits a superbubble and a rich massive star population. Our goal is to perform quantitative spectral analyses of all massive stars associated with the N 206 superbubble in order to determine their stellar and wind parameters. We compare the superbubble energy budget to the stellar energy input and discuss the star formation history of the region.

We observed the massive stars in the N 206 complex using the multi-object spectrograph FLAMES at ESO's Very Large Telescope (VLT). Available ultra-violet (UV) spectra from archives are also used. The spectral analysis is performed with Potsdam Wolf-Rayet (PoWR) model atmospheres by reproducing the observations with the synthetic spectra.

We present the stellar and wind parameters of the OB stars and the two Wolf-Rayet (WR) binaries in the N 206 complex. Twelve percent of the sample show Oe/Be type emission lines, although most of them appear to rotate far below critical. We found eight runaway stars based on their radial velocity. The wind-momentum luminosity relation of our OB sample is consistent with the expectations. The Hertzsprung-Russell diagram (HRD) of the OB stars reveals a large age spread ($1 - 30$ Myr), suggesting different episodes of star formation in the complex. The youngest stars are concentrated in the inner part of the complex, while the older OB stars are scattered over outer regions. We derived the present day mass function for the entire N 206 complex as well as for the cluster NGC 2018. The total ionizing photon flux produced by all massive stars in the N 206 complex is $Q_0 \approx 5 \times 10^{50}\,\mathrm{s}^{-1}$, and the mechanical luminosity of their stellar winds amounts to $L_{\mathrm{mec}} = 1.7 \times 10^{38}\,\mathrm{erg\,s}^{-1}$. Three very massive Of stars are found to dominate the feedback among 164 OB stars in the sample. The two WR winds alone release about as much mechanical

luminosity as the whole OB star sample. The cumulative mechanical feedback from all massive stellar winds is comparable to the combined mechanical energy of the supernova explosions that likely occurred in the complex. Accounting also for the WR wind and supernovae, the mechanical input over the last five Myr is $\approx 2.3 \times 10^{52}$ erg.

The N206 complex in the LMC has undergone star formation episodes since more than 30 Myr ago. From the spectral analyses of its massive star population, we derive a current star formation rate of $2.2 \times 10^{-3} M_{\odot}\,\mathrm{yr}^{-1}$. From the combined input of mechanical energy from all stellar winds, only a minor fraction is emitted in the form of X-rays. The corresponding input accumulated over a long time also exceeds the current energy content of the complex by more than a factor of five. The morphology of the complex suggests a leakage of hot gas from the superbubble.

3.1. Introduction

Understanding the feedback of stars on their environment is one of the key problems in star and galaxy formation. Massive stars are the main feedback agents, altering the surrounding environment on local, global, and cosmic scales. They dynamically shape the interstellar medium (ISM) around them on timescales of a few Myr. With their winds, ionizing radiation, and supernova explosions, ensembles of massive stars cause the largest structures of the ISM such as giant or multiple H II regions, superbubbles, and supergiant shells.

The interaction via winds and ionizing radiation of a single massive star with its surroundings is usually referred to as an interstellar bubble (Weaver et al. 1977). A massive star first forms an H II region around itself through its strong ionizing radiation field, and its stellar wind interacts with this ionized gas. The supersonic stellar wind (typically 2000 km/s) drives a shock into the ambient medium, while the reverse shock decelerates the wind material, and the kinetic energy of the shocked stellar wind becomes thermal energy, leading to a hot ($T > 10^6$ K), very low density bubble that emits soft X-rays. In a cluster, these hot bubbles around stars can interact with each other and form a superbubble (Tenorio-Tagle & Bodenheimer 1988; Oey et al. 2001; Chu 2008). Superbubbles are observed around many young massive star clusters with sizes of hundreds of parsecs (Tenorio-Tagle & Bodenheimer 1988; Sasaki et al. 2011).

In a series of papers, we study the superbubble associated with the giant H II region N 206 in the Large Magellanic Cloud (LMC). The LMC is one of the closest galaxies to the Milky Way with a distance modulus of only DM = 18.5 mag (Madore & Freedman 1998), allowing for detailed spectroscopy of its bright stars. Another advantage of the LMC is the marginal foreground reddening along the line of sight (Subramaniam 2005; Haschke et al. 2011). The LMC is chemically less evolved than the Milky Way with a metallicity around $Z = 0.5\,Z_{\odot}$ (Rolleston et al. 2002). This allows us to study how stellar feedback works at sub-solar metallicity.

Our target of study is the high-mass star-forming complex N 206 (alias: Henize 206, LHA 120-N 206, and DEM L 221) in the outskirts of the LMC that surrounds the star forming cluster NGC 2018 (LHA 120-N 206A). This H II region was first cataloged in an Hα objective prism survey by Karl Henize in 1956 (Henize 1956). The N 206 complex also harbors a supernova remnant (SNR) B0532-71.0 (Mathewson & Clarke 1973; Williams et al. 2005) in the eastern part. The N 206 complex has been studied in multiwavelengths by various authors. Dunne et al. (2001) reported the expansion velocity of the Hα shell to be ~30 km/s. Since the superbubble has expanded to a diameter of ~112 pc, this suggests an age of ~2 Myr. More than one hundred young stellar object (YSO) candidates were identified in this region using infrared data from *Spitzer*, and a star formation rate (SFR) of $0.25 \times 10^{-2}\,M_{\odot}\,\mathrm{yr}^{-1}$ has been estimated (Carlson et al. 2012;

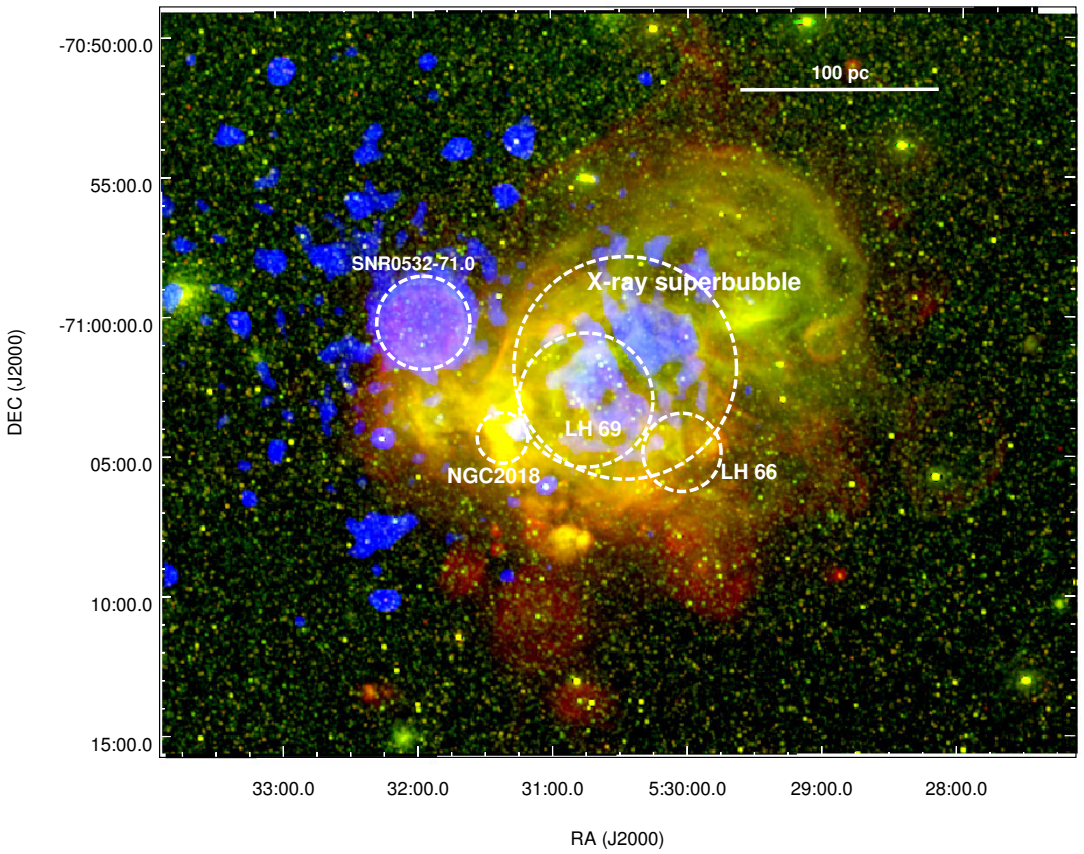

Figure 3.1.: Location of the X-ray superbubble, SNR B0532-71.0, cluster NGC 2018, and OB associations LH 66 and LH 69 in the N 206 complex. The three-color composite image (Hα (red) + [O III] (green) + X-ray (blue)) shown in the background is from the Magellanic Cloud Emission-Line Survey (MCELS, Smith et al. 2005) and *XMM-Newton* (0.3 − 1 keV).

Romita et al. 2010; Gorjian et al. 2004).

The central part of the region is filled with hot gas and has been detected in X-rays. This X-ray superbubble is excited by the winds of the massive stars in the young cluster NGC 2018 as well as the LH 66 and LH 69 OB associations (Lucke & Hodge 1970) (see Sect. 3.2 for more details of the structure of the region). Dunne et al. (2001) concluded that current star formation is taking place around the X-ray superbubble. A detailed study of the complex in X-rays using the *XMM-Newton* telescope was published by Kavanagh et al. (2012). They compared the thermal energy stored in the X-ray emitting gas of the superbubble and the mechanical input supplied by the stellar population. Moreover, they found that the pressure of the hot gas drives the expansion of the shell into the surrounding H I cloud. They estimated the overall mass and thermal energy content of the superbubble and blowout region as 741±85 $M_\odot$ and (3.5±1.3) × 10^{51} erg from soft diffuse X-ray emission and Hα emission. However, this study was lacking information about the energetics of the complete massive star population in this region.

For a better understanding of a star-forming complex, we need to probe its stellar content in

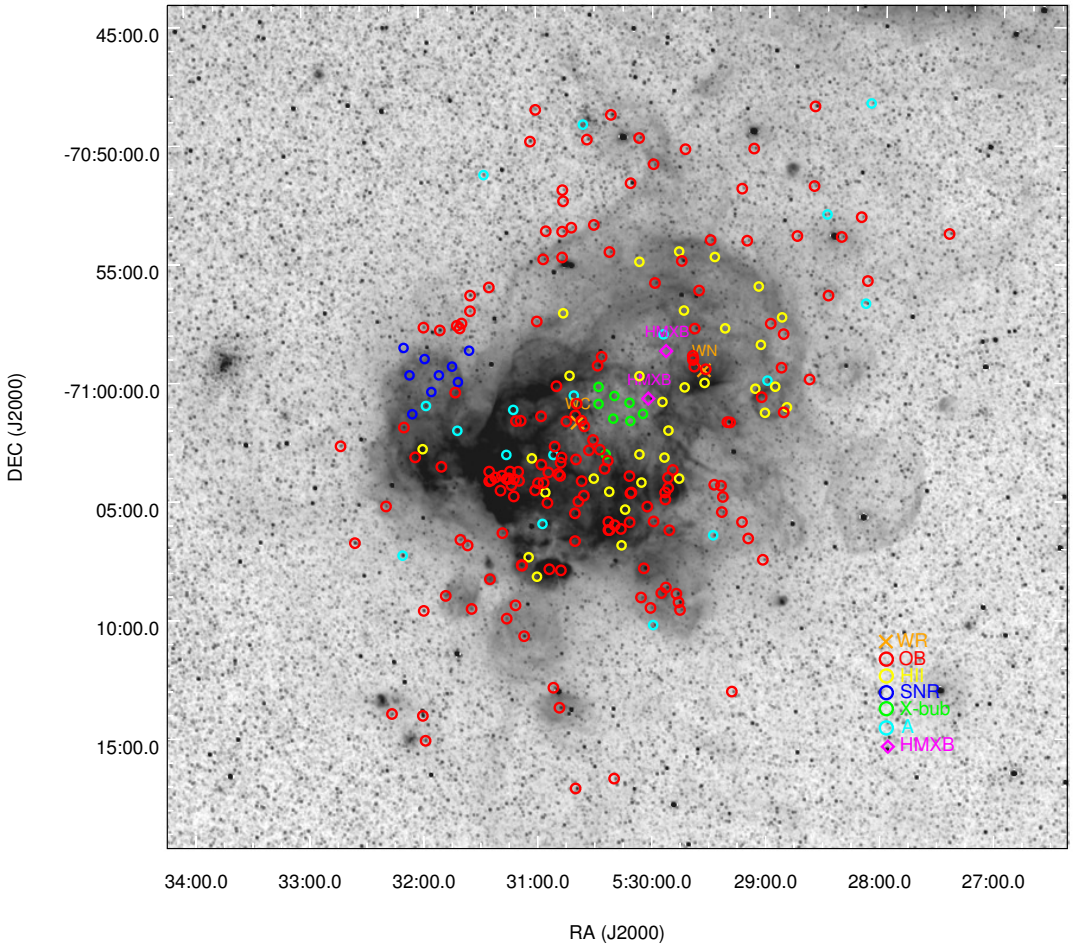

Figure 3.2.: Position of all VLT-FLAMES MEDUSA fibers on the N 206 complex, including the OB-type stars (red circle), WR (orange cross), H II region (yellow circle), SNR (blue circle), X-ray superbubble (green circle), A-type stars (cyan circle), and candidate HMXBs (magenta diamond). The background image shown is Hα emission from the Magellanic Cloud Emission-Line Survey (MCELS, Smith et al. 2005).

detail. In terms of brightness and youth, OB stars are excellent tracers of star formation. Their feedback effects can also lead to sequential star formation in these regions (Gouliermis et al. 2008; Smith et al. 2010; Chen et al. 2007). Therefore, the quantitative spectroscopy of OB star populations associated with superbubbles is essential to provide constraints on their fundamental parameters. By analyzing the massive star content of N 206 using sophisticated model atmospheres, we can derive the stellar and wind parameters of the individual stars as well as their ionizing fluxes. This, in turn, will enable us to compare the energy budget of the cluster with the energy stored in the X-ray superbubble.

This is the second paper in the series that presents the spectroscopic analysis of the entire massive star population in the N 206 superbubble. In the first paper of the series, we focused on the Of-type stars (Ramachandran et al. 2018a, hereafter Paper I). Here we present the spectroscopic analysis of all remaining massive stars in this region, and finally discuss the total stellar feedback and the energy budget of the superbubble.

Section 3.2 briefly describes the spatial structure of the complex. The spectroscopic observations and spectral classifications are presented in Sections 4.2 and 4.2. In Sect. 4.3 and Sect. 3.6, we quantitatively analyze the OB star spectra and the Wolf-Rayet (WR) binary spectra using Potsdam Wolf-Rayet (PoWR) atmosphere models. In Sect. 3.7, the results are presented and discussed. The final Sect. 3.8 provides a summary and general conclusions. The Appendices encompass tables with all stellar parameters and figures with the spectral fits of the analyzed stars.

3.2. Spatial structure of the N 206 complex

A color composite image of the N 206 superbubble in Hα (red), O III (green), and in 0.3 − 1 keV X-ray (blue) is shown in Fig. 3.1. The Hα emission basically traces the H II region in the complex. The entire structure is distributed over an approximately circular region with a diameter of ≈32′, corresponding to 465 pc. The complex encompasses an X-ray superbubble, a supernova remnant (SNR), the young cluster NGC 2018, and the OB associations LH 66 and LH 69.

The superbubble has been studied by many authors using Chandra and *XMM-Newton* data. It has a circular shell of diameter ≈ 8′ (120 pc). The brightest Hα emission originates in the eastern and southern sides of the bubble (Dunne et al. 2001). According to Dunne et al. (2001), the brightest X-ray emitting region of the superbubble is confined by an Hα structure. A soft diffuse X-ray emission is detected across both the remnant and the superbubble. Kavanagh et al. (2012) noticed that no X-ray emission is detected from the major part of the superbubble region, and the hot X-ray emitting gas is distributed in a non-uniform manner.

The X-ray superbubble is surrounded by and overlaps with the young cluster NGC 2018 and the OB associations LH 66 and LH 69. This region contains 41 OB stars including four Of-type stars (N206-FS 111, 131, 162, and 178 analyzed in Paper I). Two WR binaries are present in the N 206 complex. The WC binary is located nearly at the center and the WN binary near the edge of the X-ray superbubble. The OB associations LH 66 and LH 69 occupy an approximately circular region of 3.3′ and 4.8′ in diameter. They harbor 12 and 29 OB stars, respectively. The entire LH 69 OB association is located within the boundaries of the X-ray superbubble region. The young cluster NGC 2018 is very bright in Hα. The emission spans over a region of ≈ 2′ in diameter. This cluster encompasses 14 OB stars, mostly young O stars including three Of-type stars (N206-FS 180, 187, and 193).

The 30 pc×30 pc SNR B0532-71.0 is located on the eastern side of the nebular complex and has a faint circular Hα shell (Dunne et al. 2001). Williams et al. (2005) have done a detailed study of this SNR in X-ray and radio. Their estimate of the thermal energy would yield an initial explosion energy of 8×10^{50} erg. They estimated the age of the SNR to be in the range of 17 000-40 000 years.

3.3. Spectroscopy

The presented study is largely based on spectroscopic data obtained with the Fiber Large Array Multi-Element Spectrograph (FLAMES) at ESO-VLT. Accounting for a typical color excess of $E_{B-V} \approx 0.1 - 0.2$ mag, implying an extinction of $A_V \approx 0.3 - 0.6$ mag, we targeted the blue hot stars (i.e., with spectral subtypes earlier than B2V) by selecting all sources with $B - V < 0.20$ mag and $V < 16$ mag. Therefore, for spectral types later than B2V our sample is incomplete. Apart from this, a few blue stars in the dense parts of the region were missed because the allocation of the Medusa fibers is constrained by the physical size of the fiber buttons. More details of the

observations and the data reduction are given in Paper I. In total, 2918 spectra (including multiple exposures) were normalized, co-added, and cleaned for cosmic rays. The final spectra refer to 234 individual fiber positions as indicated in Fig. 3.2. The sample of spectra consists of:

- Nine Of stars (analyzed in Paper I)
- 155 other OB-type stars (see Sect. 4.3)
- 17 A-type stars (not considered in this work)
- Two WR binaries WN+O and WC+O, see Sect. 3.6
- Two candidate high mass X-ray binary (HMXB) positions (see Sect. 3.7.6)
- 32 fiber positions in the H II region (not considered in this work)
- Eight fiber positions in the X-ray superbubble (not considered in this work)
- Nine fiber positions in the SNR (not considered in this work).

From the fibers that have been placed at the diffuse background, one can extract and analyze the nebular emission lines. This will be subject to a separate study.

All the objects observed in this survey are labeled by a prefix N206-FS (N 206 FLAMES Survey) along with a number corresponding to the ascending order of their right ascension (1–234). We identified and analyzed all the OB-type stars among them. Their coordinates and spectral types are listed in Table 1. More details on the spectral classification schemes are given Sect. 4.2.

Apart from the VLT optical spectra, eight of the OB stars in our sample have available UV spectra in the Mikulski Archive for Space Telescopes (MAST[1]). The stars N206-FS 58, 60, 65, 93, and 134 have available Hubble Space Telescope (HST) /STIS (Space Telescope Imaging Spectrograph) spectra. These were taken with the far ultra-violet Multi-Anode Microchannel Array (FUV-MAMA) detector (G140L grating), with 25×25 arcsecond square field of view (FOV), operating in the near ultraviolet from 1140 to 1730 Å. We retrieved an IUE (International Ultraviolet Explorer) short-wavelength spectrum in the wavelength range 1150–2000 Å from the archive for the star N206-FS 147, which is taken with a large aperture ($21'' \times 9''$). We also used available far-UV FUSE (Far Ultraviolet Spectroscopic Explorer) spectra of the stars N206-FS 90 and 119 in the wavelength range 905–1187 Å, taken with a medium aperture ($4'' \times 20''$). It should be noted that the UV spectra from the archive are flux-calibrated, while our VLT-FLAMES spectra are not.

The WR binary N206-FS 128 has available FUSE, IUE short, and IUE long (2000–3200 Å) spectra. Additionally, a FOcal Reducer/low dispersion Spectrograph 2 (FORS2) spectrum in the 4590–9290 Å wavelength range is available from the ESO archive.

In addition to the spectra, we used various photometric data from the VizieR archive to construct the spectral energy distribution (SED). UV and optical (U, B, V, and I) photometry was taken from Massey (2002), Zaritsky et al. (2004), Girard et al. (2011), and Zacharias et al. (2012). The infrared magnitudes (JHK_s and *Spitzer-IRAC*) of the sources are taken from the catalogs Kato et al. (2007), Bonanos et al. (2009), and Cutri et al. (2012).

[1] http://archive.stsci.edu/.

Table 3.1.: Coordinates and spectral types of OB stars in our sample

N206-FS #	RA (J2000) (°)	DEC (J2000) (°)	Spectral type
1	81.861792	-70.896000	B1.5 V
3	82.036292	-70.929639	B2.5 IV
5	82.050750	-70.884806	B1 V
6	82.093167	-70.898833	B2.5 IV
7	82.120750	-70.940083	B0.5 V
9	82.151542	-70.807222	B1.5 (III)e
10	82.152417	-70.863194	B0.5 V
11	82.160250	-70.999139	B2 IV
12	82.188458	-70.898389	B2.5 IV
14	82.215750	-71.022361	B2 (IV)e
15	82.216792	-70.967389	B2.5 IV
17	82.221000	-70.990972	B2 IV
19	82.244750	-70.960083	B2.5 IV
22	82.259167	-71.126028	B2.5 V
23	82.263500	-71.011778	O8 V
27	82.282167	-70.837083	O9.5 IV
28	82.291167	-71.111111	B7 IV
29	82.296208	-70.901861	B5 IV
30	82.304833	-71.099583	B0.5 V

Notes. Continues in Table B.1.

3.4. Spectral classification

The spectral classification of OB stars is primarily based on the blue optical wavelength range. We mainly follow the classification schemes proposed in Sota et al. (2011), Sota et al. (2014), and Walborn et al. (2014).

3.4.1. O stars

We identified 31 O stars in the whole sample (excluding the nine Of stars described in Paper I). The main diagnostic line ratios used for their subtype classification are He I λ4388/ He II λ4542, He I λ4144/ He II λ4200 and He I λ4713/ He II λ4686. An example of an O star spectrum is shown in Fig. 3.3 (a).

The luminosity-class criteria of O stars are mainly based on the strength of He II 4686. Two O supergiants are identified in the sample, N206-FS 90 and N206-FS 134. Absent or very weak He II λ4686 absorption together with Hα emission reveals their supergiant nature. The Si IV absorption lines are very strong in these spectra. Compared to these objects, N206-FS 62 and N206-FS 192 have stronger He II λ4686 absorption, and therefore are classified as giants. Additionally, these spectra are contaminated with disk emission, suggesting their Oe nature. Furthermore, two main sequence O stars are also identified with Oe features.

We found six stars that exhibit special characteristics typical for the Vz class, namely, N206-FS 64, 107, 145, 154, 184, and 198. According to Walborn (2006), these objects may be near

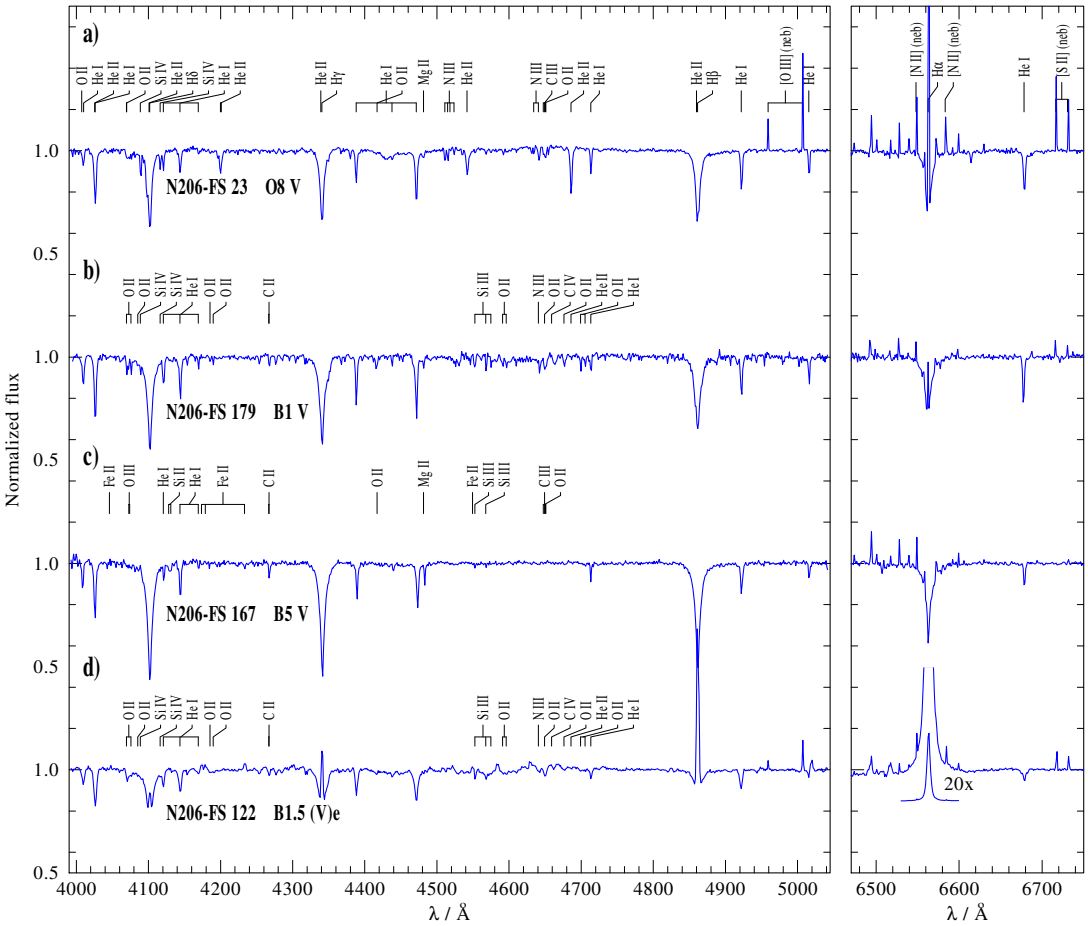

Figure 3.3.: Example spectra of O, early B, late B, and Be stars in the N 206 superbubble. The [O III], [N II], and [S II] lines are from nebular emission (neb).

or on the zero-age main sequence (ZAMS). As described in Walborn et al. (2014), the main characteristic of the Vz class is the prominent He II λ4686 absorption feature that is stronger than any other He line in the blue-violet region.

3.4.2. Early B stars

Stars with spectral subtype B0 to B2 are considered as early B stars in this paper. We identified 102 such stars in the whole sample. The main classification schemes for B stars are taken from Evans et al. (2015) and McEvoy et al. (2015). The classification is based on the ionization equilibrium of helium and silicon. The spectral subtypes are mainly determined from Si III λ4553/ Si IV λ4089 line ratio and the strength of He II λ4686, He II λ4542, and Mg II λ4481. An example of an early B-type spectrum is shown in Fig. 3.3 (b). Here the Si III lines are stronger and the He II lines are weaker than in the O star spectrum in Fig. 3.3 (a).

For B stars, luminosity classes were mainly determined from the width of the Balmer lines

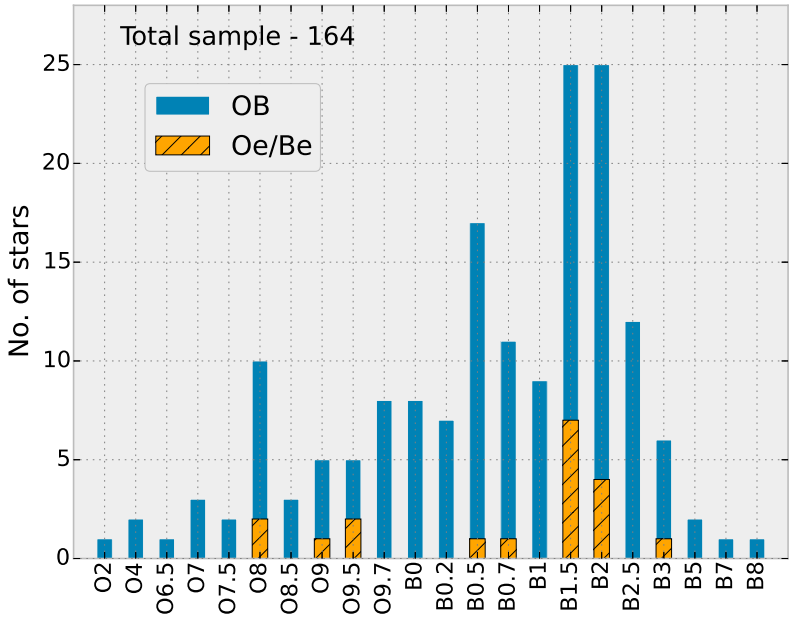

Figure 3.4.: Spectral subtype distribution of all OB stars in our sample. For each spectral subtype, the number of included Oe/Be star is represented in a different color.

and from the intensity of the silicon absorption lines (Si IV and Si III). The B supergiants and bright giants show rich absorption-line spectra. For more details on the luminosity and subtype classification, we refer the reader to Table 1 and Table 2 of Evans et al. (2015).

3.4.3. Late B stars

Stars with spectral subtypes ranging from B2.5 to B9 are considered as late B stars in this paper. We identified a total of 22 such objects. It should be noted that this sample is not complete because of its color and magnitude cut-offs (see Sect. 4.2). The main diagnostic lines for late B stars are Si II $\lambda\lambda$4128-4132. We used the line ratios of Si II $\lambda\lambda$4128-4132 to He I λ4144 and of Mg II λ4481 to He I λ4471 for classifying their spectral subtypes. An example of a late B-type star (B5 V) is shown in Fig. 3.3 (c).

3.4.4. Oe/Be stars

The characteristic features of Oe/Be stars are the strong and broad emission of Hα and other Balmer lines (see Fig. 3.3(d)), which are attributed to a circumstellar decretion disk (Struve 1931) fed by the ejected matter from the central star. We identified 19 such disk-originating emission-line stars in the whole sample, where five of them are classified as Oe stars (including the Oef star in Paper I). Among this Oe/Be sample, three stars are giants or bright giants, while the rest are dwarfs. Most of the Be stars have spectral subtype B1.5–B2.

Thus, the fraction of Oe/Be stars in this region is ~12%. Since the Be stars have a transient nature and the emission line profiles are usually variable, this fraction is just a lower limit. According to

McSwain et al. (2008), approximately 25 to 50% of the Be stars may go undetected in a single epoch spectroscopic observation.

The Hα and Hβ lines of these Be stars also show different profiles depending on the disk viewing angle (see Rivinius et al. 2013, for more details). Seven stars (N206-FS 9, 119, 121, 122, 181, 192, 233) show Hα and Hβ line profiles close to pole-on view. All the other twelve Oe/Be stars show line profiles that indicate higher inclinations because the Hα and Hβ emission lines are double-peaked. Four of these stars (N206-FS 62, 113, 186, 192) additionally show characteristics of B[e] stars, defined by Balmer lines in emission plus forbidden emission lines (Lamers et al. 1998).

A histogram of the spectral types of all investigated stars in the superbubble N 206 (including the Of stars from Paper I) is shown in Fig. 4.2. The number of stars gradually increases with spectral subtypes starting from O2, until B2. One exception is a local maximum at spectral subtype O8. The most populated spectral subtypes are B1.5 and B2. The sudden decrease in the number of stars towards later B subtypes is due to the incompleteness of the sample.

3.5. Analysis of OB stars

We performed spectral analyses of all OB stars in our sample, determining their physical parameters. This was achieved by reproducing the observed spectra with synthetic spectra, calculated with the Potsdam Wolf-Rayet (PoWR) model atmosphere code.

3.5.1. The models

The PoWR code for expanding stellar atmospheres is an advanced non-local thermodynamic equilibrium (non-LTE) code that accounts for mass loss, line blanketing, and wind clumping. It can be employed for a wide range of hot stars at arbitrary metallicities (e.g. Hainich et al. 2014, 2015; Oskinova et al. 2011; Shenar et al. 2015), since the hydrostatic and wind regimes of the atmosphere are treated consistently (Sander et al. 2015). The non-LTE radiative transfer is calculated in the co-moving frame. Any model can be specified by its luminosity L, stellar temperature T_*, surface gravity g_*, and mass-loss rate $\dot{M}$ as main parameters.

In the subsonic region, the velocity field is defined such that a hydrostatic density stratification is approached (Sander et al. 2015). In the supersonic region, the wind velocity field $v(r)$ is pre-specified assuming the so-called β-law (Castor et al. 1975b) with $\beta = 0.8$ (Puls et al. 2008). For establishing the non-LTE population numbers, the Doppler broadening v_{Dop} is set to 30 km s^{-1} throughout the atmosphere. In the formal integration that yields the synthetic spectra, the Doppler broadening varies with depth and consists of the thermal motion and a "microturbulence" $\xi(r)$. We adopt $\xi(r) = max(\xi_{min}, 0.1\, v(r))$ for OB star models with $\xi_{min} = 20$ km s^{-1} (Shenar et al. 2016). For all the OB stars in our study, we account for wind clumping assuming that clumping starts at the sonic point, increases outwards, and reaches a density contrast of $D = 10$ at a radius of $R_{\mathrm{D}} = 10\, R_*$. The models account for complex atomic data of H, He, C, N, O, Mg, Si, P, S, and Fe group elements. More details of the PoWR models used for the analysis of our program stars are described in Paper I.

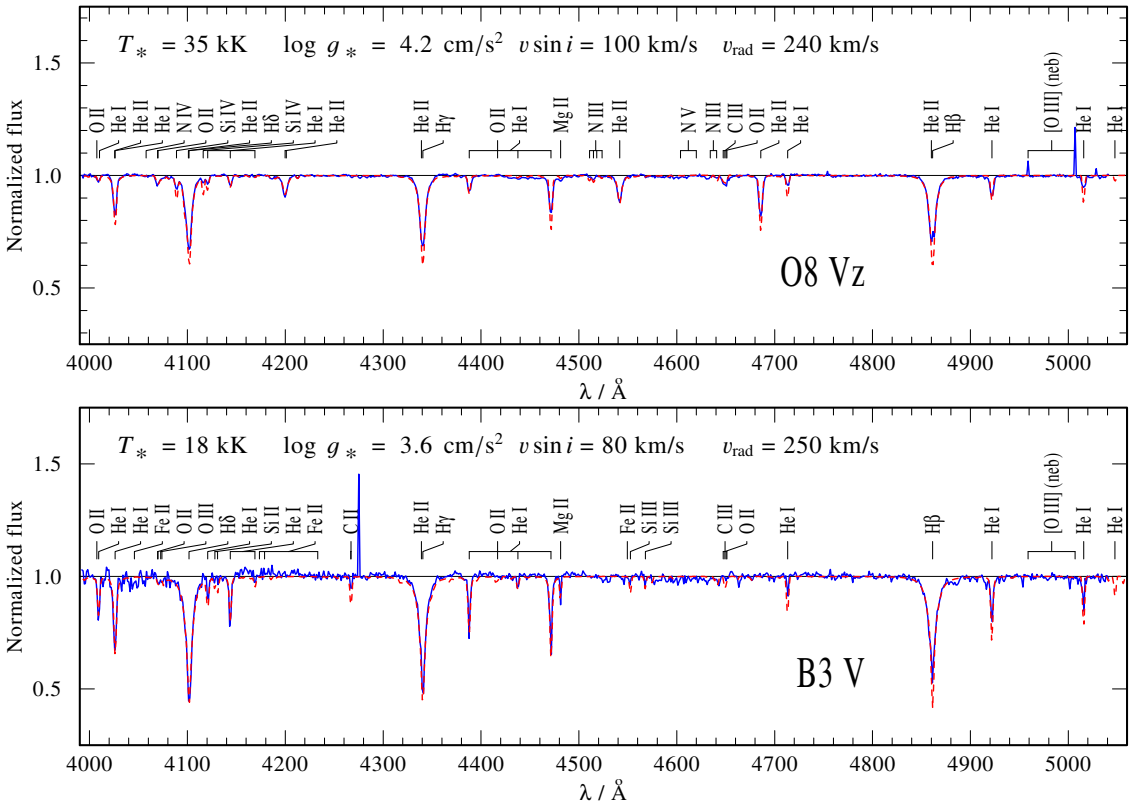

Figure 3.5.: Normalized VLT-FLAMES blue optical spectra (blue solid) for the O star N206-FS 64 (upper panel) and the B star N206-FS 221 (lower panel), respectively. Over-plotted are the synthetic PoWR model spectra (red dashed). The stellar parameters of these best fitting models are given in each panel. The observed spectra are contaminated with nebular emission lines as indicated by "(neb)".

3.5.2. Spectral fitting

We performed the spectral analysis by iteratively fitting the observed spectra with PoWR models. In order to do that, we constructed OB-star grids with the stellar temperature T_* and the surface gravity $\log g_*$ as the main parameters. For the metallicity of the LMC, we adopted the values from Trundle et al. (2007). Since the model spectra of OB stars are mostly sensitive to T_*, $\log g_*$, and L, these parameters are varied to find the best-fit model systematically. The other parameters, namely the chemical composition and the mass-loss rate, are kept constant within the model grids. The stellar mass M and luminosity L in the grid models are chosen according to the evolutionary tracks calculated by Brott et al. (2011). The LMC OB star grid[2], which is also available online, spans from $T_* = 13$ kK to 54 kK with a spacing of 1 kK, and $\log g_* = 2.2$ to 4.4 with a spacing of 0.2 dex. For individual stars, we also calculated models with adjusted C, N, O, and Si abundances when necessary. More details about deriving the stellar and wind parameters are described in the following subsections.

[2] www.astro.physik.uni-potsdam.de/PoWR.html

Effective temperature

We constrain the stellar temperature mainly from the silicon and helium ionization balance. In the temperature range from 20 to 30 kK, the line ratio Si III λ4553/ Si IV λ4089 decreases with an increase in temperature. In the case of hotter stars (>30 kK), the temperature determination is mainly based on the helium line ratios He I λ4388/ He II λ4542, He I λ4144/ He II λ4200 and He I λ4713/ He II λ4686.

For the hottest O stars, where the He I lines are absent or very weak, the temperature diagnostic must rely on nitrogen line ratios (see Paper I). For late B subtypes (13-20 kK), He II lines are absent. The main diagnostic line, in this case, is the multiplet Si II $\lambda\lambda$4128-4132, which increases as the stellar temperature goes down from 20 kK to 10 kK. Furthermore, the line ratio Mg II λ4481 to He I λ4471 increases with decreasing temperatures and is employed for an accurate determination of the stellar temperature in this range.

As examples, the FLAMES spectra of an O star and a B star are shown in Fig. 3.5 together with the corresponding PoWR model. The upper panel shows the spectrum of a typical O star with strong He II lines. The Si IV lines are weak, Si III lines are absent, and the He I/ He II ratio is small indicating a high stellar temperature. The observation is reproduced best by a model with $T_* =$ 35 kK. The lower panel depicts a typical late B star spectrum fitted by a model with $T_*=$ 18 kK. The main indicators are the presence of Si II absorption lines, strong Mg II lines, and weak Si III lines. Here He II is completely absent and the He I lines are prominent (see Fig. 3.5).

The fit procedure usually gives a clear preference for one specific grid model. Hence the uncertainty in the temperature determination is limited by the grid resolution of ±1 kK. However, the uncertainty in log g_* (see below) also propagates to the temperature and leads to a total uncertainty of about ±2 kK.

In the case of Oe/Be stars, the stellar temperature is not of the same precision, because He I, Si III, and Si II lines can be partially filled with emission. Furthermore, the Balmer wings are affected by the disk emission, so that a larger uncertainty in log g_* additionally affects the temperature estimates.

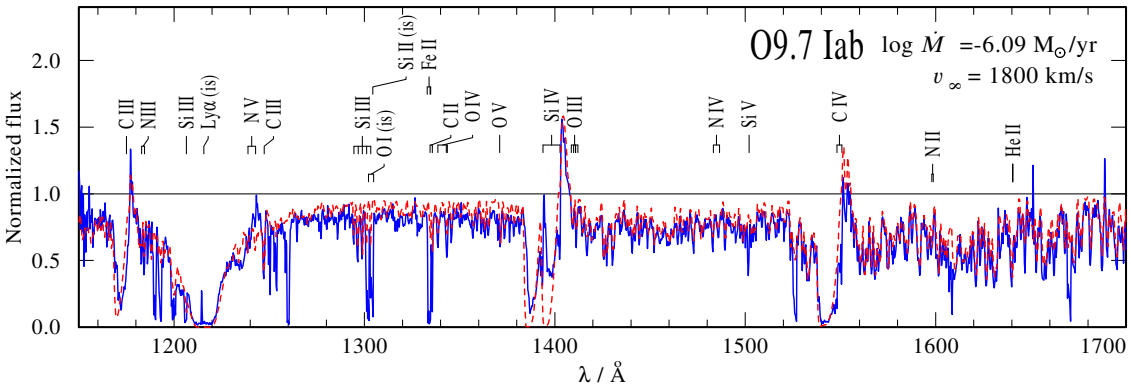

Figure 3.6.: Normalized UV (HST/STIS) spectrum (blue solid line) of an O supergiant (N206-FS 134) is over-plotted with the PoWR model (red dashed line). The wind parameters of this best-fit model are given in the panel. The observed spectrum also contains interstellar absorption lines (is).

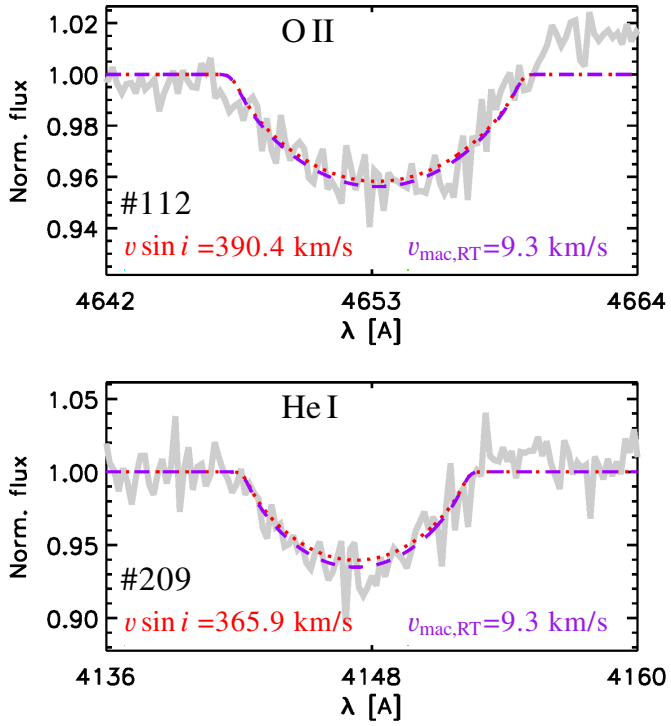

Figure 3.7.: Rotation velocity $v \sin i$ from the line profile fitting of two fast rotating stars (N206-FS 112 and N206-FS 209) in the sample using the `iacob-broad` tool. The gray curves show the observed line profile. The $v \sin i$ is calculated from line profile fitting based on the Fourier transform method (red dotted line) and goodness-of-fit analysis (violet dashed line). See text for more details.

Surface gravity

The Balmer lines are broadened by the Stark effect; we mainly use their wings to measure the surface gravity log g_*. Since the Hα line is often affected by wind emission, Hγ and Hδ are better suited for this purpose. The typical uncertainty for log g_* is ±0.2 dex. For example, the Balmer lines of the star shown in the upper panel of Fig. 3.5 are broad, and the best model fit gives log g_* = 4.2. The Balmer absorption lines in the observation are less deep than in the model because they are partially filled with nebular emission. Similarly, broad Balmer lines of the B-type star in the lower panel are fitted with a model for log g_*= 3.6, since the stellar temperature is much lower for this object compared to an O star.

For the Oe/Be stars in our sample, the methods described above to measure stellar temperature and log g_* are not always successful because the equivalent widths of the Balmer lines may be reduced by disk emission. Therefore, the uncertainty in the surface gravity of these stars is relatively high.

Mass-loss rate

We calculated two model grids: one with a "high" mass-loss rate of $10^{-7} M_\odot\,\mathrm{yr}^{-1}$ and another one with a "low" value of $10^{-8}\ M_\odot\,\mathrm{yr}^{-1}$. The mass-loss rate can be estimated from the P-Cygni

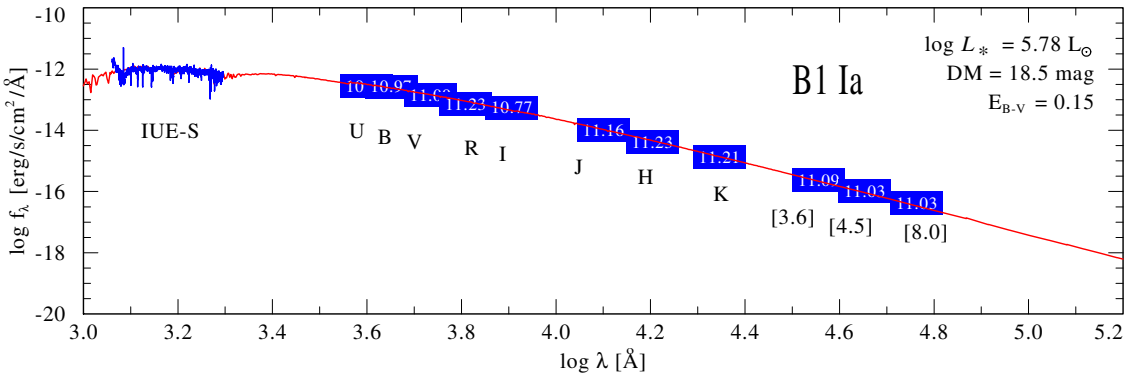

Figure 3.8.: Spectral energy distribution fit of a sample B star (N206-FS 147). The model SED (red) is fitted to the available photometry from optical ($UBVRI$), near-infrared (JHK_s), and mid-infrared ($IRAC$ 3.6, 4.5, and 8.0 μm) bands (blue boxes) as well as the flux calibrated UV spectra from the HST. The luminosity L and the color excess E_{B-V} of the best-fitting model are given in the figure.

profiles of the UV resonance lines. For eight of our sample stars, UV spectra are available. The main diagnostic lines are the resonance doublets C IV $\lambda\lambda$1548–1551 and Si IV $\lambda\lambda$1393–1403 in the HST / IUE range. Useful wind lines in the FUSE range are P V $\lambda\lambda$1118–1128, C IV λ1169, and C III λ1176.

As an example, the UV spectrum of the O supergiant N206-FS 134 is shown in Fig. 3.6. The normalized high-resolution HST/STIS data are fitted with a PoWR model. This spectrum was consistently normalized with the reddened model continuum. The mass-loss rate is estimated to be log $\dot{M}$ = -6.1 [$M_\odot$ yr^{-1}], on the basis of the shown UV fit and in accordance with Hα.

Without UV spectra, the mass-loss rate estimates can only rely on wind emission in Hα and He II λ4686. In case we have UV observations or, at least, the Hα line is in emission, we calculate additional models with adjusted mass-loss rates for the individual stars and precisely determine $\dot{M}$. The error in log $\dot{M}$ is approximately ±0.1 dex if obtained with the help of UV spectra, and ±0.2 dex if only based on Hα and He IIλ4686.

Most of the stars in our sample have neither Hα in emission nor available UV spectra. In these cases, we adopt the "high" mass-loss rate of $10^{-7} M_\odot$ yr^{-1} for the O stars and the"low" $\dot{M} = 10^{-8} M_\odot$ yr^{-1} for B stars and consider these values as upper limits.

Terminal velocity

For stars with available UV spectra, we measured the terminal velocities (v_∞) from the blue edge of the absorption trough of the P-Cygni profiles and recalculated the models accordingly. The main diagnostic P-Cygni profiles are from the doublets C IV $\lambda\lambda$1548–1551, P V $\lambda\lambda$1118–1128, and S V $\lambda\lambda$1122–1134. The typical uncertainties in v_∞ from these measurements are ± 100 km s^{-1}. Figure 3.6 shows an example UV spectrum, where v_∞ is measured from the best fit of the blue edge of C IV $\lambda\lambda$1548–1551 as 1800 ± 50 km s^{-1}. Since this line is saturated, it is not sensitive to clumping.

For those stars for which we have only optical spectra, the terminal velocities are estimated theoretically from the escape velocity $v_{\rm esc}$. The ratio between terminal and escape velocity has been studied for Galactic massive stars both theoretically and observationally and found to be

$v_\infty/v_{\rm esc} \simeq 2.6$ for stars with $T_* \geq 21$ kK, while for stars with $T_* < 21$ kK the ratio is $\approx$1.3 (Lamers et al. 1995; Kudritzki & Puls 2000). The terminal velocity is expected to depend slightly on metallicity, $v_\infty \propto (Z/Z_\odot)^q$, where $q = 0.13$ (Leitherer et al. 1992), and we adopted this scaling to account for the LMC metallicity.

Radial velocity

We measured the radial velocity of all sample stars based on the absorption lines in the VLT-FLAMES spectra. These measurements are performed manually by fitting a number of line centers of the synthetic spectra to the observation. Generally, hydrogen lines are poor indicators for radial velocity measurements, because they are broad, sensitive to wind effects, and possibly affected by nebular emission (Sana et al. 2013b). Metal lines, on the other hand, are very weak in O-star spectra. So, we can use Si and Mg lines to measure radial velocity only in B- star spectra . Mainly, we use the He I lines at 4026, 4387, 4471, and 4922 Å and the He II lines at 4200 and 4541 Å for measuring the radial velocities. Examples can be seen in Fig. 3.5, where the radial velocity for the O star (upper panel) is estimated to be 240 km s^{-1} and for the B star to be 250 km s^{-1} (lower panel).

The typical uncertainty of v_{rad} is about $\pm$10 km s^{-1}. However, in a few cases, where stars have large rotational velocities or the spectra are noisy, the precise determination of the line centers is more difficult and the uncertainty can increase up to $\pm$20 km s^{-1}.

Projected rotational velocity

We constrain the projected rotation velocity $v \sin i$ of all OB stars from the line profile shapes, using the `iacob-broad` tool written in IDL (Simón-Díaz & Herrero 2014). The $v \sin i$ measurements are mainly based on absorption lines in the blue optical wavelengths. We used both implemented methods, the combined Fourier transform (FT) and the goodness-of-fit (GOF) analysis, as described in Paper I.

The primary lines selected for applying these methods are He I, Si IV and Si III. The lines used for measuring $v \sin i$ of O-stars are He I lines at 4026, 4387, 4471, and 4922 Å, and Si IV lines at 4089 and 4116 Å. For B stars, we used He I lines at 4144, 4387, 4471 and 4922 Å, the C II line at 4267 Å, the Mg II line at 4481 Å, Si III lines at 4552 to 4575 Å, the O II line at 4649 Å, and the N III line at 4641 Å.

Figure 3.7 shows rotationally broadened lines from two stars of our sample with the fastest rotation, N206-FS 112 and N206-FS 209 respectively. These stars are rotating close to their critical velocity (approximately 0.7 $v_{critical}$). The typical uncertainty in $v \sin i$ is $\sim 10\%$. Finally, we adopt these measured velocities and convolve our model spectra to account for rotational and macroturbulent broadening. This leads to line profile fits consistent with the observations (e.g., Fig 3.5) in all cases.

Luminosity and reddening

The luminosity L and the color excess E_{B-V} of the individual OB stars were determined by fitting the model SED to the photometry. The model flux is diluted with the LMC distance modulus of 18.5 mag (Pietrzyński et al. 2013). The uncertainty in the luminosity depends on the uncertainty in the color excess (which is typically small for LMC stars), the temperature, and the observed photometry. The total uncertainty is about 0.2 in $\log L$. If flux-calibrated UV spectra (HST, IUE,

Table 3.2.: Main diagnostics used in our spectral fitting process.

Parameter	O stars	Early B stars	Late B stars
T_*	He I/He II line ratios	Si III/Si IV line ratios	Si II/Si III, Mg II/He I line ratios
log g_*	Hγ and Hδ line wings	Hγ and Hδ line wings	Hγ and Hδ line wings
$\dot{M}$	Hα, He II 4686, Si IV 1393–1403	Hα, He II 4686, Si IV 1393–1403	Hα, He II 4686, Si IV 1393–1403
	P V 1118–1128, C IV 1169, C III 1176 C IV 1548–1551	C IV 1548–1551	
v_∞	Hα, N V 1238–1242, C IV 1548–1551	Hα, C IV 1548–1551	Hα, Si IV 1393–1403
	Si IV 1393–1403, P V 1118–1128	Si IV 1393–1403	
$v \sin i$	He I lines, N III 4510–4525	He I lines, N III 4641	He I lines, C II 4267
	Si IV 4089–4116	Si III 4552–4575, O II 4649	Mg II 4481
v_{rad}	He I and He II lines	He I lines, Si III 4552–4575	He I lines, C II 4267, Mg II 4481

or FUSE) are available, this gives additional information on the SED, and the uncertainty in the luminosity is only ≈0.1 dex in these cases.

An example SED fit of a B supergiant is given in Fig. 3.8. The figure shows the theoretical SED fitted to multi-band photometry and flux calibrated UV spectra. We appropriately adjusted the reddening and the luminosity of the model's SED to the observed data. Reddening includes the contribution from the Galactic foreground (E_{B-V} = 0.04 mag) adopting the reddening law from Seaton (1979), and from the LMC using the reddening law described in Howarth (1983) with R_V = 3.2. The total E_{B-V} is a fitting parameter.

Table 3.2 summarizes the main diagnostic lines used for the different aspects of the fitting process. This iterative procedure yields the stellar and wind parameters of the O, early B and late B stars in our sample. In the course of this procedure, individual models with refined stellar parameters and abundances are calculated for each of these stars. The fitting process is iterated until no further improvement of the fit is possible.

Table 3.3.: Stellar parameters of OB stars in N 206

N206-FS #	Spectral type	T_* [kK]	log L [$L_\odot$]	log g_* [cm s^{-2}]	log $\dot{M}$ [$M_\odot$ yr^{-1}]	E_{B-V} [mag]	M_V [mag]	R_* [$R_\odot$]	v_∞ [km s^{-1}]	$v \sin i$ [km s^{-1}]	v_{rad} [km s^{-1}]	M_* [$M_\odot$]	log Q_0 [s^{-1}]	L_{mec} [$L_\odot$]
1	B1.5 V	20.0	4.23	3.6	-7.78	0.18	-3.96	10.9	800	100	280	17	45.7	0.9
3	B2.5 IV	18.0	3.93	3.6	-8.00	0.12	-3.29	9.5	800	130	250	13	45.4	0.5
5	B1 V	25.0	4.06	4.2	-7.78	0.12	-2.67	5.7	2500	100	270	19	46.3	8.7
6	B2.5 IV	20.0	4.13	3.6	-7.85	0.12	-3.50	9.7	800	180	280	14	45.6	0.7
7	B0.5 V	29.0	4.44	4.2	-6.78	0.08	-3.64	6.6	2500	229	240	25	47.2	86.6
9	B1.5 (III)e	20.0	4.48	3.2	-7.00	0.25	-4.20	14.5	600	130	290	12	46.5	3.0
10	B0.5 V	27.0	4.22	4.2	-6.80	0.05	-3.12	5.9	2400	90	250	20	46.6	74.5
11	B2 IV	21.0	4.20	3.8	-7.70	0.10	-3.61	9.5	2000	120	280	21	45.8	6.6
12	B2.5 IV	20.0	4.38	3.6	-7.66	0.24	-3.98	12.9	900	80	260	24	45.9	1.5
14	B2 (IV)e	20.0	4.43	3.6	-7.62	0.18	-4.03	13.7	1000	130	260	27	46.0	2.0
15	B2.5 IV	19.0	3.93	3.8	-8.00	0.13	-3.24	8.5	1000	90	250	17	45.3	0.8
17	B2 IV	20.0	4.33	3.6	-7.70	0.23	-3.71	12.2	900	160	260	22	45.8	1.3
19	B2.5 IV	18.0	4.03	3.4	-7.93	0.12	-3.42	10.7	700	160	280	10	45.4	0.5
22	B2.5 V	20.0	4.13	3.6	-7.85	0.08	-3.29	9.7	800	80	240	14	45.6	0.7
23	O8 V	35.0	4.86	4.2	-6.65	0.24	-3.79	7.3	2500	60	230	31	48.3	115.5
27	O9.5 IV	32.0	4.76	4.0	-6.93	0.20	-4.11	7.8	1900	21	280	22	47.9	35.4
28	B7 IV	14.0	3.86	3.4	-8.11	0.22	-3.47	14.5	800	90	240	19	44.9	0.4
29	B5 IV	17.0	3.60	3.6	-8.15	0.12	-2.78	7.3	700	120	280	8	45.0	0.3
30	B0.5 V	27.0	4.16	4.2	-6.85	0.08	-2.86	5.5	2300	75	250	18	46.6	61.7

Notes. Continues in Table B.2.

3.6. Analysis of WR binaries

The two WR binaries present in this region are analyzed using PoWR models. The detailed analysis of the binary system N206-FS 45 (BAT99 49) with spectral type WN4:b+O will be given in Shenar et al. (in prep.), and we are adopting the derived parameters in this paper. The second binary, N206-FS 128 (BAT99 53), is classified as WC4+O (Bartzakos et al. 2001; Kavanagh et al. 2012). We perform the analysis of this WC star using our LMC-WC grid models[3]. Most of the descriptions of PoWR models given in Sect. 3.5.1 are also applicable in the case of WR stars, with few special aspects as given below.

3.6.1. The model

In the case of WR models, the parameter log g_* is not as important as for OB star models, since the spectral lines originate primarily in the wind. The outer boundary is taken to be R_{max}=1000 R_* for WR models. Accounting for the very strong microturbulence in WR winds, the Doppler velocity is set to 100 km/s (e.g. Hamann et al. 2006). For the velocity law exponent (see Equation 2 in Paper I), we adopt $\beta = 1$ as usual for WR winds.

For the chemical composition of the WC star, we assume mass fractions of 55% helium, 40% carbon, 5% oxygen, 0.1% neon, and 0.07% iron-group elements. For the published WC grid, the terminal wind velocity was set to 2000 km/s. For the WC star in N206-FS 128, we calculated models with higher terminal velocities to fit the spectrum.

3.6.2. Spectral fitting

The observed spectrum is a sum of a WC spectrum and an O star spectrum (see Fig. B.1 and B.2). In order to reproduce this, we add the fluxes of a WC and an O star model. The light ratio is mainly constrained by the strength of the He I absorption features which are clearly associated with the O star component (secondary), while the broad emission features are from the WC star (primary). For fitting the light ratio, we separately adjust the luminosities of both stars, under the constraint that the sum of the fluxes, after reddening, fits the observed SED (see Fig. B.1).

The main diagnostic of the temperature of the WC star is the C III to C IV line ratio. The C IV λ5808 emission is stronger than the C III λ4648 emission. The strong O V line emission also indicates a very high stellar temperature (>100 kK). The best-fit model has a temperature of 158 kK. The terminal velocity is determined to be $\sim$ 3400 km s^{-1}, based on the width of the prominent C III and C IV features in the UV and optical spectra. The clumping contrast D must be chosen as high as 40. With the standard value of $D = 10$ (Sander et al. 2012), the model predicts much stronger electron scattering wings of the blend complex at $\lambda \approx$4686 Å and the C IV line at 7721 Å. Most of the emission lines in the spectra are reproduced by a model with a mass-loss rate of $2 \times 10^{-5}\ M_\odot\ \mathrm{yr}^{-1}$. The effective temperature of the O star, $T_* = 33$ kK, is derived from the ratio between the He I and He II absorption lines.

For the WC component, our final model has a luminosity of log $L = 5.35\ L_\odot$, which is relatively low compared to that of single WC stars in the LMC (Crowther et al. 2002). However, stars of the same spectral type in the Milky Way show such low luminosities (Sander et al. 2012). The O star component has a luminosity of log $L = 5.22\ L_\odot$, which corresponds to luminosity class V.

[3] http://www.astro.physik.uni-potsdam.de/~wrh/PoWR/LMC-WC/.

Table 3.4.: Stellar parameters of WR binaries in N 206

N206-FS #	Spectral type	T_* [kK]	log L [$L_\odot$]	log g_* [cm s^{-2}]	log $\dot{M}$ [$M_\odot$ yr^{-1}]	E_{B-V} [mag]	D	R_* [$R_\odot$]	v_∞ [km s^{-1}]	$v \sin i$ [km s^{-1}]	v_{rad} [km s^{-1}]	M_* [$M_\odot$]	log Q_0 [s^{-1}]	L_{mec} [$L_\odot$]
45[1]	WN4:b	100	5.4	5	-5.4	0.1	10	1.6	1700	-	250	18	49.3	955
	O8 III	33	5.2	3.6	-7.0	0.1	10	12.2	2100	280	250	27	48.8	37
128	WC4	158	5.35	6.0	-4.67	0.1	40	0.6	3400	-	220	13	49.1	20400
	O9 V	33	5.22	3.8	-7.0	0.1	10	11.3	2400	200	220	29	48.5	27

Notes. [1] Parameters are taken from Shenar et al. (in prep.)

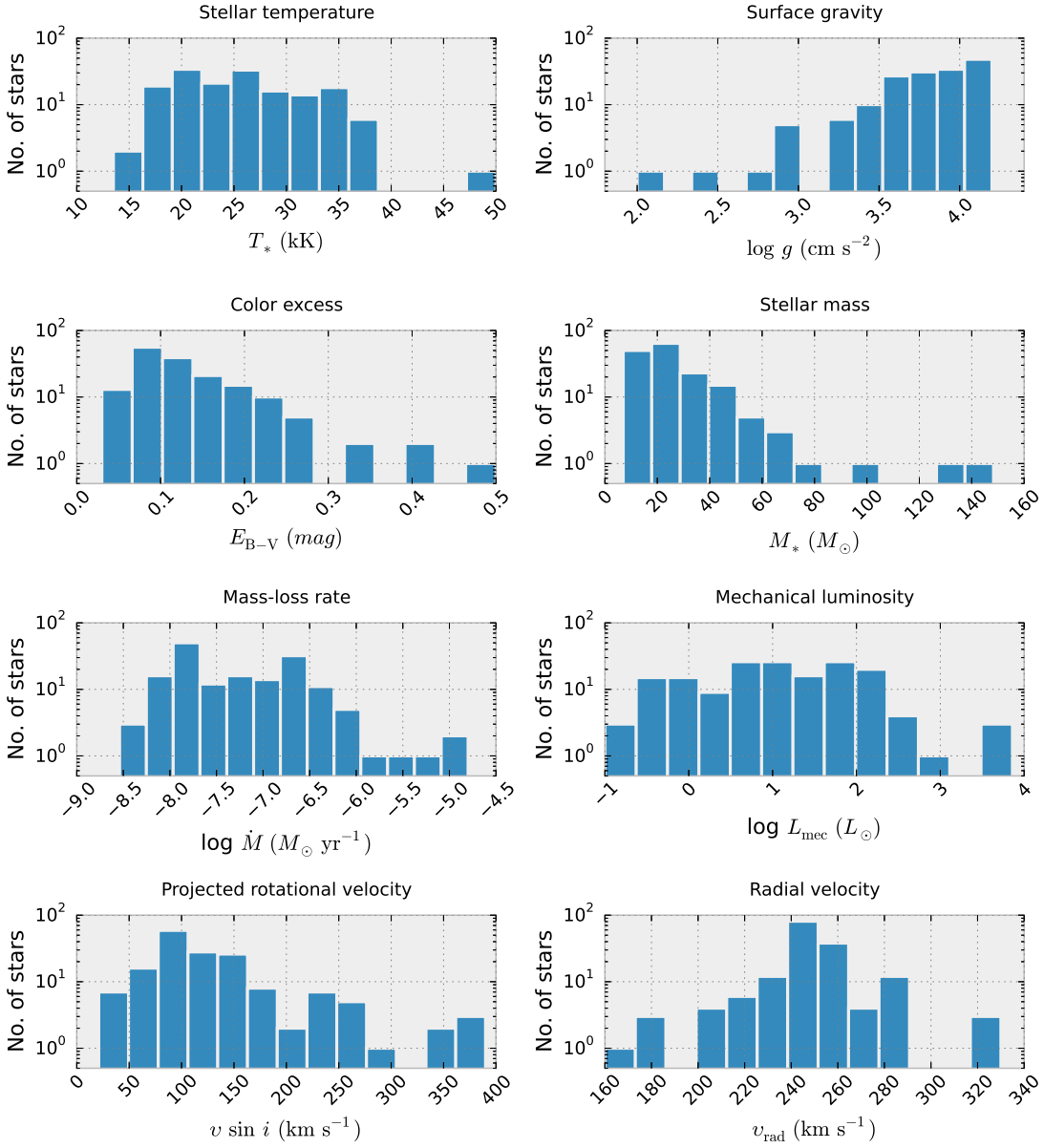

Figure 3.9.: Histograms of stellar temperature, surface gravity, color excess, projected rotational velocity, radial velocity, stellar mass, mass-loss rate, and mechanical luminosity of OB stars in N 206 superbubble. The number of stars in the y-axis are shown in logarithmic scale. We used the square root (of data size) estimator method to calculate the optimal bin width and consequently the number of bins.

3.7. Results and discussions

3.7.1. Stellar parameters

The fundamental parameters for the individual stars are given in Table 3.3. The rate of hydrogen ionizing photons (log Q_0) and the rate at which the kinetic energy is carried away by the stellar winds (mechanical luminosity $L_{\rm mec} = 0.5\,\dot{M}\,v_\infty^2$) are also tabulated. The derived parameters of the WR binaries are compiled in Table 3.4.

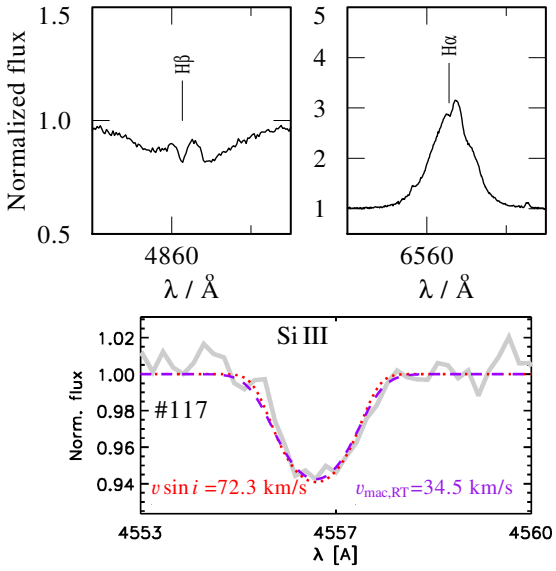

Figure 3.10.: Upper panel shows the Hβ and Hα line profiles of one of the slow rotating Be stars, N206-FS 117. The lower panel shows $v \sin i$ from the profile fitting of the Si III absorption line using the `iacob-broad` tool. The gray curves show the observed line profile. The $v \sin i$ is calculated from line profile fitting based on the Fourier transform method (red dotted line) and goodness-of-fit analysis (violet dashed line).

For the whole sample, we plot histograms for the distributions of stellar temperature, surface gravity, color excess, projected rotational velocity, radial velocity, stellar mass, mass-loss rate, and mechanical luminosity (Fig. 4.5). The stellar temperature of the OB stars (including the Of stars) ranges from 14 to 50 kK. In the surface gravity histogram (Fig. 4.5), most of the stars are found at surface gravities log g_* between 4.0 and 4.2. Only 15% of the stars have $\log g \leq 3.4\,\mathrm{cm\,s^{-2}}$, indicating giants or supergiants. The color excess histogram reveals that most of the stars in the N 206 superbubble have a very low color excess of $E_{B-V} \approx 0.1$. Stars that belong to the young cluster NGC 2018 are found to have comparatively higher extinction, with five cluster members showing $E_{B-V} > 0.25$. These young stars in the cluster are still surrounded by the reminder of their parental cloud. This is consistent with the far infrared Herschel images and CO intensity maps that reveal a distribution of cold dense gas around this cluster (see Fig. 3.27).

The histogram of the stellar masses (Fig. 4.5) refers to spectroscopic masses, calculated from log g_* and R_* ($g_* = G\,M_*\,R_*^{-2}$). These masses vary in the range of $7 - 150\,M_\odot$. The number of objects decreases with increasing mass. We note that the lowest mass bin is not complete.

From the mass-loss rate histogram, we can see that the OB stars in the sample have log $\dot{M}$

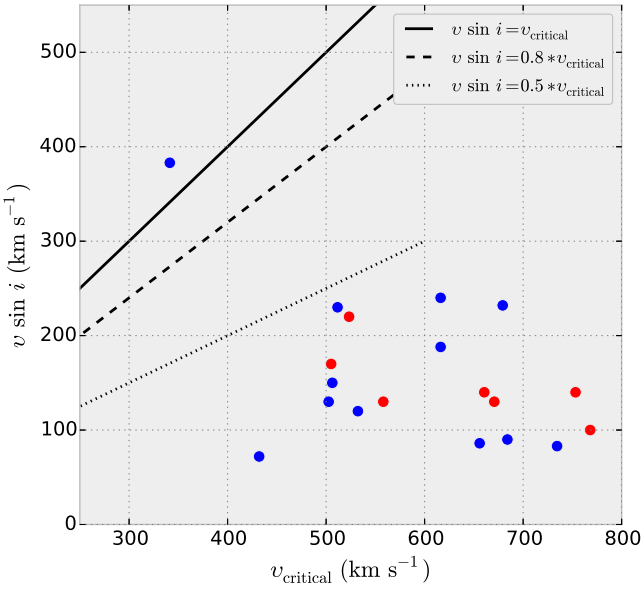

Figure 3.11.: Projected rotational velocity ($v \sin i$) versus critical velocity ($v_{critical}$) of Oe/Be stars. The red dots represent stars with a pole-on view as deduced from the Hβ and Hα line profiles, while the remaining stars are represented by blue dots. The solid, dashed, and dotted lines represent 100%, 80%, and 50% of $v_{critical}$, respectively.

[$M_\odot$yr^{-1}] in the range of −8.5 to −4.8. Stars with the highest mass-loss rates are either super-giants or bright giants. The statistics of the mechanical luminosity, $L_{mec} = 0.5 \dot{M} v_\infty^2$, are also plotted as a histogram in Fig. 4.5. This distribution suggests that most of the OB stars in our sample release $L_{mec} < 20\, L_\odot$ to the surrounding ISM. This is 10 − 100 times lower than the mechanical luminosities of any of the Of stars analyzed in Paper I. The mechanical luminosities of the WR stars are even larger (see below).

Stellar rotation

The distribution of projected rotational velocities ($v \sin i$) covers 30 to 400 km s^{-1} (Fig. 4.5, bottom). Most of the stars have a $v \sin i$ of around ∼100 km s^{-1}. The presence of a low-velocity peak and a high-velocity tail is consistent with studies of other massive star forming regions (Ramírez-Agudelo et al. 2013; Penny 1996).

Fifteen OB stars of the sample are rotating faster than 200 km s^{-1}, and five of them (3%) exhibit very fast rotation with $v \sin i$ in the range 340-400 km s^{-1}. Interestingly, only the Oe star, N206-FS 62, is rotating very fast. All other 18 Oe/Be stars in our sample show only a moderately enhanced rotation with an average $v \sin i$ of about 160 km s^{-1}, while the average for the other B stars is ≈ 120 km s^{-1}. As an example, the line profiles and projected rotational velocity measurements of one of the sample Be stars with slow rotation are shown in Fig. 3.10.

For the Oe/Be stars in our sample, we compared $v \sin i$ with the critical rotational velocity $v_{critical} = (2GM_*/(3R_*))^{0.5}$ (see Fig. 3.11). Interestingly, most of the Oe/Be stars rotate significantly below their critical velocity with $v \sin i \sim (0.1 \ldots 0.5)\, v_{critical}$. Here $v_{critical}$ is calculated from the spectroscopic masses. For a comparison, we also calculated the critical velocities using

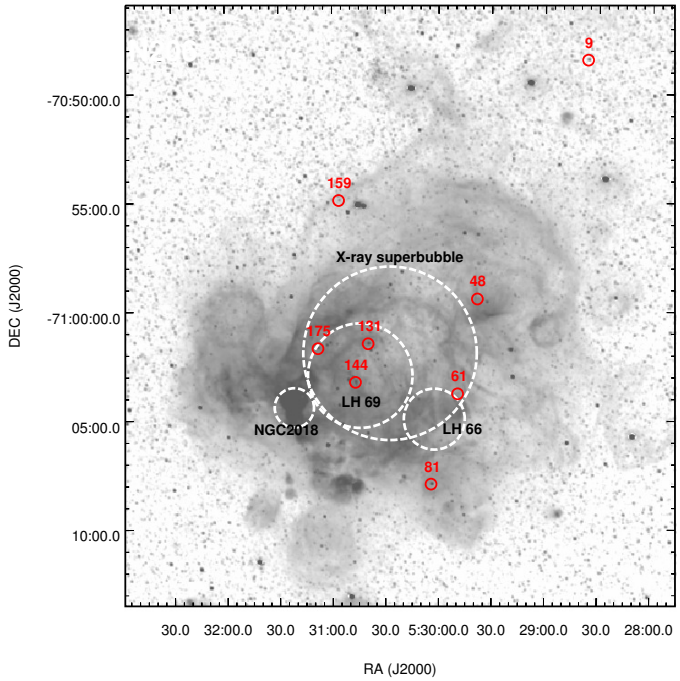

Figure 3.12.: Eight candidate runaway OB stars in the sample. The underlying Hα image is from the Magellanic Cloud Emission-Line Survey (MCELS, Smith et al. 2005).

evolutionary masses, which are generally lower (see Sect. 4.5). Even in this case, 75% of the Oe/Be stars are rotating with $v \sin i < 0.5\, v_{critical}$.

The Oe and Be stars in our sample in general rotate sub-critically. Our result is in line with the statistical study by Cranmer (2005) who concluded that this strongly constrains the physical models of angular momentum deposition in Be star disks. However, many observations of Be stars in the Galaxy and Magellanic Clouds suggest that most of them are rotating at almost their critical velocity (Rivinius et al. 2013; Martayan et al. 2006, 2010).

One possible reason for finding a low $v \sin i$ could be an accidental pole-on view ($\sin i \approx 0$). From inspecting the Balmer emission line profiles, we distinguish between double-peak disk emissions and single peaks. For the latter, one may suggest a low inclination angle. Typically, the disk emission of Hα shows up by double peaks that are separated by up to 4 Å in the case of large inclination. Given the limited spectral resolution of our data, we cannot resolve double peaks with separations below 0.8 Å. Therefore, our category of pole-on stars (red dots in Fig. 3.11) comprises stars with $\sin i \leq 0.2$ corresponding to $i \leq 10°$.

However, the statistically probability of observing an inclination below the angle i scales with $1 - \cos i$. This implies that the chance of catching a star with an inclination $i \leq 10°$ is only about 2%. The likely reason that we find seven out of 19 Oe/Be stars with apparently low inclination is the contamination by nebular emission, so that the double peaks of the Balmer profiles cannot be recognized. Nevertheless, it is puzzling that nearly all Oe/Be stars of the sample with higher inclination also show $v \sin i < 0.5\, v_{critical}$. The only exception is N206-FS 62, which rotates close to its critical velocity.

Table 3.5.: Candidate runaway OB stars in the N 206 superbubble

N206-FS #	v_{rad} (km s^{-1})	v_{rad} - $\bar{v}_{rad}$ (km s^{-1})	spectral type
9	300	52	B1.5 (IV)e
48	180	−68	B0.7 V
61	180	−68	B0.7 V
81	160	−88	B1 II
131[1]	185	−63	O6.5 II (f)
144	320	72	B0 II Nwk
159	320	72	B2 V
175	330	82	B0 III

Notes. (1) One of the Of stars analyzed in Paper I

Radial velocity and candidate runaway stars

The radial velocity of OB stars in our N 206 sample ranges from 160 to 330 km s^{-1} (see Fig. 4.5), with a peak of the distribution at about ~240-270 km s^{-1}. Runaway stars are usually defined by peculiar velocities in excess of 40 km/s (Blaauw 1961) compared to the systemic velocity. Their velocity is either a result of dynamical ejection from a young cluster or of ejection from a binary system due to a supernova.

To identify runaway candidates in our sample, we compared the radial velocity estimates for each star with the mean radial velocity of all program stars and the corresponding standard deviation. By accounting for a threshold of $|\delta v_{rad}| > 3\sigma$, we identify runaway candidates. Then we recalculate the mean velocity and standard deviation excluding these objects, continuing this process until no more stars with $|\delta v_{rad}| > 3\sigma$ remain. We find eight runaway candidates among the total sample. This includes the Of binary N206-FS 131 described in Paper I. All other runaways are early B-type stars. Their positions are marked in Fig. 4.10; their radial velocities as well as the deviation from the mean velocity are given in Table C.3.

The mean radial velocity of the OB stars (excluding the runaway candidates) in this region is found to be ≈248±16 km s^{-1}. This dispersion of ±16 km s^{-1} includes the ±10 km s^{-1} uncertainty of the v_{rad} measurement, meaning that the actual velocity dispersion is smaller. The radial velocities do not show any obvious correlation with spatial structures in the complex.

3.7.2. The wind momentum-luminosity relationship

We quantitatively investigate the wind properties of our sample OB stars by plotting the modified wind momentum-luminosity relation (WLR) and compared our results to previous studies and theoretical predictions. Figure 4.15 depicts the modified stellar wind momentum, which is defined as $D_{\rm mom} \equiv \dot{M} v_\infty R_*$ (Kudritzki & Puls 2000), as a function of the stellar luminosity. The wind momentum of eight stars, which have available UV spectra, and nine OB stars with Hα partially or completely in emission, are empirically determined and plotted in the figure. For all other stars, only an upper limit for the wind momentum can be estimated, as marked by upside-down triangles. A linear regression to the logarithmic values of the modified wind momenta obtained in this work, accounting for the individual error bars, gives a slope of 1.61 ± 0.22, which is less steep than the theoretically predicted slope of 1.83 for LMC OB stars (Vink et al. 2000) given in Fig. 4.15

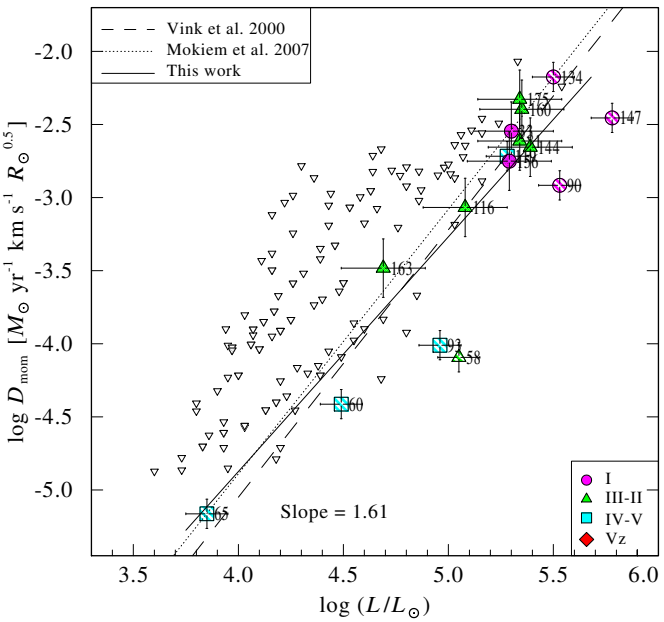

Figure 3.13.: Modified wind momentum ($D_{\rm mom}$) in units of $M_\odot$/yr km s^{-1} $R_\odot^{0.5}$ as a function of stellar luminosity for analyzed LMC OB stars. The filled and hatched symbols are wind momenta determined from Hα or nitrogen emission lines and from UV P-Cygni profiles with individual error bars, while open triangles (up-side down) indicate upper limits. A power-law (solid line) fit to the observations yields a slope of 1.61. The theoretical WLR from Vink et al. (2000) (dashed line) and an empirical WLR from Mokiem et al. (2007a) for LMC stars are also plotted. Luminosity classes are distinguished by different symbols as given in the legend.

(dashed line). The empirical WLR obtained by Mokiem et al. (2007a) for LMC OB stars with a slope of 1.81 is also marked in the figure (dotted line) for comparison. Figure 3.14 shows the WLR of the whole OB star sample including the Of stars from Paper I. This yields a linear regression of

$$\log D_{\rm mom} = (1.82 \pm 0.18) \log (L_*/L_\odot) + (-12.25 \pm 0.95) \tag{3.1}$$

which is close to the theoretical and empirical relations shown.

However, this agreement might be just fortuitous. First of all, the empirical wind momenta show a large scatter. Moreover, they are based on different diagnostics, which have their specific issues. The Balmer line emission is fed by the recombination cascade and therefore subject to the microclumping effect. The empirical mass-loss rate derived from a given observed emission line scales roughly with the square root of the adopted clumping contrast (e.g. Hamann & Koesterke 1998). For our analyses, we adopted a clumping contrast of $D = 10$, while the WLR from Mokiem et al. (2007a) shown in Figs. 4.15 and 3.14 have been obtained with smooth-wind models.

On the other hand, part of our empirical mass-loss rates have been derived from fitting the P-Cygni profiles of UV lines (hatched symbol filling in Figs. 4.15 and 3.14). These resonance lines are not affected by microclumping, but here the usual neglect of macroclumping ("porosity") can lead to an underestimation of mass-loss rates (Oskinova et al. 2007).

Another uncertainty refers to the actual metallicity of the individual stars. The theoretical prediction from Vink et al. (2000) has been calculated for a canonical LMC metallicity of 0.5

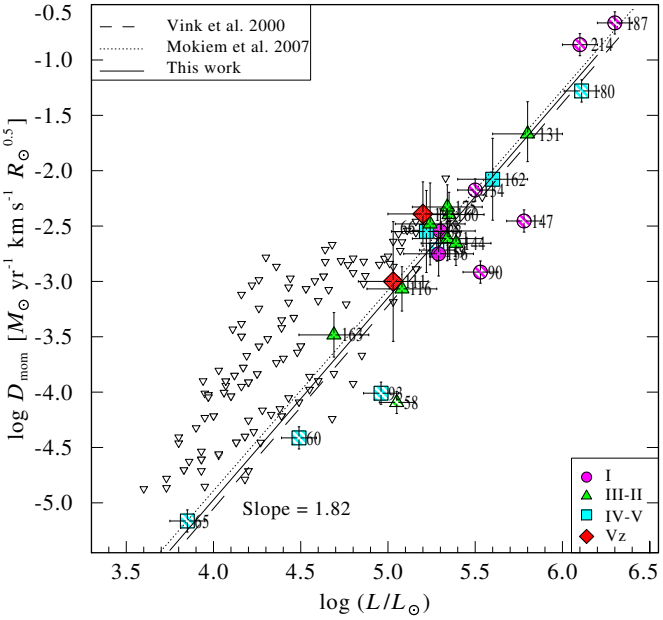

Figure 3.14.: Same as Fig. 4.15, but including the Of stars from Paper I.

solar. Our young stars, and especially the two most luminous Of stars in our sample, might have formed already with higher metallicity. Our spectral data allow only very limited abundance measurements, and the total metallicity cannot be precisely determined. On the other hand, Vink mass-loss rates have been often found to over-predict $\dot{M}$ by about a factor of two for early OB-type stars (e.g. Šurlan et al. 2013) and by more than an order of magnitude for late OB-type stars (Martins et al. 2009; Shenar et al. 2017).

3.7.3. OB stars in the Hertzsprung-Russell diagram

The evolutionary status of all hot OB stars in the N 206 complex are investigated using the Hertzsprung-Russell diagram (HRD). Figure 4.13 shows our sample of OB stars with the effective temperatures and luminosities as given in Table 3.3. The nine 'Of stars' from Paper I are also included.

The evolutionary tracks and isochrones are adapted from Brott et al. (2011) and Köhler et al. (2015), which were calculated for an initial rotational velocity of $\sim 100\,\mathrm{km\,s^{-1}}$. This seems roughly adequate since the $v \sin i$ histogram in Fig. 4.5 revealed an average of $\sim 126\,\mathrm{km\,s^{-1}}$. The evolutionary tracks are shown for stars with initial masses of $5 - 100\ M_\odot$, while the isochrones are shown for ages of 0, 1, 2, 3, 4 5, 7, 10, 20, and 30 Myr, respectively.

Figure 4.13 shows that most of the O stars have ages between 1 and 7 Myr, with initial evolutionary masses ranging from 15 to 40 $M_\odot$. In the case of B stars, ages extend from 5 to 30 Myr. Interestingly, most of the Be stars are close to the terminal age main sequence as indicated by the loops in the evolutionary tracks.

The most massive stars in our sample (N206-FS 180, N206-FS 187, and N206-FS 214) are the youngest ones. This supports a scenario described in Bouret et al. (2013), where the most massive stars of the cluster form last, and after their formation, they quench subsequent star formation. However, our finding could also be due to the V-magnitude ($V < 16$ mag) cut-off of the sample,

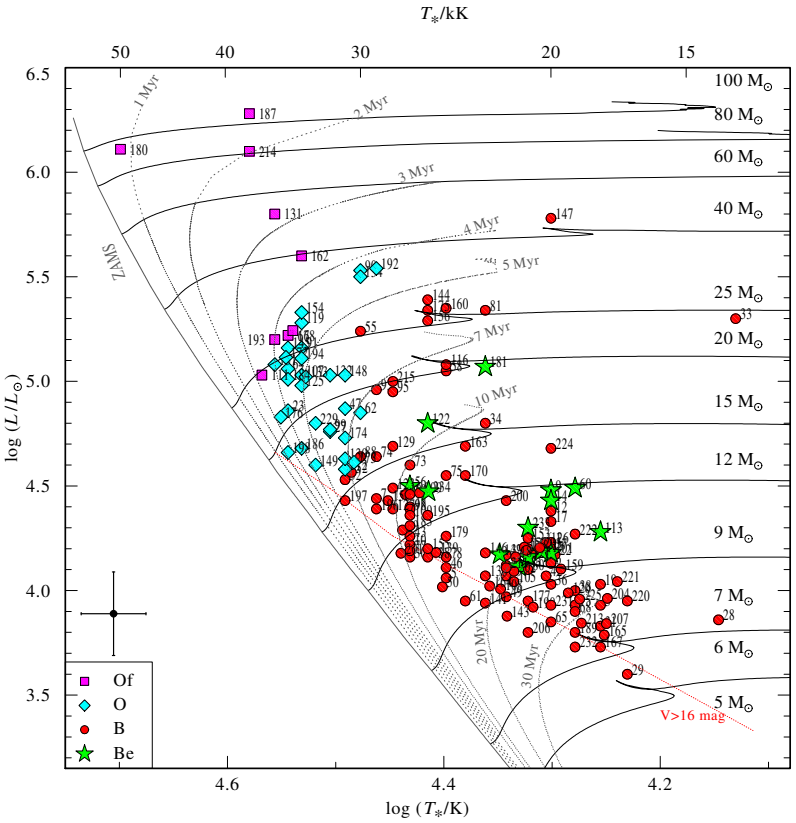

Figure 3.15.: Hertzsprung-Russell diagram for OB stars in the N 206 superbubble in the LMC. The nine Of stars from Paper I are also included. The evolutionary tracks (thin solid lines) are labeled with their initial mass. Isochrones are represented by gray dotted lines. Tracks and isochrones are based on evolutionary models accounting for rotation with $v_{\rm rot,init} \sim 100$ km s^{-1} (Brott et al. 2011; Köhler et al. 2015). Different spectral types are distinguished by different colors and shapes of the symbols (see legend). The typical uncertainties of the stellar temperatures and luminosities are indicated by the error bars in the lower left of the HRD. The red dotted line represents the visual-magnitude cut-off of the observed sample.

since we might miss very young B-type stars.

Figure 3.16 shows also the HRD of the OB stars, but now color-coded with their respective projected rotational velocity. Five fast rotators with $v \sin i$ >300 km s^{-1} (N206-FS 62, 112, 155, 190, and 209) are found to have initial evolutionary masses less than 20 $M_\odot$ (see dark-blue circles in the diagram). The most massive and youngest stars (<5 Myr) are found to be slower rotators than the rest of the sample. Interestingly, one slow rotator (N206-FS 52) with $v \sin i \approx$35 km s^{-1} and the fastest rotator (N206-FS 112) with $v \sin i \approx$390 km s^{-1} fall on nearly the same position in the HRD. However, both of these stars have similar spectral type and mass.

HR diagram of substructures

As discussed above, the empirical HRD indicates a spread of stellar ages rather than a coeval population of OB stars. This raises the question of multiple or progressing star formation throughout

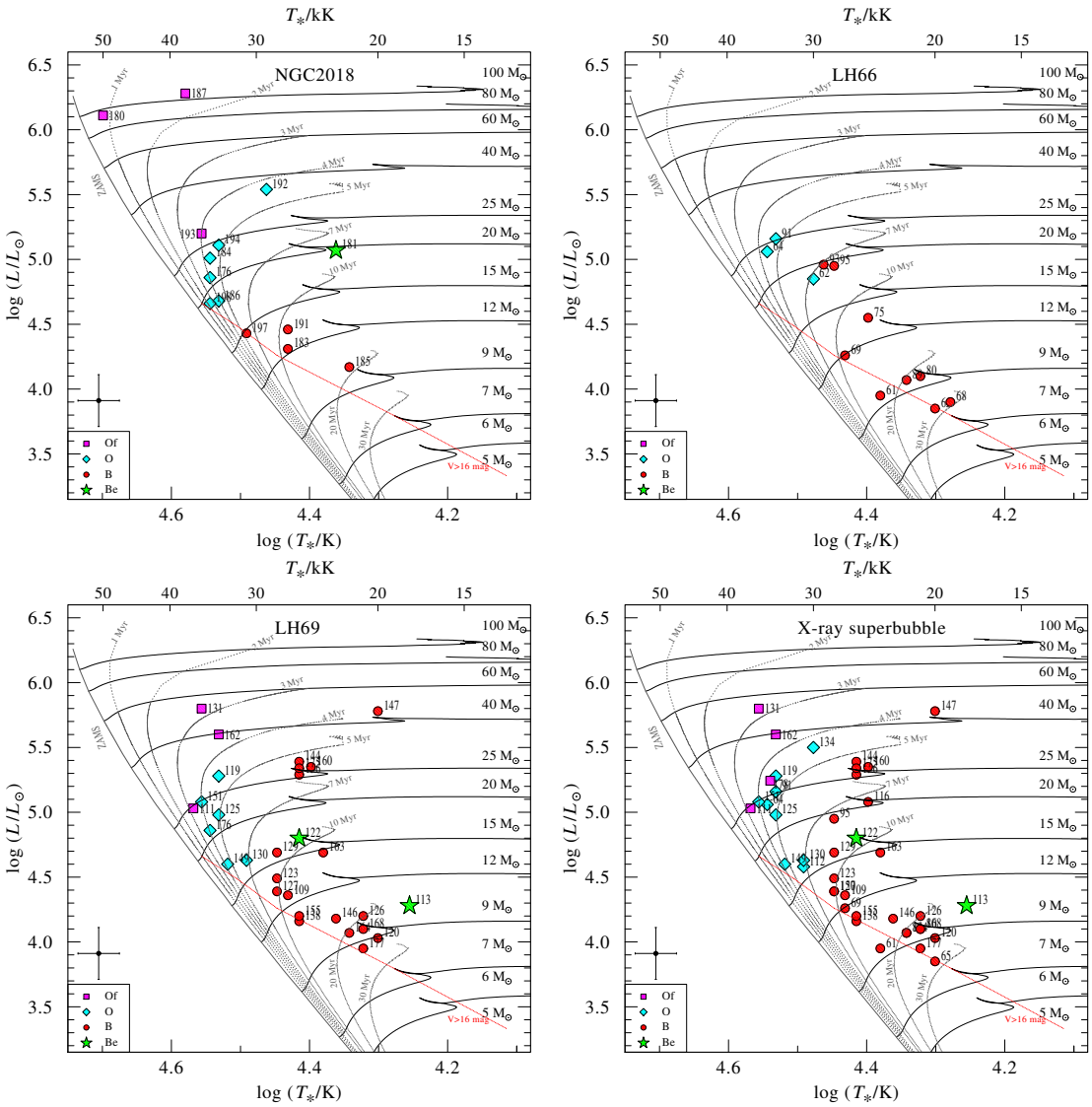

Table 3.6.: Hertzsprung-Russell diagram for stars in subregions of N 206 (circular regions shown for NGC 2018, LH 66, LH 69, and X-ray superbubble in Fig. 3.1). The evolutionary tracks, isochrones, and symbols have the same meaning as in Fig. 4.13.

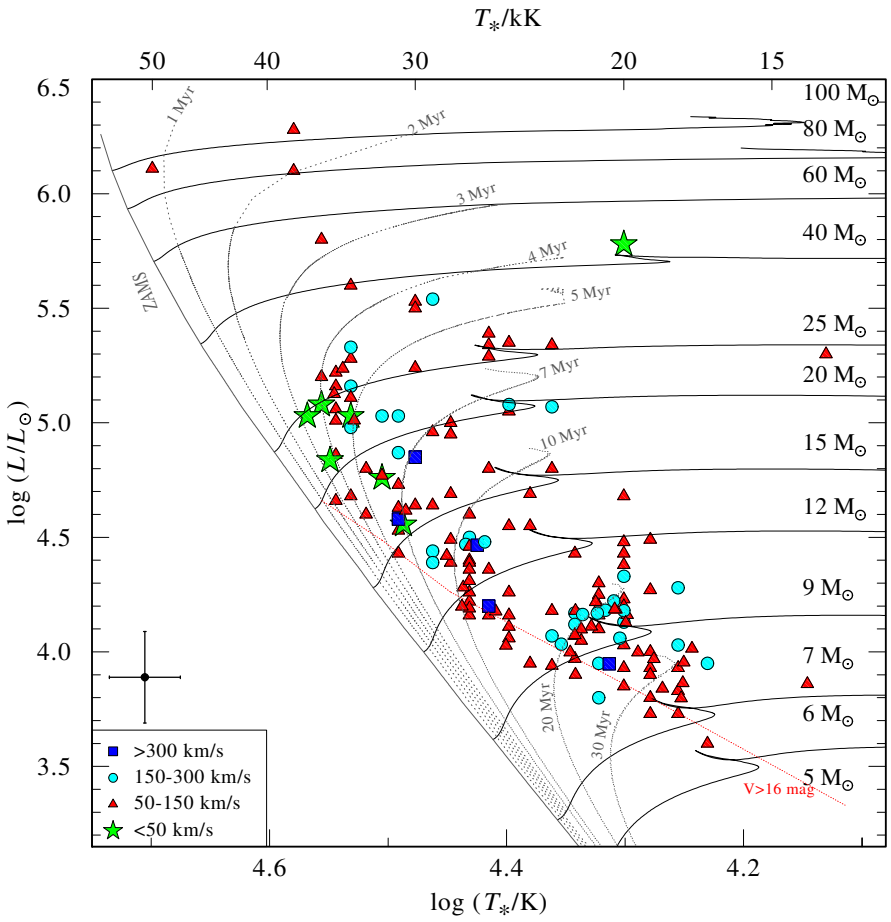

Figure 3.16.: Same as Fig. 4.13 with symbol shapes and colors referring to the projected rotational velocity (see legend).

this large region. Therefore, we split our sample into different spatial regions as given in Fig. 3.1, and plot their respective HRDs (Fig. 3.6).

The upper-left panel refers to the cluster NGC 2018, which contains mostly O stars and especially the three most massive stars of the whole sample. Most of the stars in this cluster fall in the age range of 2 – 4 Myr. The cluster shows a large age dispersion from ≤1 Myr (N206-FS180) to ~20 Myr (N206-FS185).

Most stars in the OB association LH 66 (Fig. 3.6, upper-right panel) have ages in the range 7 – 10 Myr, with no star being younger than 5 Myr. The OB association LH 69 (lower-left panel) contains multiple populations with ages of 4, 5, 10, and 20 Myr. The youngest star in this association is ≤3 Myr old. Most of the stars in LH 69 are part of the somewhat larger X-ray superbubble region, which shows an age dispersion in the range 3 – 30 Myr.

Summarizing this investigation revealed that each of the subregions of the N 206 complex had multiple episodes of star formation over the last 30 Myr. However, only the cluster NGC 2018 formed stars as recently as 1 Myr ago.

The evolutionary status of the WC+O binary N206-FS 128

We compare the HRD positions of the binary components of N206-FS 128 with evolutionary tracks from Eldridge et al. (2008), which account for binary interaction (see Fig. 3.17). These binary tracks are defined by three parameters : the initial mass of the primary $M_{i,1}$, the initial orbital period P_i, and the mass ratio $q_i = M_{i,2}/M_{i,1}$. Using the χ^2 minimization algorithm described in Shenar et al. (2016), we found the best fitting parameters for the binary track to be $M_{i,1} = 35 M_\odot$, $P_i = 10$ days, and $q_i = 0.7$. After 6 Myr of evolution, this binary track reproduces not only the observed HRD positions but also the current surface hydrogen and carbon abundances of both components very well. The current period of the binary system predicted by the model is ≈ 5 days, and thus slightly higher than the observed value of 3.23 days measured by Mowlavi et al. (2017).

According to the best-fitting binary track, the WC component N206-FS 128a started its evolution with an initial mass of $35 M_\odot$ and stayed on the main sequence (pre WR phase) for 5.4 Myr. Before it entered into the WR phase, it had undergone a Roche lobe overflow (RLOF) phase (dashed magenta lines in Fig. 3.17) over ~20,000 years. During this phase, the primary looses more than half of its mass, and the secondary accretes a few solar masses. After this, N206-FS 128a entered the WNL stage with a low hydrogen mass fraction $0 < X_{\rm H} < 0.2$ at the surface. The WNE phase is reached when the surface hydrogen has vanished. When the helium-burning products appear at the surface, the star proceeds to the WC/WO phase.

During the last 0.6 Myr, the primary experienced very high mass loss, which decreased its mass to about $10\,M_\odot$, while the mass of the secondary remained roughly constant. This is the current state of the system, at an estimated age of roughly 6 Myr.

If, hypothetically, the star N206-FS 128a had evolved without mutual interaction with its companion, it would have evolved as represented in Fig. 3.17 by the black dashed line. In that case, the star would end up as a WC star with a higher luminosity.

The secondary, N206-FS 128b, is an O9 star with an initial mass of $25 M_\odot$, which is still in the hydrogen burning stage. The binary track of the secondary does not continue to further evolutionary stages, since the primary explodes as a supernova in a few ten thousand years. After this, the secondary may evolve like a single star of $M = 25 M_\odot$ (see black dashed line in Fig. 3.17).

Evidence for sequential star formation?

In the HRD (Fig. 4.13), we have included the isochrones for evolutionary tracks with an initial rotational velocity of $\sim 100\,{\rm km\,s^{-1}}$(Brott et al. 2011; Köhler et al. 2015). The same models have been used to estimate the ages and evolutionary masses for most of our sample stars as given in Table B.3. However, the adopted initial rotation affects the isochrones and thus the age determination of the individual stars. In order to test this effect, we consider three stars with different measured $v \sin i = 35$, 264, and 390 $\rm km\,s^{-1}$, respectively, but similar HRD positions. (Fig. 3.18). In each of the HRDs we show the matching isochrone for $v_{rot} \sim 100\,{\rm km\,s^{-1}}$. Additionally, we plot an isochrone that is selected from the set of tracks that is more suitable for the respective star according to its measured $v \sin i$. In the first two cases, the difference in the determined age is relatively small (< 0.4 Myr). However, in the case of the rapidly rotating star N206-FS 112, the isochrone corresponding to $v_{rot} = 100\,{\rm km\,s^{-1}}$ yields an age that is higher by about 1 Myr. Therefore, we finally applied isochrones for an initial rotational velocity of $\geq 300\,{\rm km\,s^{-1}}$ for those stars with measured $v \sin i > 300\,{\rm km\,s^{-1}}$ for determining the age and evolutionary mass. The uncertainties in the age are approximately 20-40%, which are due to the uncertainties of the derived parameters (temperature, luminosity, $v \sin i$) as well as uncertainty in choosing the

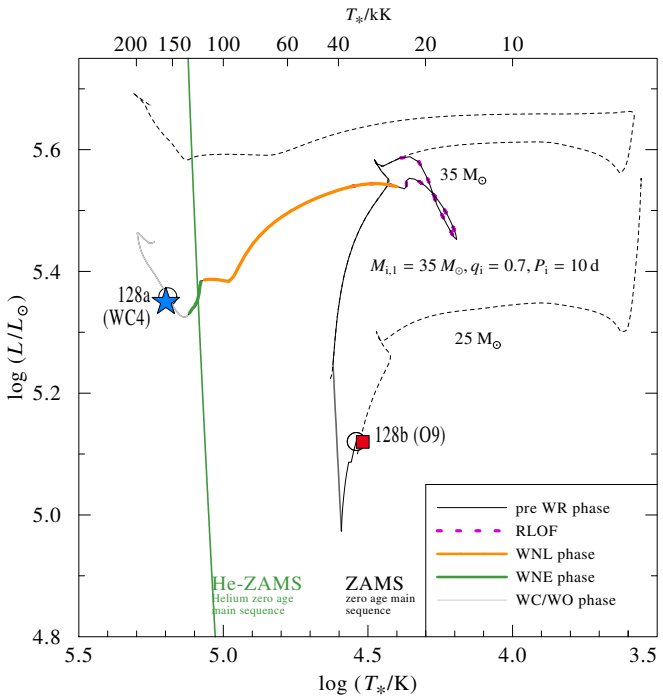

Figure 3.17.: HRD positions of N206-FS 128a (WC4, blue asterisk) and N206-FS 128b (O9, red square). The solid lines represent binary evolutionary tracks from Eldridge et al. (2008) for the respective components. The circles denote the best-fitting positions along the tracks after 6 Myr of evolution. For comparison, the dashed lines show how the components would evolve without mutual interaction. See text for more details

adequate isochrones.

The distribution of ages of all OB stars in our sample is displayed in Fig. 4.17. It clearly shows multiple peaks across stellar ages, with a maximum in the age range 3-7 Myr. From the HRD we can see that the stars in this age range are mostly O stars and B supergiants. So, massive star formation in the N 206 complex must have peaked in this time period. There are also local maxima at ages 10, 20, and 30 Myr populated by B stars.

We checked our results for correlations between stellar ages and location. Figure 3.20 shows the position of the OB stars, color-coded with their respective estimated age. For this purpose, we grouped the stars into four different age categories 0-4 Myr, 4-10 Myr, 10-20 Myr, and above 20 Myr, respectively. We can see that the youngest stars are concentrated in the central parts of the complex, especially in the NGC 2018 cluster. Most of the older OB stars are located in the periphery of the N 206 complex.

To investigating the variation of ages with location, we divided the region into four annuli with radii of 80, 300, 670, and 1300″, respectively, centered at the young cluster NGC 2018. The median of the ages of all OB stars inside each annulus is calculated and plotted in Fig. 3.21. The radial distances are converted from arc seconds to pc using the LMC distance. Interestingly, we can see a clear trend of the age increasing with distance from the cluster center throughout the whole complex.

We propose two possible explanations for this correlation. One is that the star formation process

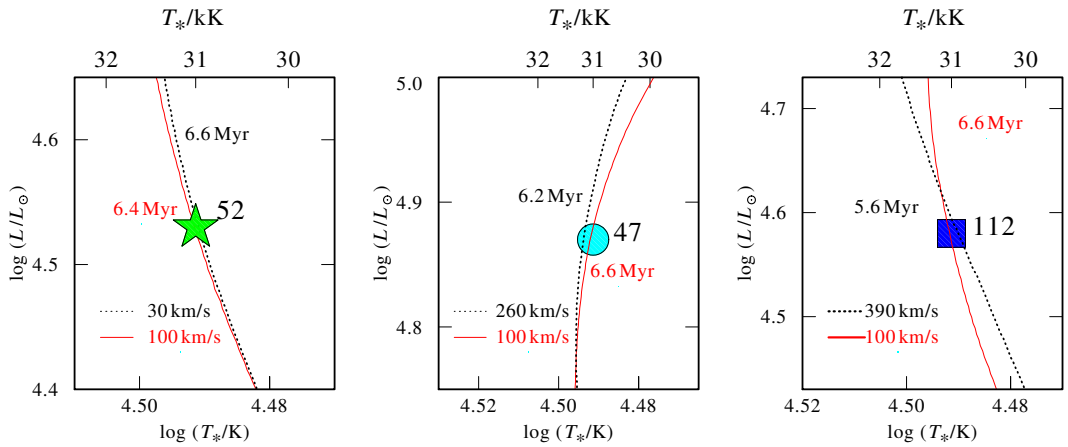

Figure 3.18.: Effect of adopted initial rotation velocity on age determination. The HRDs of N206-FS 52 ($v \sin i \approx 35\,\mathrm{km\,s^{-1}}$), N206-FS 47 ($v \sin i \approx 264\,\mathrm{km\,s^{-1}}$), and N206-FS 112 ($v \sin i \approx 390\,\mathrm{km\,s^{-1}}$) are plotted from left to right. The black dashed lines represent the isochrones with $v \sin i$ corresponding to each star, and solid red lines are the isochrones with $v_{rot} \sim 100\,\mathrm{km\,s^{-1}}$.

began in the outer parts. The massive OB stars formed at this time period must have already cleared out their surrounding molecular cloud, and the star formation propagated inwards, where dense molecular gas was left. Another possible scenario is that the star formation happened near the center of the complex, and these stars migrated outward during their lifetime. Given the average radial velocity dispersion of $16\,\mathrm{km\,s^{-1}}$, a star could travel a projected distance of 240 pc (∼ radius of the complex) in 15 Myr. The dynamical ejection of massive stars from young clusters are also supported by Oh et al. (2015) and Oh & Kroupa (2016).

Mass discrepancy

In Paper I we discussed the mass discrepancy noticed for the Of stars. The same discrepancy is also found here for the whole OB sample. The evolutionary masses of the individual stars are derived from the HRD as described above (see Sect. 4.5). The evolutionary mass (see Table B.3) represents the current stellar mass of the star as predicted by the track, while the spectroscopic mass (see Table 3.3) is inferred from log g.

In order to check for the discrepancy that we encountered in Paper I, we compared both masses for all OB stars (Fig. 3.22). We can see a systematic difference between evolutionary and spectroscopic masses, even though the uncertainties are quite high. This mass discrepancy is a well known problem in astrophysics, especially in the case of OB stars in the Magellanic Clouds (McEvoy et al. 2015; Bouret et al. 2013; Massey et al. 2009, 2013). In our sample, the evolutionary masses are systematically lower than the spectroscopic masses. Moreover, the evolved stars (giants and supergiants) show much smaller discrepancies than the main sequence stars. It should be noted that spectroscopic masses have a much higher uncertainty than the evolutionary masses. The one-to-one correlation of the masses falls within this error limit. The study of Galactic B stars by Nieva & Przybilla (2014) gives similar results, where the spectroscopic masses appear to be larger

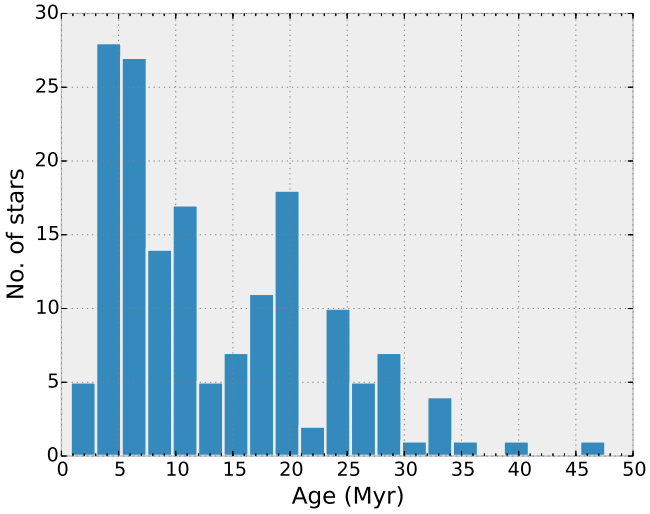

Figure 3.19.: Histogram of ages of the OB stars in the N 206 complex, with bin width of ~2 Myr.

than corresponding evolutionary masses for $M_{spec} > 15 M_{\odot}$.

Moreover, we cannot rule out the possibility of undetected companion(s) in the spectra, which would also affect the mass determinations. Also we know that a significant fraction of the OB stars in clusters or associations are binaries (Sana et al. 2013a, 2011). Some O stars studied by Bouret et al. (2013) also showed higher spectroscopic than evolutionary masses, and turned out to be binaries. They concluded that the bias toward higher spectroscopic masses is probably related to the binary status of the objects. However, it seems unlikely that all stars in our sample are biased this way.

3.7.4. Present day mass function

The spectral analysis of hot OB stars in the N 206 region gives a good sample to reveal the present day mass function. Figure 3.23 (upper panel) shows the present day mass function (PDMF) for the massive stars based on both spectroscopic and evolutionary masses. The corresponding power-law fits give a slope of $\Gamma \approx -2.0$ in both cases. Since the sample becomes incomplete at the lowest masses, the power-law fit is restricted to masses above 20 $M_{\odot}$ in the case of spectroscopic masses, and 10 $M_{\odot}$ for evolutionary masses. It should be noted that the PDMF plotted here might be biased due to unresolved binaries (Weidner et al. 2009). Moreover, the PDMF discussed here is distinct from the initial mass function (IMF), because stars lose mass over their lives, and some disappear after supernova explosions. Since multiple episodes of star formation have occurred in this region, the number of lower mass stars will increase over time and therefore lead to a steeper slope than in the IMF (Kroupa et al. 2013).

In Figure 3.23 (lower panel) we plot the PDMF only for the young cluster NGC 2018. For this subset of stars, the power-law fit gives a very shallow slope of ≈ 0.9. This is substantially flatter than the Salpeter slope of the IMF Γ = -1.35, and could indicate a top-heavy IMF for this young cluster. In a recent work, Schneider et al. (2018b) found a similarly flat IMF for the 30 Doradus starburst in the LMC. Moreover, Marks et al. (2012) deduced a variation of the IMF as becoming top-heavy with decreasing metallicity.

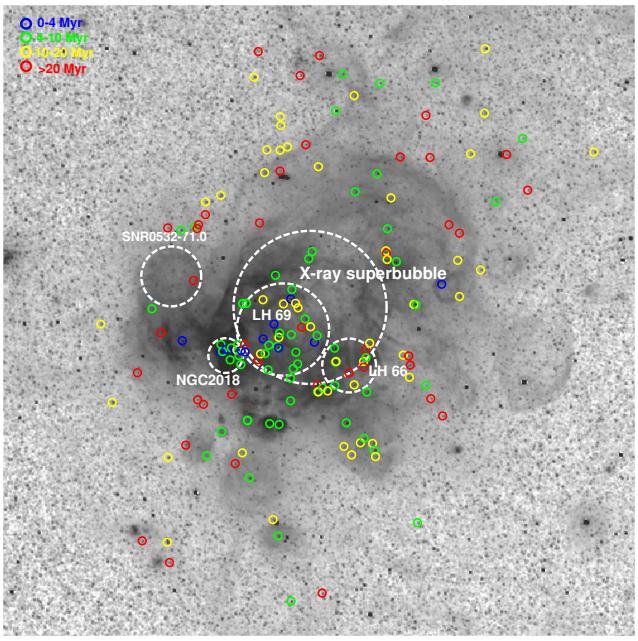

Figure 3.20.: Distribution of the OB stars in the N 206 complex, color-coded with their age

Thus we find a substantial variation of the mass function for different parts of the N 206 complex. To quantify this, we calculate the slopes of the PDMF as a function of distance from NGC 1028. Similar to the analysis in Sect. 3.7.3, we divide the region into four annuli and determine the PDMF for each of the different areas. From the central young cluster to the outer parts of the complex, the slopes are -0.9, -1.4, -1.9, and -2.3, respectively. So, the slope of the PDMF gets gradually steeper with distance from the NGC 2018 cluster. This could indicate mass segregation in the complex. Similar trends are also observed in other clusters like NGC 346 (Sabbi et al. 2008), NGC 3603 (Harayama et al. 2008), and Westerlund 2 (Zeidler et al. 2017).

3.7.5. Present star formation rate

The distribution of stellar ages (Fig. 4.17) indicates a phase of vivid star formation over the last 7.5 Myr. We extract from our results the spectroscopic masses of all OB stars younger than 7.5 Myr. Together with the two WR binaries, their total mass adds to 2600 $M_\odot$. Neglecting the mass lost by winds and SNe, the mass that has been assembled per year into massive stars is thus 2600 $M_\odot$/7.5 Myr = 3.6×10^{-4} $M_\odot$yr^{-1}.

Our sample contains the stars with spectroscopic masses above 20 $M_\odot$ (see Fig. 3.23). For a rough estimate of the mass which went into any stars including those with masses lower than this limit, we adopt a Salpeter IMF and compare the integral from 20 to 150 $M_\odot$ with the integral starting from a lower mass cut-off of 0.5 $M_\odot$ (e.g. Kroupa 2002). This calculation indicates a correction factor of about six. Thus, the total star formation rate we obtain is about 2.2×10^{-3} $M_\odot$ yr^{-1}. This number compares very well with the estimate of 2.5×10^{-3} $M_\odot$ yr^{-1} derived from infrared data on young stellar objects, as reported in the Introduction (Sect. 4.1).

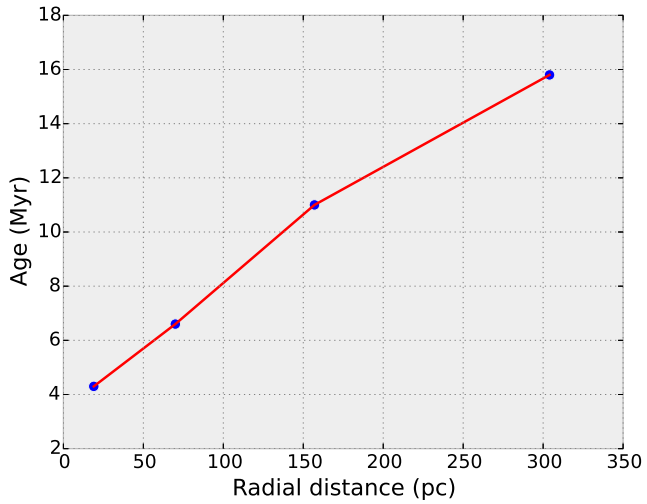

Figure 3.21.: Median age of the OB stars as function of their radial distance from the cluster NGC 2018.

3.7.6. Stellar feedback in the N 206 complex

We quantify the total stellar feedback of the N 206 complex from our spectroscopic study of its massive star population. The interstellar environment consists roughly of three phases: the cold, neutral, or molecular gas, the ionized H II regions, and the shock-heated plasma that emits X-rays. Neglecting mutual interactions, the H II regions are powered by the ionizing radiation of stars, while the X-ray plasma is created by the shocked stellar wind and supernova explosions.

The ionizing photon fluxes generated by the massive stars in our sample will be discussed in Sect. 3.7.6. These ionizing fluxes could be used for constructing photoionization models, and their predictions could be compared with the diffuse emission observed in this complex. In fact, we have placed a number of FLAMES fibers on the diffuse background and plan to do such modeling in the future, but this is beyond the scope of the present paper.

In Sect. 3.7.6, we calculate the total mechanical luminosity produced by the stellar winds of all sample stars as well as the integrated kinetic energy of the winds over the life of the star. In Sect. 3.7.6, we discuss the possible supernova rate in the complex and estimate the input energy. Assuming no interaction between different phases of the ISM, we discuss the energy budget of the superbubble in Sect. 3.7.6 by comparing with the stored energy calculated by Kavanagh et al. (2012).

Ionizing feedback from the WR and OB stars

The rate of hydrogen ionizing photons (Q_0) for each OB star predicted by their final model is given in the Table. 3.3. This ionizing photon flux strongly varies with the spectral subtypes of the OB stars as shown in Fig. 4.12 (upper panel). The present-day total ionizing photon flux produced by all the OB stars in our sample is $Q_0 \approx 4 \times 10^{50}\,\mathrm{s}^{-1}$. More than 65% of this total ionizing photon flux is contributed by the three very massive Of stars (N206-FS 180, N206-FS 187, and N206-FS 214). The ionizing photon flux generated by the two WR binaries in the complex is $Q_0 \approx 5 \times 10^{49}\,\mathrm{s}^{-1}$, which contributes about twelve percent to the combined ionizing feedback

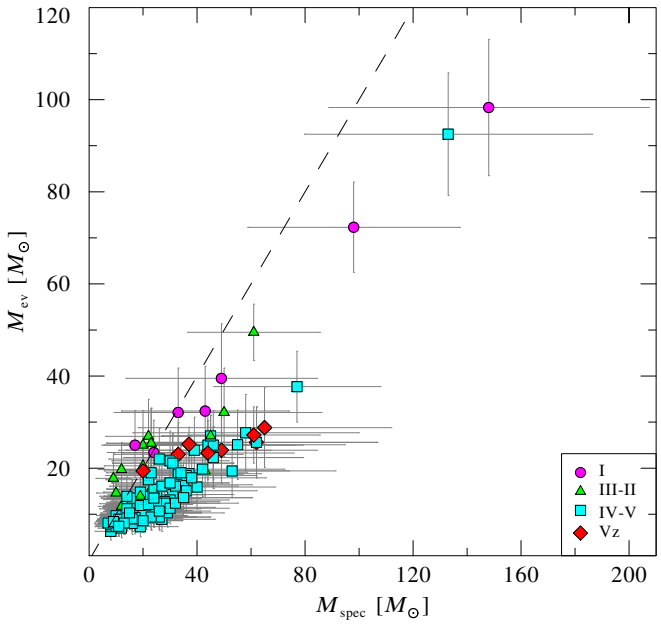

Figure 3.22.: Spectroscopic versus evolutionary masses. The one-to-one correlation of spectroscopic and evolutionary masses is indicated by the dashed line. The sample also includes the Of stars from Paper I. Different luminosity classes are denoted using different shapes and colors as given in the legend.

from WR and OB stars.

The three Of stars are the only stars in our sample that produce a significant number of He II ionizing photons. The number rate of such photons with $\lambda < 228$ Å is about $\approx 6 \times 10^{45}$ s^{-1}.

Mechanical feedback from stellar winds

The mechanical luminosities of the OB stars in the N 206 complex as a function of their spectral subtype are shown in Fig. 4.12 (lower panel). The total mechanical luminosity generated by all sample OB stars is estimated to be $L_{mec} = 0.5\,\dot{M}\,v_\infty^2 \approx 2.34 \times 10^4\,L_\odot$. Similar to the ionizing photon flux, the total mechanical luminosity is also dominated (~62%) by the three very massive Of stars.

Since we know the ages (see Sect. 3.7.3) and the mechanical luminosity (see Table 3.3) of the individual OB stars, we can construct a diagram for the evolution of the mechanical luminosity in the entire complex with time (see Fig. 3.25). The red line illustrates the total mechanical luminosity of all OB stars at a particular time. Here we assume that all our sample OB stars had a constant mechanical output since their formation. Since most of our sample OB stars are still in their hydrogen burning phase (before reaching the terminal age main sequence) as evident from the HRD, this assumption is justified for a rough estimate. Therefore, if only accounting for those OB stars which still exist today, the total mechanical luminosity would have increased over the past five Myr. Of course, this curve might change a lot due to previous generations of massive stars which are no longer present today.

In order to calculate the total mechanical energy released by all presently existing OB stars via stellar winds throughout their life, we must integrate their mechanical luminosity over their age. We obtained a total mechanical feedback from our sample OB stars of $E_{mec} = 0.5\,\dot{M}\,v_\infty^2\,t \approx$

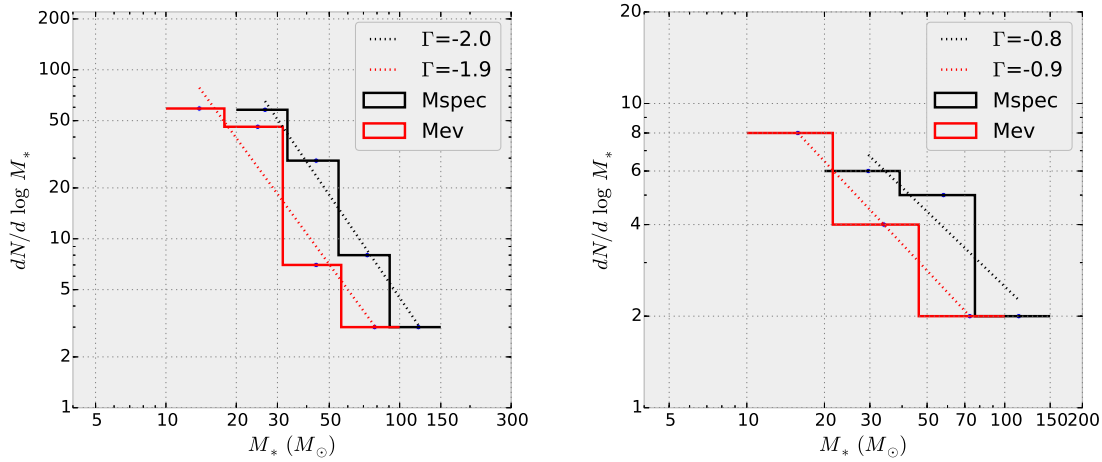

Figure 3.23.: Present day mass function of the whole OB stars in the sample (upper panel) and only for the NGC 2018 cluster (lower panel). The histograms are for spectroscopic (black) and evolutionary (red) masses, respectively. Power laws are fitted to the mass functions (dashed lines) with their slopes Γ as given in the legends.

1.1×10^{52} erg. Even if we are considering only the past five Myr, the accumulated mechanical feedback is $E_{\rm mec} \approx 9.5 \times 10^{51}$ erg. However, these estimates of mechanical feedback only consider those massive stars that are still present in the N 206 complex today, and does not account for those massive stars which have already disappeared. Therefore, these estimates are only lower limits to the stellar wind feedback.

Table 3.7.: Feedback from the WR binaries

		N206-FS 45	N206-FS 128
pre-WR phase	$\log \dot{M}$ $[M_\odot\,{\rm yr}^{-1}]$	-6.5	-6.1
	v_∞ $[{\rm km\,s}^{-1}]$	2600	2800
	L_{mec} $[L_\odot]$	177	514
	t [Myr]	6.2	5.4
	E_{mec} $[10^{50}{\rm erg}]$	1.3	3.3
WR phase	$\log \dot{M}$ $[M_\odot\,{\rm yr}^{-1}]$	-5.4	-4.67
	v_∞ $[{\rm km\,s}^{-1}]$	1700	3400
	L_{mec} $[L_\odot]$	950	20400
	t [Myr]	0.3	0.6
	E_{mec} $[10^{50}{\rm erg}]$	0.34	14.75

The WR stars make a significant contribution to the mechanical feedback of the region. Here we only discuss the feedback from the primary (WR) component, since the contribution from the secondary component (late O star) is comparatively much smaller. The details of the feedback parameters of the WR stars N206-FS 45 and N206-FS 128 are given in Table 3.7.

The evolutionary tracks predict (see Sect. 3.7.3) the initial parameters of the star N206-FS 128a at the ZAMS as $T_* = 39\,{\rm kK}$, $\log g_* = 4.1$, $\log(L/L_\odot) = 5.2$, $\log \dot{M} \sim -6.1\,[M_\odot\,{\rm yr}^{-1}]$, and

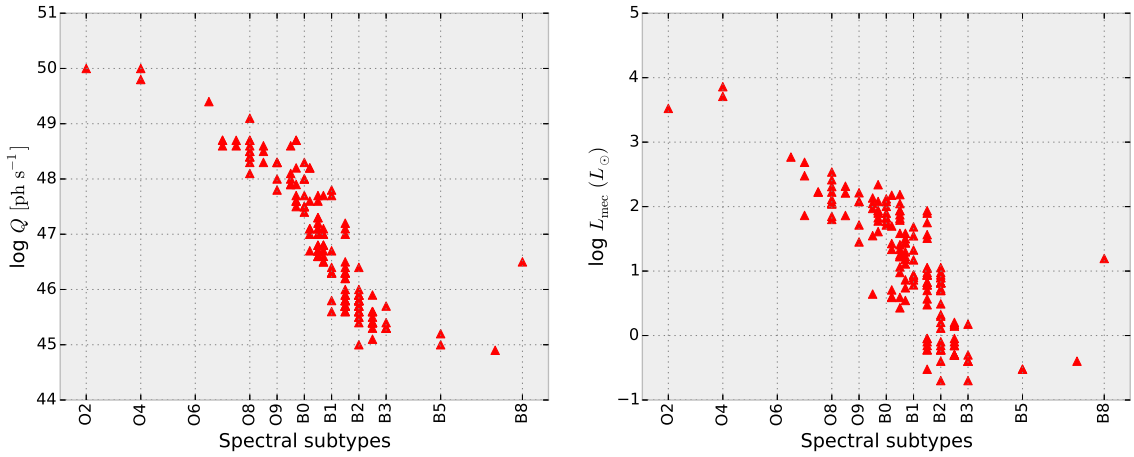

Figure 3.24.: Ionizing photon flux (upper panel) and mechanical luminosity (lower panel) as a function of spectral subtypes.

$v_\infty \sim 2800\,\mathrm{km\,s^{-1}}$. Here, v_∞ is calculated theoretically from v_{esc}. The mechanical energy produced by this star is about 3.3×10^{50} erg over the first 5.4 Myr. The star then stayed in the WR stage for the last 0.6 Myr, imparting a wind energy of approximately 1.5×10^{51} erg to the surroundings. Thus, the mechanical feedback from N206-FS 128 throughout its life is $E_{mec} \approx 1.8 \times 10^{51}$ erg.

The feedback contribution from the WN component of the binary N206-FS 45 has been estimated by Shenar et al. (in prep.) on the basis of a spectral analysis. The current period of the system is 36.9 days (Foellmi et al. 2003). For the derived parameters (see Table 3.4), the binary evolutionary tracks by Eldridge & Stanway (2009) suggest an age of ≈ 6.5 Myr and an initial mass of the WN component of 30 $M_\odot$. The star spent ≈ 6.2 Myr in the hydrogen burning phase. The mechanical luminosity estimated for this time period is ≈ 177 $L_\odot$, and the integrated mechanical energy amounts to $E_{\rm mec} \approx 1.3 \times 10^{50}$ erg. The star has stayed in the WR stage over the last 0.3 Myr. The mechanical energy released by the WR wind during this time period is $\approx 3.4 \times 10^{49}$ erg. Therefore, the model predicts the accumulated mechanical energy output of this star in both stages to be $E_{\rm mec} \approx 1.6 \times 10^{50}$ erg.

Table 3.7 summarizes the feedback from N206-FS 45 and N206-FS 128 in both the pre-WR and WR phase. Now we add these contributions to the mechanical luminosity over time plotted in (Fig. 3.25). From the diagram, we can see that the two WR stars contribute to the feedback about as much as the whole sample of hundreds of OB stars. The total mechanical luminosity is about $L_{\rm mec} = 4.5 \times 10^4\,L_\odot = 1.7 \times 10^{38}\,\mathrm{erg\,s^{-1}}$.

The integrated mechanical energy over the lifetime of both WR stars in our sample is ≈ 2×10^{51} erg. So, the total accumulated mechanical feedback over the lifetimes of the current WR and OB stars becomes $E_{\rm mec} \approx 1.3 \times 10^{52}$ erg. Even if we consider only the past five Myr, the total integrated mechanical feedback is $\approx 1.2 \times 10^{52}$ erg.

From the size and expansion velocity of the X-ray superbubble, Dunne et al. (2001) suggest an age of ∼2 Myr. According to Kavanagh et al. (2012), the expansion of the superbubble must have undergone induced acceleration in its history, and therefore it is likely to be older than 2 Myr. The HRD of the stars in the X-ray superbubble region (Fig. 3.6, lower right) reveals many O stars within the age range 4 − 5 Myr. Therefore we speculate that the age of the superbubble is about 2 − 4 Myr. This time interval is marked in Fig. 3.25 by a shaded area. As seen in Fig. 4.17, the star

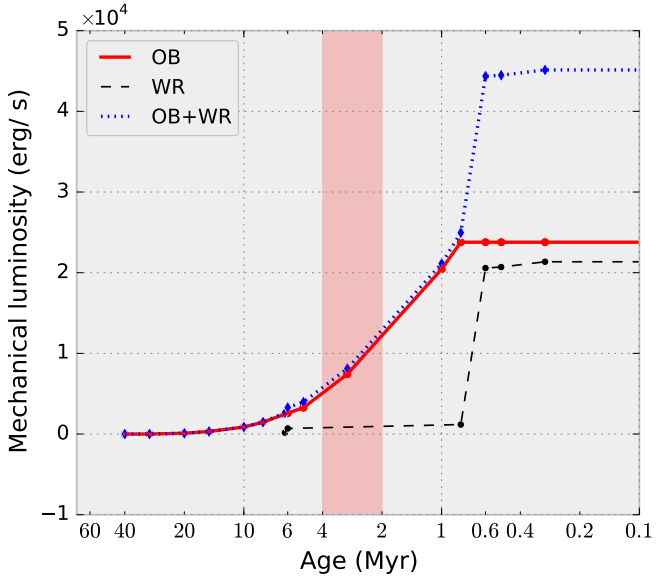

Figure 3.25.: Evolution of the mechanical luminosity in the N206 complex, only considering the present stellar content. The mechanical luminosity from WR and OB stars is shown in black dashed and red solid lines, respectively. The combined mechanical luminosity is represented by the blue dotted line. The red shaded area indicates the time interval in which the superbubble formation has begun.

formation in the N 206 complex peaked 3 – 5 Myr ago. In this period, the stellar winds from this population must have caused a rapid increase in the overall mechanical luminosity.

Regarding the times more than five Myr ago, it should be noted that we are not aware of the full star formation history. There might have been other time intervals of peak star formation. However, considering only the present stellar content, $L_{\rm mec}$ was negligible before 5 Myr, then it started to grow and led to the formation of the superbubble. The huge increase in $L_{\rm mec}$ over the last 0.6 Myr is due to the two WR stars.

Feedback from supernovae

A single supernova (SN) injects typically 10^{51} erg of mechanical energy into the ISM (Woosley & Weaver 1995). Therefore, for our study we need to estimate the number of supernovae that have already occurred in the N 206 complex.

Currently, there is only one SNR situated in this complex, which suggests that a SN that occurred within the last few ten thousand years. Older SNRs would have already faded below the observational limit.

Indirect evidence for previous SNe could come from the detection of X-ray binaries. The formation of their compact component, a black hole or neutron star, might have been accompanied by a SN explosion. Previous studies by Shtykovskiy & Gilfanov (2005) and Kavanagh et al. (2012) have identified two HMXB candidates, namely XMMU J052952.9-705850 and USNO-B1.0 0189-00079195, by the X-ray analysis of the region using *XMM-Newton* telescope data. In order to check the nature of these objects, we have taken VLT-FLAMES spectra at the positions of both X-ray sources (Fig. 3.26). In both cases, no stellar features can be detected, neither lines nor

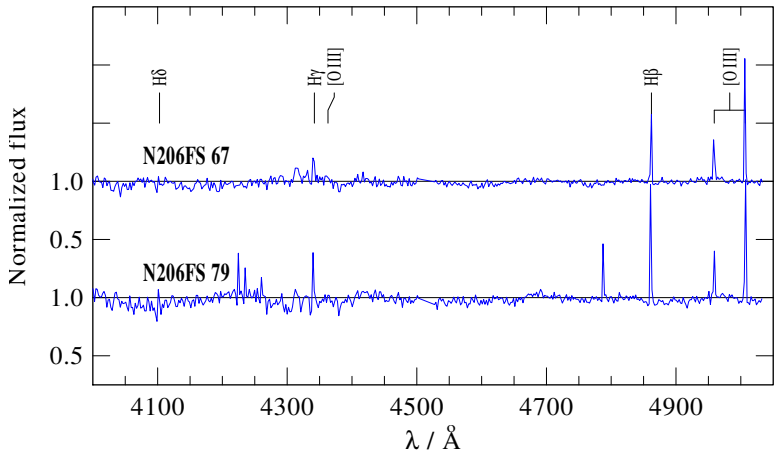

Figure 3.26.: Normalized VLT-FLAMES LR02+LR03 spectra taken at the positions of the X-ray sources XMMU J052952.9-705850 (upper panel) and USNO-B1.0 0189-00079195 (lower panel)

a continuum. The data show only nebular emission from the diffuse background in both cases. Hence we do not support the identification of these X-ray sources with HMXBs. Our conclusion is supported by the Million Optical - Radio/X-ray Associations (MORX) Catalog (Flesch 2016), which also suggests that these X-ray sources are most probably contaminations from background quasars or external galaxies.

Further indirect evidence for previous SN occurrences is given by OB runaways. These stars might have been ejected from a binary system, when the SN explosion of the primary disrupted the system. In Sect. 4.4 we identified eight runaway candidates with radial velocities in excess of $\pm 48\,\mathrm{km\,s^{-1}}$. Interestingly, most of these stars are located inside or at the periphery of the X-ray superbubble as shown in Fig. 4.10.

Considering the evolutionary masses of the OB stars, there are about 36 stars in the $20 - 40\,M_\odot$ bins and five stars with masses $\geq 40\,M_\odot$, which must become SNe within the next ten and five Myr, respectively. Additionally, there are two WR binaries in the complex. These numbers are higher than predicted by Kavanagh et al. (2012) from the IMF. If the SFR was roughly constant in time, there should have been a similar number of massive stars in the past.

In Ferrand & Marcowith (2010), the rate of supernovae in massive clusters or OB associations is expressed to first approximation as

$$\frac{\mathrm{d}n}{\mathrm{d}t_{SN}} \approx \frac{N_*}{\Delta t^*_{OB}}. \tag{3.2}$$

Here $\Delta t^*_{OB} = t_{SN}(m_{min}) - t_{SN}(m_{max})$ is the active lifetime of the cluster, where m_{min} and m_{max} are the minimum and maximum initial mass of the stars in the region that explode as SNe. The symbol N_* is the number of stars with masses between m_{min} and m_{max}. Regarding the SN rate in the N 206 complex, we can take $m_{min} = 8\,M_\odot$ and $m_{max} = 100\,M_\odot$. This gives $t_{SN}(m_{min}) \approx 37$ Myr and $t_{SN}(m_{max}) \approx 3.5$ Myr. From the HRD, 162 stars have $M_{ini} \geq 8\,M_\odot$ (including binary companions). So, the supernova rate is ≈ 4.8 per Myr or one SN per 210,000 years. Even if we consider only stars with initial masses below $40\,M_\odot$, because more massive stars might collapse silently (Heger et al. 2003), the rate is $\approx$ five supernovae per Myr. This number is in statistical agreement with the presence of just one SNR today.

If we do the same calculation only for massive stars within or close to the X-ray superbubble (including stars in NGC 2018, LH 66, and LH 69), the estimated SN rate is ≈2.2 per Myr. So, if we consider only the past five Myr and massive stars close to the X-ray superbubble, the accumulated mechanical input by supernova explosions is estimated to be $E_{\rm mec} \approx 1.1 \times 10^{52}$ erg, and hence contributes approximately the same amount to the mechanical feedback as the massive star winds.

Superbubble energy budget

We compare our energy feedback results with the X-ray analysis of the superbubble by Kavanagh et al. (2012). Using XMM-*Newton* data, they estimated the X-ray luminosity of the N 206 superbubble as $\approx 7 \times 10^{35}$ erg s^{-1}. In young star clusters, the unresolved X-ray emission from the population of active pre-main sequence stars could be significant (Nayakshin & Sunyaev 2005; Wang et al. 2006), also at sub-solar metallicities (Oskinova et al. 2013). Kavanagh et al. (2012) estimated the contribution from the unresolved low-mass population to the observed X-ray emission as ∼ 6%. Moreover, the distribution of YSO candidates (Carlson et al. 2012) shows that they are not concentrated in the X-ray superbubble area.

To estimate the contribution of young active stars of low mass to the extended X-ray emission in N 206, we use the scaling provided in Oskinova (2005). Their figure 5 compares the relative contributions to the X-ray emission from the hot cluster wind with the emission from the unresolved population of low-mass stars. As can be seen in this figure, in clusters younger than ∼ 2.5 Myr (assuming an instantaneous burst of star formation), the collective X-ray luminosity of low-mass stars dominates the cluster X-ray luminosity. However, for older clusters, the input of mechanical energy from massive stars dominantly powers the diffuse X-ray emission. We estimated the age of the X-ray superbubble in N 206 as higher than 2 Myr (see Fig. 3.25). Moreover, we found that star formation has been ongoing in this region for a longer time. Hence, it is most likely that the observed soft diffuse X-ray emission is dominated by the mechanical energy input from massive stars.

The observed X-ray luminosity is only 0.4% of the combined mechanical luminosity of the WR and OB stellar winds (see Sect. 3.7.6). The uncertainty in $L_{\rm mec}$ is about 30% reflecting the error margins of the stellar wind parameters ($\dot{M}, v_\infty$). Previous studies on other massive star forming regions such as the Omega Nebula, the Rosette Nebula (Townsley et al. 2003), 30 Doradus (Lopez et al. 2010; Doran et al. 2013), and the Carina Nebula (Smith 2006; Townsley et al. 2011) also revealed similar trends, where only a small portion of the wind energy is converted into X-ray emission. Rosen et al. (2014) published a detailed study about missing stellar wind energy from massive star clusters. They suggest that turbulent mixing at the hot-cold interface or physical leakage of the shock heated gas can efficiently remove the kinetic energy injected by the massive star winds and supernovae.

Kavanagh et al. (2012) also estimated the total energy stored in the superbubble in the form of thermal energy of the shock-heated gas and the kinetic energies of the expanding Hα and H I shells to be $(4.7 \pm 1.3) \times 10^{51}$ erg. The feedback calculations discussed in the previous sections reveal a much higher mechanical energy input by the massive stars to the N 206 complex. Adding the mechanical energy input during the last five Myr from the OB and WR star winds (Sect. 3.7.6) and the SNe (Sect. 3.7.6), we obtain $\approx 2.3 \times 10^{52}$ erg, which is almost five times higher than the stored energy content observed by Kavanagh et al. (2012). Even more, the feedback estimates are only a lower limit, as discussed in Sect. 3.7.6. With the SN rate estimated in Sect. 3.7.6, about 25 supernovae might have occurred in the entire complex during the past five Myr. Also, there would be a contribution from stellar winds of their progenitors. Considering these numbers, the

total $E_{\rm mec}$ can increase by a factor of roughly two. However, this does not include the contribution from stars which already died as SNe between 5 to 50 Myr ago (Fig. 3.25). According to the SNe estimation given in Sect. 3.7.6, about 250 stars might have already exploded as SNe. Here we assumed a constant star formation rate over the past 50 Myr, as high as the current rate. During their evolutionary stages, stellar winds (OB/WR) of these stars would have provided a significant amount of mechanical feedback. Supernovae and stellar winds together might have released about 15 times more mechanical energy than our estimated value of 2.3×10^{52} erg. As we have seen above, the radiative cooling by X-ray emission is negligible. Hence, this comparison shows that most of the mechanical energy input has been consumed by other processes or escaped from the X-ray superbubble.

The hot X-ray emitting gas could not escape, if it were fully confined by surrounding cold and dense molecular material. Figure 3.27 shows a multiwavelength image of the N 206 complex at far-infrared, optical, and X-ray wavelengths, over-plotted with CO intensity contours. The CO intensity map taken from the Magellanic Mopra Assessment (MAGMA) (Wong et al. 2011) traces the dense molecular gas. This map reveals that the X-ray superbubble is only partially confined by the dense molecular cloud. In the 2D projection, it seems that the X-ray emitting gas leaks out in northern directions. Figure 3.27 also gives a general picture of ongoing star formation in this region. When comparing this with Fig. 3.20, we can see that now the star formation is presently progressing at the rim of the cloud. This could be an indication of a triggered star formation in the complex by the expansion of the superbubble when it hits the rim of the cloud. The young cluster NGC 2018 is also located in this dense part of the molecular cloud. At the other side of the superbubble, the cold molecular gas is already removed, which might be due to the energetic winds of massive stars or SNe that occurred in the past. So, mostly older stars are left there, and there is not enough material available for further star formation.

3.8. Summary and conclusions

We have identified and analyzed the OB stars and WR binaries in the N 206 complex located in the LMC. The stellar and wind parameters of the individual stars are determined using PoWR model atmospheres. We also present a detailed binary analysis of the WC4+O9 system, and discuss its evolutionary status. Our main conclusions are:

- Approximately 12% of the whole sample are found to be emission-line stars with a disk. However, our analysis shows that the projected rotational velocities of most of these Oe/Be stars are far below their critical velocity.
- From the radial velocity distribution of the OB stars, we suspect eight stars to be runaways.
- The wind momentum-luminosity relation of most of the sample OB stars is consistent with expectations within uncertainties.
- The HRD of our OB star sample in the complex reveals multiple populations of different ages. Moreover, each of the clusters and OB associations inside the region also shows large age dispersions, indicating multiple star formation events.
- The current stellar masses as derived from evolutionary tracks are systematically lower than the masses that we obtain from our spectroscopic analyses. This discrepancy is higher for main sequence stars than for evolved stars.

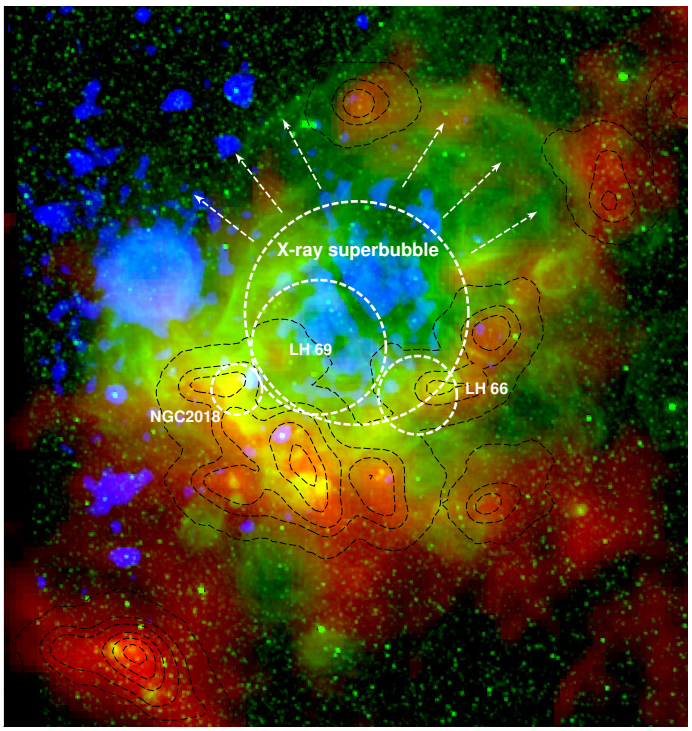

Figure 3.27.: Color composite image of the N 206 complex, constructed from the Herschel spire data (red: 500 μm), Hα (green: MCELS, Smith et al. 2005), and X-rays (blue: XMM-*Newton* 0.3 − 1 keV). CO intensity contours taken from the MAGMA survey are over-plotted to the image. The arrows suggest the possible leakage of hot gas from the X-ray superbubble.

- We find indications of sequential star formation in the region. The youngest stars are mostly distributed inside the young clusters and the inner part of the complex, whereas outer parts contain slightly older populations.
- The current star formation is taking place at the rim of the superbubble, where it hits the molecular cloud.
- The present day mass function of the entire region shows a steeper slope than the Salpeter IMF. However, the cluster NGC 2018 shows a top-heavy mass function.
- We derive the current star formation rate of the complex as $2.2 \times 10^{-3} M_{\odot}\,\mathrm{yr}^{-1}$.
- The total ionizing photon flux produced by all massive stars in the N 206 complex is $Q_0 \approx 5 \times 10^{50}\,\mathrm{s}^{-1}$.
- Three very massive Of stars out of 164 OB stars contribute >60% of the total ionizing photon flux and the stellar wind mechanical luminosity.
- The integrated mechanical energy feedback from all OB stars over the past five Myr is estimated to be $\approx 1.3 \times 10^{52}$ erg. This is more than the energy that is found to be stored in the superbubble.

- The two WR binaries contribute about as much mechanical luminosity as all the 164 OB stars in the sample.
- The rate of supernova explosions in the complex is estimated to be about five per Myr.
- The X-ray luminosity of the N 206 superbubble is only 0.4% of the current mechanical luminosity from the stellar winds of the OB + WR stars.
- The energy input accumulated over time from the OB stars, WR stars, and SNe is found to be more than five times higher than the energy stored in the X-ray superbubble.
- The morphology of the complex, with the X-ray superbubble not being fully enclosed by the cold molecular gas, gives the impression that the hot gas has the possibility to escape from the complex.
- The fact that a few of the most massive stars dominate the energetics of the N 206 complex would not have been revealed without spectroscopic information.

3.9. acknowledgements

We wish to thank the referee, Daniel Q. Wang, for very constructive suggestions to improve the paper. Based on observations collected at the European Organization for Astronomical Research in the Southern Hemisphere under ESO program 096.D-0218(A) (P.I.: L. Oskinova). V.R. is grateful for financial support from Deutscher Akademischer Austauschdienst (DAAD), as a part of Graduate School Scholarship Program. LMO acknowledges support by the DLR grant 50 OR 1508. A.A.C.S. is supported by the Deutsche Forschungsgemeinschaft (DFG) under grant HA 1455/26. T.S. acknowledges support from the German "Verbundforschung" (DLR) grant 50 OR 1612. This research made use of the VizieR catalog access tool, CDS, Strasbourg, France. The original description of the VizieR service was published in A&AS 143, 23. Some data presented in this paper were retrieved from the Mikulski Archive for Space Telescopes (MAST). STScI is operated by the Association of Universities for Research in Astronomy, Inc., under NASA contract NAS5-26555. Support for MAST for non-HST data is provided by the NASA Office of Space Science via grant NNX09AF08G and by other grants and contracts.

Chapter 4.

Testing massive star evolution, star-formation history and feedback at low metallicity Spectroscopic analysis of OB stars in the SMC Wing (Manuscript III)

Varsha Ramachandran, W.-R. Hamann, L. M. Oskinova, J. S. Gallagher, R. Hainich, T. Shenar, A. A. C. Sander, H. Todt, and L. Fulmer

*A*stronomy & Astrophysics, 2019, Volume 625

Abstract

Stars that start their lives with spectral types O and early B are the progenitors of core-collapse supernovae, long gamma-ray bursts, neutron stars, and black holes. These massive stars are the primary sources of stellar feedback in star-forming galaxies. At low metallicities, the properties of massive stars and their evolution are not yet fully explored. Here we report a spectroscopic study of 320 massive stars of spectral types O (23 stars) and B (297 stars) in the Wing of the Small Magellanic Cloud (SMC). The spectra, which we obtained with the ESO Very Large Telescope, were analyzed using state-of-the-art stellar atmosphere models, and the stellar parameters were determined. We find that the stellar winds of our sample stars are generally much weaker than theoretically expected. The stellar rotation rates show broad, tentatively bimodal distributions. The upper Hertzsprung-Russell diagram (HRD) is well populated by the stars of our sample from a specific field in the SMC Wing. A few very luminous O stars are found close to the main sequence, while all other, slightly evolved stars obey a strict luminosity limit. Considering additional massive stars in evolved stages, with published parameters and located all over the SMC, essentially confirms this picture. The comparison with single-star evolutionary tracks suggests a dichotomy in the fate of massive stars in the SMC. Only stars with an initial mass below $\sim 30\,M_{\odot}$ seem to evolve from the main sequence to the cool side of the HRD to become a red supergiant and to explode as type II-P supernova. In contrast, stars with initially more than $\sim 30\,M_{\odot}$ appear to stay always hot and might evolve quasi chemically homogeneously, finally collapsing to relatively massive black holes. However, we find no indication that chemical mixing is correlated with rapid rotation.

We measured the key parameters of stellar feedback and established the links between the rates of star formation and supernovae. Our study demonstrates that in metal-poor environments stellar feedback is dominated by core-collapse supernovae in combination with winds and ionizing

radiation supplied by a few of the most massive stars. We found indications of the stochastic mode of massive star formation, where the resulting stellar population is fully capable of producing large-scale structures such as the supergiant shell SMC-SGS 1 in the Wing. The low level of feedback in metal-poor stellar populations allows star formation episodes to persist over long timescales.

4.1. Introduction

Massive stars ($M_{init} \gtrsim 8\,M_{\odot}$) are cosmic engines that play a pivotal role in the physical and chemical evolution of the interstellar medium (ISM) and galaxies via UV radiation, stellar winds, and supernovae (SNe). These stars are among the main sources of reionization of the universe (Barkana 2006). Massive stars are the progenitors of neutron stars and black holes, formed by their core-collapse. Detection of gravitational waves from coalescing black holes further highlighted a need for better understanding of massive stars, especially at low metallicity.

The evolution of a star is mainly decided by its mass, mass-loss history, composition, rotation rate, and binary status. Mass-loss rates ($\dot{M}$) derived empirically are often lower compared to standard prescriptions, especially for low-luminosity OB stars ('weak wind stars', Bouret et al. 2003; Martins et al. 2005b; Marcolino et al. 2009). The variation of $\dot{M}$ with evolutionary phase and metallicity is still under debate. Especially at highest masses, the evolution of massive stars at low metallicity and their remnant mass at collapse depends critically on the mass loss by winds and eruptions.

Stellar evolution models predict rotationally induced chemical mixing in massive main sequence stars and homogeneous evolution channels, predominantly at low metallicity. The presence of a companion can also alter the evolutionary paths (Sana et al. 2012).

The quantitative spectroscopy of massive stars in metal-poor environments is a key to understand their properties, evolution, and feedback in detail. Up to now, the largest spectroscopically analyzed samples refer to the Large Magellanic Cloud (LMC) with metallicity $Z \sim 0.5\,Z_{\odot}$ (Schneider et al. 2018a; Ramachandran et al. 2018b). In this paper, we analyze 320 OB stars in the Small Magellanic Cloud (SMC), significantly enlarging the previous studies (Hunter et al. 2008a; Bouret et al. 2013; Castro et al. 2018). Our sample stars belong to the Wing of the SMC, which is the nearest (DM =18.7 mag) (Cignoni et al. 2009) low density (Stanimirovic et al. 2000) and low reddening region at low metallicity. The chemical composition of B stars (C, N, O, Mg, Si and Fe) obtained by Hunter et al. (2007) and Trundle et al. (2007) compared to solar values (Asplund et al. 2009) suggest the metallicity of SMC to be $\sim 1/7\,Z_{\odot}$. The properties of the Wing match with the typical conditions for low-metallicity dwarf irregular galaxies, which are the most common among star-forming galaxies (Gallagher et al. 1984).

Among the spectacular manifestations of massive star feedback are the large-scale structures in the ISM, such as the Hα "supergiant shell" (SGS) in the SMC (SMC-SGS 1, Meaburn 1980), which contains the majority of our sample stars (Fig. 4.1). It has a closed ring-like morphology (r $\sim$ 300 pc) with a bright rim in the southeast. It is associated with a H I supershell, which shows a central radial velocity of 173 km s^{-1} and expansion velocity of $\sim$ 10 km s^{-1} (Stanimirovic et al. 1999; Fulmer et al. 2019 submitted). However, the formation mechanism of such large structures is still a subject of debate. One source responsible for the huge amount of energy needed for their formation could be the combined effect of ionizing radiation and winds from young clusters or OB associations and SN explosions. Alternative mechanisms include the distortion of the ISM by γ-ray bursts (Efremov et al. 1999), collisions of high-velocity clouds (HVCs) (Tenorio-Tagle 1981;

Tenorio-Tagle et al. 1986), stochastic star formation propagation (Seiden et al. 1979; Matteucci & Chiosi 1983; Harris & Zaritsky 2008), and the turbulent nature of the ISM (Elmegreen 1997). Quantitative feedback studies are necessary to unveil which of the possible mechanisms plays a key role.

The nebular complexes of the region were first identified by Davies et al. (1976) and classified into eight different emission regions DEM 160-167. Three H II regions, N 88, N 89, and N 90, are located in the rim of the shell (see Fig. 4.1). A well-studied and prominent site of star formation in the SMC-SGS 1 is the group of young clusters NGC 602. The main cluster NGC 602a and the adjacent cluster NGC 602b are immersed in the emission nebula N 90, while NGC 602c is located in the northeast (Westerlund 1964). The cluster hosts few of the most massive stars in the SMC , including a rare pre-SN star of WO type (Sk 188) in NGC 602c and an early-type O3 star (Sk 183) in NGC 602a (Evans et al. 2012). Many of the OB stars within the SGS do not appear to be bound to any of the clusters and it was suggested that they related to the same triggering event (McCumber et al. 2005).

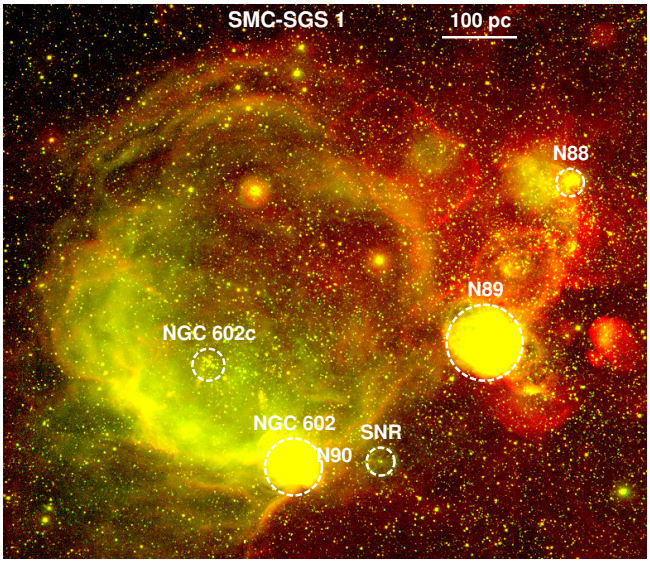

Figure 4.1.: Supergiant shell SMC-SGS1 in the Wing of the SMC. The H II regions (N 88,89, and 90), clusters (NGC 602 and NGC 602c), and the supernova remnant (SNR) in the region are indicated on the color composite (Hα, [O III]) image, taken from the Magellanic Cloud Emission-Line Survey (MCELS, Winkler et al. 2005).

The quantitative spectroscopy of OB star populations in the SMC allows us to test massive star evolution, their feedback, and star formation in low-metallicity galaxies. Through the analyses of OB stars using sophisticated model atmospheres, we provide the stellar and wind parameters of the individual stars and their energy feedback. The spectroscopic observations and data reduction are presented in Sect. 4.2. In Sect. 4.3, we quantitatively analyze the OB star spectra using the Potsdam Wolf-Rayet (PoWR) model atmospheres. We present the main results and discussions in Sect. 4.5 to Sect. 4.8. The final Sect. 4.9 provides a summary and general conclusions. The Appendices encompass additional data, figures and tables.

4.2. Observations and data reduction

We obtained the optical spectra of the OB stars associated with SMC-SGS 1 on 2010 October 24-26 with the Fiber Large Array Multi-Element Spectrograph (FLAMES) on ESO's Very Large Telescope (VLT). Using the Medusa-fiber mode of FLAMES (Pasquini et al. 2002), spectra on 132 targets were simultaneously recorded, where each fiber has an aperture of 1.2″ on the sky. Three of the standard settings of the Giraffe spectrograph LR02 (resolving power $R = 6000$, 3960–4567 Å), LR03 ($R = 7500$, 4501–5071 Å), and HR15N ($R = 19200$, 6442–6817 Å) were used for this survey. The higher resolution spectra of Hα serve for the determination of the wind parameters and to distinguish nebular emission from the stellar component.

Our observation constraint was a magnitude cut of $V \leq 17$ mag (based on Massey 2002), corresponding to unreddened O and early B-type stars at the distance of the SMC. We could not apply further constraints since no other photometry data were available at the time of observation. The exposure time for each pointing is 1800 s in all three spectrograph settings. We took three to six exposures for each target to get an S/N> 50.

The ESO Common Pipeline Library (CPL)[1] FLAMES reduction routines were executed for the standard data processing stages, i.e., bias subtraction, fiber location, summed extractions, division by a normalized flat-field, and wavelength calibration. All these spectra were then corrected to the heliocentric frame. A number of fibers was placed on the sky background. Each sky fiber was inspected and the contaminated sky fibers were rejected prior to the creation of a median sky spectrum for each observation. This median sky spectrum was then subtracted from all stellar spectra. However, because of the prominent nebular regions in the shell, the majority of the spectra are still contaminated by nebular emission lines such as Hα, [O III], [N II], and [S II].

To clean the extracted spectra of cosmic rays, we calculated the ratio of the two exposures for each spectrum. Since these exposures were consecutive, we assumed that any unexpected and significant deviations in the ratio are indicative of a cosmic ray. The pixels identified as suspect were rejected, then replaced with the value from the sister exposure, appropriately scaled by the ratio of the surrounding pixel.

The obtained spectra are not flux-calibrated. The spectra were rectified by fitting the stellar continuum with a cubic spline function. For each star, the LR02 and LR03 spectra were merged to form the medium resolution blue spectrum from 3960 to 5071 Å. We obtained spectra of 543 individual stars. Since we only applied a V magnitude cutoff, the sample also contains late-type stars, foreground stars, and objects with poor S/N. By inspection of the blue spectra, we eliminated them from our final catalog. We are only interested in hot blue stars in this study. The final catalog contains 320 OB stars. The survey covers a large part of the SGS with a total area of 0.28 kpc^2. We adopt a naming convention for all the objects in the survey starting with SMCSGS-FS (SMC supergiant shell FLAMES Survey) and a number in ascending order with their right ascension (1–320). The full catalog of the survey targets are given in Table C.1 with their names, positions, and spectral types.

Flux-calibrated UV spectra are available in the Mikulski Archive for Space Telescopes (MAST[2]) for nine OB stars of our sample. All these stars (SMCSGS-FS 96, 216, 231, 284, 287, 288, 292, 298, and 310) have an International Ultraviolet Explorer (IUE) spectrum in the wavelength range 1150–2000 Å. For SMCSGS-FS 310, there exists an HST/Space Telescope Imaging Spectrograph (STIS) spectrum, a far-UV Far Ultraviolet Spectroscopic Explorer (FUSE), and a high-resolution

[1] http://www.eso.org/observing/cpl
[2] http://archive.stsci.edu/

Ultraviolet and Visual Echelle Spectrograph (UVES) spectrum. The HST spectrum was taken with the G130M grating in the wavelength range 1135–1429 Å, with an effective resolving power of $R = 18000$. The FUSE spectrum was taken with a large aperture ($30'' \times 30''$), and extends over the wavelength range 905–1187 Å. The UVES spectra cover wavelength ranges of 3750–5000 Å, 4600–6600 Å, and 6700–11000 Å with a resolving power of $R \sim 35000$.

In addition to the spectra, we adopted various photometric data from the VizieR archive, for constructing the spectral energy distributions (SEDs). Ultraviolet and optical (U, B, V, and I) photometry was taken from Massey (2002), Zaritsky et al. (2004), Girard et al. (2011), and Zacharias et al. (2012). The infrared magnitudes (JHK_s and *Spitzer-IRAC*) of the OB stars are taken from the catalogs Kato et al. (2007), Bonanos et al. (2009), and Cutri et al. (2012).

Spectral classification

We visually compared the blue optical spectra of our sample stars to those of classified stars from Sota et al. (2011, 2014), Walborn et al. (2014), Evans et al. (2015), and McEvoy et al. (2015), while also taking into account the low metallicity of the SMC compared to the Galaxy and the LMC. Detailed descriptions of the subtype classification of OB stars are given in Ramachandran et al. (2018a) and Ramachandran et al. (2018b). The spectral classifications of all stars are tabulated in Table C.2.

We identified 23 O stars and 297 B stars in the whole sample based on He I/He II ionization equilibrium. In O stars, the He I lines get weaker and He II lines get stronger as going toward the earliest subclasses. So, for the classification of early O subtypes, we used the strength and morphology of the optical nitrogen lines N III $\lambda\lambda$4634–4642 (hereafter N III) and N IV λ4058 (hereafter N IV) (Mihalas et al. 1972; Walborn et al. 2002). We identified these nitrogen emission lines in four of our sample stars, known as Of stars. The nitrogen emission lines of these stars are weaker than the LMC stars of similar spectral subtype.

The sample contains a very early-type O3 star, SMCSGS-FS 231 (Sk 183), which shows N IV and N III emission lines in the spectra. Part of our team has studied this star in detail previously (see Evans et al. 2012). We identified another early spectral subtype O6 star, SMCSGS-FS 287, which shows weak N III emission lines and very strong He II absorption lines. Two O7 stars (SMCSGS-FS 241 and 292) are present in the sample, where only SMCSGS-FS 292 is identified as an Of star based on very weak N III emission lines (no available LR03 spectra for SMCSGS-FS 241 to assign this classification). All these three Of stars have a prominent He II 4686 absorption feature that is stronger than any other He line in the blue-violet spectra. This characteristic represents the Vz luminosity class. Stars of this class are expected to be very young and may be near or on the zero-age main sequence (ZAMS) (Walborn 1973, 2009). However, analysis of O Vz stars in 30 Doradus by Sabín-Sanjulián et al. (2014) revealed that they might be in more evolved phases because of weaker O-star winds in the low-metallicity environment of the LMC compared to the Galaxy.

A peculiar Of supergiant, SMCSGS-FS 310 (Sk 190) is part of the sample. We classified this star as O7.5 based on its strong He II absorption lines and very weak N III emission lines. The He I absorption lines are very weak in the blue optical spectrum. The weak He II 4686 emission wings in the spectrum qualify its Onfp nature. This spectral class was introduced by Walborn (1973) to describe a composite emission + absorption profile at He II 4686. In this case "f" denotes He II 4686 and N III emission, "p" refers to peculiar early-type spectra and the broadened absorption lines due to rapid rotation is indicated with "n" (Walborn 1973; Walborn et al. 2010). Since the He II 4686 absorption line is negligible or very weak compared to the emission wings, the star might be an Of

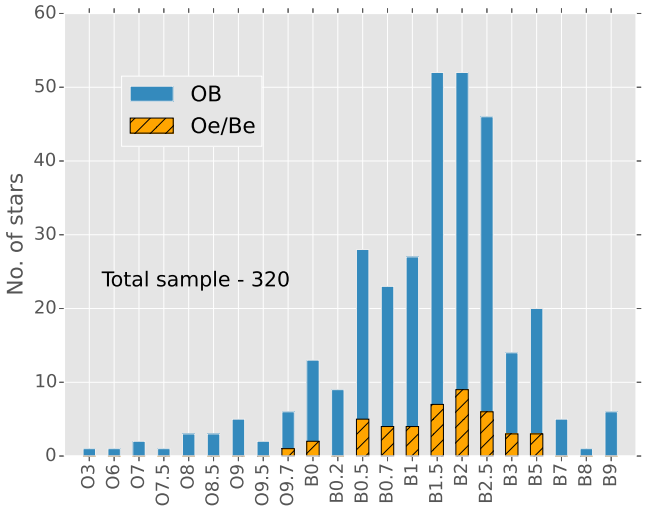

Figure 4.2.: Spectral subtype distribution of all OB stars in our sample. For each spectral subtype, the number of detected Oe/Be stars are represented in orange with black lines.

supergiant. Hence we assigned a spectral type of O7.5 In(f)p to the star. Such evolved stars are not expected to rotate rapidly because of strong mass loss. Walborn et al. (2010) discussed possible reasons for their rapid rotation such as binarity and stellar mergers. These types of stars are also considered as gamma-ray-burst progenitors.

All other 18 O stars are of late subtype O8–9.7. These are mostly main sequence stars since their He II 4686 absorption line is strong. One of these, SMCSGS-FS 269, is identified to be a Vz luminosity class star. Because of the weak He II 4686 absorption, SMCSGS-FS 288 is classified as a giant.

We subclassified all sample B stars into B0–9 based on the ionization equilibrium of helium and silicon. The main diagnostics used for early B types (B0–2) are the Si III λ4553/ Si IV λ4089 line ratio and the strength of He II λ4686, He II λ4542, and Mg II λ4481. Approximately two-thirds of the sample are in the early B-star category, as highlighted by the histogram shown in Fig. 4.2. The spectral subtype with highest number of sample stars is B2. This is because, the sample is not complete in the case of late B stars (B2.5–9). We identified a total of 95 stars later than B2. The main diagnostic lines used to subclassify these late B-type stars are Si II $\lambda\lambda$4128-4132, He I λ4144, He I λ4471, and Mg II λ4481.

The main criteria used for determining the luminosity classes of B stars are the width of the Balmer lines and the intensity of the Si IV and Si III absorption lines (Evans et al. 2015). We identified five B supergiants in the sample, which show rich absorption-line spectra. Among these, four are late B9 supergiants and one is a B2 supergiant. There are also 20 giants / bright giants present in the sample and the rest are main sequence B stars. Ramachandran et al. (2018b) and Evans et al. (2015) provide a detailed description of spectral and luminosity classifications of B stars.

We identified 44 stars with strong emission lines among the whole sample. The optical spectra of these non-supergiant stars exhibit broad Balmer emission lines, especially Hα. These are characteristic features of Be (or Oe) stars, which emerge from their circumstellar decretion disk. The high-resolution Hα observations (HR15N) helped us to distinguish disk emission profiles. In

some cases, we observed a double-horn profile in Hα and Hβ. Some spectra are contaminated by nebular emission.

The fraction of Be stars in the sample is about 15%. This is slightly higher than that of our LMC sample described in Ramachandran et al. (2018b). This fraction is just a lower limit since we have only single epoch spectroscopic observations of our sample stars. We might have missed a fraction of Be stars owing to their transient nature and variability in the emission line profiles (about one-third to one-half, McSwain et al. 2008). Among this Be sample, 15 stars are identified as giants or bright giants, while the rest are dwarfs. These Be stars have spectral subtypes ranging from B0 to B5 (see Fig. 4.2). Interestingly, 15 out of 25 B-type giants are Be stars.

The statistics of spectral subtypes of all investigated OB stars is shown in Fig. 4.2. Emission line stars in each subtype are also illustrated. We can see a gradual increase in the number of stars with spectral subtypes starting from O3, until B2. Stars with spectral subtype B2 are the most common, while this spectral class also encompasses more Be stars than any other. The number of stars declines toward late B subtypes most probably because of our brightness limit.

4.3. Quantitative analysis

We performed the spectral analysis of all 320 sample OB stars in SMC-SGS 1 using the PoWR model atmosphere code. By fitting the model spectra to the observational data, we derive stellar and wind parameters of the individual OB stars.

4.3.1. Models

PoWR is a state-of-the-art stellar atmosphere code suitable for the spectroscopic analysis of any hot stars with and without winds, across a broad range of metallicities (Hainich et al. 2014, 2015; Oskinova et al. 2011). The PoWR models have already been used to analyze the complete sample of Wolf-Rayet (WR) stars and binaries in the SMC (Hainich et al. 2015; Shenar et al. 2016). The PoWR code solves the radiative transfer equation for a spherically expanding atmosphere and the statistical equilibrium equations simultaneously under the constraint of energy conservation. Stellar parameters were determined iteratively. Details of the PoWR code are described in Gräfener et al. (2002), Hamann & Gräfener (2004), Sander et al. (2015), and Todt et al. (2015).

A PoWR model is specified by the star's luminosity L, stellar temperature T_*, surface gravity g_*, and mass-loss rate $\dot{M}$ as the main parameters. The stellar temperature relates to R_* and L via the Stefan-Boltzmann law $L = 4\pi\sigma_{\rm SB} R_*^2 T_*^4$. In this case the "stellar temperature" T_* is the effective temperature $T_{\rm eff}$ corresponding to the stellar radius R_*. We place the latter at the Rosseland continuum optical depth of 20. In the case of our program stars, the winds are optically thin and the differences between T_* and $T_{\rm eff}$ ($\tau = 2/3$) are negligible.

In the subsonic region of the stellar atmosphere, a velocity field is defined such that a hydrostatic density stratification is approached (Sander et al. 2015). In the supersonic region, the prespecified wind velocity field $v(r)$ is assumed to follow the so-called β -law (Castor et al. 1975b) In this work, we adopt β=0.8, which is a typical value for O-type stars (Kudritzki et al. 1989).

In the non-LTE iteration in the co-moving frame, the line opacity and emissivity profiles are Gaussians with a constant Doppler width $v_{\rm Dop}$. We set this parameter to $30\,{\rm km\,s^{-1}}$ for our OB sample. In the formal integral for the calculation of the emergent spectrum, the Doppler velocity is split into the depth-dependent thermal velocity and a "microturbulence velocity" $\xi(r)$. The pressure broadening is also taken into account by means of microturbulent velocity. We adopt

$\xi(r) = max(\xi_{min}, 0.1v(r))$ for OB models, where ξ_{min} =20 km s^{-1} (Shenar et al. 2016). For main-sequence B stars, ξ_{min} can be low as 5 km s^{-1} (Hunter et al. 2008a; Dufton et al. 2006). By constructing some models with lower microturbulence velocities, we found that this effect is within the uncertainty limits of our grid parameters.

Optically thin inhomogeneities in the model iterations are described by the "clumping factor" D by which the density in the clumps is enhanced compared to a homogeneous wind of the same $\dot{M}$ (Hamann & Koesterke 1998). For all the OB stars in our study, we account for depth-dependent clumping assuming that clumping begins at the sonic point, increases outward, and reaches a density contrast of $D = 10$ at a radius of $R_D = 10\,R_*$ (Runacres & Owocki 2002). We note that the empirical mass-loss rates when derived from Hα emission scale with $D^{-1/2}$, since this line is mainly fed via recombination.

The models are calculated using complex atomic data of H, He, C, N, O, Si, Mg, S, P, and Fe group elements. The iron group elements are treated with the so-called superlevel approach as described in Gräfener et al. (2002). We adopt the following chemical abundance based on Trundle et al. (2007): $X_H = 0.7375$, $X_C = 2.1 \times 10^{-4}$, $X_N = 3.26 \times 10^{-5}$, $X_O = 1.13 \times 10^{-3}$, $X_{Si} = 1.3 \times 10^{-4}$, $X_{Mg} = 9.9 \times 10^{-5}$, $X_S = 4.42 \times 10^{-5}$, $X_P = 8.32 \times 10^{-7}$, and $X_{Fe} = 3.52 \times 10^{-4}$.

4.3.2. Spectral fitting

For a systematic spectral analysis, we constructed grids of OB-star model atmospheres for SMC metallicity with the stellar temperature T_* and the surface gravity log g_* as main parameters. The grid spans from $T_* = 10$ kK to 50 kK with a spacing of 1 kK, and log $g_* = 2.0$ to 4.4 [cm s^{-2}] with a spacing of 0.2 dex. For a given value of (T_*,log g_*), the stellar mass M and luminosity L are chosen according to the evolutionary tracks calculated by Brott et al. (2011). While the chemical composition is kept constant within the model grid, we also calculate specific models with adjusted C, N, O, Si abundances, when necessary. The SMC OB star grid is also available online[3]. More details of the PoWR model grids for OB stars are given in Hainich et al. (2018).

For all the 320 OB stellar spectra in the sample, we determined the best-fitting model by a careful iterative visual comparison of observed spectra with the model. We considered only single-star models for the fits. Our first step was to find the main parameters, i.e., the stellar temperature and surface gravity of the model that best represents the observed spectrum. The primary constraint we used is the helium and silicon ionization balance to determine whether the spectrum represents a very hot O star or cooler B star. For the hottest stars in the sample, we derived the stellar temperature by consistently fitting nitrogen emission lines and He II lines. In the case of cooler stars (10-20 kK), we determined the temperature by fitting Si II, Mg II, and He I lines. For intermediate temperature stars, we used the Si III to Si IV and He I / He II line ratios. The precision in the temperature is limited by the grid resolution of ±1 kK. After getting a constraint on the temperature, we measured the surface gravity using the pressure-broadened wings of the Balmer lines. The main diagnostic lines are Hγ and Hδ, since they are less affected by wind as well as disk emission. The typical uncertainty for log g_* is ±0.2 dex. Since the ionization balance also reacts on log g_*, the temperature might need to readjust accordingly. The uncertainty in log g_* therefore propagates to the temperature and leads to a total uncertainty of about ±2 kK. As example, the spectra of an O8 star (blue lines) is shown in Fig. 4.3 overplotted with a model (red lines) with $T_* = 35$ kK and log $g_* = 4.2$ [cm s^{-2}]. It should be noted that the above method of spectral fitting is not successful in the case of Be stars, since their Balmer absorption lines may be

[3] www.astro.physik.uni-potsdam.de/PoWR

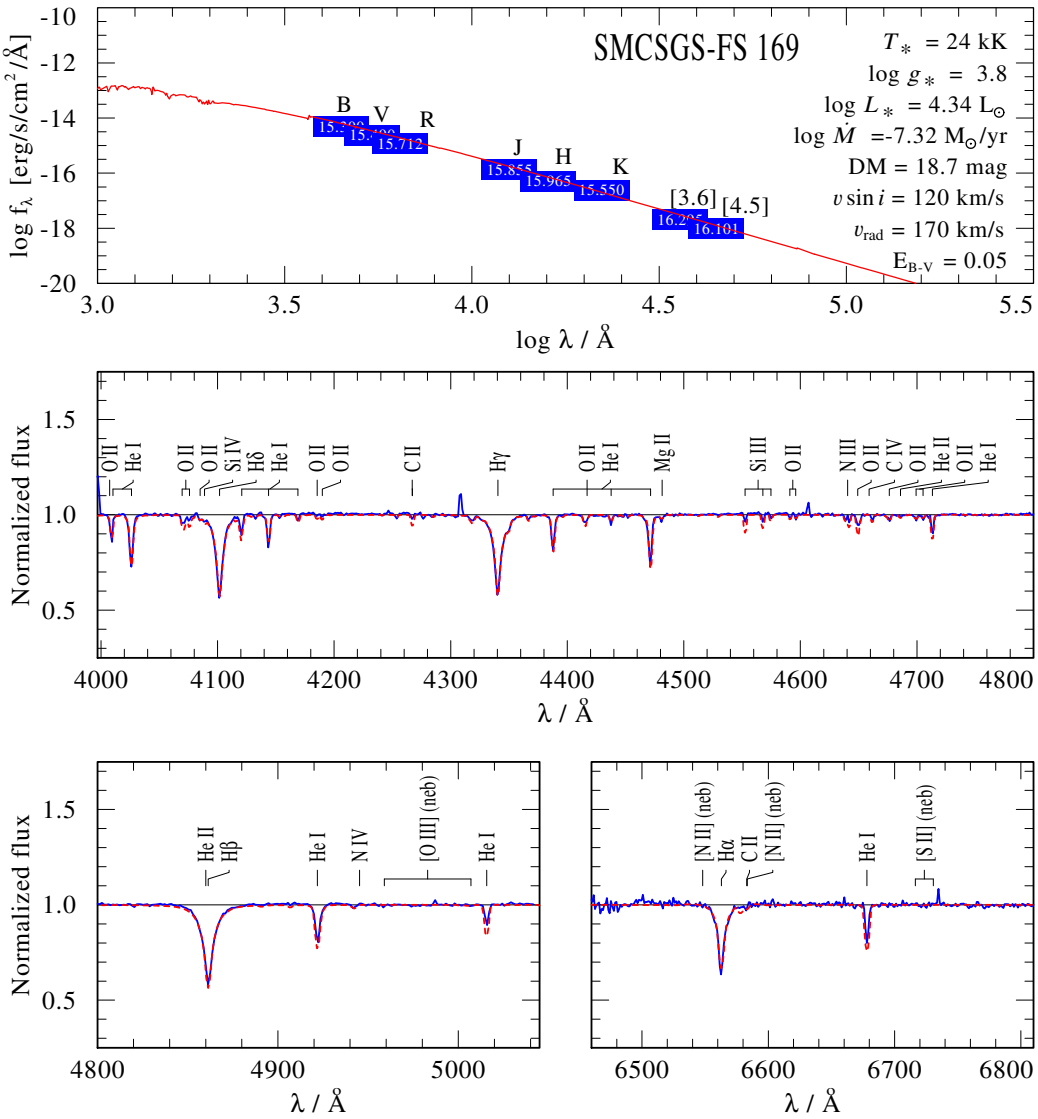

Figure 4.3.: Spectral fit for SMCSGS-FS 169. Top panel: The model SED (red) fitted to the available photometry from optical (*UBV* and *I*), and infrared (*JHK*$_s$ and *IRAC* 3.6 & 4.5 μm) bands (blue boxes). Botton panels: The VLT-FLAMES spectra (blue solid line), overplotted with the PoWR model (red dashed line). The parameters of this best-fit model are given in Table C.2.

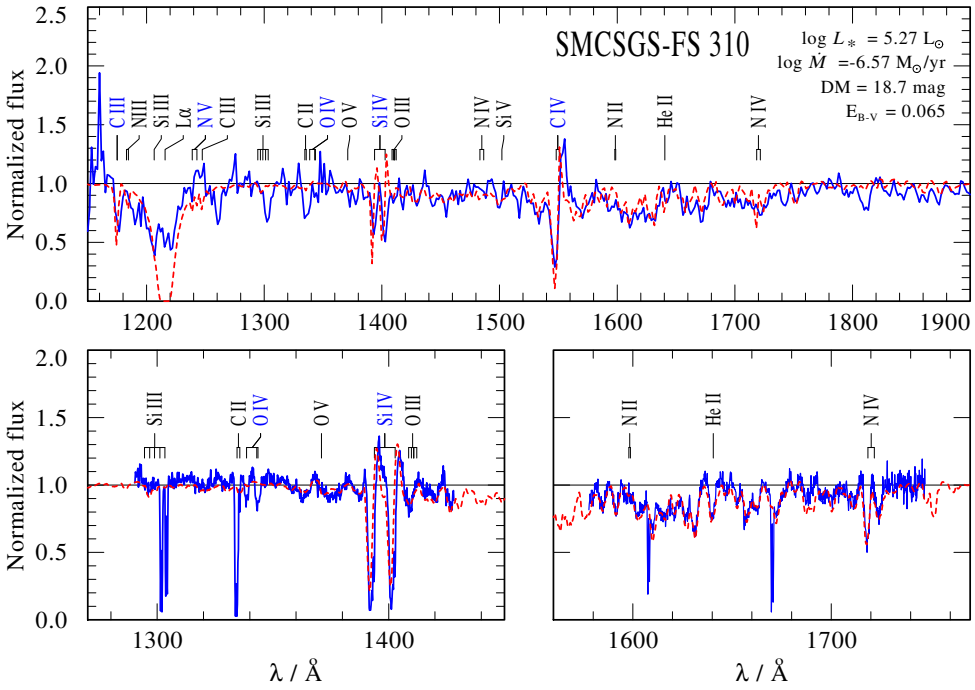

Figure 4.4.: Spectral fit for SMCSGS-FS 310. The panels show the normalized HST (blue solid line), overplotted with the PoWR model (red dashed line). The parameters of this best-fit model are given in Table C.2.

filled by disk emission. Therefore, the uncertainty in the stellar temperature and surface gravity of these stars is relatively high.

After fixing T_* and $\log g_*$, we determined the wind parameters whenever possible. The mass-loss rate and terminal velocities (v_∞) can be estimated from the UV P-Cygni profiles. For nine of our sample stars, UV spectra are available. We used the main diagnostic lines C IV $\lambda\lambda$1548–1551 and Si IV $\lambda\lambda$1393–1403 in the HST / IUE range and P V $\lambda\lambda$1118–1128, C IV λ1169, and C III λ1176 in the FUSE range. The typical uncertainties are ±0.2 dex in $\log \dot{M}$ and ± 100 km s^{-1} v_∞. Since UV spectra are not available for most of the sample stars, we need to constrain $\dot{M}$ and v_∞ based on optical lines such as Hα and He II λ4686. In fact none of the stars in the sample shows wind emission in Hα or He II λ4686 (do not confuse with disk emission in Be stars). In these cases, the adopted mass-loss rate is only an upper limit. For stars with no available UV spectra, we estimated the terminal velocities theoretically from the escape velocity $v_{\rm esc}$. For Galactic massive stars with $T_* \geq 21$ kK, the ratio $v_\infty/v_{\rm esc}$ is 2.6 and for stars with $T_* < 21$ kK the ratio is ≈1.3 (Lamers et al. 1995; Kudritzki & Puls 2000). We adopt a scaling for SMC metallicity using the relation, $v_\infty \propto (Z/Z_\odot)^q$, where $q = 0.13$ (Leitherer et al. 1992). The UV spectrum of the sample star SMCSGS-FS 310 is shown in Fig. 4.4. The derived mass-loss rate and v_∞ from the UV P-Cygni profiles are $\log \dot{M}$ = -6.6 [$M_\odot$ yr^{-1}] and 550 km s^{-1}, respectively.

We determined the luminosity L and color excess E_{B-V} of the individual OB stars by fitting the model SED to the photometry (see first panel of Fig. 4.4). In this case the model flux is diluted with the SMC distance modulus of 18.7 mag. We consistently adjusted the color excess and luminosity of the model's SED to reproduce the observed data. The typical uncertainty in $\log L/L_\odot$ is about

0.2 dex. For stars with available flux-calibrated UV spectra (HST, IUE, or FUSE), the uncertainty in the luminosity is only ≈0.1 dex in these cases. The color excess of OB stars in the Wing of the SMC is very small, typically 0.05 mag.

Subsequently, we chose a best-fit model for each individual OB star in the sample and overplotted the selected model with the observed spectra (eg. Fig. 4.3 and Fig. 4.4). There is a systematic shift between synthetic models and observed spectra owing to the radial velocities of sample stars. We measured the radial velocity of individual stars by fitting a number of absorption line centers of the synthetic spectra to the observation. The primary lines used for these measurements are absorption lines of He I, He II, and Si III. The typical uncertainty of v_{rad} varies from ±10 to 20 km s^{-1}.

Finally, we estimated the projected rotation velocity $v \sin i$ of all OB stars from their line profile shapes. The measurements are based on the Fourier transform (FT) method using the `iacob-broad` tool (Simón-Díaz & Herrero 2014). The primary lines selected for applying these methods are He I, Si IV and Si III. The typical uncertainty in $v \sin i$ is $\sim 10\%$. We convolved our model spectra with measured $v \sin i$ to account for rotational broadening, which results in a consistent fit with the observations. For example, the model spectra shown in Fig. 4.3 is convolved with a $v \sin i$ of 300 km s^{-1}.

We applied these spectral fitting methods in an iterative manner for individual OB star spectrum. More detailed explanations of the fitting procedure for each parameter is given in Ramachandran et al. (2018b). We also calculated individual models with refined stellar parameters and abundances for each of these stars, when necessary. The fitting procedure continued until no further improvement of the fit was possible. The final best-fit models yield the stellar and wind parameters of all OB stars in our sample.

4.4. Stellar parameters

The stellar and wind parameters of individual OB stars derived from spectral analysis are given in Table C.2. The PoWR model also gives the rate of hydrogen ionizing photons Q_0. We calculated the values of mass-loss rate, terminal velocity, and the mechanical luminosity $L_{\rm mec} = 0.5\,\dot{M}\,v_\infty^2$ produced by the stellar winds only for nine stars with available UV spectra. For the rest of the stars we adopted values from the derived relation of these nine stars. The distribution of some of these derived parameters in the total sample is illustrated in Fig. 4.5. Since we obtained only single-epoch spectra, we are not able to detect binarity.

The stellar temperature statistics of the sample is shown in the top left panel of Fig. 4.5. The temperature of our sample stars ranges from 10 kK to 46 kK, with a peak around 20 kK. It has to be emphasized that stars in the low temperature regime are incomplete owing to the observation limit. The earliest type O3 star has the highest stellar temperature of 46 kK. The sample also contains late B supergiants of temperature ≈ 10 kK. The surface gravities of sample stars are in the range of $10^{2.6}$ to $10^{4.4}$ cm s^{-2}, while most of the stars are found at log g_* of 4.2. This indicates that majority of the sample are young main sequence stars, while only a few percent of the stars are in evolved stages.

The mean color excess of our sample stars is only about 0.05 mag, which can be mainly attributed to the Galactic foreground. Hence the dust content in the Wing of the SMC is significantly low. Only six percent of the sample shows a color excess higher than 0.1 mag. The star, SMCSGS-FS 45, with highest $E_{B-V} \approx 0.45$ mag is a B supergiant located close to the highly extincted H II region N 88 (Heydari-Malayeri et al. 1999).

The histogram of the stellar masses given in Fig. 4.5 ranges from 4 $M_\odot$ to 50 $M_\odot$. In this figure

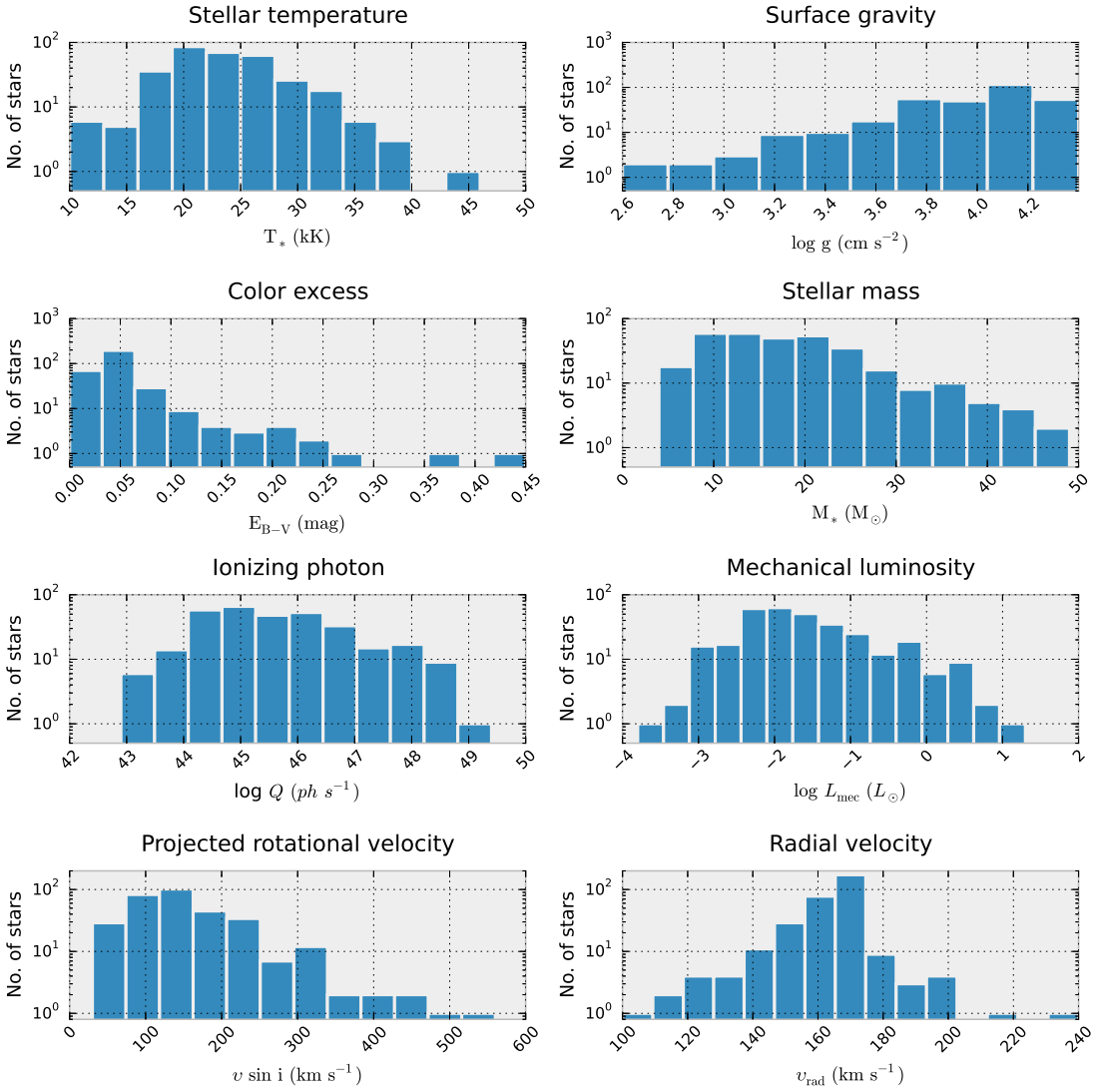

Figure 4.5.: Histograms of stellar temperature, surface gravity, color excess, projected rotational velocity, radial velocity, stellar mass, mass-loss rate, and mechanical luminosity of OB stars in SMC-SGS 1. The bin widths used are 3 kK, 0.18 dex, 0.03 mag, 4 $M_\odot$, 0.6 dex, 0.4 dex, 45 km s^{-1}, and 10 km s^{-1}, respectively. The number of stars in the y-axis are shown in logarithmic scale.

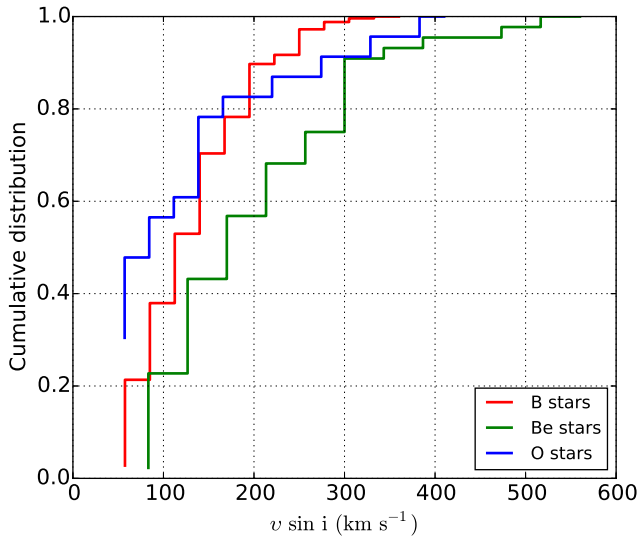

Figure 4.6.: Comparison of CDFs of $v \sin i$ between B, Be, and O stars

the stellar mass refers to the spectroscopic mass calculated from log g_* and R_* ($g_* = G\,M_*\,R_*^{-2}$). We note that the lowest mass bins are incomplete owing to the observational constraint. Most of the stars in the sample have masses in the range of 10–20 $M_\odot$.

The typical ionizing photon flux provided by an OB star in our sample is 10^{45} s^{-1}. One O3 star dominates the ionization of the region by releasing photons at a rate of 10^{49} s^{-1}.

We also plotted the statistics of the mechanical luminosity L_{mec} released by the stellar winds of our sample stars in Fig. 4.5. The OB stellar winds in SMC-SGS 1 provide only $L_{mec} < 10\,L_\odot$ to the surrounding ISM. Most of the stars produce mechanical luminosities a hundred times less than one solar luminosity. This is much lower than the mechanical luminosities of LMC OB stars (Ramachandran et al. 2018a).

4.4.1. Observed $v \sin i$ distributions

We derive the projected rotational velocities ($v \sin i$) of our sample stars from their optical line profiles. The $v \sin i$ distribution shows a main peak at ∼120 km s^{-1}, and the tail of the distribution extends to high rotational velocities up to 550 km s^{-1}. The fastest rotator in the sample is a Be star SMCSGS-FS 283, which has $v \sin i \approx 550$ km s^{-1}. We identified 20 very rapidly rotating stars with $v \sin i > 300$ km s^{-1}, which constitute 6% of the whole sample. This is double compared to that of our LMC (Ramachandran et al. 2018b). Among these rapid rotators, 12 stars have Oe/Be characteristics. Moreover, we can see a low but noteworthy peak around 300 km s^{-1} , which might be related to the effects of mergers and mass transfer in binary evolution (de Mink et al. 2013, 2014).

For further understanding, we constructed the cumulative distribution functions (CDFs) of the projected rotational velocities of our sample stars. The $v \sin i$ CDFs of O, B, and Be stars are compared in Fig. 4.6. As expected, Be stars exhibit a faster rotation compared to the normal B and O stars in the sample. The mean projected rotational velocities of Be stars in our SMC-SGS 1 sample is ≈230 km s^{-1}, which is significantly higher than the mean $v \sin i$ ≈140 km s^{-1} of normal

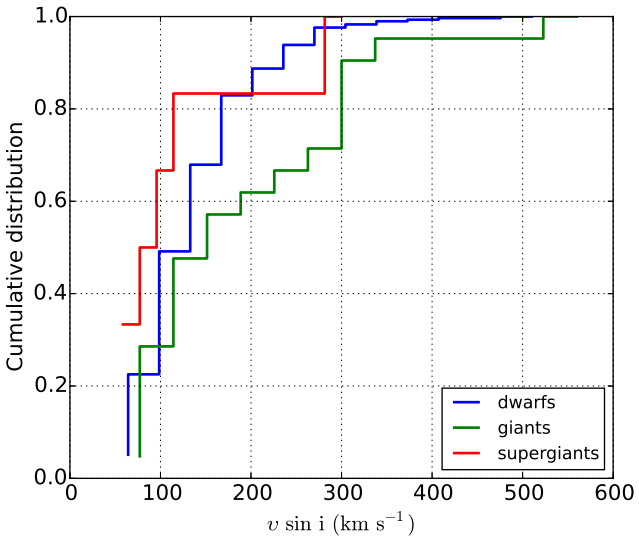

Figure 4.7.: Comparison of $v \sin i$ CDFs of dwarfs, giants, and supergiants

B stars. Most of the Be stars in this sample rotate close to their critical velocity.

We constructed $v \sin i$ CDFs of stars with different luminosity classes as shown in Fig. 4.7. About 40% of the giants have a $v \sin i > 200\,\mathrm{km\,s^{-1}}$. On average, they show a higher rotational velocity than unevolved dwarfs or evolved supergiants. Interestingly, 70% of these giants are found to be emission line Be stars. In a study of early-type stars in the SMC, Mokiem et al. (2006) found that very fast and very slow rotators are unevolved with respect to the group of evolved objects. However, in our sample, dwarfs are found to be less fast rotating than giants.

The simulated distribution of projected rotational velocities has a bimodal structure de Mink et al. (2013). Theory predicts that the majority of stars have low to intermediate rotational velocities, whereas nearly one-fourth have rotational velocities in excess of $200\,\mathrm{km\,s^{-1}}$. The VLT-FLAMES Tarantula Survey (VFTS) of massive stars in the LMC by Ramírez-Agudelo et al. (2013) and Dufton et al. (2013) also found a bimodal $v \sin i$ distribution. In order to check this trend in our sample, we plotted the probability density distribution of OB stars in Fig. 4.8 (blue solid curve). This reveals a two-component structure with about 26% of stars have $v \sin i > 200\,\mathrm{km\,s^{-1}}$.

For a comparison, the probability density distribution of $v \sin i$ of OB stars for various metallicities (Galaxy, LMC, and SMC) taken from our results and from previous papers are shown in Fig. 4.8. All these distributions are bimodal. However, there are noticeable differences in the main peak of the distribution (most probable velocity) as well as in the tail of the distribution. At SMC metallicities ($0.14\,Z_\odot$), the distribution consists of two broad peaks and the tail of the distribution extends to velocities as high as $500\,\mathrm{km\,s^{-1}}$. The $v \sin i$ distributions of LMC samples ($0.5\,Z_\odot$) have peaks at lower velocities than the the SMC sample. The Galactic samples show main peaks at relatively low velocities ($< 50\,\mathrm{km\,s^{-1}}$), the secondary peak is not very pronounced compared to the lower metallicity samples. Obviously, OB stars in the SMC sample have higher rotational velocities. This is a possible consequence of lower SMC metallicity, where the stars are more compact, stellar winds are weaker compared to LMC stars, hence suffer less angular momentum loss and therefore rotate faster (Meynet & Maeder 2002; Massey 2003; Ekström et al. 2008).

The subplot in Fig. 4.8 (top) shows a linear relationship between the peak of the distribution

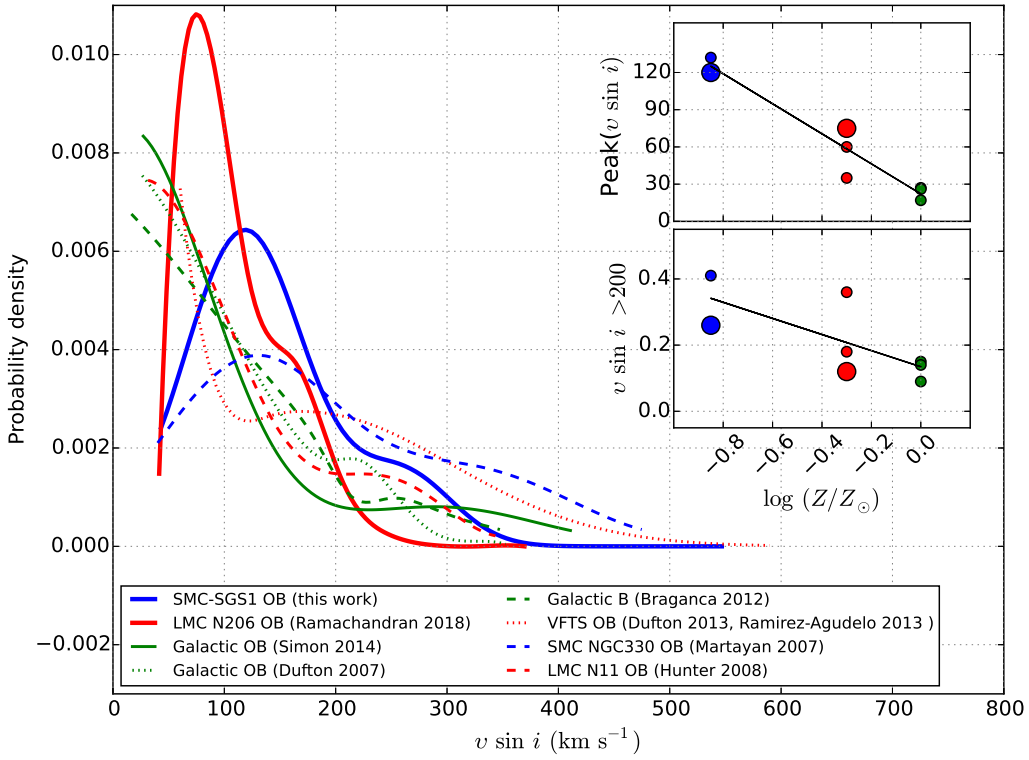

Figure 4.8.: Probability density distribution of projected rotational velocities for metallicities $Z = Z_\odot$ (Galactic, green curve), $Z = 0.5Z_\odot$ (LMC, red curve), and $Z = 0.2Z_\odot$ (SMC, blue curve). The subplots in the top and bottom show the effect of metallicity with the peak of $v \sin i$ distribution / most probable velocity and the fraction of stars with $v \sin i$ higher than 200 km s^{-1}, respectively. The Galactic, LMC and, SMC samples are represented using green, red, and blue dots, respectively. Our SMC (this work) and LMC (Ramachandran et al. 2018b) samples are shown as enlarged dots. See Sect. 4.4.1 for further information.

with the metallicity as given below,

$$\text{Peak}\,(v \sin i)/(\text{km s}^{-1}) \simeq -121 \times \log\,(Z/Z_\odot) + 22. \tag{4.1}$$

The fraction of fast rotating stars above 200 km s^{-1} also decreases with increasing metallicity, and can be written in the form,

$$\text{Fraction}\,(v \sin i > 200) \simeq -0.2 \times \log\,(Z/Z_\odot) + 0.1. \tag{4.2}$$

The OB star sample in the VFTS survey shows a very high fraction of rapidly rotating stars compared to other LMC samples. It should be emphasized that these OB star samples from various papers have different selection criteria, observational biases, and different age distributions, etcetera.

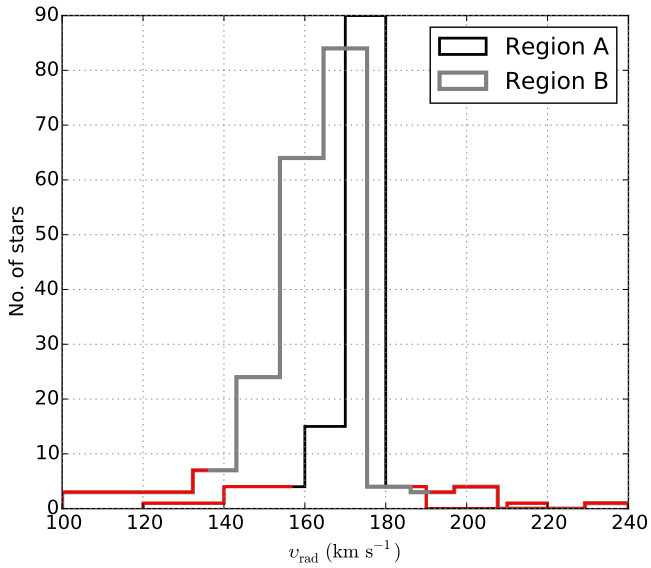

Figure 4.9.: Radial velocity distribution of stars located in region A and B. We used velocity bins of 10 km s^{-1} to construct the histogram. The value $|v_{rad}| > 3\sigma$ is represented by red lines in both histograms.

4.4.2. Radial velocity and runaway candidates

The radial velocities in our SMC-SGS 1 sample range from 100 to 240 km s^{-1} (see Fig. 4.5). The peak of the distribution is about ~170 km s^{-1}, which is close to the central velocity of the associated H I supershell (Staveley-Smith et al. 1997). The ionized gas shell associated with SMC-SGS 1 also has a heliocentric velocity of 173 km s^{-1} (Fulmer et al. 2019 submitted). The OB stars in the SMC show a radial velocity gradient, where the velocity distribution of stars in the Wing is more redshifted than in the Bar of the SMC (Evans & Howarth 2008; Lamb et al. 2016). In order to check for the velocity gradient within the SGS, we plotted the radial velocity distribution of stars located near the center of the SGS or close to NGC 602 (region A) and stars located in the western part of the SGS close to N 88 (region B). We can see a small velocity gradient between stars in these two regions (see Fig. 4.9). Stars in region B exhibit lower radial velocities and higher dispersion than in region A. The region A is within the SGS and has a more sharply peaked velocity distribution. The velocity spread between the stars is similar to the expansion velocity of the present day shell (see Fulmer et al. 2019 submitted, for details about velocity of the shell).

The radial velocities can be used to reveal runaway stars in a region. These are isolated stars or binaries that have escaped from clusters or OB associations as a result of a binary SN (Blaauw 1961) or dynamical ejection (Leonard & Duncan 1990). In order to identify possible runaway candidates, we compared the radial velocity of each star to the mean and standard deviation of all sample stars. Since region A and B have different radial velocity distributions, we decided to check for runaway stars separately in these regions. We defined a velocity threshold of $|\delta v_{rad}| > 3\sigma$ so that stars with outlying radial velocities are identified as runaway candidates. By excluding these stars, we continued to recalculate the mean velocity and standard deviation, until no more stars with $|\delta v_{rad}| > 3\sigma$ remain. Using this method, we found 11 and 14 candidate runaway stars in region A and B, respectively. This also includes the HMXB SMCSGS-FS 203 (alias SXP 1062).

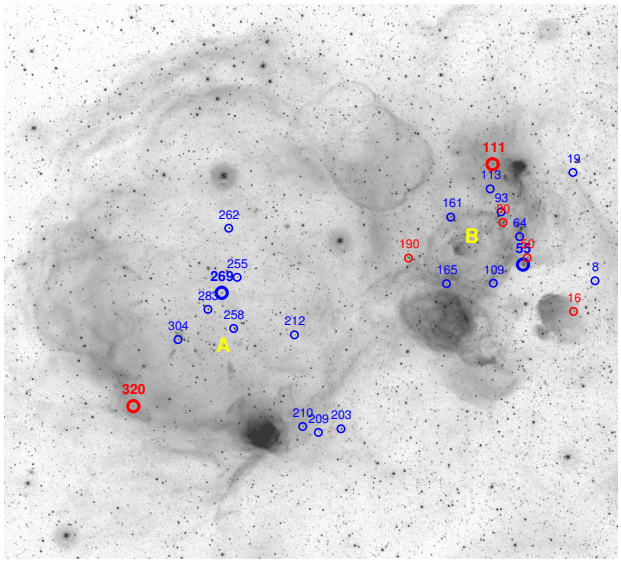

Figure 4.10.: Candidate runaway stars in the sample. The underlying Hα image is from the Magellanic Cloud Emission-Line Survey (MCELS, Smith et al. 2005). stars with redshifted and blueshifted velocities are indicated with red and blue circles, respectively. Small circles represent candidate runaway stars with $|\delta v_{rad}| > 3\sigma$, and large circles for stars with $|\delta v_{rad}| > 4\sigma$.

Their positions are denoted in Fig. 4.10, while their radial velocities and the deviation from the mean velocity are listed in Table C.3 along with their spectral types. Stars with positive and negative radial velocity deviations from the mean are denoted separately in Fig. 4.10. The mean radial velocity of the OB stars (excluding the runaway candidates) in region A and region B are 169±4 km s^{-1} and 163±9 km s^{-1}, respectively. The velocity dispersions in both regions are very small considering their size. Therefore, we also defined a higher velocity threshold of $|\delta v_{rad}| > 4\sigma$, which limits the possible runaway stars to four (large circles in Fig. 4.10). The estimated radial velocity gradient in the region is $\lesssim 3$ km s^{-1} deg^{-1} along RA and $\lesssim 13$ km s^{-1} deg^{-1} along Dec.

4.4.3. Spectral calibrations for OB stars at SMC metallicity

With a sample of 320 OB stars in the Wing of the SMC, our study offers a unique opportunity to calibrate the physical parameters of OB stars. This will be helpful for characterizing massive stars in extragalactic dwarf galaxies. It is not possible to obtain parameters such as temperature and ionizing flux by using optical photometry alone. Using quantitative spectroscopy, we measured these parameters and then calibrated with spectral types. Such studies have been pursued for Galactic (Martins et al. 2005b; Repolust et al. 2004), LMC (Ramírez-Agudelo et al. 2017; Mokiem et al. 2007b), and SMC (Mokiem et al. 2006; Bouret et al. 2003) massive stars. However, these studies mainly focused on O stars. In this work we extend this up to late B-type stars with a larger sample at SMC metallicity.

Figure 4.11 shows how the effective temperature correlates with the spectral subtypes. Different luminosity classes are denoted using different colors and symbols as given in the legends. As expected, the evolved stars (III-II and I) systematically possess lower stellar temperatures than dwarfs (Vz and V-IV) of corresponding spectral types. Moreover, we cannot define a single

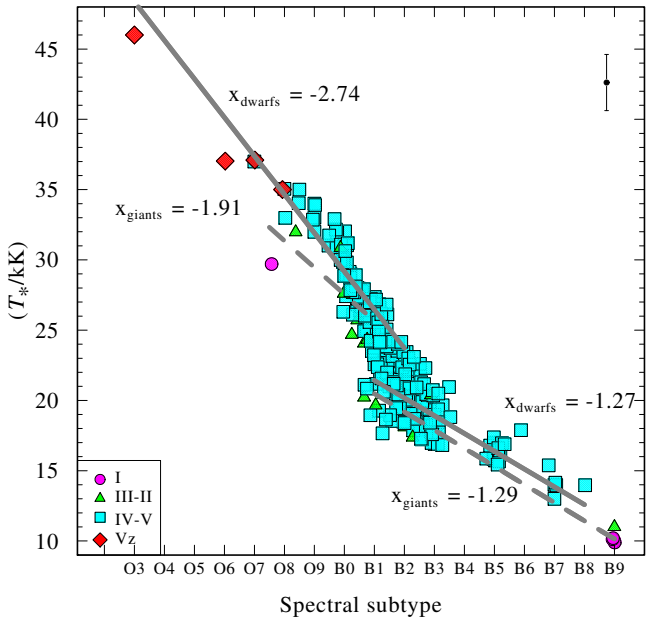

Figure 4.11.: Effective temperature vs. spectral type. The rhombi, squares, triangles, and, circles refer to luminosity classes Vz, V-IV, III-II, and, I, respectively. Typical uncertainties are indicated by the error bar in the top right corner. Gray thick lines represent linear regressions for different subgroups of stars (see text).

slope for temperature-spectral type relationship from O3 to B9, rather it changes around B1-B2. For stars with spectral type earlier than B1, the relationship is much steeper, and stars with later spectral types than B2 show a shallower relation. For stars with spectral type B1-B2, the temperature determination is more uncertain. The linear regression (see Fig. 4.11) yields the following relations:

For O3-B1 stars,

$$T_*[\mathrm{kK}] = \begin{cases} 56.60 - 2.74 \times \mathrm{ST} & (IV - Vz) \\ 46.61 - 1.91 \times \mathrm{ST} & (I - III) \end{cases} . \tag{4.3}$$

For B2-B9 stars,

$$T_*[\mathrm{kK}] = \begin{cases} 35.40 - 1.27 \times \mathrm{ST} & (IV - Vz) \\ 34.67 - 1.29 \times \mathrm{ST} & (I - III) \end{cases} . \tag{4.4}$$

In this case the spectral subtype is represented by an integer; for example, ST = 3 for an O3 star and ST = 13 for a B3 star. Effective temperature scales of B-type stars in the SMC presented by Trundle et al. (2007) agrees with our calibration within uncertainty limits of ±2 kK.

The PoWR models predict the rate of hydrogen ionizing photons (Q) for each individual OB star in our sample (see Table. C.2). We give calibrations of log Q with spectral types in Fig. 4.12 (top panel). Even though log Q decreases continuously to lower spectral subtypes, we can see breaks near B0 and B3. For O stars and late-type B stars (~ B3-B9), the slope of the relationship is much shallower than that for early-type B stars (B0-B3). An approximate fit to our data (see top panel in Fig. 4.12) is

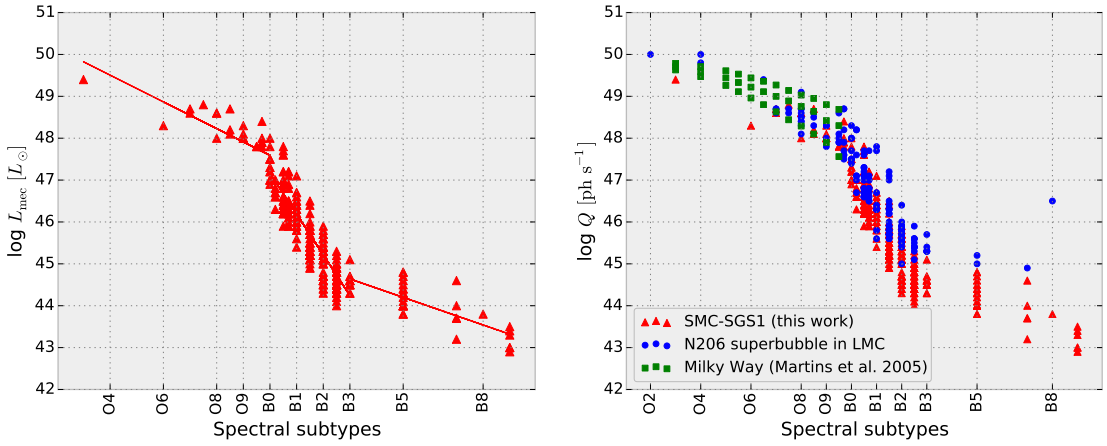

Figure 4.12.: Ionizing photon flux as a function of spectral subtypes (top panel) and the comparison with OB stars at LMC (Ramachandran et al. 2018b) and theoretically predicted values for O stars from Martins et al. (2005b).

$$\log\ Q\,[\mathrm{s}^{-1}] = \begin{cases} 50.8 - 0.32 \times \mathrm{ST} & (O\ stars) \\ 56.9 - 0.97 \times \mathrm{ST} & (B0 - B3) \\ 47.5 - 0.22 \times \mathrm{ST} & (B3 - B9) \end{cases} . \tag{4.5}$$

This log Q versus spectral subtype relation shows a similar trend as we found for the N 206 complex in the LMC (Ramachandran et al. 2018b). To check the effect of metallicity on the ionizing photon flux, we plotted the same diagram (see Fig. 4.12, bottom panel) but include values from Ramachandran et al. (2018b) (LMC stars) and Martins et al. (2005b) (Galactic stars). OB stars from the LMC sample (blue circles) also show similar breaks in the diagram. For comparison, theoretically calculated log Q for O stars from Martins et al. (2005b) (green squares) are also shown in the plot. Both LMC and Galactic data points match well. However, log Q values of SMC stars for a given spectral subtype are found to be systematically lower compared to the LMC and Galactic samples. Especially, log Q values of the late B stars in LMC and SMC, differ by more than 1 dex.

4.5. Indications for a dichotomy in massive star evolution independent of rotation

4.5.1. Observed Hertzsprung-Russell diagram

Based on the results of our spectral analyses, we construct the Hertzsprung-Russell diagram (Fig. 4.13) for our sample of 320 OB stars in the SMC. The sample comprises 23 O-type stars, among them four classified as Of, and 297 B-type stars including 44 stars with emission lines (type Be). This gives a well populated upper HRD of hydrogen burning stars with evolutionary masses (M_{ev}) in the range of ~5–50 $M_\odot$ (see Table C.4) and covering the parameter space from the ZAMS to the terminal age main sequence (TAMS). The most massive star in our sample is an O3 star (Sk 183), located close to the ZAMS with $M_{ev} \sim 47\ M_\odot$ and $\log(L/L_\odot) \sim 5.6$. All other stars have $M_{ev} \lesssim 30\ M_\odot$ ($\log(L/L_\odot) \lesssim 5.4$). The sample is complete for $V \lesssim 17$ mag, which translates

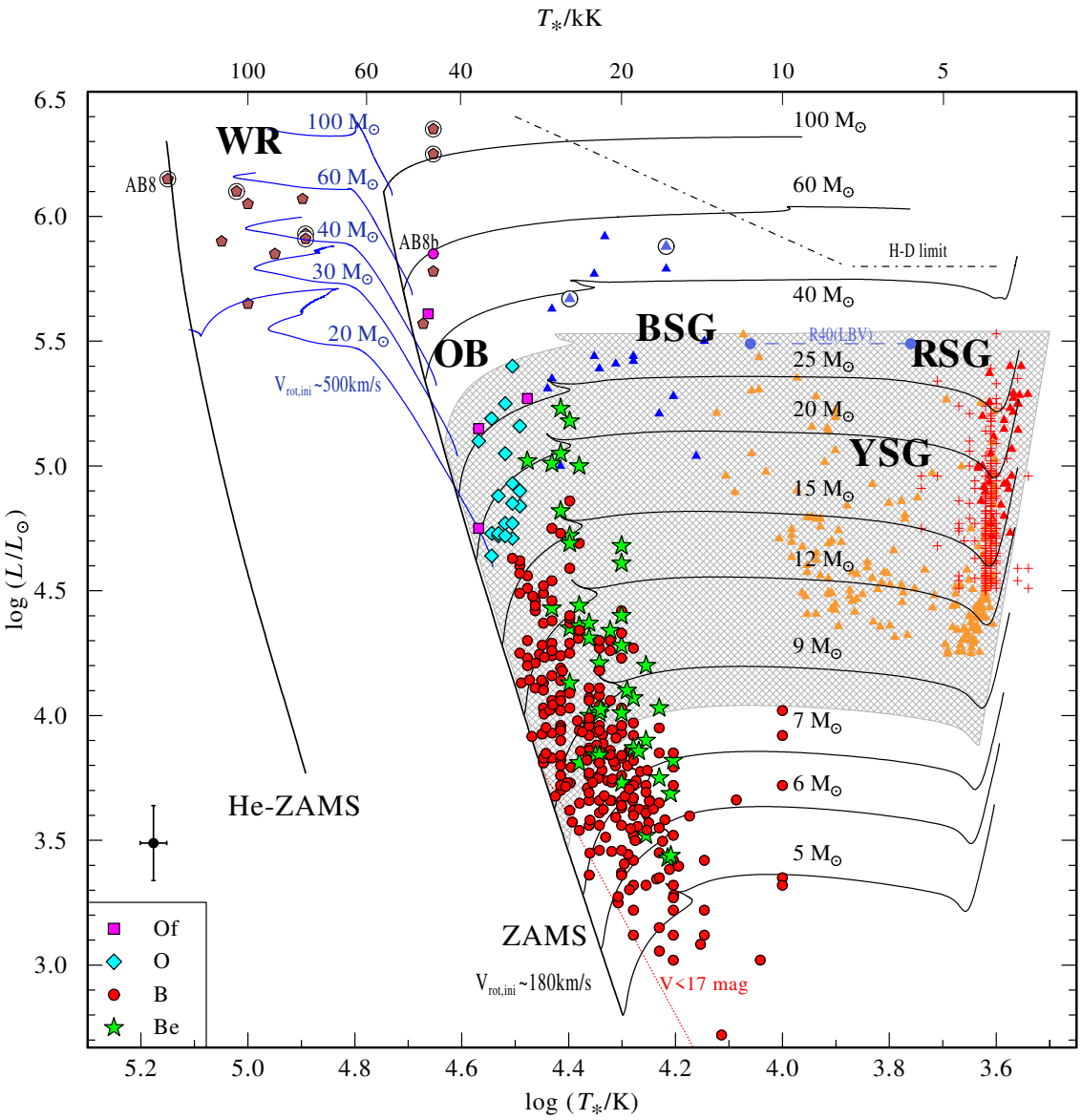

Figure 4.13.: Hertzsprung-Russell diagram for massive stars in the SMC. The OB stars analyzed in this work are represented by different symbols as explained in the legend. The typical error bar is shown in the bottom left corner, above the legend. The brown pentagons represent WR stars (encircled if in binary systems) (Hainich et al. 2015; Shenar et al. 2016), while yellow symbols stand for YSGs (Neugent et al. 2010), blue triangles for BSG (Trundle et al. 2004; Trundle & Lennon 2005) red crosses (Davies et al. 2018) and red triangles (Levesque et al. 2006) for RSGs. The HRD also includes the positions of the only confirmed LBV in the SMC, R40, at different epochs (Kalari et al. 2018). Our OB sample is limited to the SGS in the Wing of the SMC, while as all other samples spread across the whole SMC. Theoretical stellar evolutionary tracks with $v_{init} \approx 180\,\mathrm{km\,s^{-1}}$ are shown by solid lines (Brott et al. 2011; Köhler et al. 2015). The initial masses are indicated above each track. The black tracks show standard evolutionary paths, while the blue tracks with $v_{init} \approx 550\,\mathrm{km\,s^{-1}}$ show the tracks of quasi-chemically homogeneously evolving (QCHE) stars. The ZAMS and He-ZAMS are also shown. The shaded gray area indicates the region where, according to standard stellar evolution tracks, stars become RSGs and explode as SNe II-P. However, the more massive star above the gray shaded area do not seem to follow the standard evolutionary tracks. Instead, their location on the HRD is in agreement with QCHE (blue tracks). These stars remain very massive and may undergo core collapse . The figure demonstrates the dichotomy between the SMC stars with initial masses above $\sim 30\,M_\odot$ and below, suggesting that the former experience QCHE (blue tracks), while the latter do not.

into a steep limit in the HRD (red dotted line in Fig. 4.13) due to the temperature dependence of the bolometric correction.

To obtain a comprehensive picture of stellar evolution, we incorporate into the HRD samples of red supergiants (RSG), yellow supergiants (YSG), blue supergiants (BSG), luminous blue variables (LBV), and WR stars from previous studies (references are given in the figure caption). While the OB stars of our sample all reside in the supergiant shell SGS1 in the Wing of the SMC (cf. Sect. 4.7), the other samples are from the whole SMC. The WR (both single and binary) sample is complete for the whole SMC. The shown samples at RSG, YSG, BSG and LBV stages are also complete or nearly complete at high luminosities for this entire galaxy. In the Appendix (Fig. 4.18) we present a version of the HRD which additionally includes further samples of OB stars from various locations in the body of the SMC, taken from the literature.

All YSG, LBV and RSG stars in the SMC were reported with $\log(L/L_\odot) \lesssim 5.5$. The sample of RSGs in the SMC (complete for $\log(L/L_\odot) > 5.0$) has maximum luminosity of $\log(L/L_\odot) \sim 5.5$ (Davies et al. 2018). The region in the HRD above $\log(L/L_\odot) \sim 5.6$ (or $M_{init} \gtrsim 30\,M_\odot$) is populated mostly by stars close to the ZAMS or even hotter. Only six luminous BSGs ($\log(L/L_\odot) \gtrsim 5.5$) are seen to the right of ZAMS. These supergiants belong to the brightest blue objects in the SMC, and therefore have ~100% detection probability. Two of these supergiants are reported (Gvaramadze et al. 2011) as runaways (encircled blue triangles in Fig. 4.13) and, therefore, are most likely products of binary evolution. Another three BSGs show radial velocities that differ by more than $\pm 50\,\mathrm{km\,s^{-1}}$ from the systemic velocity of the SMC. Such large runaway velocity likely also indicates a binary past. Clearly, further studies on the nature of these BSGs are required.

The empirical HRD (Fig. 4.13) shows a remarkable pattern: while a few very luminous O stars are found close to the main sequence, all other OB stars as well as the BSGs, YSGs, and RSGs obey strict luminosity limits ($\log L/L_\odot < 6.0$ for BSGs, and < 5.5 for the cooler classes). The comparison with single-star evolutionary tracks suggest a dichotomy in the fate of massive stars in the SMC. Only stars with an initial mass below $\sim 30\,M_\odot$ seem to evolve from the main sequence to the cool side of the HRD to become a red supergiant. In contrast, stars with initially more than $\sim 30\,M_\odot$ appear to stay always hot.

In comparison the tracks for single-star evolution, this would imply that only stars with initially $\lesssim 30\,M_\odot$ evolve according to the standard tracks to become red supergiants. For stars with $\gtrsim 30\,M_\odot$ such evolution towards the cool side of the HRD is apparently inhibited.

A similar void region in the Galactic HRD is confined by the Humphreys-Davidson (HD) limit, as was empirically established by Humphreys & Davidson (1979b) long ago. A couple of stars that are found in the Galaxy, LMC, M31, and M33 which are close to or even slightly beyond the HD limit are considered as unstable stars (LBVs) (e.g. Groh et al. 2013; Martins & Palacios 2013; Urbaneja et al. 2017; Kourniotis et al. 2018; Humphreys et al. 2017, 2016). Our empirical HRD suggests that for the SMC the void region is even more extended than for galaxies with higher metallicity.

Why the SMC stars with initially $\gtrsim 30\,M_\odot$ stay at the blue side of the HRD? A tentative explanation is offered by the WR stars. The single WR stars, analyzed by Hainich et al. (2015), all reside between the ZAMS for hydrogen-rich stars and the theoretical He-ZAMS for hypothetical pure-helium stars. Such HRD position can be reached if a star evolves quasi chemically homogeneously, i.e. with efficient internal mixing, as demonstrated by the corresponding tracks in Fig. 4.13.

All single WR stars in the SMC are hydrogen depleted, but not free of hydrogen. In contrast, WN stars (i.e. WR stars of the nitrogen sequence) in the Galaxy or LMC either reside at the cool side of the ZAMS if showing some hydrogen, or on the hot side of the ZAMS if hydrogen-free.

Remarkably, all WR stars in the SMC are very luminous ($\log L/L_\odot \gtrsim 5.6$). There are no WR stars with lower luminosities, in contrast to the LMC and the Galaxy (Hainich et al. 2014; Hamann et al. 2006). Considered as a whole, in the SMC the population of single WR stars is strikingly different from higher metallicity environments.

Hence, the large void in the upper HRD, i.e. the absence of any cool stars at high luminosity, together with the presence of luminous, chemically homogeneous WR stars at such high luminosities, leads us to the working hypothesis that, at SMC metallicity, stellar evolution is governed by internal mixing for initial mass $\gtrsim 30\,M_\odot$.

4.5.2. Predictions from stellar evolution models

For comparison with the predictions of stellar evolution models, we consider recent stellar evolutionary tracks (Brott et al. 2011; Köhler et al. 2015). The tracks with an initial rotational velocity of $v_{init} \approx 180\,\mathrm{km\,s^{-1}}$ which is consistent with the current average rotational velocity ($\approx 150\,\mathrm{km\,s^{-1}}$) of our sample (see Fig. 4.13, 4.14) show significant deviations from our empirical HRD for stars with initial masses $M_{init} \gtrsim 30\,M_\odot$. The lack of luminous RSGs is supported by detections of SNe II-P progenitors that are consistent with an upper mass limit of $M_{init} \lesssim 25\,M_\odot$ (Davies & Beasor 2018) for RSGs, even at low metallicity ($Z \lesssim 0.1\,Z_\odot$) (Anderson et al. 2018).

While the standard evolutionary tracks cannot explain the location of putatively single WR stars in the HRD (Hainich et al. 2015; Martins et al. 2009), these are better reproduced by QCHE tracks (see however, discussions in Schootemeijer & Langer 2018). Even if a star is not fully mixed, a thin envelope could be removed by the stellar wind.

We ask ourselves what could be the possible reasons for this apparent empiric dichotomy in stellar evolution. Among the main factors that strongly affect massive star evolution, we focus on rotation, binarity, mass-loss rate (see Sect. 4.6) , and star formation history (see Sect. 4.7). Rapid rotation leads to efficient mixing of the stellar interior, leading to QCHE (Maeder & Meynet 2000) from the hydrogen ZAMS toward higher temperatures approaching the helium ZAMS toward the end of hydrogen burning (Yoon & Langer 2005). Quasi-chemically homogeneous evolution is expected to be more common among massive stars at low Z (Brott et al. 2011). The minimum rotation rate required for QCHE decreases with increasing mass (Yoon et al. 2006). At SMC metallicity, the theoretical minimum mass necessary for a star to experience QCHE is about $17 M_\odot$ with an initial $v_{rot} \approx 550\,\mathrm{km\,s^{-1}}$ or higher (blue tracks in Fig. 4.13). It should be noted that this minimum initial velocity is very model dependent, in particular, it depends on how rotation is implemented in the stellar models (Song et al. 2016).

4.5.3. Impact of stellar rotation

The distribution of stellar rotation rates of our sample stars show a bimodal distribution (see Sect. 4.4.1). Approximately 30% of stars in the secondary peak are Be stars, which rotate close to their critical velocity. It is likely that some of the fast rotating stars, including members of the Be class, experienced binary interaction during their evolution (de Mink et al. 2013). According to single-star evolutionary tracks, their evolutionary masses range from 6 to 25 $M_\odot$ and they reside close to the TAMS (indicated by the hooks in the evolutionary tracks in Figure 4.13). These Be stars are also likely evolving toward a YSG/RSG phase.

Figure 4.14 shows $v \sin i$ for our sample of stars versus their evolutionary mass. First, we consider stars with masses above $30\,M_\odot$. The $v \sin i$ values for these stars decline sharply with mass and become relatively low. Such slow rotators are not expected to experience QCHE. Yet,

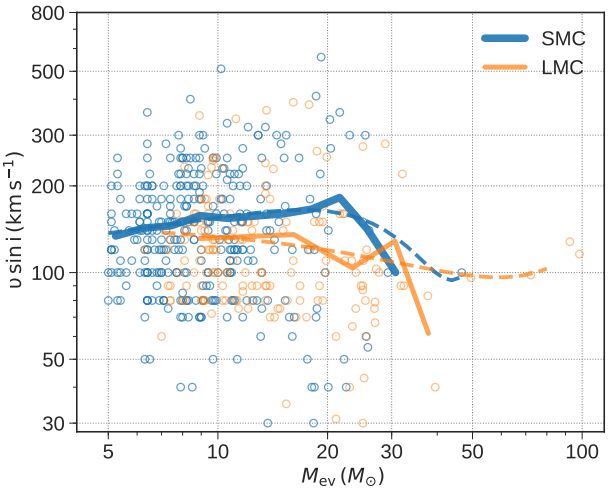

Figure 4.14.: Projected rotational velocities of OB stars as functions of stellar mass (blue circles) on logarithmic scales. The LMC OB star sample (Ramachandran et al. 2018b) is also shown for comparison. Solid lines represent mean velocities averaged over logarithmic mass bins, while dashed lines give nonlinear fits to the data.

we do see these stars close to the QCHE tracks in the HRD, suggesting that the mixing is not solely associated with rotation. Second, we consider stars with lower masses, $M_{init} \sim 17 - 25\,M_\odot$. Among these stars are a group of fast rotating OB stars with $v \sin i$ in the range 300–550 km s^{-1}. Despite their fast rotation, these stars do not follow QCHE tracks, but are located on the cool side of the ZAMS. Therefore, we conclude that SMC stars with $M_{init} \lesssim 30\,M_\odot$ follow standard evolution, independent of their current rotation rates.

The evolution of a star depends on its initial rotation rather than the current rotation. Unfortunately, it is hard to get a good handle on the initial rotation velocity of a star. It is different from the measured surface rotation because stellar mass loss (through line driven winds, mechanical mass loss by fast rotation, or induced by close binary evolution) can slow down the star throughout its evolution. We can state that our sample stars are still young and that their present-day mass-loss rates are very small (see Sect. 4.6). Hence, in case their present mass-loss rate would be representative for their whole previous lifetime, we would not expect a significant loss of angular momentum. We conclude that the evolutionary dichotomy observed in the HRD is independent of rotation.

Significantly, the upper limits on the rotational velocities of WR stars in the SMC are lower than that predicted for QCHE (Hainich et al. 2015). We may speculate that these WN stars had higher rotational velocities while on the ZAMS, but had slowed down since then. Our measurements of massive O stars do not support this (Fig. 4.14); a similar trend is also observed at LMC metallicity (Ramachandran et al. 2018b). Therefore, rapid rotation alone cannot be the crucial factor responsible for the observed dichotomy. Our results confirm the spectropolarimetric study of WR stars in Magellanic clouds, where no evidence for rotationally induced QCHE was found (Vink & Harries 2017).

4.5.4. Impact of a companion

Stellar evolution is also affected by the presence of a companion. So, the mass transfer in close binaries could also be another channel for the formation of WR stars. However, this channel cannot explain the apparently single massive WR stars in the SMC, which are all very massive and contain hydrogen, exactly as predicted by QCHE models. In case of WR stars in binary systems the situation is different.

While the spectra of our sample OB stars are satisfactorily fit by single-star models and do not clearly indicate binarity, it is likely that many of our targets are in fact binary systems (Sana et al. 2012). According to the Optical Gravitational Lensing Experiment (OGLE) survey (Pawlak et al. 2016), about 7% of our sample are eclipsing binaries, setting a firm lower limit on the binary fraction. A significant binary fraction may indeed affect our results. Our derived luminosities would be overestimated (e.g., by 0.3 dex for a binary with two identical stars) and this may result if the continuum of a companion dilutes the emission line spectrum. Lower luminosities would imply lower masses, and the uncertainty in T_* is irrelevant in the context of the observed dichotomy. We conclude that our main results are not affected by uncertain binary statistics. However, close binary evolution can produce stars that occupy the same positions on the HRD as single stars, for example, via merging. In this case, single-star evolutionary models can mislead the interpretation. At present, the physics of merging is not well understood, but it is important to keep in mind that, in principle, merger products could contaminate our sample, for example, as extraluminous BSGs (Menon & Heger 2017; Farrell et al. 2019).

Summarizing, our empirical HRD of the SMC and comparisons with evolutionary tracks indicate two different paths of massive star evolution at low metallicity. Stars with initial mass below 30 $M_\odot$ evolve without full mixing toward a RSG phase, where they are likely to explode as SN II-P. In contrast, massive single stars ($M \gtrsim 30 M_\odot$) expand only a little during their main sequence evolution, and then evolve toward WR stages remaining mixed, hot, and compact, in accordance with the predictions of the QCHE model. The lack of SNe with corresponding progenitors provides support to the idea that stars at the end of their QCHE may collapse to black holes directly (Heger et al. 2003; Marchant et al. 2016; Hainich et al. 2018). We suggest that the main factors for the evolutionary dichotomy are low metallicity and the initial mass of the star, rather than rotation.

4.6. Weak winds of massive stars at low metallicity

The spectroscopic analysis allows us to quantitatively measure stellar mass-loss rates. Observations in the UV are especially suitable for this. For nine stars with available UV spectra (see Sect. 4.2), we supplemented the optical spectra with the UV observations, and analyzed these spectra in a consistent manner using various diagnostic lines. Figure 4.15 shows the mass-loss rate ($\dot{M}$) versus luminosity of these nine OB stars (B2 to O3). A linear regression to this $\log \dot{M} - \log L$ relation, which accounts for the individual error bars, shows an order of magnitude systematic offset compared to the theoretical predictions (Vink et al. 2001) for SMC OB stars. The only exception is an Of supergiant (green diamond in Fig. 4.15). Excluding this star would result in an even higher offset compared to the predictions. Our results confirm previous spectroscopic studies of massive stars in the SMC (Bouret et al. 2003; Martins et al. 2004) and other low-metallicity dwarf galaxies like IC 1613 and WLM (Bouret et al. 2015; Lucy 2012). This is also in agreement with X-ray observations of NGC602 cluster (Oskinova et al. 2013), where they revealed that the emission is mainly coming from young low-mass stars, while the winds of the massive stars are

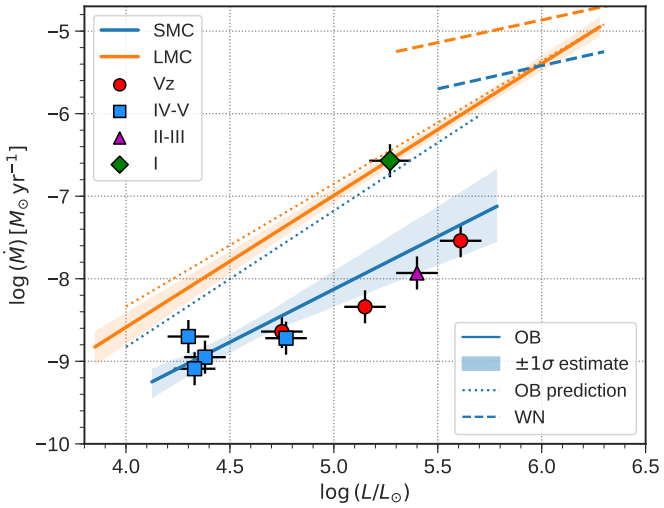

Figure 4.15.: Mass-loss rate as a function of stellar luminosity for the analyzed SMC OB stars with available UV data. Luminosity classes are distinguished by different symbols as given in the legend. A power-law fit to the empiric relation is represented by the blue solid line. For comparison, we include the empirical relation for LMC OB stars (Ramachandran et al. 2018b) along with theoretical predictions (Vink et al. 2001) (dotted lines) at SMC and LMC metallicities. The empirical relations for WN stars in the SMC and LMC (Hainich et al. 2017) are also illustrated in the plot (dashed lines).

not sufficient to power the detected extended X-ray emission.

In many OB-type dwarfs, the mass-loss rates derived empirically are much lower than predicted by the standard mass-loss recipes. At solar metallicity (or even LMC), this problem is limited to the late O- and early B-type dwarfs, and is often dubbed as the weak wind problem (Martins et al. 2005b; Marcolino et al. 2009; Oskinova et al. 2011).

Among our subsample of OB stars with UV-based mass-loss rates, eight out of nine stars exhibit the weak wind phenomenon (cf. Fig. 4.15), with the exception of the supergiant SMCSGS-FS 310. The objects with weak wind comprise not only dwarfs, but also one star of luminosity class III (SMCSGS-FS 288). One of the stars (the most luminous one indicated in Fig. 4.15) has even the very early subtype O3 (SMCSGS-FS 231). In support of our finding, we mention that Bouret et al. (2013) obtained a low $\dot{M}$ even for the most luminous O-star in the SMC, MPG 355. Thus, it seems that at SMC metallicity the weak-wind phenomenon is ubiquitous, and concerns all OB subtypes and all luminosities except supergiants.

All hot star winds are clumpy (Hamann et al. 2008; Puls et al. 2008). Our model calculations account for such inhomogeneities in the *microclumping* approximation. We adopt depth dependent clumping with a density contrast $D = 10$ (i.e. volume filling factor $f = 0.1$). Details were given in Sect. 4.3.1. Clumping enhances emission lines which are fed by recombination cascades (Hamann & Koesterke 1998). Compensating for this effect, one derives a mass-loss rate that is smaller by the factor $\sqrt{D}$ than with a smooth-wind model. Such clumping dependence would apply if we would have derived $\dot{M}$ from, e.g., an Hα emission line.

Fortunately, our empirical mass-loss rates shown in Fig. 4.15 and discussed above have been

derived from resonance lines in the UV. These wind lines are mainly formed by line scattering. Since the corresponding opacities scale linearly with density, these lines do not react on micro-clumping at all. Hence, the mass-loss rates we obtained are independent of the adopted clumping parameters.

Theoretical considerations predict a power-law dependence of the mass-loss rate on metallicity, $\dot{M} \propto Z^{\alpha}$, with α=0.69 for O-type stars (Vink et al. 2001), whereas empirical studies found α=0.83 (Mokiem et al. 2007b). However, our analysis suggests a much steeper relation with $\alpha \sim 2$. The WN winds show a metallicity dependence of $\dot{M} \propto Z^{1.2}$ (Hainich et al. 2017). Since WR winds are much stronger than the winds of O stars, it is important to consider by how much the mass loss increases while a star evolves from the O to the WR stage. Figure 4.15 shows empirical and theoretical mass-loss rates for O and WR stars in the LMC and SMC. It is striking that the difference between mass-loss rates of O and WR stars is significantly larger at the lower SMC metallicity compared to the LMC.

Very weak winds of OB stars should have only low impact on their fates. However, it may change our current understanding on stellar evolution, because theoretical evolutionary tracks, as a rule, are calculated using the standard mass-loss recipes, and hence are based on strongly overestimated mass-loss rates. After the first detection of gravitational waves, it has been argued that black hole pairs as massive as 60 $M_{\odot}$ can only form if the mass loss is relatively low (Abbott et al. 2016). For instance, according to SMC metallicity tracks by Eldridge et al. (2008), a star with initially 60 $M_{\odot}$ ends with only 22 $M_{\odot}$ short before core collapse. This prediction depends on the adopted mass-loss rate prescriptions for the different evolutionary phases. Additionally, a star might loose a significant amount of mass by eruptions in the LBV stage (Smith & Owocki 2006), which is not taken into account by standard tracks. However, if a star evolves quasi chemically homogeneously, the phase of LBV instability can be avoided. The weak winds in the OB phase reported here are not sufficient to remove the hydrogen envelope, and therefore not lead to a WR phase. This is in agreement with the suggested dichotomy in evolution, where apparently single WR stars are formed by strong internal mixing. Very weak OB winds and QCHE above a certain mass limit suggest that massive black holes can form even at SMC-like metallicity.

4.7. Mode of star formation in the SMC Wing

Spectroscopy of massive stars allows us to investigate the star formation modes in the SMC Wing and the SMC-SGS 1. Using the evolutionary tracks and isochrones (Brott et al. 2011), we estimated the individual ages of all OB stars (see Fig. 4.16, Table C.4). The uncertainties in the age are mostly in the range of 20-40%, which comes from the uncertainties in temperature, luminosity, and $v \sin i$. Five stars in this complex are found to be very young, and are less than 2 Myr in age, including the O3-type star (Sk 183) in NGC 602. From ages and masses of the individual OB stars, and by extrapolation to lower masses (0.5 $M_{\odot}$) using the Salpeter initial mass function (IMF), we estimate the present day star formation rate (SFR) of the complex to be $\approx 10^{-3}\, M_{\odot}\,\mathrm{yr}^{-1}$. With the area of the two observed fields in SMC-SGS 1 (~0.2 kpc^2) the SFR surface density becomes $\approx 4 \times 10^{-3}\, M_{\odot}\,\mathrm{yr}^{-1}\,\mathrm{kpc}^{-2}$.

A comparison of the empirical HRD with the evolutionary isochrones gives an age spread from 0 to 100 Myr for the OB stars in the complex. The age histogram (Fig. 4.17) indicates persistent star formation in this large-scale low density region over a long time. The distribution shows active star formation ongoing since 30–40 Myr, with a peak at about 6–7 Myr ago. Of course, the present age distribution is biased by the expired lifetimes of the more massive stars. It is tempting to suggest

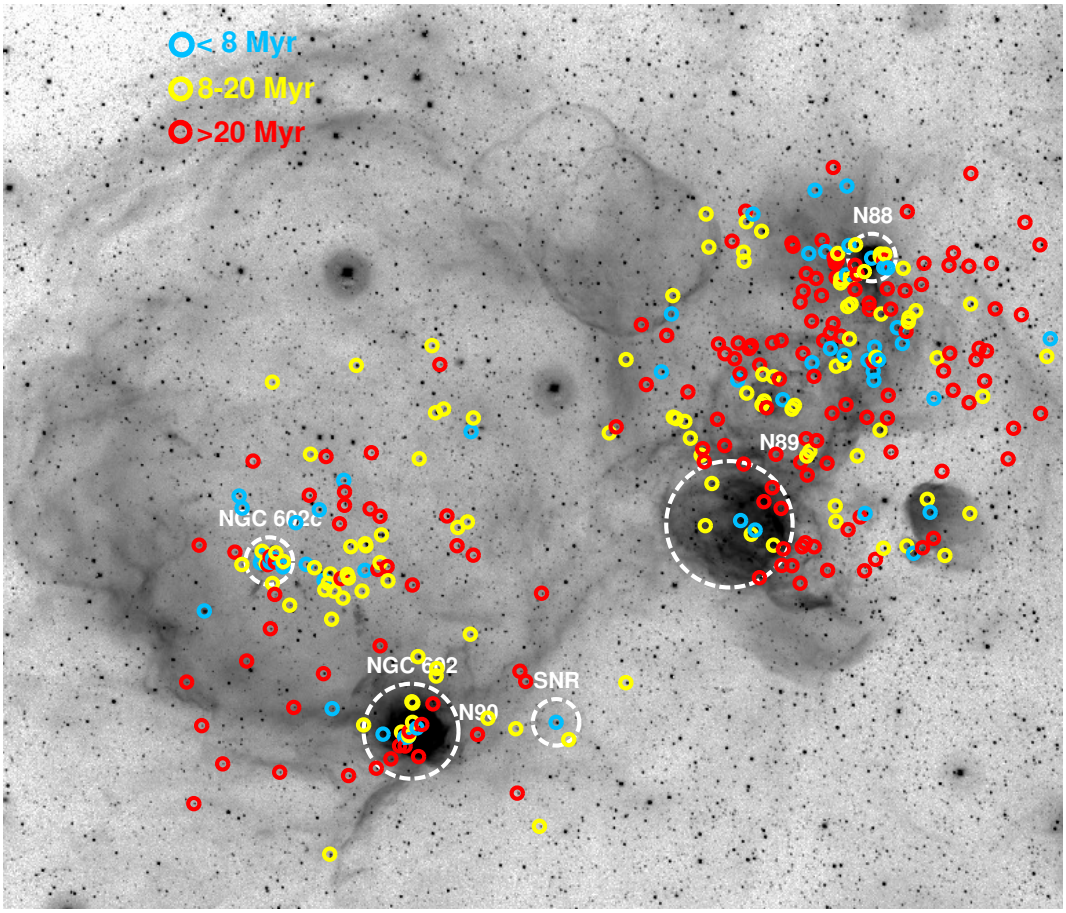

Figure 4.16.: Distribution of the OB stars in the SGS, color coded with their age

that the feedback from massive stars that formed 30–40 Myr ago, but already disappeared, have created this SGS, which expands and triggers the formation of present massive stars near its rim. However, as can be seen from Fig. 4.16, there is no obvious age gradient across the SMC-SGS 1 (see also Fulmer et al. 2019 submitted). We found many young massive stars close to the central parts of the complex, especially in the NGC 602c cluster, and also in the western regions near N 88. On the other hand, there is a high concentration of the relatively old B-star population in the western nebular regions. Such spatial distribution in the complex nullifies SGS induced star formation at the rim. Instead, it supports a stochastic mode of star formation. Altogether, we invalidate the central source/cluster scenario for the formation of the SGS. Moreover, we found that the Hα emission in the complex does not fully trace the distribution of young massive stars. Only faint, filamentary Hα emission is observed in the central part of SGS, which hosts a relatively high number of young massive stars.

We ask ourselves whether the apparent dichotomy in the empirical HRDs (Figs. 4.13 and 4.18) in fact reflects a specific star formation history instead of a bifurcation in stellar evolution. We believe that this is unlikely because the stars in the empirical HRD are located in different parts of the SMC; while our OB star sample is in the Wing of the SMC, other stars are distributed throughout the SMC and include runaway and cluster members. Therefore, there is no reason to suspect that all stars with masses above $\sim 30\,M_{\odot}$ are produced in the same coherent star burst

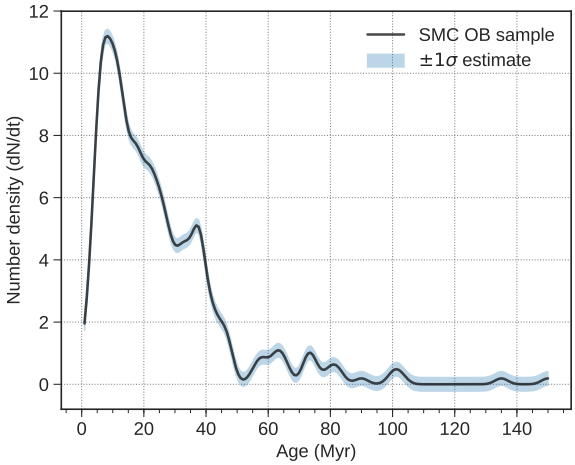

Figure 4.17.: Distribution of stellar ages of OB stars in our sample

episodes.

4.8. Feedback from massive stars and the energy budget of the supergiant shell

The total ionizing photon flux produced by all the OB stars in our sample is $\Sigma Q \approx 8 \times 10^{49}\,\mathrm{s}^{-1}$, and 30% are contributed by the O3 star located in NGC 602 alone. The SGS also encompasses AB 8, the WO-type binary in the NGC 602c cluster. By releasing a hydrogen ionizing photon flux of $Q \approx 1.5 \times 10^{50}\,\mathrm{s}^{-1}$ and He II ionizing photon flux of $\approx 5 \times 10^{47}\,\mathrm{s}^{-1}$, the WO+O4 system dominates the radiative feedback in SMC-SGS 1 (Shenar et al. 2016). However, the H II region associated with NGC 602c and its WO binary consists only of small, relatively faint emission regions scattered around the cluster. The integrated Hα luminosity of the SGS (Kennicutt et al. 1995) corresponds to an ionizing photon flux of $Q = 10^{50}\,\mathrm{s}^{-1}$. This is only half of the total Lyman continuum flux emitted by the stars we analyzed.

The winds of SMC OB stars are quite weak (Sect. 4.6). Therefore it is not surprising that the mechanical feedback by OB stars in this region is significantly lower than in star-forming regions in the LMC (Ramachandran et al. 2018b) and the Galaxy. The total mechanical luminosity generated by all OB stars in our sample is estimated to be $\Sigma L_{\mathrm{mec}} = \Sigma\, 0.5\, \dot{M}\, v_\infty^2 \sim 3 \times 10^{35}\mathrm{erg\,s}^{-1}$. The accumulated mechanical energy from all sample OB stellar winds throughout their life is $\Sigma E_{\mathrm{mec}} = \Sigma\, 0.5\, \dot{M}\, v_\infty^2 t \approx 6 \times 10^{49}\,\mathrm{erg}$. We estimate the radial momentum contribution to be $\Sigma p = \dot{M}\, v_\infty t \approx 5 \times 10^{41}\,\mathrm{g\,cm\,s}^{-1}$. We emphasize that these feedback estimates only consider current OB stars in the complex and do not account for those massive stars that already disappeared. In addition, our sample does not include massive stars in the northern regions of the SGS.

The WO+O system, AB 8, alone supplies a current mechanical luminosity of $\approx 7 \times 10^{37}\,\mathrm{erg\,s}^{-1}$. This is more than two orders of magnitude higher than the mechanical luminosity produced by all 320 OB stars in the sample together. In order to estimate the mechanical energy released by the WO star during its lifetime, we need information about its progenitor. We estimated this with the help of binary evolutionary tracks (Eldridge & Stanway 2009), by giving the current parameters

of the primary and secondary as input. The mechanical energy contribution is $\approx 1.6 \times 10^{51}$erg in the pre-WR phase and $\approx 4 \times 10^{50}$erg in the WR phase. Interestingly, the accumulated energy and momentum from this WO binary are also two orders of magnitude higher than those generated from all OB stars together (see Table 4.1). Hence, a single WR star (contribution of the secondary is negligible) is responsible for the vast majority of feedback in the complex, exceeding by far from the contribution from the whole OB population (see Table 4.1). Existing X-ray observations do not detect diffuse emission from a hot wind blown bubble around AB 8 or in the SMC-SGS 1 (Oskinova et al. 2013). This is possibly due to the low density in the SGS, or to leakage of hot gas.

To estimate the full energy budget in the SGS, knowledge of SN rate in the complex is required. Two confirmed high mass X-ray binaries (HMXBs) in this complex serve as an evidence for past SNe. Interestingly, these HMXBs, SXP 1062 and RX J0123.4-7321, are located outside of the SGS. Following our empirical HRD (Sect. 4.5), stars with masses in the range of 8 to 30 $M_{\odot}$ become SNe II-P. There are about 190 such stars in our sample as well as additional B stars without spectra in the photometric study (Fulmer et al. 2019 submitted) which will become SNe II-P in the next 40 Myr. Thus the current rate is $\gtrsim 5$ SNe per Myr, assuming a constant SFR. If we only consider stars that are located inside the SGS, the rate becomes $\gtrsim 2.5$ per Myr. This is a lower limit since our spectroscopic survey did not cover the full extent of the SGS.

It is difficult to accurately estimate the age of SMC-SGS 1. We do not detect SN remnants or HMXBs within the shell, and there is a high likelihood of off-center SNe along with the possibility of molecular clouds inside the shell that add extra cooling. It seems that an age of 20-40 Myr is likely (Fulmer et al. 2019 submitted), which is in line with the dynamic age of the shell and the age of the stellar population (Fig. 4.17). We adopt an age of 30 Myr for the feedback estimates, which is also the time-scale of active star formation in the complex. According to our estimated rate, at least 75 SNe must have contributed to the feedback in the SGS. A typical SNe II-P releases 10^{51} erg. The accumulated mechanical energy by SNe is then $E_{\rm mec} \approx 7.5 \times 10^{52}$ erg, which is huge compared to stellar wind contribution. However, the energy released by the SNe reduces over time owing to radiative cooling. In low density and low-metallicity environments, the radiative losses are small (Geen et al. 2015). Therefore, in 30 Myr , the SN energy may decline only up to $E_{\rm SN} \approx 10^{50}$ erg. Considering this effect, the total energy feedback from SNe to the SMC-SGS 1 becomes $\approx 10^{52}$ erg. Supernovae also injects a huge amount of momentum into the ISM and drive turbulence, which cannot be radiated away (Geen et al. 2015). Following Kimm & Cen (2014) and Kimm et al. (2015), the total momentum released by SNe is $p \approx 5 \times 10^{45}$ g cm s^{-1}. This is again significantly higher than the momentum provided by massive star winds.

From neutral hydrogen observations, the surface density of the H I shell is $\sim 3\ M_{\odot}$ pc^{-2} (Stanimirovic et al. 1999; Fulmer et al. 2019 submitted). With a radius of about 300 pc, the total mass of H I gas in the SGS is $M_{SGS} \sim 3 \times 10^6\ M_{\odot}$. At an expansion velocity of 10 km s^{-1}, the total momentum and kinetic energy in the SGS is about $p_{SGS} \approx 6 \times 10^{45}$ g cm s^{-1} and $E_{SGS} \approx 6 \times 10^{51}$erg, i.e, comparable to the contributions from SNe explosions in the past 30 Myr. The kinetic energy of the expanding SGS is a factor of two smaller compared to the estimated mechanical energy input. This might be because of radiative cooling or leakage of hot gas. These estimates show that the SN feedback plays a crucial role in the formation of the SMC-SGS 1.

Table 4.1 summarizes the estimated energy feedback from OB stars, WR stars, and SNe and includes a comparison with values derived from observations in the SGS. In our study of massive stars in the LMC superbubble N 206 (Ramachandran et al. 2018a,b) we found that the contribution of young OB stars is very high in terms of both ionizing photon flux and mechanical luminosity. The contributions from massive stars and SNe were almost equal, while this SMC study reveals a different feedback situation. In SMC-SGS 1, the WO star dominates all other OB stars in terms of

Table 4.1.: Ionizing flux, mechanical luminosity, momentum, and accumulated mechanical energy contributions by the OB stars, WO binary, and previous SNe, compared to the values observed in the SGSl.

	Q [s^{-1}]	L_{mec} [erg s^{-1}]	p [g cm s^{-1}]	E_{mec} [erg]
OB	8×10^{49}	3×10^{35}	5×10^{41}	6×10^{49}
WO	1.5×10^{50}	7×10^{37}	1.4×10^{43}	2×10^{51}
SN			5×10^{45}	10^{52}
Total	2×10^{50}	7×10^{37}	5×10^{45}	1.2×10^{52}
Observation	$\sim 10^{50}$ (a)	$< 5 \times 10^{32}$ (b)	6×10^{45} (c)	6×10^{51} (c)

Notes. (a) from Hα luminosity (b) from X-ray luminosity (c) from the expansion of the H I shell

ionization and mechanical feedback. The energy and momentum contribution from SNe over the last 30 Myr (age of the SGS) is significantly higher than the stellar wind feedback in the complex and this contribution is similar to the observed energy and momentum stored in the SGS. We conclude that at low-metallicity dwarf galaxies, SN explosions seem to be the dominant source for most of the mechanical feedback. The low levels of feedback in metal-poor stellar populations may promote the growth and survival of molecular clouds, thereby allowing star formation episodes to persist over long timescales. Such extended star formation can result in a continuous supply of ionizing photons, which can leak out into the circumgalactic medium via SN created holes or channels.

4.9. Summary

We present the results of a spectroscopic survey of massive stars in the SMC Wing. The spectra of 320 OB stars were analyzed using modern stellar atmosphere models to derive their fundamental stellar parameters as well as their contributions to feedback through ionizing radiation and stellar winds. We derive calibrations for the temperature and ionizing flux of OB stars as a functions of their spectral subtype. Complementing the results of our study by previous analyses of evolved massive stars in the WR and RSG evolutionary stages, we obtain a well-populated empiric HRD of massive stars in the SMC.

Comparison with evolutionary tracks reveals an apparent dichotomy in massive star evolution: stars initially less massive than 30 $M_\odot$ evolve to red supergiants. These stars are likely SNe II-P progenitors. In contrast, stars (single) initially more massive than 30 $M_\odot$ likely follow a QCHE. These stars might collapse and form black holes directly, without a SN explosion.

We find no evidence that the most-massive SMC stars evolving quasi-chemically homogeneously are fast rotators. Also, we do not find evidence that the fast rotating stars among the less massive objects evolve quasi-chemically homogeneously. Hence, there is no empirical support for the idea that QCHE is governed mainly by rotation. The bifurcation in evolutionary paths rather seems to be unrelated to rotation. We suggest that the main factors for the evolutionary dichotomy are low metallicity and the initial mass of the star.

The mass-loss rates of OB stars empirically estimated from the spectral analysis are significantly lower than theoretically predicted. This result calls for a revision of stellar evolutionary calculations

that routinely rely on overestimated mass-loss rates at low metallicities.

The ages and spatial distribution of massive stars in the SMC Wing shows that star formation is proceeding in this quiescent low density region since more than 100 Myr, and suggests that massive star formation is stochastic there and not spatially progressing. The weakness of OB-star winds at low metallicity make the SN explosions the dominant sources of mechanical energy and momentum input into the ISM. However, we find that the large population of OB stars produced during the star formation peak in the past ~50 Myr is fully capable of producing the SMC-SGS 1 supershell. Star-forming complexes with extended histories will leave their mark on the surrounding ISM even in low-metallicity systems.

4.10. acknowledgements

Based on observations collected at the European Organization for Astronomical Research in the Southern Hemisphere under ESO programme 086.D-0167(A) (P.I.: L. Oskinova). We would like to thank the anonymous referee for providing helpful comments. V.R. is grateful for financial support from Deutscher Akademischer Austauschdienst (DAAD), as a part of the Graduate School Scholarship Program. J.S.G appreciates support for this study from the University of Wisconsin-Madison College of Arts and Science and through his Rupple Bascom Professorship. LMO acknowledges support by the DLR grant 50 OR 1508. A.A.C.S. is supported by the Deutsche Forschungsgemeinschaft (DFG) under grant HA 1455/26. TS acknowledges funding from the European Research Council (ERC) under the European Union's DLV_772225_MULTIPLES Horizon 2020 research and innovation programme. We thank C. J. Evans and V. Hénault-Brunet for taking the observations and helpful discussions. This research made use of the VizieR catalog access tool, CDS, Strasbourg, France. The original description of the VizieR service was published in A&AS 143, 23. Some data presented in this paper were retrieved from the Mikulski Archive for Space Telescopes (MAST). STScI is operated by the Association of Universities for Research in Astronomy, Inc., under NASA contract NAS5-26555. Support for MAST for non-HST data is provided by the NASA Office of Space Science via grant NNX09AF08G and by other grants and contracts.

4.11. Additional figures

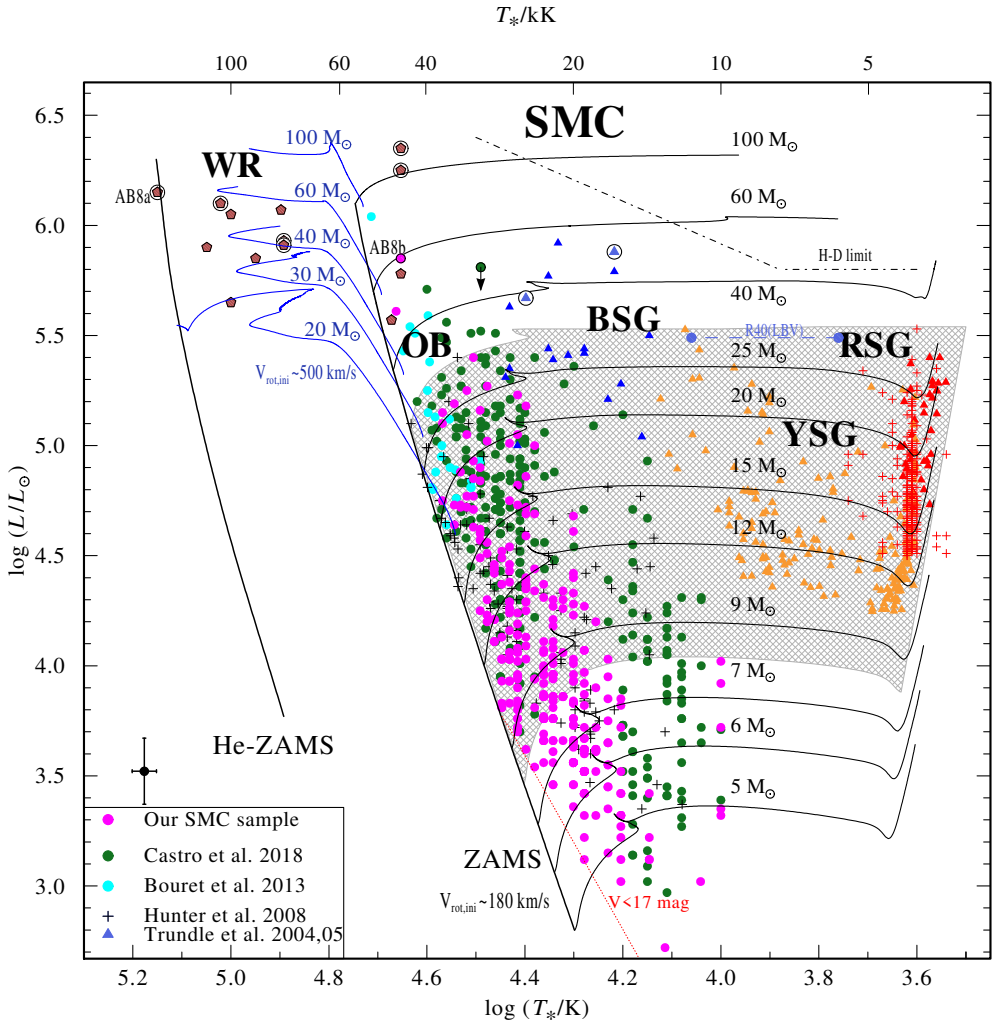

Figure 4.18.: Same as Fig. 4.13, but including additional OB stars from Castro et al. (2018), Bouret et al. (2013), and Hunter et al. (2008b), bringing the total number of OB stars to about ∼ 800. While our sample is restricted to the SGS in the Wing of the SMC (see Sect. 4.7), the other samples spread all over the SMC. The only outstanding star that seems to reside in the void region was obviously confused in the catalog by (Castro et al. 2018); we added a downward arrow because the observed SED definitely indicates $\log L/L_\odot < 5.2$. The additional samples also support our conclusions on stellar evolution.

Chapter 5.

Discussion

Initially, the goal of the thesis was to provide synthetic spectra, ionizing radiation, mechanical feedback and chemical yields of young stellar populations for specific metallicities, ages, and SFR, and then compare these with observations. In the course of the project, we extended our research to massive star evolution, stellar winds, stellar feedback comparisons with multi-wavelength observations, and eventually to a better understanding of the formation and evolution of large scale structures such as superbubbles and supergiant shells. We presented quantitative spectroscopic analyses of the young stellar populations associated with the superbubble N 206 in the LMC and the supergiant shell SMC-SGS1 in the Wing of the SMC. Comparing stellar populations at two different metallicities eventually gave us a chance to understand how massive star properties, evolution and feedback depend on the metal content of the environment.

5.1. Massive star evolution at different metallicities

Massive stars, their evolution, and their final fate are still puzzling, and less well understood than the lower mass counterparts. In this section, we discuss various factors which affect the evolutionary paths of massive stars such as the metallicity, mass, rotation, mass-loss rate, and binarity.

To understand the role of metallicity in massive stars evolution, we compare our results from the LMC and SMC analyses. We incorporate additional samples from the literature along with our OB samples discussed in Chapters 2, 3, and 4. Figure 5.1 shows two comprehensive HRDs for massive stars in the LMC and SMC, respectively. The locations of massive stars at various evolutionary stages suggest a different picture in the LMC and the SMC. These differences point to the effect of metallicity.

The LMC stars at various evolutionary stages populate the HRD below and bluewards of the HD-limit. In contrast, SMC massive stars appear to be more limited to specific parameter ranges in the HRD. Cool-luminous evolved stars in the SMC are well below the standard (Galactic) HD-limit. Moreover, the positions of SMC WR stars are apparently restricted to higher luminosities, and their properties were found to be quite different from their LMC siblings. In the LMC HRD, we do see many young stars which are very luminous and massive, including our Of samples from Chapter 2. These are progenitors of WR stars. However, such luminous massive O stars in the SMC which are potential progenitors of WR stars are very few in number. This might indicate that the evolutionary paths are different in the SMC.

We compared the empirical HRDs with single-star evolutionary tracks corresponding to the respective LMC and SMC metallicity. Empirically, LMC stars appear to follow the ‘standard’ evolutionary paths. In the standard evolutionary scenario, massive stars evolve to the right part of the HRD toward the RSG phase (very massive stars until LBV). After losing the envelope, they become hot WR stars, evolving back toward the left part of the HRD.

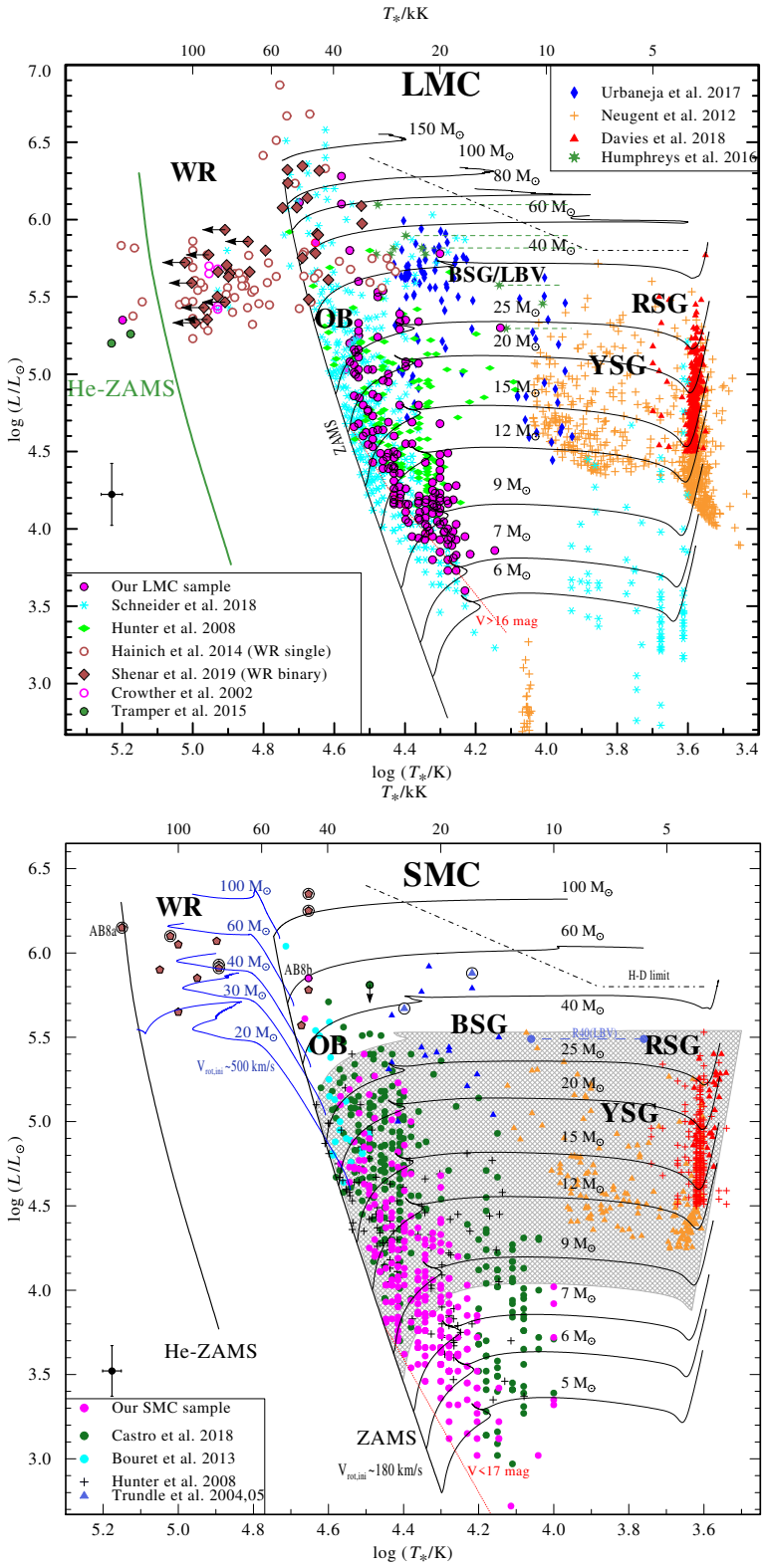

Figure 5.1.: (top) Comprehensive HRD for massive stars in the LMC. The diagram showcases massive stars at different evolutionary stages such as OB stars, BSGs, LBVs, YSGs, RSGs, and WR stars. The evolutionary tracks (black solid lines) accounting for rotation with $v_{\rm rot,init} \sim 100$ km s^{-1} (Brott et al. 2011; Köhler et al. 2015) are labeled with their initial mass. Samples from the literature are marked by different colors and symbols (see legend). (bottom) SMC HRD repeated from Fig. 4.18 to facilitate comparison.

In comparison to the LMC, the evolutionary paths seem to be different for SMC stars as discussed in Chapter 4. In the SMC, only those stars below $\sim 30\,M_{\odot}$ are found to evolve toward the cool side of the HRD to become a RSG. Apparently they do not make it to the WR phase. Different from our general understanding of massive star evolution, we see that SMC stars with initially more than $\sim 30\,M_{\odot}$ appear to stay always hot. It seems that after the main sequence, they directly evolve toward the WR phase, possibly after a little expansion in the main sequence band during which they shed their thin hydrogen envelope.

We postulate such dichotomy in the evolutionary paths to be typical for low metallicity galaxies, while the stars in high metallicity local group members such as the Galaxy, LMC, M31, and M33 are following the standard evolutionary paths. So, the metallicity might have a significant role in deciding the evolution and fate of the stars.

The initial mass of a star plays the key role in its evolution. The evolution and fate of massive stars are completely different from their low mass counterpart. Among massive stars, whether they evolve to RSG, LBV or WR phases and whether they end up as a neutron star or black hole, is mainly decided by their initial mass. At low metallicity, now we see an additional dichotomy in evolution, above and below a certain mass threshold. In the SMC, this threshold is $\sim 30\,M_{\odot}$. At higher metallicity, we don't see such limiting mass. As discussed in Chapter 4, SMC stars above $\sim 30\,M_{\odot}$ appear to evolve quasi chemically homogeneously. They seem to have efficient internal mixing. This in turn suggests that chemical mixing in stellar interior becomes very efficient above a certain mass threshold.

One would expect efficient mixing of the stellar interior for fast rotating massive stars, so that they follow a (quasi) homogeneous evolution. Such stars evolve directly to the left of the HRD, towards the helium zero age main sequence (He-ZAMS). We do see such stars above $\sim 30\,M_{\odot}$ in the SMC, namely the WR stars.

To understand the impact of rotation, we estimated the rotation rates of individual massive stars in the LMC and SMC. One of the main outcomes of Chapter 4 is that the rotation is less important for the evolution than expected. Very massive SMC stars ($\gtrsim 30\,M_{\odot}$) follow QCHE, independent of their rotation. Even some of the bright BSGs, which have a binary history, are consistent with the idea of QCHE, in which stars only slightly evolve to the red and then continue to evolve to the blue as homogeneous stars. The putatively single WR stars are only gradually hydrogen-deficient, and their positions in the HRD suggest QCHE. So, empirically we see that massive (single) stars ($M \gtrsim 30\,M_{\odot}$) expand only little during their main-sequence evolution and then evolve towards WR stages remaining mixed, hot, and compact, in accordance with the predictions of the QCHE model.

However, QCHE seems not to be correlated with fast rotation. There are many fast rotating stars below $\lesssim 30\,M_{\odot}$. But we find no evidence that these stars evolve quasi-chemically homogeneously. Rather they follow a standard evolution towards the RSG stage. A fraction of these stars are fast rotating Be stars which are located close to the terminal age main sequence (TAMS). LMC Be stars are also found near to the TAMS, but are far from critical rotation. The interesting point is that the redward/blueward evolution of stars seems to not depend (or weakly depend) on rotation - there's something else going on in stars with $M \gtrsim 30\,M_{\odot}$, which presumably causes their extra mixing. Moreover, the Of stars discussed in Chapter 2 have highly enriched surface nitrogen, indicating efficient mixing. However, these very massive and young stars in the LMC comlex N 206 (Chapters 2 and 3) are among the slowest rotators. So, in both LMC and SMC, internal mixing is more depended on initial mass than surface rotation. Therefore, our analysis of OB stars in the Magellanic Clouds suggests that stellar rotation alone does not cause the internal mixing. In stellar evolution theory, there are recent claims that core overshooting might be strongly mass dependent (Claret & Torres 2019; Sukhbold & Adams 2019). In combination with rotation, core

overshooting is a candidate for explaining fully mixed massive stars at low metallicity.

Chapters 2, 3, and 4 discuss the mass-loss rates of our LMC and SMC samples. The mass-loss rates of LMC stars are found to be in-line with theoretical expectations. However, we suspect that in an active star-forming cluster like NGC 2018, the current metallicity can be higher than standard for the LMC, especially in the case of very young massive Of stars. Indeed, previous studies show a good agreement between empirically estimated mass-loss rates and theoretical predictions for LMC and Milky Way stars, except for late O dwarfs.

Due to the low metallicity of the SMC, we generally expect weak winds in the OB stars. However, our SMC sample (Chapter 4) reveals that the mass-loss rates are even more than one order of magnitude weaker than theoretically predicted for SMC metallicity, except of one supergiant. Comparing our LMC and SMC OB samples suggests a much steeper relation between mass-loss rates and metallicity. Unlike in the LMC and Galaxy, the weak-wind regime at SMC metallicity is obviously not restricted to specific luminosities or spectral types. Only evolved stars (supergiants, WR) show strong winds, all other have very weak winds. This calls for an update of mass-loss recipes used in evolutionary model calculations.

Very weak winds of OB stars have little or no impact on their evolution. Such low mass-loss rates, in turn, questions the formation of single WR stars from O stars, because the winds of O stars can no longer be considered strong enough to remove the envelope. This could be another evidence for the dichotomy in evolution, where apparently single WR stars are formed by strong internal mixing. The signs of homogeneous evolution and weak winds of massive stars at SMC metallicity suggest that massive black holes can form even in our local universe. Since at low metallicity, massive stars above a certain mass follow QCHE and keep most of their initial mass, it is unlikely that they finally explode as supernova. Most probably they collapse to black holes without any explosions (Sukhbold et al. 2016).

Among many factors, metallicity and initial mass of a star have the main impact on their evolution. The mass loss of a star becomes only important at high metallicity. It is not yet clear which mechanisms are behind the observed dichotomy in evolutionary paths of SMC stars. This needs further investigations.

5.2. Different modes of star formation and the emergence of large scale ISM structures

The age of the OB samples in both studied regions suggest a significant age spread and multiple episodes of star formation in these complexes. Of course, these stellar populations are not just part of a single cluster but distributed over a larger spatial scale. Even at small spatial scales or in sub-structures of these regions, age spread is evident. Since we cannot attribute them to a single age, both of these massive star populations are not representing a single burst of star formation.

The two studied complexes exhibit completely different modes of star formation. The HRD of the OB stars in the N 206 region of the LMC reveals an age spread 1–30 Myr, with the youngest stars being concentrated in the inner part of the complex (NGC 2018, rim of the superbubble), and comparatively older OB stars scattered over outer regions. This might indicate sequential star formation or the migration of stars from their parental cluster. As discussed in Chapter 3, current star formation occurs at the rim of the superbubble.

Hence, we suggest the following formation scenario for the superbubble. The first generation of OB stars clustering near the center of the N 206 complex might have initiated the formation of this superbubble. While the most massive stars lived short and vanished after core-collapse, the less

massive stars, which have enough lifetime to migrate, are now located in the outer parts of the complex. Subsequently, the expansion of the superbubble might have initiated the collapse of dense clumps at the rim, forming very massive stars in the NGC 2018 cluster. A number of massive stars in the cluster and the rim are found to be much younger than the age of the superbubble, supporting this picture. This situation indicates a positive feedback scenario, where energy feedback from massive stars created the superbubble. Its subsequent expansion triggered new episodes of star formation. As this process continues, hot gas in the superbubble can completely engulf the dense molecular cloud and will terminate star formation in this region in the future. The scenario we see in the N 206 complex is the standard what we expect for a superbubble/shell formation, and shows how massive star feedback affects subsequent star formation.

We originally expected a similar formation story for the supergiant shell in the Wing of the SMC, because the Hα image of SMC-SGS 1 indicates active star formation at the rim. However, our results presented in Chapter 4 indicate a completely different situation. The star formation episodes in the SMC-SGS 1 is extended in space and time, indicating a different mode of star-formation than a starburst. The similar age distribution across the region supports a stochastic mode of star formation. The present-day star formation rate surface density of the complex is $\approx 4 \times 10^{-3}\,M_{\odot}\,\mathrm{yr}^{-1}\,\mathrm{kpc}^{-2}$. This is an order of magnitude lower than what we derived for the N 206 region ($\approx 3 \times 10^{-2}\,M_{\odot}\,\mathrm{yr}^{-1}\,\mathrm{kpc}^{-2}$). However, given the low density in the SMC Wing, this star-formation activity is remarkable!

The low metallicity in the SMC might be prerequisite for this mode of star formation. Because the feedback from massive stars is much lower, star formation can persist over 100 Myr instead of triggering very active star formation over a short period of time. So, the metallicity and density of the ISM decide on the mode and duration of star formation.

Comparing with observations, we see that the Hα emission in the SGS-SMC 1 does not fully trace active star formation. Although many of the young massive stars are concentrated in and around NGC 602c, even including the very massive WO+O4 binary, the Hα emission of the region is negligible. Depending on the environment, one should be careful when using Hα emission as a star formation tracer, at least in low-density, low-metallicity galaxies. This can also affect the SFR estimates. Nestingen-Palm et al. (2017) calculated the star formation rate surface density of the SMC from Hα and 24 μm images. Their SFR plot shows peak values of $\geq 4 \times 10^{-3}\,M_{\odot}\,\mathrm{yr}^{-1}\,\mathrm{kpc}^{-2}$ at the N 90, 89, and 88 regions, while for the rest of the SGS the values are very low ($\leq 4 \times 10^{-4}\,M_{\odot}\,\mathrm{yr}^{-1}\,\mathrm{kpc}^{-2}$). This is an order of magnitude lower than our derived values. Studies like Lee et al. (2011) and McQuinn et al. (2010) also discussed the large discrepancy between SFR estimated from Hα and UV in dwarf galaxies. McQuinn et al. (2010) conclude that the significantly lower Hα SFR is due to the short lifetime of the Hα emission. However, in our study, we can clearly see an example where the Hα emission under-predicts the SFR by not tracing many young massive stars. In contrast, the Hα + 24 μm SFR map of the LMC in Skibba et al. (2012) is in good agreement with our derived SFR values in the N 206 complex. So, the discrepancy occurs only for the low-density, low-metallicity environment.

5.3. Feedback: which are the key agents?

The feedback parameters of whole stellar ensembles encompassed by large-scale ISM structures were not previously measured at low metallicities. While SN feedback is routinely included in ISM, star- and galaxy-formation models, there were no firm quantitative foundations for this assumption – chiefly because feedback parameters for the majority of massive stars (late-O and

Table 5.1.: Ionizing feedback

Total Q [s^{-1}]	N206-LMC	SMC-SGS 1
OB	4×10^{50} (89%)	8×10^{49} (35%)
WR	5×10^{49} (11%)	1.5×10^{50} (65%)
observed (Hα)	2.7×10^{50} (60%)	10^{50} (44%)

Table 5.2.: Stellar wind feedback rates

Total $L_{\rm mec}$	N206-LMC	SMC-SGS 1
OB	8×10^{37} (51%)	3×10^{35} (0.5%)
WR	7×10^{37} (49%)	7×10^{37} (99.5%)
observed (X-rays)	7×10^{35} (0.4%)	$< 5 \times 10^{32}$

early-B) were not measured yet from individual stellar spectroscopy.

A comparison of ionizing and stellar wind feedback from OB and WR stars between N 206 and SGS is given in Tables 5.1 and 5.2, respectively. The N 206 complex is more active in star formation than the SGS in the SMC. Few young Of stars power the ionization of the N 206 H II region. Since the winds of OB stars in the LMC are much stronger than in the SMC, wind feedback in N 206 is dominated by OB stars, especially the massive Of stars (Chapter 2). The stellar wind feedback from the two WR stars in N 206 is comparable to that from all young OB stars together.

The situation is completely different in the SMC supergiant shell, where the ionizing and mechanical luminosity is dominated by one particular WO star. Apart from this WO, an O3 star in NGC 602 dominates the ionization of the N 90 H II region. The observed Hα emission reflects almost half of the ionizing flux provided by the massive stars – the other half of the Ly continuum photons obviously escapes.

Metal-poor massive stars are believed to be one of the key agents of ionization in the Universe, and are expected to provide higher ionizing fluxes than corresponding high metallicity stars. However, we don't find that the ionizing contributions of the SMC stars are particularly higher than of the LMC stars. Instead, we suggest that low metallicity galaxies promote extensive star formation over long timescales, which eventually provide significant amounts of ionizing photons. Some fraction of these photons might escape to the intergalactic space.

SMC stars have very weak winds, even for earliest spectral types. Such weak winds translate to low feedback, as seen in the distribution of mechanical luminosities. At low metallicity, only the winds of very massive stars in their late evolutionary stages (supergiants, WR) are strong enough to contribute significantly to the feedback. Even the hot gas detected in the N 90 H II region is not provided by massive stars, but rather by pre-main sequence stars. LMC OB stars provide much higher feedback to the ISM. Consequently, active star-forming regions in the LMC are known for hosting bubbles, superbubbles, or large-scale shells filled with diffuse hot gas. Even though the superbubble N 206 is bright in diffuse X-rays, the energy content of the hot gas reflects only a small fraction of the stellar feedback. There must be a leakage of hot gas from this structure.

The total energy feedback from OB stars, WR stars and supernovae in the N 206 and SGS complexes are compared in Table 5.3. The X-ray superbubble in the LMC is equally powered

Table 5.3.: Total energy feedback integrated over time

Total $E_{\rm mec}$	N206-LMC	SMC-SGS 1
OB	10^{52} (43%)	6×10^{49} (0.5%)
WR	10^{51} (9%)	2×10^{51} (16%)
SNe	1.2×10^{52} (48%)	10^{52} (83%)
Observed	4.7×10^{51} (20%)	6×10^{51} (50%)

by stellar winds and supernovae. In contrast, the overall energy feedback of the supergiant shell in the SMC is dominated by supernovae, implying that hundreds of OB stars do not have much impact on the feedback before their final explosion. Thus, at low metallicities, feedback is chiefly governed by supernova explosions and only few very massive stars. The comparison of the total stellar input with X-ray, radio and Hα observations shows that only a fraction the input energy accumulated over time is currently still present in these regions. The rest might have escaped or leaked out of the complex.

The low-density low-metallicity SGS region is a good proxy for low-metallicity dwarf irregular galaxies. This result has significant importance for feedback in such galaxies, where we can now neglect the contribution from OB stars. However, at LMC like metallicities, young OB stars have a significant contribution in terms of ionizing and mechanical feedback. In that case, neglecting their contribution and considering only supernovae is not justified.

Concluding, the metallicity decides whether the stellar winds or supernovae become the key agents of feedback. But, as we speculated, the low feedback at low metallicity might allow for long lasting modes of star formation, which eventually imprint giant structures to the ISM.

5.4. Outlook

We started to conduct a similar massive star study for the most massive and young low-metallicity star cluster in the Local Group, NGC 346. This will significantly increase the sample of studied massive stars in the SMC. MUSE (optical) and HST (UV) spectra have been secured and will provide stellar and wind parameters of nearly half of all O-type stars in the entire SMC. The integral-field MUSE observations of the ionized gas in the region will allow to study feedback in this low metallicity starburst region.

In order to understand the impact of a companion on stellar evolution, we need binary analyses of massive stars, especially at low metallicity. Unfortunately, quantitative knowledge about massive binary statistics at metallicities lower than $0.5\,Z_{\odot}$ is missing. We will continue our investigations for the SMC by taking multi-epoch observations of the SMC Wing and of NGC 346.

Only a handful of massive stars have been spectroscopically analyzed in galaxies with poorer metal-content than the SMC. In the future, quantitative spectroscopy of massive stars at different evolutionary stages in galaxies such as IC 1613, Sext-A, IZw18, LeoP, etc., can bring more insights on stellar evolution in the early Universe.

Chapter 6.

Summary

The goal of this thesis is to broaden the empirical basis for a better, comprehensive understanding of massive star evolution, star formation and feedback at low metallicity. Low metallicity massive stars are a key to understand the early universe. Quantitative information on metal-poor massive stars was sparse before. The quantitative spectroscopic studies of massive star populations associated with large-scale ISM structures were not performed at low metallicity before, but are important to investigate star-formation histories and feedback in detail. We aim to connect and compare fundamental properties, evolution, star formation and feedback to get a global picture of massive stars and their interaction with their environment.

Much of this work relies on spectroscopic observations with VLT-FLAMES of ~500 OB stars in the Magellanic Clouds. When available, the optical spectroscopy was complemented by UV spectra from the HST, IUE, and FUSE archives. The two representative young stellar populations that have been studied are associated with the superbubble N 206 in the Large Magellanic Cloud (LMC) and with the supergiant shell SMC-SGS 1 in the Wing of the Small Magellanic Cloud (SMC), respectively. We performed spectroscopic analyses of the massive stars using the non-LTE Potsdam Wolf-Rayet (PoWR) model atmosphere code. We estimated the stellar, wind, and feedback parameters of the individual massive stars and established their statistical distributions.

The analysis of Of stars, OB stars, and Wolf-Rayet (WR) stars associated with the N 206 complex in the LMC were presented in Chapters 2 and 3. The mass-loss rates of most of the sample OB stars are consistent with theoretical expectations for LMC metallicity. The most massive and youngest stars show nitrogen enrichment at their surface, and are found to be slower rotators than the rest of the sample. We found twelve percent of the sample being Oe/Be stars. Most of them are evolved, located near the terminal age main sequence, and appear to rotate far below their critical velocity. The N 206 complex has undergone star formation episodes since more than 30 Myr, with a current star formation rate higher than average in the LMC. The spatial age distribution of stars across the complex possibly indicates triggered star formation due to the expansion of the superbubble. Three very massive, young Of stars in the region dominate the ionizing and mechanical feedback among hundreds of other OB stars in the sample. The current stellar wind feedback rate from the two WR stars in the complex is comparable to that released by the whole OB sample. We see only a minor fraction of this stellar wind feedback converted into X-ray emission. In this LMC complex, stellar winds and supernovae equally contribute to the total energy feedback, which eventually powered the central superbubble. However, the total energy input accumulated over the time scale of the superbubble significantly exceeds the observed energy content of the complex. The lack of energy along with the morphology of the complex suggests a leakage of hot gas from the superbubble.

A detailed spectroscopic study of massive stars has also been performed for the supergiant shell SMC-SGS 1 in the SMC (Chapter 4). Previous spectral studies of massive stars in the SMC were not large enough and were lacking spectral information on B-type main sequence stars. For

the first time at low metallicity, we provide the stellar and wind parameters along with rotation velocities for a large sample of OB stars, including those in the lower mass-range. The stellar rotation velocities show a broad, tentatively bimodal distribution, with Be stars being among the fastest. We incorporate additional samples from the literature and obtain the most well-populated spectroscopic Hertzsprung-Russell diagram (HRD) of massive stars in the SMC. The comparison with stellar evolution models suggests a dichotomy in the fate of massive stars in the SMC. Stars with initial masses below 30 solar masses seem to evolve to the cool side of the HRD to become a red supergiant and finally explode as type II-P supernova. However, stars above this mass range appear to stay always hot and compact, seem to evolve chemically-homogeneously and are expected to collapse to relatively massive black holes without explosion. We find no correlation between stellar rotation and evolutionary path. The massive stars above 30 solar masses which appear to follow quasi-chemically homogeneous evolution (QCHE) are generally found to be slow or moderate rotators. In contrast, massive stars below this mass limit follow the standard evolutionary path towards red supergiants, even if they rotate very fast. Hence we find no indication that chemical mixing is correlated with rapid rotation. Mass and metallicity are likely to play the key role in the observed dichotomy. This is an extremely important result with far-reaching implications on stellar evolution.

Although it was previously known that the strength of OB winds decreases with decreasing metallicity, we report a systematic, order of magnitude shortfall in our SMC sample. Here, the "weak-wind problem" systematically extends to nearly all early-type stars. These results can overturn the conventional mass-loss recipes used in evolutionary codes at low Z. The ages and spatial distribution of massive stars show that star-formation is proceeding in the quiescent low-density region of the SMC since more than 100 Myr. We found that the massive star formation in the supergiant shell is stochastically progressing rather than sequential. The estimated SFR is relatively high for a low-density region, and is not reflected by the diffuse Hα emission. The feedback parameters of the whole stellar ensembles encompassed by large scale ISM structures were not previously measured at SMC metallicities. We estimate the feedback from OB stars, WR stars, and SNe, and compare the values with multi-wavelength observations of the supergiant shell. The ionization of the giant shell is mostly caused by one WO star alone. Due to their weak winds, stellar wind feedback from OB stars is negligible compared to the supernova feedback. The low levels of feedback in metal-poor stellar populations may promote the growth and survival of molecular clouds, thereby allowing star formation episodes to persist over long time. Such extended star-formation can result in a continuous supply of ionizing photons which can leak out via SN-created holes or channels into the circum-galactic medium. Our study suggests that, star-forming complexes with extended histories will leave their mark on the surrounding ISM even in low metallicity systems.

Our study showcases the importance of quantitative spectroscopy of massive stars with adequate stellar-atmosphere models in order to understand star-formation, evolution, and feedback. The stellar population analyses in the LMC and SMC make us understand that massive stars and their impact can be very different depending on their environment. Obviously due to their different metallicity, the massive stars in the LMC and the SMC follow different evolutionary paths. Their winds differ significantly, and the key feedback agents are different. As a consequence the star formation can proceed in different modes. Future large scale spectroscopic studies of more distant galaxies with even lower metallicities can improve our current understanding of massive stars, especially regarding their role in the early Universe.

Bibliography

Abbott, B. P., Abbott, R., Abbott, T. D., et al. 2016, The Astrophysical Journal Letters, 818, L22
Anderson, J. P., Dessart, L., Gutiérrez, C. P., et al. 2018, Nature Astronomy, 2, 574
Asplund, M., Grevesse, N., Sauval, A. J., & Scott, P. 2009, ARA&A, 47, 481
Barkana, R. 2006, Science, 313, 931
Bartzakos, P., Moffat, A. F. J., & Niemela, V. S. 2001, MNRAS, 324, 18
Baum, E., Hamann, W.-R., Koesterke, L., & Wessolowski, U. 1992, A&A, 266, 402
Bestenlehner, J. M., Gräfener, G., Vink, J. S., et al. 2014, A&A, 570, A38
Blaauw, A. 1961, Bull. Astron. Inst. Netherlands, 15, 265
Bomans, D. J., Dennerl, K., & Kurster, M. 1994, A&A, 283, L21
Bonanos, A. Z., Massa, D. L., Sewilo, M., et al. 2009, AJ, 138, 1003
Bouret, J.-C., Lanz, T., Hillier, D. J., et al. 2003, ApJ, 595, 1182
Bouret, J.-C., Lanz, T., Hillier, D. J., et al. 2015, MNRAS, 449, 1545
Bouret, J.-C., Lanz, T., Martins, F., et al. 2013, A&A, 555, A1
Brott, I., de Mink, S. E., Cantiello, M., et al. 2011, A&A, 530, A115
Carlson, L. R., Sabbi, E., Sirianni, M., et al. 2007, ApJ, 665, L109
Carlson, L. R., Sewiło, M., Meixner, M., Romita, K. A., & Lawton, B. 2012, A&A, 542, A66
Carlson, L. R., Sewiło, M., Meixner, M., et al. 2011, ApJ, 730, 78
Cassinelli, J. P. & Olson, G. L. 1979, ApJ, 229, 304
Castor, J., McCray, R., & Weaver, R. 1975a, ApJ, 200, L107
Castor, J. I., Abbott, D. C., & Klein, R. I. 1975b, ApJ, 195, 157
Castro, N., Oey, M. S., Fossati, L., & Langer, N. 2018, ApJ, 868, 57
Chen, C.-H. R., Chu, Y.-H., Gruendl, R. A., & Heitsch, F. 2007, in IAU Symposium, Vol. 237, Triggered Star Formation in a Turbulent ISM, ed. B. G. Elmegreen & J. Palous, 401–401
Chu, Y.-H. 2008, in IAU Symposium, Vol. 250, Massive Stars as Cosmic Engines, ed. F. Bresolin, P. A. Crowther, & J. Puls, 341–354
Chu, Y.-H., Chang, H.-W., Su, Y.-L., & Mac Low, M.-M. 1995, ApJ, 450, 157
Cignoni, M., Sabbi, E., Nota, A., et al. 2009, AJ, 137, 3668
Claret, A. & Torres, G. 2019, arXiv e-prints
Conti, P. S. 1975, Memoires of the Societe Royale des Sciences de Liege, 9, 193
Cranmer, S. R. 2005, ApJ, 634, 585
Crowther, P. A., Dessart, L., Hillier, D. J., Abbott, J. B., & Fullerton, A. W. 2002, A&A, 392, 653
Cutri, R. M., Skrutskie, M. F., van Dyk, S., et al. 2012, VizieR Online Data Catalog, 2281, 0
Dale, J. E., Ercolano, B., & Bonnell, I. A. 2012, Monthly Notices of the Royal Astronomical Society, 424, 377
Davies, B. & Beasor, E. R. 2018, MNRAS, 474, 2116
Davies, B., Crowther, P. A., & Beasor, E. R. 2018, MNRAS, 478, 3138
Davies, R. D., Elliott, K. H., & Meaburn, J. 1976, MmRAS, 81, 89
de Avillez, M. A. & Breitschwerdt, D. 2005, A&A, 436, 585
de Mink, S. E., Langer, N., Izzard, R. G., Sana, H., & de Koter, A. 2013, ApJ, 764, 166
de Mink, S. E. & Mandel, I. 2016, MNRAS, 460, 3545

de Mink, S. E., Sana, H., Langer, N., Izzard, R. G., & Schneider, F. R. N. 2014, ApJ, 782, 7
Doran, E. I., Crowther, P. A., de Koter, A., et al. 2013, ArXiv e-prints
Dufton, P. L., Langer, N., Dunstall, P. R., et al. 2013, A&A, 550, A109
Dufton, P. L., Smartt, S. J., Lee, J. K., et al. 2006, A&A, 457, 265
Dunne, B. C., Chu, Y.-H., Chen, C. H. R., et al. 2003, ApJ, 590, 306
Dunne, B. C., Points, S. D., & Chu, Y.-H. 2001, ApJS, 136, 119
Dyson, J. E. & de Vries, J. 1972, A&A, 20, 223
Efremov, Y. N., Ehlerová, S., & Palouš , J. 1999, A&A, 350, 457
Ekström, S., Georgy, C., Meynet, G., Groh, J., & Granada, A. 2013, in EAS Publications Series, Vol. 60, EAS Publications Series, ed. P. Kervella, T. Le Bertre, & G. Perrin, 31–41
Ekström, S., Meynet, G., Maeder, A., & Barblan, F. 2008, A&A, 478, 467
Eldridge, J. J., Izzard, R. G., & Tout, C. A. 2008, MNRAS, 384, 1109
Eldridge, J. J. & Stanway, E. R. 2009, MNRAS, 400, 1019
Elmegreen, B. G. 1997, ApJ, 477, 196
Evans, C. J., Hainich, R., Oskinova, L. M., et al. 2012, ApJ, 753, 173
Evans, C. J. & Howarth, I. D. 2008, MNRAS, 386, 826
Evans, C. J., Howarth, I. D., Irwin, M. J., Burnley, A. W., & Harries, T. J. 2004, MNRAS, 353, 601
Evans, C. J., Kennedy, M. B., Dufton, P. L., et al. 2015, A&A, 574, A13
Evans, C. J., Taylor, W. D., Hénault-Brunet, V., et al. 2011, A&A, 530, A108
Farrell, E. J., Groh, J. H., Meynet, G., et al. 2019, A&A, 621, A22
Ferrand, G. & Marcowith, A. 2010, A&A, 510, A101
Flesch, E. W. 2016, PASA, 33, e052
Foellmi, C., Moffat, A. F. J., & Guerrero, M. A. 2003, MNRAS, 338, 1025
Frank, A., Ray, T. P., Cabrit, S., et al. 2014, Protostars and Planets VI, 451
Fulmer, L. M., Gallagher, J. S., Hamann, W. R., et al. 2019 submitted, A&A
Gabler, R., Gabler, A., Kudritzki, R. P., & Mendez, R. H. 1992, A&A, 265, 656
Gallagher, III, J. S., Hunter, D. A., & Tutukov, A. V. 1984, ApJ, 284, 544
Geen, S., Hennebelle, P., Tremblin, P., & Rosdahl, J. 2016, MNRAS, 463, 3129
Geen, S., Rosdahl, J., Blaizot, J., Devriendt, J., & Slyz, A. 2015, MNRAS, 448, 3248
Girard, T. M., van Altena, W. F., Zacharias, N., et al. 2011, AJ, 142, 15
Gorjian, V., Werner, M. W., Mould, J. R., et al. 2004, ApJS, 154, 275
Gouliermis, D. A., Chu, Y.-H., Henning, T., et al. 2008, ApJ, 688, 1050
Graczyk, D., Soszyński, I., Poleski, R., et al. 2011, Acta Astron., 61, 103
Gräfener, G. & Hamann, W.-R. 2005, A&A, 432, 633
Gräfener, G., Koesterke, L., & Hamann, W.-R. 2002, A&A, 387, 244
Groh, J. H., Meynet, G., Georgy, C., & Ekström, S. 2013, Astronomy & Astrophysics, 558, A131
Gruendl, R. A. & Chu, Y.-H. 2009, ApJS, 184, 172
Guerrero, M. A. & Chu, Y.-H. 2008, ApJS, 177, 216
Gvaramadze, V. V., Pflamm-Altenburg, J., & Kroupa, P. 2011, A&A, 525, A17
Hainich, R., Oskinova, L. M., Shenar, T., et al. 2018, A&A, 609, A94
Hainich, R., Pasemann, D., Todt, H., et al. 2015, A&A, 581, A21
Hainich, R., Rühling, U., Todt, H., et al. 2014, A&A, 565, A27
Hainich, R., Shenar, T., Sander, A., Hamann, W.-R., & Todt, H. 2017, in IAU Symposium, Vol. 329, The Lives and Death-Throes of Massive Stars, ed. J. J. Eldridge, J. C. Bray, L. A. S. McClelland, & L. Xiao, 171–175
Hamann, W.-R., Duennebeil, G., Koesterke, L., Wessolowski, U., & Schmutz, W. 1991, A&A,

249, 443
Hamann, W.-R., Feldmeier, A., & Oskinova, L. M. 2008
Hamann, W.-R. & Gräfener, G. 2004, A&A, 427, 697
Hamann, W.-R., Gräfener, G., & Liermann, A. 2006, A&A, 457, 1015
Hamann, W.-R. & Koesterke, L. 1998, A&A, 335, 1003
Harayama, Y., Eisenhauer, F., & Martins, F. 2008, ApJ, 675, 1319
Harris, J. & Zaritsky, D. 2008, Publications of the Astronomical Society of Australia, 25, 116
Haschke, R., Grebel, E. K., & Duffau, S. 2011, AJ, 141, 158
Heger, A., Fryer, C. L., Woosley, S. E., Langer, N., & Hartmann, D. H. 2003, ApJ, 591, 288
Hénault-Brunet, V., Oskinova, L. M., Guerrero, M. A., et al. 2012, MNRAS, 420, L13
Henize, K. G. 1956, ApJS, 2, 315
Herrero, A., Kudritzki, R. P., Vilchez, J. M., et al. 1992, A&A, 261, 209
Heydari-Malayeri, M., Charmandaris, V., Deharveng, L., Rosa, M. R., & Zinnecker, H. 1999, A&A, 347, 841
Hill, G. M., Moffat, A. F. J., St-Louis, N., & Bartzakos, P. 2000, MNRAS, 318, 402
Howarth, I. D. 1983, MNRAS, 203, 301
Howarth, I. D. 2013, A&A, 555, A141
Humphreys, R. M. & Davidson, K. 1979a, ApJ, 232, 409
Humphreys, R. M. & Davidson, K. 1979b, ApJ, 232, 409
Humphreys, R. M., Davidson, K., Hahn, D., Martin, J. C., & Weis, K. 2017, The Astrophysical Journal, 844, 40
Humphreys, R. M., Weis, K., Davidson, K., & Gordon, M. S. 2016, The Astrophysical Journal, 825, 64
Hunter, I., Brott, I., Lennon, D. J., et al. 2008a, ApJ, 676, L29
Hunter, I., Dufton, P. L., Smartt, S. J., et al. 2007, A&A, 466, 277
Hunter, I., Lennon, D. J., Dufton, P. L., et al. 2008b, A&A, 479, 541
Hutchings, J. B. 1980, ApJ, 235, 413
Hutchings, J. B. 1982, ApJ, 255, 70
Kalari, V. M., Vink, J. S., Dufton, P. L., & Fraser, M. 2018, A&A, 618, A17
Kato, D., Nagashima, C., Nagayama, T., et al. 2007, PASJ, 59, 615
Kavanagh, P. J., Sasaki, M., & Points, S. D. 2012, A&A, 547, A19
Kennicutt, Jr., R. C., Bresolin, F., Bomans, D. J., Bothun, G. D., & Thompson, I. B. 1995, AJ, 109, 594
Kim, S., Staveley-Smith, L., Dopita, M. A., et al. 1998, ApJ, 503, 674
Kimm, T. & Cen, R. 2014, ApJ, 788, 121
Kimm, T., Cen, R., Devriendt, J., Dubois, Y., & Slyz, A. 2015, MNRAS, 451, 2900
Köhler, K., Langer, N., de Koter, A., et al. 2015, A&A, 573, A71
Kourniotis, M., Kraus, M., Arias, M. L., Cidale, L., & Torres, A. F. 2018, Monthly Notices of the Royal Astronomical Society, 480, 3706
Kroupa, P. 2002, Science, 295, 82
Kroupa, P., Weidner, C., Pflamm-Altenburg, J., et al. 2013, The Stellar and Sub-Stellar Initial Mass Function of Simple and Composite Populations, ed. T. D. Oswalt & G. Gilmore, 115
Krumholz, M. R. & Matzner, C. D. 2009, The Astrophysical Journal, 703, 1352
Kudritzki, R. P. 2002, ApJ, 577, 389
Kudritzki, R. P., Pauldrach, A., Puls, J., & Abbott, D. C. 1989, A&A, 219, 205
Kudritzki, R.-P. & Puls, J. 2000, ARA&A, 38, 613
Lamb, J. B., Oey, M. S., Segura-Cox, D. M., et al. 2016, ApJ, 817, 113

Lamers, H. J. G. L. M. & Cassinelli, J. P. 1999, Introduction to Stellar Winds (Cambridge, UK: Cambridge University Press, June 1999.), 452
Lamers, H. J. G. L. M., Snow, T. P., & Lindholm, D. M. 1995, ApJ, 455, 269
Lamers, H. J. G. L. M., Zickgraf, F.-J., de Winter, D., Houziaux, L., & Zorec, J. 1998, A&A, 340, 117
Langer, N. 1992, A&A, 265, L17
Larsen, S. S., Clausen, J. V., & Storm, J. 2000, A&A, 364, 455
Lee, J. C., Gil de Paz, A., Kennicutt, Jr., R. C., et al. 2011, ApJS, 192, 6
Leitherer, C., Robert, C., & Drissen, L. 1992, ApJ, 401, 596
Leonard, P. J. T. & Duncan, M. J. 1990, AJ, 99, 608
Levesque, E. M., Massey, P., Olsen, K. A. G., et al. 2006, ApJ, 645, 1102
Lindsay, E. M. 1963, Irish Astronomical Journal, 6, 127
Liu, Q. Z., van Paradijs, J., & van den Heuvel, E. P. J. 2005, A&A, 442, 1135
Lopez, L. A., Krumholz, M., Bolatto, A., Prochaska, J. X., & Ramirez-Ruiz, E. 2010, in Bulletin of the American Astronomical Society, Vol. 42, American Astronomical Society Meeting Abstracts #215, 261
Lopez, L. A., Krumholz, M. R., Bolatto, A. D., et al. 2014, ApJ, 795, 121
Lucke, P. B. & Hodge, P. W. 1970, AJ, 75, 171
Lucy, L. B. 2012, A&A, 543, A18
Mac Low, M., Balsara, D. S., Kim, J., & de Avillez, M. A. 2005, The Astrophysical Journal, 626, 864
Mac Low, M.-M., Chang, T. H., Chu, Y.-H., et al. 1998, ApJ, 493, 260
Mac Low, M.-M. & McCray, R. 1988, ApJ, 324, 776
Madore, B. F. & Freedman, W. L. 1998, ApJ, 492, 110
Maeder, A. 1987, A&A, 178, 159
Maeder, A. & Meynet, G. 1988, A&AS, 76, 411
Maeder, A. & Meynet, G. 2000, ARA&A, 38, 143
Maeder, A. & Meynet, G. 2005, A&A, 440, 1041
Maeder, A., Meynet, G., Ekström, S., & Georgy, C. 2009, Communications in Asteroseismology, 158, 72
Maíz Apellániz, J., Negueruela, I., Barbá, R. H., et al. 2015, A&A, 579, A108
Marchant, P., Langer, N., Podsiadlowski, P., Tauris, T. M., & Moriya, T. J. 2016, A&A, 588, A50
Marcolino, W. L. F., Bouret, J.-C., Martins, F., et al. 2009, A&A, 498, 837
Marks, M., Kroupa, P., Dabringhausen, J., & Pawlowski, M. S. 2012, MNRAS, 422, 2246
Martayan, C., Baade, D., & Fabregat, J. 2010, A&A, 509, A11
Martayan, C., Frémat, Y., Hubert, A.-M., et al. 2006, A&A, 452, 273
Martínez-Núñez, S., Kretschmar, P., Bozzo, E., et al. 2017, Space Sci. Rev.
Martins, F. 2011, Bulletin de la Societe Royale des Sciences de Liege, 80, 29
Martins, F., Hillier, D. J., Bouret, J. C., et al. 2009, A&A, 495, 257
Martins, F., Mahy, L., Hillier, D. J., & Rauw, G. 2012, A&A, 538, A39
Martins, F. & Palacios, A. 2013, Astronomy & Astrophysics, 560, A16
Martins, F., Schaerer, D., & Hillier, D. J. 2005a, A&A, 436, 1049
Martins, F., Schaerer, D., Hillier, D. J., & Heydari-Malayeri, M. 2004, A&A, 420, 1087
Martins, F., Schaerer, D., Hillier, D. J., et al. 2005b, A&A, 441, 735
Martizzi, D., Faucher-Giguère, C.-A., & Quataert, E. 2015, MNRAS, 450, 504
Massey, P. 2002, ApJS, 141, 81
Massey, P. 2003, ARA&A, 41, 15

Massey, P., Lang, C. C., Degioia-Eastwood, K., & Garmany, C. D. 1995, ApJ, 438, 188
Massey, P., Neugent, K. F., Hillier, D. J., & Puls, J. 2013, ApJ, 768, 6
Massey, P., Puls, J., Pauldrach, A. W. A., et al. 2005, ApJ, 627, 477
Massey, P., Zangari, A. M., Morrell, N. I., et al. 2009, ApJ, 692, 618
Mathewson, D. S. & Clarke, J. N. 1973, ApJ, 180, 725
Matteucci, F. & Chiosi, C. 1983, A&A, 123, 121
Matzner, C. D. 2007, The Astrophysical Journal, 659, 1394
McCumber, M. P., Garnett, D. R., & Dufour, R. J. 2005, AJ, 130, 1083
McEvoy, C. M., Dufton, P. L., Evans, C. J., et al. 2015, A&A, 575, A70
McLeod, A. F., Dale, J. E., Evans, C. J., et al. 2018, MNRAS
McQuinn, K. B. W., Skillman, E. D., Cannon, J. M., et al. 2010, ApJ, 721, 297
McSwain, M. V., Huang, W., Gies, D. R., Grundstrom, E. D., & Townsend, R. H. D. 2008, ApJ, 672, 590
Meaburn, J. 1980, MNRAS, 192, 365
Menon, A. & Heger, A. 2017, MNRAS, 469, 4649
Meynet, G. & Maeder, A. 2002, A&A, 390, 561
Mihalas, D., Hummer, D. G., & Conti, P. S. 1972, ApJ, 175, L99
Moffat, A. F. J. 1989, ApJ, 347, 373
Mokiem, M. R., de Koter, A., Evans, C. J., et al. 2007a, A&A, 465, 1003
Mokiem, M. R., de Koter, A., Evans, C. J., et al. 2006, A&A, 456, 1131
Mokiem, M. R., de Koter, A., Vink, J. S., et al. 2007b, A&A, 473, 603
Mowlavi, N., Lecoeur-Taïbi, I., Holl, B., et al. 2017, A&A, 606, A92
Murray, N., Quataert, E., & Thompson, T. A. 2010, The Astrophysical Journal, 709, 191
Najarro, F., Kudritzki, R. P., Cassinelli, J. P., Stahl, O., & Hillier, D. J. 1996, A&A, 306, 892
Nayakshin, S. & Sunyaev, R. 2005, MNRAS, 364, L23
Nestingen-Palm, D., Stanimirović, S., González-Casanova, D. F., et al. 2017, ApJ, 845, 53
Neugent, K. F., Massey, P., Skiff, B., et al. 2010, ApJ, 719, 1784
Nieva, M.-F. & Przybilla, N. 2014, A&A, 566, A7
Nigra, L., Gallagher, J. S., Smith, L. J., et al. 2008, PASP, 120, 972
Oey, M. S., Clarke, C. J., & Massey, P. 2001, in Dwarf galaxies and their environment, ed. K. S. de Boer, R.-J. Dettmar, & U. Klein, 181
Oh, S. & Kroupa, P. 2016, A&A, 590, A107
Oh, S., Kroupa, P., & Pflamm-Altenburg, J. 2015, ApJ, 805, 92
Oskinova, L. M. 2005, MNRAS, 361, 679
Oskinova, L. M., Hamann, W.-R., & Feldmeier, A. 2007, A&A, 476, 1331
Oskinova, L. M., Sun, W., Evans, C. J., et al. 2013, ApJ, 765, 73
Oskinova, L. M., Todt, H., Ignace, R., et al. 2011, MNRAS, 416, 1456
Pasquini, L., Avila, G., Blecha, A., et al. 2002, The Messenger, 110, 1
Pawlak, M., Soszyński, I., Udalski, A., et al. 2016, Acta Astron., 66, 421
Penny, L. R. 1996, ApJ, 463, 737
Pietrzyński, G., Graczyk, D., Gieren, W., et al. 2013, Nature, 495, 76
Points, S. D., Chu, Y. H., Snowden, S. L., & Staveley-Smith, L. 2000, ApJ, 545, 827
Portegies Zwart, S. F., Pooley, D., & Lewin, W. H. G. 2002, ApJ, 574, 762
Puls, J., Springmann, U., & Lennon, M. 2000, A&AS, 141, 23
Puls, J., Vink, J. S., & Najarro, F. 2008, A&A Rev., 16, 209
Ramachandran, V., Hainich, R., Hamann, W.-R., et al. 2018a, A&A, 609, A7
Ramachandran, V., Hamann, W. R., Hainich, R., et al. 2018b, A&A, 615, A40

Ramírez-Agudelo, O. H., Sana, H., de Koter, A., et al. 2017, A&A, 600, A81
Ramírez-Agudelo, O. H., Simón-Díaz, S., Sana, H., et al. 2013, A&A, 560, A29
Repolust, T., Puls, J., & Herrero, A. 2004, A&A, 415, 349
Rhode, K. L., Salzer, J. J., Westpfahl, D. J., & Radice, L. A. 1999, AJ, 118, 323
Rivero González, J. G., Puls, J., Massey, P., & Najarro, F. 2012a, A&A, 543, A95
Rivero González, J. G., Puls, J., Najarro, F., & Brott, I. 2012b, A&A, 537, A79
Rivinius, T., Carciofi, A. C., & Martayan, C. 2013, A&A Rev., 21, 69
Rogers, H. & Pittard, J. M. 2013, Monthly Notices of the Royal Astronomical Society, 431, 1337
Rolleston, W. R. J., Trundle, C., & Dufton, P. L. 2002, A&A, 396, 53
Romita, K. A., Carlson, L. R., Meixner, M., et al. 2010, ApJ, 721, 357
Rosen, A. L., Lopez, L. A., Krumholz, M. R., & Ramirez-Ruiz, E. 2014, MNRAS, 442, 2701
Rosen, S. R., Webb, N. A., Watson, M. G., et al. 2016, A&A, 590, A1
Runacres, M. C. & Owocki, S. P. 2002, A&A, 381, 1015
Sabbi, E., Sirianni, M., Nota, A., et al. 2008, AJ, 135, 173
Sabín-Sanjulián, C., Simón-Díaz, S., Herrero, A., et al. 2014, A&A, 564, A39
Sana, H., de Koter, A., de Mink, S. E., et al. 2013a, A&A, 550, A107
Sana, H., de Mink, S. E., de Koter, A., et al. 2012, Science, 337, 444
Sana, H., James, G., & Gosset, E. 2011, MNRAS, 416, 817
Sana, H., van Boeckel, T., Tramper, F., et al. 2013b, MNRAS, 432, L26
Sander, A., Hamann, W.-R., & Todt, H. 2012, A&A, 540, A144
Sander, A., Shenar, T., Hainich, R., et al. 2015, A&A, 577, A13
Sasaki, M., Breitschwerdt, D., Baumgartner, V., & Haberl, F. 2011, A&A, 528, A136
Schneider, F. R. N., Ramírez-Agudelo, O. H., Tramper, F., et al. 2018a, ArXiv e-prints
Schneider, F. R. N., Sana, H., Evans, C. J., et al. 2018b, Science, 359, 69
Schootemeijer, A. & Langer, N. 2018, A&A, 611, A75
Seaton, M. J. 1979, MNRAS, 187, 73P
Seiden, P. E., Schulman, L. S., & Gerola, H. 1979, ApJ, 232, 702
Shenar, T., Hainich, R., Todt, H., et al. 2016, A&A, 591, A22
Shenar, T., Hamann, W.-R., & Todt, H. 2014, ArXiv e-prints
Shenar, T., Oskinova, L., Hamann, W.-R., et al. 2015, ApJ, 809, 135
Shenar, T., Oskinova, L. M., Järvinen, S. P., et al. 2017, A&A, 606, A91
Shtykovskiy, P. & Gilfanov, M. 2005, A&A, 431, 597
Simón-Díaz, S. & Herrero, A. 2014, A&A, 562, A135
Skibba, R. A., Engelbracht, C. W., Aniano, G., et al. 2012, ApJ, 761, 42
Smartt, S. J. 2015, PASA, 32, e016
Smith, D. A. & Wang, Q. D. 2004, ApJ, 611, 881
Smith, N. 2006, MNRAS, 367, 763
Smith, N. 2014, ARA&A, 52, 487
Smith, N. & Owocki, S. P. 2006, The Astrophysical Journal Letters, 645, L45
Smith, N., Povich, M. S., Whitney, B. A., et al. 2010, MNRAS, 406, 952
Smith, R. C., Points, S., Chu, Y.-H., et al. 2005, in Bulletin of the American Astronomical Society, Vol. 37, American Astronomical Society Meeting Abstracts, #145.01
Song, H. F., Meynet, G., Maeder, A., Ekström, S., & Eggenberger, P. 2016, A&A, 585, A120
Sota, A., Maíz Apellániz, J., Morrell, N. I., et al. 2014, ApJS, 211, 10
Sota, A., Maíz Apellániz, J., Walborn, N. R., et al. 2011, ApJS, 193, 24
Springel, V. & Hernquist, L. 2003, MNRAS, 339, 289
Stanimirovic, S., Staveley-Smith, L., Dickey, J. M., Sault, R. J., & Snowden, S. L. 1999, MNRAS,

302, 417
Stanimirovic, S., Staveley-Smith, L., van der Hulst, J. M., et al. 2000, MNRAS, 315, 791
Staveley-Smith, L., Sault, R. J., Hatzidimitriou, D., Kesteven, M. J., & McConnell, D. 1997, MNRAS, 289, 225
Struve, O. 1931, ApJ, 73, 94
Sturm, R., Haberl, F., Pietsch, W., & Udalski, A. 2013, A&A, 551, A96
Subramaniam, A. 2005, A&A, 430, 421
Sukhbold, T. & Adams, S. 2019, arXiv e-prints
Sukhbold, T., Ertl, T., Woosley, S. E., Brown, J. M., & Janka, H.-T. 2016, ApJ, 821, 38
Tenorio-Tagle, G. 1981, A&A, 94, 338
Tenorio-Tagle, G. & Bodenheimer, P. 1988, ARA&A, 26, 145
Tenorio-Tagle, G., Bodenheimer, P., Rozyczka, M., & Franco, J. 1986, A&A, 170, 107
Toalá, J. A. & Arthur, S. J. 2011, The Astrophysical Journal, 737, 100
Todt, H., Sander, A., Hainich, R., et al. 2015, A&A, 579, A75
Townsley, L. K., Broos, P. S., Chu, Y.-H., et al. 2011, ApJS, 194, 16
Townsley, L. K., Feigelson, E. D., Montmerle, T., et al. 2003, ApJ, 593, 874
Trundle, C., Dufton, P. L., Hunter, I., et al. 2007, A&A, 471, 625
Trundle, C. & Lennon, D. J. 2005, A&A, 434, 677
Trundle, C., Lennon, D. J., Puls, J., & Dufton, P. L. 2004, A&A, 417, 217
Urbaneja, M. A., Kudritzki, R.-P., Gieren, W., et al. 2017, The Astronomical Journal, 154, 102
Šurlan, B., Hamann, W.-R., Aret, A., et al. 2013, A&A, 559, A130
Vacca, W. D., Garmany, C. D., & Shull, J. M. 1996, ApJ, 460, 914
Vink, J. S., de Koter, A., & Lamers, H. J. G. L. M. 2000, A&A, 362, 295
Vink, J. S., de Koter, A., & Lamers, H. J. G. L. M. 2001, A&A, 369, 574
Vink, J. S. & Harries, T. J. 2017, A&A, 603, A120
Wada, K., Spaans, M., & Kim, S. 2000, ApJ, 540, 797
Walborn, N. R. 1971, ApJ, 167, 357
Walborn, N. R. 1973, AJ, 78, 1067
Walborn, N. R. 2006, in IAU Joint Discussion, Vol. 4, IAU Joint Discussion
Walborn, N. R. 2009, Optically observable zero-age main-sequence O stars, ed. M. Livio & E. Villaver, Space Telescope Science Institute Symposium Series (Cambridge University Press), 167–177
Walborn, N. R., Howarth, I. D., Evans, C. J., et al. 2010, AJ, 139, 1283
Walborn, N. R., Howarth, I. D., Lennon, D. J., et al. 2002, AJ, 123, 2754
Walborn, N. R., MacKenty, J. W., Saha, A., White, R. L., & Parker, J. W. 1995, ApJ, 439, L47
Walborn, N. R., Morrell, N. I., Howarth, I. D., et al. 2004, ApJ, 608, 1028
Walborn, N. R., Sana, H., Simón-Díaz, S., et al. 2014, A&A, 564, A40
Walch, S. & Naab, T. 2015, MNRAS, 451, 2757
Walch, S., Whitworth, A. P., Bisbas, T. G., Wünsch, R., & Hubber, D. A. 2013, Monthly Notices of the Royal Astronomical Society, 435, 917
Walch, S. K., Whitworth, A. P., Bisbas, T., Wünsch, R., & Hubber, D. 2012, MNRAS, 427, 625
Wang, Q. D., Dong, H., & Lang, C. 2006, MNRAS, 371, 38
Weaver, R., McCray, R., Castor, J., Shapiro, P., & Moore, R. 1977, ApJ, 218, 377
Weidner, C., Kroupa, P., & Maschberger, T. 2009, MNRAS, 393, 663
Westerlund, B. E. 1964, MNRAS, 127, 429
Williams, R. M., Chu, Y.-H., Dickel, J. R., et al. 2005, ApJ, 628, 704
Winkler, P. F., Young, A. L., Braziunas, D., et al. 2005, in Bulletin of the American Astronomical

Society, Vol. 37, American Astronomical Society Meeting Abstracts, 1380
Wong, T., Hughes, A., Ott, J., et al. 2011, ApJS, 197, 16
Woosley, S. E. & Weaver, T. A. 1995, ApJS, 101, 181
Yoon, S.-C. & Langer, N. 2005, A&A, 443, 643
Yoon, S.-C., Langer, N., & Norman, C. 2006, A&A, 460, 199
Zacharias, N., Finch, C. T., Girard, T. M., et al. 2012, VizieR Online Data Catalog, 1322
Zaritsky, D., Harris, J., Thompson, I. B., & Grebel, E. K. 2004, AJ, 128, 1606
Zeidler, P., Nota, A., Grebel, E. K., et al. 2017, AJ, 153, 122

Appendix

The full appendix can be found in the electronic version of this thesis. It comprises the appendices published with Manuscript I (Appendix A), Manuscript II (Appendix B), and Manuscript III (Appendix C). The appendices contain additional tables and figure containing spectral fits of all sample stars.

Appendix A.

A.1. Spectral fitting

In this section, we present the spectral fits of all stars analyzed in this study. The upper panel shows the SED with photometry from UV, optical and infrared bands. Lower panels show the normalized VLT-FLAMES spectrum depicted by blue solid lines. The observed spectrum is overplotted with PoWR spectra shown by red dashed lines. Main parameters of the best-fit model are given in Table 2.3.

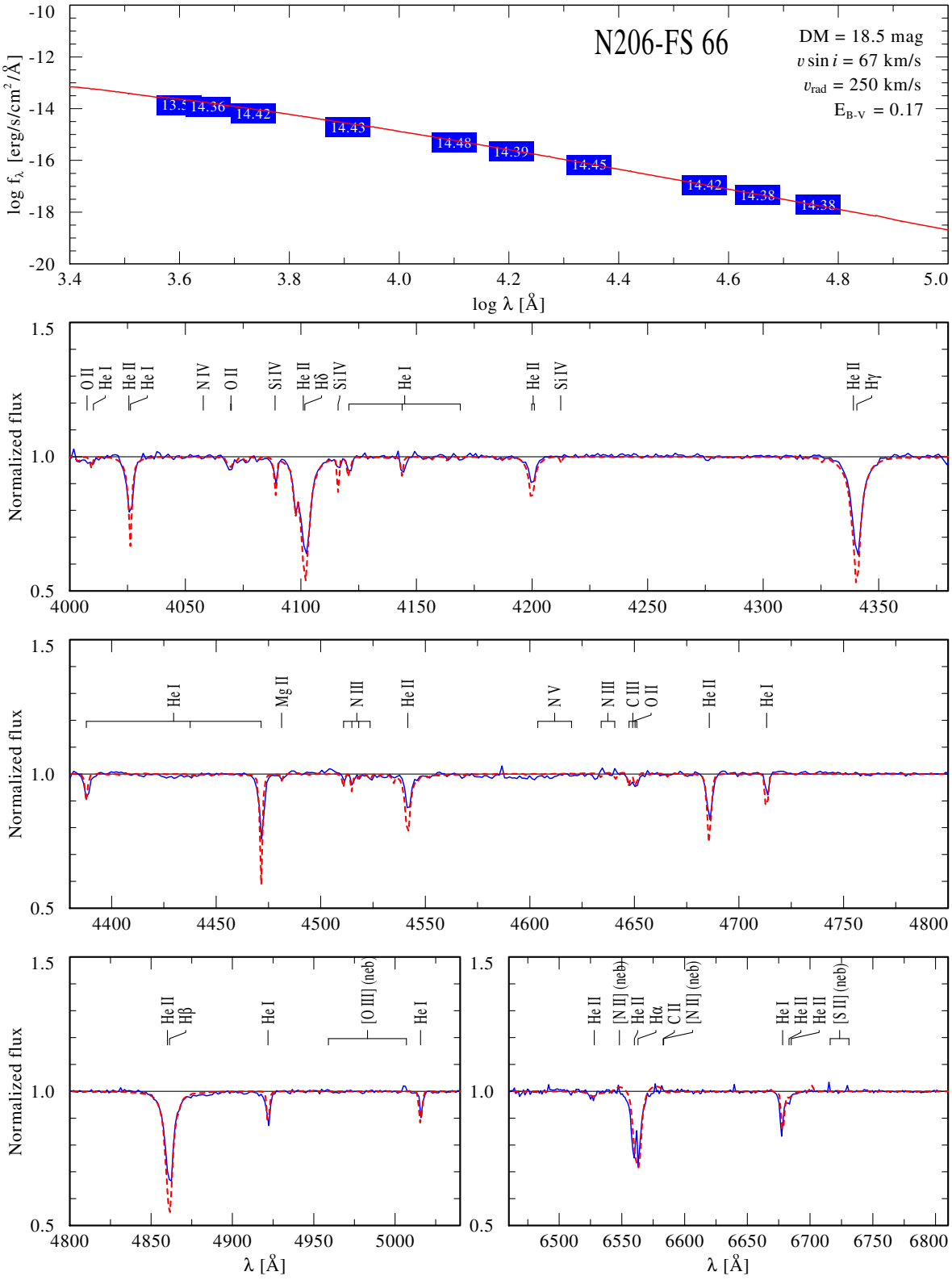

Figure A.1.: Spectral fit for N206-FS 66

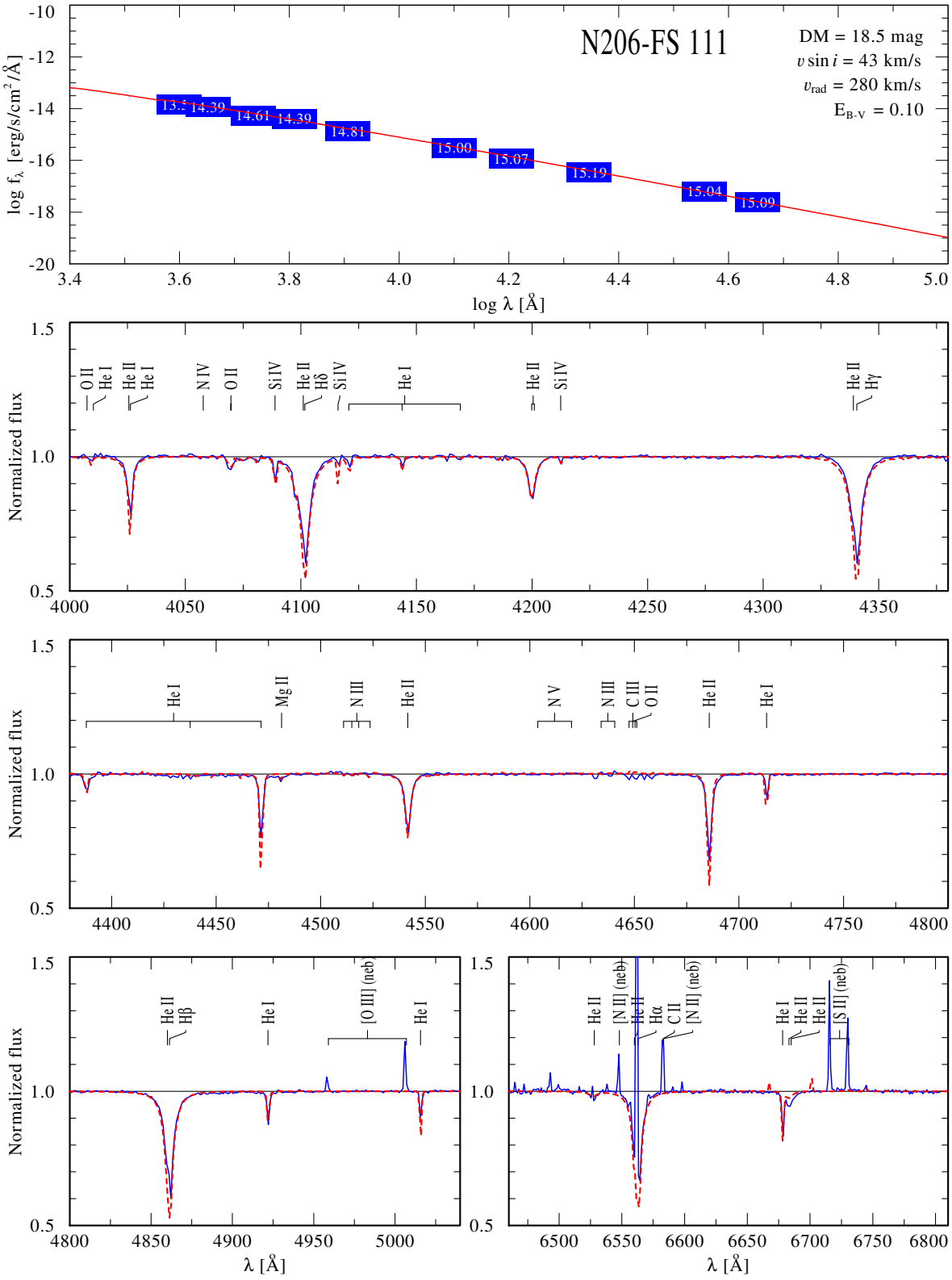

Figure A.2.: Spectral fit for N206-FS 111

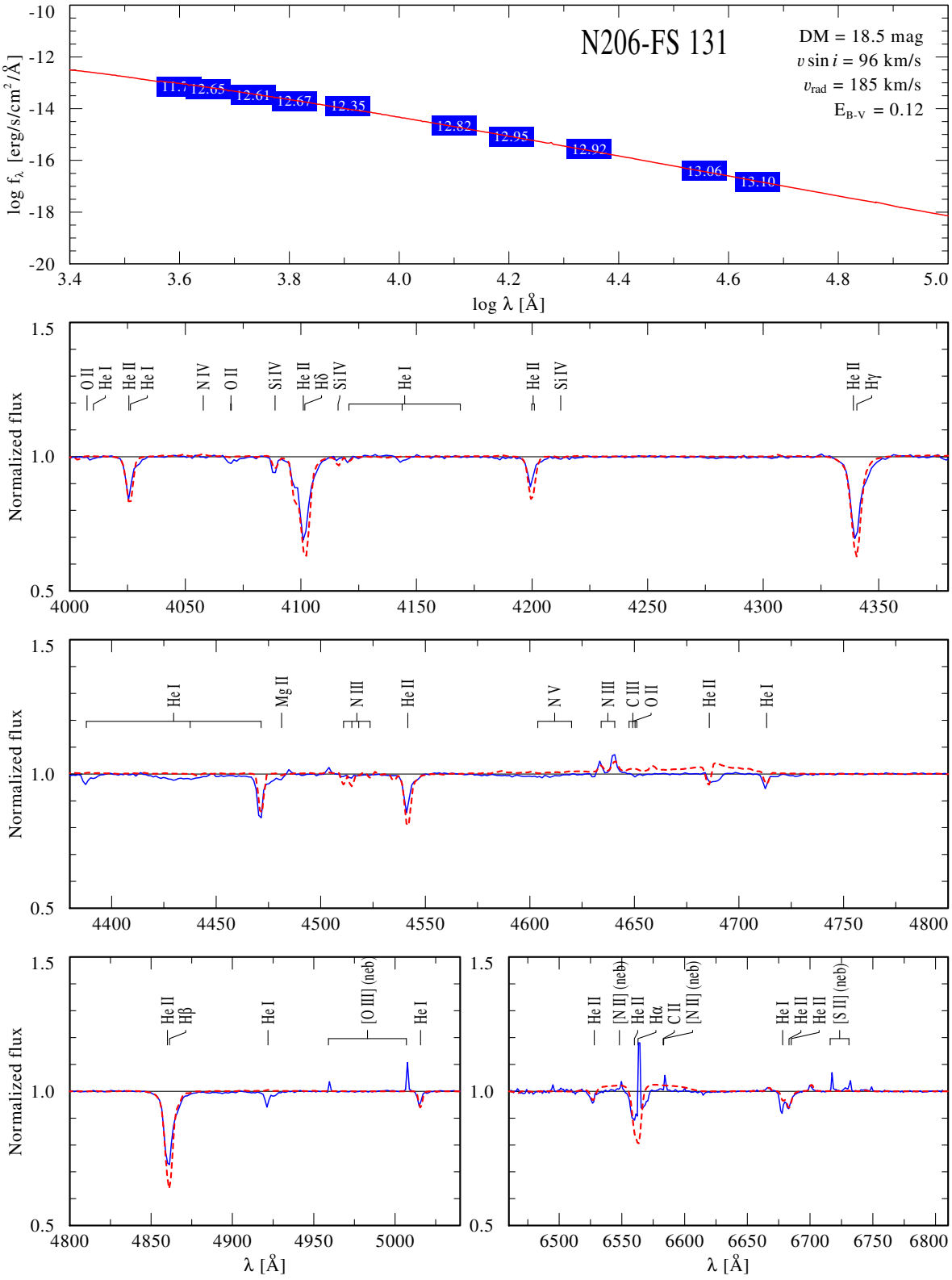

Figure A.3.: Spectral fit for N206-FS 131, which is suspected to be a binary (see Chapter 2.7 and next figure)

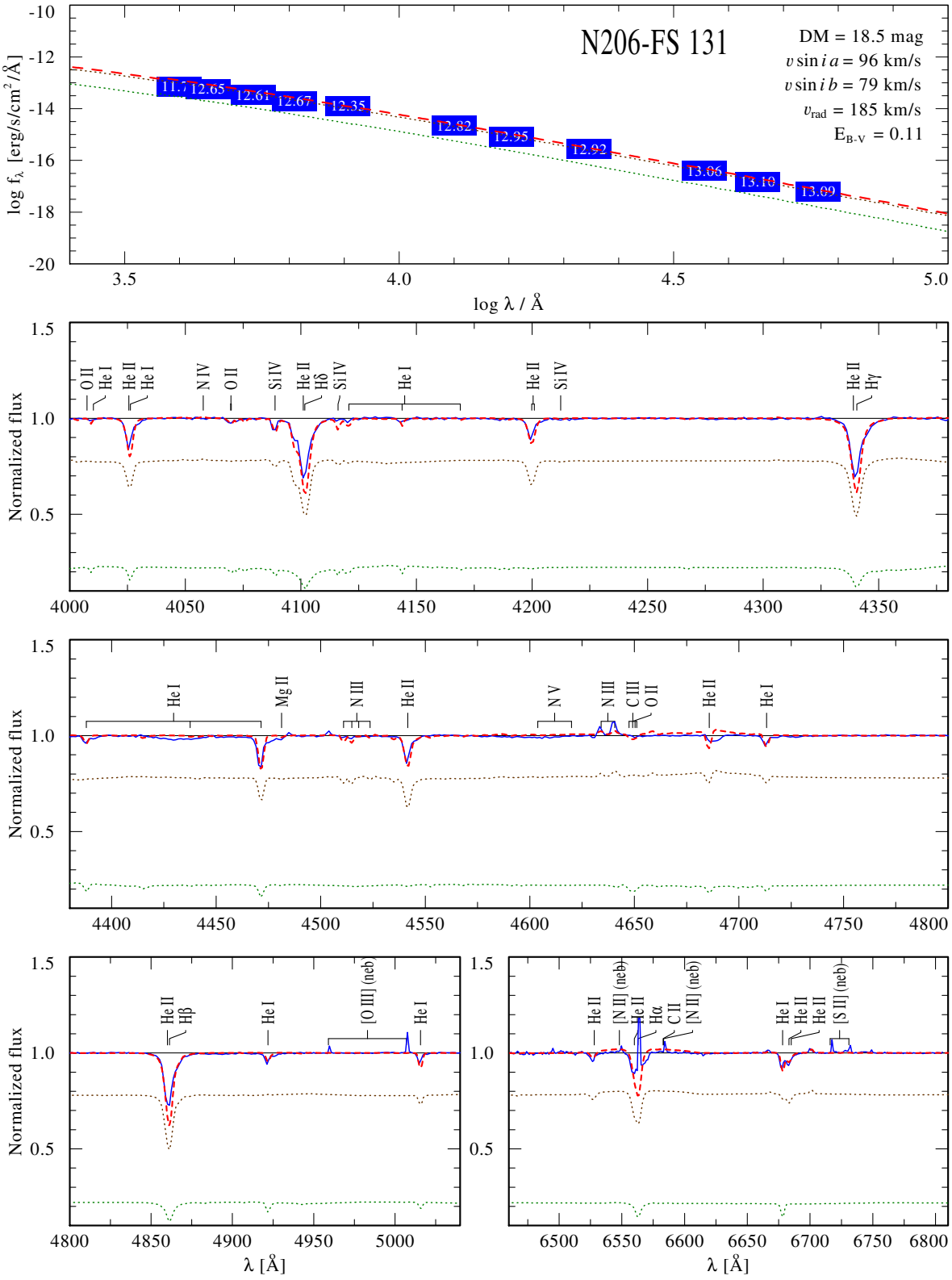

Figure A.4.: Composite model (red dashed line) for N206-FS 131. The primary Of star (brown dotted line) is fitted with $T_* = 38$ kK model and secondary component (green dotted line) to a model with $T_* = 30$ kK. See Table 2.3 for more information.

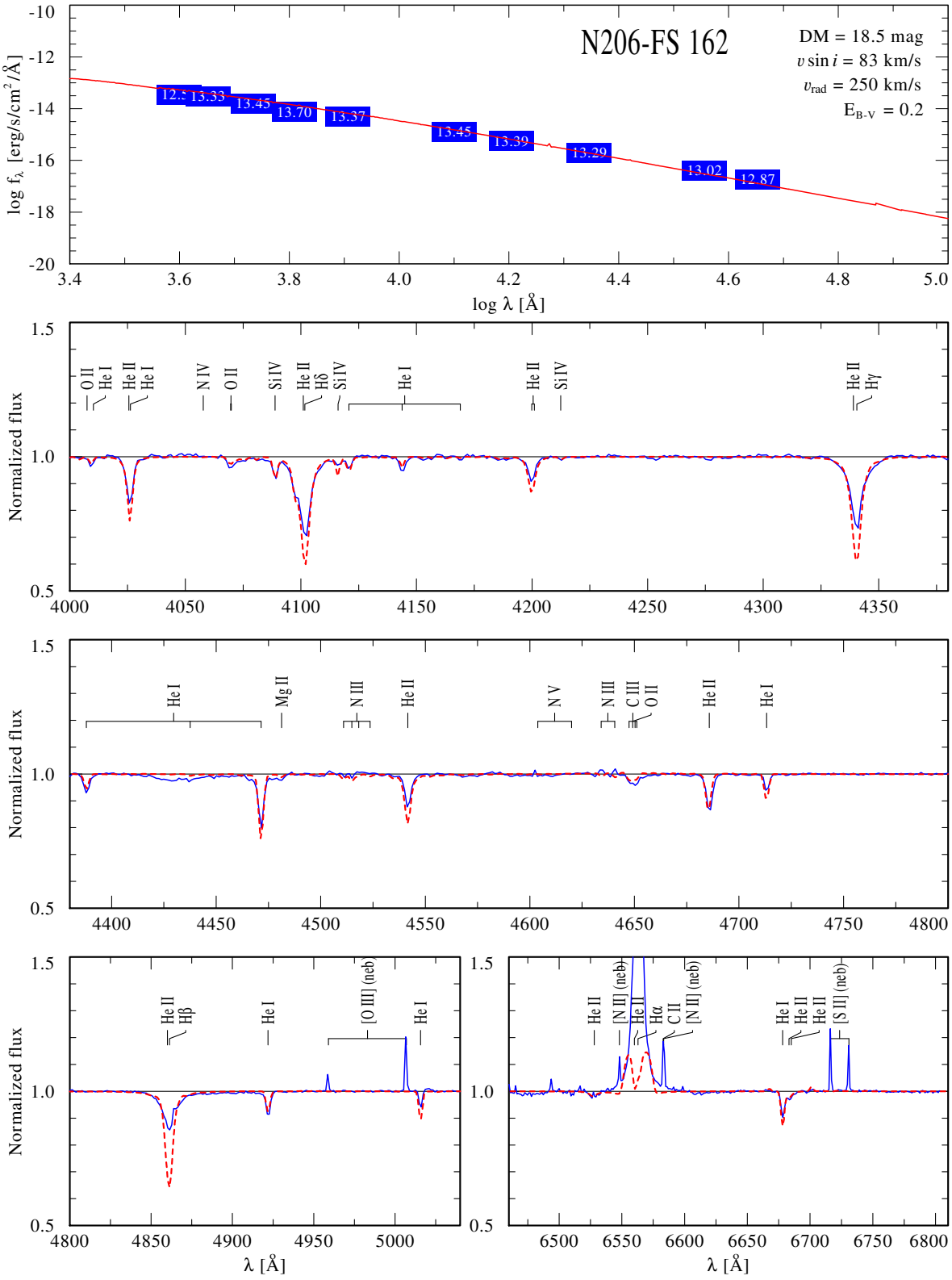

Figure A.5.: Spectral fit for N206-FS 162

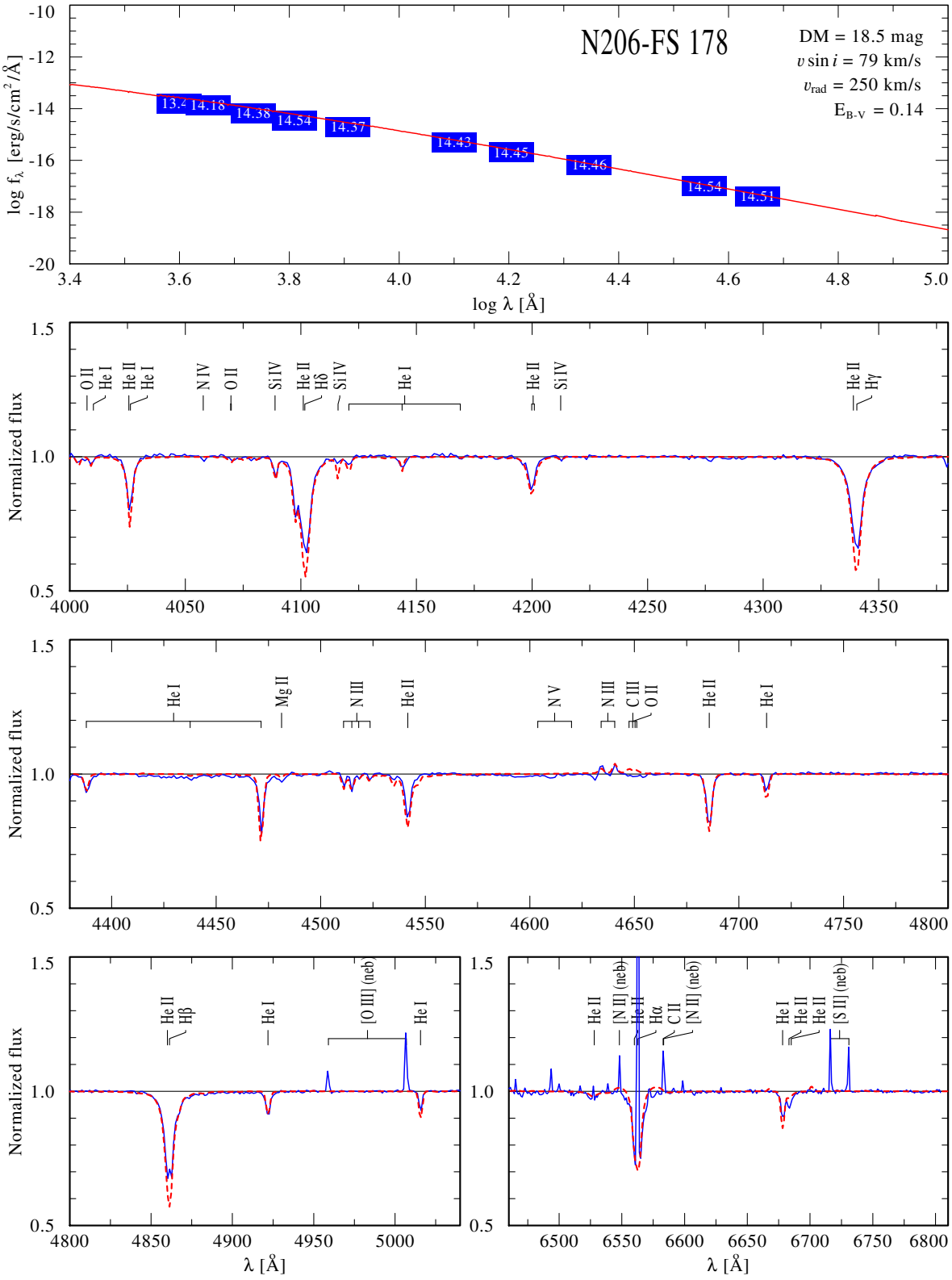

Figure A.6.: Spectral fit for N206-FS 178.

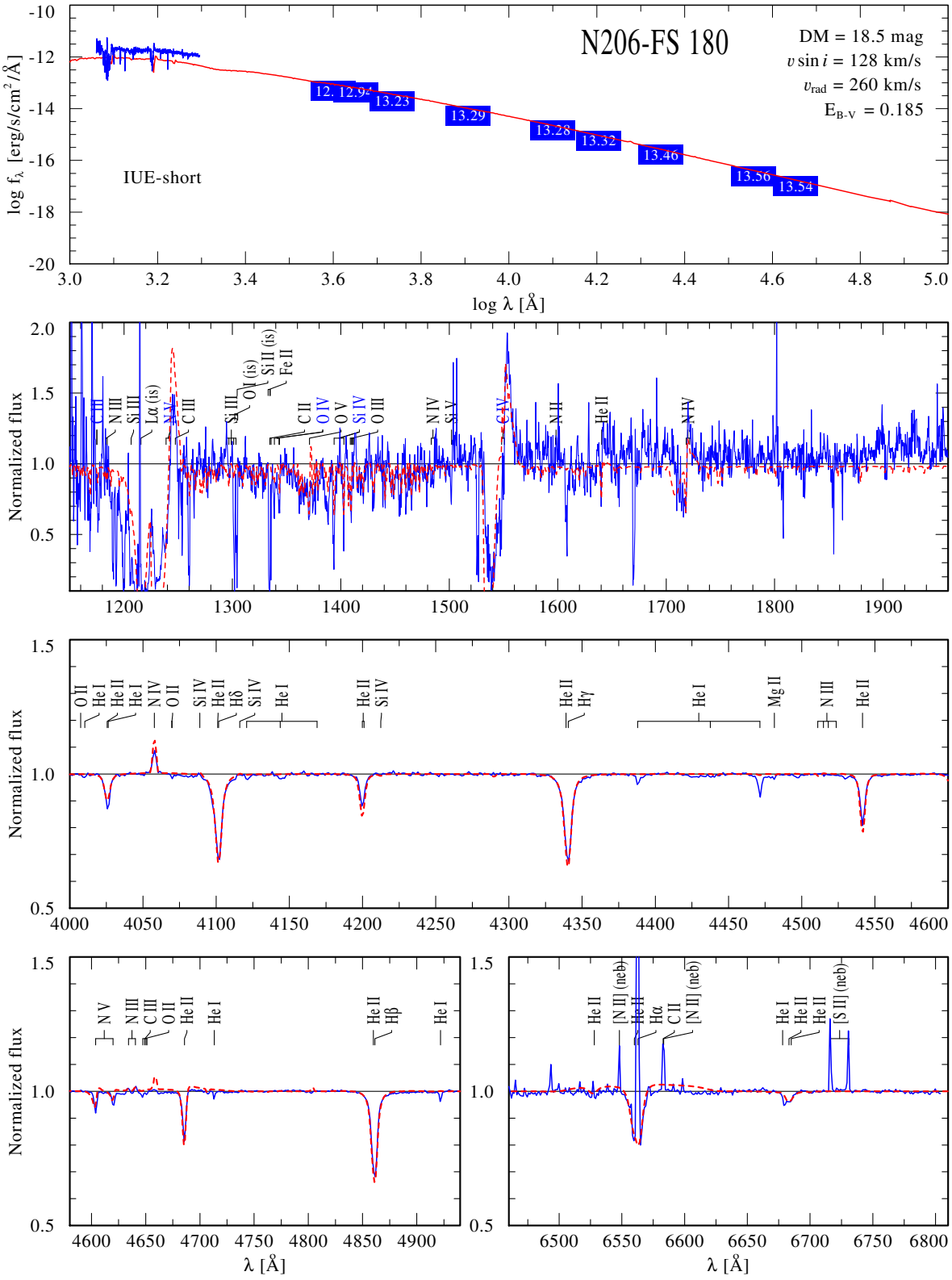

Figure A.7.: Spectral fit for N206-FS 180 with a single star model. The He I lines in the observation are absent in the model, indicating the contamination from a secondary component. See next figure for the composite model.

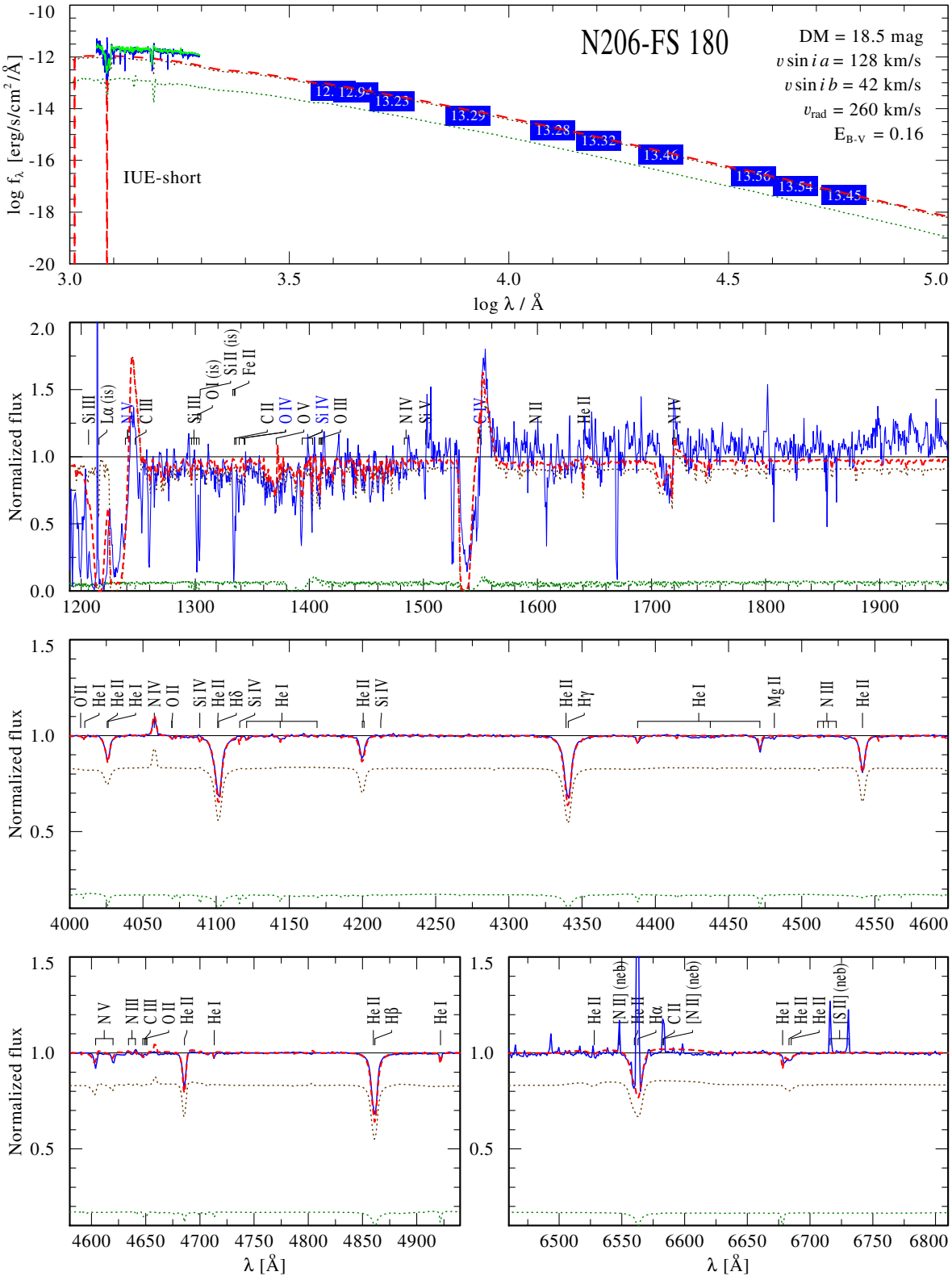

Figure A.8.: Composite model (red dashed line) for N206-FS 180 is the weighted sum of O2 V((f*)) (brown dotted line) and O8 IV (green dotted line) model spectra with effective temperature 50 kK and 32 kK, respectively. The relative offsets of the model continua correspond to the light ratio between the two stars. See Table 2.3 for more details.

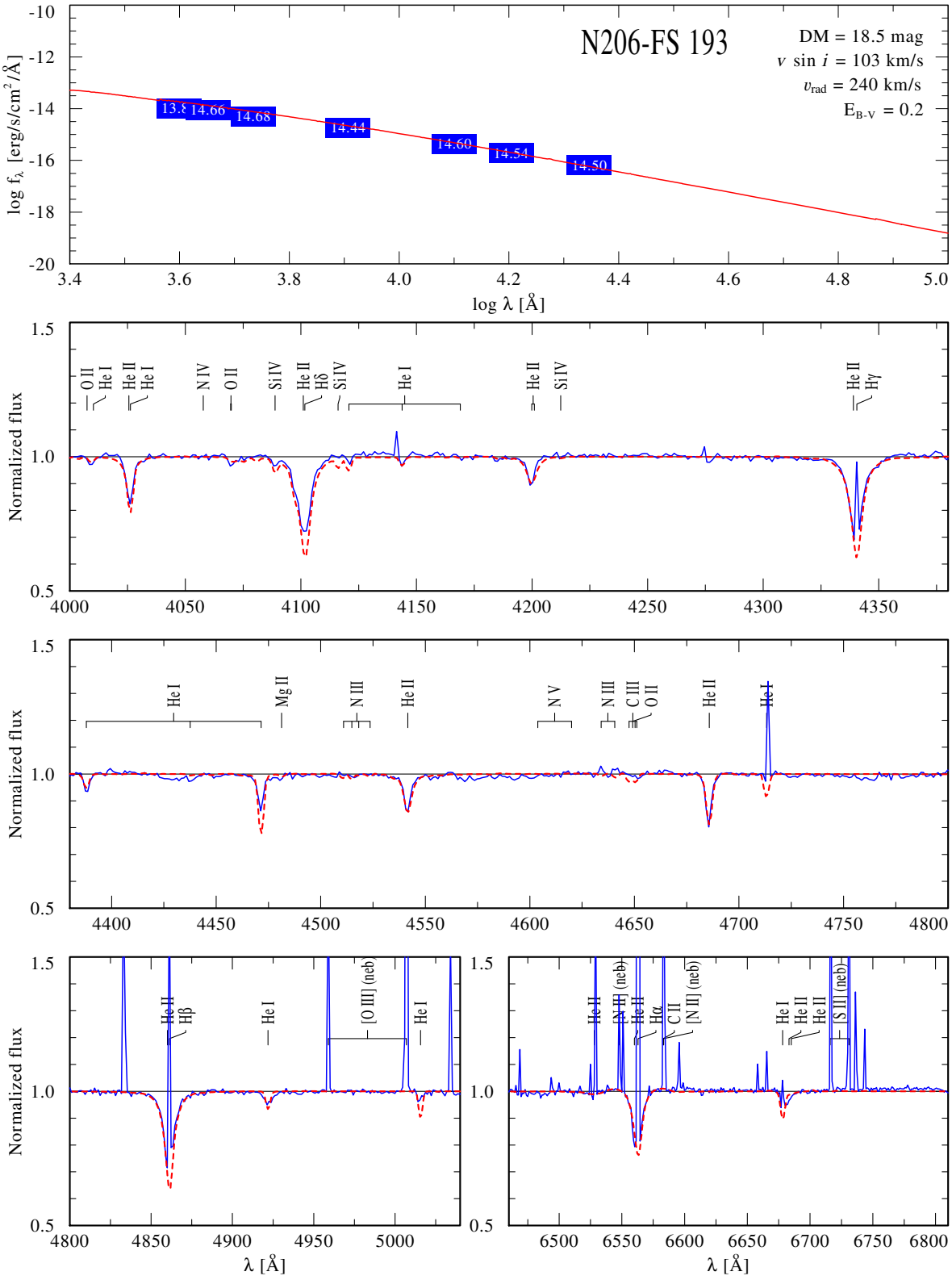

Figure A.9.: Spectral fit for N206-FS 193

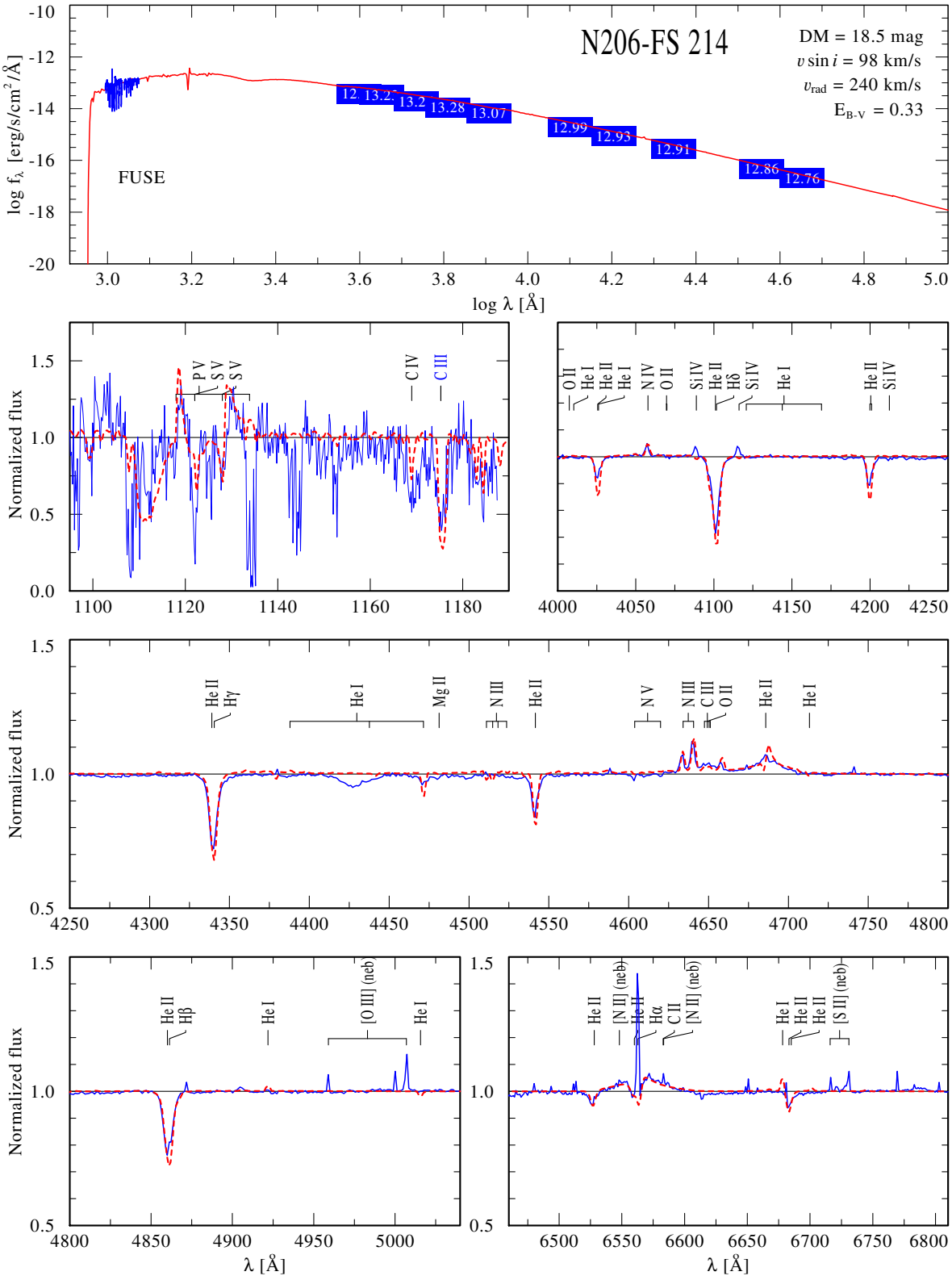

Figure A.10.: Spectral fit for N206-FS 214. The SED is best fitted to flux calibrated FUSE FUV spectra. The second panel shows the FUSE spectrum normalized with the model continuum.

Appendix B.

B.1. Additional tables

Table B.1.: Coordinates and spectral types of OB stars in the N 206 sample (continuation of Table 3.1)

N206-FS #	RA (J2000) (°)	DEC (J2000) (°)	Spectral type
31	82.307375	-70.865306	B3 IV
32	82.325375	-71.218750	B0 V
33	82.331500	-71.029611	B8 Ia
34	82.337333	-71.029389	B1.5 III Nwk
36	82.346625	-71.082000	B2 IV
37	82.348583	-71.092639	B1.5 IV
38	82.350667	-71.074139	B2 V
39	82.365375	-71.073444	B1.5 V
42	82.374917	-70.901500	B2 IV
43	82.384500	-70.992333	B0.5 V
46	82.399375	-70.937000	B1.5 V
47	82.408458	-70.963778	O9.7 V
48	82.409125	-70.990472	B0.7 V
49	82.411208	-70.985083	B1.5 V
50	82.412125	-70.985778	B1 V
51	82.412458	-70.982944	B2 IV
52	82.429292	-70.837722	B0 V
55	82.436708	-70.916278	B0.2 IV
56	82.438917	-71.161500	B0.7 (IV)e
58	82.442250	-71.156111	B0.5 II
60	82.446917	-71.150111	B1.5 (IV)e
61	82.455208	-71.063139	B1.5 V
62	82.462500	-71.105500	O9.5 (III)e
64	82.464958	-71.075722	O8 Vz
65	82.465500	-71.068611	B2 IV
68	82.471250	-71.083889	B2.5 IV
69	82.471583	-71.079000	B0.2 V
73	82.479625	-71.149639	B0.7 IV
74	82.494250	-70.931778	B0.5 V
75	82.496542	-71.099333	B0.7 IV
77	82.497500	-70.848306	B0.5 V

Table B.1.: continued.

N206-FS #	RA (J2000) (°)	DEC (J2000) (°)	Spectral type
78	82.503083	-71.160111	B1 V
80	82.510292	-71.088917	B1.5 V
81	82.517667	-71.132278	B1 II
84	82.523792	-71.152778	B1.5 IV
88	82.528583	-70.829889	B0 V
89	82.544917	-71.079056	B2 IV
90	82.546875	-70.861667	O9.7 Iab
91	82.546958	-71.079583	O8 IV
93	82.548625	-71.099917	B0.2 V
95	82.549083	-71.067472	B0.5 IV
98	82.567542	-71.104611	B0.7 IV
99	82.581125	-71.102000	O9.5 V
101	82.582333	-71.280056	B1.5 (IV)e
103	82.589083	-70.813639	B2 (IV)e
104	82.592167	-70.910028	B0.5 V
105	82.592250	-71.105389	B1.5 V
107	82.594583	-71.105417	O8 Vz
108	82.594708	-71.099611	B1.5 V
109	82.596000	-71.056639	B0.5 V
112	82.609125	-70.983639	O9.7 V
113	82.613167	-71.048917	B3 (V)e
116	82.617792	-70.989889	B0.7 III
117	82.625625	-70.890972	B2 (IV)e
119	82.627875	-71.042083	O8 (V)e
120	82.636708	-71.049361	B2 IV
121	82.640458	-70.831000	B1.5 (V)e
122	82.646792	-71.032472	B1.5 (IV)e
123	82.647833	-71.081194	B0.2 V
125	82.652583	-71.071000	O9 V
126	82.653000	-71.028583	B2 V
127	82.659750	-71.085278	B0.2 V
129	82.663083	-71.016611	B0.5 IV
130	82.664750	-71.055778	O9.7 V
132	82.666750	-71.286972	O9 IV
133	82.667125	-71.113139	O9 V
134	82.667250	-71.093611	O9.7 Iab
136	82.674125	-70.892889	B1 V
138	82.685458	-71.029000	B0.7 V
139	82.691667	-70.874306	B0.7 V
141	82.693083	-70.866500	B1.5 V
142	82.693750	-70.895667	B2 (V)e
143	82.694000	-70.913778	B1.5 V

Table B.1.: continued.

N206-FS #	RA (J2000) (°)	DEC (J2000) (°)	Spectral type
144	82.696042	-71.054333	B0 II Nwk
145	82.697958	-71.133667	O8 Vz
146	82.697958	-71.058083	B1.5 IV
147	82.699083	-71.067278	B1 Ia Nwk
148	82.701792	-71.230222	O9.7 IV
149	82.703083	-71.065917	O9 IV
150	82.706750	-71.004278	B0.5 V
151	82.710958	-71.046639	O7.5 V
153	82.714833	-71.216167	B2 IV
154	82.723083	-71.132889	O7 Vz
155	82.724667	-71.064833	B0.7 V
156	82.726875	-71.086278	B0.2 I
157	82.728917	-70.895361	B2 V
159	82.734792	-70.915111	B2 V
160	82.734917	-71.072167	B0 II Nwk
163	82.740167	-71.025389	B0.5 III
164	82.747125	-71.072389	B1.5 V
165	82.748792	-70.958750	B3 V
167	82.750750	-70.810028	B5 V
168	82.753417	-71.077389	B2 V
170	82.762250	-70.832333	B1 IV
172	82.778292	-71.179861	O8.5 V
173	82.782458	-71.130361	O9.7 V
174	82.783083	-71.129889	O9.7 V
175	82.784208	-71.028500	B0 III
176	82.788292	-71.070694	O8.5 V
177	82.789958	-71.064306	B2 V
179	82.796833	-71.158167	B1 V
181	82.799750	-71.081639	B1.5 (III)e
183	82.804833	-71.073722	B0.5 V
184	82.807750	-71.064167	O8 Vz
185	82.810333	-71.068875	B2 V
186	82.813100	-71.069500	O9 (V)e
189	82.816125	-71.167472	B2.5 V
190	82.824708	-71.107389	B2 V
191	82.825125	-71.067111	B0.5 V
192	82.828458	-71.077500	O9.5 (III)e
194	82.848833	-71.070194	O8.5 V
195	82.851708	-70.934694	B0.7 V
196	82.852250	-71.139750	B0.2 IV
197	82.852792	-71.064139	B0 V
198	82.852833	-71.070889	O8 Vz

Table B.1.: continued.

N206-FS #	RA (J2000) (°)	DEC (J2000) (°)	Spectral type
200	82.892125	-70.940389	B1.5 IV
201	82.892458	-71.160556	B0.5 V
202	82.892583	-70.951361	B2 V
204	82.900333	-71.115917	B2.5 V
205	82.910917	-70.959972	B1.5 V
206	82.915042	-70.963417	B2 V
207	82.916000	-71.111972	B2.5 V
209	82.921000	-70.961556	B0.7 V
211	82.925333	-71.008500	B1 V
213	82.948583	-71.151278	B3 V
215	82.957792	-70.964722	B0 IV
220	82.993000	-70.962694	B3 IV
221	82.994625	-71.253000	B3 V
222	82.996583	-71.161722	B1.5 IV
224	83.000167	-71.235472	B2 III
225	83.012833	-71.053778	B2.5 V
229	83.036750	-71.032778	O9.5 V
231	83.067583	-71.234000	B2 V
232	83.076792	-71.088139	B2.5 V
233	83.145083	-71.113722	B1.5 (V)e
234	83.174125	-71.045583	B0.5 (V)e

Table B.2.: Stellar parameters of all OB stars in the N 206 superbubble (continuation of Table 3.3)

N206-FS #	Spectral type	T_* [kK]	$\log L$ [$L_\odot$]	$\log g_*$ [cm s^{-2}]	$\log \dot{M}$ [$M_\odot$ yr^{-1}]	E_{B-V} [mag]	M_V [mag]	R_* [$R_\odot$]	v_∞ [km s^{-1}]	$v \sin i$ [km s^{-1}]	v_{rad} [km s^{-1}]	M_* [$M_\odot$]	$\log Q_0$ [s^{-1}]	L_{mec} [$L_\odot$]
31	B3 IV	18.0	3.83	3.6	-8.07	0.12	-3.03	8.5	800	90	290	10	45.3	0.4
32	B0 V	31.0	4.53	4.2	-6.85	0.15	-3.18	6.4	2400	150	260	24	47.5	67.1
33	B8 Ia	13.5	5.30	2.0	-6.28	0.12	-7.19	81.9	600	65	270	24	46.5	15.68
34	B1.5 III Nwk	23.0	4.80	3.4	-7.70	0.12	-5.08	15.9	1500	80	220	23	47.0	3.7
36	B2 IV	20.0	4.03	3.6	-7.93	0.15	-3.29	8.6	800	150	260	11	45.6	0.6
37	B1.5 IV	20.0	4.20	3.4	-8.00	0.12	-3.76	10.5	600	130	260	10	45.7	0.3
38	B2 V	19.0	4.00	3.8	-7.70	0.10	-3.47	9.3	1000	100	260	20	45.6	1.6
39	B1.5 V	22.0	4.17	4.0	-7.62	0.12	-3.16	8.4	2400	160	240	26	45.9	11.3
42	B2 IV	20.0	4.03	4.0	-7.35	0.12	-3.51	8.6	1200	180	250	27	45.9	5.3
43	B0.5 V	27.0	4.26	4.2	-6.78	0.10	-3.03	6.2	2500	75	240	22	46.7	86.6
46	B1.5 V	25.0	4.11	4.2	-7.24	0.11	-2.93	6.1	2600	100	260	21	46.3	32.3
47	O9.7 V	31.0	4.87	4.0	-6.78	0.07	-4.39	9.5	2200	264	240	33	47.9	67.0
48	B0.7 V	27.0	4.40	4.0	-7.45	0.10	-3.78	7.3	2100	100	180	19	47.0	12.9
49	B1.5 V	22.0	3.97	4.0	-7.78	0.08	-2.97	6.7	2100	80	240	16	45.6	6.1
50	B1 V	25.0	4.06	4.2	-7.78	0.08	-3.12	5.7	2500	100	250	19	46.3	8.7
51	B2 IV	21.0	4.20	3.8	-7.70	0.05	-3.71	9.5	2000	245	240	21	45.8	6.6
52	B0 V	31.0	4.53	4.2	-6.85	0.08	-3.68	6.4	2400	35	240	24	47.5	67.1
55	B0.2 IV	30.0	5.24	3.8	-6.43	0.12	-5.05	15.5	2200	110	270	55	48.2	150.1
56	B0.7 (IV)e	27.0	4.50	4.0	-7.38	0.22	-3.35	8.1	2200	188	260	24	47.1	16.8
58	B0.5 II	25.0	5.05	3.0	-7.95	0.20	-5.34	17.9	1700	100	240	12	47.7	2.69
60	B1.5 (IV)e	19.0	4.49	3.4	-7.90	0.23	-4.07	16.3	760	86	240	24	46.2	0.6
61	B1.5 V	24.0	3.95	4.2	-7.78	0.03	-2.82	5.5	2500	120	180	17	46.0	8.7
62	O9.5 (III)e	30.0	4.85	3.4	-7.07	0.18	-3.97	9.9	800	383	260	9	48.1	4.4
64	O8 Vz	35.0	5.06	4.2	-6.50	0.09	-4.65	9.2	2800	100	240	49	48.5	204.6
65	B2 IV	20.0	3.85	3.8	-8.54	0.10	-2.88	7.0	900	100	260	11	45.0	0.2
68	B2.5 IV	19.0	3.90	3.8	-7.78	0.10	-2.94	8.2	1000	80	230	16	45.5	1.4
69	B0.2 V	27.0	4.26	4.2	-7.38	0.09	-3.07	6.2	2500	150	210	22	46.7	21.7
73	B0.7 IV	27.0	4.60	4.0	-7.70	0.12	-3.89	9.1	2100	70	240	31	47.0	7.3
74	B0.5 V	29.0	4.64	4.2	-6.62	0.12	-3.80	8.3	2800	100	240	40	47.3	153.4
75	B0.7 IV	25.0	4.55	3.8	-7.78	0.15	-4.06	10.1	2000	150	250	23	46.8	5.5
77	B0.5 V	27.0	4.19	4.2	-7.43	0.07	-2.99	5.7	2400	150	240	19	46.6	17.8
78	B1 V	25.0	4.16	4.2	-7.20	0.08	-3.07	6.4	2600	80	240	24	46.3	35.2
80	B1.5 V	21.0	4.10	3.8	-7.78	0.12	-3.33	8.5	1900	100	220	17	45.7	5.0
81	B1 II	23.0	5.34	2.8	-5.95	0.12	-6.06	29.5	400	87	160	20	47.8	14.9
84	B1.5 IV	22.0	4.12	4.0	-7.66	0.14	-3.44	7.9	2300	218	230	23	45.8	9.5
88	B0 V	30.0	4.64	4.2	-6.70	0.06	-4.08	7.8	2700	70	260	35	47.5	120.0
89	B2 IV	22.0	4.07	4.0	-7.70	0.12	-3.07	7.5	2300	130	260	20	45.8	8.7
90	O9.7 Iab	30.0	5.53	3.4	-6.86	0.12	-5.86	21.6	1891	90	260	43	48.7	40.9
91	O8 IV	34.0	5.16	4.0	-6.75	0.26	-4.31	11.0	2200	274	260	44	48.5	70.6
93	B0.2 V	29.0	4.96	4.0	-7.78	0.21	-4.60	12.0	1700	80	240	53	47.6	3.98
95	B0.5 IV	28.0	4.95	3.8	-6.70	0.12	-4.80	12.7	2000	80	260	37	47.6	65.9
98	B0.7 IV	27.0	4.39	4.2	-7.28	0.03	-3.65	7.2	2700	100	250	30	46.8	31.7
99	O9.5 V	32.0	4.77	4.2	-6.73	0.20	-3.50	7.9	2700	150	240	36	47.9	112.0
101	B1.5 (IV)e	20.0	4.18	3.6	-7.81	0.24	-3.30	10.3	800	232	230	15	45.7	0.8
103	B2 (IV)e	21.0	4.10	3.8	-7.78	0.16	-3.41	8.5	1900	150	280	17	45.7	5.0
104	B0.5 V	27.0	4.50	4.0	-7.38	0.04	-3.72	8.1	2200	200	230	24	47.1	16.8
105	B1.5 V	22.0	4.07	4.0	-7.70	0.12	-3.00	7.5	2300	100	240	20	45.8	8.7

Table B.2.: continued.

N206-FS #	Spectral type	T_* [kK]	$\log L$ [$L_\odot$]	$\log g_*$ [cm s^{-2}]	$\log \dot{M}$ [$M_\odot$ yr^{-1}]	E_{B-V} [mag]	M_V [mag]	R_* [$R_\odot$]	v_∞ [km s^{-1}]	$v \sin i$ [km s^{-1}]	v_{rad} [km s^{-1}]	M_* [$M_\odot$]	$\log Q_0$ [s^{-1}]	L_{mec} [$L_\odot$]
107	O8 Vz	34.0	5.03	4.0	-6.45	0.14	-4.39	9.5	2100	40	250	33	48.4	129.1
108	B1.5 V	22.0	3.97	4.0	-7.78	0.10	-2.99	6.7	2200	140	240	16	45.7	6.7
109	B0.5 V	27.0	4.36	4.2	-6.70	0.15	-3.10	6.9	2600	90	250	28	46.8	111.3
112	O9.7 V	31.0	4.58	4.2	-6.81	0.08	-3.68	6.8	2500	390	260	27	47.5	79.4
113	B3 (V)e	18.0	4.28	3.6	-7.74	0.20	-3.51	14.2	1000	230	240	29	45.7	1.5
116	B0.7 III	25.0	5.08	3.0	-6.78	0.12	-5.27	18.5	1200	252	260	13	47.7	19.83
117	B2 (IV)e	20.0	4.18	3.6	-7.81	0.16	-3.73	10.3	800	72	260	15	45.7	0.8
119	O8 (V)e	34.0	5.28	4.0	-6.66	0.17	-5.10	12.6	2470	100	240	58	48.7	110.78
120	B2 IV	20.0	4.03	3.6	-7.93	0.08	-3.32	8.6	800	110	250	11	45.6	0.6
121	B1.5 (V)e	21.0	4.16	3.8	-7.73	0.23	-3.42	9.1	2000	140	260	19	45.8	6.1
122	B1.5 (IV)e	26.0	4.80	3.8	-6.66	0.28	-4.44	12.4	2100	140	240	36	47.2	79.2
123	B0.2 V	28.0	4.49	4.0	-7.85	0.10	-3.49	7.5	2100	90	240	20	47.1	5.1
125	O9 V	34.0	4.98	4.2	-6.70	0.13	-4.38	8.9	2700	160	290	46	48.3	120.0
126	B2 V	21.0	4.20	3.8	-7.70	0.03	-3.76	9.5	2000	251	230	21	45.8	6.6
127	B0.2 V	28.0	4.39	4.0	-7.93	0.10	-3.23	6.7	2000	80	260	16	47.0	3.9
129	B0.5 IV	28.0	4.69	4.0	-7.70	0.10	-4.22	9.4	2400	110	200	32	47.3	9.5
130	O9.7 V	31.0	4.63	4.2	-6.78	0.07	-3.67	7.2	2500	80	260	30	47.6	86.6
132	O9 IV	32.0	5.03	3.8	-6.93	0.12	-4.61	10.7	1700	160	260	26	48.3	28.3
133	O9 V	34.0	4.98	4.2	-6.70	0.40	-3.91	8.9	2700	110	260	46	48.3	120.0
134	O9.7 Iab	30.0	5.50	3.4	-6.09	0.16	-6.22	20.9	1800	90	260	40	48.7	218.58
136	B1 V	23.0	4.07	4.0	-7.70	0.07	-2.84	6.8	2200	180	250	17	45.8	8.0
138	B0.7 V	26.0	4.16	4.2	-7.28	0.05	-2.75	5.9	2500	140	260	20	46.5	27.4
139	B0.7 V	26.0	4.16	4.2	-7.28	0.08	-3.02	5.9	2500	110	250	20	46.5	27.4
141	B1.5 V	23.0	3.94	4.2	-7.70	0.06	-2.74	5.9	2600	80	240	20	46.2	11.1
142	B2 (V)e	21.0	4.20	3.8	-7.70	0.14	-3.72	9.5	2000	120	240	21	45.8	6.6
143	B1.5 V	22.0	3.97	4.0	-7.78	0.10	-3.18	6.7	2200	120	270	16	45.7	6.7
144	B0 II Nwk	26.0	5.39	3.0	-6.55	0.25	-5.84	24.5	1585	75	320	22	48.3	58.76
145	O8 Vz	35.0	5.16	4.2	-6.43	0.18	-4.97	10.4	2900	120	250	62	48.6	260.8
146	B1.5 IV	23.0	4.18	3.8	-8.49	0.10	-3.36	7.8	1800	120	220	14	46.3	0.9
147	B1 Ia Nwk	20.0	5.78	2.5	-6.13	0.15	-7.88	64.8	588	40	260	49	47.7	21.2
148	O9.7 IV	31.0	5.03	3.8	-6.65	0.12	-4.66	11.4	1800	160	220	30	48.2	59.8
149	O9 IV	33.0	4.60	4.2	-6.93	0.12	-3.27	6.1	2300	70	260	22	47.8	51.9
150	B0.5 V	28.0	4.39	4.0	-7.93	0.08	-3.48	6.7	2000	90	250	16	47.0	3.9
151	O7.5 V	36.0	5.08	4.2	-6.55	0.10	-4.44	8.9	2700	30	240	46	48.6	168.6
153	B2 IV	21.0	4.25	3.8	-7.66	0.20	-3.79	10.1	2100	130	230	24	45.9	7.9
154	O7 Vz	34.0	5.33	4.0	-6.03	0.40	-4.91	13.4	2500	280	260	65	48.7	486.8
155	B0.7 V	26.0	4.20	4.0	-7.93	0.08	-2.91	6.2	1900	342	220	14	46.6	3.5
156	B0.2 I	26.0	5.29	3.0	-6.62	0.16	-5.57	21.8	1585	90	240	17	48.2	50.0
157	B2 V	21.0	4.25	3.8	-7.66	0.08	-3.89	10.1	2100	80	230	24	45.9	7.9
159	B2 V	21.0	4.20	3.8	-7.70	0.10	-3.93	9.5	2000	100	320	21	45.8	6.6
160	B0 II Nwk	25.0	5.35	3.0	-6.28	0.12	-5.97	25.3	1522	80	240	23	48.0	100.9
163	B0.5 III	24.0	4.69	3.2	-7.22	0.10	-4.18	12.8	1527	75	250	10	47.0	11.6
164	B1.5 V	22.0	4.07	4.0	-7.70	0.08	-3.19	7.5	2300	250	240	20	45.8	8.7
165	B3 V	18.0	3.83	3.6	-8.07	0.10	-2.93	8.5	800	80	280	10	45.3	0.4
167	B5 V	18.0	3.73	3.6	-8.15	0.10	-2.95	7.6	700	120	250	8	45.2	0.3
168	B2 V	21.0	4.10	3.8	-7.78	0.08	-3.53	8.5	1900	180	240	17	45.7	5.0
170	B1 IV	24.0	4.55	3.8	-7.70	0.06	-4.30	10.9	2100	80	240	28	46.7	7.3
172	O8.5 V	35.0	5.16	4.2	-6.53	0.12	-4.75	10.4	2900	60	230	62	48.6	207.2

Table B.2.: continued.

N206-FS #	Spectral type	T_* [kK]	$\log L$ [$L_\odot$]	$\log g_*$ [cm s^{-2}]	$\log \dot{M}$ [$M_\odot$ yr^{-1}]	E_{B-V} [mag]	M_V [mag]	R_* [$R_\odot$]	v_∞ [km s^{-1}]	$v \sin i$ [km s^{-1}]	v_{rad} [km s^{-1}]	M_* [$M_\odot$]	$\log Q_0$ [s^{-1}]	L_{mec} [$L_\odot$]
173	O9.7 V	31.0	4.63	4.2	-6.78	0.23	-3.55	7.2	2500	90	240	30	47.6	86.6
174	O9.7 V	31.0	4.73	4.2	-6.70	0.15	-3.49	8.1	2700	120	250	38	47.7	120.0
175	B0 III	26.0	5.34	3.2	-6.22	0.12	-5.87	23.1	1624	90	330	31	48.0	131.9
176	O8.5 V	35.0	4.86	4.2	-6.85	0.12	-3.83	7.3	2500	31	260	31	48.3	72.8
177	B2 V	21.0	3.95	3.8	-7.89	0.10	-2.81	7.2	1700	160	200	12	45.6	3.1
179	B1 V	25.0	4.26	4.2	-7.12	0.08	-3.43	7.2	2800	80	240	30	46.4	48.5
181	B1.5 (III)e	23.0	5.07	3.4	-6.62	0.34	-5.06	21.6	1700	170	250	43	47.1	56.5
183	B0.5 V	27.0	4.31	4.2	-7.34	0.10	-3.44	6.5	2600	140	240	25	46.7	25.6
184	O8 Vz	35.0	5.01	4.2	-6.74	0.26	-3.99	8.7	2700	110	240	44	48.4	110.1
185	B2 V	22.0	4.17	4.0	-7.62	0.14	-3.57	8.4	2400	170	250	26	45.9	11.3
186	O9 (V)e	34.0	4.68	4.2	-6.43	0.10	-6.41	6.3	2300	90	240	23	48.0	164.0
189	B2.5 V	19.0	3.80	3.8	-7.85	0.12	-3.01	7.4	900	60	240	12	45.4	0.9
190	B2 V	20.0	4.03	3.6	-7.93	0.06	-3.11	8.6	800	351	250	11	45.5	0.6
191	B0.5 V	27.0	4.46	4.2	-7.22	0.28	-3.53	7.8	2800	90	250	35	46.8	38.5
192	O9.5 (III)e	29.0	5.54	3.4	-6.07	0.50	-5.64	23.4	1400	220	260	50	48.6	136.1
194	O8.5 V	34.0	5.11	4.0	-6.39	0.18	-4.62	10.4	2200	75	260	39	48.5	162.7
195	B0.7 V	26.0	4.36	4.2	-7.62	0.06	-3.69	7.5	2800	90	220	32	46.7	15.3
196	B0.2 IV	29.0	4.39	4.0	-7.00	0.12	-3.02	6.2	1800	180	240	14	47.1	26.7
197	B0 V	31.0	4.43	4.2	-6.93	0.12	-2.96	5.7	2300	75	250	19	47.4	51.9
198	O8 Vz	35.0	4.66	4.2	-6.80	0.12	-3.78	5.8	2200	150	200	20	48.1	63.3
200	B1.5 IV	22.0	4.43	3.6	-6.81	0.08	-4.31	11.3	1700	100	240	19	46.3	36.7
201	B0.5 V	27.0	4.26	4.2	-7.38	0.08	-3.11	6.2	2500	150	240	22	46.7	21.7
202	B2 V	22.0	4.12	4.0	-7.66	0.20	-3.47	7.9	2300	120	260	23	45.8	9.5
204	B2.5 V	18.0	3.93	3.6	-8.00	0.10	-3.39	9.5	800	140	240	13	45.4	0.5
205	B1.5 V	20.0	4.13	3.6	-7.85	0.16	-3.54	9.7	800	80	240	14	45.6	0.7
206	B2 V	21.0	3.80	3.8	-8.00	0.07	-3.01	6.0	1600	160	230	8	45.4	2.1
207	B2.5 V	18.0	3.93	3.6	-8.00	0.12	-3.06	9.5	800	110	240	13	45.4	0.5
209	B0.7 V	27.0	4.46	4.2	-7.22	0.10	-3.75	7.8	2800	366	260	35	46.8	38.5
211	B1 V	22.0	3.97	4.0	-7.78	0.12	-2.97	6.7	2100	90	240	16	45.6	6.1
213	B3 V	18.0	3.83	3.6	-8.07	0.10	-3.17	8.5	800	80	250	10	45.3	0.4
215	B0 IV	28.0	5.00	3.8	-6.66	0.10	-4.90	13.5	2100	110	260	42	47.7	79.2
220	B3 IV	17.0	3.95	3.2	-8.07	0.10	-3.39	10.9	500	233	240	7	45.3	0.2
221	B3 V	18.0	3.93	3.6	-8.00	0.08	-3.53	9.5	800	80	250	13	45.4	0.5
222	B1.5 IV	19.0	4.27	3.4	-7.85	0.12	-4.10	12.6	700	90	240	15	45.9	0.6
224	B2 III	20.0	4.68	3.2	-7.65	0.05	-4.76	18.3	600	70	250	19	46.4	0.7
225	B2.5 V	19.0	4.00	3.8	-7.70	0.10	-3.28	9.3	1000	150	240	20	45.6	1.6
229	O9.5 V	33.0	4.80	4.2	-6.78	0.08	-4.12	7.7	2600	150	230	34	48.0	93.6
231	B2 V	20.0	3.93	3.6	-8.00	0.10	-3.33	7.7	700	150	240	9	45.5	0.4
232	B2.5 V	19.0	3.73	3.8	-8.15	0.09	-2.92	6.8	900	130	240	11	45.1	0.5
233	B1.5 (V)e	21.0	4.30	3.8	-6.62	0.17	-3.61	10.7	2100	130	260	26	46.4	86.3
234	B0.5 (V)e	27.0	4.50	4.0	-7.38	0.14	-3.18	8.1	2200	240	260	24	47.1	16.8

Table B.3.: Ages and evolutionary masses of the OB stars determined from isochrones (see Sect. 3.7.3)

N206-FS #	Age [Myr]	M_{ev} [$M_\odot$]
1	18.5	10
3	28.2	8.1
5	7.3	10.6
6	23.2	9.2
7	7.8	14.2
9	16.4	11.7
10	11.0	11.7
11	19.4	9.7
12	16.8	11.2
14	14.8	11.5
15	26.8	8.2
17	17.2	10.8
19	26.6	8.6
22	23.2	9.2
23	4.0	21.1
27	6.2	18.4
28	35.8	7.3
29	47.6	6.3
30	9.2	11.4
31	33.0	7.4
32	7.0	15.4
33	6.7	23.4
34	10.3	15.5
36	24.2	8.9
37	19.5	9.7
38	25.8	8.6
39	19.2	9.4
42	24.2	8.9
43	9.5	12.1
46	10.8	10.6
47	6.4	18.7
48	11.6	13.2
49	20.3	9
50	7.3	10.6
51	19.3	9.7
52	6.6	15.4
55	5.3	25.1
56	10.4	13.5
58	7.8	19.7
60	16.7	11.7

Table B.3.: continued.

N206-FS #	Age [Myr]	M_{ev} [$M_\odot$]
61	14.6	9.5
62	6.7	17.8
64	4.2	23.9
65	28.2	7.8
68	27.6	8
69	11.3	12.1
73	10.2	14.3
74	8.1	15.9
75	13.9	12.6
77	10.7	11.5
78	13.0	10.5
80	20.5	9.3
81	6.2	25
84	18.0	9.4
88	7.3	16.4
89	14.2	9.8
90	4.2	32.4
91	4.5	25
93	6.9	19.4
95	7.4	18.8
98	11.9	13.1
99	5.7	18.4
101	20.5	9.6
103	20.9	9.3
104	10.5	13.5
105	14.2	9.8
107	4.3	23
108	20.3	9
109	8.5	12.8
112	5.6	16.1
113	18.8	10.3
116	6.9	19.9
117	20.4	9.6
119	4.2	27.7
120	24.2	8.9
121	23.3	9.2
122	11.9	15.1
123	9.1	13.9
125	4.9	22.3
126	19.6	9.7
127	10.0	13.5
129	6.6	16.1

Table B.3.: continued.

N206-FS #	Age [Myr]	M_{ev} [$M_\odot$]
130	6.8	16.8
132	4.9	22
133	5.0	22.3
134	4.3	31.8
136	11.6	10.1
138	10.9	11
139	10.9	11
141	20.0	9.1
142	19.4	9.7
143	20.3	9
144	5.6	26.9
145	4.3	25.6
146	18.3	9.9
147	4.0	39.5
148	5.3	21.6
149	4.4	17.5
150	9.6	13.5
151	4.0	25
153	17.5	10.3
154	4.3	28.8
155	9.6	11.2
156	5.9	25
157	17.5	10.3
159	19.4	9.7
160	6.1	25.4
163	11.1	14.6
164	17.0	9.8
165	33.0	7.4
167	33.2	7.3
168	20.9	9.3
170	14.4	12.4
172	4.2	25.6
173	7.0	16.8
174	4.5	17.9
175	6.3	24.7
176	3.2	21.1
177	23.3	8.7
179	13.2	11.3
181	8.1	19.4
183	8.9	12.4
184	4.2	23.3
185	19.5	9.4

Table B.3.: continued.

N206-FS #	Age [Myr]	M_{ev} [$M_\odot$]
186	3.9	19
189	39.6	7
190	23.2	8.9
191	8.9	13.6
192	4.3	32.1
194	4.7	23.9
195	12.4	12.4
196	7.2	13.9
197	5.3	14.8
198	2.3	19.4
200	15.3	11.9
201	9.5	12.1
202	20.2	9.4
204	28.2	8.1
205	23.2	9.2
206	26.7	7.7
207	28.2	8.1
209	9.7	13.6
211	20.3	9
213	33.0	7.4
215	7.1	19.8
220	31.0	8.1
221	28.2	8.1
222	18.3	10.3
224	12.6	13.9
225	25.8	8.6
229	4.9	19
231	25.2	8.4
232	29.5	7.4
233	16.8	10.7
234	10.4	13.5

B.2. Spectral fits of the WR binary N206-FS 128

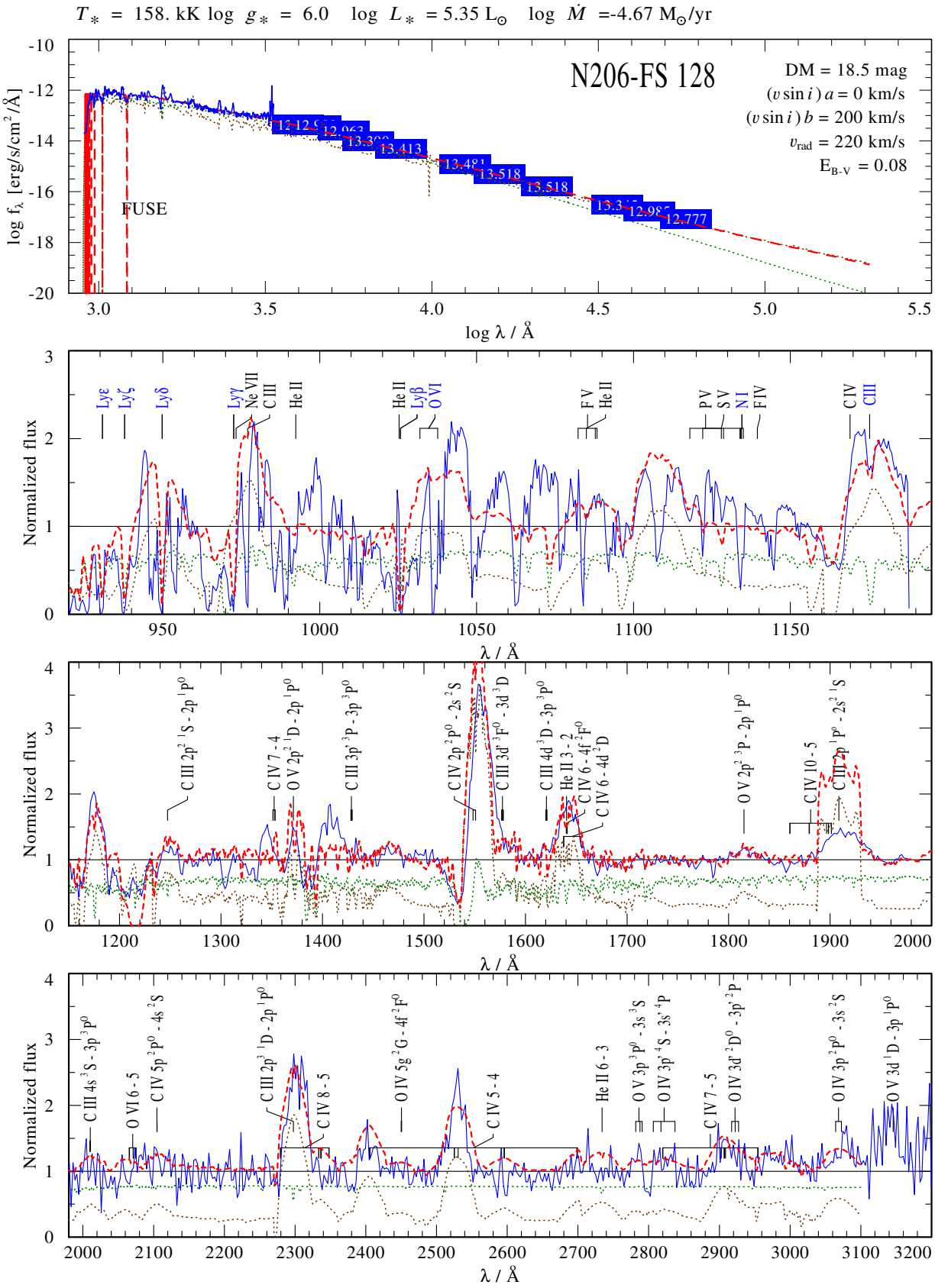

Figure B.1.: Spectral fit for N206-FS 128. The upper panel shows the spectral energy distribution with photometry from UV, optical, and infrared bands as well as the flux calibrated UV spectra. Lower panels show the normalized UV spectra from FUSE, IUE-short, and IUE-long (blue solid lines), fitted by composite model (red dashed lines). The WC and O star models are represented with brown and green dotted lines respectively.

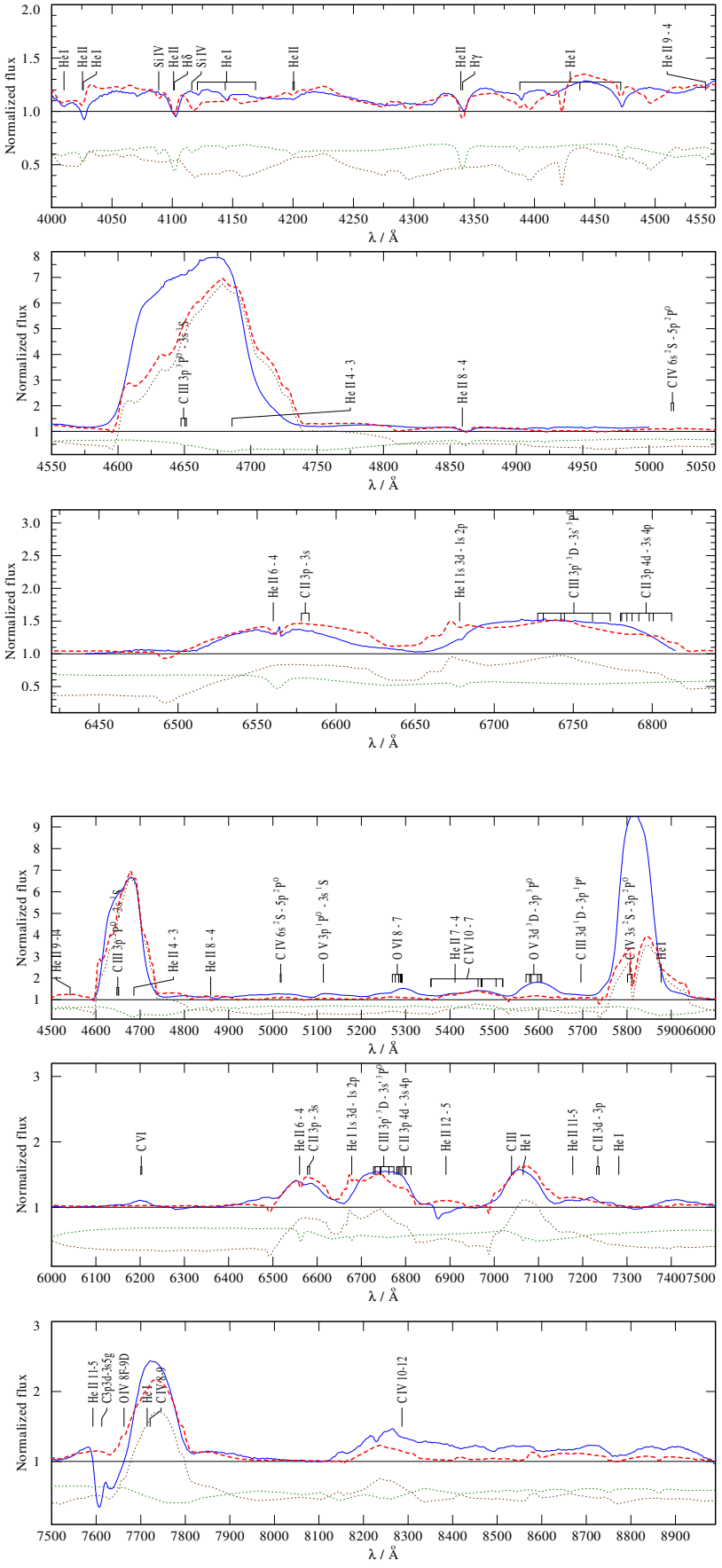

Figure B.2.: Same as Fig. B.1, but shows the normalized FLAMES (panel 1-3) and FORS2 (panel 4-6) spectra.

B.3. Spectral fits of LMC OB stars

We present the spectral fits of all the OB stars in the N 206 complex analyzed in this study. The upper panel shows the spectral energy distribution with photometry from UV, optical, and infra-red bands. Lower panels show the normalized VLT-FLAMES spectra depicted by blue solid lines. For a few stars the available UV spectra from HST, FUSE, IUE are also included in the lower panels. The observed spectra are over-plotted with PoWR model spectra (red dashed lines). The main parameters of the best-fit models are compiled in Table 3.3, continued in Table B.2

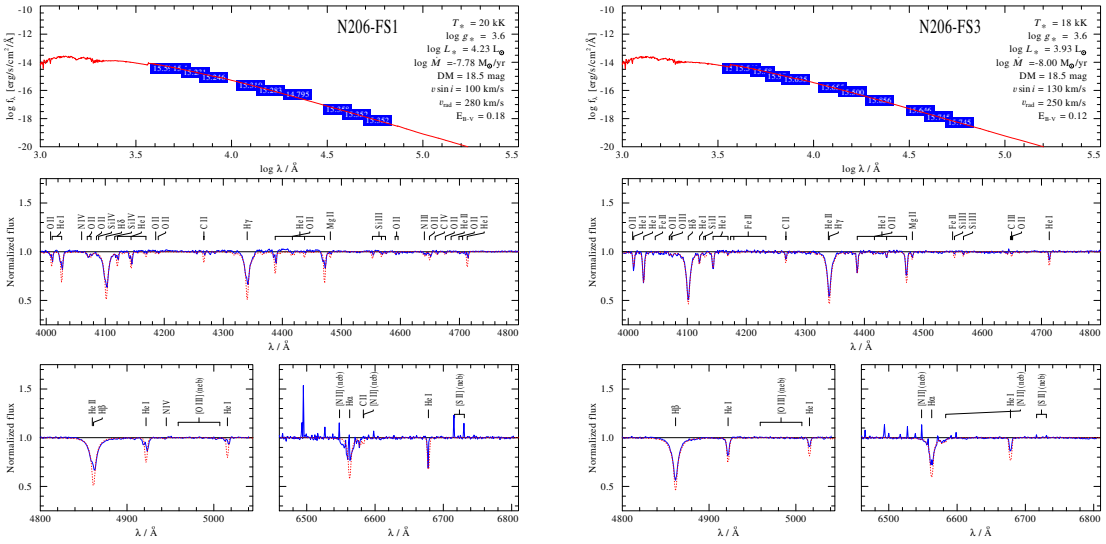

Figure B.3.: Spectral fit for N206-FS 1 and N206-FS 3

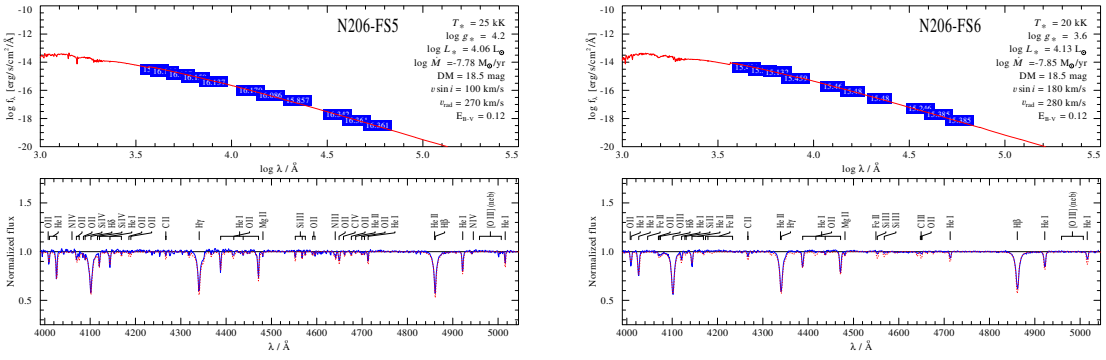

Figure B.4.: Spectral fit for N206-FS 5 and N206-FS 6

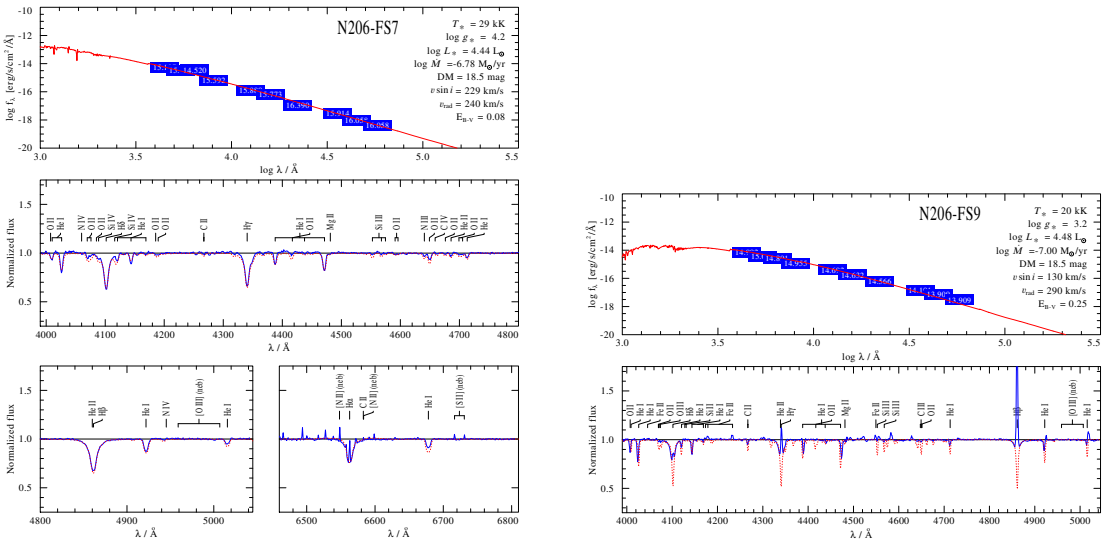

Figure B.5.: Spectral fit for N206-FS 7 and N206-FS 9

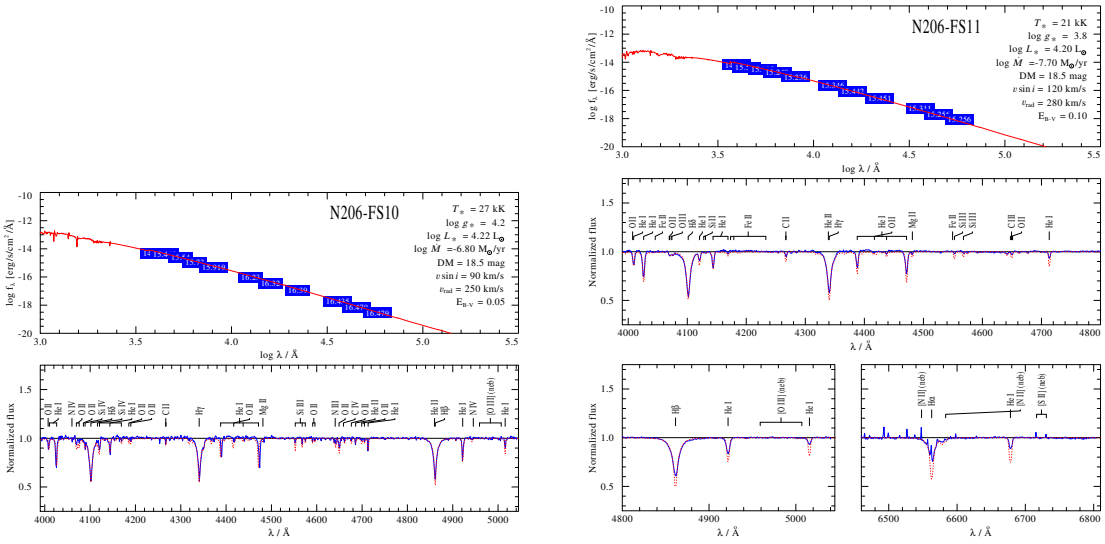

Figure B.6.: Spectral fit for N206-FS 10 and N206-FS 11

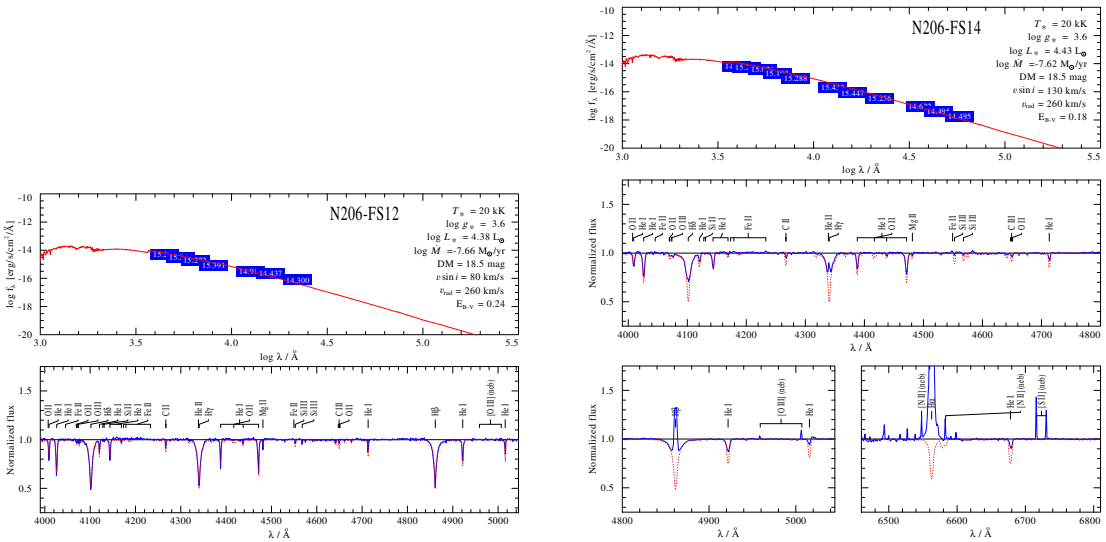

Figure B.7.: Spectral fit for N206-FS 12 and N206-FS 14

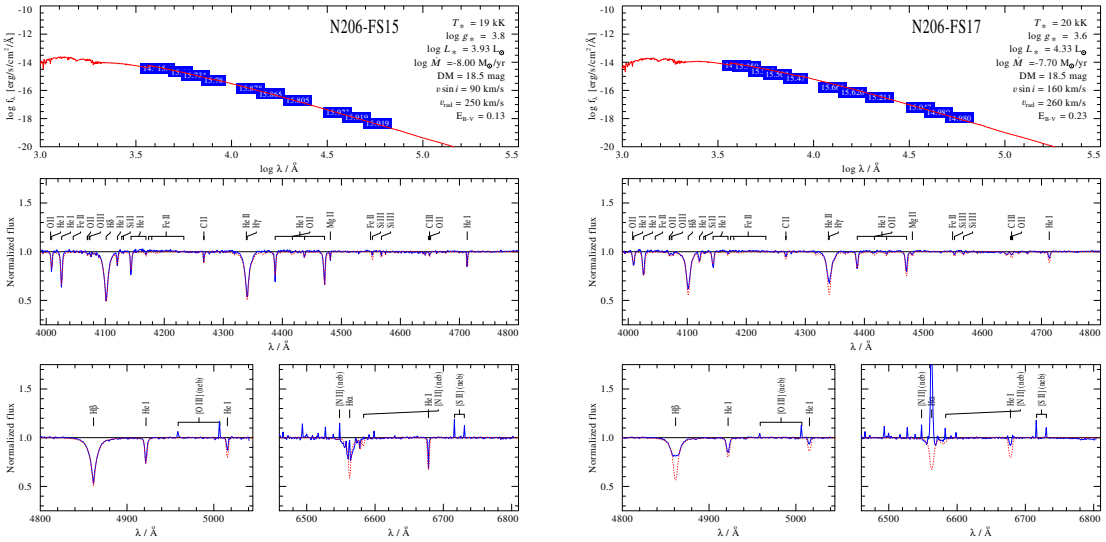

Figure B.8.: Spectral fit for N206-FS 15 and N206-FS 17

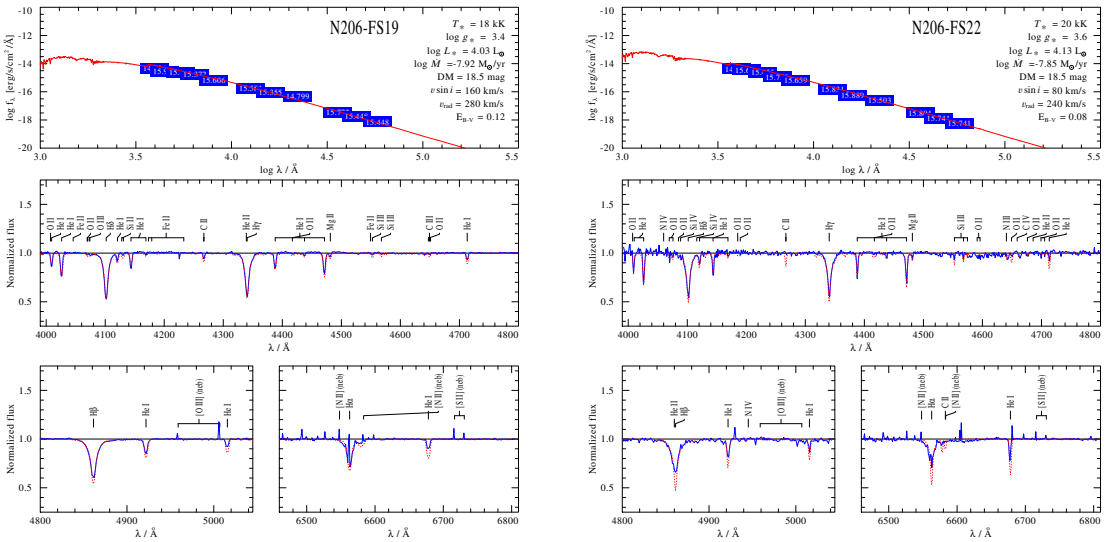

Figure B.9.: Spectral fit for N206-FS 19 and N206-FS 22

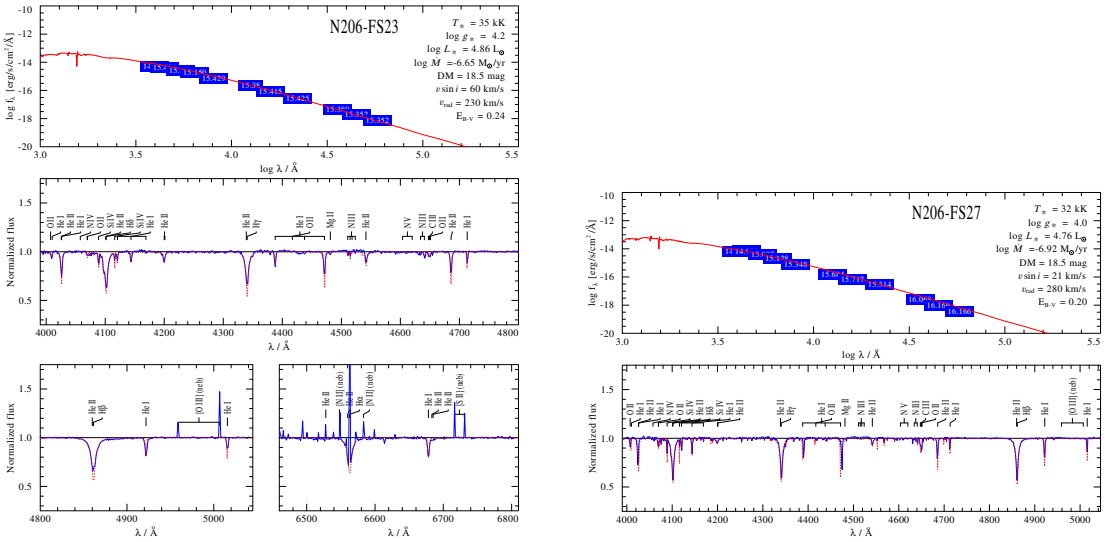

Figure B.10.: Spectral fit for N206-FS 23 and N206-FS 27

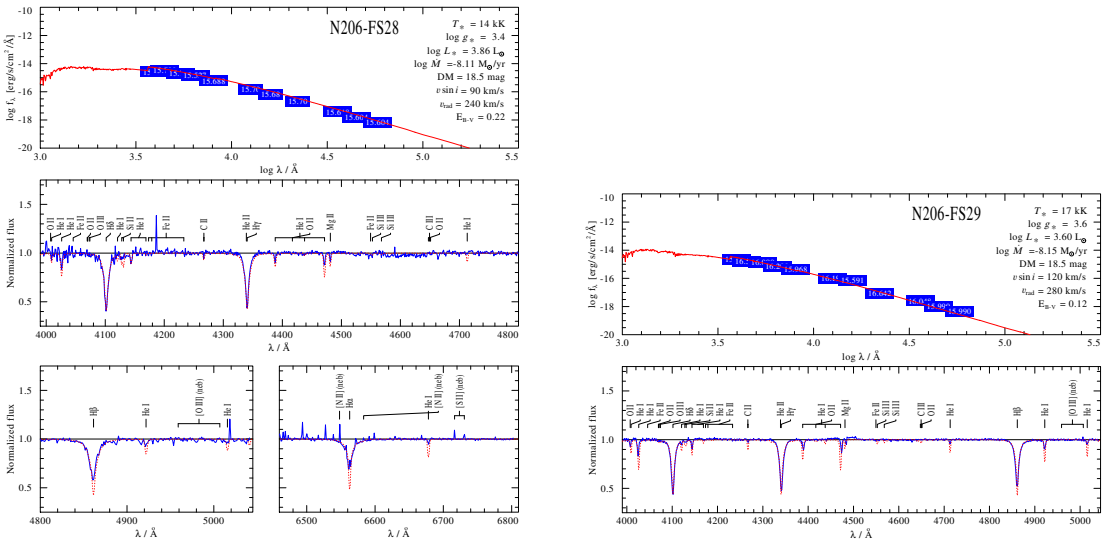

Figure B.11.: Spectral fit for N206-FS 28 and N206-FS 29

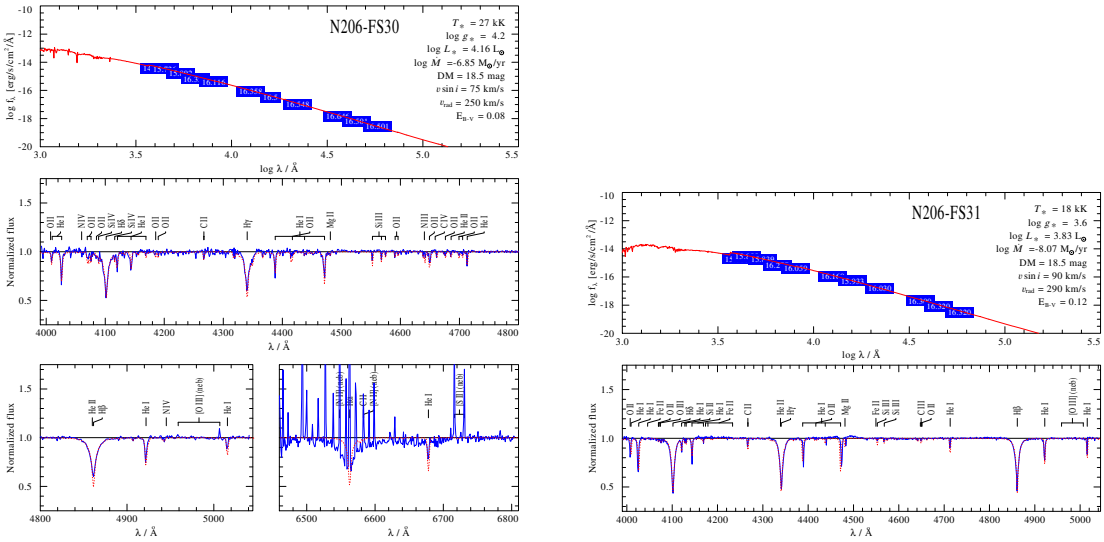

Figure B.12.: Spectral fit for N206-FS 30 and N206-FS 31

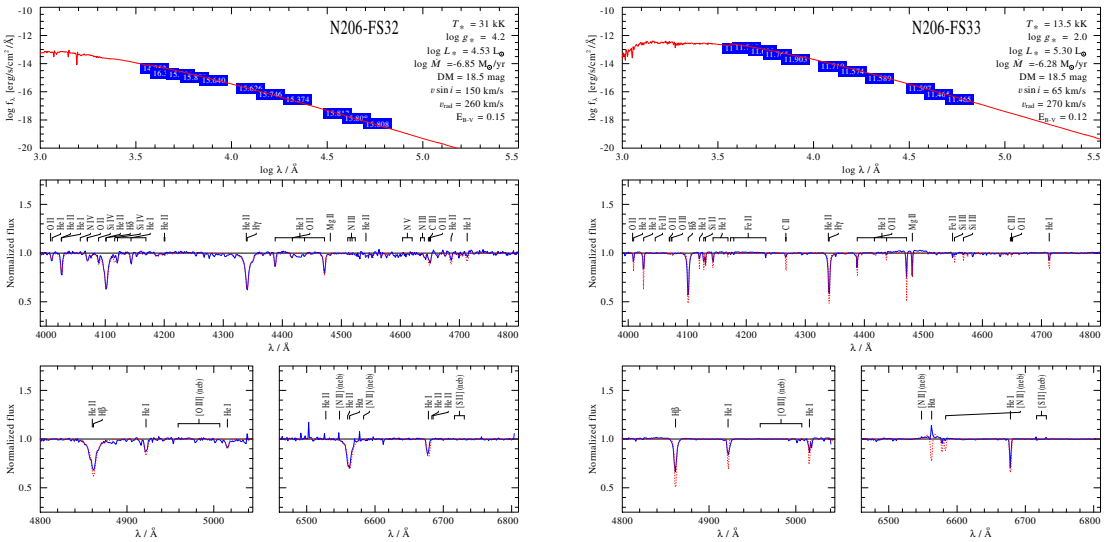

Figure B.13.: Spectral fit for N206-FS 32 and N206-FS 33

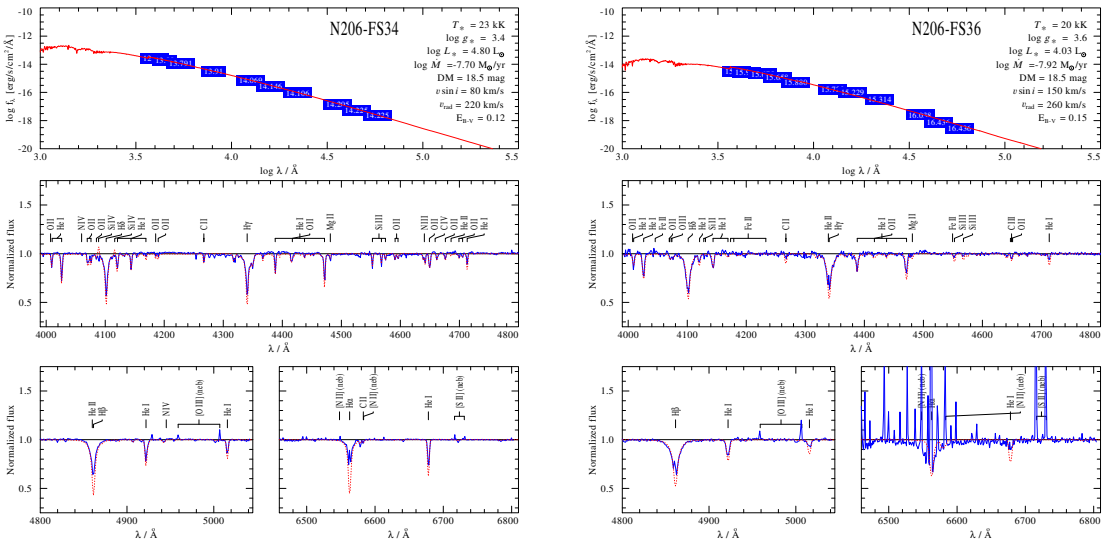

Figure B.14.: Spectral fit for N206-FS 34 and N206-FS 36

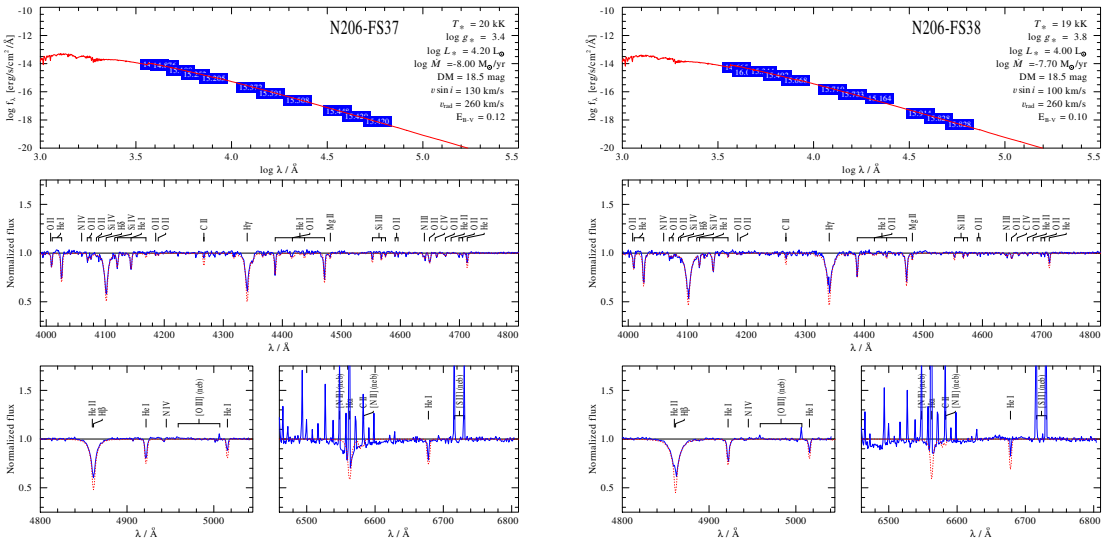

Figure B.15.: Spectral fit for N206-FS 37 and N206-FS 38

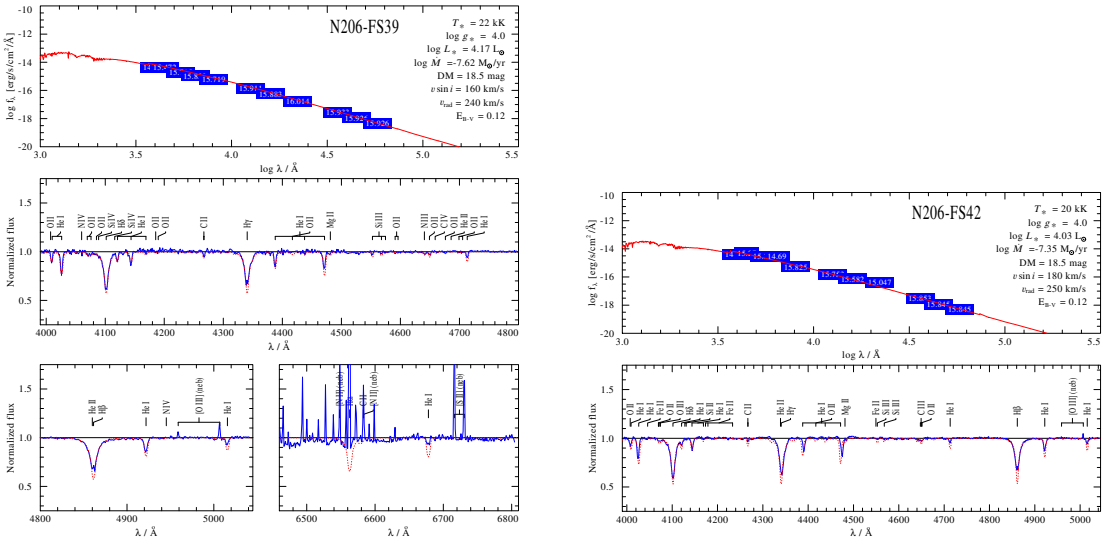

Figure B.16.: Spectral fit for N206-FS 39 and N206-FS 42

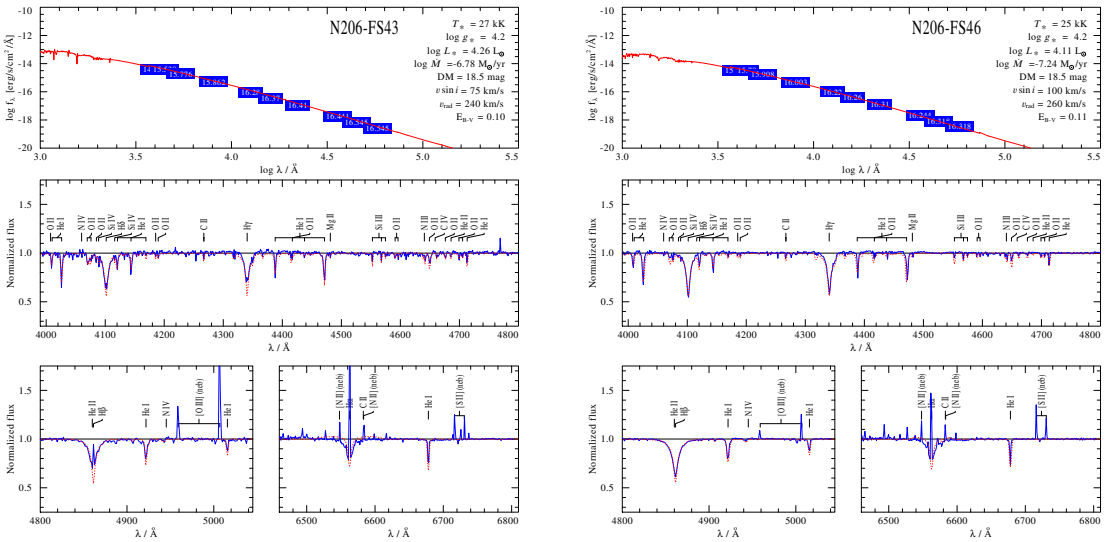

Figure B.17.: Spectral fit for N206-FS 43 and N206-FS 46

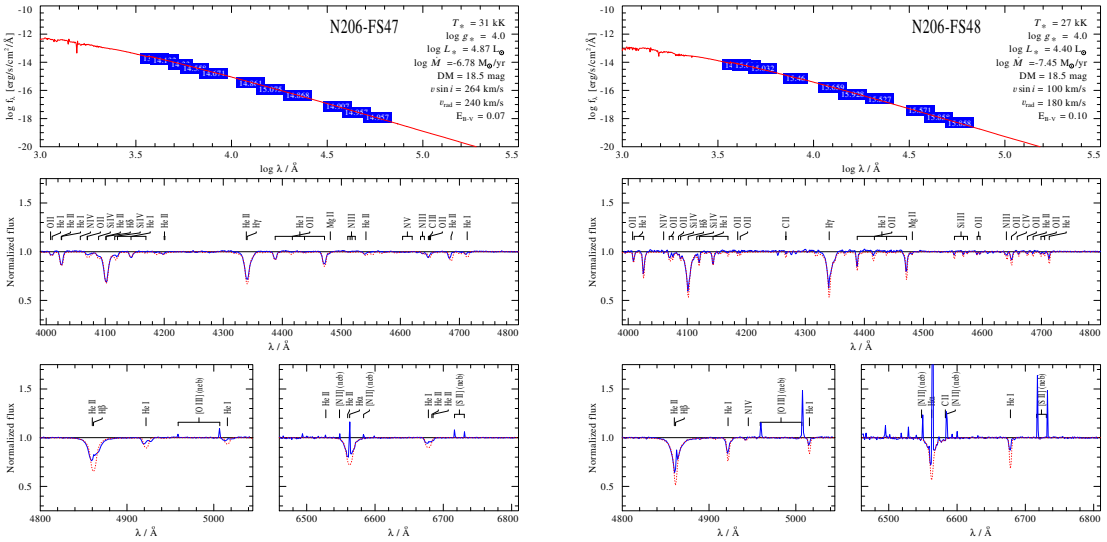

Figure B.18.: Spectral fit for N206-FS 47 and N206-FS 48

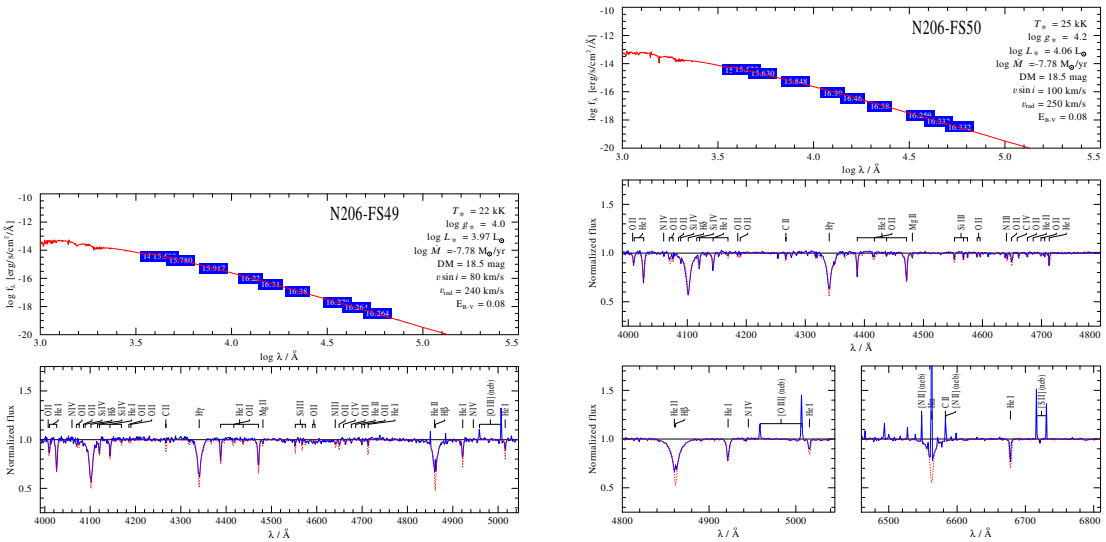

Figure B.19.: Spectral fit for N206-FS 49 and N206-FS 50

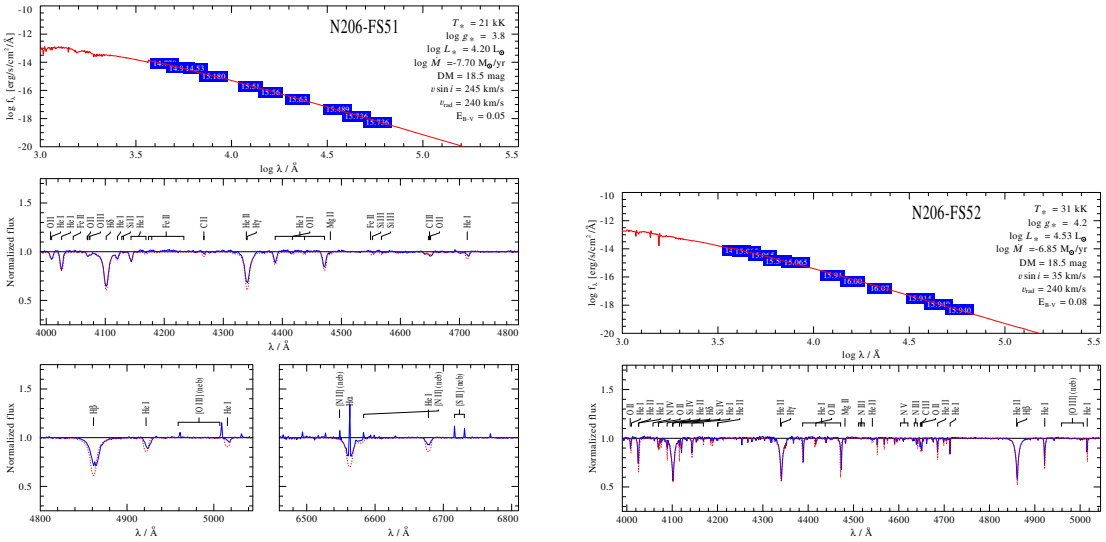

Figure B.20.: Spectral fit for N206-FS 51 and N206-FS 52

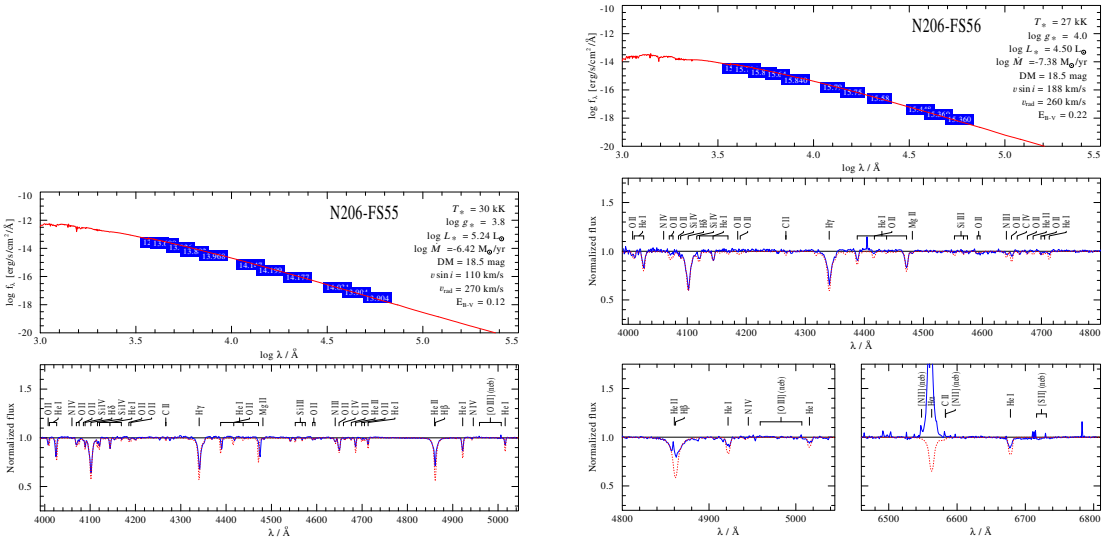

Figure B.21.: Spectral fit for N206-FS 55 and N206-FS 56

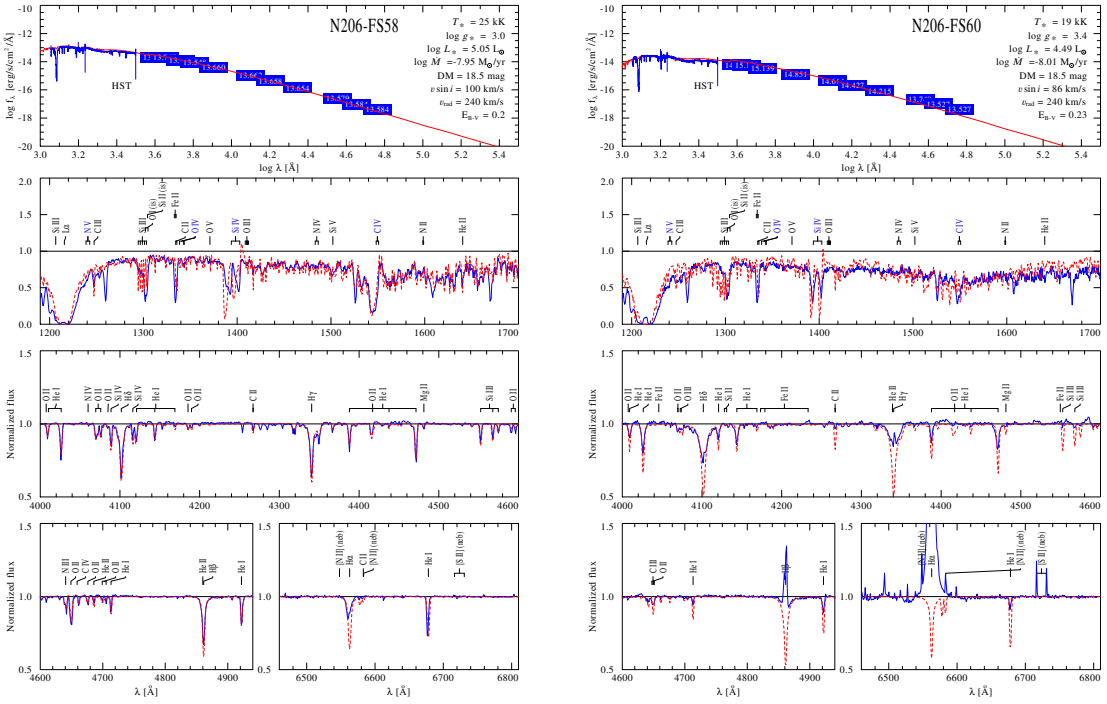

Figure B.22.: Spectral fit for N206-FS 58 and N206-FS 60

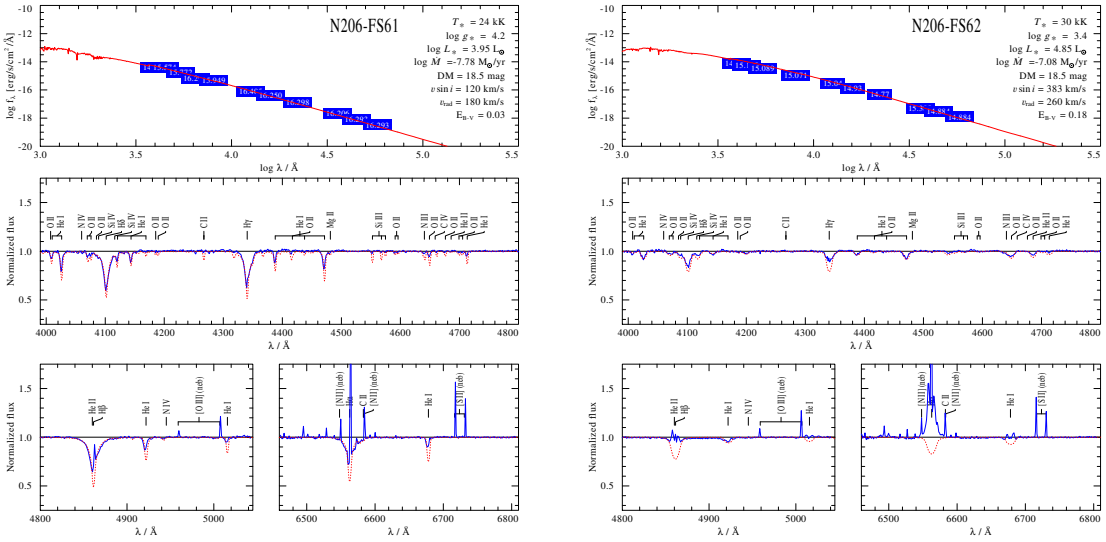

Figure B.23.: Spectral fit for N206-FS 61 and N206-FS 62

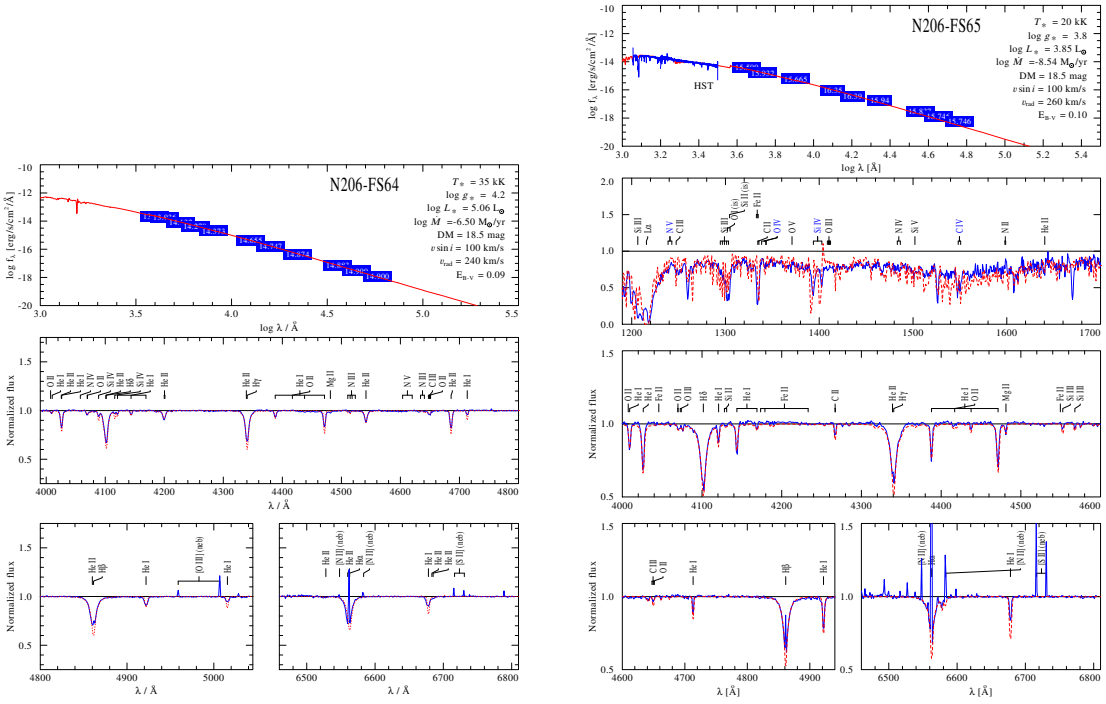

Figure B.24.: Spectral fit for N206-FS 64 and N206-FS 65

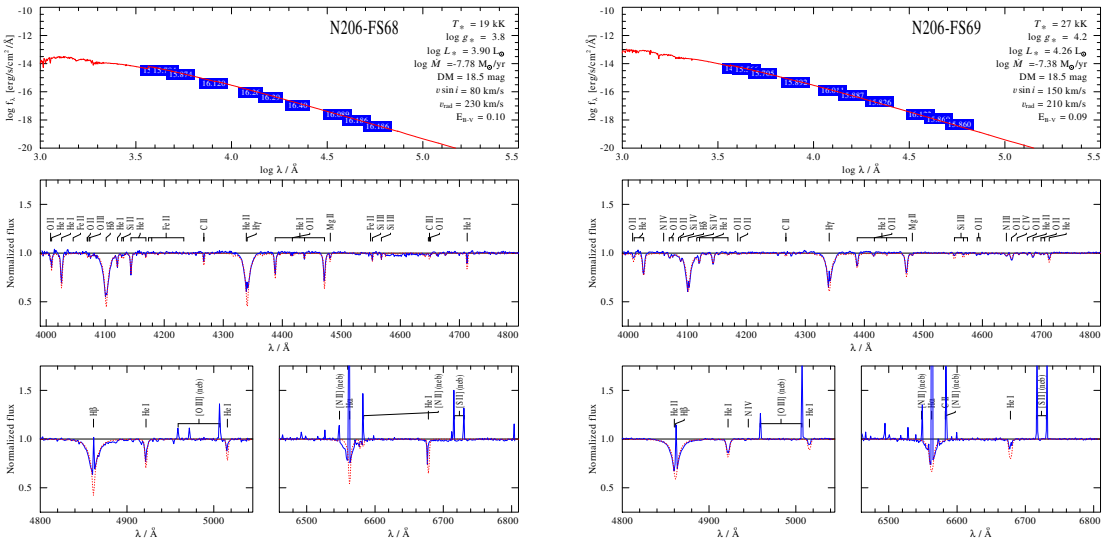

Figure B.25.: Spectral fit for N206-FS 68 and N206-FS 69

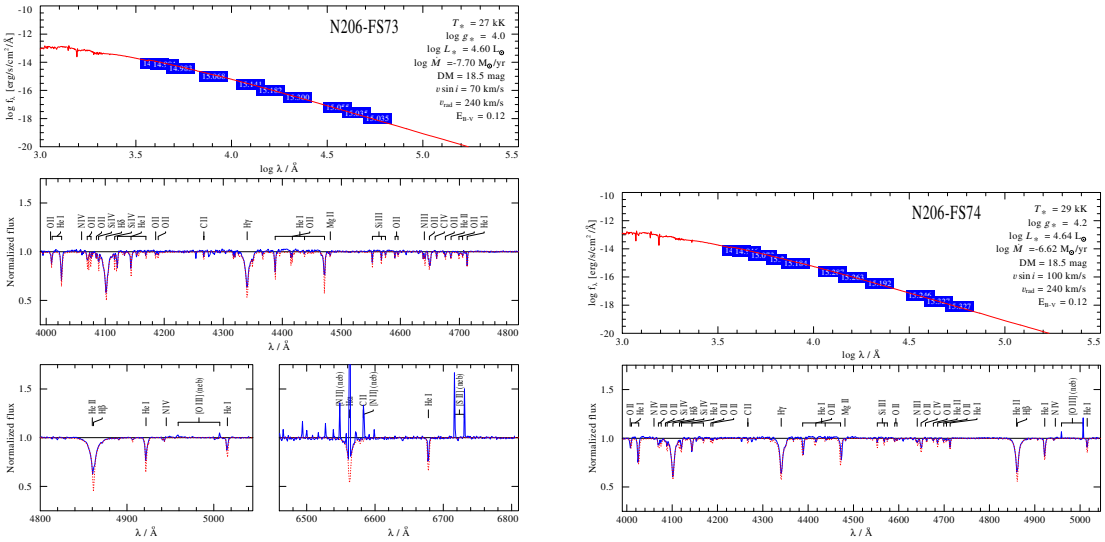

Figure B.26.: Spectral fit for N206-FS 73 and N206-FS 74

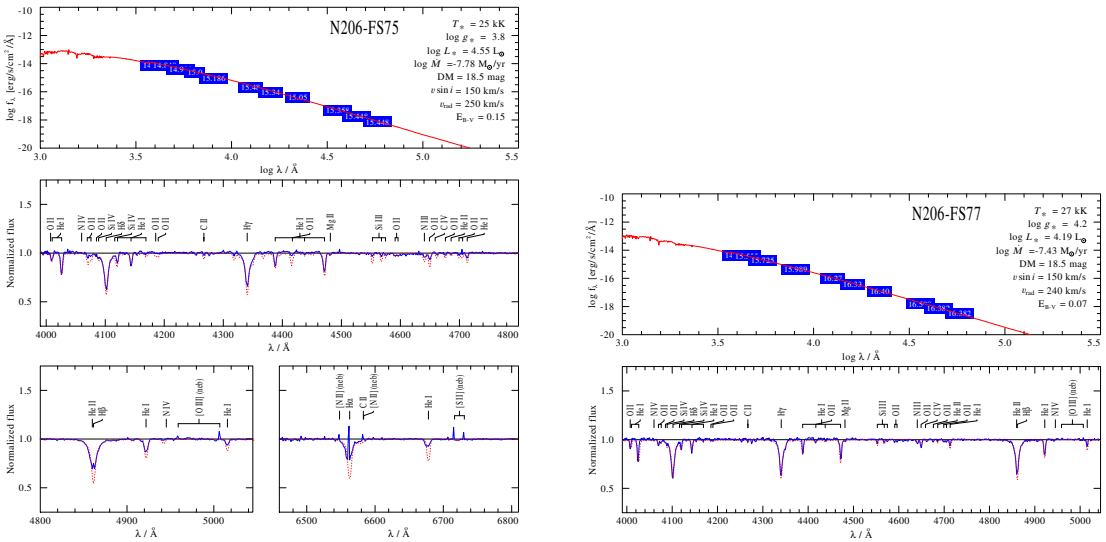

Figure B.27.: Spectral fit for N206-FS 75 and N206-FS 77

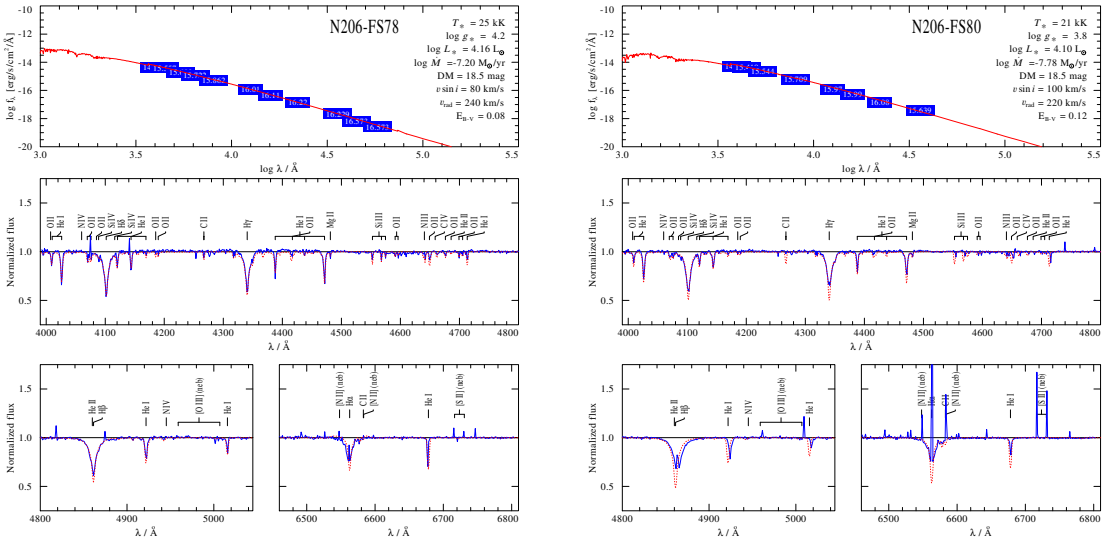

Figure B.28.: Spectral fit for N206-FS 78 and N206-FS 80

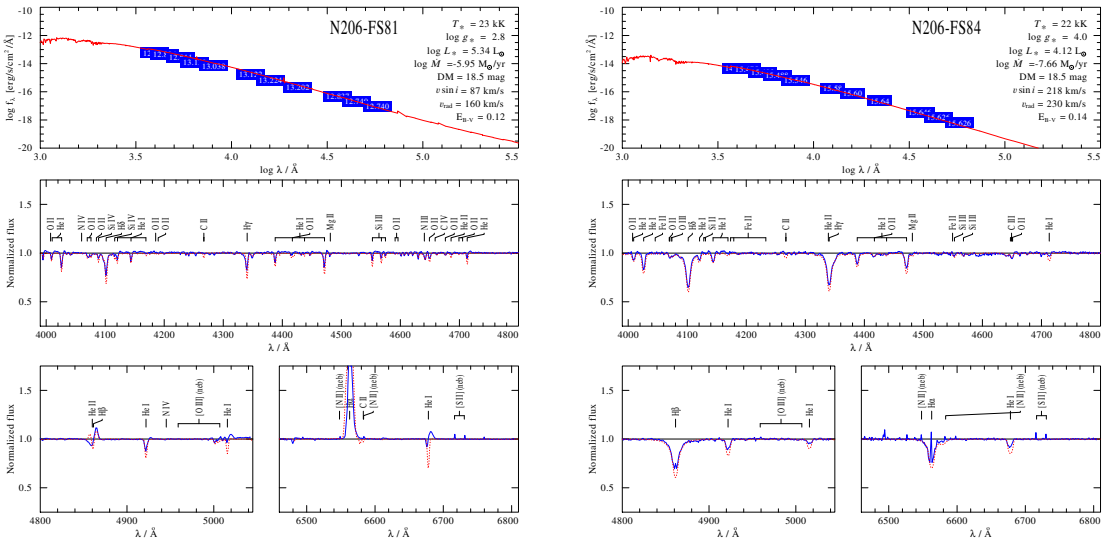

Figure B.29.: Spectral fit for N206-FS 81 and N206-FS 84

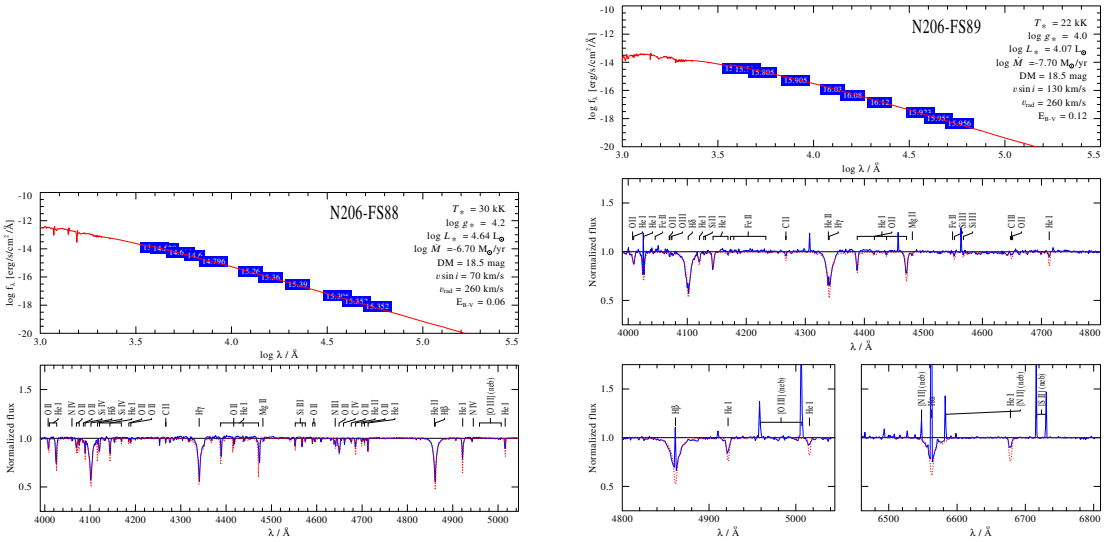

Figure B.30.: Spectral fit for N206-FS 88 and N206-FS 89

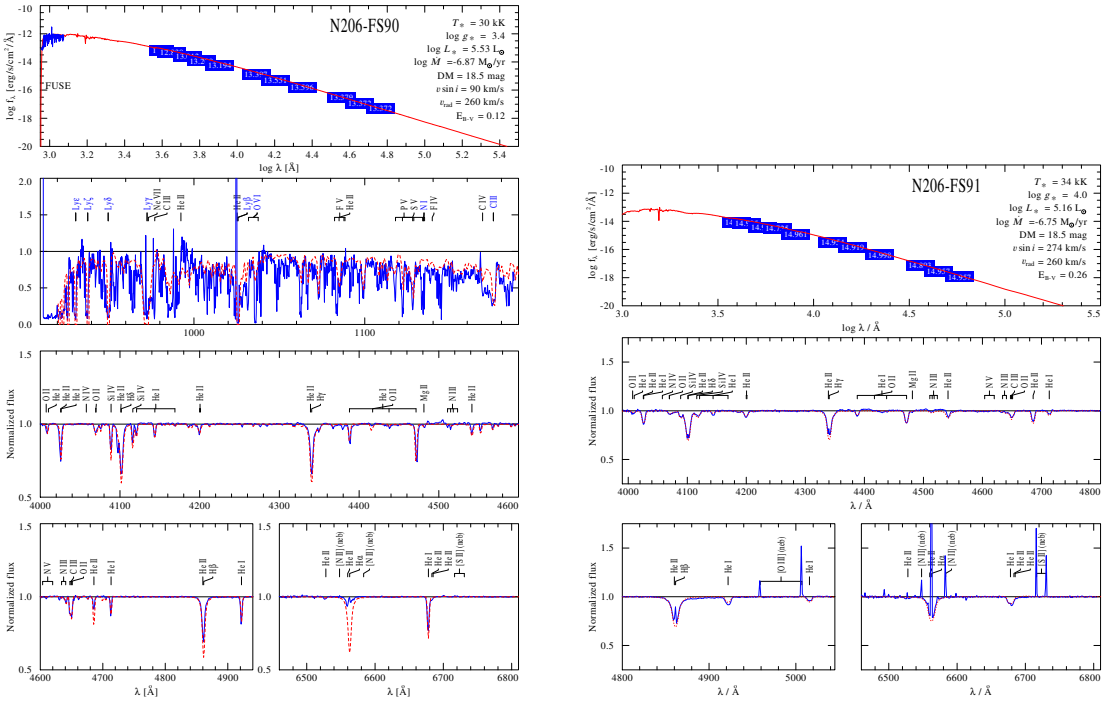

Figure B.31.: Spectral fit for N206-FS 90 and N206-FS 91

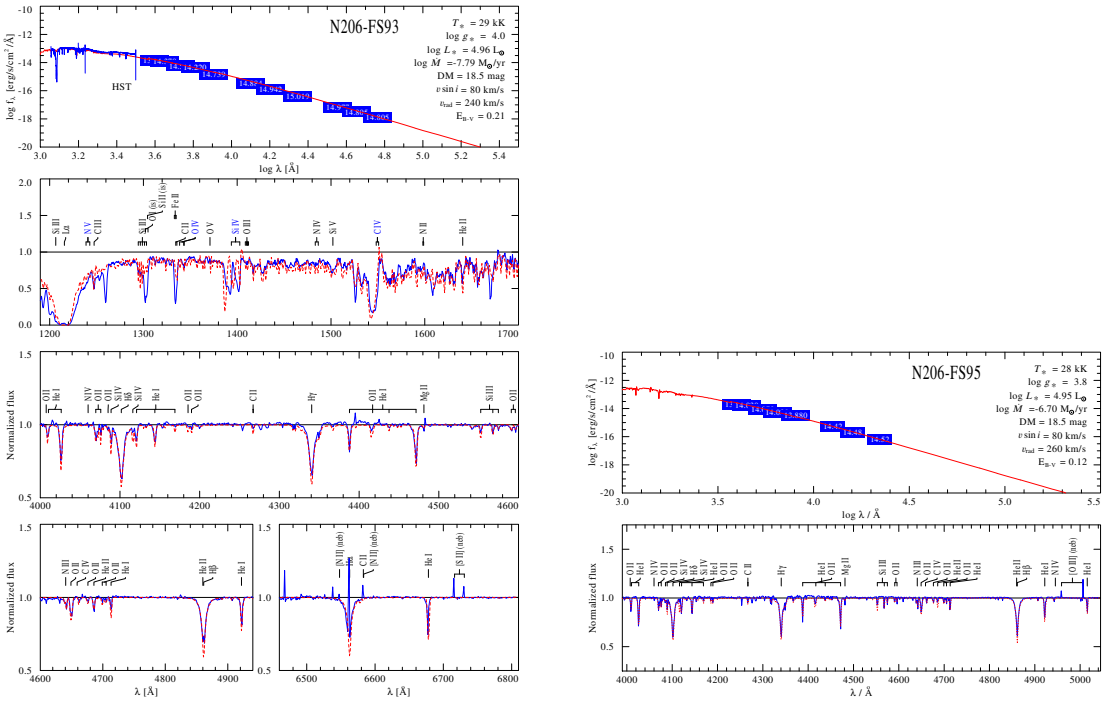

Figure B.32.: Spectral fit for N206-FS 93 and N206-FS 95

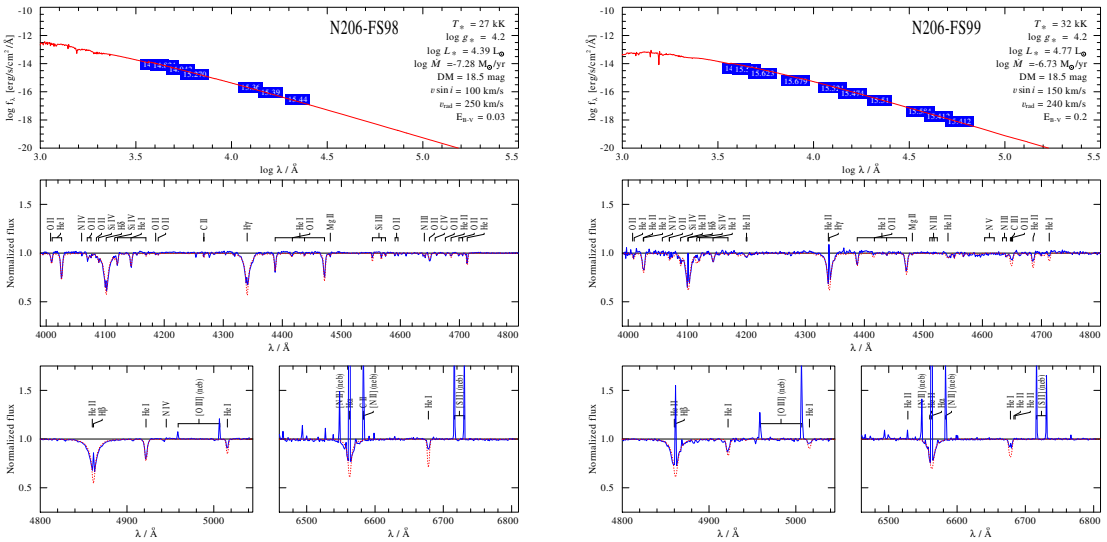

Figure B.33.: Spectral fit for N206-FS 98 and N206-FS 99

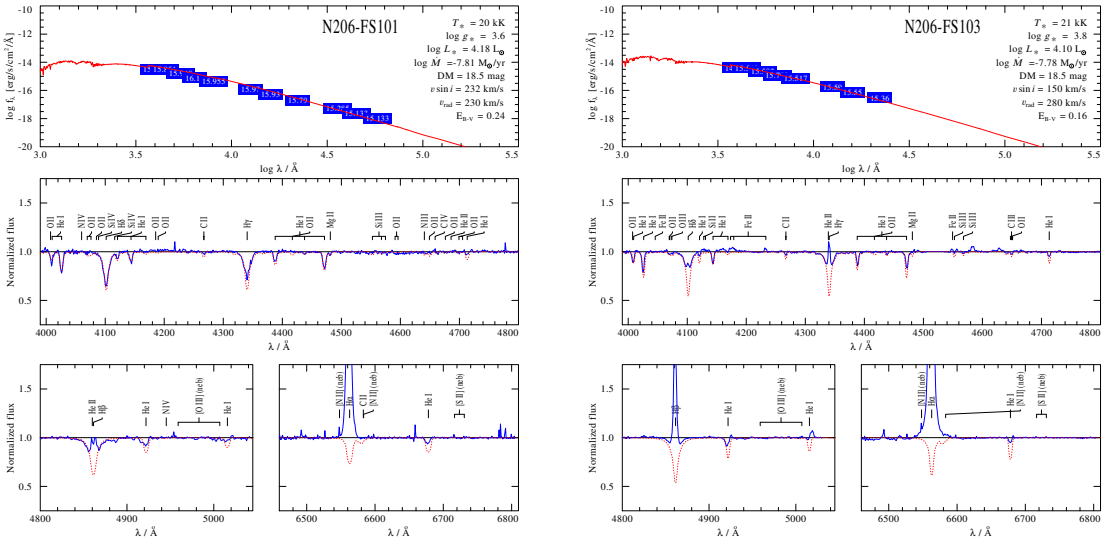

Figure B.34.: Spectral fit for N206-FS 101 and N206-FS 103

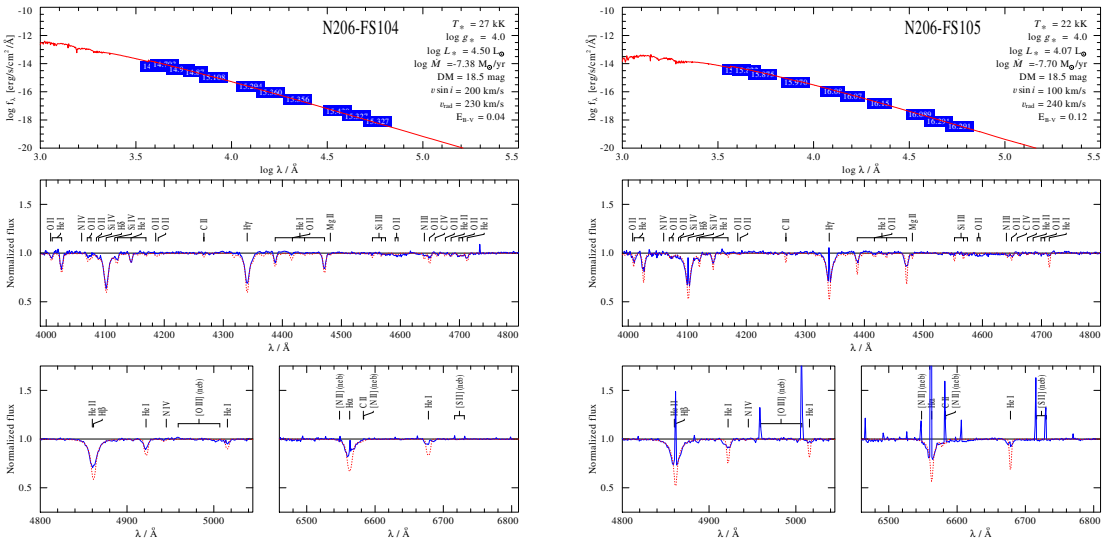

Figure B.35.: Spectral fit for N206-FS 104 and N206-FS 105

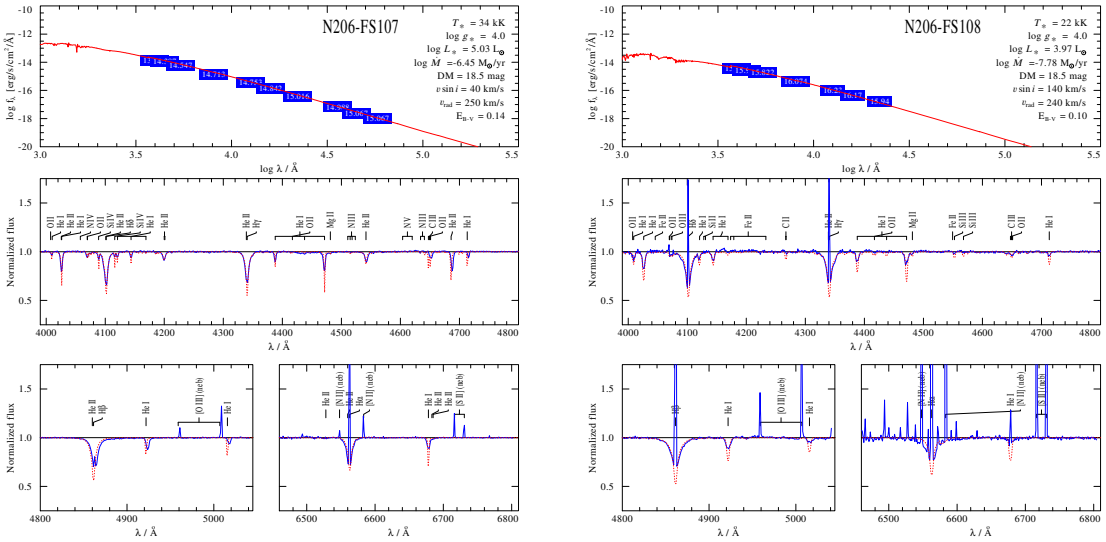

Figure B.36.: Spectral fit for N206-FS 107 and N206-FS 108

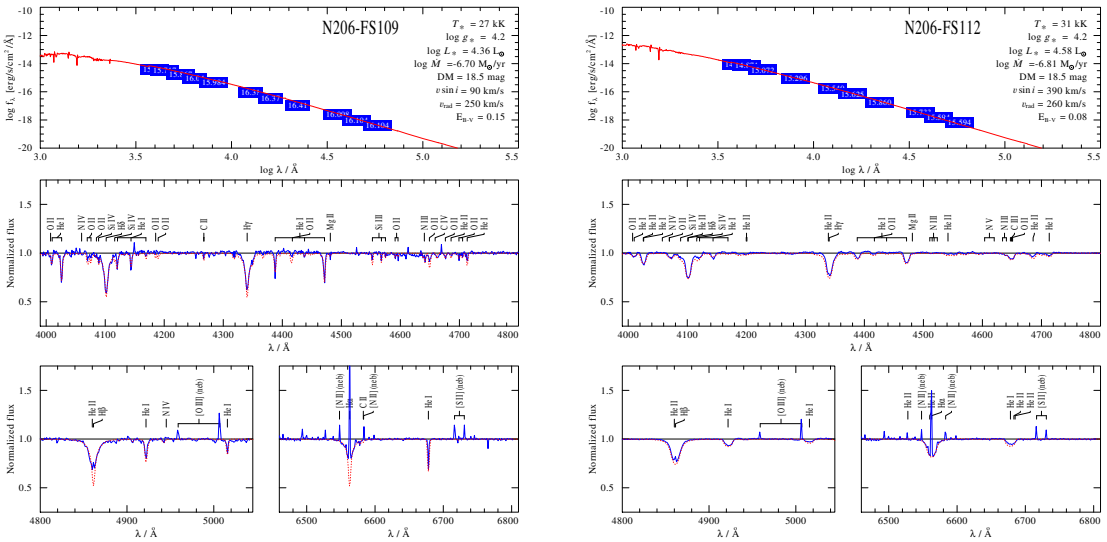

Figure B.37.: Spectral fit for N206-FS 109 and N206-FS 112

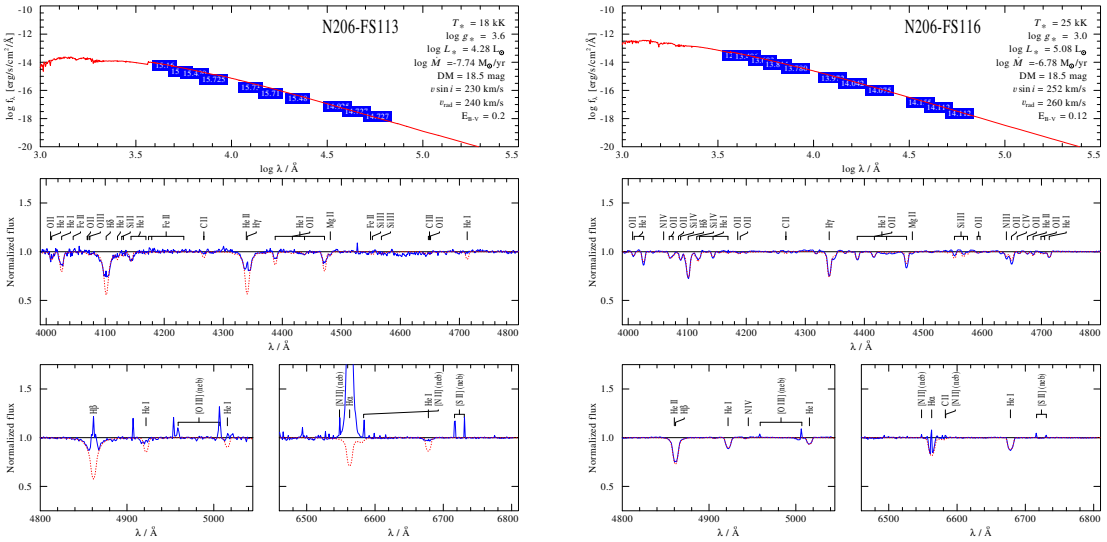

Figure B.38.: Spectral fit for N206-FS 113 and N206-FS 116

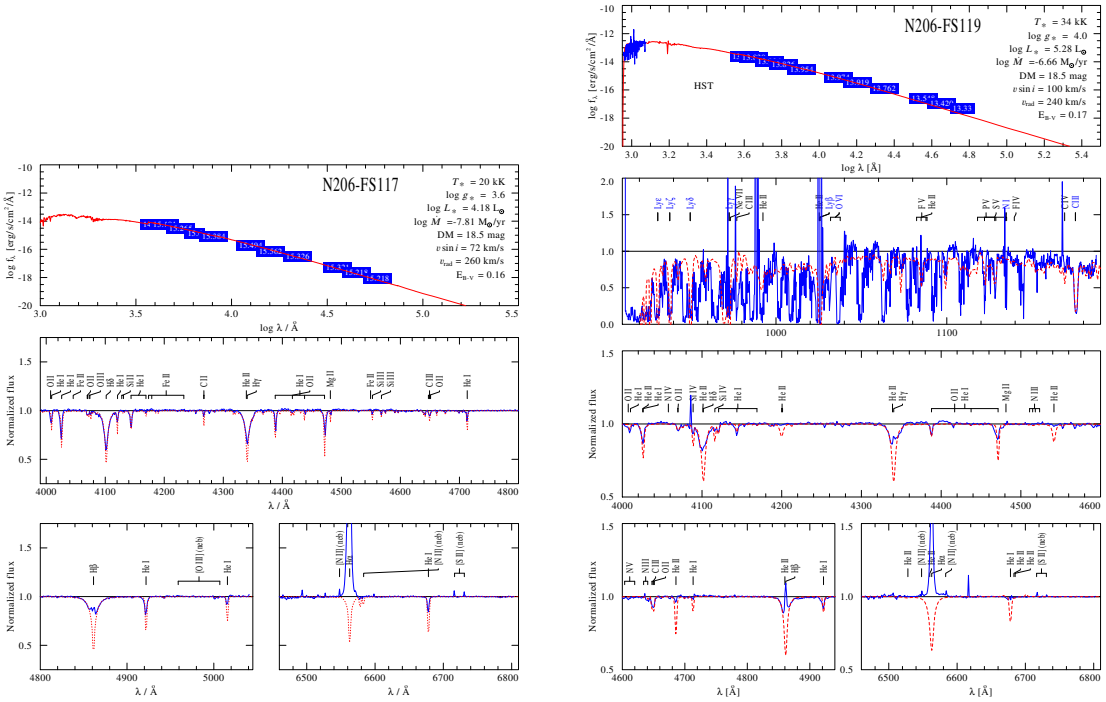

Figure B.39.: Spectral fit for N206-FS 117 and N206-FS 119

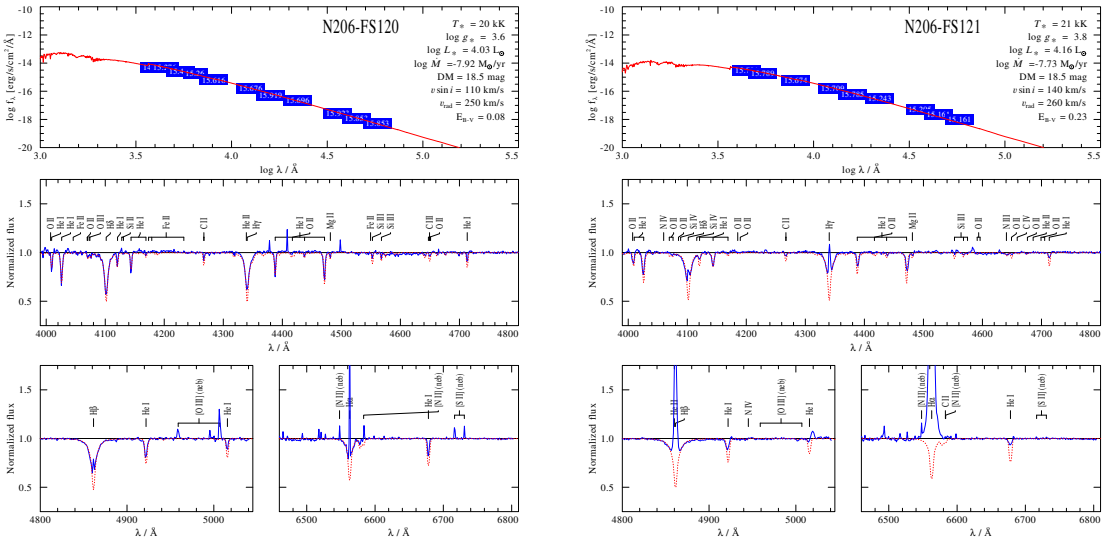

Figure B.40.: Spectral fit for N206-FS 120 and N206-FS 121

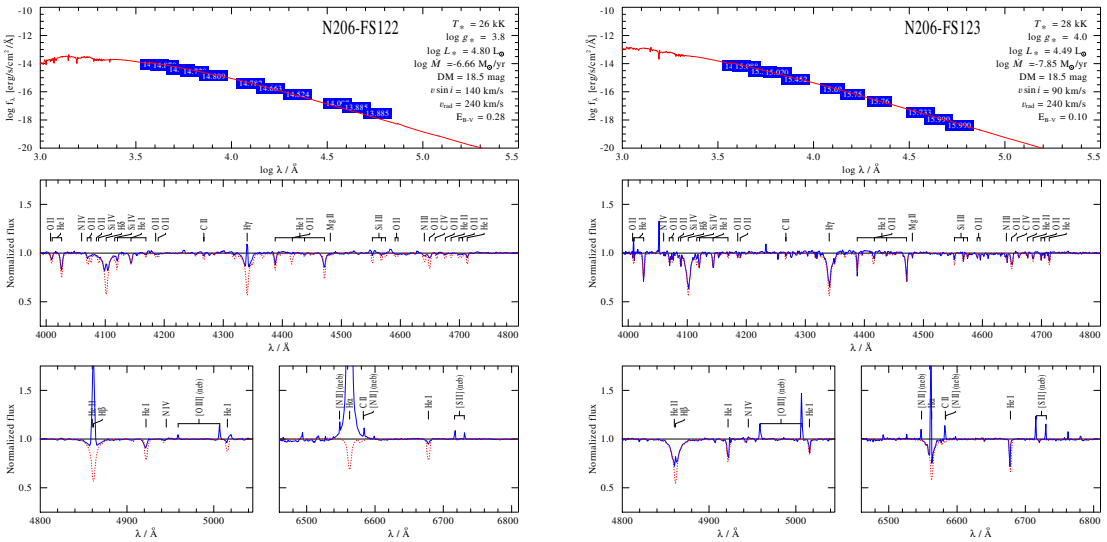

Figure B.41.: Spectral fit for N206-FS 122 and N206-FS 123

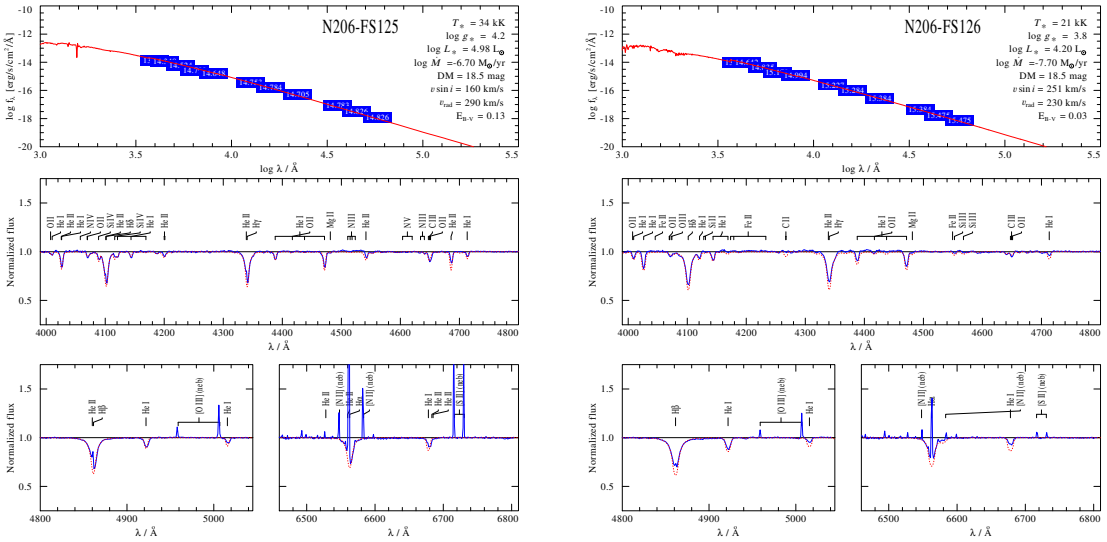

Figure B.42.: Spectral fit for N206-FS 125 and N206-FS 126

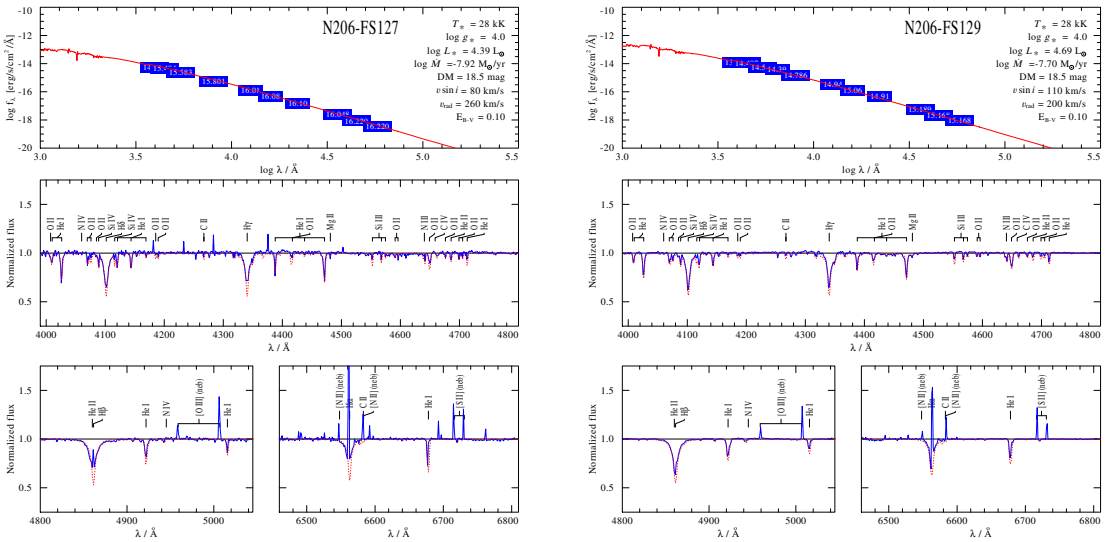

Figure B.43.: Spectral fit for N206-FS 127 and N206-FS 129

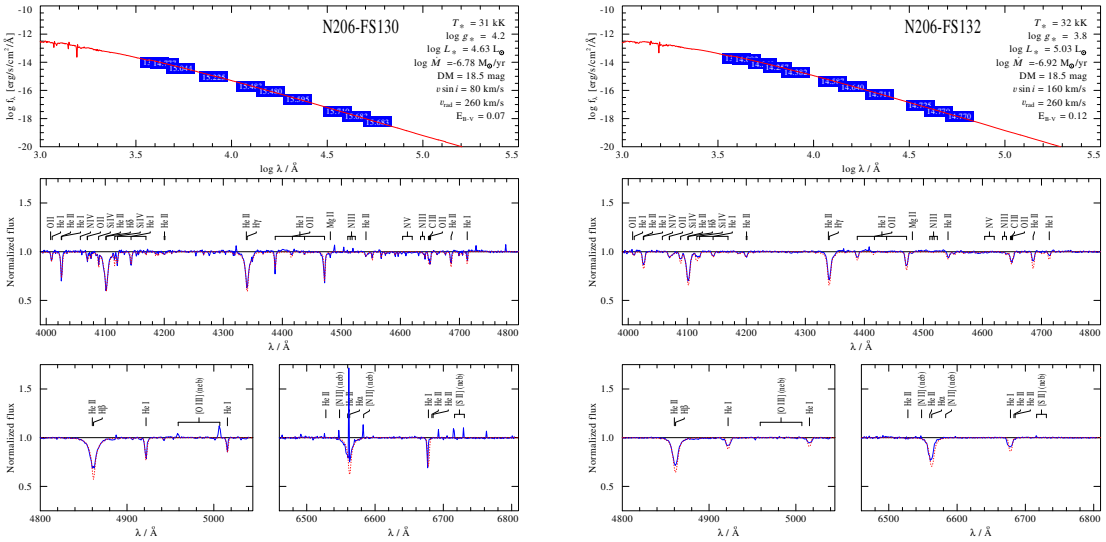

Figure B.44.: Spectral fit for N206-FS 130 and N206-FS 132

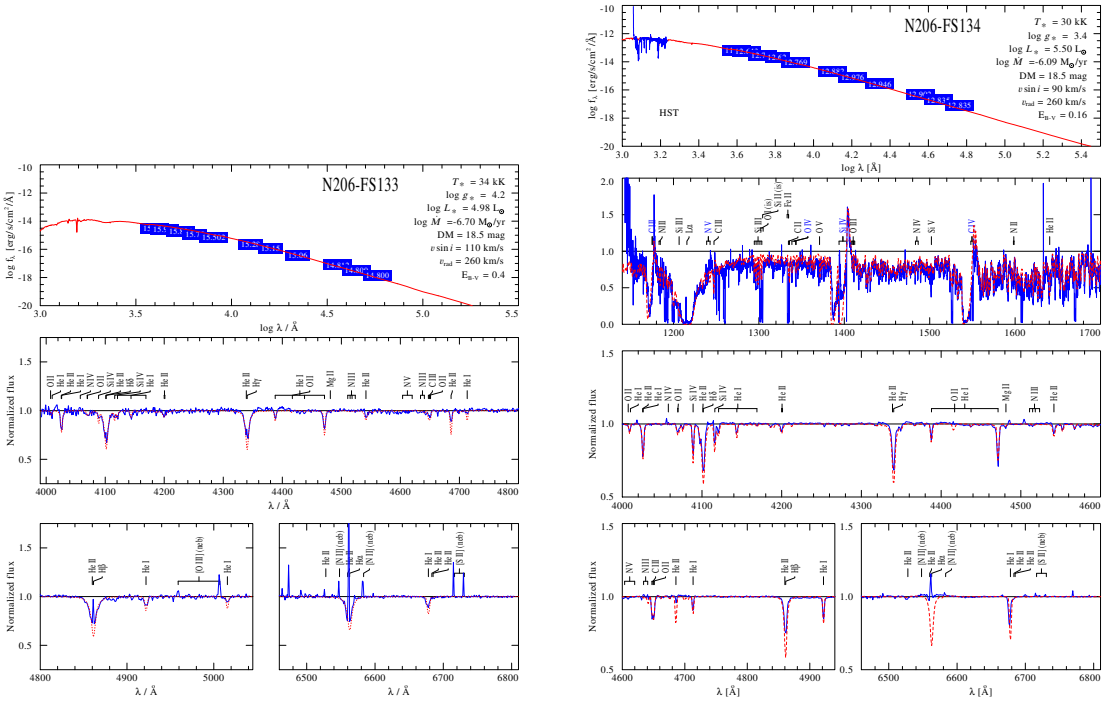

Figure B.45.: Spectral fit for N206-FS 133 and N206-FS 134

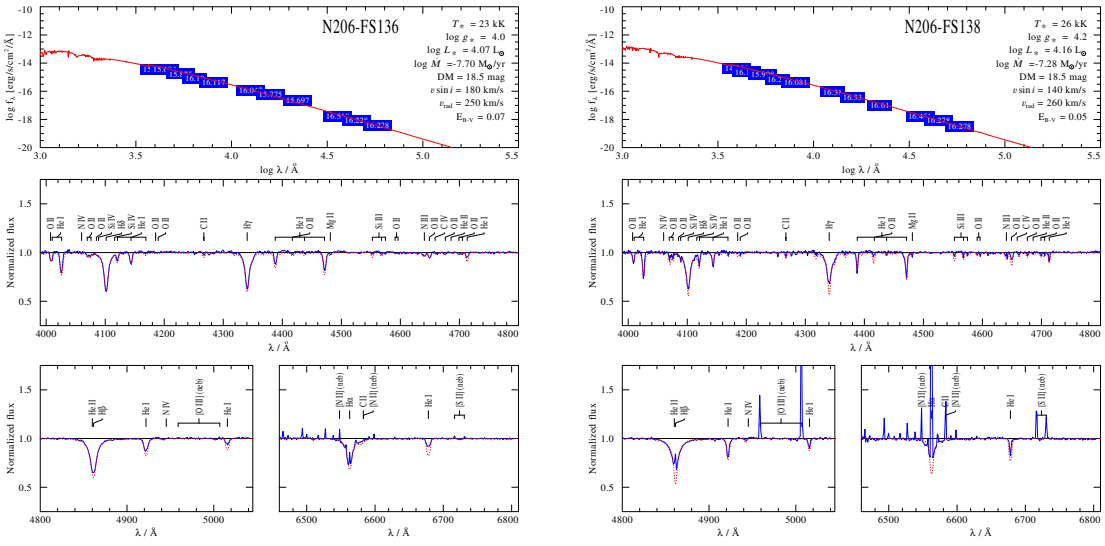

Figure B.46.: Spectral fit for N206-FS 136 and N206-FS 138

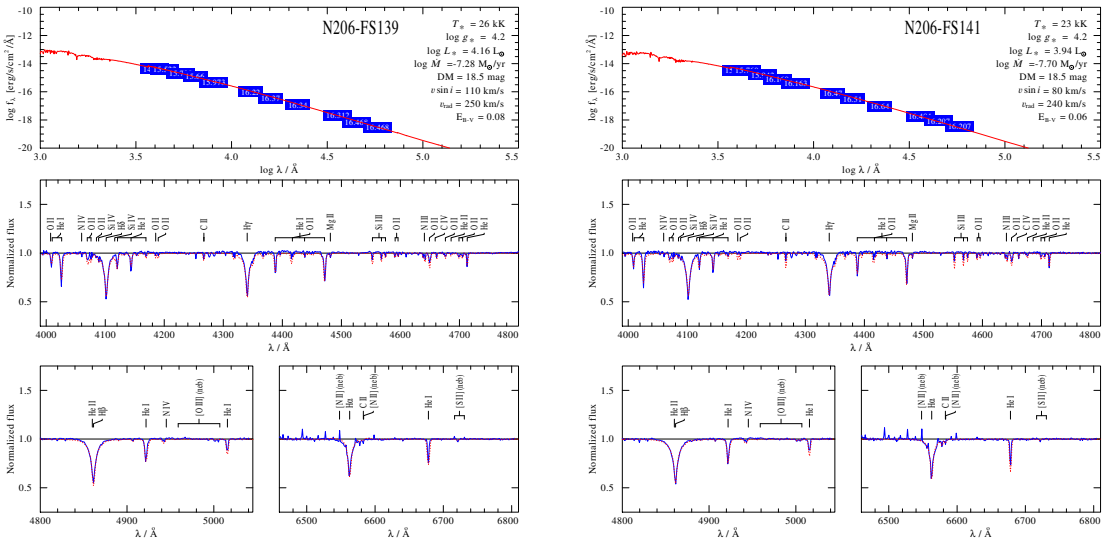

Figure B.47.: Spectral fit for N206-FS 139 and N206-FS 141

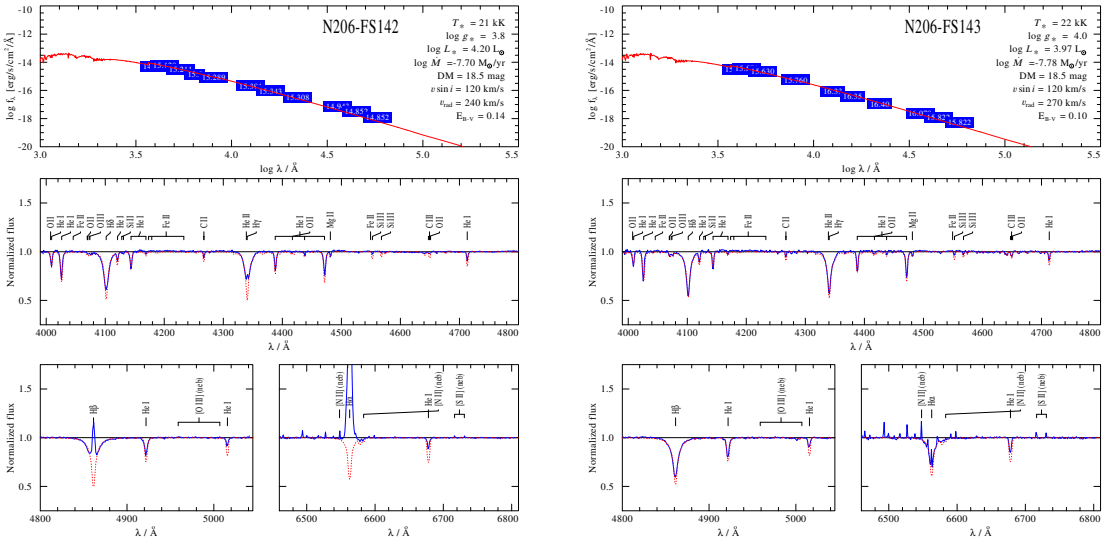

Figure B.48.: Spectral fit for N206-FS 142 and N206-FS 143

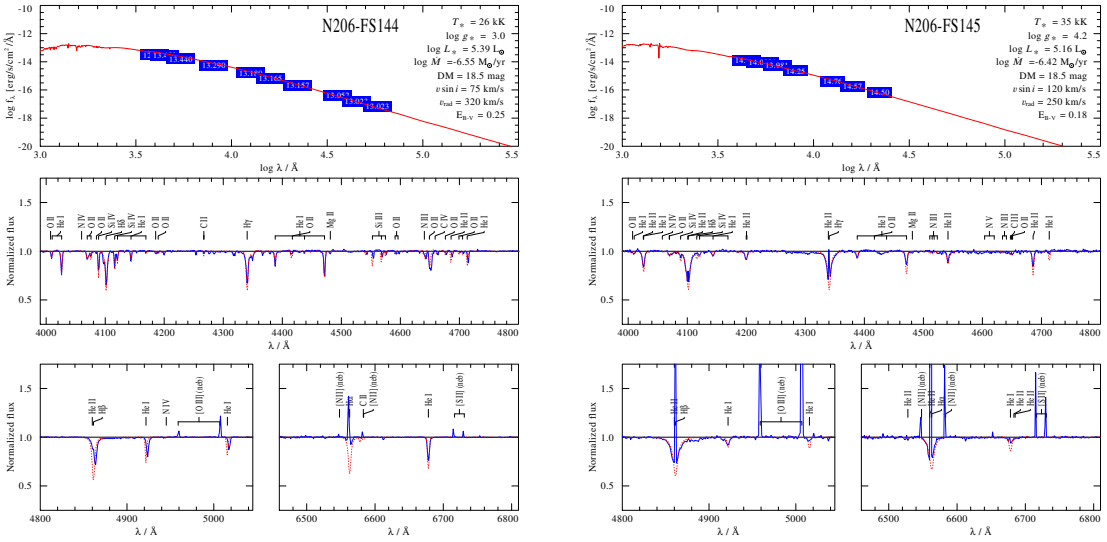

Figure B.49.: Spectral fit for N206-FS 144 and N206-FS 145

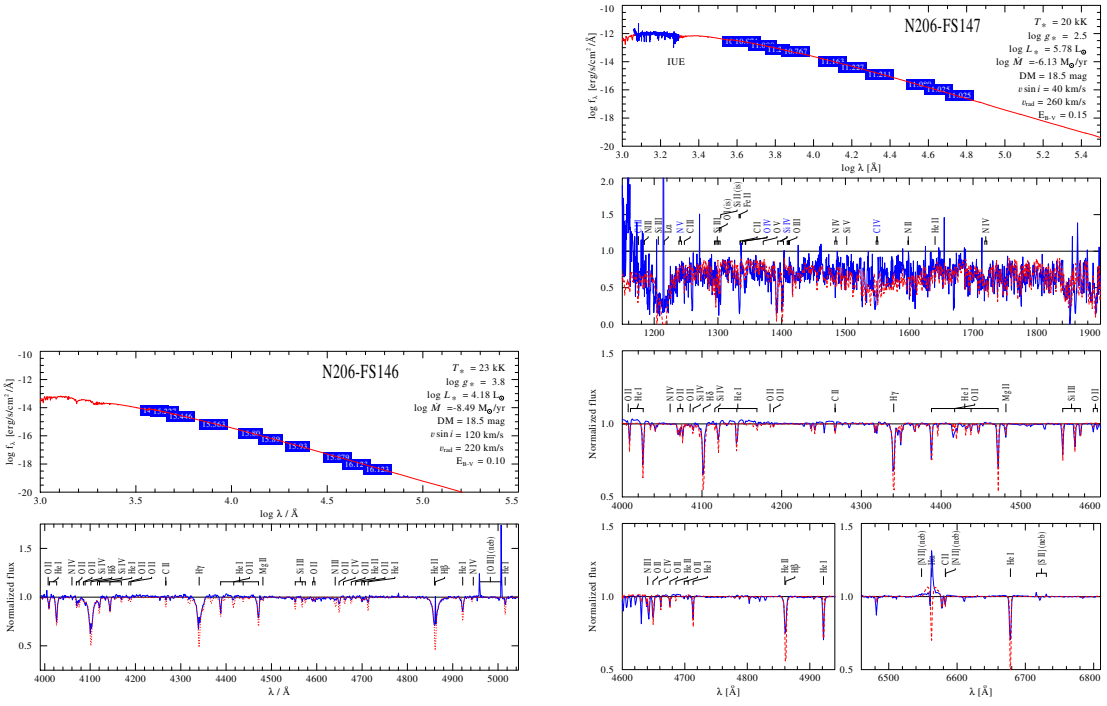

Figure B.50.: Spectral fit for N206-FS 146 and N206-FS 147

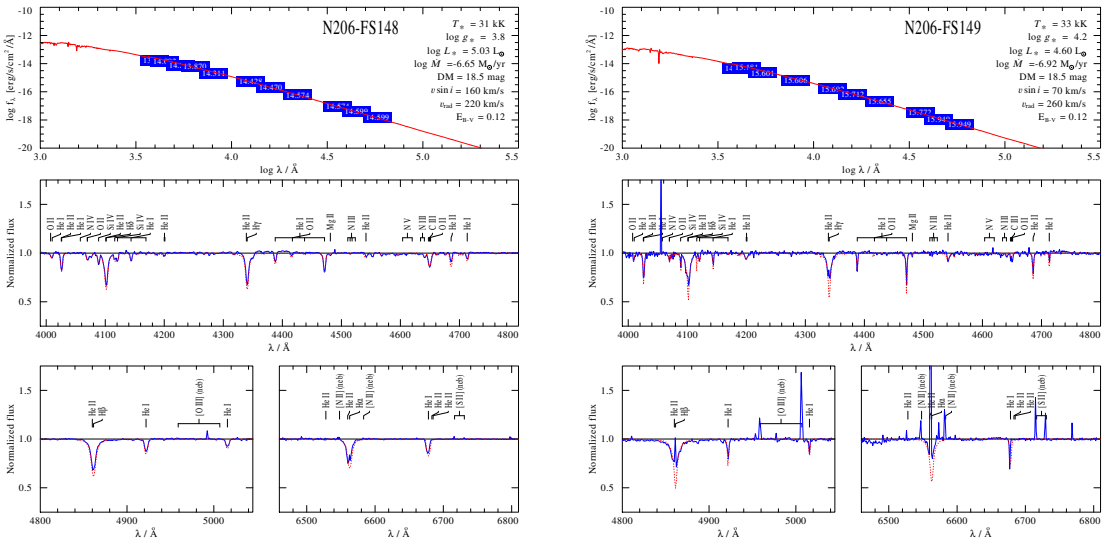

Figure B.51.: Spectral fit for N206-FS 148 and N206-FS 149

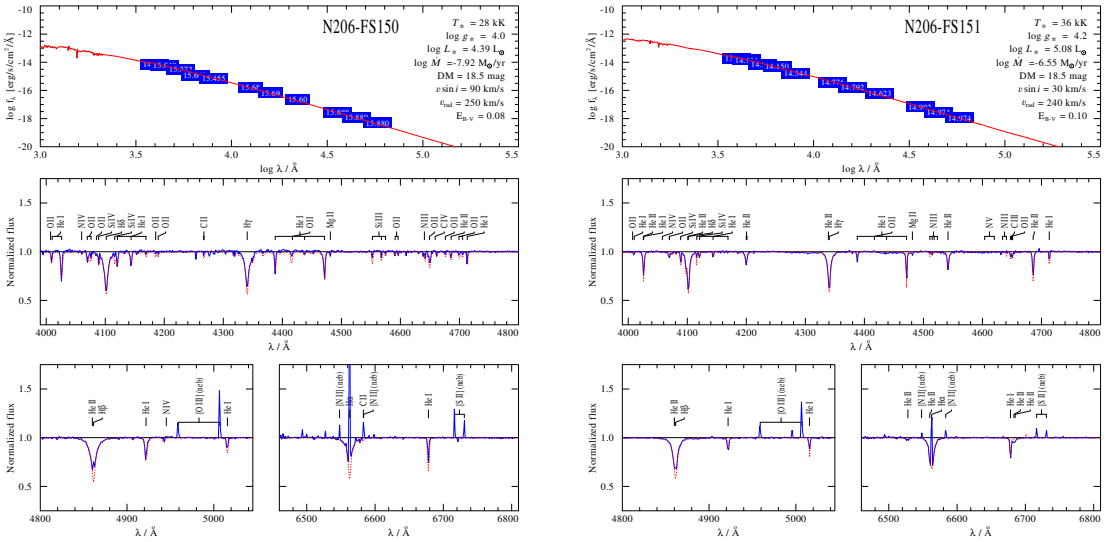

Figure B.52.: Spectral fit for N206-FS 150 and N206-FS 151

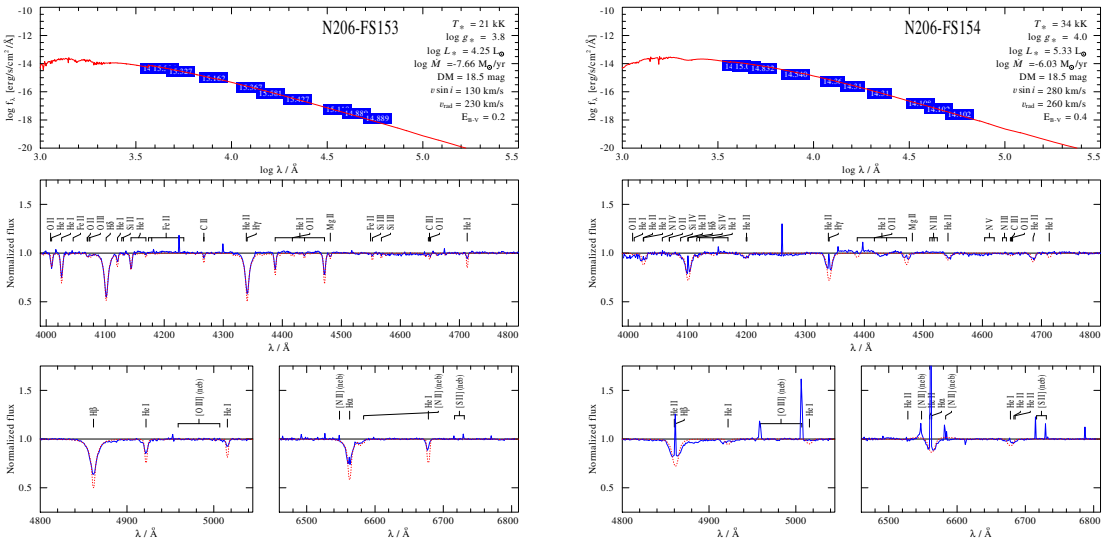

Figure B.53.: Spectral fit for N206-FS 153 and N206-FS 154

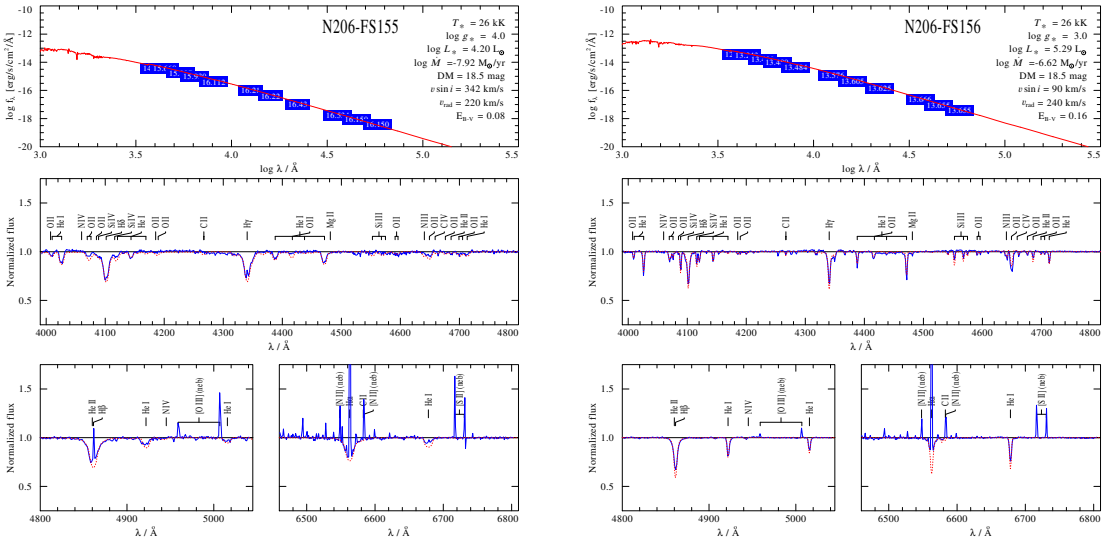

Figure B.54.: Spectral fit for N206-FS 155 and N206-FS 156

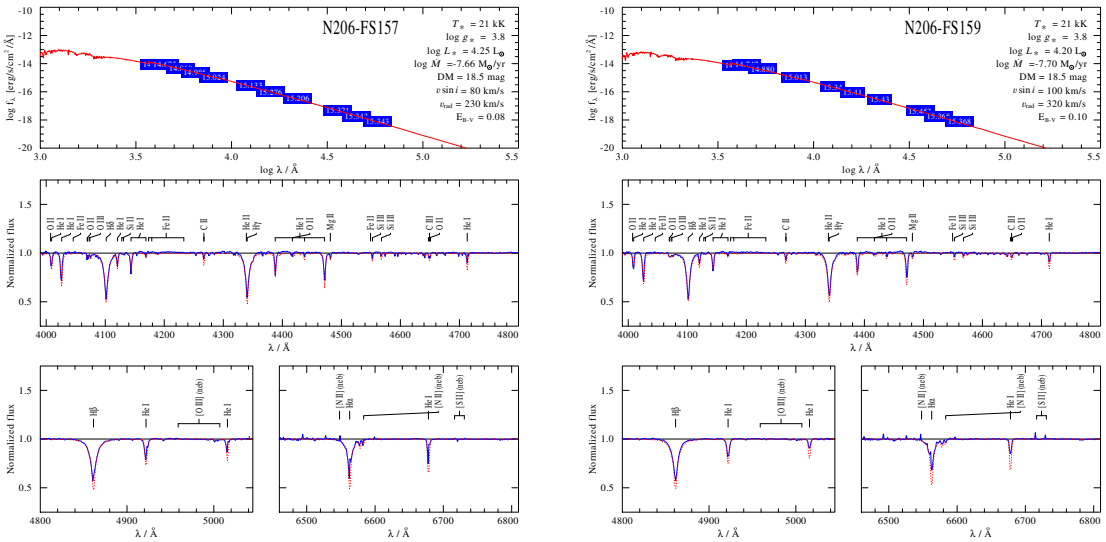

Figure B.55.: Spectral fit for N206-FS 157 and N206-FS 159

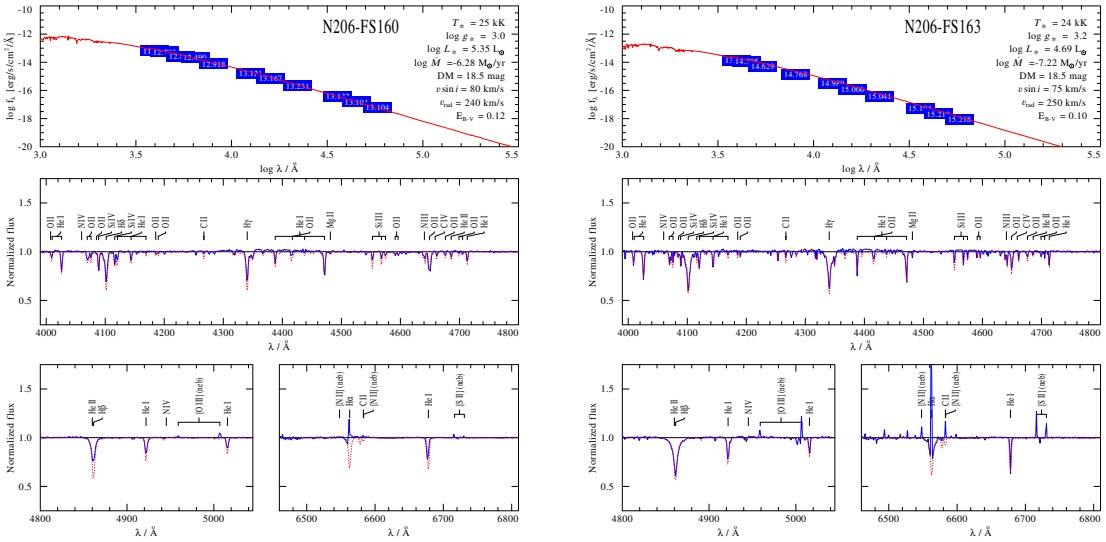

Figure B.56.: Spectral fit for N206-FS 160 and N206-FS 163

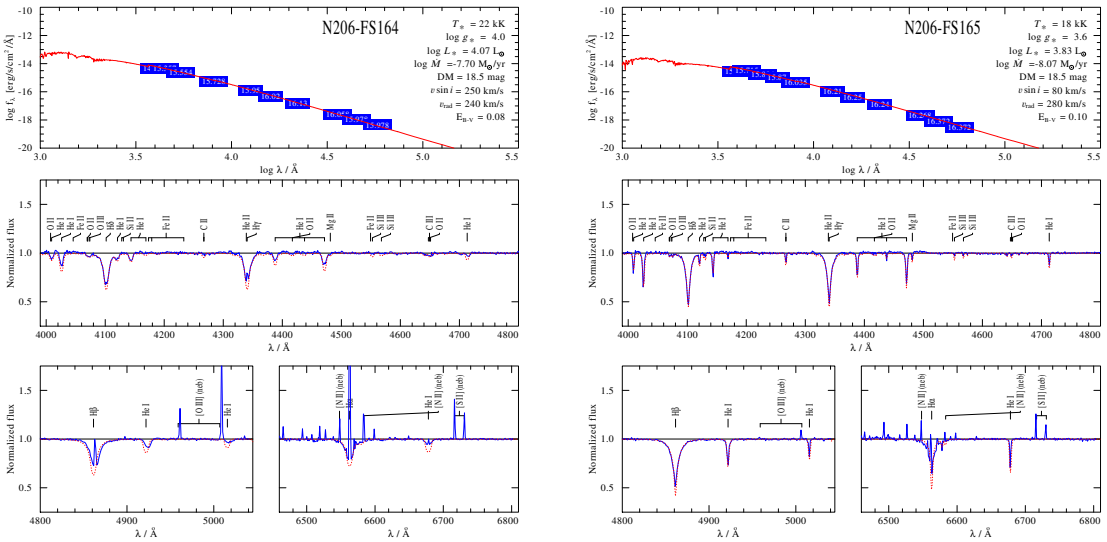

Figure B.57.: Spectral fit for N206-FS 164 and N206-FS 165

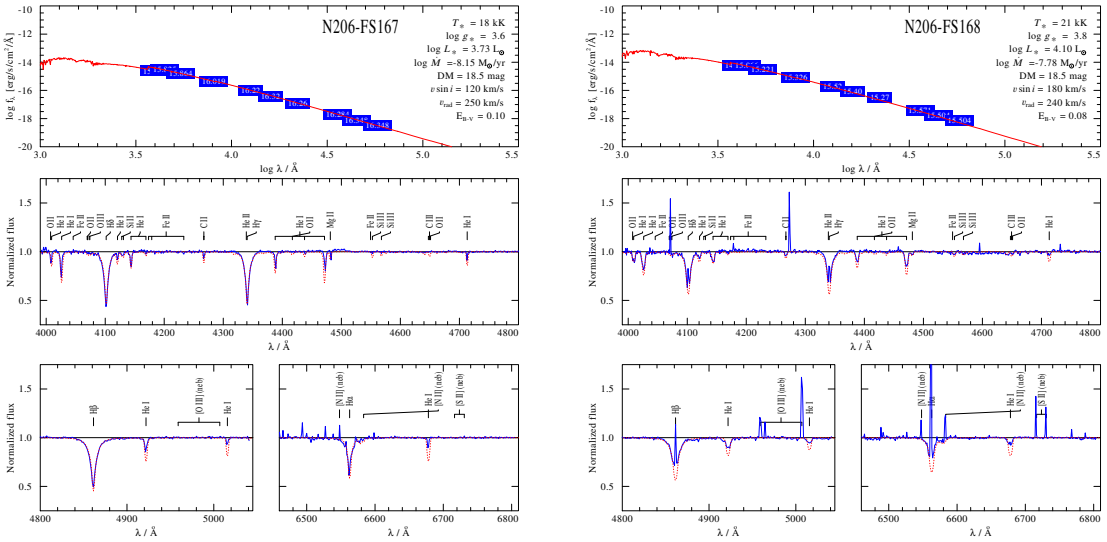

Figure B.58.: Spectral fit for N206-FS 167 and N206-FS 168

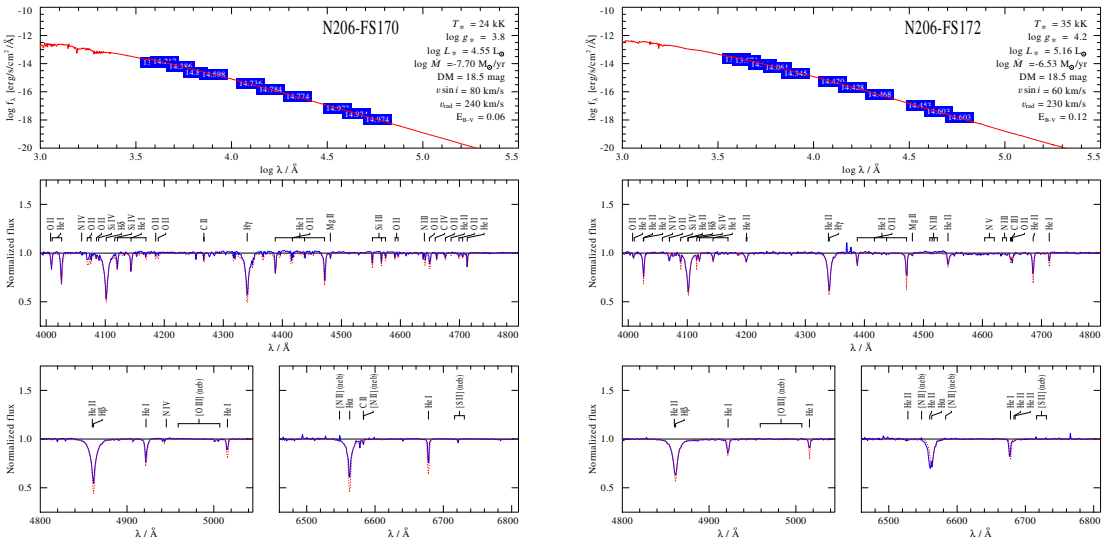

Figure B.59.: Spectral fit for N206-FS 170 and N206-FS 172

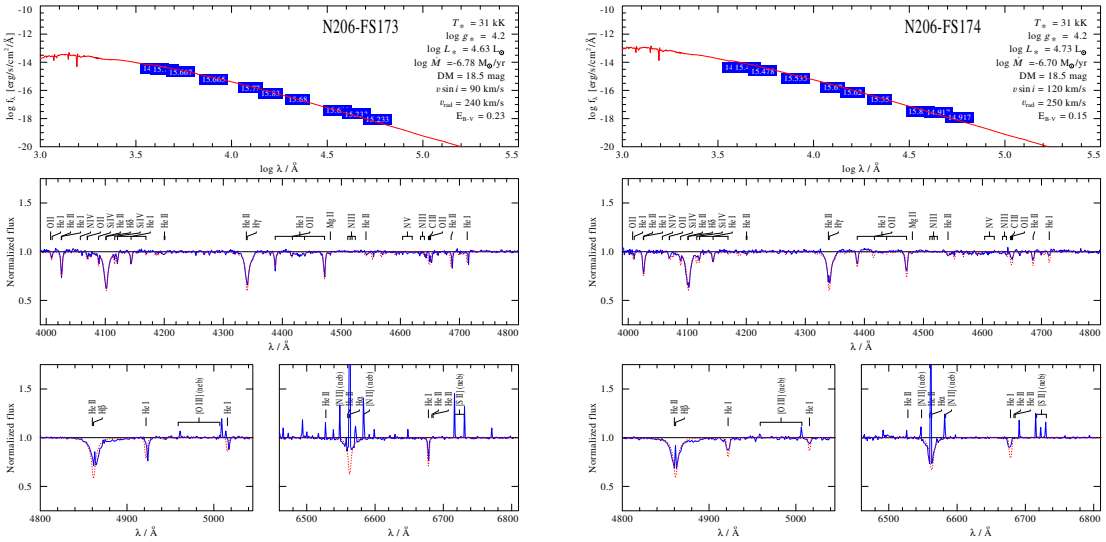

Figure B.60.: Spectral fit for N206-FS 173 and N206-FS 174

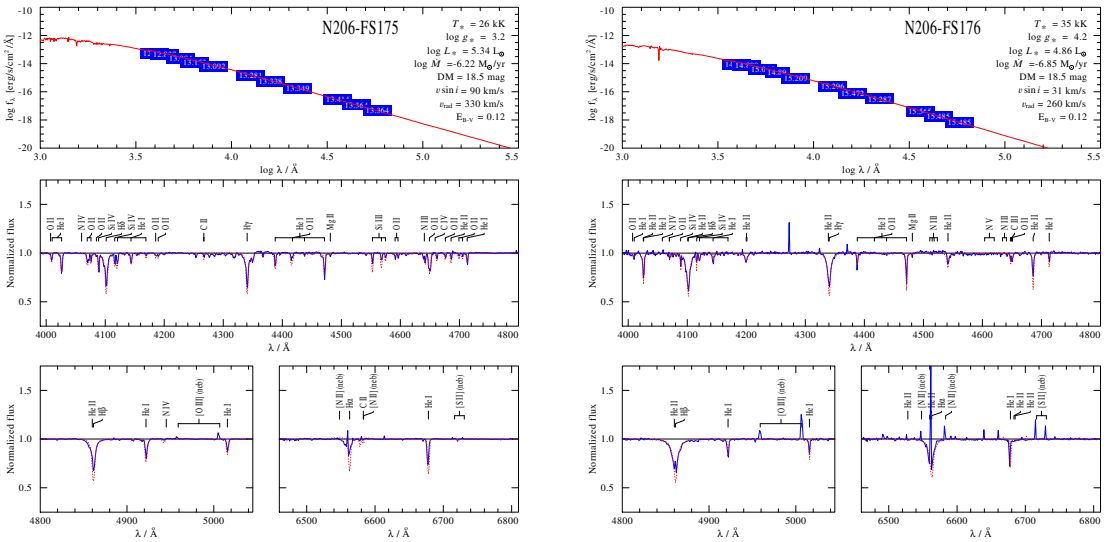

Figure B.61.: Spectral fit for N206-FS 175 and N206-FS 176

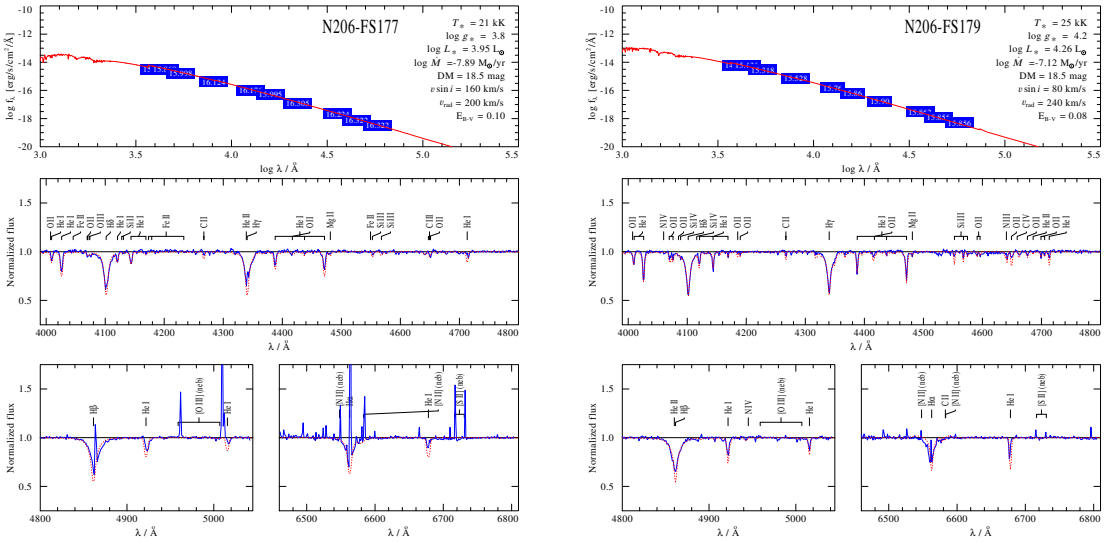

Figure B.62.: Spectral fit for N206-FS 177 and N206-FS 179

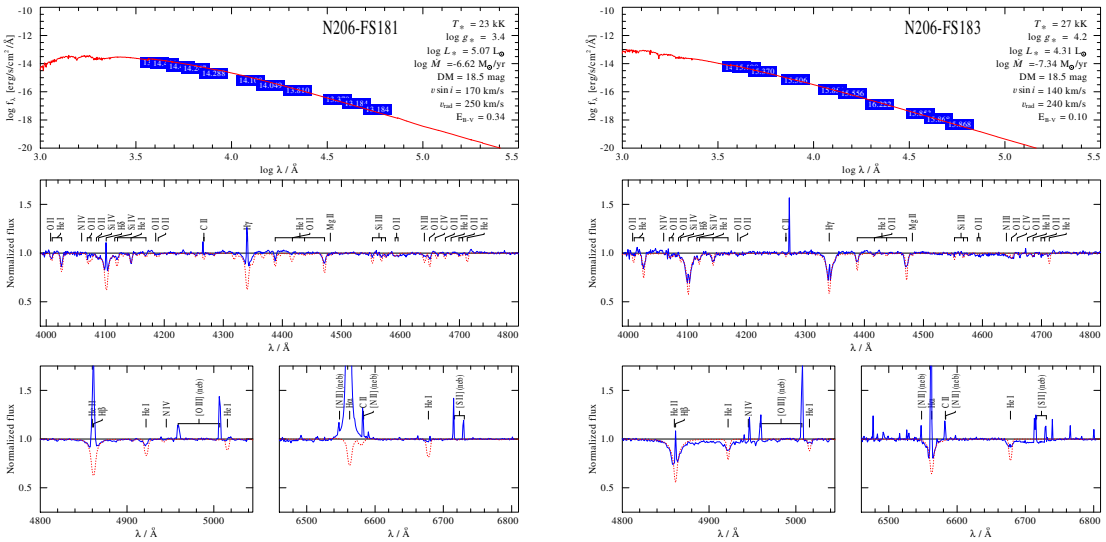

Figure B.63.: Spectral fit for N206-FS 181 and N206-FS 183

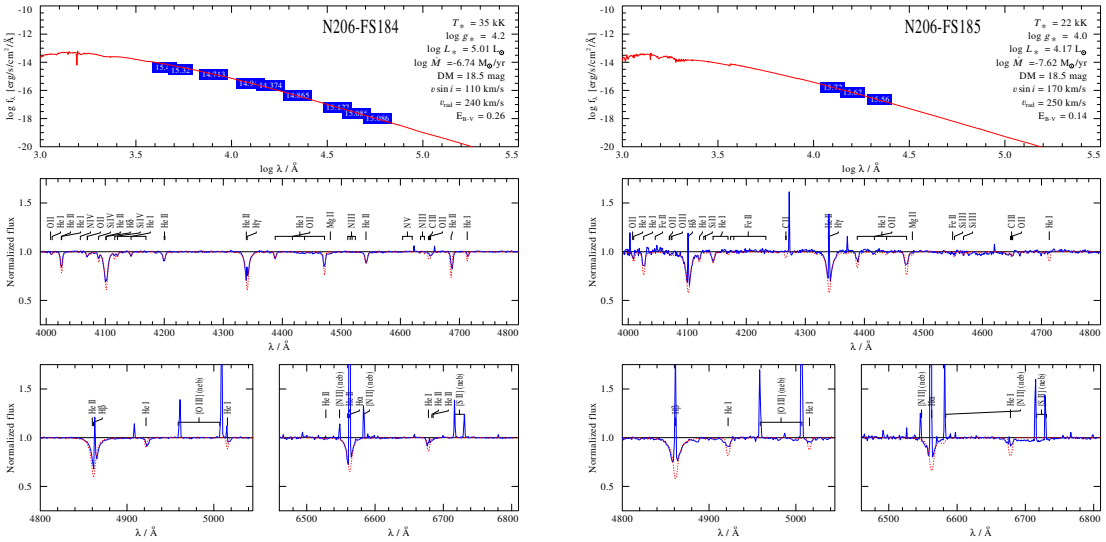

Figure B.64.: Spectral fit for N206-FS 184 and N206-FS 185

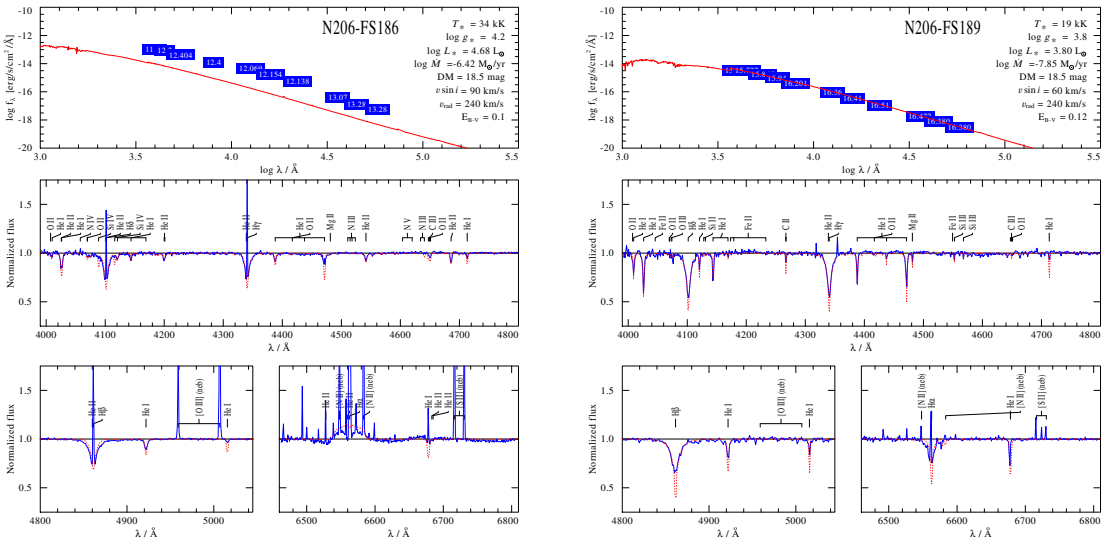

Figure B.65.: Spectral fit for N206-FS 186 and N206-FS 189

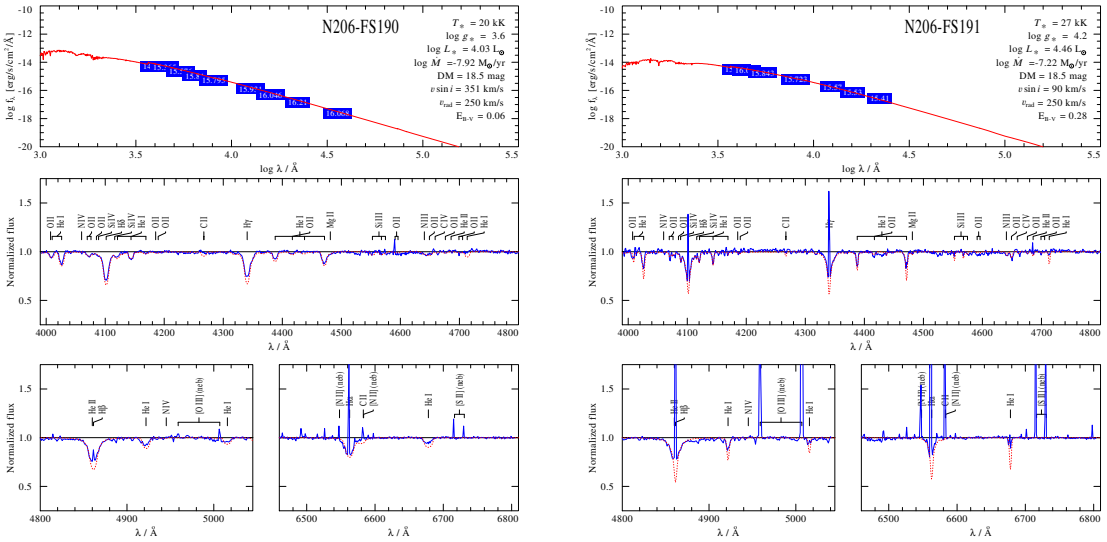

Figure B.66.: Spectral fit for N206-FS 190 and N206-FS 191

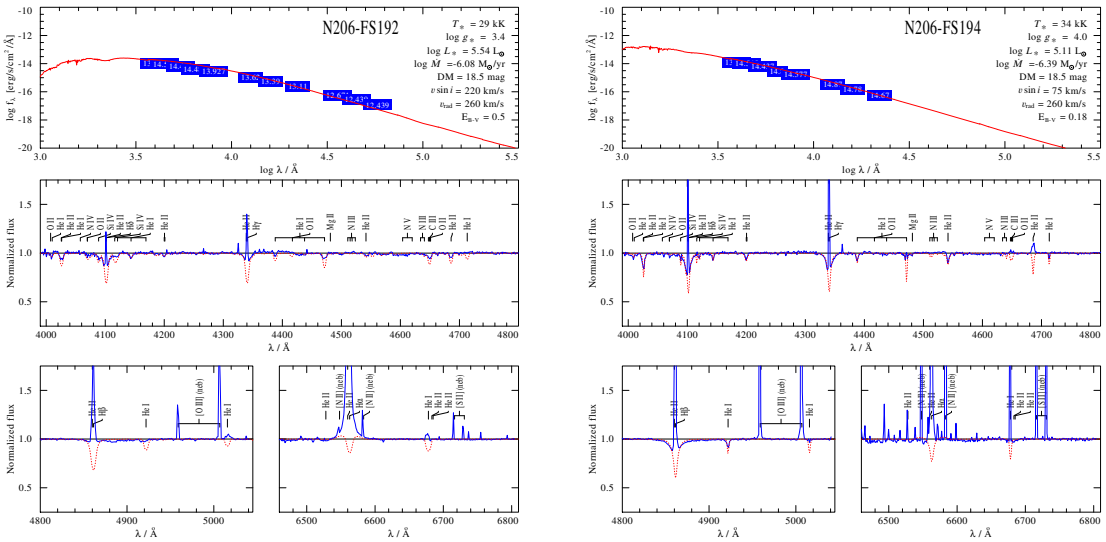

Figure B.67.: Spectral fit for N206-FS 192 and N206-FS 194

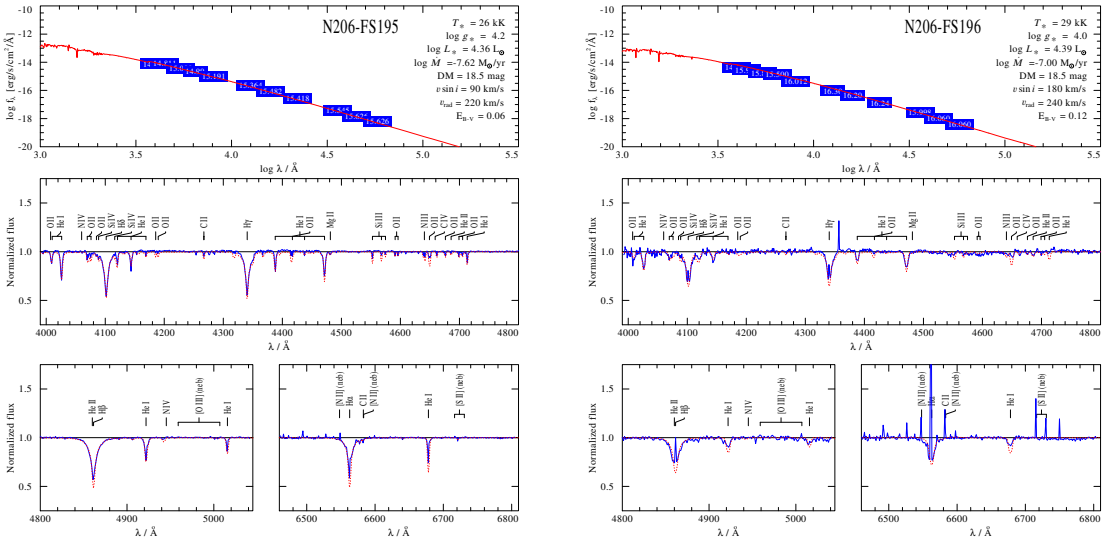

Figure B.68.: Spectral fit for N206-FS 195 and N206-FS 196

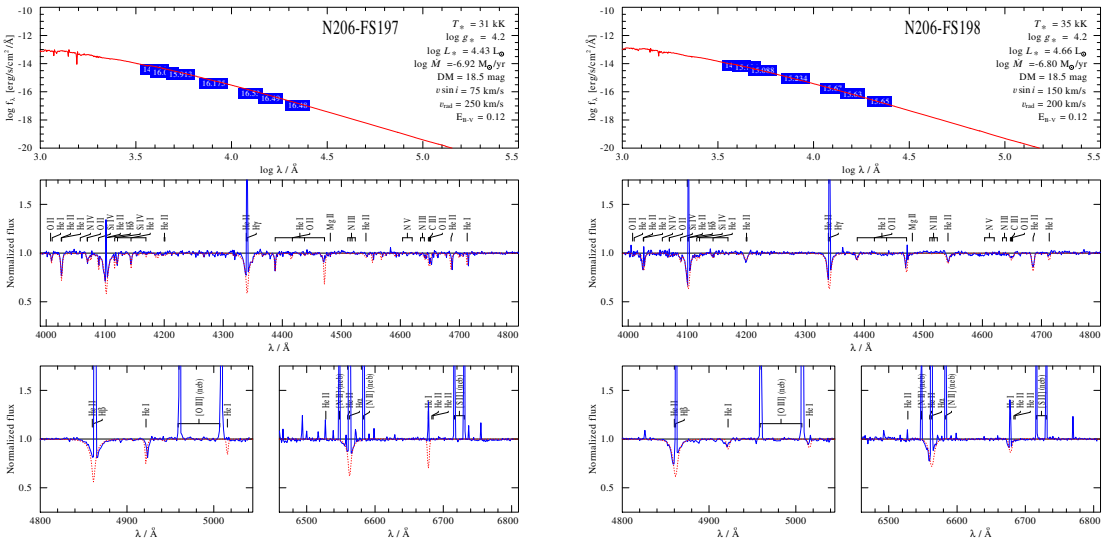

Figure B.69.: Spectral fit for N206-FS 197 and N206-FS 198

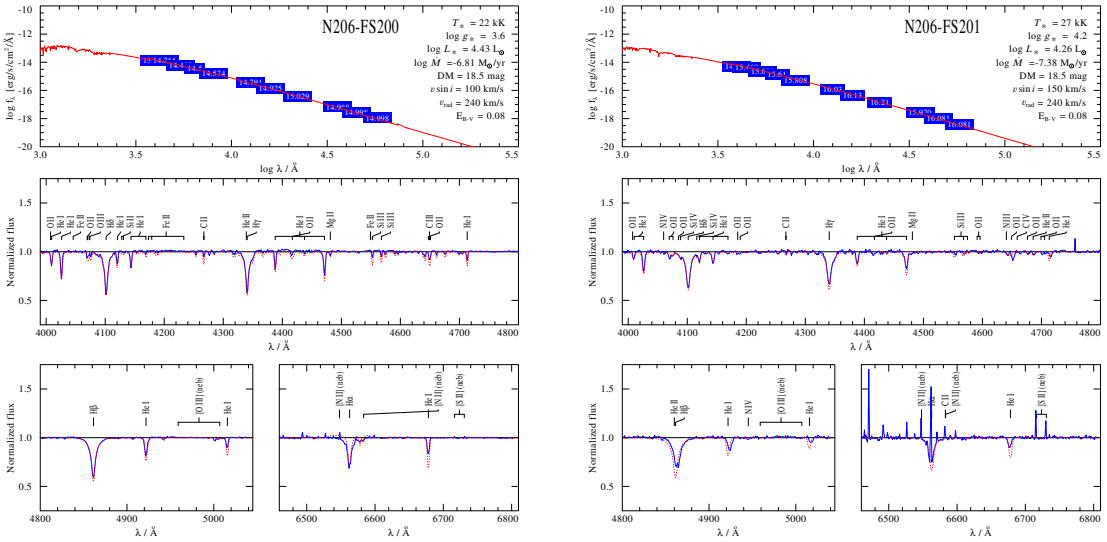

Figure B.70.: Spectral fit for N206-FS 200 and N206-FS 201

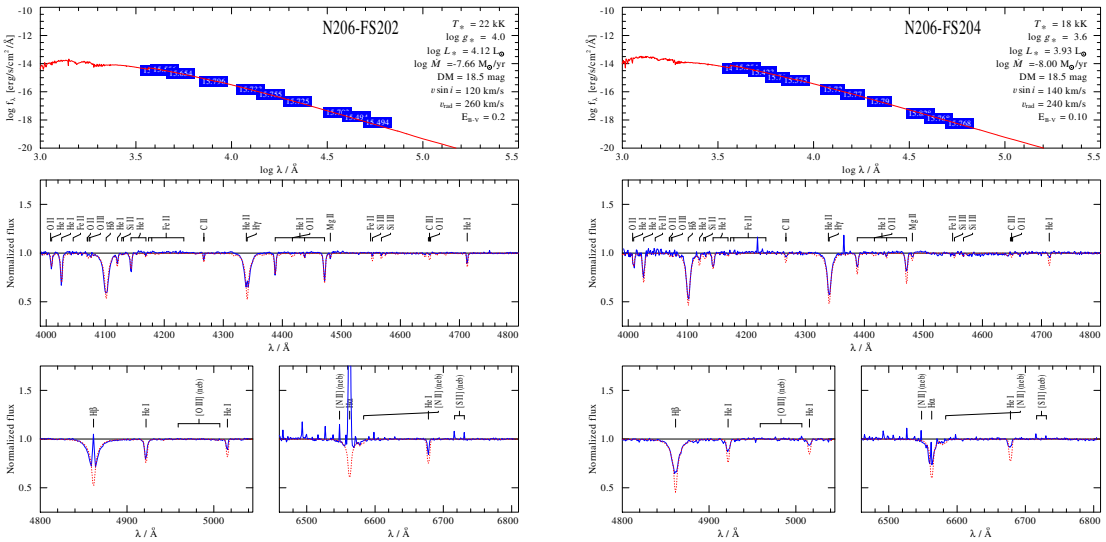

Figure B.71.: Spectral fit for N206-FS 202 and N206-FS 204

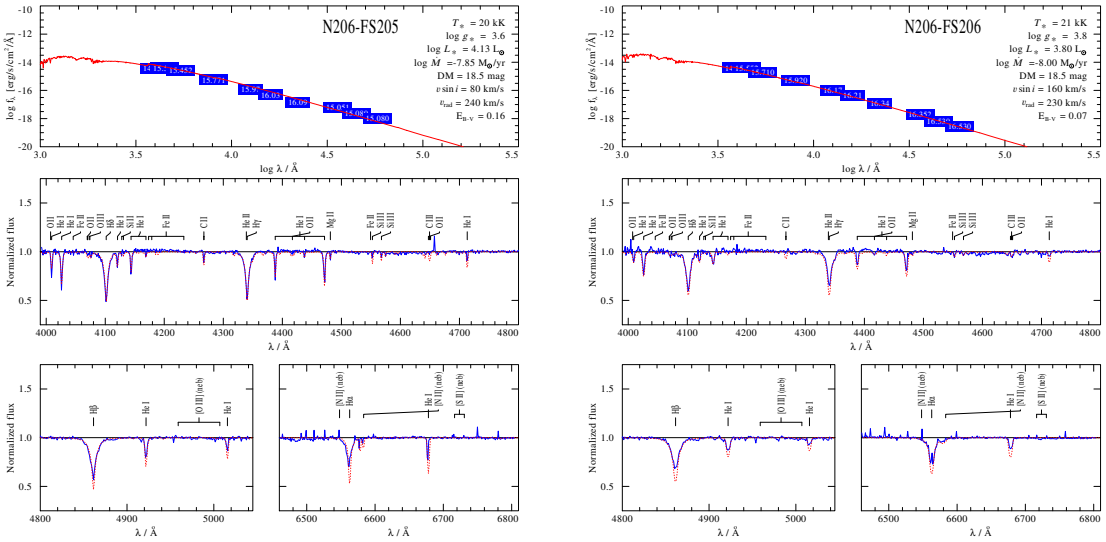

Figure B.72.: Spectral fit for N206-FS 205 and N206-FS 206

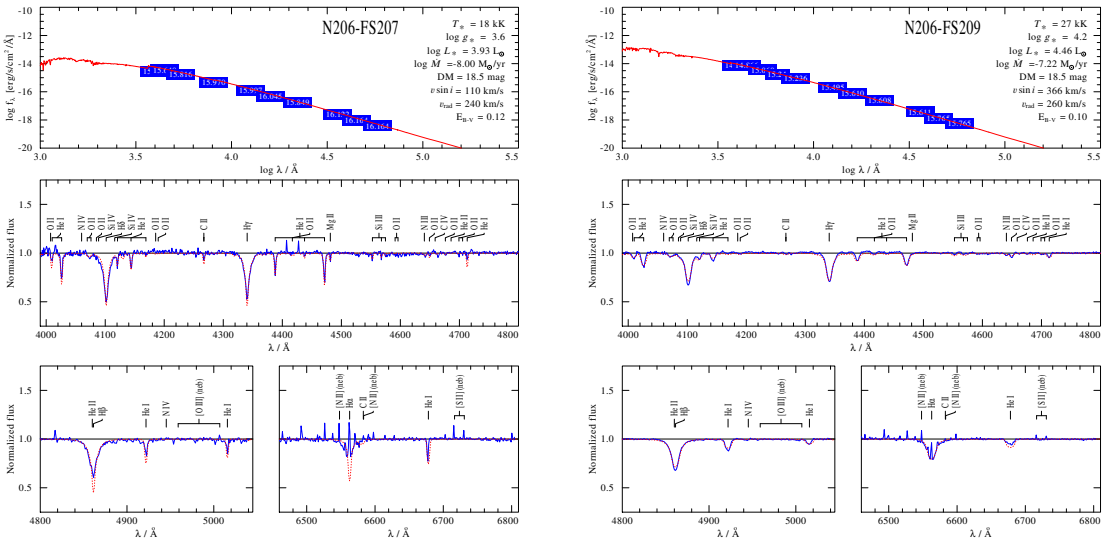

Figure B.73.: Spectral fit for N206-FS 207 and N206-FS 209

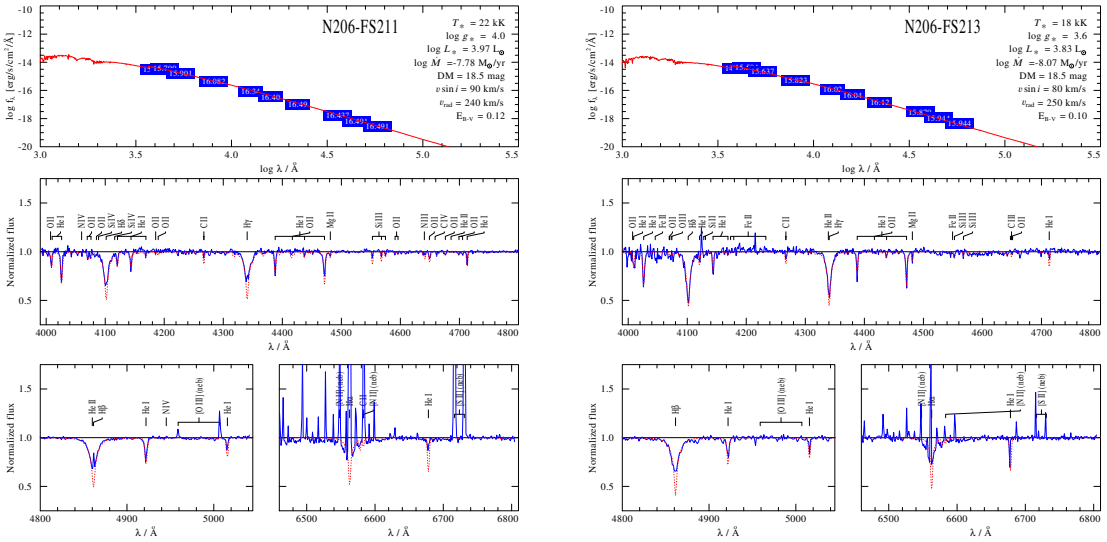

Figure B.74.: Spectral fit for N206-FS 211 and N206-FS 213

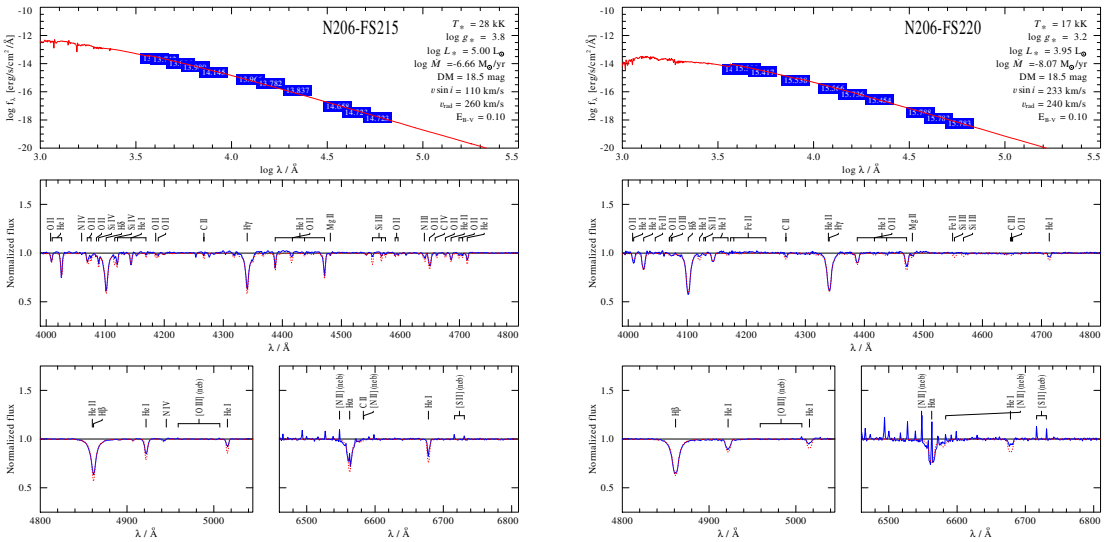

Figure B.75.: Spectral fit for N206-FS 215 and N206-FS 220

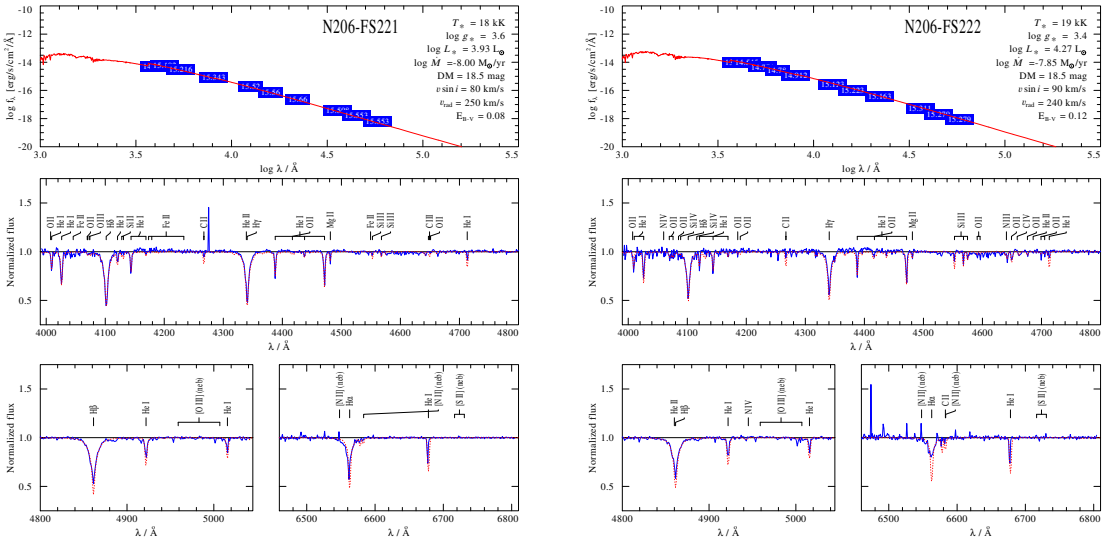

Figure B.76.: Spectral fit for N206-FS 221 and N206-FS 222

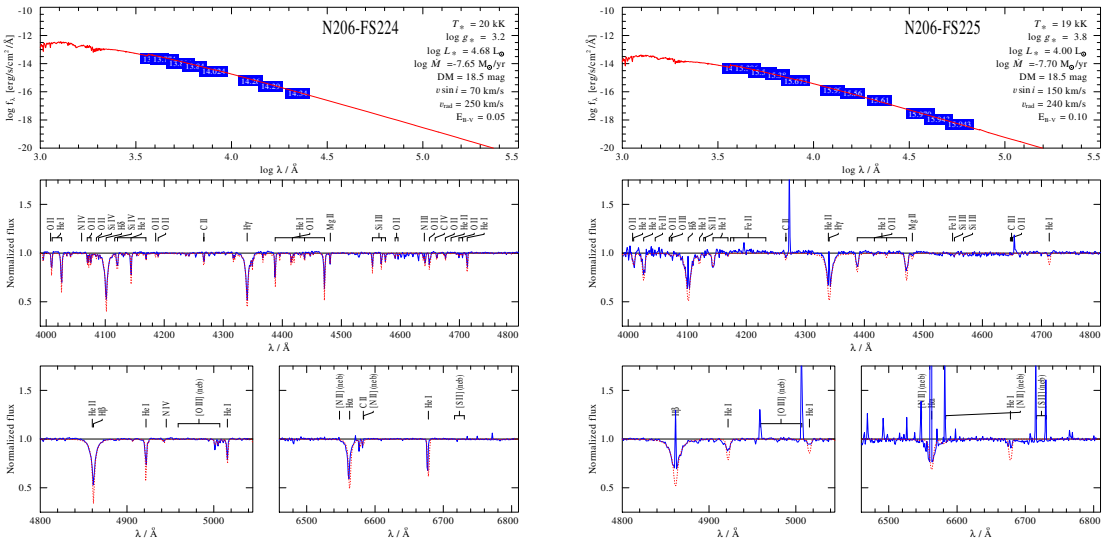

Figure B.77.: Spectral fit for N206-FS 224 and N206-FS 225

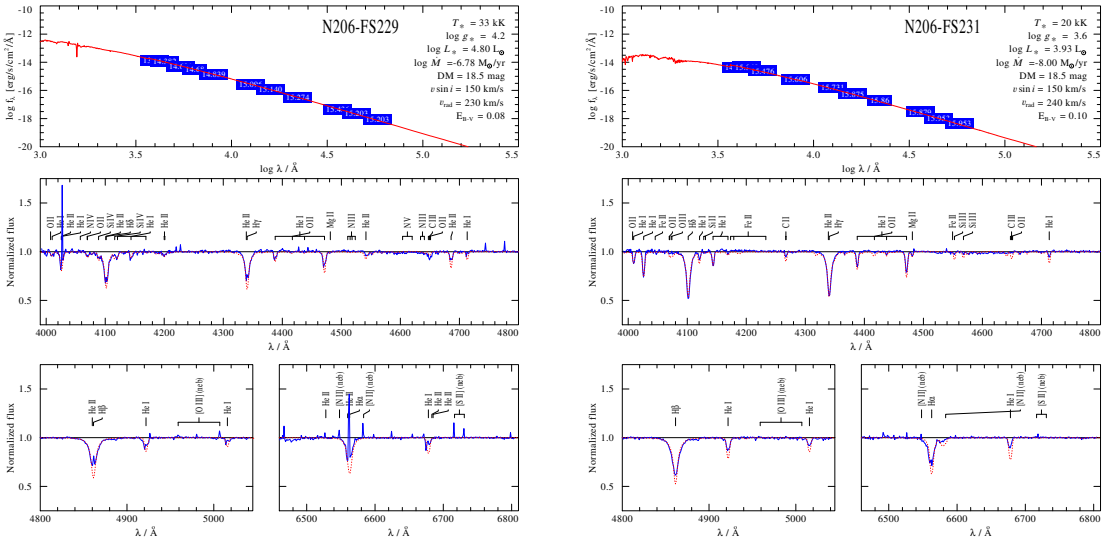

Figure B.78.: Spectral fit for N206-FS 229 and N206-FS 231

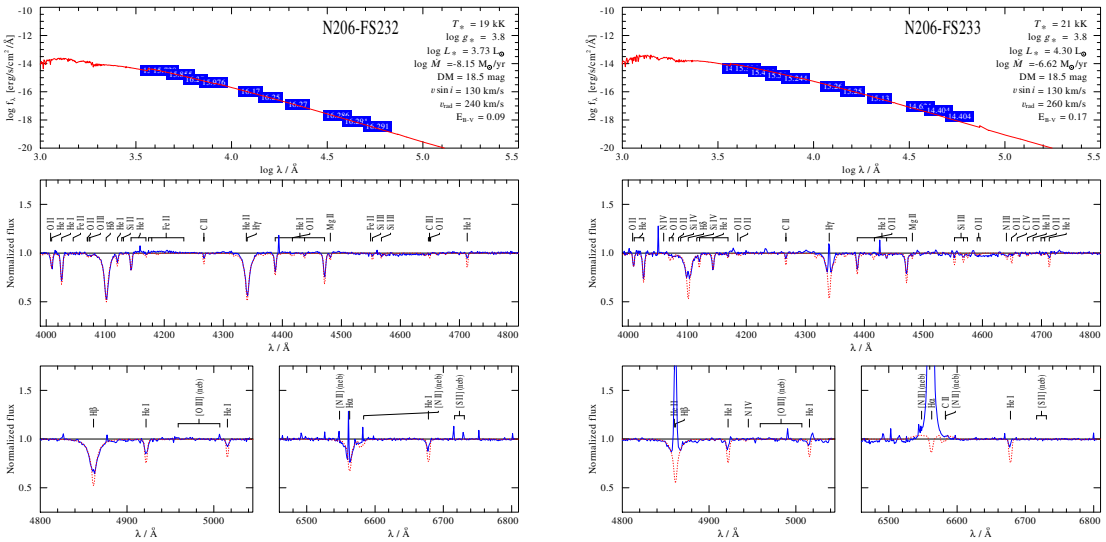

Figure B.79.: Spectral fit for N206-FS 232 and N206-FS 233

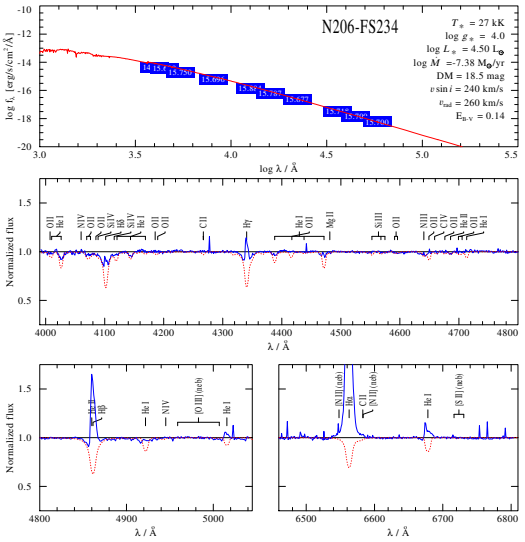

Figure B.80.: Spectral fit for N206-FS 234

Appendix C.

C.1. Additional tables

Table C.1.: Coordinates and spectral types of OB stars in our sample

SMCSGS-FS #	RA (J2000) (°)	DEC (J2000) (°)	Spectral type
1	20.521458	-73.218556	B0.7 V
2	20.529708	-73.233361	B0.2 V
3	20.54225	-73.281333	B2.5 V
4	20.560708	-73.140333	B2 III
5	20.60625	-73.121917	B2 V
6	20.6075	-73.199278	B1.5 IV
7	20.619125	-73.294472	B2 V
8	20.63225	-73.320222	B2 V
9	20.683708	-73.195111	B2 (IV)e
10	20.699083	-73.157222	B7 V
11	20.705042	-73.230472	B2 V
12	20.707792	-73.255667	B8 V
13	20.71175	-73.268667	B1.5 IV
14	20.726542	-73.228556	B2.5 V
15	20.734792	-73.238056	B2.5 IV
16	20.738625	-73.366917	B1.5 V
17	20.750958	-73.274194	B5 V
18	20.755458	-73.191639	B1.5 (IV)e
19	20.763833	-73.160111	B5 V
20	20.766375	-73.082472	B5 V
21	20.7985	-73.264278	B5 V
22	20.807917	-73.402639	B0.5 V
23	20.80975	-73.149361	B9 III
24	20.811333	-73.233389	B7 V
25	20.821208	-73.159889	B3 V
26	20.823792	-73.332306	B5 V
27	20.827917	-73.248333	B2.5 V
28	20.842833	-73.388639	B5 V
29	20.847708	-73.237528	B0.7 V
30	20.8535416667	-73.2716388889	B1 V
31	20.854792	-73.366917	O9 V
32	20.864208	-73.356139	B0.7 (III)e

Table C.1.: continued.

SMCSGS-FS #	RA (J2000) (°)	DEC (J2000) (°)	Spectral type
33	20.874	-73.396722	B3 V
34	20.893625	-73.158861	B3 (V)e
35	20.899125	-73.176583	B1.5 V
36	20.899792	-73.401583	B0.5 (III)e
37	20.913292	-73.198667	B0.7 V
38	20.920083	-73.395667	B0.2 V
39	20.9325	-73.204556	B0.5 V
40	20.934333	-73.20825	B0.7 V
41	20.939917	-73.216139	B2.5 V
42	20.945958	-73.182139	B2 IV
43	20.946	-73.115972	B2 (V)e
44	20.949625	-73.226389	B0 V
45	20.953083	-73.1635	B2 Ib Nwk
46	20.965542	-73.21325	B0 V
47	20.974042	-73.317417	B2 V
48	20.98625	-73.197889	B2 V
49	20.986458	-73.270056	B3 (IV)e
50	20.987125	-73.289056	B9 Ib
51	20.9885	-73.398111	B1.5 (V)e
52	20.99775	-73.1635	B0.5 V
53	20.997792	-73.180972	B2 V
54	21.007375	-73.152111	B1.5 V
55	21.007708	-73.299333	B1.5 IV
56	21.009458	-73.16325	B0.5 V
57	21.010167	-73.157083	B5 V
58	21.010833	-73.407556	B2.5 V
59	21.013583	-73.202222	B0 V
60	21.017042	-73.240667	B0.2 V
61	21.019958	-73.152028	B1.5 V
62	21.020375	-73.154167	B0 V
63	21.0255	-73.238528	B0.5 V
64	21.029333	-73.257861	O9 V
65	21.029875	-73.230083	B0.2 V
66	21.031667	-73.242083	B2 V
67	21.032042	-73.250222	B0 V
68	21.042042	-73.417361	B2 V
69	21.044875	-73.369389	B0.5 (II)e
70	21.045333	-73.155722	B0 V
71	21.046875	-73.288944	B1.5 IV
72	21.04775	-73.198583	B2 (II)e
73	21.04825	-73.241222	B0 (IV)e
74	21.049125	-73.193333	B2 V

Table C.1.: continued.

SMCSGS-FS #	RA (J2000) (°)	DEC (J2000) (°)	Spectral type
75	21.058875	-73.372472	B1.5 V
76	21.065208	-73.167083	B0.7 V
77	21.072083	-73.321361	B1.5 IV
78	21.085875	-73.169417	B2 V
79	21.090875	-73.182278	B2.5 V
80	21.092458	-73.162028	B2.5 V
81	21.092542	-73.144861	B1.5 V
82	21.093125	-73.383306	B2 IV
83	21.101083	-73.194444	B1.5 V
84	21.1035	-73.223722	B1.5 V
85	21.105042	-73.173583	B0.7 V
86	21.108458	-73.278694	B9 III
87	21.111083	-73.196667	B2 V
88	21.111542	-73.145639	B0.5 V
89	21.116667	-73.170278	O9.5 V
90	21.116708	-73.237556	O9.7 V
91	21.117333	-73.244139	B0.7 (IV)e
92	21.121667	-73.095889	B0.5 V
93	21.128292	-73.221694	B2.5 V
94	21.129667	-73.376722	B1.5 V
95	21.132458	-73.173556	B1.5 V
96	21.132458	-73.36375	B1.5 V
97	21.133333	-73.177111	B1.5 V
98	21.139458	-73.246778	B0.5 V
99	21.143417	-73.1525	B1 IV
100	21.144	-73.158194	B2.5 V
101	21.146333	-73.1725	B2.5 V
102	21.1485	-73.28625	B3 V
103	21.149958	-73.160528	B2.5 V
104	21.150333	-73.41775	B5 V
105	21.151917	-73.211194	B2.5 V
106	21.153667	-73.156056	B1.5 V
107	21.158125	-73.23225	B0 V
108	21.159125	-73.218917	B2.5 V
109	21.159458	-73.328167	B2.5 V
110	21.162417	-73.080639	B2.5 (III)e
111	21.178125	-73.151167	O8.5 V
112	21.178167	-73.225667	B3 V
113	21.187167	-73.187944	B7 V
114	21.189458	-73.141861	B2.5 V
115	21.191208	-73.398333	B1.5 V
116	21.191333	-73.309472	B2.5 V

Table C.1.: continued.

SMCSGS-FS #	RA (J2000) (°)	DEC (J2000) (°)	Spectral type
117	21.203625	-73.25575	B5 (IV)e
118	21.204083	-73.173806	B2.5 V
119	21.2102916667	-73.2444166667	B0 V
120	21.210375	-73.318389	B0.2 V
121	21.213417	-73.100111	O9.7 V
122	21.213958	-73.209639	B2 V
123	21.216458	-73.3385	B2 IV
124	21.217917	-73.395139	B2.5 (V)e
125	21.21925	-73.322556	B0.5 V
126	21.222333	-73.308083	B5 V
127	21.2265	-73.398583	B2.5 V
128	21.227042	-73.153167	O9 V
129	21.230042	-73.429111	B3 V
130	21.233	-73.169889	B2.5 V
131	21.236583	-73.327889	B1.5 V
132	21.237125	-73.23675	B2 V
133	21.240583	-73.184722	B2 V
134	21.248542	-73.193917	B2.5 V
135	21.255083	-73.414583	B2 IV
136	21.25825	-73.280417	B1 (IV)e
137	21.265208	-73.283639	B1.5 IV
138	21.272833	-73.147361	B1.5 V
139	21.276375	-73.144667	B2.5 (V)e
140	21.2812916667	-73.4006944444	B2 V
141	21.284958	-73.414528	B1.5 V
142	21.290667	-73.366861	B2 V
143	21.292625	-73.275889	O8 V
144	21.301208	-73.226278	B2.5 V
145	21.304042	-73.258667	B2 V
146	21.309125	-73.321694	B2.5 V
147	21.3107916667	-73.3977777778	B1 V
148	21.317833	-73.349667	B2 V
149	21.321042	-73.256889	B0.5 V
150	21.32625	-73.228528	B3 V
151	21.339292	-73.282917	B1.5 V
152	21.34125	-73.361528	B2.5 V
153	21.346792	-73.277333	B2.5 IV
154	21.349625	-73.425222	B2 V
155	21.352292	-73.254944	B0.5 V
156	21.352958	-73.280528	B0.2 V
157	21.361958	-73.247306	B2.5 (V)e
158	21.364458	-73.135361	B0.7 (III)e

Table C.1.: continued.

SMCSGS-FS #	RA (J2000) (°)	DEC (J2000) (°)	Spectral type
159	21.365208	-73.385472	B0.7 V
160	21.376292	-73.389	B1 IV
161	21.387292	-73.231194	B5 IV
162	21.390375	-73.121139	B1 V
163	21.393458	-73.233667	B2.5 V
164	21.397917	-73.271	B1 V
165	21.402667	-73.330417	B5 V
166	21.408292	-73.37775	O8 IV
167	21.409292	-73.127667	B0.7 (II)e
168	21.411542	-73.118861	B1.5 V
169	21.413292	-73.160778	B1 IV
170	21.415417	-73.153194	B0.7 V
171	21.418583	-73.255	B1 (V)e
172	21.425042	-73.26025	B0 V
173	21.425417	-73.229167	B2.5 V
174	21.435083	-73.2425	B2.5 V
175	21.449125	-73.144167	B9 Ib
176	21.45925	-73.315278	B7 V
177	21.463458	-73.238444	B5 (V)e
178	21.481583	-73.293389	B2 V
179	21.482833	-73.230361	B2.5 (IV)e
180	21.494292	-73.347194	B2 V
181	21.51125	-73.382583	B2 V
182	21.51575	-73.149472	B1 V
183	21.51775	-73.329028	B5 (V)e
184	21.523	-73.31825	B2.5 V
185	21.525458	-73.121833	B0.7 V
186	21.527167	-73.323722	B0.7 V
187	21.559458	-73.309639	B0.5 IV
188	21.568958	-73.270944	B5 V
189	21.576375	-73.295694	B2 (III)e
190	21.601708	-73.293417	B0.7 IV
191	21.610292	-73.292306	B0.5 V
192	21.617583	-73.190583	B1.5 IV
193	21.620667	-73.205972	B0.7 V
194	21.633167	-73.224	B5 V
195	21.647	-73.254556	O9.7 IV
196	21.690333	-73.265389	B3 IV
197	21.707292	-73.215333	B1.5 IV
198	21.7370833333	-73.5150555556	B1 V
199	21.750083	-73.244722	B1 V
200	21.775958	-73.301111	B2 V

Table C.1.: continued.

SMCSGS-FS #	RA (J2000) (°)	DEC (J2000) (°)	Spectral type
201	21.795958	-73.30625	B0.7 V
202	21.9034166667	-73.5633027778	B1 V
203	21.941375	-73.5490055556	B0.5 (III)e
204	21.9874166667	-73.6361277778	B1 V
205	21.988375	-73.441108	B2.5 V
206	22.032417	-73.515008	B3 IV
207	22.04975	-73.506539	B3 IV
208	22.0542083333	-73.6085444444	B2.5 V
209	22.060333	-73.554683	B1.5 V
210	22.1428333333	-73.5460972222	B0.5 III
211	22.173292	-73.559731	B5 V
212	22.189625	-73.409742	B2.5 V
213	22.19225	-73.294933	B1.5 (V)e
214	22.19675	-73.4759083333	B1 (V)e
215	22.198417	-73.3064	O9.7 IV
216	22.207417	-73.381936	B0.7 IV
217	22.235583	-73.386661	B1 IV
218	22.23725	-73.401928	B3 V
219	22.267208	-73.377064	B9 Ia
220	22.27875	-73.287578	B1.5 V
221	22.2904583333	-73.2503861111	B2.5 V
222	22.294833	-73.504828	B0.5 V
223	22.296208	-73.511025	B0.5 (IV)e
224	22.302417	-73.290767	B1.5 (II)e
225	22.305625	-73.534356	B2 (V)e
226	22.3134583333	-73.2346222222	B1 (IV)e
227	22.338125	-73.551694	B2 V
228	22.347333	-73.578567	B2.5 V
229	22.349292	-73.329328	B1.5 V
230	22.350375	-73.494928	B1 IV
231	22.352333	-73.554564	O3 V((f∗))z
232	22.364875	-73.533775	B0.5 V
233	22.365625	-73.5499166667	B1.5 (IV)e
234	22.367708	-73.435	B3 IV
235	22.3677916667	-73.5326861111	B2 (IV)e
236	22.375292	-73.557622	B2.5 V
237	22.3762916667	-73.5609083333	B0.7 V
238	22.379333	-73.562036	O8.5 V
239	22.380625	-73.5618416667	O9 V
240	22.3872083333	-73.5697777778	B2 V
241	22.3887083333	-73.5624194444	O7 V
242	22.397875	-73.5581611111	B1.5 V

Table C.1.: continued.

SMCSGS-FS #	RA (J2000) (°)	DEC (J2000) (°)	Spectral type
243	22.397917	-73.558575	B2.5 V
244	22.403667	-73.569606	B2 V
245	22.42925	-73.580575	B1.5 (IV)e
246	22.43925	-73.431517	B1 V
247	22.441958	-73.419681	B5 V
248	22.452667	-73.559853	B0.2 V
249	22.458833	-73.393142	B2 (III)e
250	22.462	-73.485925	B2 V
251	22.462833	-73.4164	B1.5 V
252	22.463208	-73.377597	B9 Ia
253	22.4693333333	-73.4219833333	B1.5 V
254	22.472375	-73.588392	B1.5 V
255	22.488958	-73.324414	B2 V
256	22.492292	-73.371314	B1.5 V
257	22.504292	-73.402286	B0.5 V
258	22.5065416667	-73.4006083333	B0.5 (III)e
259	22.507125	-73.422864	B0.7 V
260	22.510125	-73.552217	B0.5 V
261	22.515333	-73.440167	B0.7 V
262	22.533083	-73.251328	B2 (III)e
263	22.548625	-73.403031	B0.2 V
264	22.554542	-73.594572	B2.5 III
265	22.555375	-73.429317	B0.5 IV
266	22.5591666667	-73.4262611111	B1 V
267	22.5669166667	-73.3684333333	B2 V
268	22.567	-73.3572694444	B2 V
269	22.569208	-73.347561	O8 Vz
270	22.571458	-73.446061	B0.7 V
271	22.577042	-73.429733	B3 (IV)e
272	22.581667	-73.3839	B2.5 IV
273	22.597083	-73.4403	B1.5 V
274	22.603125	-73.538586	B0.5 V
275	22.604708	-73.463744	B0.7 V
276	22.60875	-73.425892	B0.5 V
277	22.610375	-73.6603722222	B1 IV
278	22.614375	-73.433778	B1 IV
279	22.621083	-73.327653	B2 V
280	22.624875	-73.4391388889	B1 V
281	22.627	-73.431239	B0.2 V
282	22.62875	-73.509333	B2.5 (IV)e
283	22.6408333333	-73.3721916667	B0.5 (III)e
284	22.654875	-73.420669	B1.5 IV

Table C.1.: continued.

SMCSGS-FS #	RA (J2000) (°)	DEC (J2000) (°)	Spectral type
285	22.666542	-73.325708	B1.5 V
286	22.669875	-73.360042	B7 IV
287	22.6795	-73.417817	O6 V((f))z
288	22.709292	-73.382958	O8.5 III
289	22.716625	-73.537558	B1.5 (IV)e
290	22.727875	-73.451983	B1 V
291	22.7460416667	-73.4153472222	B1 V
292	22.747625	-73.419914	O7 V((f))z
293	22.7585	-73.591744	B2 V
294	22.768083	-73.408225	B1 V
295	22.769917	-73.415786	B2 V
296	22.77175	-73.442961	B5 V
297	22.777	-73.265336	B1.5 V
298	22.778208	-73.412917	O9.5 V
299	22.778583	-73.433769	B1.5 V
300	22.785	-73.471639	B1.5 V
301	22.7851666667	-73.4113666667	B1.5 V
302	22.7852916667	-73.4160444444	B0 V
303	22.791625	-73.41805	B1.5 V
304	22.796625	-73.4170805556	B0.5 V
305	22.80825	-73.406858	B1.5 V
306	22.808792	-73.410603	B0 V
307	22.8137916667	-73.4164416667	B0.5 V
308	22.834042	-73.33135	B5 V
309	22.855042	-73.498622	B2.5 V
310	22.866542	-73.370617	O7.5 In(f)p
311	22.8679166667	-73.4178138889	B1 V
312	22.875083	-73.360547	O9 IV
313	22.888125	-73.407439	B2.5 V
314	22.927208	-73.584561	B2 V
315	22.978875	-73.456525	O9.7 (III)e
316	22.988708	-73.552478	B2 (V)e
317	22.9901666667	-73.2716722222	B0 V
318	22.992833	-73.401447	B2 V
319	23.0135	-73.6177	B1.5 V
320	23.032208	-73.515939	B2 V

Table C.2.: Stellar parameters of all OB stars in the SMC-SGS 1

SMCSGS-FS #	Spectral type	T_* [kK]	log L [$L_\odot$]	log g_* [cm s^{-2}]	log $\dot{M}^{(1)}$ [$M_\odot$ yr^{-1}]	E_{B-V} [mag]	M_V [mag]	R_* [$R_\odot$]	$v_\infty{}^{(2)}$ [km s^{-1}]	v sin i [km s^{-1}]	v_{rad} [km s^{-1}]	M_* [$M_\odot$]	log Q_0 [s^{-1}]	*olog* $L_{mec}{}^{(3)}$ [$L_\odot$]
1	B0.7 V	27	3.83	4.4	−9.5	0.03	−1.8	3.8	2300	120	170	13	46.1	−1.9
2	B0.2 V	29	4.21	4.4	−9.1	0.02	−3.0	5.1	2600	80	160	23	46.7	−1.2
3	B2.5 V	19	3.52	4.0	−9.8	0.03	−2.2	5.3	900	130	150	10	44.5	−2.4
4	B2 III	19	4.27	3.4	−9.0	0.03	−3.8	12.6	600	130	160	15	45.4	−1.1
5	B2 V	20	3.56	4.2	−9.7	0.05	−1.9	5.0	1100	100	170	15	44.6	−2.4
6	B1.5 IV	23	3.87	4.0	−9.4	0.03	−3.0	5.4	1700	70	170	11	45.6	−1.8
7	B2 V	22	3.76	4.2	−9.5	0.05	−2.2	5.2	2200	70	170	16	45.2	−2.0
8	B2 V	20	3.66	4.2	−9.6	0.05	−2.0	5.6	1100	130	120	18	44.7	−2.2
9	B2 (IV)e	22	4.01	3.8	−9.3	0.09	−2.8	7.0	1500	250	170	11	45.6	−1.6
10	B7 V	14	3.12	3.8	−10.2	0.05	−2.0	6.2	800	80	170	9	43.7	−3.1
11	B2 V	20	3.66	4.2	−9.6	0.05	−2.0	5.6	1100	100	170	18	44.7	−2.2
12	B8 V	14	3.22	3.8	−10.1	0.05	−2.1	6.9	800	100	170	11	43.8	−3.0
13	B1.5 IV	22	4.08	3.6	−9.2	0.03	−3.0	7.6	1200	140	155	8	45.7	−1.4
14	B2.5 V	19	3.52	4.0	−9.8	0.05	−2.2	5.3	900	200	170	10	44.5	−2.4
15	B2.5 IV	20	3.63	3.6	−9.7	0.10	−2.2	5.5	500	140	160	4	44.9	−2.2
16	B1.5 V	22	4.11	3.8	−9.2	0.05	−3.1	7.8	1600	150	200	14	45.7	−1.4
17	B5 V	16	3.52	4.0	−9.8	0.05	−2.3	7.5	1000	130	140	21	44.2	−2.4
18	B1.5 (IV)e	24	4.44	3.8	−8.9	0.09	−3.5	9.6	1800	320	170	21	46.4	−0.8
19	B5 V	16	3.32	4.0	−10.0	0.02	−2.4	6.0	900	150	120	13	44.0	−2.8
20	B5 V	16	3.12	4.0	−10.2	0.05	−1.9	4.7	800	140	160	8	43.8	−3.1
21	B5 V	16	3.32	4.0	−10.0	0.03	−1.8	6.0	900	200	190	13	44.0	−2.8
22	B0.5 V	27	4.54	4.0	−8.8	0.04	−3.8	8.5	2100	80	170	27	46.9	−0.6
23	B9 III	11	3.02	3.5	−10.3	0.03	−2.2	8.9	600	110	180	9	43.0	−3.3
24	B7 V	14	3.42	3.8	−9.9	0.05	−1.9	8.7	900	100	160	18	44.0	−2.6
25	B3 V	18	3.32	3.8	−10.0	0.05	−2.0	4.7	600	180	170	5	44.3	−2.8
26	B5 V	17	3.45	3.8	−9.9	0.04	−1.9	6.1	700	160	190	9	44.4	−2.6
27	B2.5 V	19	3.52	4.2	−9.8	0.05	−1.9	5.3	1100	140	170	16	44.4	−2.4
28	B5 V	17	3.65	3.8	−9.7	0.05	−2.7	7.7	800	220	160	14	44.6	−2.2
29	B0.7 V	26	4.02	4.4	−9.3	0.03	−2.6	5.1	2700	230	170	23	46.2	−1.5
30	B1 V	26	3.7	4.4	−9.6	0.02	−2.0	3.5	2200	70	170	11	45.9	−2.1
31	O9 V	32	4.93	4.0	−8.4	0.02	−4.3	9.5	2000	340	160	33	48.1	0.1
32	B0.7 (III)e	25	4.72	3.6	−8.6	0.22	−4.2	12.2	1500	280	170	22	46.9	−0.3
33	B3 V	17	3.65	3.8	−9.7	0.05	−2.1	7.7	800	50	160	14	44.6	−2.2
34	B3 (V)e	18	3.52	3.8	−9.8	0.08	−2.0	5.9	700	200	170	8	44.5	−2.4
35	B1.5 V	22	3.76	4.2	−9.5	0.05	−2.6	5.2	2200	180	170	16	45.2	−2.0
36	B0.5 (III)e	26	5.23	3.2	−8.1	0.19	−5.1	20.4	1000	300	160	24	47.8	0.6
37	B0.7 V	26	4.14	4.2	−9.2	0.05	−3.1	5.8	2200	330	170	20	46.3	−1.3
38	B0.2 V	28	4.37	4.2	−8.9	0.02	−3.0	6.5	2300	80	150	25	46.8	−0.9
39	B0.5 V	27	4.29	4.2	−9.0	0.02	−3.0	6.4	2300	230	170	24	46.6	−1.1
40	B0.7 V	25	4.29	4.0	−9.0	0.05	−3.6	7.5	2000	130	170	20	46.4	−1.1
41	B2.5 V	19	3.22	4.2	−10.1	0.03	−1.5	3.8	900	160	170	8	44.1	−3.0
42	B2 IV	20	4.03	3.8	−9.3	0.05	−3.1	8.6	900	80	170	17	45.1	−1.5
43	B2 (V)e	20	4.01	3.8	−9.3	0.11	−3.3	8.4	900	180	170	16	45.7	−1.6
44	B0 V	30	4.51	4.2	−8.8	0.03	−3.6	6.7	2300	130	160	26	47.2	−0.7
45	B2 Ib	20	4.42	2.8	−8.9	0.45	−3.5	13.5	300	50	170	4	45.7	−0.8
46	B0 V	30	4.3	4.4	−9.0	0.02	−3.2	5.2	2600	250	170	25	46.9	−1.0
47	B2 V	22	3.86	4.2	−9.4	0.03	−2.7	5.9	2300	70	140	20	45.3	−1.8
48	B2 V	22	3.96	4.2	−9.3	0.05	−3.0	6.6	2400	130	160	25	45.4	−1.7
49	B3 (IV)e	17	3.75	3.4	−9.6	0.23	−2.6	8.7	500	150	170	7	44.7	−2.0
50	B9 Ib	10	3.72	2.8	−9.6	0.03	−3.6	24.2	500	80	200	13	43.3	−2.1
51	B1.5 (V)e	22	4.21	3.8	−9.1	0.08	−3.0	8.8	1700	250	170	18	45.8	−1.2
52	B0.5 V	28	4.03	4.4	−9.3	0.05	−2.6	4.4	2500	150	170	18	46.4	−1.5

Table C.2.: continued.

SMCSGS-FS #	Spectral type	T_* [kK]	log L [$L_\odot$]	log g_* [cm s^{-2}]	log $\dot{M}^{(1)}$ [$M_\odot$ yr^{-1}]	E_{B-V} [mag]	M_V [mag]	R_* [$R_\odot$]	$v_\infty{}^{(2)}$ [km s^{-1}]	$v \sin i$ [km s^{-1}]	v_{rad} [km s^{-1}]	M_* [$M_\odot$]	log Q_0 [s^{-1}]	*olog* $L_{mec}{}^{(3)}$ [$L_\odot$]	
53	B2 V	19	3.52	4.0	−9.8	0.02	−2.0	5.3	900	80	170	10	44.5	−2.4	
54	B1.5 V	23	3.66	4.4	−9.6	0.05	−2.0	4.3	2500	220	160	17	45.1	−2.2	
55	B1.5 IV	22	4.18	3.6	−9.1	0.02	−3.6	8.5	1300	270	100	10	45.8	−1.3	
56	B0.5 V	28	3.81	4.4	−9.5	0.09	−2.0	3.4	2200	100	150	11	46.2	−1.9	
57	B5 V	16	3.22	4.0	−10.1	0.03	−2.1	5.3	900	120	160	10	44.0	−3.0	
58	B2.5 V	19	3.32	4.2	−10.0	0.05	−2.2	4.2	1000	140	160	10	44.2	−2.8	
59	B0 V	29	4.42	4.2	−8.9	0.05	−3.3	6.4	2300	200	170	24	47.0	−0.8	
60	B0.2 V	28	3.93	4.4	−9.4	0.05	−2.6	3.9	2300	120	170	14	46.3	−1.7	
61	B1.5 V	23	4.07	4.0	−9.2	0.02	−4.1	6.8	1900	80	160	17	45.8	−1.5	
62	B0 V	29	4.46	4.2	−8.9	0.05	−3.7	6.7	2300	140	170	26	47.0	−0.8	
63	B0.5 V	27	4.03	4.4	−9.3	0.05	−2.6	4.7	2600	100	160	21	46.3	−1.5	
64	O9 V	33	5.05	4.0	−8.3	0.05	−4.6	10.3	2000	50	120	39	48.3	0.3	
65	B0.2 V	29	4.11	4.4	−9.2	0.03	−2.7	4.5	2500	120	170	19	46.6	−1.4	
66	B2 V	19	3.92	4.2	−9.4	0.09	−2.5	8.4	1400	250	170	41	44.8	−1.7	
67	B0 V	31	4.6	4.2	−8.7	0.05	−3.9	6.9	2300	70	150	28	47.5	−0.5	
68	B2 V	20	3.56	4.2	−9.7	0.05	−2.0	5.0	1100	130	160	15	44.6	−2.4	
69	B0.5 (II)e	26	5.05	3.2	−8.3	0.05	−5.0	16.6	900	100	160	16	47.6	0.3	
70	B0 V	30	4.56	4.2	−8.8	0.05	−3.4	7.1	2300	170	160	29	47.3	−0.6	
71	B1.5 IV	22	3.61	3.8	−9.7	0.05	−2.0	4.4	1200	250	160	4	45.2	−2.3	
72	B2 (II)e	18	4.2	3.0	−9.1	0.05	−3.9	13.0	400	150	170	6	45.2	−1.2	
73	B0 (IV)e	30	5.02	3.8	−8.3	0.08	−4.6	12.0	1700	270	160	33	48.0	0.2	
74	B2 V	19	3.52	4.2	−9.8	0.02	−2.2	5.3	1100	160	170	16	44.4	−2.4	
75	B1.5 V	22	3.86	4.2	−9.4	0.05	−2.2	5.9	2300	250	170	20	45.3	−1.8	
76	B0.7 V	26	3.96	4.2	−9.3	0.03	−2.7	4.7	2000	160	150	13	46.1	−1.7	
77	B1.5 IV	22	4.27	3.8	−9.0	0.02	−3.8	9.4	1800	160	150	20	45.9	−1.1	
78	B2 V	20	3.56	4.2	−9.7	0.03	−2.2	5.0	1100	140	160	15	44.6	−2.4	
79	B2.5 V	19	3.52	4.2	−9.8	0.05	−2.2	5.3	1100	120	160	16	44.4	−2.4	
80	B2.5 V	19	3.52	4.0	−9.8	0.07	−2.3	5.3	900	160	160	10	44.5	−2.4	
81	B1.5 V	23	3.96	4.4	−9.3	0.05	−1.9	6.0	3000	180	190	33	45.4	−1.7	
82	B2 IV	20	3.83	3.6	−9.5	0.08	−2.7	6.9	600	120	160	7	45.1	−1.9	
83	B1.5 V	23	3.76	4.4	−9.5	0.05	−2.0	4.8	2600	170	160	21	45.2	−2.0	
84	B1.5 V	23	3.76	4.4	−9.5	0.05	−2.2	4.8	2600	250	170	21	45.2	−2.0	
85	B0.7 V	26	4.19	4.2	−9.1	0.03	−3.3	6.2	2300	70	170	22	46.3	−1.2	
86	B9 III	10	3.35	3.4	−10.0	0.03	−2.9	15.8	800	80	170	23	43.0	−2.7	
87	B2 V	22	3.66	4.2	−9.6	0.03	−2.4	4.7	2000	120	180	13	45.1	−2.2	
88	B0.5 V	26	3.72	4.4	−9.6	0.05	−2.2	3.6	2200	220	170	12	45.9	−2.1	
89	O9.5 V	31	4.84	4.0	−8.5	0.02	−5.1	9.1	2000	120	160	31	47.8	−0.1	
90	O9.7 V	31	4.9	4.0	−8.4	0.02	−4.6	9.8	2100	70	200	35	47.9	0.0	
91	B0.7 (IV)e	25	4.35	3.8	−9.0	0.09	−3.2	8.0	1600	150	170	15	46.5	−1.0	
92	B0.5 V	28	3.83	4.4	−9.5	0.05	−2.4	3.5	2200	90	160	11	46.2	−1.9	
93	B2.5 V	19	3.42	4.2	−9.9	0.08	−2.0	4.7	1000	140	130	13	44.3	−2.6	
94	B1.5 V	23	4.06	4.4	−9.3	0.05	−3.1	6.8	3100	80	160	42	45.5	−1.5	
95	B1.5 V	23	3.76	4.4	−9.5	0.05	−2.2	4.8	2600	220	160	21	45.2	−2.0	
96	B1.5 V	22	4.3	4.0	−8.7	* 0.08	−3.7	9.8	900*	250	170	35	46.5	−1.0	*
97	B1.5 V	23	3.56	4.4	−9.7	0.05	−1.6	3.8	2300	170	170	13	45.0	−2.4	
98	B0.5 V	26	4.08	4.2	−9.2	0.02	−2.9	5.4	2100	130	150	17	46.2	−1.4	
99	B1 IV	24	4.69	3.6	−8.6	0.05	−4.8	12.8	1600	120	170	24	46.7	−0.4	
100	B2.5 V	19	3.42	4.2	−9.9	0.02	−2.2	4.7	1000	180	160	13	44.3	−2.6	
101	B2.5 V	20	3.56	4.2	−9.7	0.05	−2.3	5.0	1100	200	170	15	44.6	−2.4	
102	B3 V	17	3.35	3.8	−10.0	0.02	−1.8	5.5	700	200	150	7	44.3	−2.7	
103	B2.5 V	19	3.42	4.2	−9.9	0.05	−2.0	4.7	1000	150	140	13	44.3	−2.6	
104	B5 V	16	3.02	4.0	−10.3	0.05	−1.8	4.2	800	250	160	7	43.8	−3.3	

Table C.2.: continued.

SMCSGS-FS #	Spectral type	T_* [kK]	log L [$L_\odot$]	log g_* [cm s^{-2}]	log $\dot{M}^{(1)}$ [$M_\odot$ yr^{-1}]	E_{B-V} [mag]	M_V [mag]	R_* [$R_\odot$]	$v_\infty{}^{(2)}$ [km s^{-1}]	v sin i [km s^{-1}]	v_{rad} [km s^{-1}]	M_* [$M_\odot$]	log Q_0 [s^{-1}]	*olog* $L_{mec}{}^{(3)}$ [$L_\odot$]
105	B2.5 V	20	3.76	4.2	−9.5	0.02	−2.4	6.3	1200	130	160	23	44.8	−2.0
106	B1.5 V	23	3.86	4.4	−9.4	0.02	−2.1	5.4	2800	180	160	27	45.3	−1.8
107	B0 V	31	4.62	4.2	−8.7	0.05	−3.6	7.1	2300	60	160	29	47.5	−0.5
108	B2.5 V	20	3.46	4.2	−9.8	0.04	−2.0	4.5	1000	140	170	12	44.5	−2.5
109	B2.5 V	19	3.62	4.2	−9.7	0.05	−1.7	6.0	1200	120	110	21	44.5	−2.3
110	B2.5 (III)e	18	3.9	3.2	−9.4	0.07	−3.4	9.2	400	220	160	5	45.0	−1.8
111	O8.5 V	35	4.73	4.4	−8.6	0.05	−3.7	6.3	2700	220	240	37	48.1	−0.3
112	B3 V	19	3.62	4.2	−9.7	0.05	−2.1	6.0	1200	100	160	21	44.5	−2.3
113	B7 V	13	2.72	3.8	−10.6	0.03	−1.1	4.5	600	100	110	5	43.2	−3.8
114	B2.5 V	19	3.52	4.0	−9.8	0.03	−2.2	5.3	900	200	170	10	44.5	−2.4
115	B1.5 V	22	3.46	4.2	−9.8	0.05	−2.0	3.7	1800	120	160	8	44.9	−2.5
116	B2.5 V	19	3.52	4.2	−9.8	0.03	−2.0	5.3	1100	80	160	16	44.4	−2.4
117	B5 (IV)e	16	3.82	3.4	−9.5	0.08	−2.8	10.6	600	180	170	10	44.8	−1.9
118	B2.5 V	19	3.67	4.0	−9.6	0.05	−2.5	6.3	1000	170	150	15	44.9	−2.2
119	B0 V	32	4.63	4.0	−8.7	0.05	−3.3	6.7	1700	250	160	17	47.8	−0.5
120	B0.2 V	29	4.44	4.2	−8.9	0.05	−2.8	6.6	2300	30	170	25	47.0	−0.8
121	O9.7 V	32	4.71	4.2	−8.6	0.05	−3.9	7.4	2300	50	170	32	47.8	−0.3
122	B2 V	20	3.46	4.2	−9.8	0.05	−1.9	4.5	1000	80	160	12	44.5	−2.5
123	B2 IV	20	3.93	3.6	−9.4	0.05	−3.0	7.7	600	100	170	9	45.2	−1.7
124	B2.5 (V)e	19	4.07	3.8	−9.2	0.08	−2.9	10.0	900	200	180	23	45.1	−1.5
125	B0.5 V	27	4.24	4.2	−9.1	0.05	−2.7	6.0	2300	220	160	21	46.5	−1.2
126	B5 V	16	3.42	3.8	−9.9	0.05	−1.7	6.7	800	100	160	10	44.3	−2.6
127	B2.5 V	20	3.83	3.8	−9.5	0.05	−2.8	6.9	800	280	160	11	44.9	−1.9
128	O9 V	34	4.72	4.2	−8.6	0.05	−3.2	6.6	2100	410	170	25	48.0	−0.3
129	B3 V	18	3.62	3.8	−9.7	0.05	−2.6	6.7	800	70	180	10	44.6	−2.3
130	B2.5 V	19	3.52	4.2	−9.8	0.02	−2.1	5.3	1100	160	160	16	44.4	−2.4
131	B1.5 V	22	3.46	4.2	−9.8	0.05	−1.5	3.7	1800	100	170	8	44.9	−2.5
132	B2 V	22	3.86	4.2	−9.4	0.05	−2.4	5.9	2300	150	170	20	45.3	−1.8
133	B2 V	22	3.86	4.2	−9.4	0.05	−1.9	5.9	2300	120	160	20	45.3	−1.8
134	B2.5 V	20	3.56	4.2	−9.7	0.05	−1.8	5.0	1100	200	160	15	44.6	−2.4
135	B2 IV	20	3.93	3.8	−9.4	0.05	−3.1	7.7	800	170	160	14	45.0	−1.7
136	B1 (IV)e	23	4.31	3.8	−9.0	0.05	−3.2	9.0	1700	120	170	19	46.2	−1.0
137	B1.5 IV	21	4.26	3.6	−9.1	0.05	−3.6	10.2	1500	180	170	15	45.7	−1.1
138	B1.5 V	22	3.76	4.2	−9.5	0.05	−2.1	5.2	2200	270	140	16	45.2	−2.0
139	B2.5 (V)e	20	3.73	3.8	−9.6	0.08	−2.3	6.1	700	150	170	9	44.8	−2.1
140	B2 V	20	3.64	4.2	−9.7	0.05	−2.0	5.5	1100	80	160	18	44.7	−2.2
141	B1.5 V	22	3.96	4.2	−9.3	0.05	−3.0	6.6	2400	200	170	25	45.4	−1.7
142	B2 V	21	3.86	4.0	−9.4	0.05	−2.5	6.4	1900	130	170	15	45.1	−1.8
143	O8 V	35	5.19	4.0	−8.1	0.03	−4.8	10.7	2000	60	150	42	48.6	0.5
144	B2.5 V	20	3.36	4.2	−9.9	0.05	−1.4	4.0	1000	200	140	9	44.4	−2.7
145	B2 V	22	3.86	4.2	−9.4	0.05	−2.7	5.9	2300	250	150	20	45.3	−1.8
146	B2.5 V	20	3.66	4.2	−9.6	0.05	−2.0	5.6	1100	120	170	18	44.7	−2.2
147	B1 V	26	3.9	4.4	−9.4	0.05	−2.3	4.4	2500	100	170	18	46.1	−1.8
148	B2 V	21	3.86	4.0	−9.4	0.10	−2.8	6.4	1900	200	170	15	45.1	−1.8
149	B0.5 V	27	4.03	4.4	−9.3	0.05	−2.3	4.7	2600	100	160	21	46.3	−1.5
150	B3 V	18	3.61	3.8	−9.7	0.05	−2.1	6.6	800	140	170	10	44.5	−2.3
151	B1.5 V	22	3.76	4.2	−9.5	0.02	−2.3	5.2	2200	200	170	16	45.2	−2.0
152	B2.5 V	19	3.52	4.2	−9.8	0.02	−2.4	5.3	1100	160	170	16	44.4	−2.4
153	B2.5 IV	20	4.23	3.8	−9.1	0.02	−4.1	10.9	1000	250	150	27	45.3	−1.2
154	B2 V	22	3.96	4.2	−9.3	0.05	−2.8	6.6	2400	150	160	25	45.4	−1.7
155	B0.5 V	27	4.06	4.2	−9.3	0.05	−2.7	4.9	2000	100	150	14	46.3	−1.5
156	B0.2 V	29	4.21	4.4	−9.1	0.03	−2.9	5.1	2600	160	170	23	46.7	−1.2

Table C.2.: continued.

SMCSGS-FS #	Spectral type	T_* [kK]	log L [$L_\odot$]	log g_* [cm s^{-2}]	log $\dot{M}^{(1)}$ [$M_\odot$ yr^{-1}]	E_{B-V} [mag]	M_V [mag]	R_* [$R_\odot$]	$v_\infty{}^{(2)}$ [km s^{-1}]	$v \sin i$ [km s^{-1}]	v_{rad} [km s^{-1}]	M_* [$M_\odot$]	log Q_0 [s^{-1}]	*olog* $L_{mec}{}^{(3)}$ [$L_\odot$]
157	B2.5 (V)e	17	4.03	3.8	−9.3	0.08	−3.8	12.0	1000	150	160	33	45.0	−1.5
158	B0.7 (III)e	26	4.82	3.4	−8.5	0.11	−4.2	12.7	1100	250	150	15	47.2	−0.1
159	B0.7 V	26	3.76	4.2	−9.5	0.05	−1.9	3.7	1800	110	140	8	45.9	−2.0
160	B1 IV	25	4.29	4.0	−9.0	0.03	−3.5	7.5	2000	220	150	20	46.4	−1.1
161	B5 IV	16	3.85	3.8	−9.5	0.02	−3.0	11.0	1000	140	130	28	44.7	−1.8
162	B1 V	25	3.62	4.4	−9.7	0.05	−2.1	3.5	2200	250	150	11	45.6	−2.3
163	B2.5 V	19	3.12	4.2	−10.2	0.05	−0.9	3.4	900	80	150	7	44.0	−3.1
164	B1 V	25	4.09	4.0	−9.2	0.05	−2.9	5.9	1800	230	170	13	46.2	−1.4
165	B5 V	16	3.32	4.0	−10.0	0.05	−2.3	6.0	900	120	130	13	44.0	−2.8
166	O8 IV	33	5.25	3.8	−8.1	0.02	−5.1	12.9	1700	140	150	39	48.6	0.6
167	B0.7 (II)e	24	5	3.2	−8.3	0.05	−5.1	18.3	1100	120	150	19	47.2	0.2
168	B1.5 V	23	3.96	4.4	−9.3	0.05	−3.0	6.0	3000	190	160	33	45.4	−1.7
169	B1 IV	24	4.34	3.8	−9.0	0.05	−3.4	8.6	1700	120	170	17	46.3	−1.0
170	B0.7 V	27	4.16	4.2	−9.2	0.05	−3.0	5.5	2200	200	170	18	46.5	−1.3
171	B1 (V)e	25	4.13	3.8	−9.2	0.22	−2.6	6.2	1400	510	160	9	46.3	−1.3
172	B0 V	30	4.23	4.2	−9.1	0.09	−2.6	4.8	1900	80	170	14	47.0	−1.2
173	B2.5 V	19	3.62	4.2	−9.7	0.05	−1.8	6.0	1200	250	150	21	44.5	−2.3
174	B2.5 V	19	3.62	4.2	−9.7	0.03	−2.6	6.0	1200	280	150	21	44.5	−2.3
175	B9 Ib	10	3.32	3.0	−10.0	0.03	−3.1	15.3	500	120	150	9	42.9	−2.8
176	B7 V	14	3.12	3.8	−10.2	0.03	−2.1	6.2	800	220	170	9	43.7	−3.1
177	B5 (V)e	17	3.45	3.8	−9.9	0.05	−1.8	6.1	700	110	150	9	44.4	−2.6
178	B2 V	22	3.56	4.2	−9.7	0.05	−1.5	4.2	1900	120	160	10	45.0	−2.4
179	B2.5 (IV)e	19	4.07	3.4	−9.2	0.10	−3.0	10.0	600	250	170	9	45.2	−1.5
180	B2 V	21	4.3	4.0	−9.0	0.00	−3.9	10.7	2400	140	160	42	45.6	−1.0
181	B2 V	22	3.66	4.2	−9.6	0.05	−1.8	4.7	2000	130	170	13	45.1	−2.2
182	B1 V	26	3.72	4.4	−9.6	0.07	−2.1	3.6	2200	70	160	12	45.9	−2.1
183	B5 (V)e	16	3.32	4.0	−10.0	0.05	−2.6	6.0	900	160	170	13	44.0	−2.8
184	B2.5 V	20	3.73	3.8	−9.6	0.05	−2.6	6.1	700	180	170	9	44.8	−2.1
185	B0.7 V	27	4.06	4.2	−9.3	0.05	−2.5	4.9	2000	80	170	14	46.3	−1.5
186	B0.7 V	27	3.93	4.4	−9.4	0.05	−2.6	4.2	2400	220	170	16	46.2	−1.7
187	B0.5 IV	28	4.49	4.0	−8.8	0.03	−3.8	7.5	1900	140	170	20	47.0	−0.7
188	B5 V	17	3.55	3.8	−9.8	0.02	−2.2	6.9	800	160	160	11	44.5	−2.4
189	B2 (III)e	20	4.4	3.4	−8.9	0.08	−4.0	13.2	600	120	160	16	45.7	−0.9
190	B0.7 IV	25	4.86	3.6	−8.5	0.05	−4.8	14.4	1600	70	200	30	47.1	−0.1
191	B0.5 V	28	4.13	4.4	−9.2	0.05	−2.7	4.9	2600	110	160	22	46.5	−1.3
192	B1.5 IV	23	4.11	4.0	−9.2	0.05	−3.1	7.2	2000	170	160	19	45.9	−1.4
193	B0.7 V	27	3.93	4.4	−9.4	0.05	−2.9	4.2	2400	80	160	16	46.2	−1.7
194	B5 V	16	3.27	4.0	−10.0	0.02	−2.0	5.6	900	120	170	12	44.0	−2.9
195	O9.7 IV	32	4.85	4.0	−8.5	0.05	−4.5	8.7	1900	30	170	28	48.0	−0.1
196	B3 IV	18	3.62	3.8	−9.7	0.03	−2.7	6.7	800	110	170	10	44.6	−2.3
197	B1.5 IV	21	3.66	3.6	−9.6	0.05	−2.0	5.1	1000	100	170	4	45.1	−2.2
198	B1 V	25	4.37	4.0	−8.9	0.02	−3.5	8.2	2100	150	170	24	46.4	−0.9
199	B1 V	25	4.03	4.2	−9.3	0.05	−2.9	5.5	2200	100	160	18	46.0	−1.5
200	B2 V	22	3.76	4.2	−9.5	0.05	−2.5	5.2	2200	130	140	16	45.2	−2.0
201	B0.7 V	27	4.03	4.4	−9.3	0.03	−2.8	4.7	2600	220	150	21	46.3	−1.5
202	B1 V	26	4.24	4.2	−9.1	0.05	−3.2	6.5	2300	80	170	25	46.4	−1.2
203	B0.5 (III)e	25	5.18	3.2	−8.1	0.25	−5.1	20.8	1100	450	130	25	47.6	0.5
204	B1 V	26	3.95	4.4	−9.4	0.02	−2.5	4.7	2500	80	170	20	46.1	−1.7
205	B2.5 V	19	3.62	4.0	−9.7	0.03	−2.1	6.0	900	360	170	13	44.6	−2.3
206	B3 IV	18	3.72	3.8	−9.6	0.03	−2.9	7.5	800	80	170	13	44.7	−2.1
207	B3 IV	19	3.97	3.4	−9.3	0.05	−3.1	8.9	500	140	170	7	45.1	−1.6
208	B2.5 V	20	3.84	4.2	−9.5	0.05	−2.5	6.9	1300	75	170	28	44.9	−1.9

Table C.2.: continued.

SMCSGS-FS #	Spectral type	T_* [kK]	log L [$L_\odot$]	log g_* [cm s^{-2}]	log $\dot{M}^{(1)}$ [$M_\odot$ yr^{-1}]	E_{B-V} [mag]	M_V [mag]	R_* [$R_\odot$]	$v_\infty{}^{(2)}$ [km s^{-1}]	v sin i [km s^{-1}]	v_{rad} [km s^{-1}]	M_* [$M_\odot$]	log Q_0 [s^{-1}]	*olog* $L_{mec}{}^{(3)}$ [$L_\odot$]	
209	B1.5 V	23	3.76	4.4	−9.5	0.05	−2.1	4.8	2600	80	150	21	45.2	−2.0	
210	B0.5 III	28	4.52	3.6	−8.8	0.18	−3.4	7.8	1100	320	145	9	47.2	−0.7	
211	B5 V	17	3.85	3.8	−9.5	0.18	−2.4	9.7	900	150	170	22	44.8	−1.8	
212	B2.5 V	20	3.66	4.2	−9.6	0.05	−2.1	5.6	1100	150	150	18	44.7	−2.2	
213	B1.5 (V)e	24	3.81	4.0	−9.5	0.05	−2.0	4.7	1600	400	170	8	45.8	−1.9	
214	B1 (V)e	23	4	4.0	−9.3	0.16	−2.5	6.3	1900	200	170	15	45.8	−1.6	
215	O9.7 IV	33	4.77	4.2	−8.6	0.05	−3.8	7.4	2300	40	170	32	47.9	−0.2	
216	B0.7 IV	27	4.38	4.0	−9.0	* 0.07	−3.4	7.1	1200*	110	170	18	46.8	−0.9	*
217	B1 IV	25	4.39	4.0	−8.9	0.05	−3.5	8.4	2100	110	160	26	46.5	−0.9	
218	B3 V	17	3.55	3.8	−9.8	0.05	−2.4	6.9	800	130	160	11	44.5	−2.4	
219	B9 Ia	10	4.02	2.6	−9.3	0.05	−5.0	34.2	400	40	170	17	43.5	−1.5	
220	B1.5 V	24	3.94	4.2	−9.4	0.05	−2.4	5.4	2200	70	160	17	45.8	−1.7	
221	B2.5 V	19	3.6	4.2	−9.7	0.05	−2.1	5.8	1200	50	170	20	44.4	−2.3	
222	B0.5 V	28	4.03	4.4	−9.3	0.05	−2.8	4.4	2500	80	170	18	46.4	−1.5	
223	B0.5 (IV)e	27	4.43	3.6	−8.9	0.05	−3.2	7.5	1100	300	170	8	46.9	−0.8	
224	B1.5 (II)e	20	4.68	3.0	−8.6	0.05	−4.5	18.3	400	160	170	12	46.0	−0.4	
225	B2 (V)e	22	3.96	4.2	−9.3	0.05	−2.7	6.6	2400	150	160	25	45.4	−1.7	
226	B1 (IV)e	25	4.37	3.8	−8.9	0.27	−2.9	8.2	1600	270	170	15	46.5	−0.9	
227	B2 V	20	3.96	4.2	−9.3	0.05	−2.6	8.0	1400	200	170	37	45.0	−1.7	
228	B2.5 V	19	3.62	4.2	−9.7	0.05	−2.2	6.0	1200	100	170	21	44.5	−2.3	
229	B1.5 V	23	3.77	4.0	−9.5	0.02	−2.3	4.8	1600	140	160	9	45.5	−2.0	
230	B1 IV	25	4.59	4.0	−8.7	0.05	−4.6	10.5	2400	180	170	41	46.7	−0.5	
231	O3 V((f*))z	46	5.61	4.1	−7.5	* 0.08	−5.1	10.1	2900*	100	170	47	49.4	1.3	*
232	B0.5 V	27	4.03	4.4	−9.3	0.05	−2.5	4.7	2600	110	170	21	46.3	−1.5	
233	B1.5 (IV)e	23	4.37	3.8	−8.9	0.15	−3.8	9.7	1800	120	170	22	46.2	−0.9	
234	B3 IV	18	3.62	3.8	−9.7	0.05	−2.6	6.7	800	100	170	10	44.6	−2.3	
235	B2 (IV)e	21	4.34	3.6	−9.0	0.15	−3.7	11.2	1500	120	170	18	45.8	−1.0	
236	B2.5 V	19	3.72	4.2	−9.6	0.05	−2.4	6.7	1200	200	170	26	44.6	−2.1	
237	B0.7 V	27	4.26	4.2	−9.1	0.05	−3.3	6.2	2300	200	170	22	46.5	−1.1	
238	O8.5 V	34	4.88	4.2	−8.4	0.05	−4.6	8.0	2300	140	170	37	48.2	0.0	
239	O9 V	34	4.73	4.2	−8.6	0.05	−3.4	6.7	2100	75	170	26	48.0	−0.3	
240	B2 V	22	4.04	4.2	−9.3	0.05	−3.4	7.2	2500	90	170	30	45.5	−1.5	
241	O7 V	37	5.1	4.2	−8.2	0.09	−4.8	8.7	2300	150	170	43	48.6	0.4	
242	B1.5 V	23	3.69	4.4	−9.6	0.05	−1.8	4.4	2500	85	170	18	45.2	−2.1	
243	B2.5 V	19	3.82	4.0	−9.5	0.05	−3.4	7.5	1000	110	160	21	44.8	−1.9	
244	B2 V	21	3.86	4.0	−9.4	0.05	−2.4	6.4	1900	100	170	15	45.1	−1.8	
245	B1.5 (IV)e	22	3.84	3.8	−9.5	0.10	−2.3	5.7	1400	300	160	8	45.5	−1.9	
246	B1 V	25	4.25	4.2	−9.1	0.03	−3.4	7.1	2500	180	180	29	46.2	−1.1	
247	B5 V	16	3.42	3.8	−9.9	0.05	−2.2	6.7	800	90	160	10	44.3	−2.6	
248	B0.2 V	30	4.2	4.4	−9.1	0.05	−2.5	4.7	2500	120	170	20	46.8	−1.2	
249	B2 (III)e	20	4.61	3.2	−8.7	0.10	−4.4	16.9	600	300	170	16	45.9	−0.5	
250	B2 V	22	3.81	3.8	−9.5	0.05	−2.2	5.5	1400	120	170	7	45.4	−1.9	
251	B1.5 V	23	3.76	4.4	−9.5	0.05	−1.7	4.8	2600	80	170	21	45.2	−2.0	
252	B9 Ia	10	3.92	2.6	−9.4	0.05	−4.4	30.5	400	100	170	13	43.4	−1.7	
253	B1.5 V	23	3.92	4.4	−9.4	0.05	−1.9	5.8	2900	130	170	30	45.4	−1.7	
254	B1.5 V	21	4.06	4.0	−9.3	0.05	−3.4	8.1	2100	120	170	24	45.3	−1.5	
255	B2 V	20	3.56	4.2	−9.7	0.05	−2.2	5.0	1100	80	140	15	44.6	−2.4	
256	B1.5 V	23	3.86	4.4	−9.4	0.05	−2.4	5.4	2800	80	170	27	45.3	−1.8	
257	B0.5 V	27	4.46	4.2	−8.9	0.05	−4.0	7.8	2600	100	170	35	46.8	−0.8	
258	B0.5 (III)e	25	4.69	3.4	−8.6	0.12	−4.8	11.8	1100	300	150	13	47.0	−0.4	
259	B0.7 V	27	4.03	4.4	−9.3	0.05	−2.5	4.7	2600	110	175	21	46.3	−1.5	
260	B0.5 V	27	4.26	4.2	−9.1	0.05	−2.9	6.2	2300	160	160	22	46.5	−1.1	

Table C.2.: continued.

SMCSGS-FS #	Spectral type	T_* [kK]	log L [$L_\odot$]	log g_* [cm s^{-2}]	log $\dot{M}^{(1)}$ [$M_\odot$ yr^{-1}]	E_{B-V} [mag]	M_V [mag]	R_* [$R_\odot$]	$v_\infty{}^{(2)}$ [km s^{-1}]	$v \sin i$ [km s^{-1}]	v_{rad} [km s^{-1}]	M_* [$M_\odot$]	log Q_0 [s^{-1}]	*olog* $L_{mec}{}^{(3)}$ [$L_\odot$]	
261	B0.7 V	26	3.82	4.4	−9.5	0.05	−2.3	4.0	2400	80	170	15	46.0	−1.9	
262	B2 (III)e	20	4.28	3.2	−9.0	0.10	−3.6	11.5	500	180	140	8	45.6	−1.1	
263	B0.2 V	29	4.44	4.2	−8.9	0.05	−3.5	6.6	2300	80	170	25	47.0	−0.8	
264	B2.5 III	17	3.95	3.2	−9.4	0.05	−3.3	10.9	500	80	170	7	45.0	−1.7	
265	B0.5 IV	27	4.75	3.8	−8.6	0.08	−4.4	10.9	1800	120	180	27	47.2	−0.3	
266	B1 V	25	4.35	4.0	−9.0	0.02	−3.6	8.0	2100	150	160	23	46.4	−1.0	
267	B2 V	20	3.64	4.2	−9.7	0.05	−2.2	5.5	1100	80	170	18	44.7	−2.2	
268	B2 V	20	3.64	4.2	−9.7	0.05	−2.1	5.5	1100	80	170	18	44.7	−2.2	
269	O8 Vz	35	4.64	4.2	−8.7	0.05	−3.5	5.7	2000	160	120	19	48.0	−0.4	
270	B0.7 V	26	3.76	4.2	−9.5	0.05	−2.1	3.7	1800	70	170	8	45.9	−2.0	
271	B3 (IV)e	18	3.62	3.8	−9.7	0.07	−2.5	6.7	800	120	170	10	44.6	−2.3	
272	B2.5 IV	19	3.67	3.8	−9.6	0.05	−2.4	6.3	700	90	170	9	44.7	−2.2	
273	B1.5 V	23	3.66	4.4	−9.6	0.05	−1.9	4.3	2500	200	170	17	45.1	−2.2	
274	B0.5 V	28	4.03	4.4	−9.3	0.05	−2.6	4.4	2500	120	160	18	46.4	−1.5	
275	B0.7 V	26	4.06	4.2	−9.3	0.05	−2.8	5.3	2100	210	170	16	46.2	−1.5	
276	B0.5 V	26	4.14	4.2	−9.2	0.05	−2.8	5.8	2200	100	170	20	46.3	−1.3	
277	B1 IV	25	4.4	3.6	−8.9	0.05	−3.2	8.5	1200	200	170	10	46.6	−0.9	
278	B1 IV	26	4.73	3.6	−8.6	0.05	−4.2	11.5	1400	300	170	19	47.1	−0.3	
279	B2 V	22	3.96	4.2	−9.3	0.05	−2.6	6.6	2400	220	180	25	45.4	−1.7	
280	B1 V	26	3.94	4.2	−9.4	0.05	−2.1	4.6	2000	50	170	12	46.1	−1.7	
281	B0.2 V	29	4.11	4.4	−9.2	0.05	−2.8	4.5	2500	70	170	19	46.6	−1.4	
282	B2.5 (IV)e	19	3.87	3.8	−9.4	0.06	−2.7	8.0	800	150	170	15	44.9	−1.8	
283	B0.5 (III)e	27	5.01	3.4	−8.3	0.38	−4.6	14.7	1100	550	140	20	47.7	0.2	
284	B1.5 IV	20	4.33	3.8	−9.1	* 0.02	−3.8	12.2	752*	140	170	34	45.9	−1.0	*
285	B1.5 V	23	3.76	4.4	−9.5	0.05	−2.1	4.8	2600	100	170	21	45.2	−2.0	
286	B7 IV	16	3.72	3.8	−9.6	0.08	−3.1	9.5	900	120	170	21	44.6	−2.1	
287	O6 V((f))z	37	4.75	4.2	−8.6	* 0.05	−3.6	5.8	2500*	40	160	19	48.3	−0.3	*
288	O8.5 III	32	5.4	3.6	−7.9	* 0.06	−5.7	16.4	1900*	100	170	39	48.7	0.9	*
289	B1.5 (IV)e	23	3.96	3.8	−9.3	0.20	−2.6	6.0	1400	300	160	8	45.8	−1.7	
290	B1 V	24	3.54	4.2	−9.8	0.05	−2.0	3.4	1700	150	170	7	45.4	−2.4	
291	B1 V	26	3.84	4.2	−9.5	0.02	−2.6	4.1	1900	300	170	10	46.0	−1.9	
292	O7 V((f))z	37	5.15	4.2	−8.3	* 0.05	−4.8	9.2	2500*	55	170	49	48.7	0.5	*
293	B2 V	19	3.52	4.2	−9.8	0.05	−2.1	5.3	1100	150	170	16	44.4	−2.4	
294	B1 V	24	3.94	4.2	−9.4	0.05	−2.5	5.4	2200	180	170	17	45.8	−1.7	
295	B2 V	21	3.86	4.0	−9.4	0.05	−2.7	6.4	1900	100	170	15	45.1	−1.8	
296	B5 V	19	3.42	4.2	−9.9	0.05	−2.1	4.7	1000	100	170	13	44.3	−2.6	
297	B1.5 V	23	3.76	4.4	−9.5	0.05	−2.4	4.8	2600	170	170	21	45.2	−2.0	
298	O9.5 V	32	4.77	4.2	−8.7	* 0.08	−3.8	7.9	1700*	180	170	36	47.8	−0.2	*
299	B1.5 V	23	3.76	4.4	−9.5	0.09	−2.5	4.8	2600	200	170	21	45.2	−2.0	
300	B1.5 V	22	3.86	4.2	−9.4	0.05	−2.8	5.9	2300	80	160	20	45.3	−1.8	
301	B1.5 V	23	3.99	4.4	−9.3	0.01	−2.6	6.2	3000	230	170	36	45.5	−1.6	
302	B0 V	31	4.57	4.2	−8.7	0.02	−3.7	6.7	2200	80	170	26	47.5	−0.6	
303	B1.5 V	23	3.86	4.4	−9.4	0.05	−2.6	5.4	2800	230	180	27	45.3	−1.8	
304	B0.5 V	27	4.29	4.2	−9.0	0.05	−3.4	6.4	2300	120	150	24	46.6	−1.1	
305	B1.5 V	23	3.66	4.4	−9.6	0.05	−2.1	4.3	2500	150	170	17	45.1	−2.2	
306	B0 V	31	4.49	4.4	−8.8	0.05	−3.3	6.1	2800	150	170	34	47.3	−0.7	
307	B0.5 V	28	3.81	4.4	−9.5	0.05	−2.1	3.4	2200	150	170	11	46.2	−1.9	
308	B5 V	17	3.15	3.8	−10.1	0.06	−1.9	4.3	600	100	160	4	44.1	−3.1	
309	B2.5 V	20	3.56	4.2	−9.7	0.05	−2.1	5.0	1100	180	170	15	44.6	−2.4	
310	O7.5 In(f)p	30	5.27	3.2	−6.6	* 0.06	−5.3	16.0	600*	300	170	15	48.8	0.7	*
311	B1 V	26	3.8	4.4	−9.5	0.05	−2.2	3.9	2300	80	170	14	46.0	−1.9	
312	O9 IV	33	4.72	4.0	−8.6	0.05	−3.6	7.0	1700	40	170	18	48.0	−0.3	

Table C.2.: continued.

SMCSGS-FS #	Spectral type	T_* [kK]	log L [$L_\odot$]	log g_* [cm s^{-2}]	log $\dot{M}^{(1)}$ [$M_\odot$ yr^{-1}]	E_{B-V} [mag]	M_V [mag]	R_* [$R_\odot$]	$v_\infty$$^{(2)}$ [km s^{-1}]	v sin i [km s^{-1}]	v_{rad} [km s^{-1}]	M_* [$M_\odot$]	log Q_0 [s^{-1}]	*olog* $L_{mec}$$^{(3)}$ [$L_\odot$]
313	B2.5 V	20	3.76	4.2	−9.5	0.05	−2.1	6.3	1200	160	170	23	44.8	−2.0
314	B2 V	19	3.52	4.0	−9.8	0.05	−2.4	5.3	900	180	170	10	44.5	−2.4
315	O9.7 (III)e	31	5.16	3.6	−8.2	0.22	−4.8	13.2	1300	440	170	25	48.4	0.5
316	B2 (V)e	19	3.62	4.0	−9.7	0.09	−2.4	6.0	900	100	170	13	44.6	−2.3
317	B0 V	31	4.25	4.2	−9.1	0.05	−2.5	4.6	1900	75	170	12	47.2	−1.1
318	B2 V	19	3.42	4.2	−9.9	0.05	−1.8	4.7	1000	150	170	13	44.3	−2.6
319	B1.5 V	22	3.94	4.2	−9.4	0.15	−2.2	6.4	2400	40	170	24	45.4	−1.7
320	B2 V	20	3.66	4.2	−9.6	0.05	−2.0	5.6	1100	100	220	18	44.7	−2.2

Notes. $^{(1)}$ log $M_\odot$ values with * are determined from UV P-Cygni profiles. We derived a relation for these measured log $M_\odot$ and log $L/L_\odot$ and applied for rest of the stars. $^{(2)}$ v_∞ values with * are determined from UV P-Cygni profiles. Other values are theoretically calculated from v_{esc}. $^{(3)}$ log L_{mec} values with * are calculated for nine stars with UV spectra. For the rest of the stars we adopted values from the derived relation of these nine stars.

Table C.4.: Ages and evolutionary masses of the OB stars determined from stellar evolutionary tracks and isochrones

SMCSGS-FS #	Age [Myr]	M_{ev} [$M_\odot$]
1	6.0	9.3
2	8.6	12.0
3	38.5	6.4
4	22.0	10.1
5	36.9	6.6
6	21.4	8.3
7	21.0	7.9
8	32.4	7.0
9	22.4	8.9
10	101.0	5.3
11	32.4	7.0
12	100.0	5.1
13	17.6	9.4
14	38.5	6.4
15	32.9	6.8
16	18.9	9.5
17	63.3	5.9
18	13.4	12.1
19	72.9	5.1
20	80.0	5.2
21	72.9	5.1
22	10.6	13.1
23	135.0	5.4
24	80.0	5.4

Table C.4.: continued.

SMCSGS-FS #	Age [Myr]	M_{ev} [$M_\odot$]
25	56.6	5.4
26	55.2	5.8
27	38.5	6.4
28	43.4	6.5
29	13.1	10.3
30	5.1	8.9
31	5.6	20.3
32	10.7	14.9
33	43.4	6.5
34	42.4	6.3
35	21.0	7.9
36	6.1	23.0
37	13.0	10.6
38	10.1	12.8
39	12.0	11.7
40	14.0	11.1
41	37.2	5.6
42	24.7	8.7
43	23.2	8.6
44	7.9	14.3
45	16.7	11.3
46	6.3	13.2
47	24.6	8.0
48	22.6	8.6
49	39.8	6.9
50	47.2	6.4
51	19.2	9.7
52	7.6	11.1
53	38.5	6.4
54	10.4	7.9
55	18.0	9.2
56	0.9	9.4
57	75.8	5.1
58	46.3	5.7
59	8.3	13.6
60	5.2	10.2
61	17.5	9.7
62	8.3	13.9
63	10.0	10.8
64	5.0	22.2
65	5.9	11.7
66	27.6	7.9

Table C.4.: continued.

SMCSGS-FS #	Age [Myr]	M_{ev} [$M_\odot$]
67	6.3	15.7
68	36.9	6.6
69	7.3	19.7
70	8.0	15.3
71	21.0	7.4
72	21.8	9.4
73	6.4	20.4
74	38.5	6.4
75	24.6	8.0
76	12.2	9.9
77	15.7	10.4
78	30.9	6.6
79	38.5	6.4
80	38.5	6.4
81	20.0	8.9
82	28.9	7.2
83	17.5	8.2
84	17.5	8.2
85	13.1	10.6
86	82.0	5.0
87	15.3	7.6
88	6.0	8.9
89	6.3	17.7
90	6.2	18.6
91	13.5	11.6
92	1.0	9.5
93	41.9	6.1
94	14.8	9.6
95	17.5	8.2
96	16.9	10.6
97	18.5	7.4
98	13.0	10.7
99	11.3	14.3
100	33.9	6.1
101	36.9	6.6
102	63.0	5.3
103	41.9	6.1
104	83.0	5.3
105	29.2	7.4
106	21.5	8.3
107	7.2	16.0
108	32.7	6.4

Table C.4.: continued.

SMCSGS-FS #	Age [Myr]	M_{ev} [$M_\odot$]
109	35.5	6.4
110	30.2	7.8
111	4.0	19.1
112	34.5	6.4
113	150.0	5.3
114	38.5	6.4
115	20.8	6.9
116	35.5	6.4
117	38.4	7.0
118	37.2	6.8
119	6.1	16.7
120	8.5	13.7
121	6.1	17.6
122	32.7	6.4
123	26.1	8.1
124	25.3	8.7
125	11.1	11.4
126	65.7	5.6
127	27.0	7.2
128	4.3	18.6
129	46.0	6.3
130	38.5	6.4
131	22.8	6.9
132	24.6	8.0
133	24.6	8.0
134	36.9	6.6
135	26.1	8.1
136	14.1	10.9
137	17.7	10.2
138	25.0	7.9
139	26.0	7.4
140	29.3	7.1
141	22.6	8.6
142	27.7	7.7
143	4.3	25.5
144	36.5	6.1
145	24.6	8.0
146	32.4	7.0
147	11.1	9.4
148	27.7	7.7
149	8.3	10.8
150	48.0	6.2

Table C.4.: continued.

SMCSGS-FS #	Age [Myr]	M_{ev} [$M_\odot$]
151	21.0	7.9
152	38.5	6.4
153	18.6	9.9
154	22.6	8.6
155	11.7	10.9
156	8.2	12.0
157	25.9	8.3
158	9.2	15.2
159	7.9	9.0
160	14.0	11.1
161	35.9	7.2
162	6.7	8.4
163	36.0	5.4
164	10.1	10.4
165	72.9	5.1
166	4.6	26.0
167	8.3	18.4
168	21.0	8.9
169	14.7	11.3
170	10.8	11.0
171	25.7	10.2
172	6.0	12.5
173	42.5	6.4
174	32.5	6.4
175	90.0	5.1
176	102.9	5.3
177	62.2	5.8
178	23.0	7.1
179	25.3	8.7
180	16.0	10.5
181	15.3	7.6
182	8.2	8.9
183	72.9	5.1
184	26.0	7.4
185	10.5	10.9
186	11.1	9.9
187	9.6	13.6
188	61.8	6.0
189	16.8	11.1
190	9.2	16.2
191	9.1	11.3
192	17.5	9.7

Table C.4.: continued.

SMCSGS-FS #	Age [Myr]	M_{ev} [$M_\odot$]
193	6.2	9.9
194	74.0	5.2
195	6.1	18.3
196	46.0	6.3
197	22.3	7.3
198	13.9	11.7
199	14.4	10.0
200	26.0	7.9
201	10.1	10.8
202	12.9	11.0
203	6.9	21.6
204	12.4	9.8
205	32.5	6.4
206	38.0	6.9
207	26.6	8.2
208	32.9	7.3
209	17.5	8.2
210	9.8	13.5
211	33.8	7.3
212	32.4	7.0
213	17.5	8.4
214	18.5	9.1
215	5.9	18.4
216	11.3	12.5
217	13.1	12.1
218	57.8	6.0
219	31.3	7.9
220	18.2	9.0
221	35.6	6.3
222	8.7	11.1
223	11.1	12.9
224	12.6	13.6
225	22.6	8.6
226	13.9	11.7
227	25.5	8.3
228	28.5	6.4
229	18.3	8.1
230	12.6	13.1
231	1.4	46.7
232	10.2	10.8
233	15.3	11.3
234	46.0	6.3

Table C.4.: continued.

SMCSGS-FS #	Age [Myr]	M_{ev} [$M_\odot$]
235	16.7	10.8
236	32.4	7.1
237	11.9	11.5
238	4.8	20.1
239	4.2	18.7
240	20.5	9.1
241	3.8	25.0
242	20.0	8.0
243	34.7	7.2
244	27.7	7.7
245	28.0	7.8
246	14.3	10.8
247	65.7	5.6
248	5.8	12.3
249	14.9	12.9
250	25.2	7.8
251	17.5	8.2
252	39.8	6.8
253	21.0	8.6
254	22.7	9.0
255	36.9	6.6
256	21.5	8.3
257	11.3	13.2
258	10.8	14.5
259	7.2	10.8
260	8.9	11.5
261	11.4	9.1
262	17.8	10.3
263	8.5	13.7
264	29.4	7.9
265	9.0	16.0
266	13.1	11.6
267	29.3	7.1
268	29.3	7.1
269	3.1	18.6
270	8.1	9.0
271	46.0	6.3
272	33.2	6.8
273	16.4	7.9
274	6.0	11.1
275	13.0	10.6
276	13.0	10.6

Table C.4.: continued.

SMCSGS-FS #	Age [Myr]	M_{ev} [$M_\odot$]
277	13.6	12.0
278	9.5	15.4
279	22.6	8.6
280	11.8	9.7
281	6.0	11.7
282	30.1	7.6
283	7.3	19.2
284	17.2	10.6
285	17.5	8.2
286	46.2	6.7
287	2.0	20.1
288	4.6	29.3
289	20.1	8.9
290	10.1	7.5
291	10.0	9.1
292	3.9	25.8
293	58.5	6.4
294	14.0	9.0
295	27.7	7.7
296	41.9	6.1
297	17.5	8.2
298	6.2	17.9
299	17.5	8.2
300	24.6	8.0
301	20.4	9.0
302	6.6	15.3
303	21.5	8.3
304	11.3	11.7
305	10.4	7.9
306	6.2	14.7
307	2.0	9.4
308	64.2	5.0
309	36.9	6.6
310	5.5	25.4
311	9.6	9.1
312	3.9	18.1
313	29.2	7.4
314	58.5	6.4
315	5.6	22.5
316	42.5	6.4
317	4.0	13.2
318	41.9	6.1

Table C.4.: continued.

SMCSGS-FS #	Age [Myr]	M_{ev} [$M_\odot$]
319	22.7	8.5
320	32.4	7.0

Table C.3.: Candidate runaway OB stars in the SMC supergiant shell.

SMCSGS-FS #	v_{rad} (km s^{-1})	$v_{rad} - \bar{v}_{rad}$ (km s^{-1})	spectral type
203	130	−39	B0.5 (III)e
209	150	−19	B1.5 V
210	145	−24	B0.5 III
212	150	−19	B2.5 V
255	140	−29	B2 V
258	150	−19	B0.5 (III)e
262	140	−29	B2 (III)e
269	120	−49	O8 Vz
283	140	−29	B0.5 (III)e
304	150	−19	B0.5 V
320	220	51	B2 V
8	120	−43	B2 V
16	200	37	B1.5 V
19	120	−43	B5 V
50	200	37	B9 Ib
55	100	−63	B1.5 IV
64	120	−43	O9 V
90	200	37	O9.7 V
93	130	−33	B2.5 V
109	110	−53	B2.5 V
111	240	77	O8.5 V
113	110	−53	B7 V
161	130	−33	B5 IV
165	130	−33	B5 V
190	200	37	B0.7 IV

C.2. Spectral fits of SMC OB stars

We present the spectral fits of all the OB stars in the SMC-SGS 1 complex analyzed in this study. The upper panel shows the spectral energy distribution with photometry from UV, optical, and infra-red bands. Lower panels show the normalized VLT-FLAMES spectra depicted by blue solid lines. For a few stars the available UV spectra from HST, FUSE, IUE are also included in the lower panels. The observed spectra are over-plotted with PoWR model spectra (red dashed lines). The main parameters of the best-fit models are compiled in Table C.2

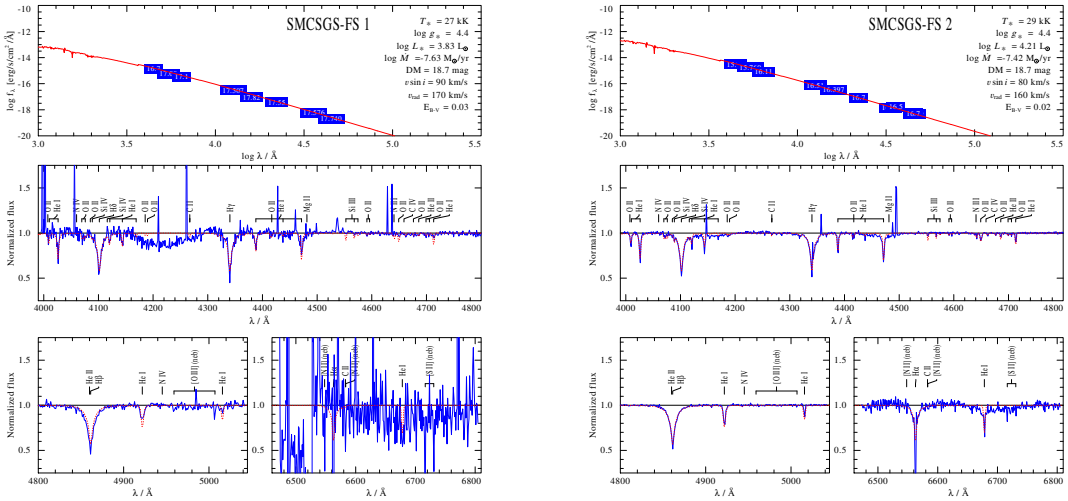

Figure C.1.: Spectral fit for SMCSGS-FS 1 and SMCSGS-FS 2

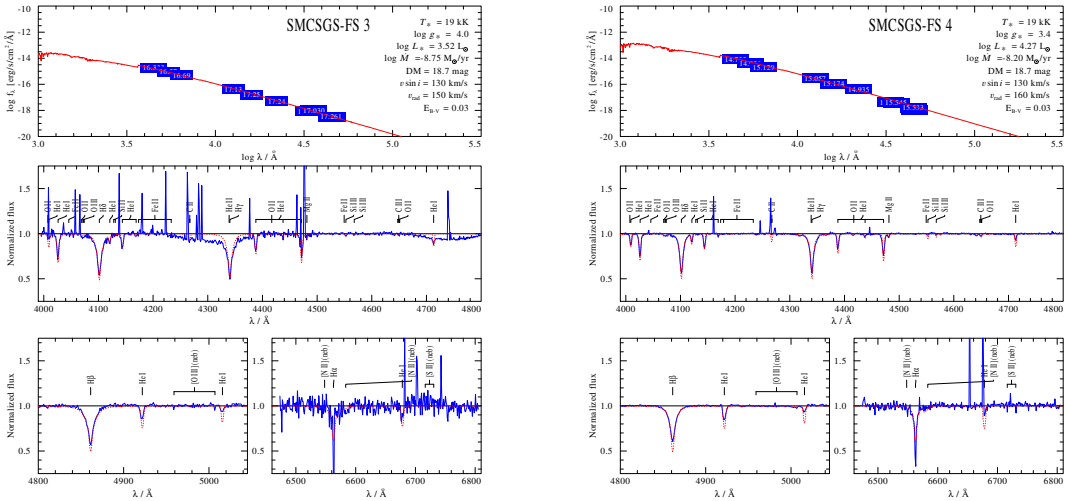

Figure C.2.: Spectral fit for SMCSGS-FS 3 and SMCSGS-FS 4

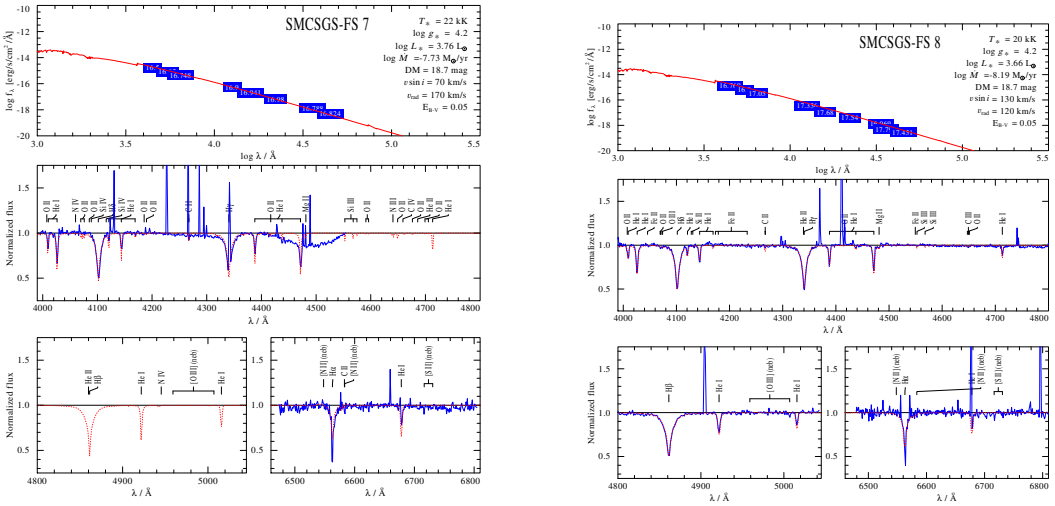

Figure C.3.: Spectral fit for SMCSGS-FS 7 and SMCSGS-FS 8

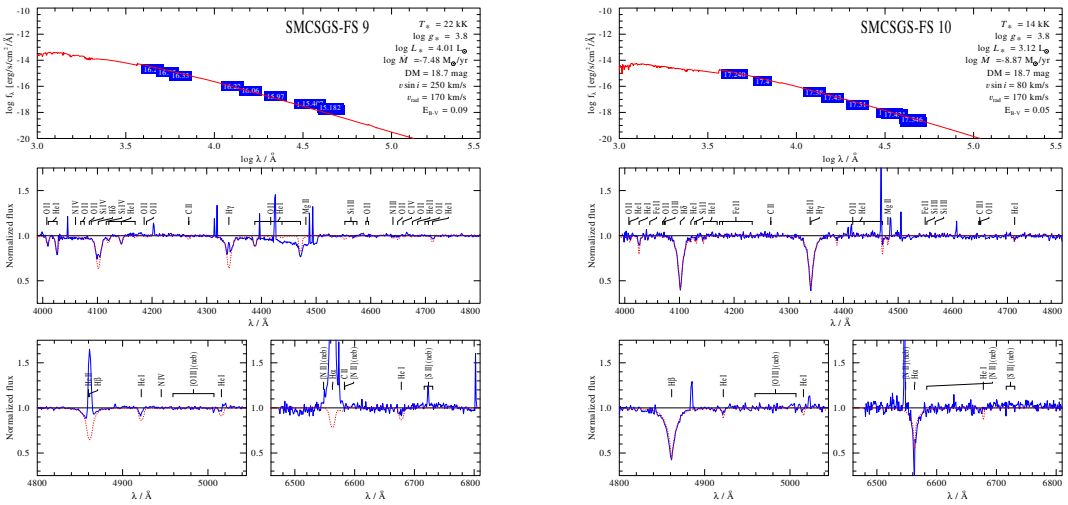

Figure C.4.: Spectral fit for SMCSGS-FS 9 and SMCSGS-FS 10

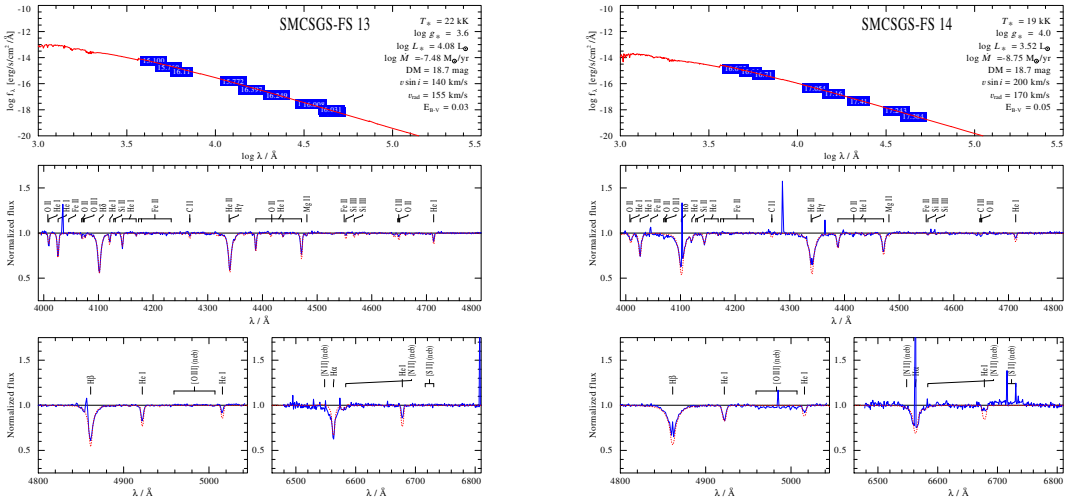

Figure C.5.: Spectral fit for SMCSGS-FS 13 and SMCSGS-FS 14

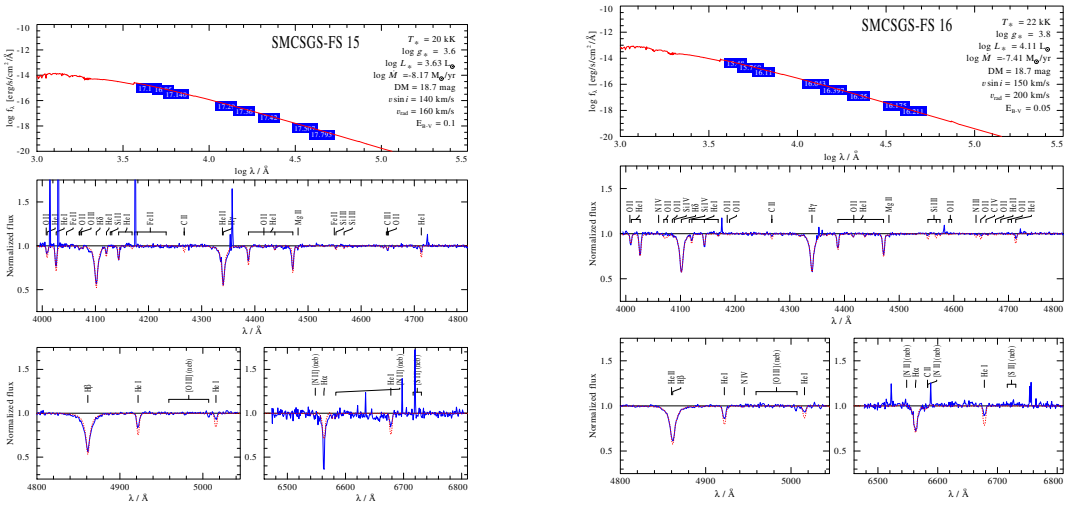

Figure C.6.: Spectral fit for SMCSGS-FS 15 and SMCSGS-FS 16

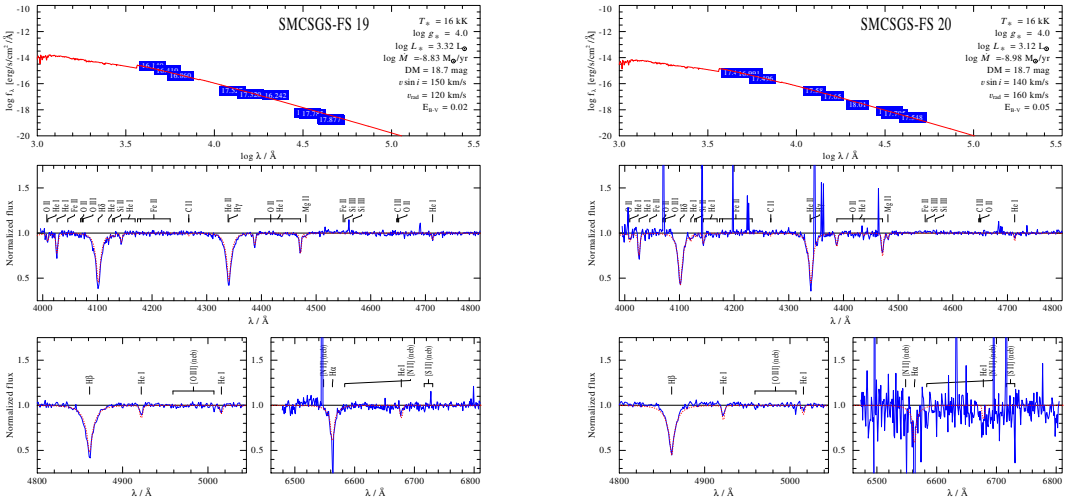

Figure C.7.: Spectral fit for SMCSGS-FS 19 and SMCSGS-FS 20

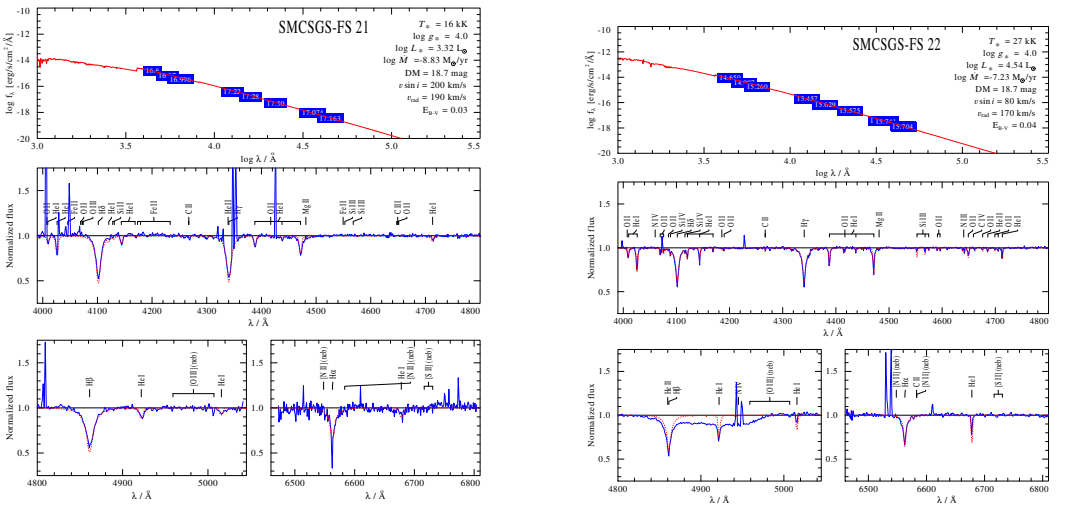

Figure C.8.: Spectral fit for SMCSGS-FS 21 and SMCSGS-FS 22

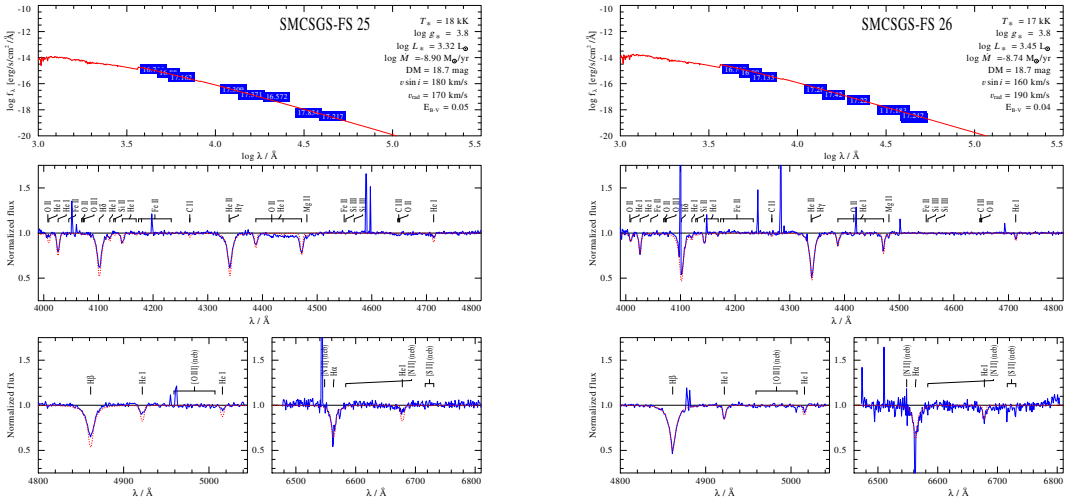

Figure C.9.: Spectral fit for SMCSGS-FS 25 and SMCSGS-FS 26

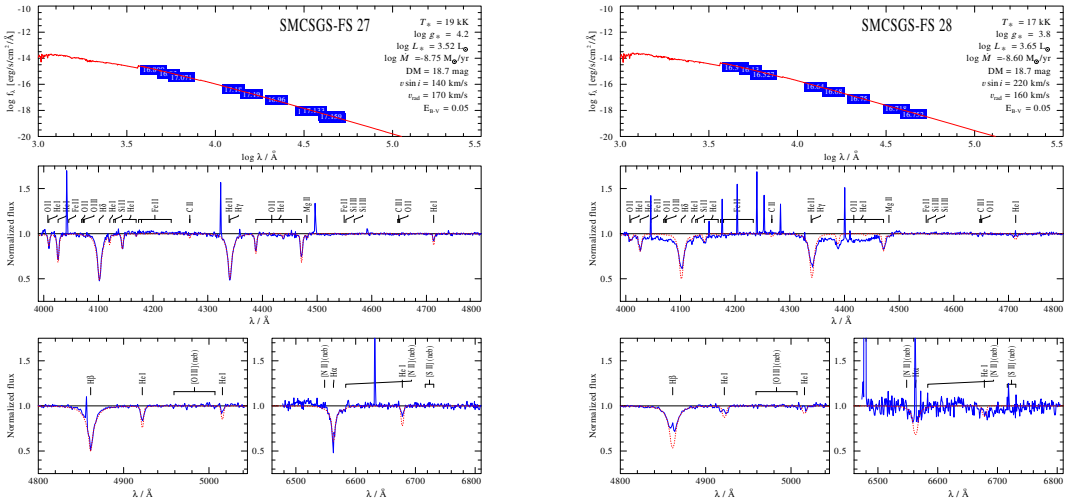

Figure C.10.: Spectral fit for SMCSGS-FS 27 and SMCSGS-FS 28

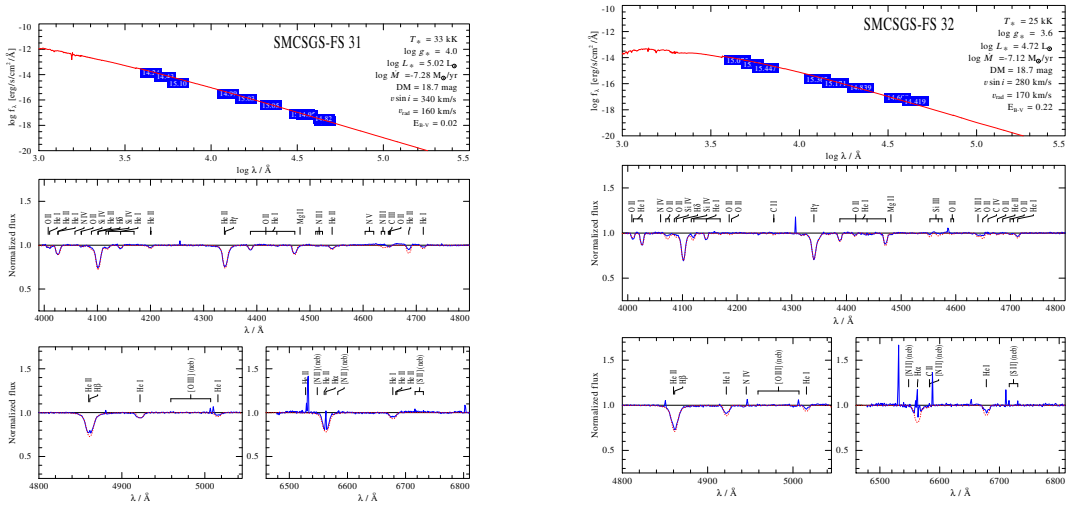

Figure C.11.: Spectral fit for SMCSGS-FS 31 and SMCSGS-FS 32

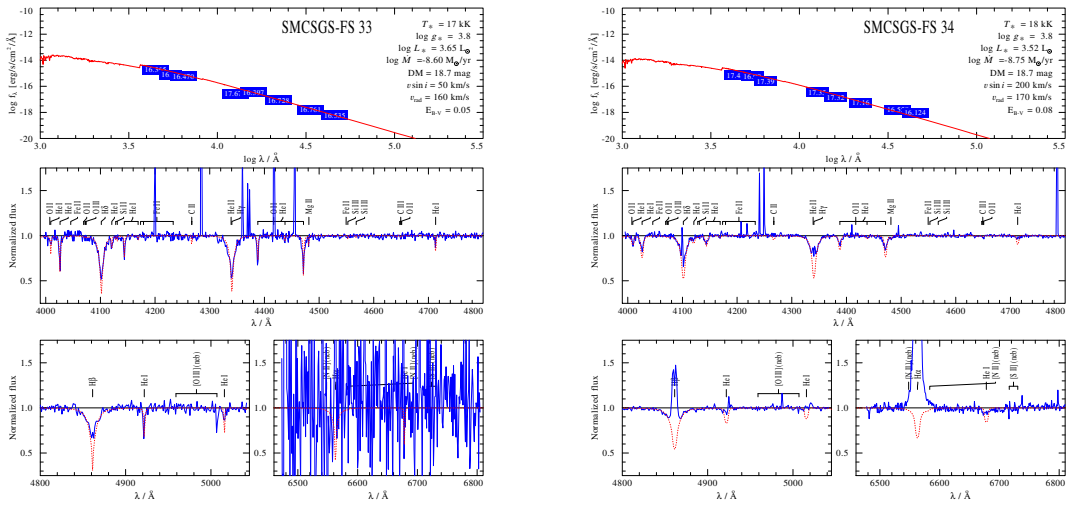

Figure C.12.: Spectral fit for SMCSGS-FS 33 and SMCSGS-FS 34

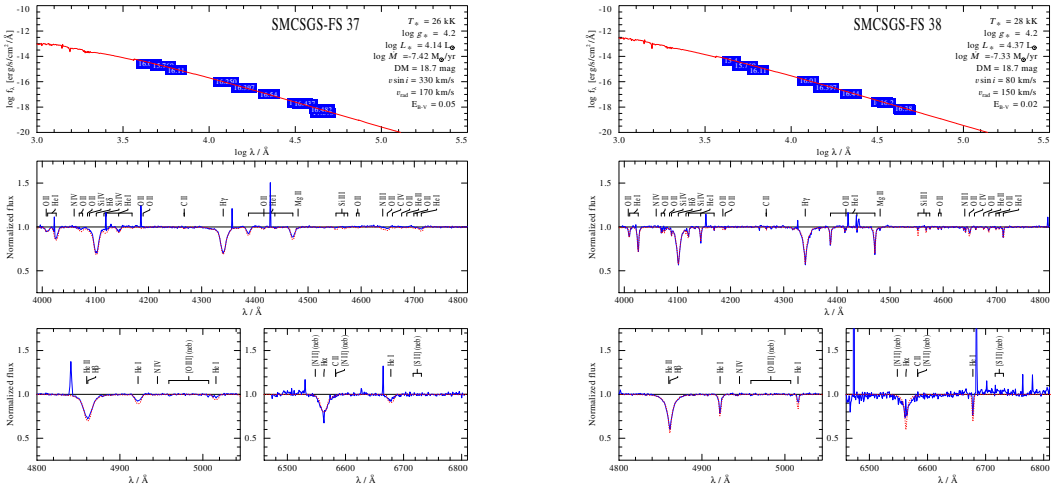

Figure C.13.: Spectral fit for SMCSGS-FS 37 and SMCSGS-FS 38

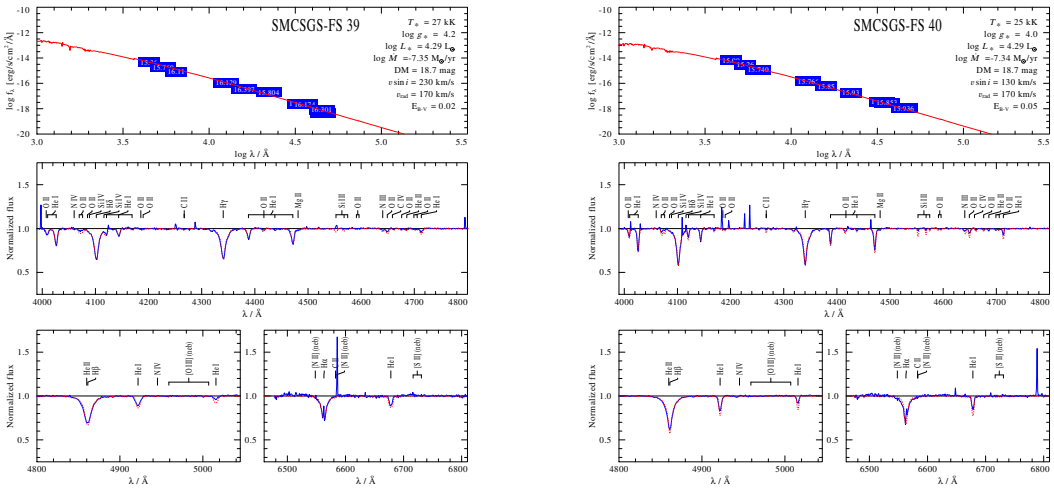

Figure C.14.: Spectral fit for SMCSGS-FS 39 and SMCSGS-FS 40

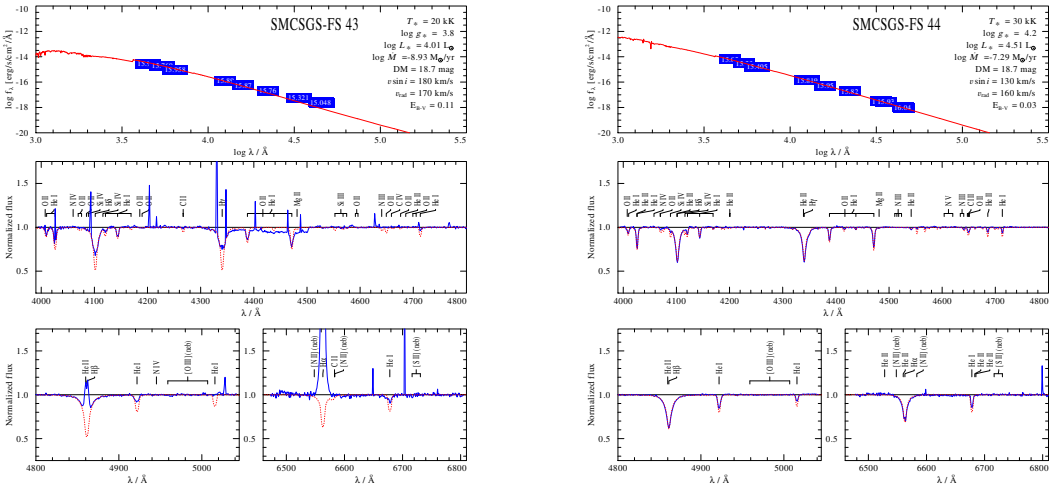

Figure C.15.: Spectral fit for SMCSGS-FS 43 and SMCSGS-FS 44

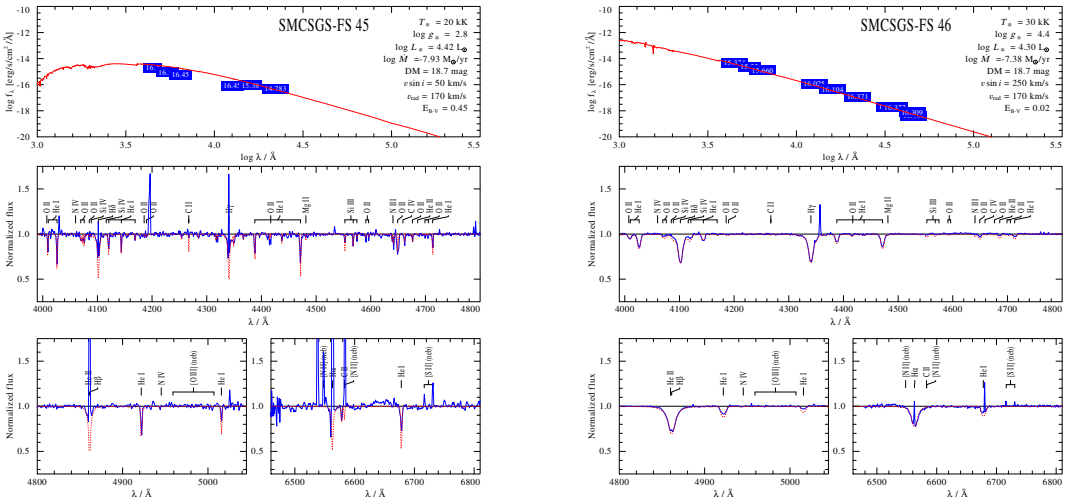

Figure C.16.: Spectral fit for SMCSGS-FS 45 and SMCSGS-FS 46

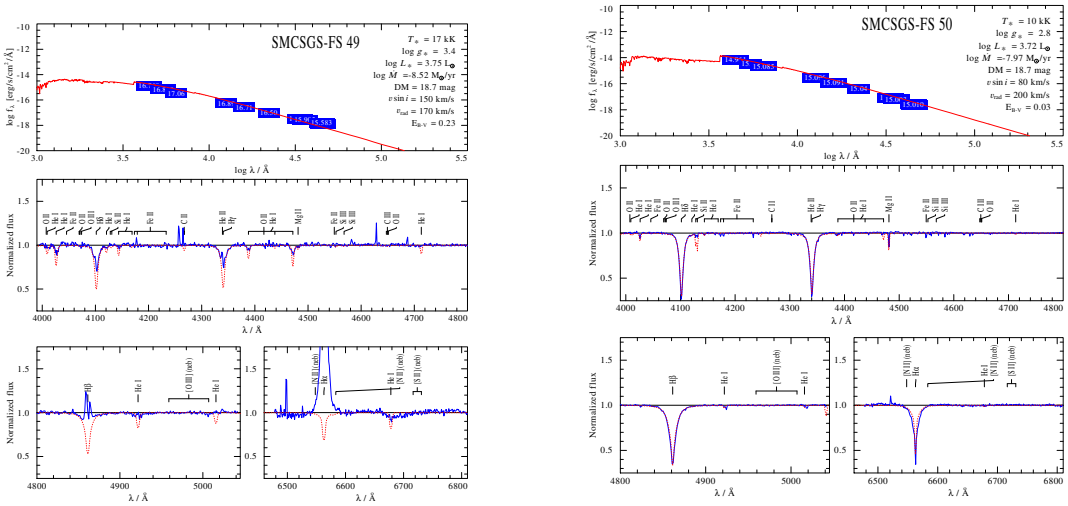

Figure C.17.: Spectral fit for SMCSGS-FS 49 and SMCSGS-FS 50

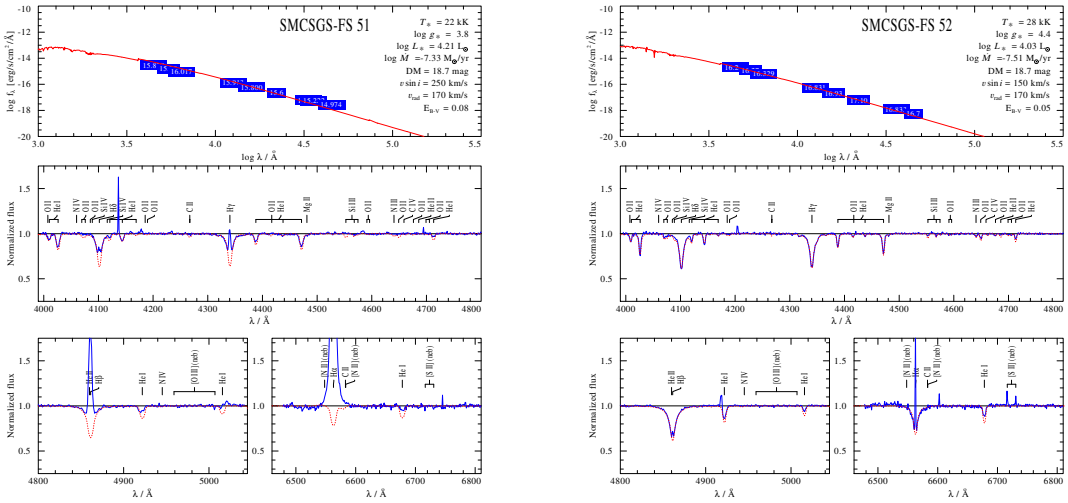

Figure C.18.: Spectral fit for SMCSGS-FS 51 and SMCSGS-FS 52

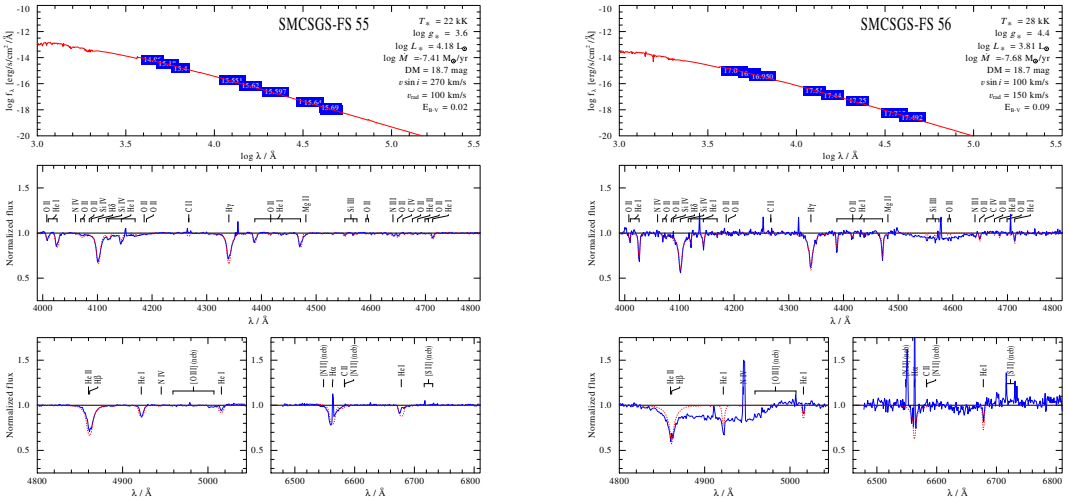

Figure C.19.: Spectral fit for SMCSGS-FS 55 and SMCSGS-FS 56

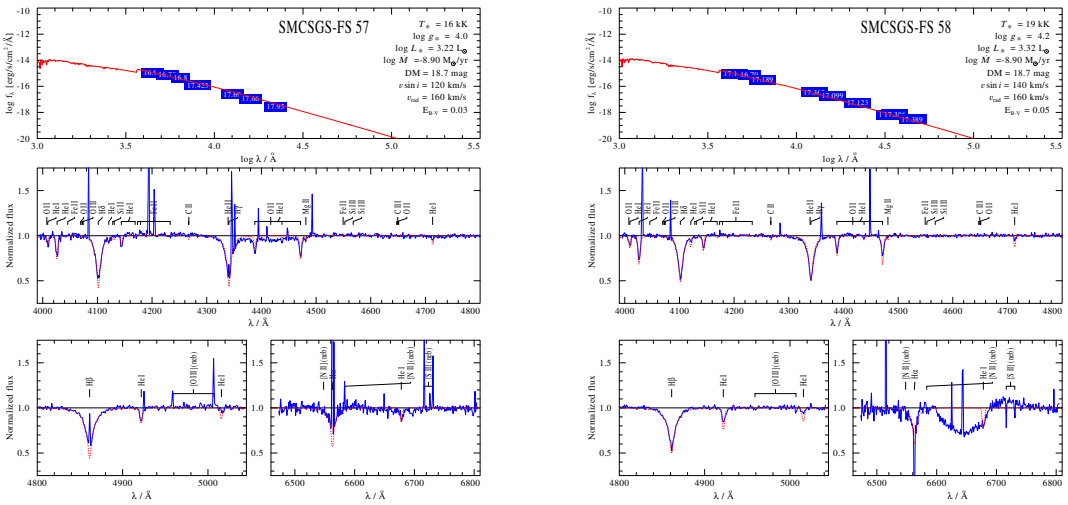

Figure C.20.: Spectral fit for SMCSGS-FS 57 and SMCSGS-FS 58

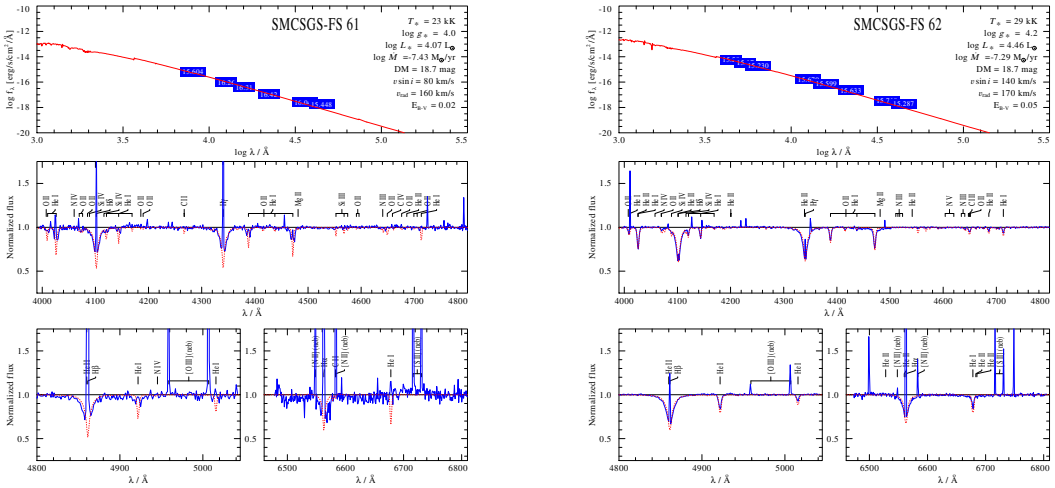

Figure C.21.: Spectral fit for SMCSGS-FS 61 and SMCSGS-FS 62

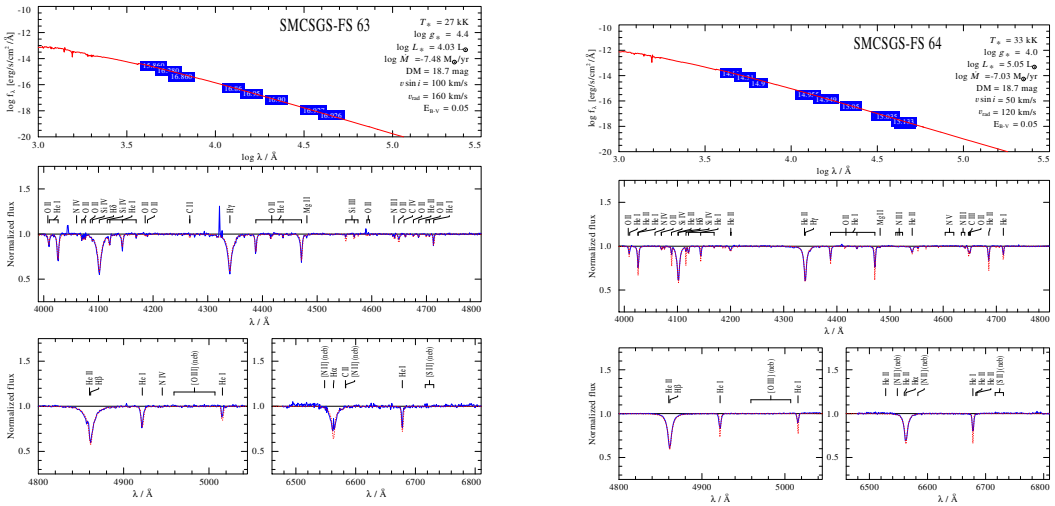

Figure C.22.: Spectral fit for SMCSGS-FS 63 and SMCSGS-FS 64

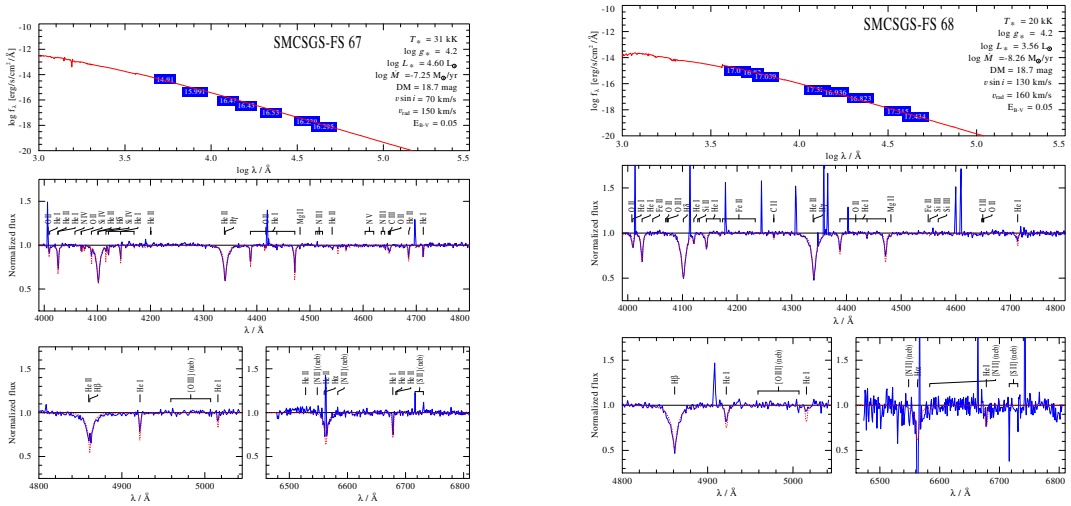

Figure C.23.: Spectral fit for SMCSGS-FS 67 and SMCSGS-FS 68

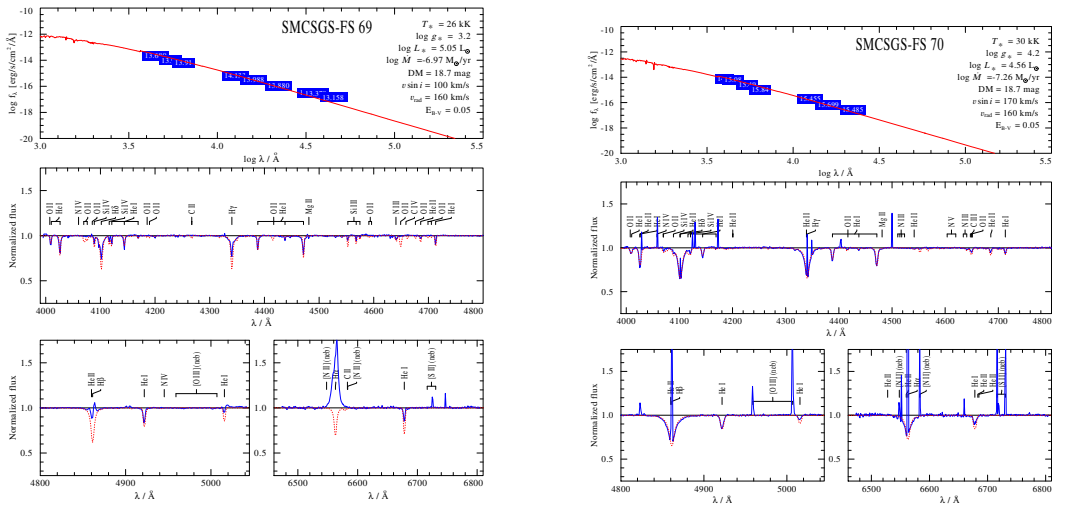

Figure C.24.: Spectral fit for SMCSGS-FS 69 and SMCSGS-FS 70

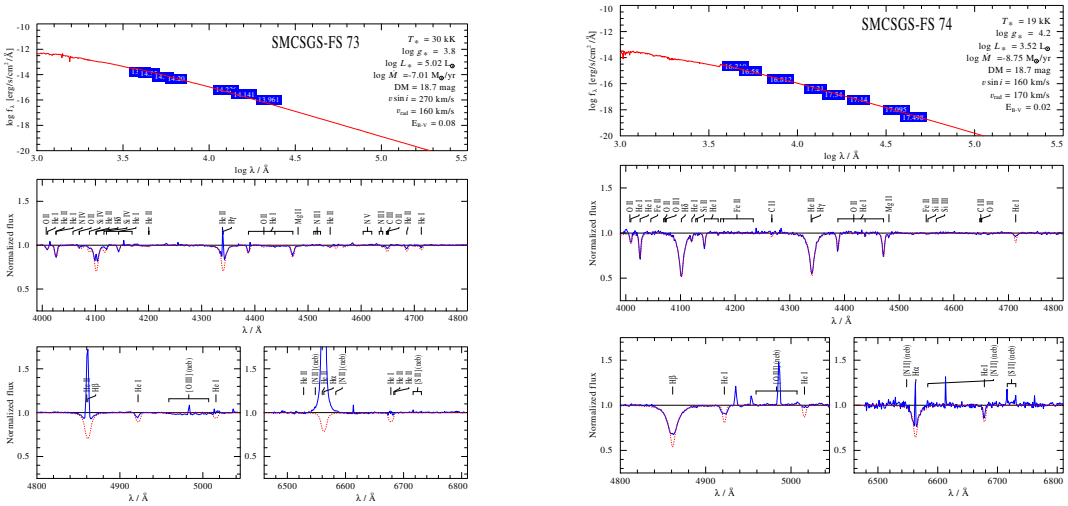

Figure C.25.: Spectral fit for SMCSGS-FS 73 and SMCSGS-FS 74

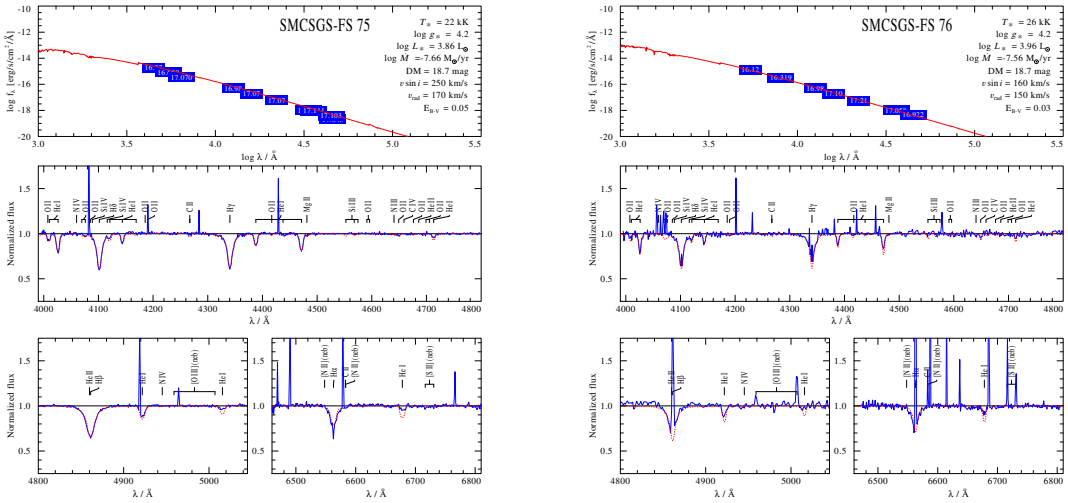

Figure C.26.: Spectral fit for SMCSGS-FS 75 and SMCSGS-FS 76

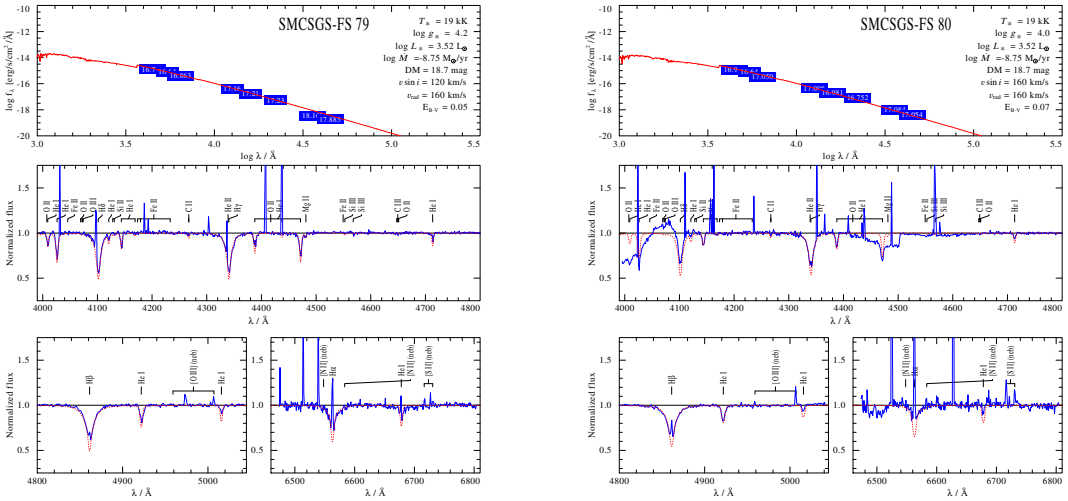

Figure C.27.: Spectral fit for SMCSGS-FS 79 and SMCSGS-FS 80

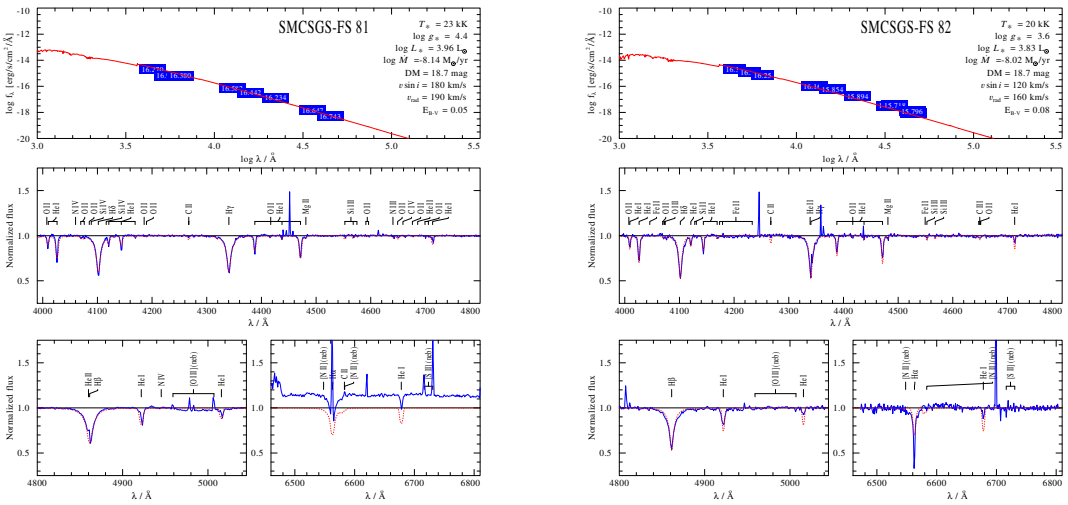

Figure C.28.: Spectral fit for SMCSGS-FS 81 and SMCSGS-FS 82

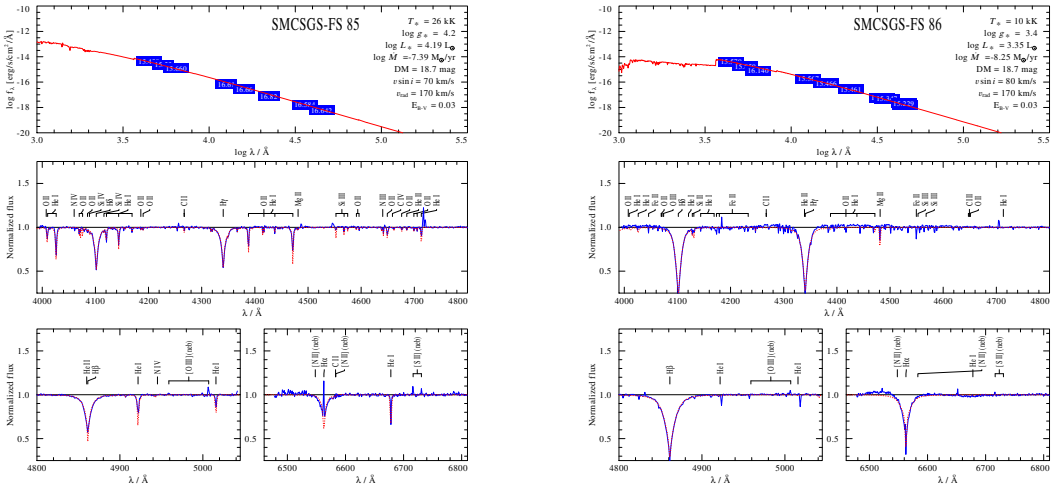

Figure C.29.: Spectral fit for SMCSGS-FS 85 and SMCSGS-FS 86

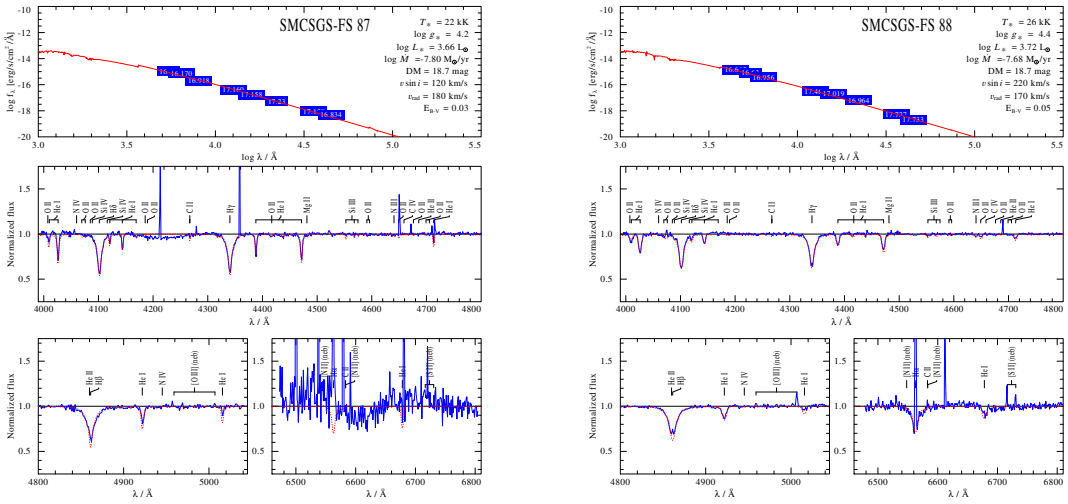

Figure C.30.: Spectral fit for SMCSGS-FS 87 and SMCSGS-FS 88

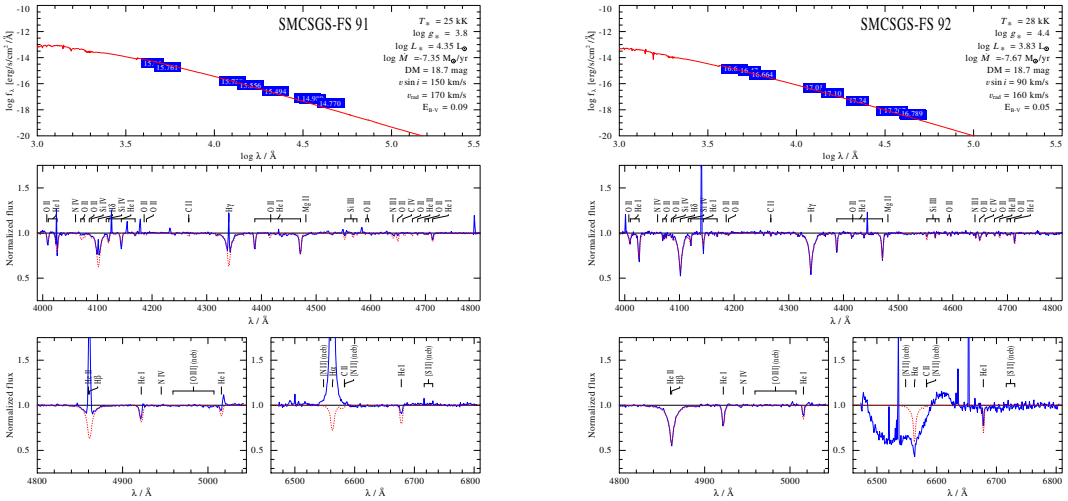

Figure C.31.: Spectral fit for SMCSGS-FS 91 and SMCSGS-FS 92

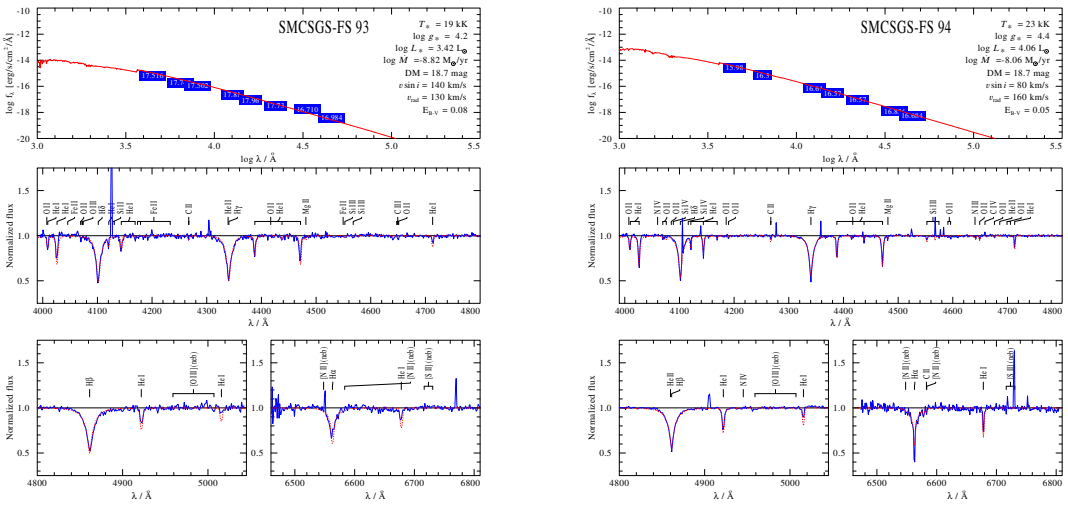

Figure C.32.: Spectral fit for SMCSGS-FS 93 and SMCSGS-FS 94

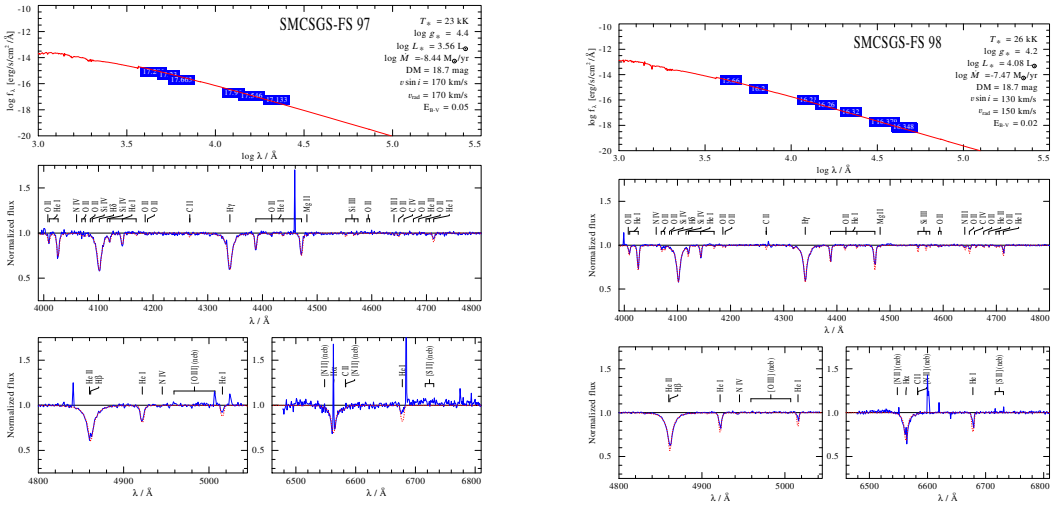

Figure C.33.: Spectral fit for SMCSGS-FS 97 and SMCSGS-FS 98

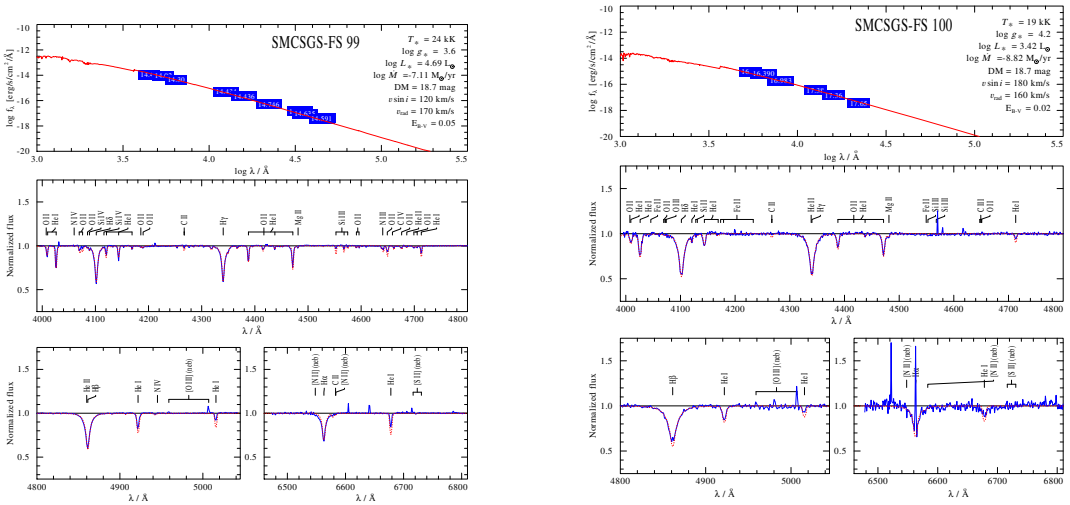

Figure C.34.: Spectral fit for SMCSGS-FS 99 and SMCSGS-FS 100

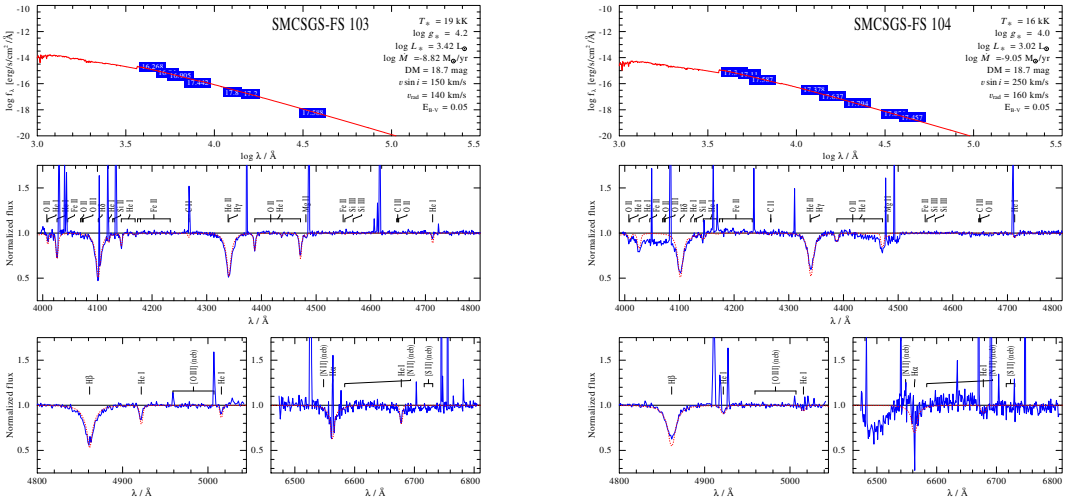

Figure C.35.: Spectral fit for SMCSGS-FS 103 and SMCSGS-FS 104

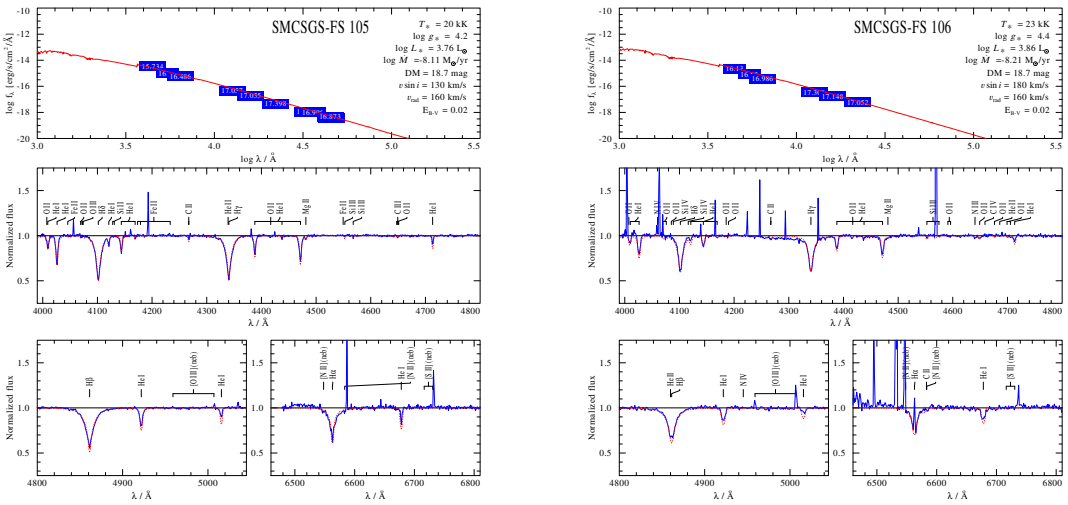

Figure C.36.: Spectral fit for SMCSGS-FS 105 and SMCSGS-FS 106

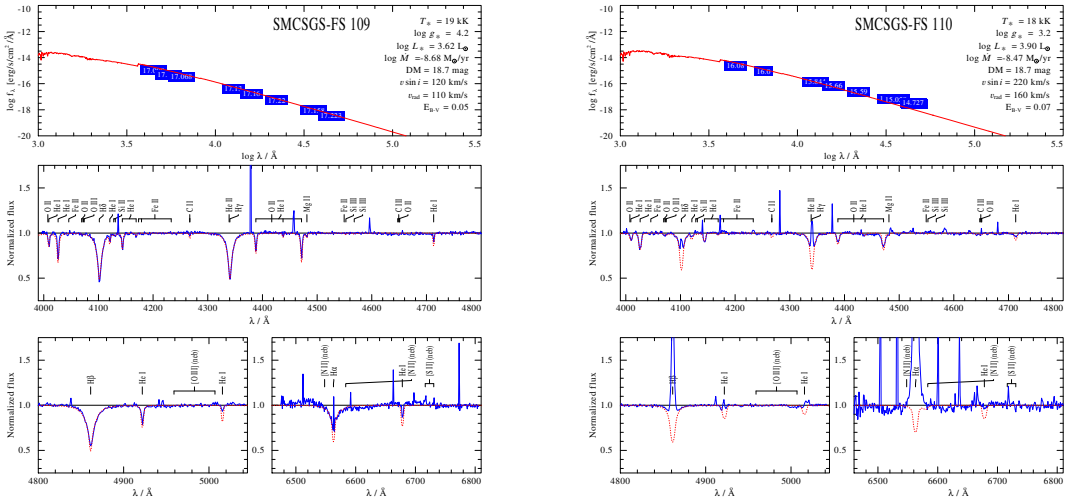

Figure C.37.: Spectral fit for SMCSGS-FS 109 and SMCSGS-FS 110

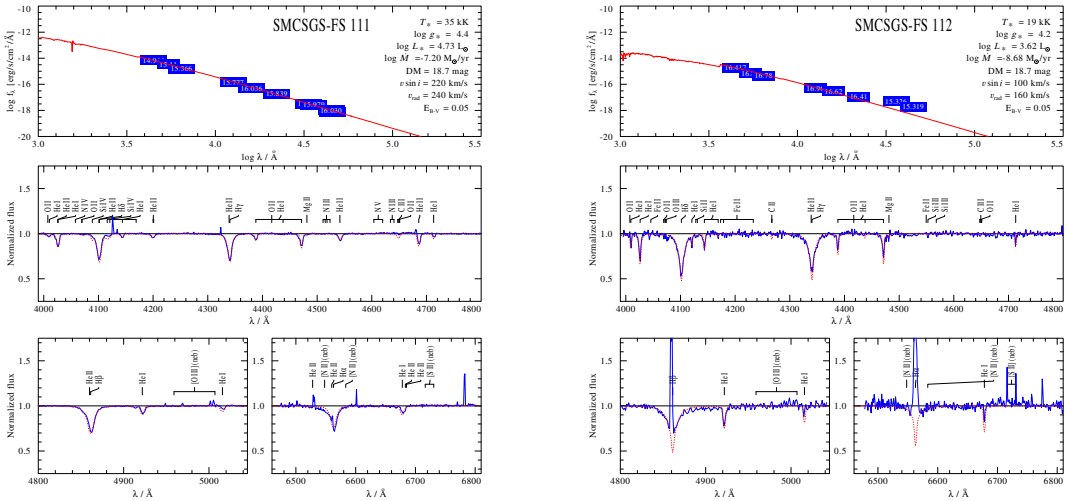

Figure C.38.: Spectral fit for SMCSGS-FS 111 and SMCSGS-FS 112

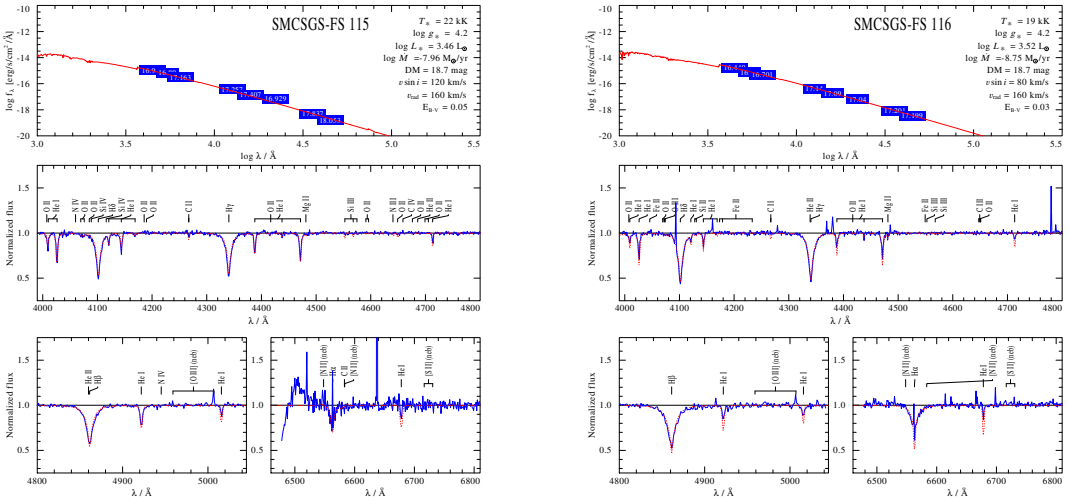

Figure C.39.: Spectral fit for SMCSGS-FS 115 and SMCSGS-FS 116

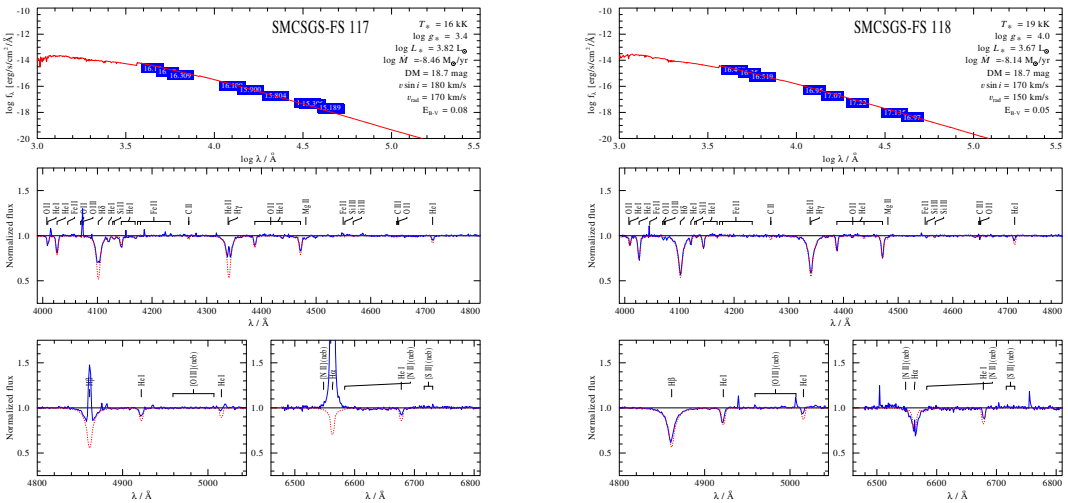

Figure C.40.: Spectral fit for SMCSGS-FS 117 and SMCSGS-FS 118

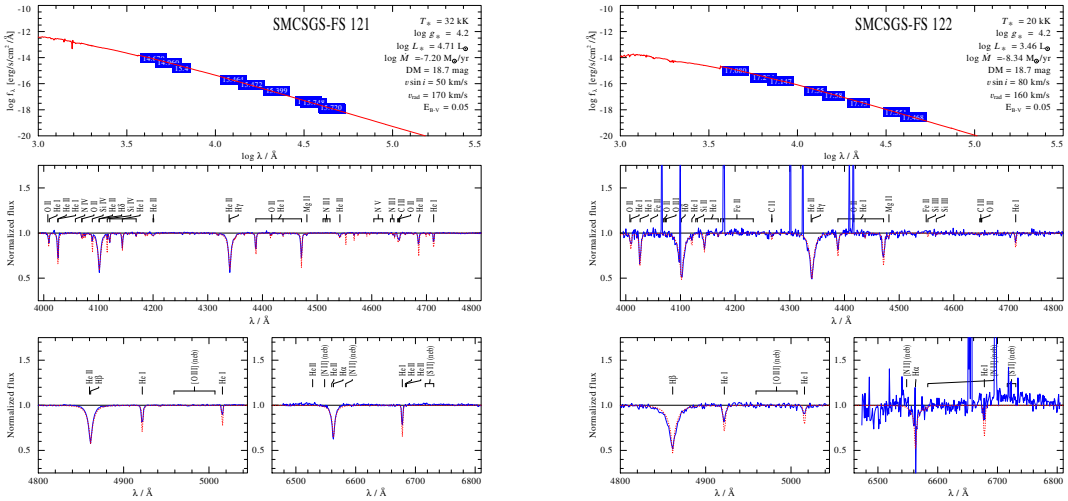

Figure C.41.: Spectral fit for SMCSGS-FS 121 and SMCSGS-FS 122

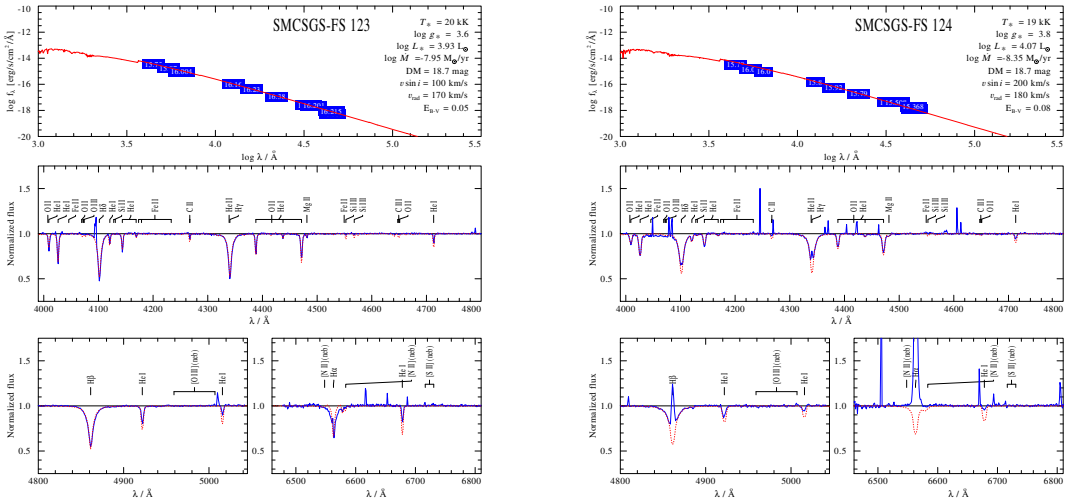

Figure C.42.: Spectral fit for SMCSGS-FS 123 and SMCSGS-FS 124

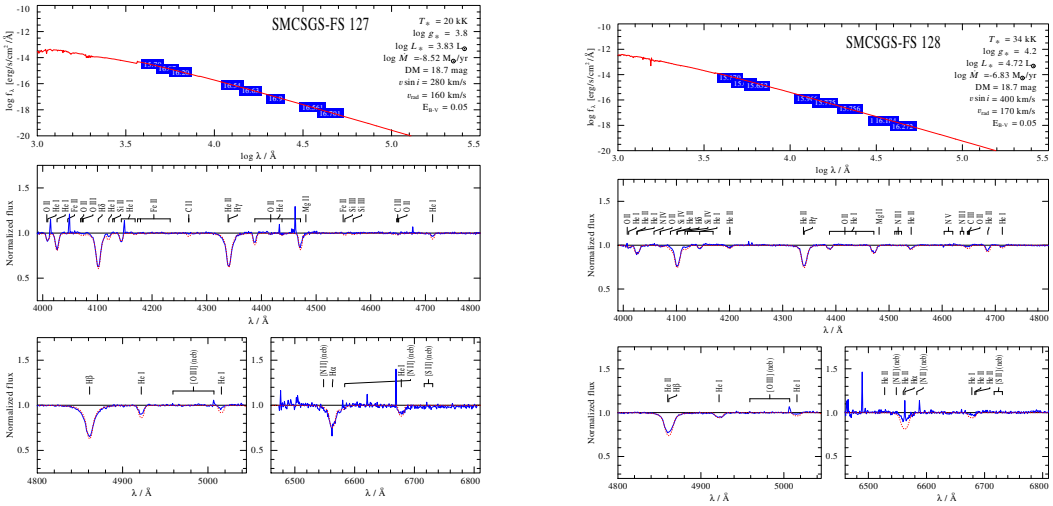

Figure C.43.: Spectral fit for SMCSGS-FS 127 and SMCSGS-FS 128

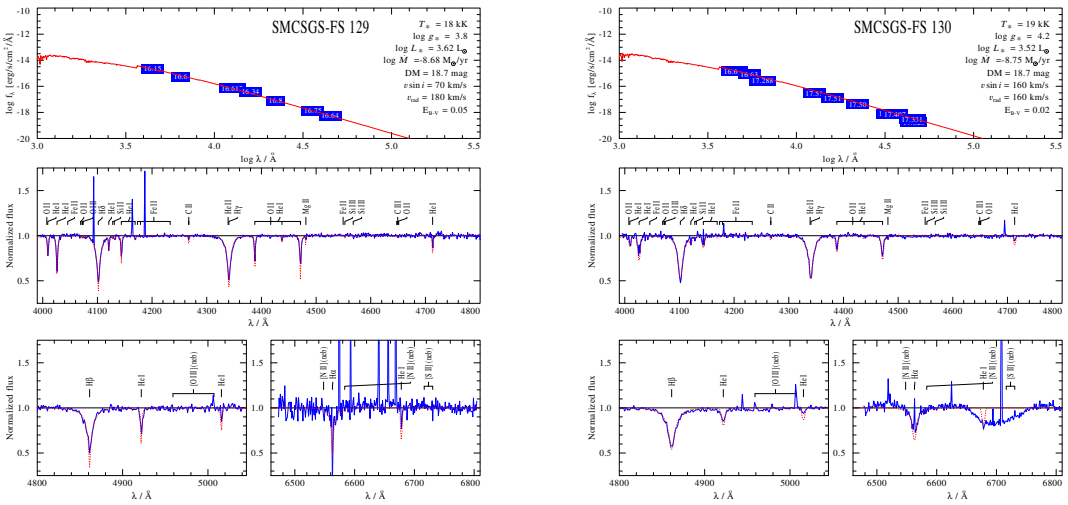

Figure C.44.: Spectral fit for SMCSGS-FS 129 and SMCSGS-FS 130

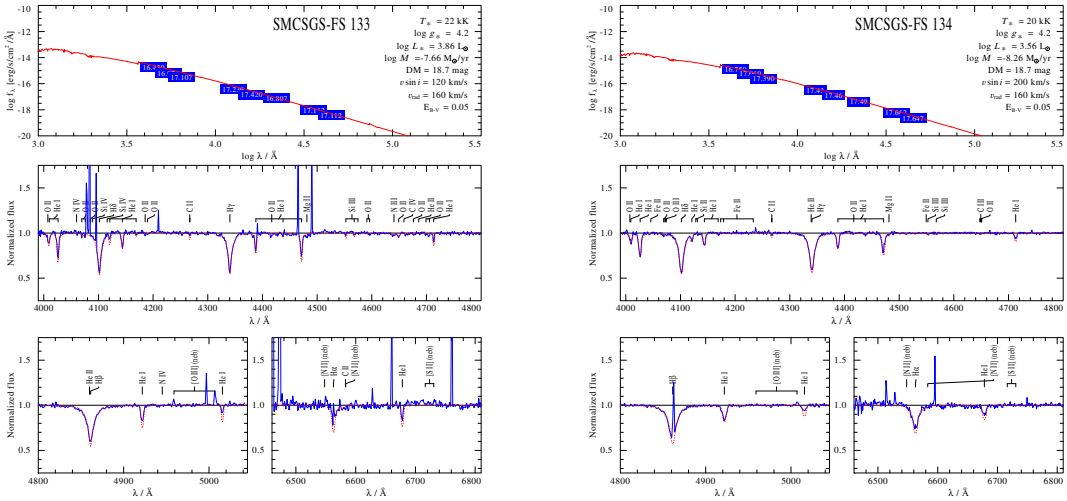

Figure C.45.: Spectral fit for SMCSGS-FS 133 and SMCSGS-FS 134

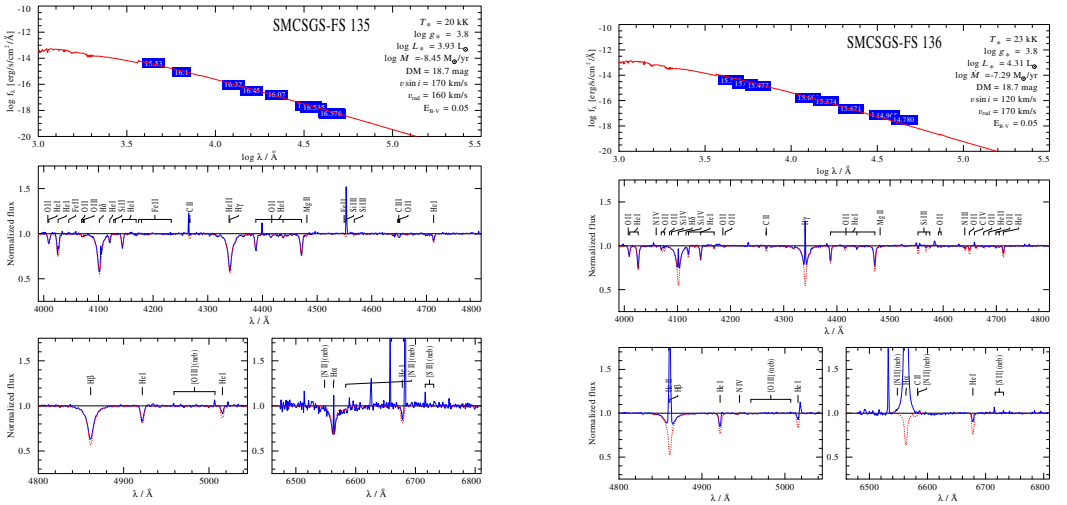

Figure C.46.: Spectral fit for SMCSGS-FS 135 and SMCSGS-FS 136

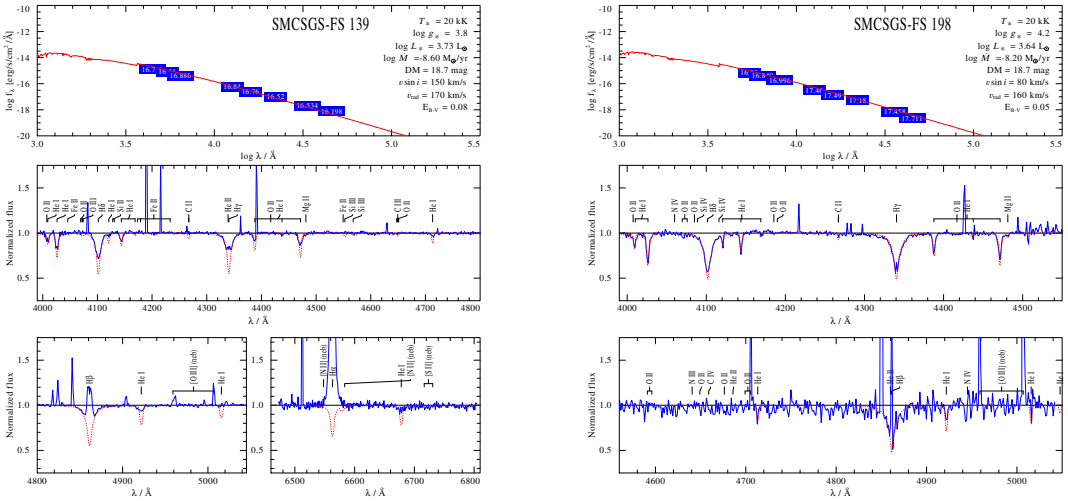

Figure C.47.: Spectral fit for SMCSGS-FS 139 and SMCSGS-FS 140

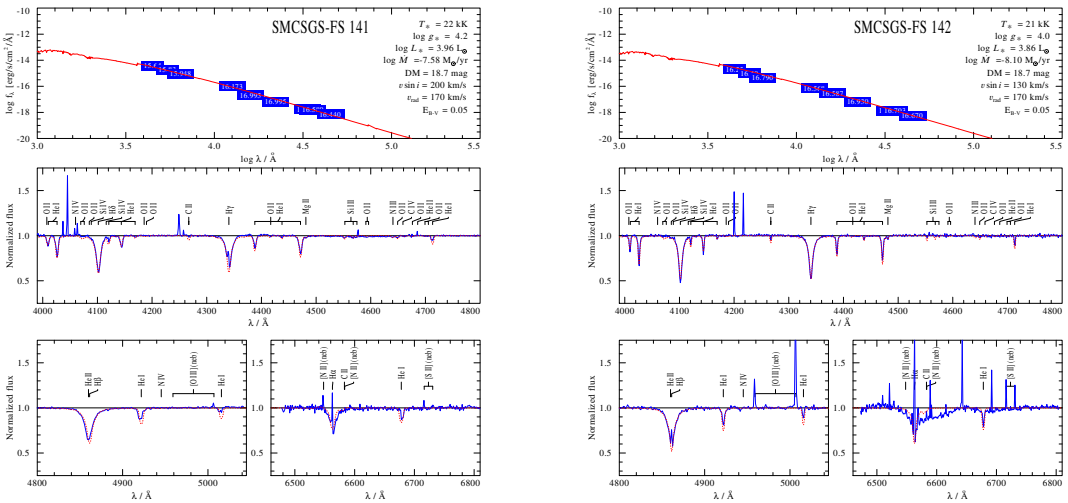

Figure C.48.: Spectral fit for SMCSGS-FS 141 and SMCSGS-FS 142

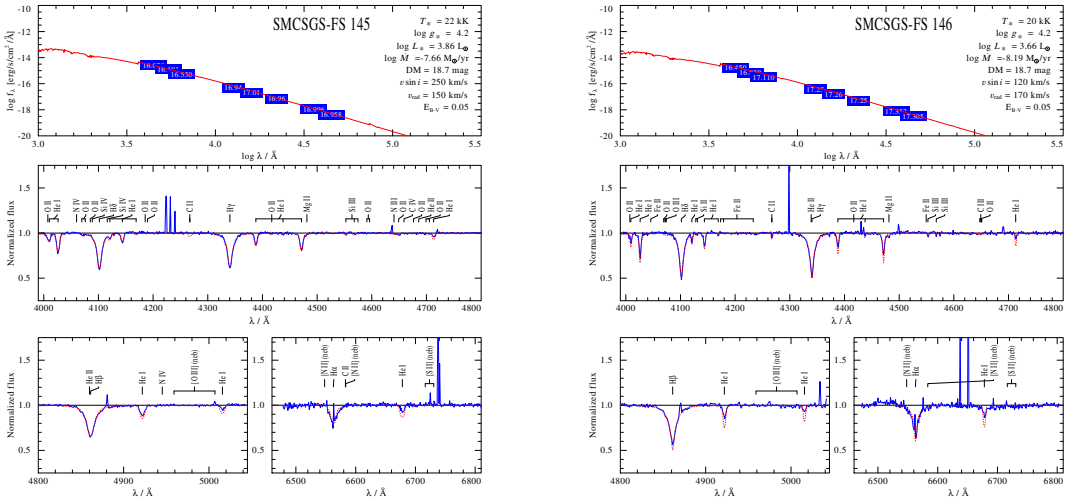

Figure C.49.: Spectral fit for SMCSGS-FS 145 and SMCSGS-FS 146

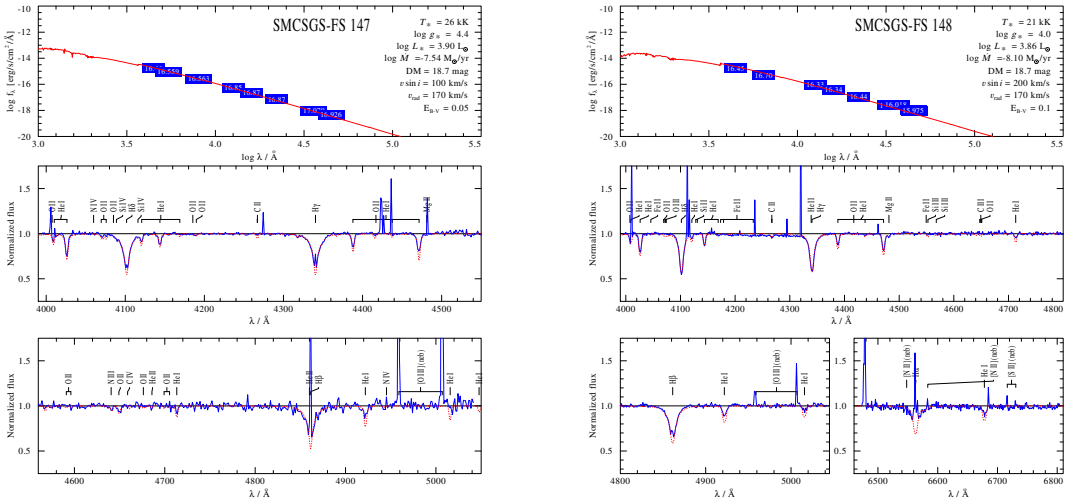

Figure C.50.: Spectral fit for SMCSGS-FS 147 and SMCSGS-FS 148

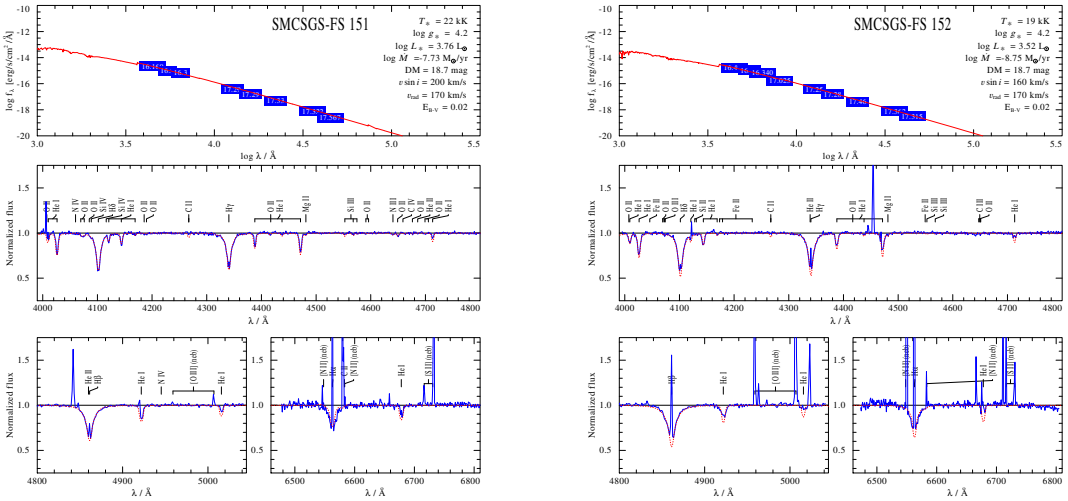

Figure C.51.: Spectral fit for SMCSGS-FS 151 and SMCSGS-FS 152

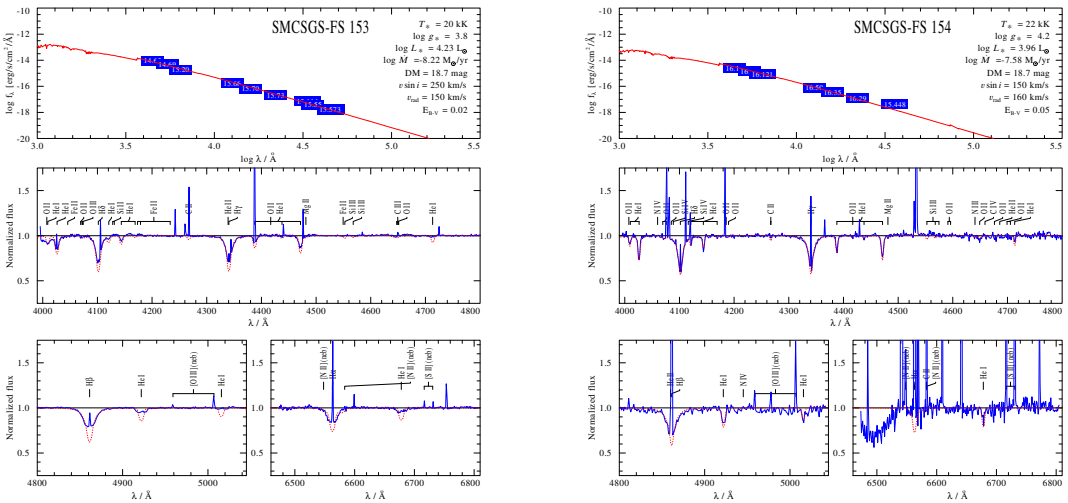

Figure C.52.: Spectral fit for SMCSGS-FS 153 and SMCSGS-FS 154

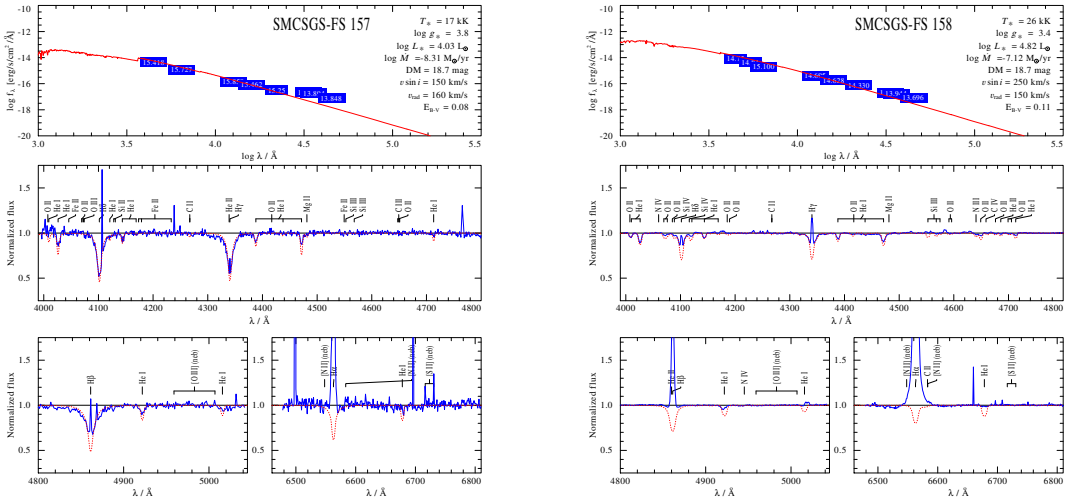

Figure C.53.: Spectral fit for SMCSGS-FS 157 and SMCSGS-FS 158

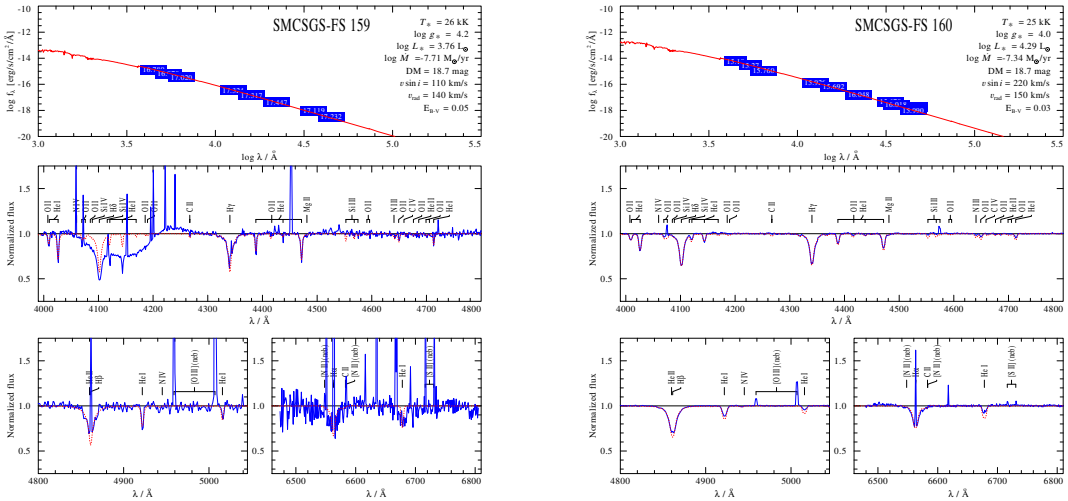

Figure C.54.: Spectral fit for SMCSGS-FS 159 and SMCSGS-FS 160

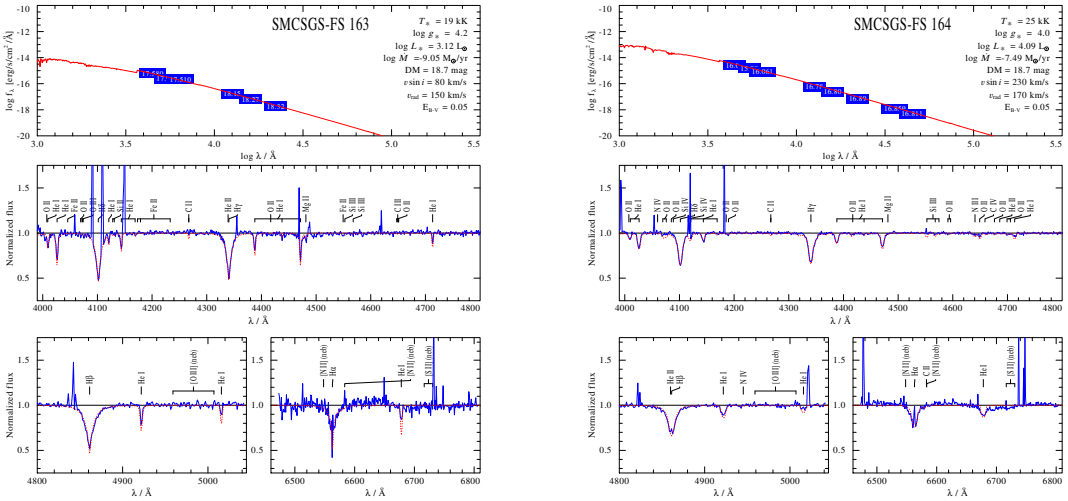

Figure C.55.: Spectral fit for SMCSGS-FS 163 and SMCSGS-FS 164

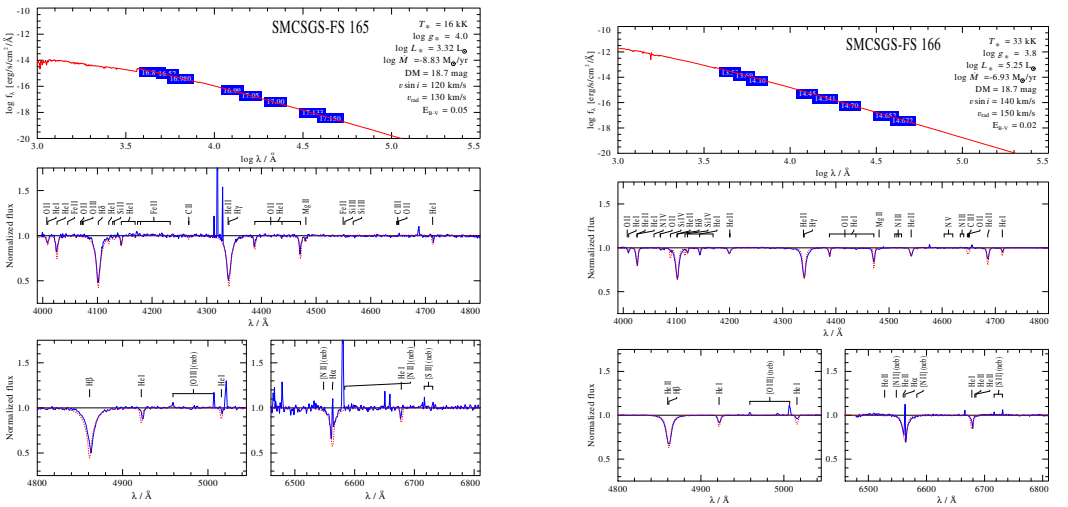

Figure C.56.: Spectral fit for SMCSGS-FS 165 and SMCSGS-FS 166

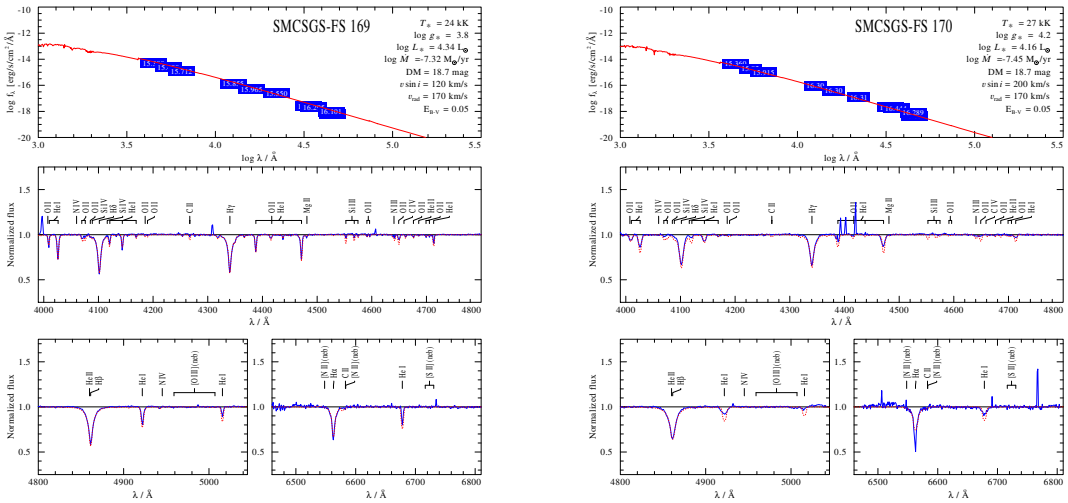

Figure C.57.: Spectral fit for SMCSGS-FS 169 and SMCSGS-FS 170

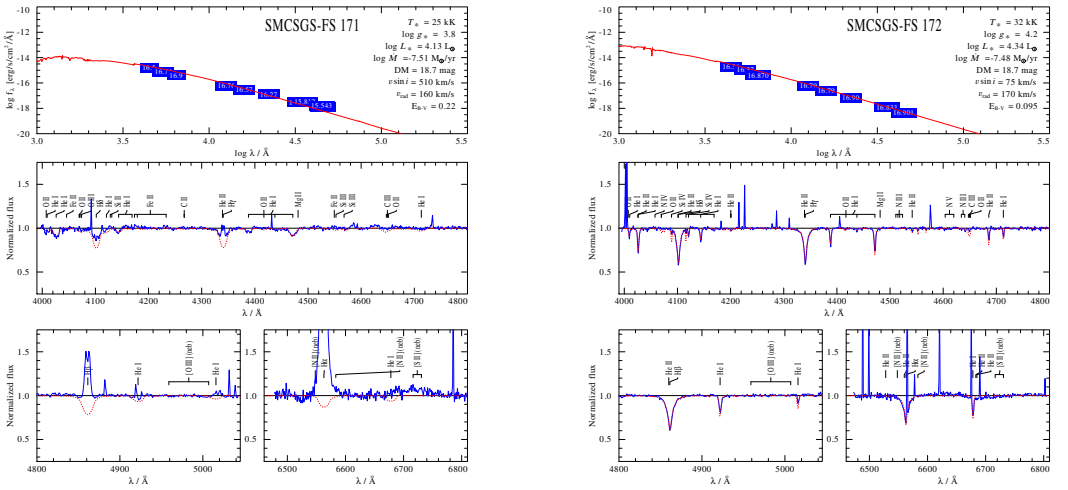

Figure C.58.: Spectral fit for SMCSGS-FS 171 and SMCSGS-FS 172

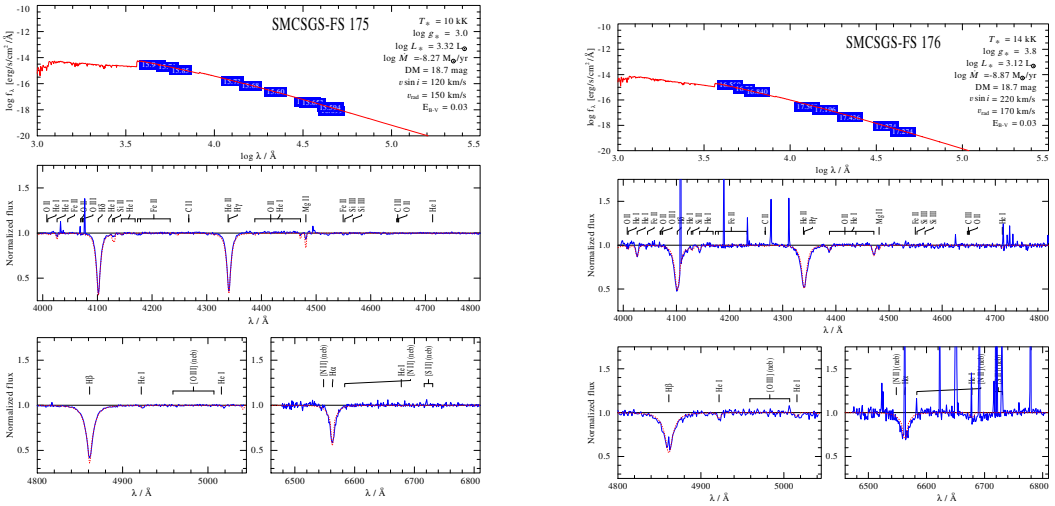

Figure C.59.: Spectral fit for SMCSGS-FS 175 and SMCSGS-FS 176

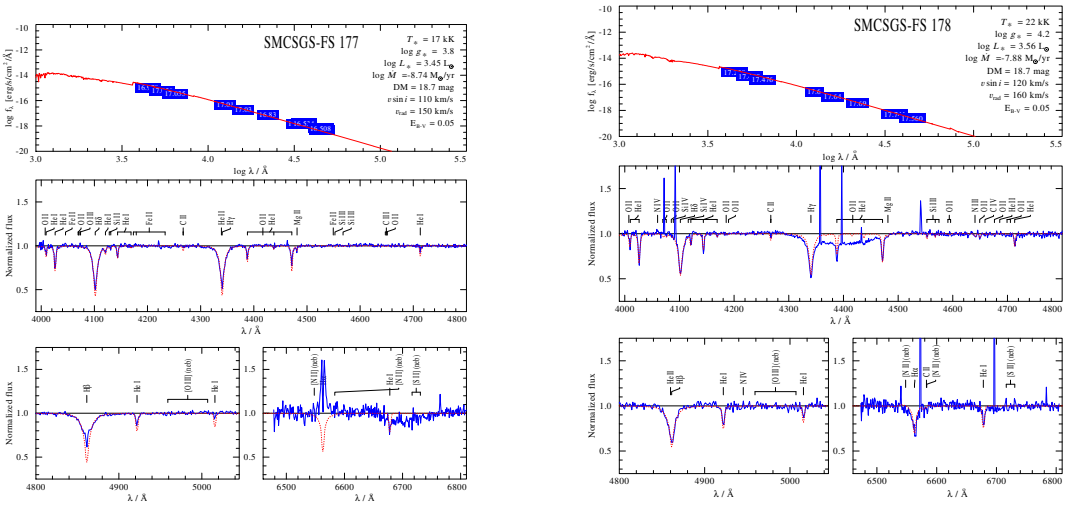

Figure C.60.: Spectral fit for SMCSGS-FS 177 and SMCSGS-FS 178

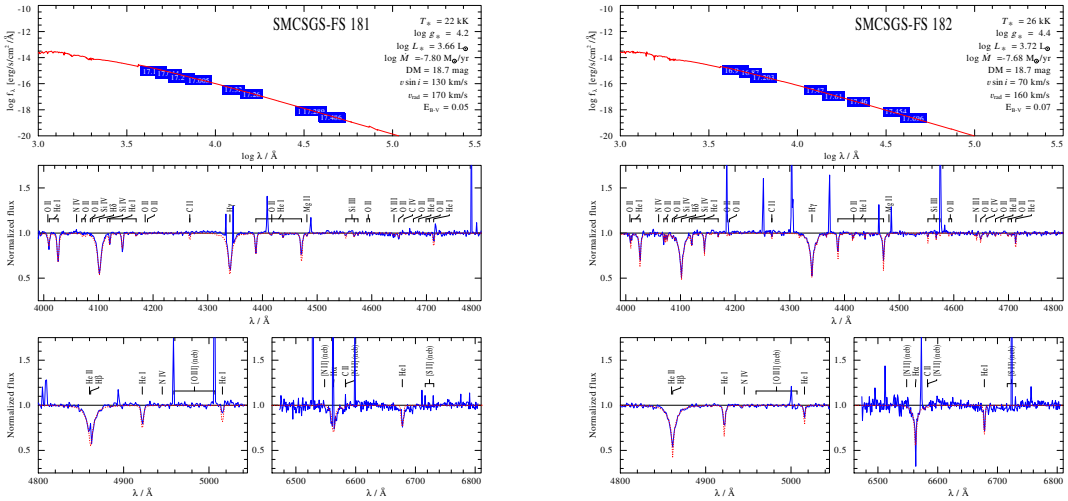

Figure C.61.: Spectral fit for SMCSGS-FS 181 and SMCSGS-FS 182

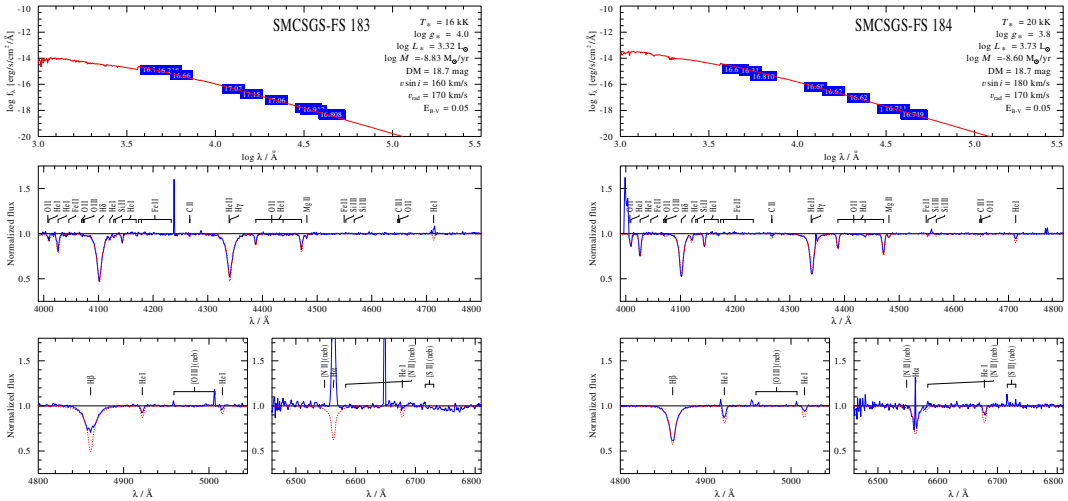

Figure C.62.: Spectral fit for SMCSGS-FS 183 and SMCSGS-FS 184

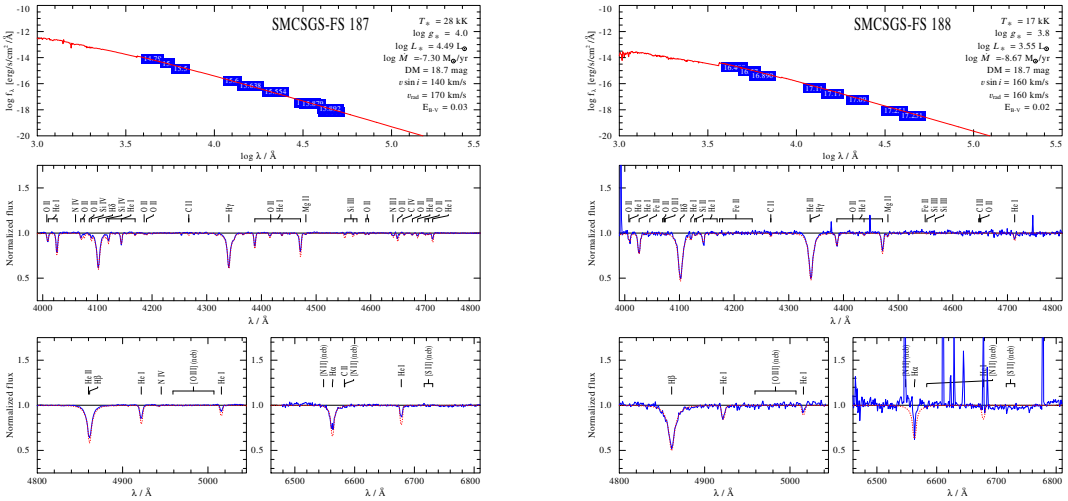

Figure C.63.: Spectral fit for SMCSGS-FS 187 and SMCSGS-FS 188

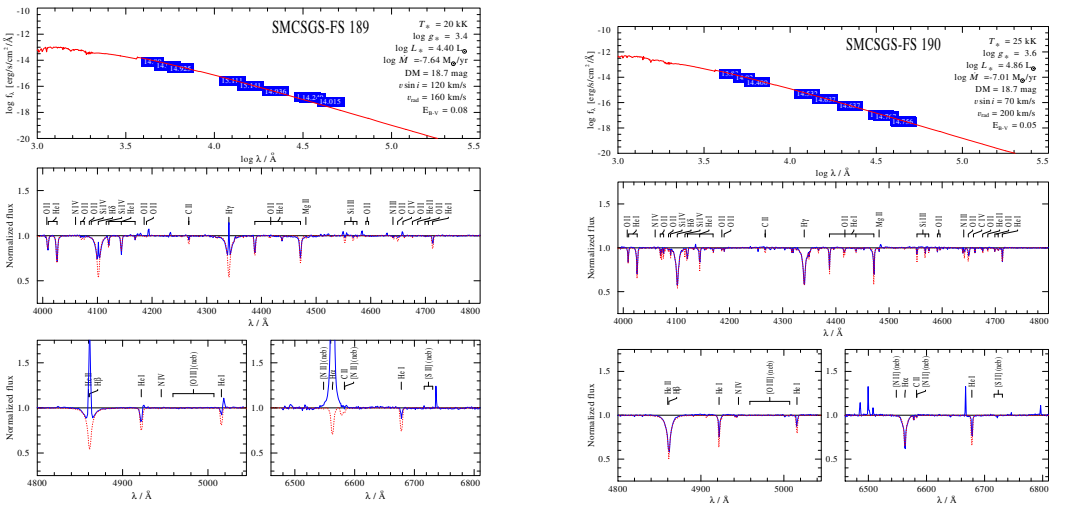

Figure C.64.: Spectral fit for SMCSGS-FS 189 and SMCSGS-FS 190

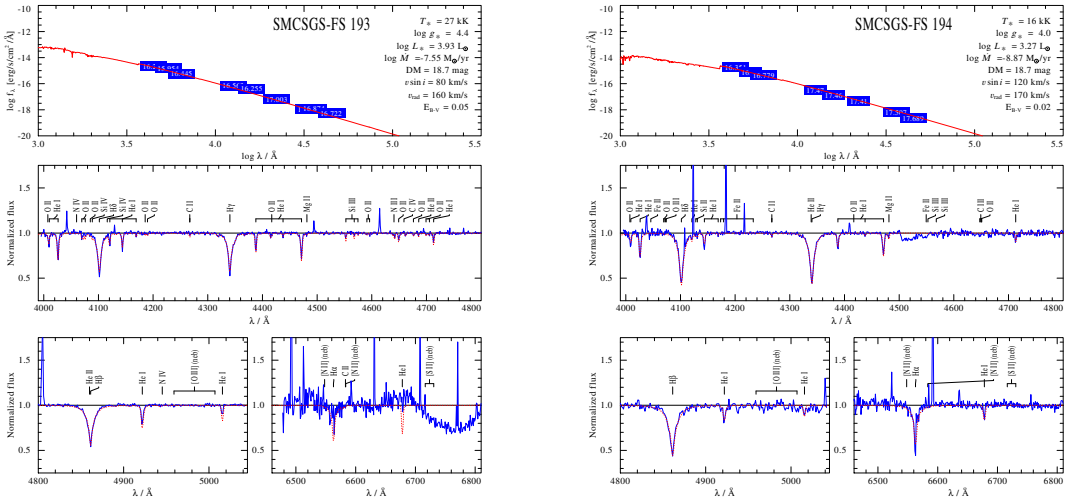

Figure C.65.: Spectral fit for SMCSGS-FS 193 and SMCSGS-FS 194

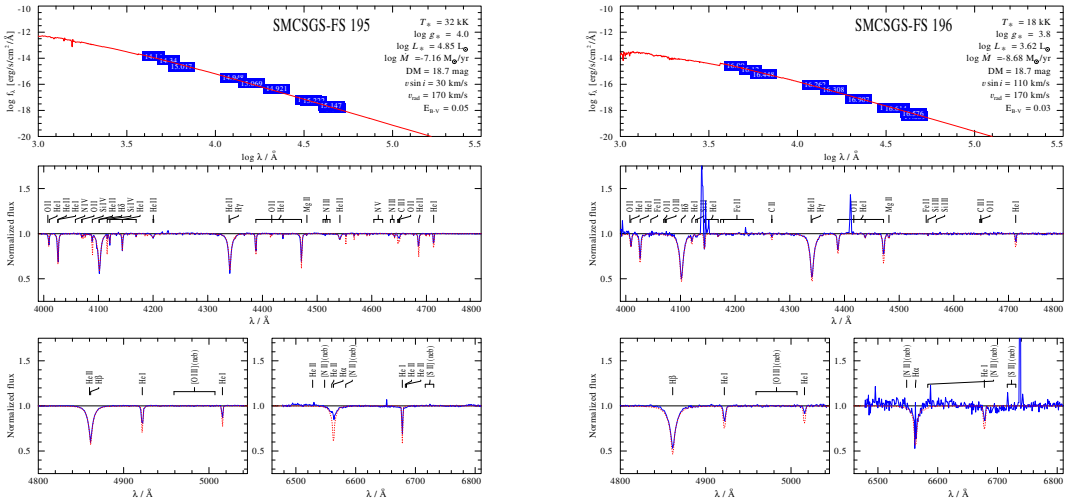

Figure C.66.: Spectral fit for SMCSGS-FS 195 and SMCSGS-FS 196

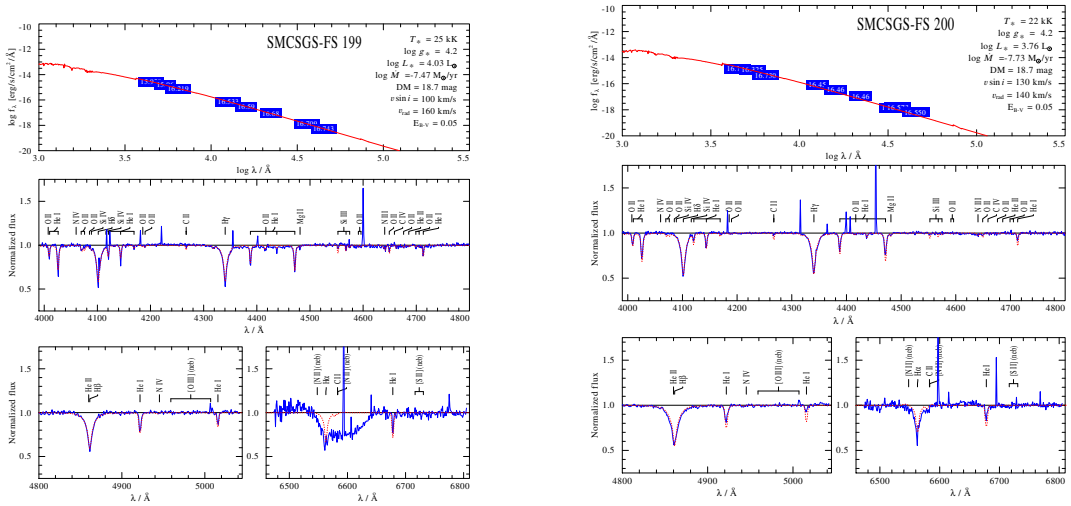

Figure C.67.: Spectral fit for SMCSGS-FS 199 and SMCSGS-FS 200

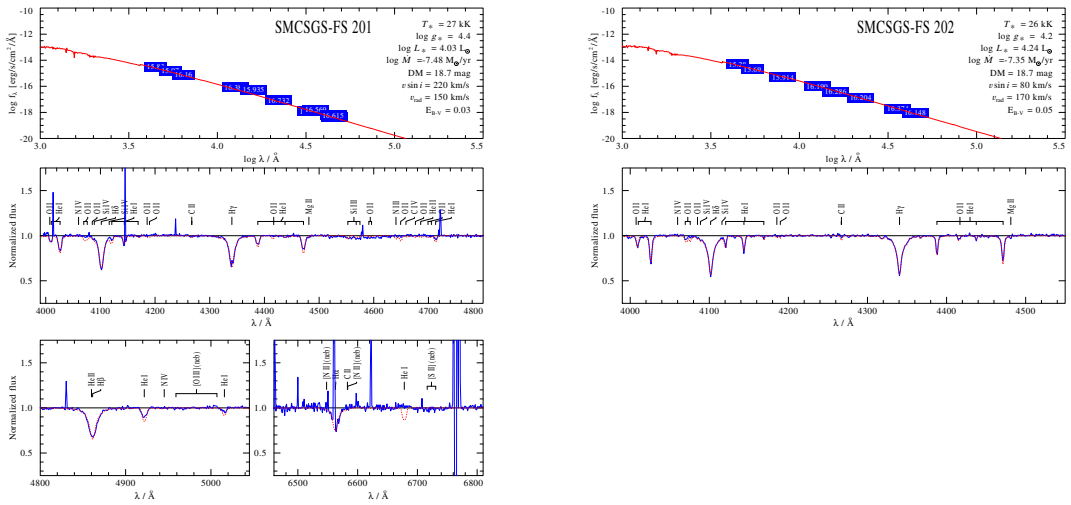

Figure C.68.: Spectral fit for SMCSGS-FS 201 and SMCSGS-FS 202

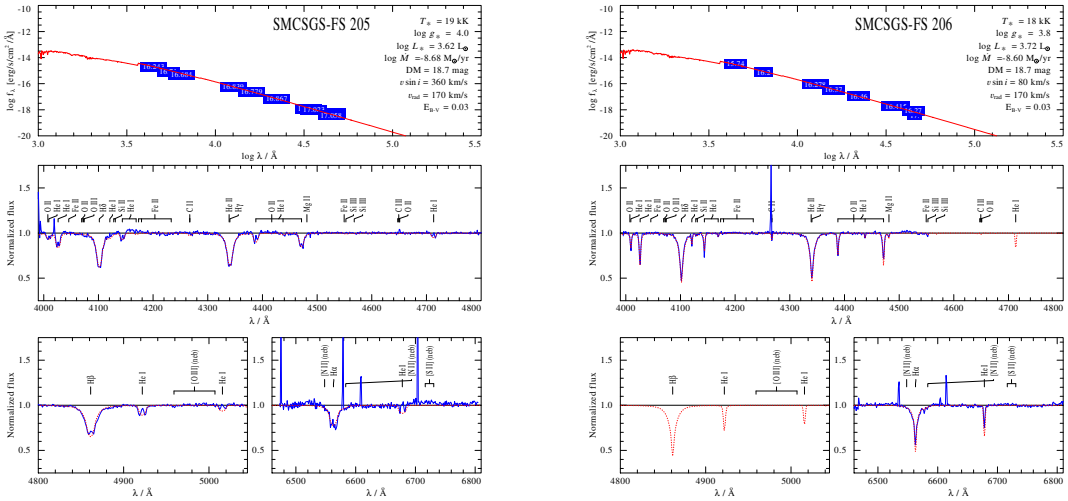

Figure C.69.: Spectral fit for SMCSGS-FS 205 and SMCSGS-FS 206

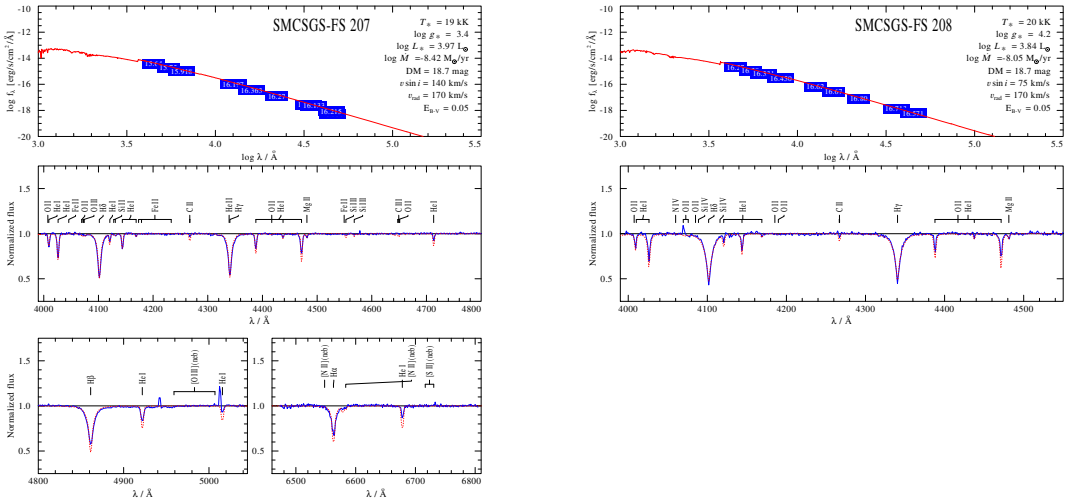

Figure C.70.: Spectral fit for SMCSGS-FS 207 and SMCSGS-FS 208

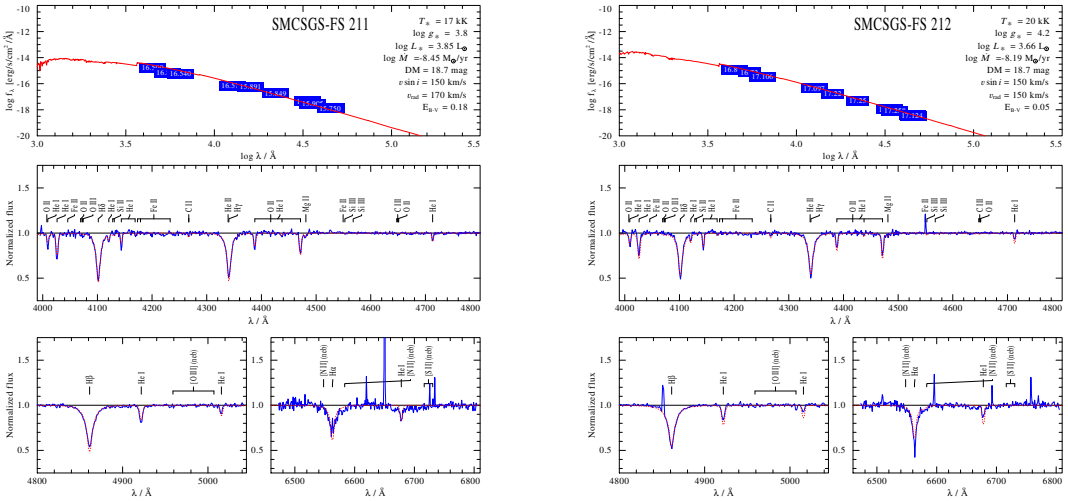

Figure C.71.: Spectral fit for SMCSGS-FS 211 and SMCSGS-FS 212

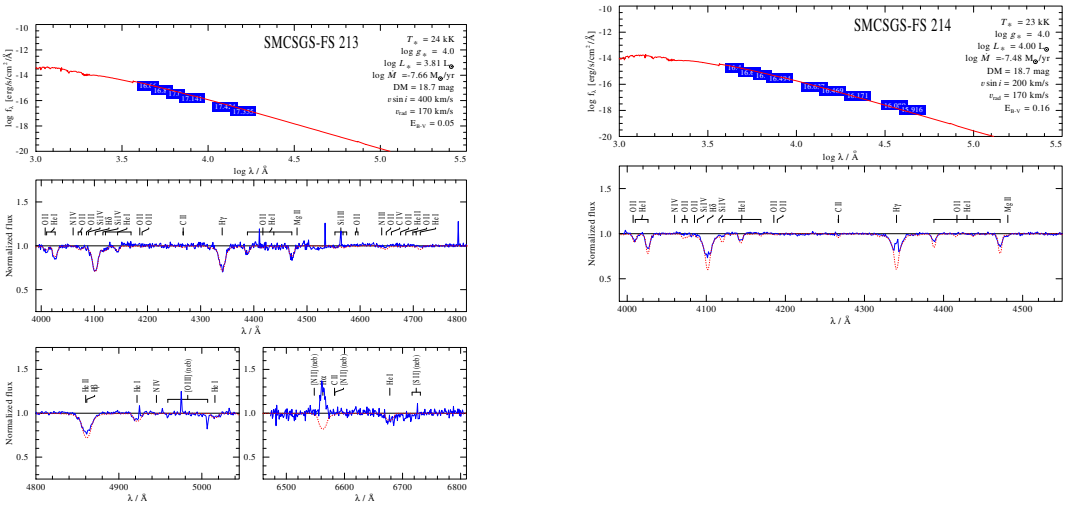

Figure C.72.: Spectral fit for SMCSGS-FS 213 and SMCSGS-FS 214

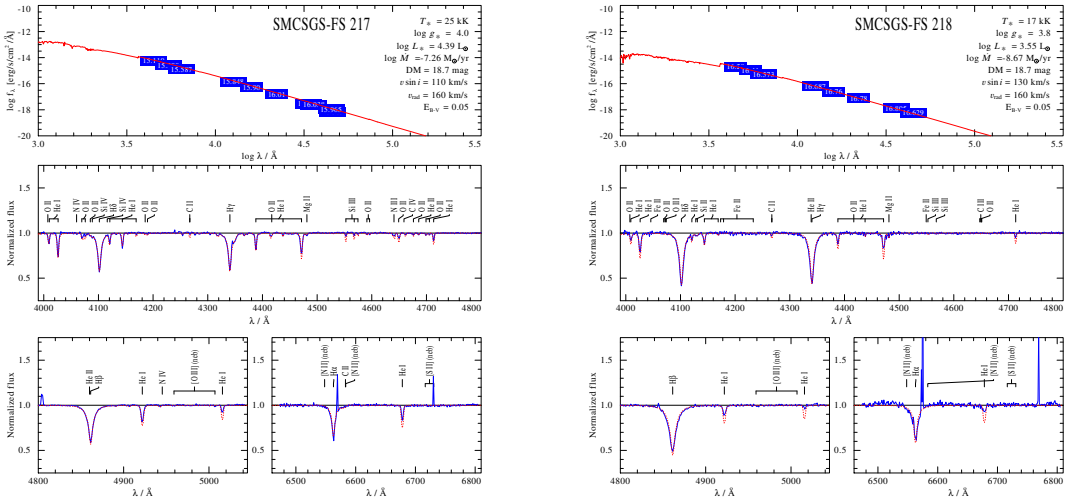

Figure C.73.: Spectral fit for SMCSGS-FS 217 and SMCSGS-FS 218

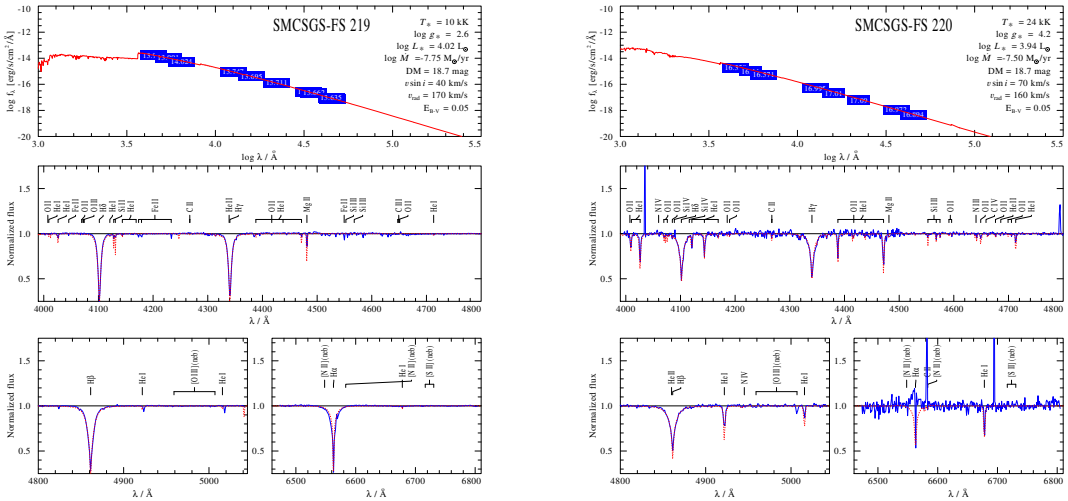

Figure C.74.: Spectral fit for SMCSGS-FS 219 and SMCSGS-FS 220

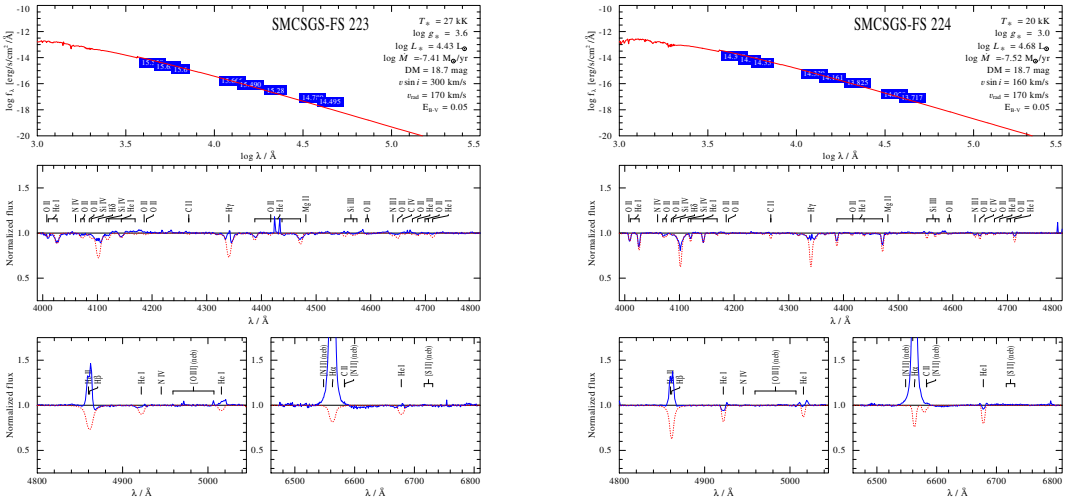

Figure C.75.: Spectral fit for SMCSGS-FS 223 and SMCSGS-FS 224

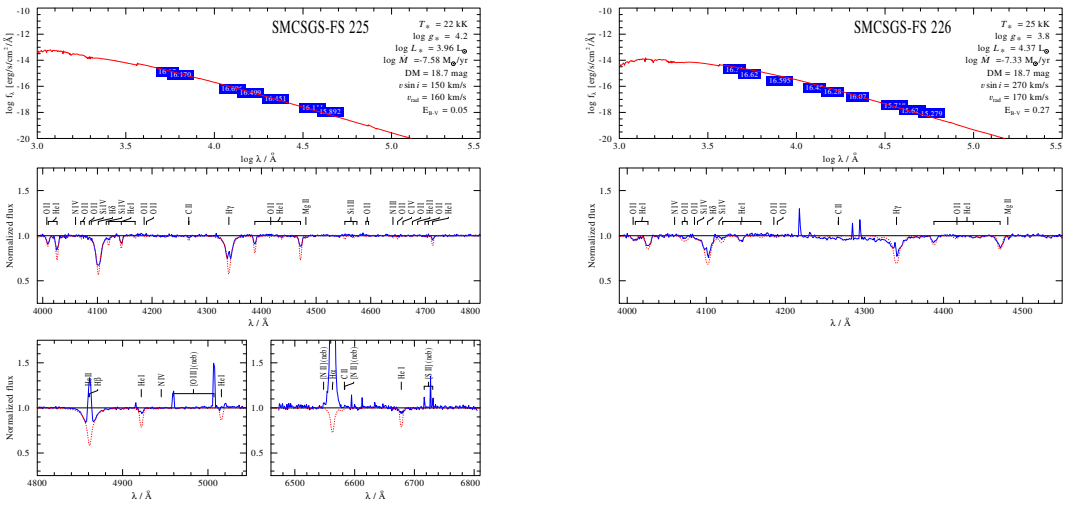

Figure C.76.: Spectral fit for SMCSGS-FS 225 and SMCSGS-FS 226

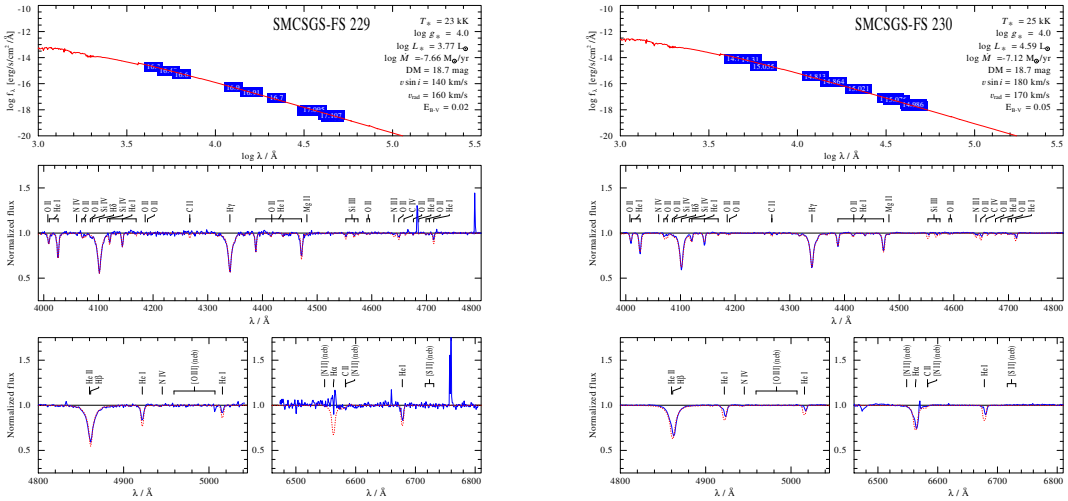

Figure C.77.: Spectral fit for SMCSGS-FS 229 and SMCSGS-FS 230

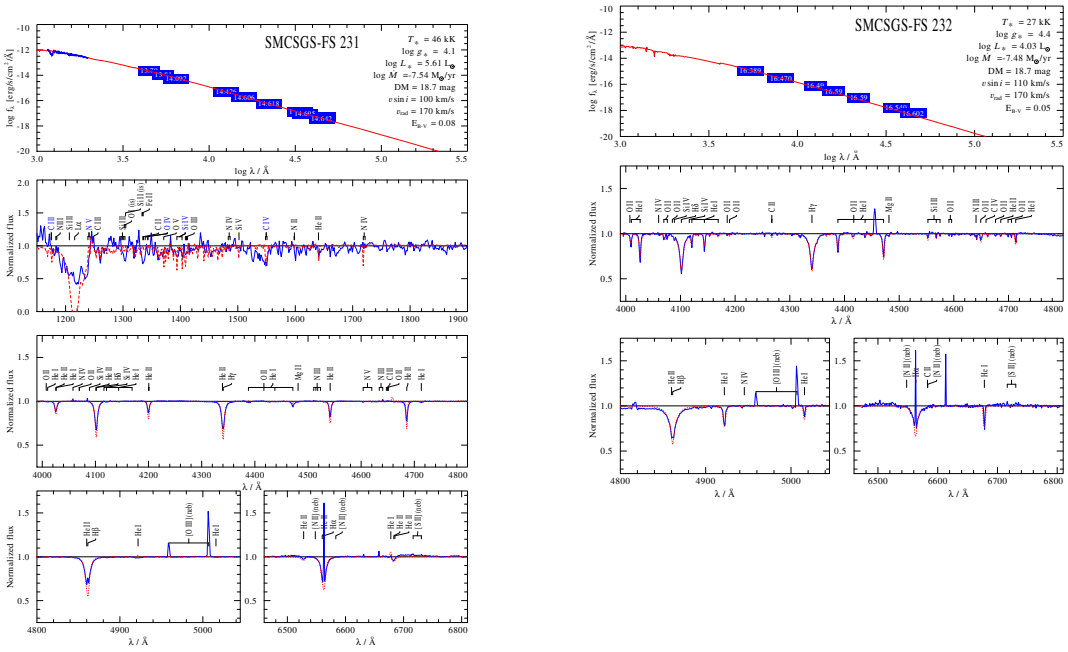

Figure C.78.: Spectral fit for SMCSGS-FS 231 and SMCSGS-FS 232

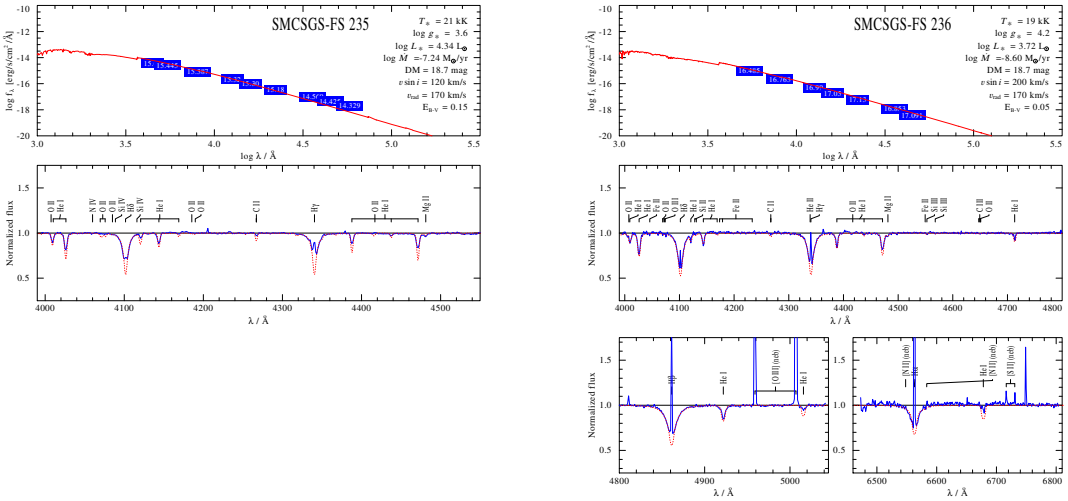

Figure C.79.: Spectral fit for SMCSGS-FS 235 and SMCSGS-FS 236

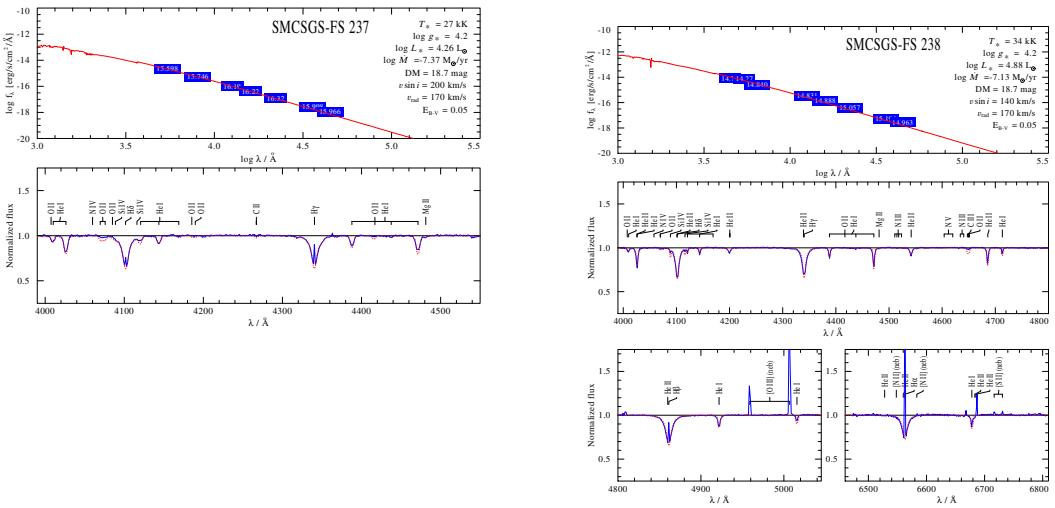

Figure C.80.: Spectral fit for SMCSGS-FS 237 and SMCSGS-FS 238

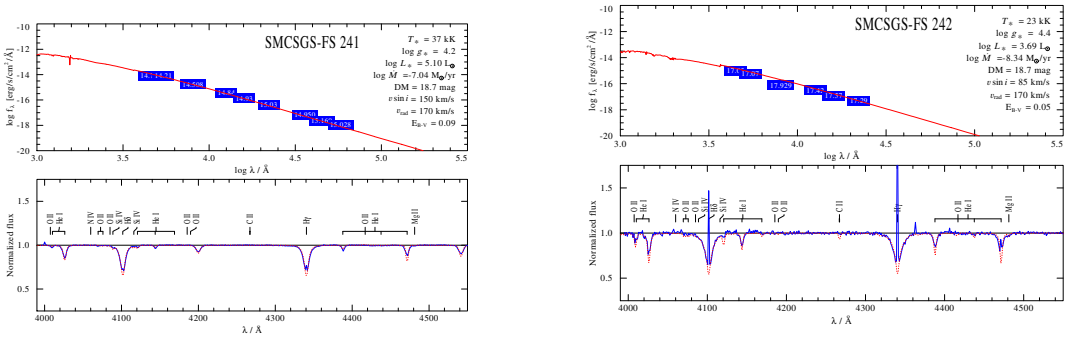

Figure C.81.: Spectral fit for SMCSGS-FS 241 and SMCSGS-FS 242

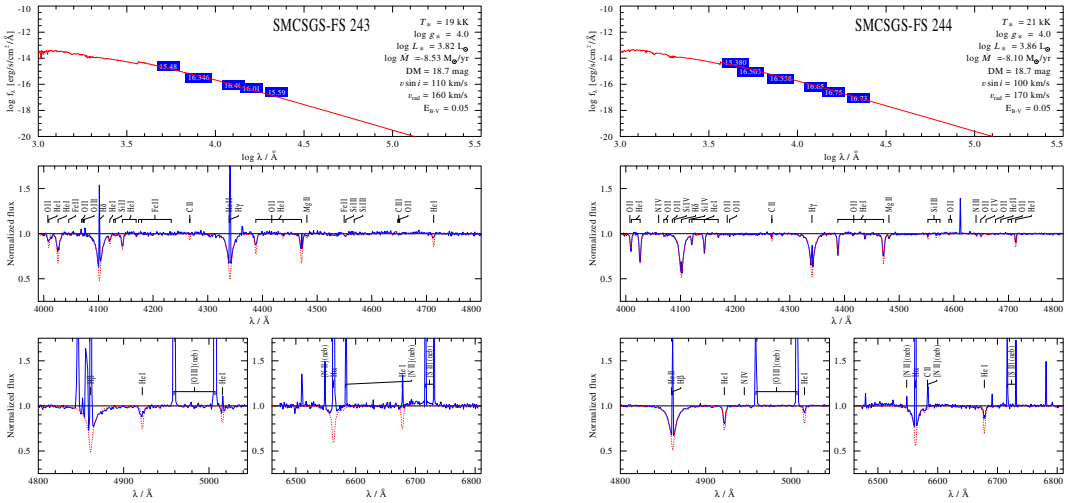

Figure C.82.: Spectral fit for SMCSGS-FS 243 and SMCSGS-FS 244

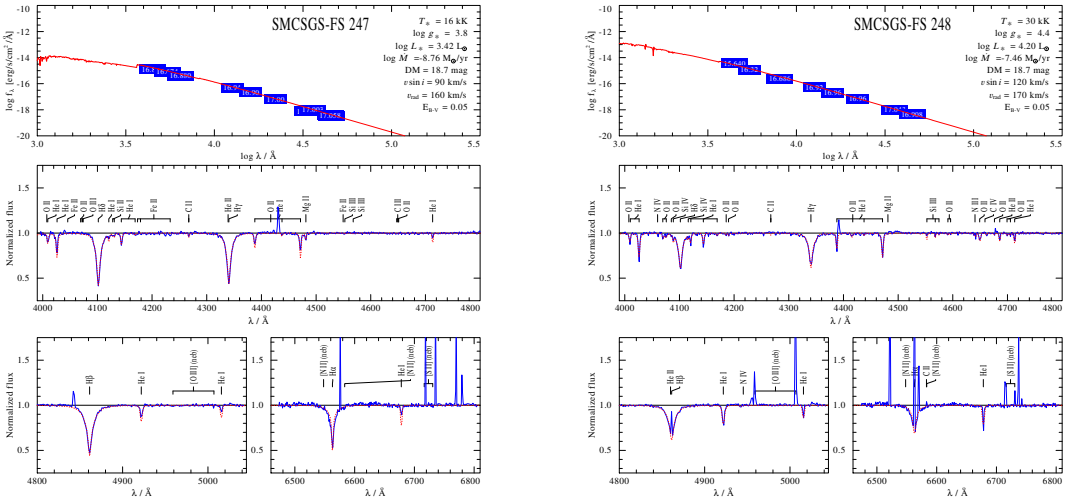

Figure C.83.: Spectral fit for SMCSGS-FS 247 and SMCSGS-FS 248

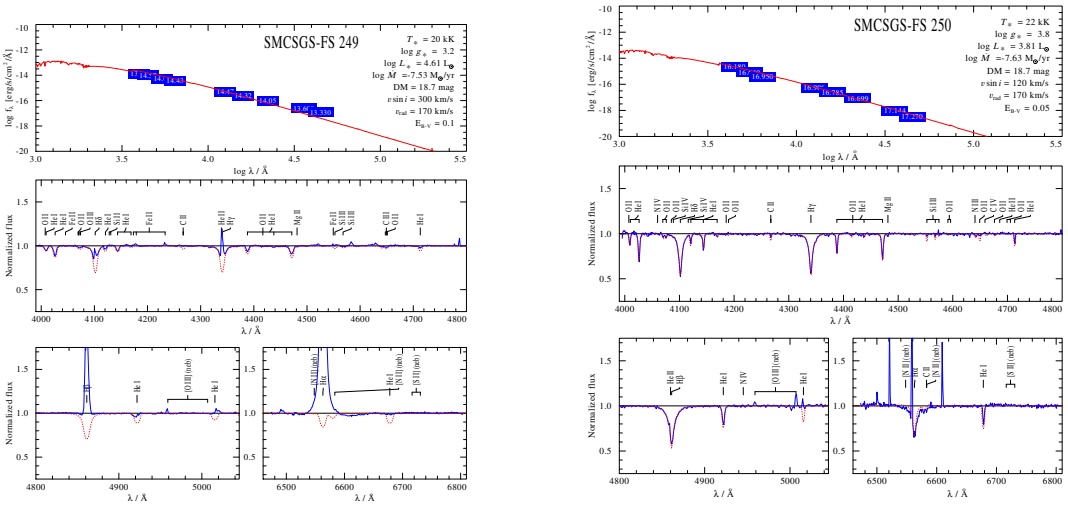

Figure C.84.: Spectral fit for SMCSGS-FS 249 and SMCSGS-FS 250

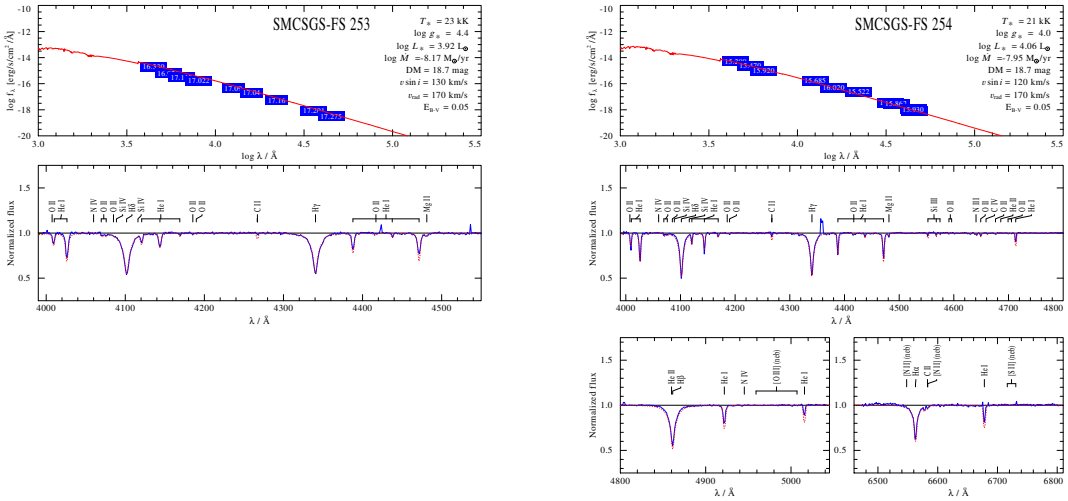

Figure C.85.: Spectral fit for SMCSGS-FS 253 and SMCSGS-FS 254

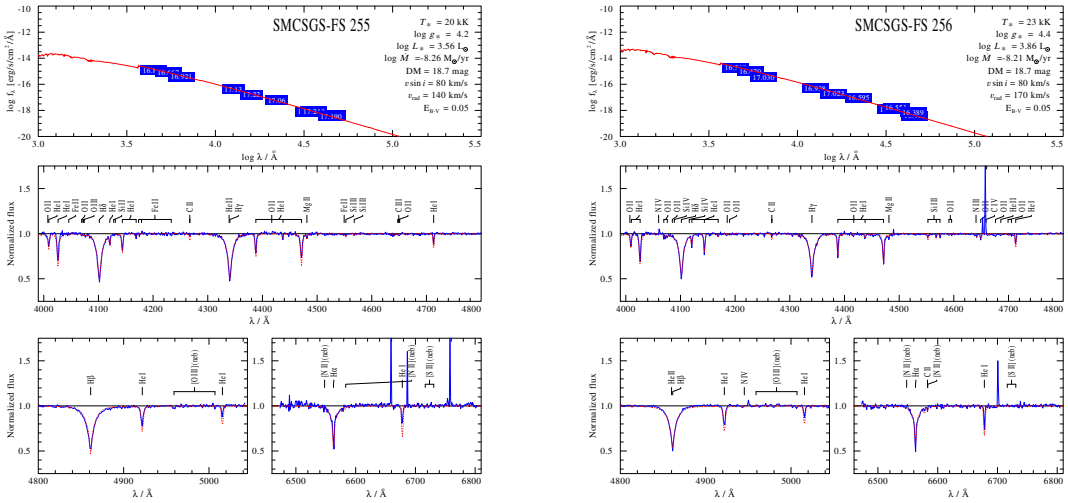

Figure C.86.: Spectral fit for SMCSGS-FS 255 and SMCSGS-FS 256

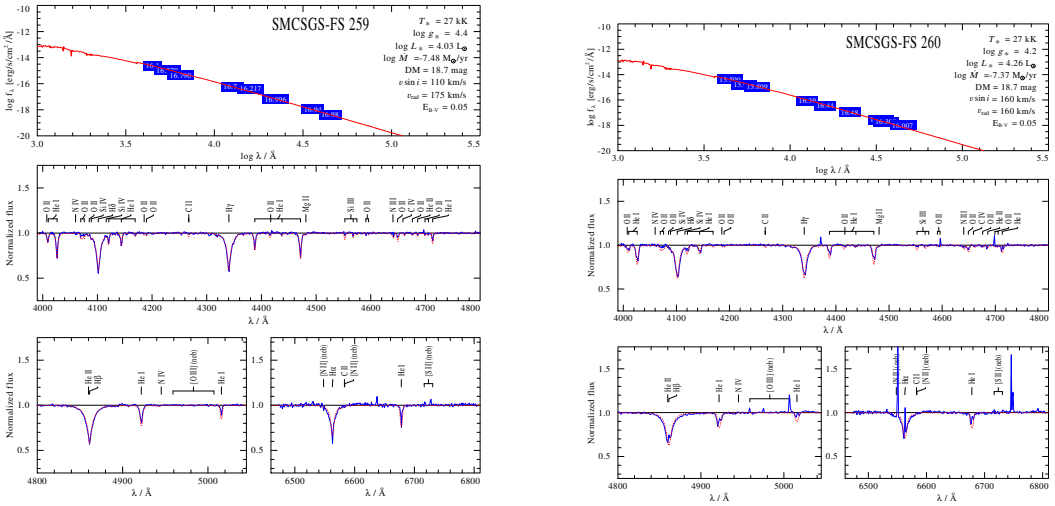

Figure C.87.: Spectral fit for SMCSGS-FS 259 and SMCSGS-FS 260

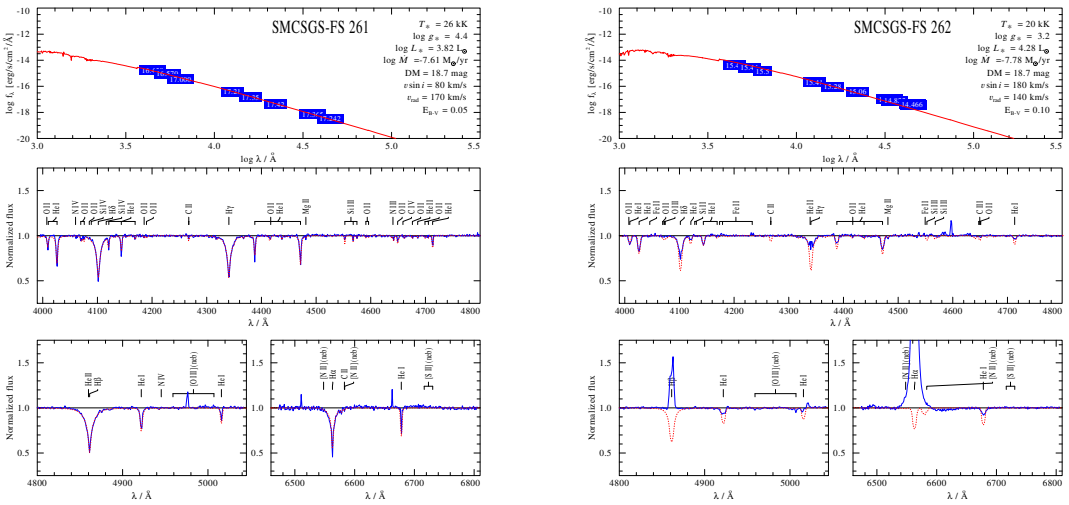

Figure C.88.: Spectral fit for SMCSGS-FS 261 and SMCSGS-FS 262

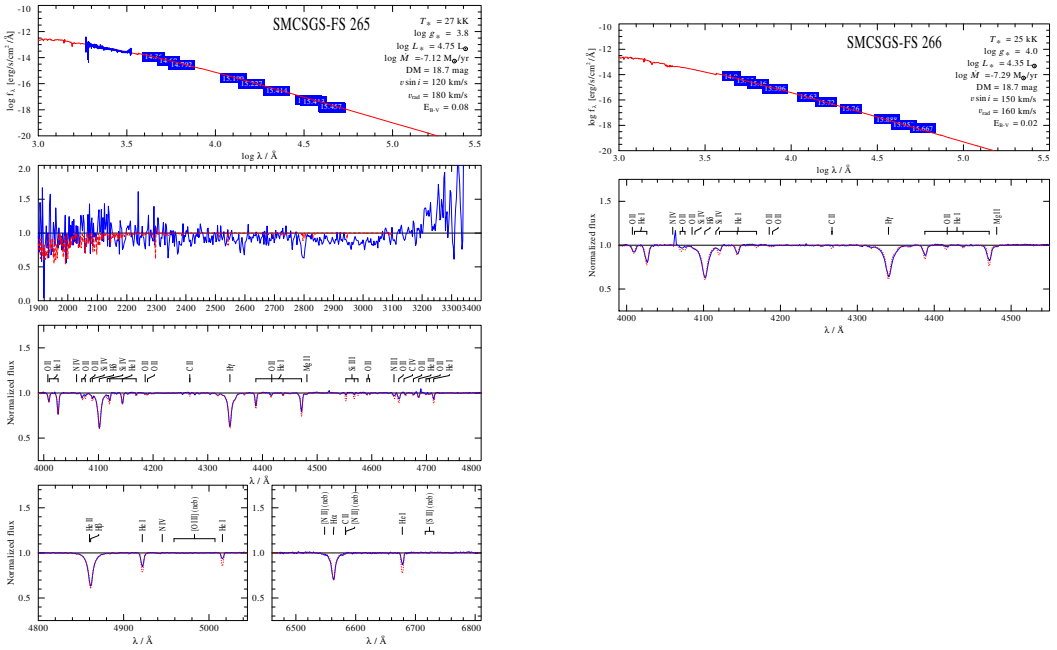

Figure C.89.: Spectral fit for SMCSGS-FS 265 and SMCSGS-FS 266

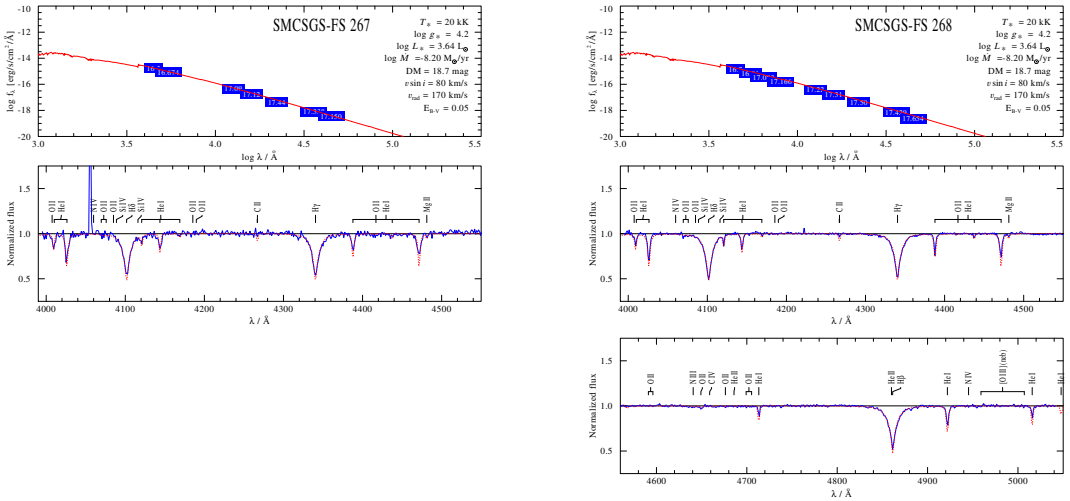

Figure C.90.: Spectral fit for SMCSGS-FS 267 and SMCSGS-FS 268

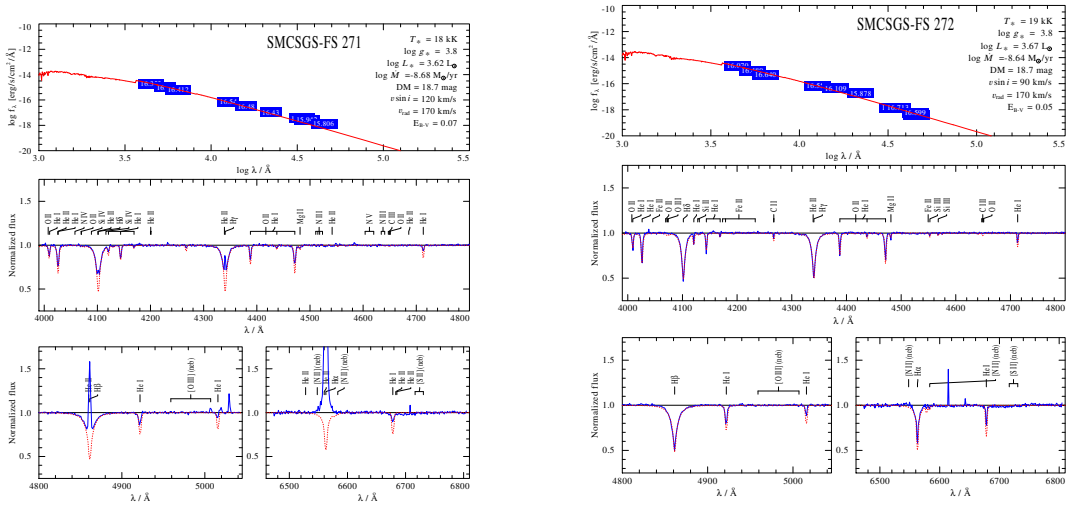

Figure C.91.: Spectral fit for SMCSGS-FS 271 and SMCSGS-FS 272

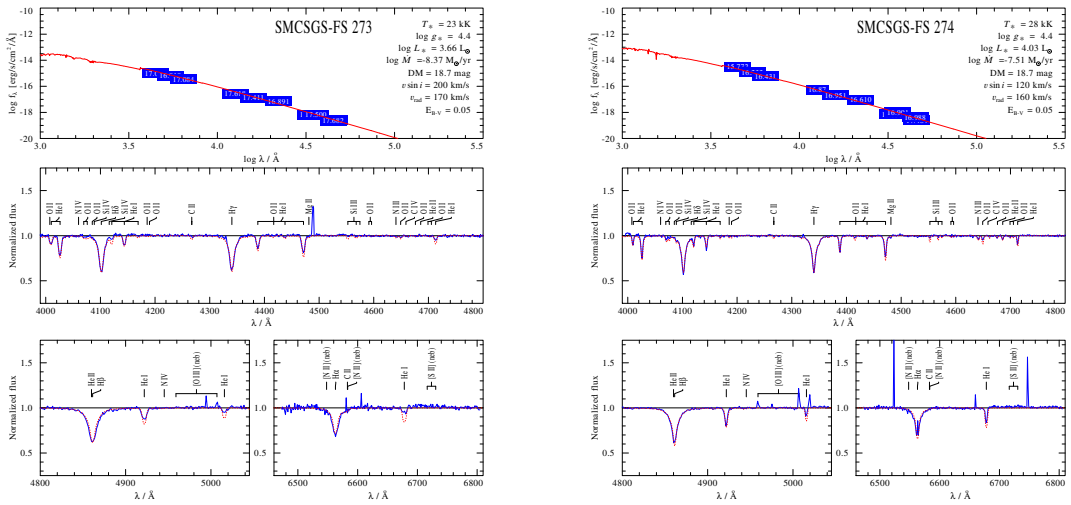

Figure C.92.: Spectral fit for SMCSGS-FS 273 and SMCSGS-FS 274

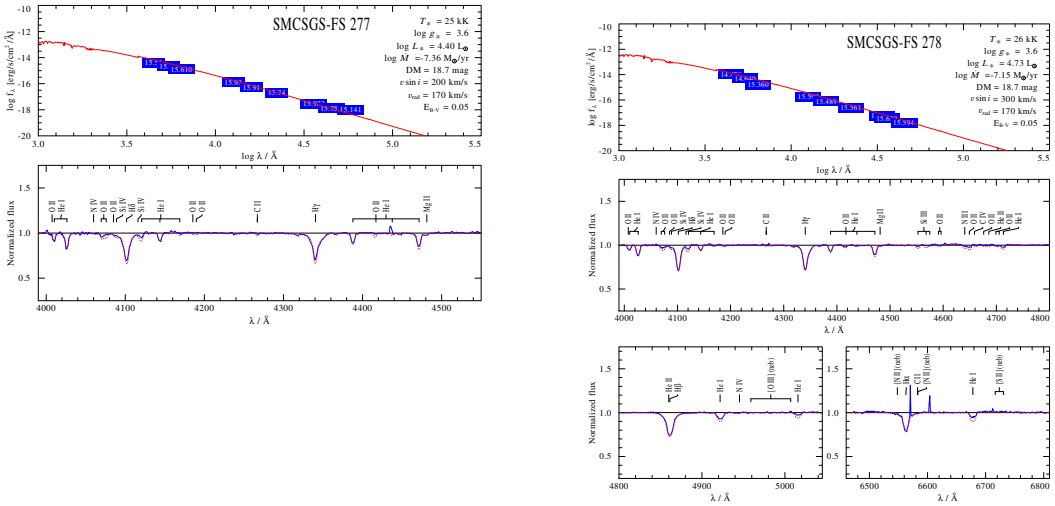

Figure C.93.: Spectral fit for SMCSGS-FS 277 and SMCSGS-FS 278

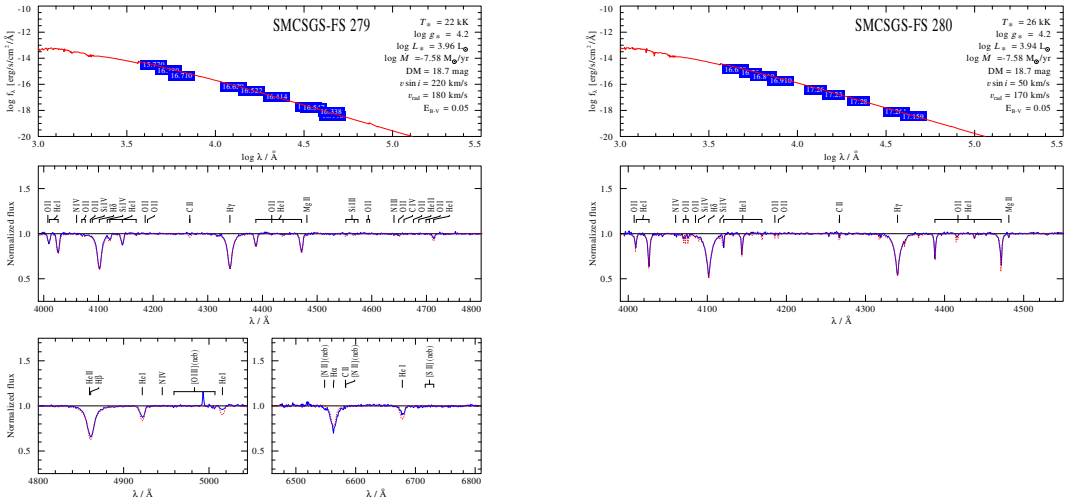

Figure C.94.: Spectral fit for SMCSGS-FS 279 and SMCSGS-FS 280

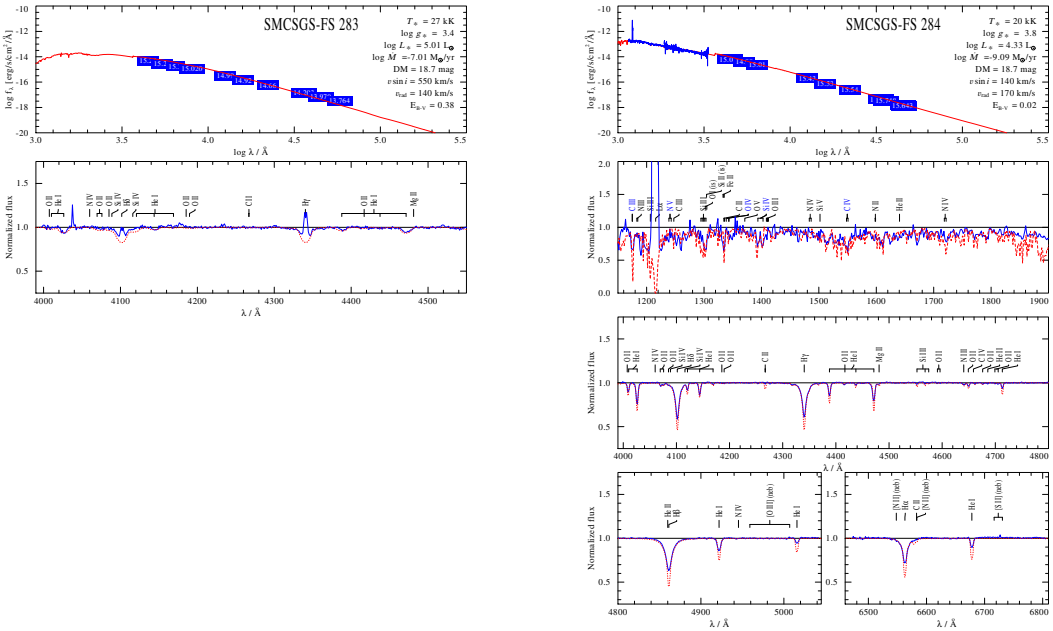

Figure C.95.: Spectral fit for SMCSGS-FS 283 and SMCSGS-FS 284

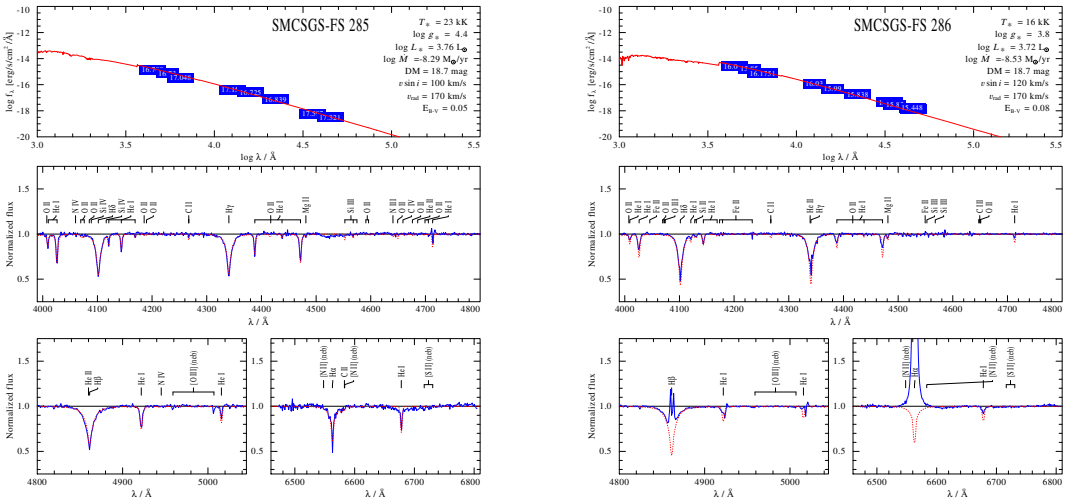

Figure C.96.: Spectral fit for SMCSGS-FS 285 and SMCSGS-FS 286

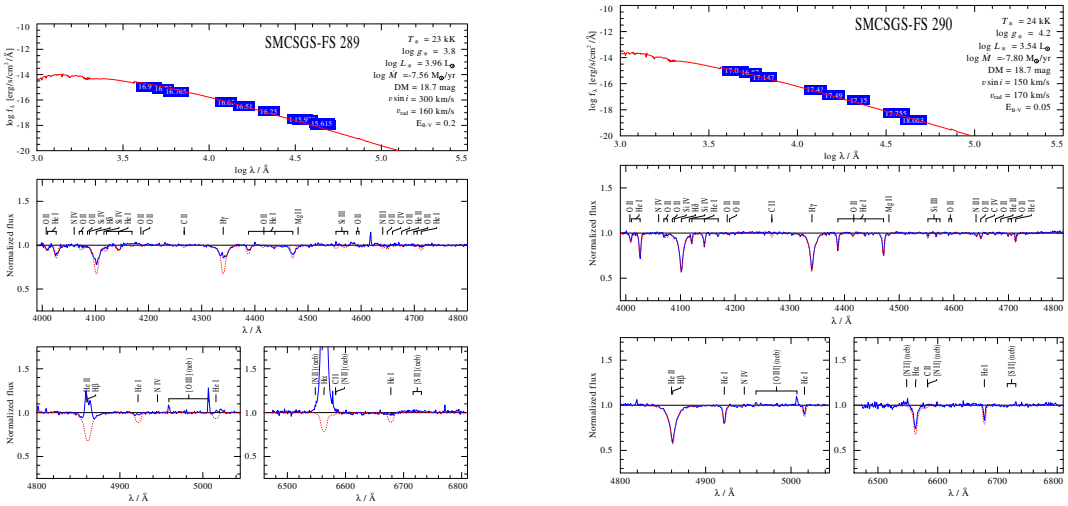

Figure C.97.: Spectral fit for SMCSGS-FS 289 and SMCSGS-FS 290

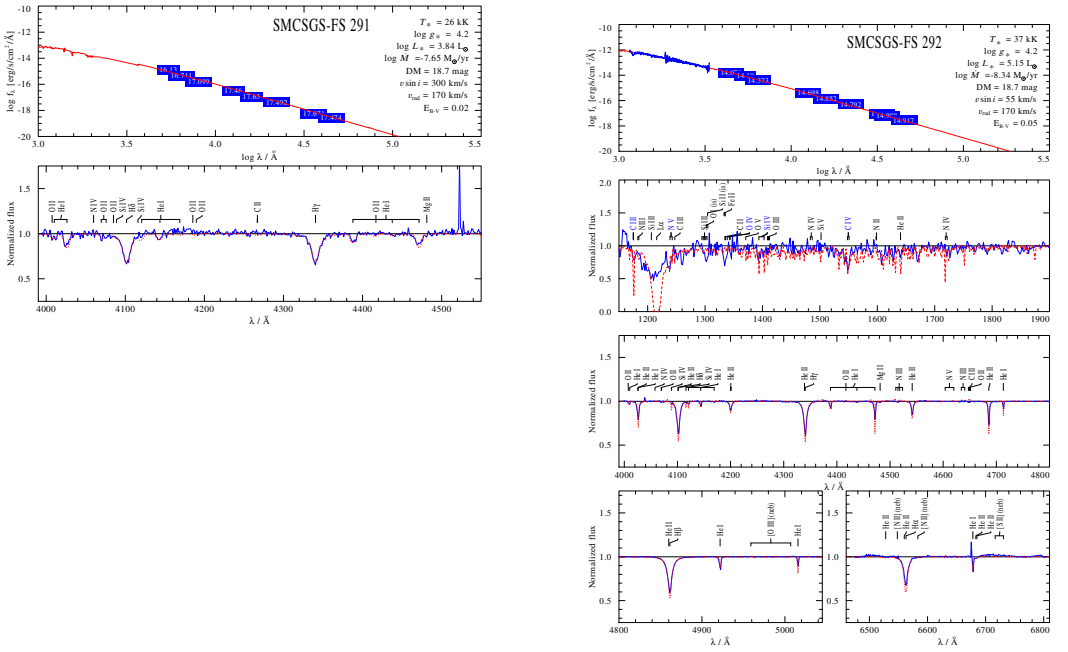

Figure C.98.: Spectral fit for SMCSGS-FS 291 and SMCSGS-FS 292

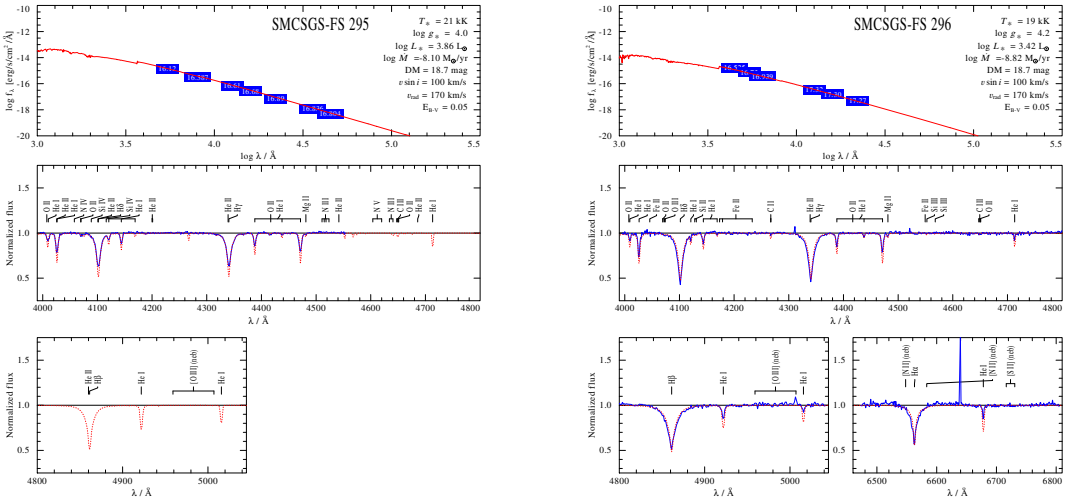

Figure C.99.: Spectral fit for SMCSGS-FS 295 and SMCSGS-FS 296

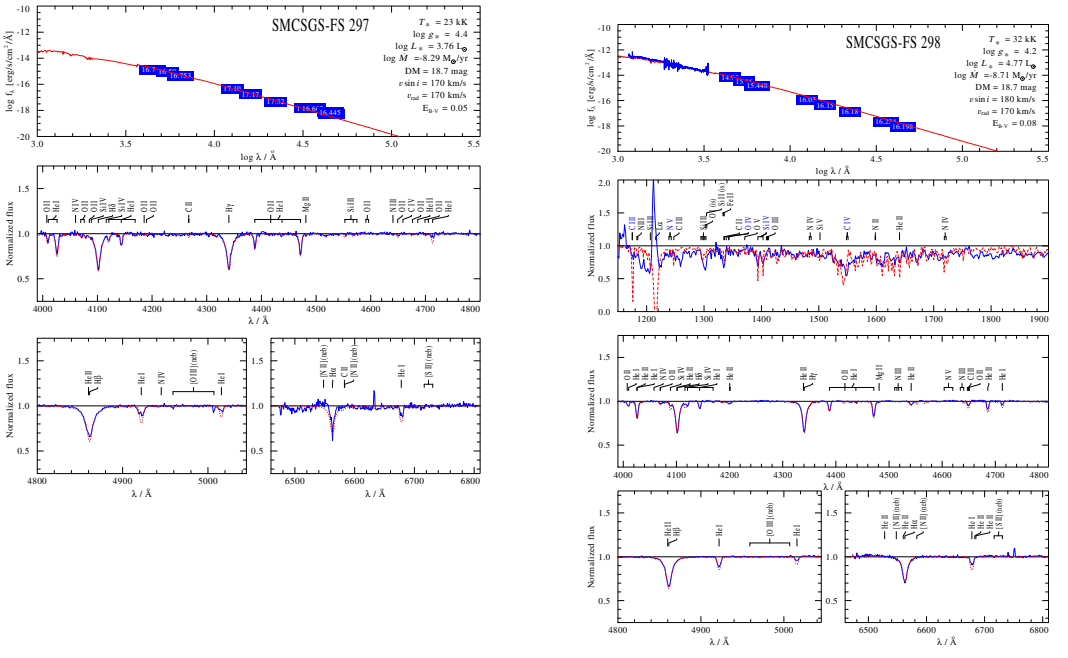

Figure C.100.: Spectral fit for SMCSGS-FS 297 and SMCSGS-FS 298

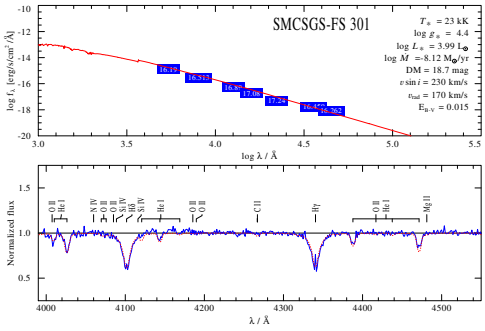

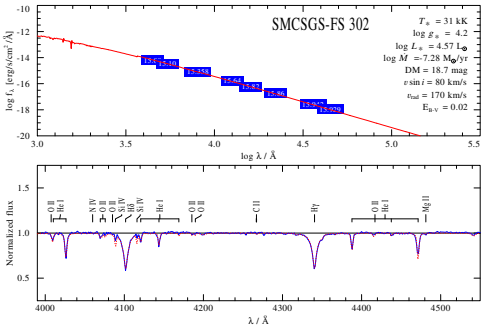

Figure C.101.: Spectral fit for SMCSGS-FS 301 and SMCSGS-FS 302

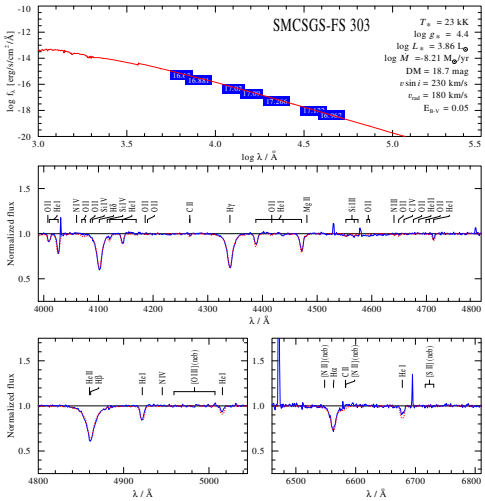

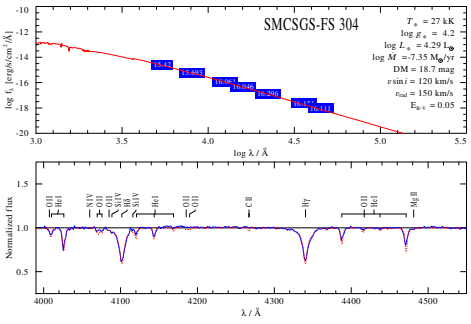

Figure C.102.: Spectral fit for SMCSGS-FS 303 and SMCSGS-FS 304

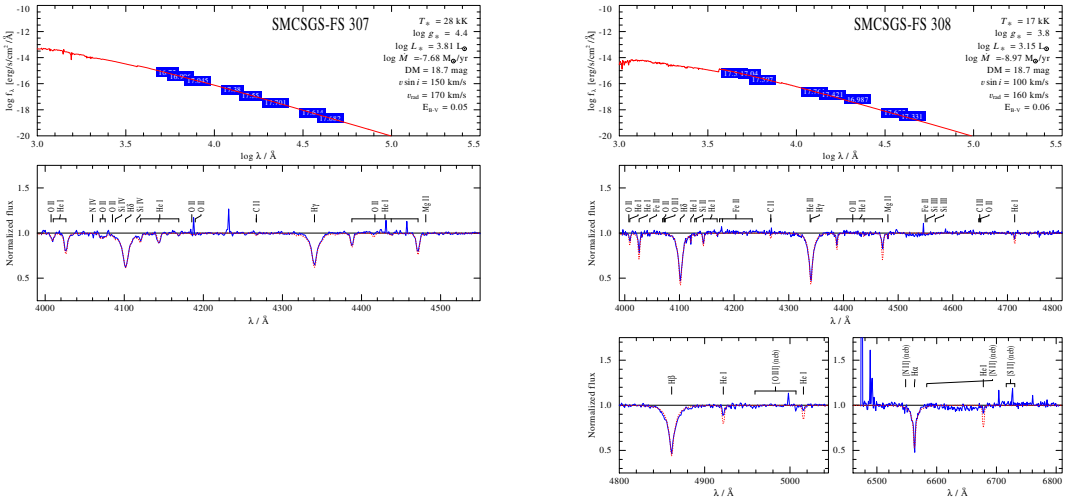

Figure C.103.: Spectral fit for SMCSGS-FS 307 and SMCSGS-FS 308

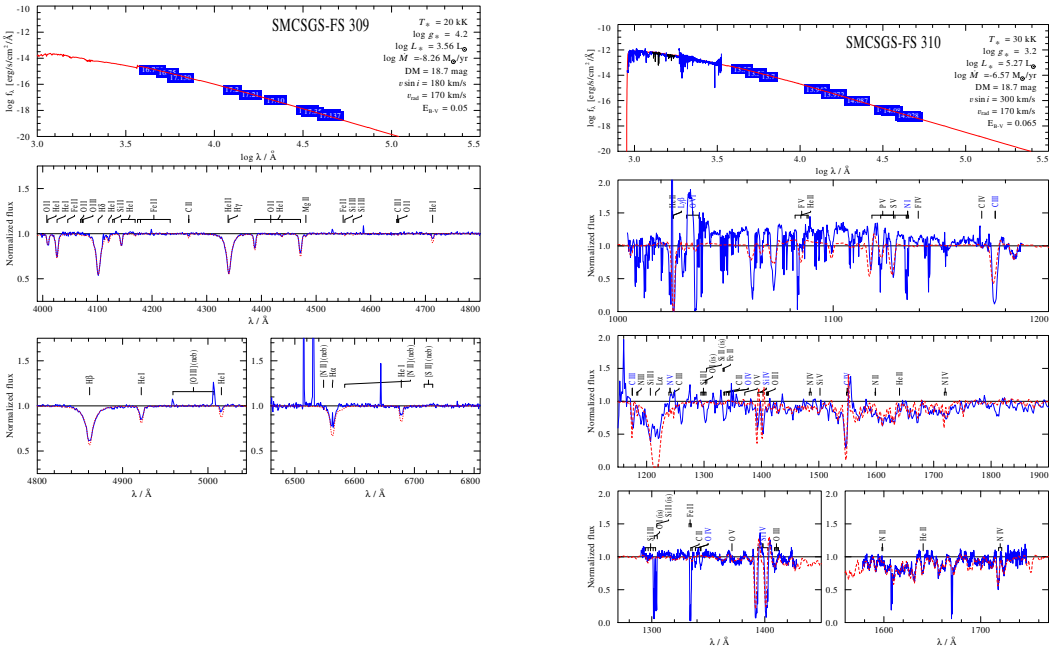

Figure C.104.: Spectral fit for SMCSGS-FS 309 and SMCSGS-FS 310

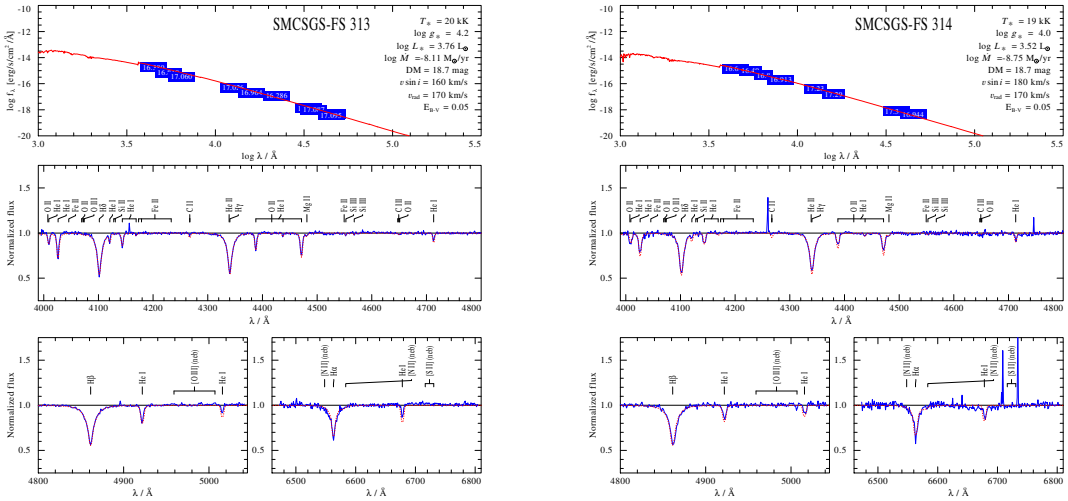

Figure C.105.: Spectral fit for SMCSGS-FS 313 and SMCSGS-FS 314

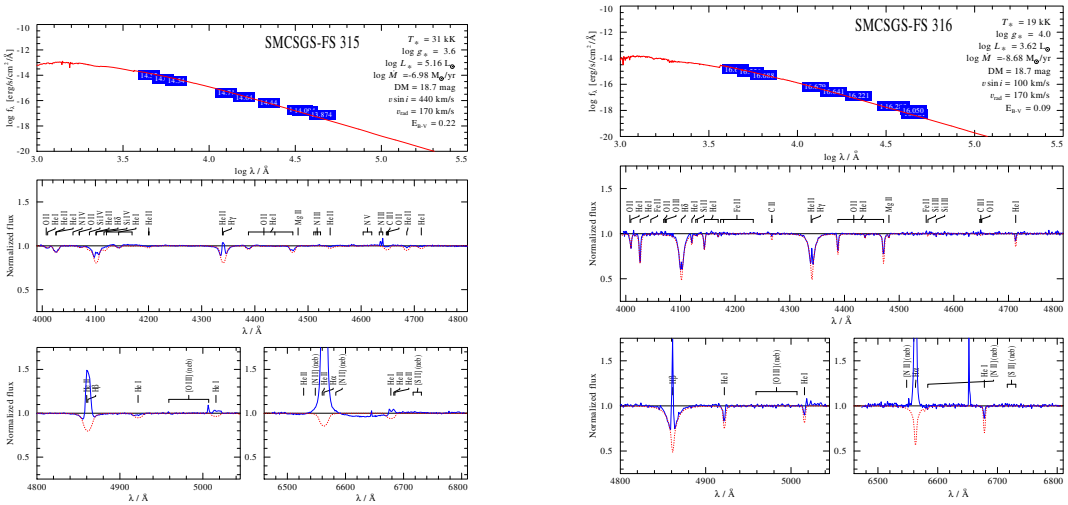

Figure C.106.: Spectral fit for SMCSGS-FS 315 and SMCSGS-FS 316

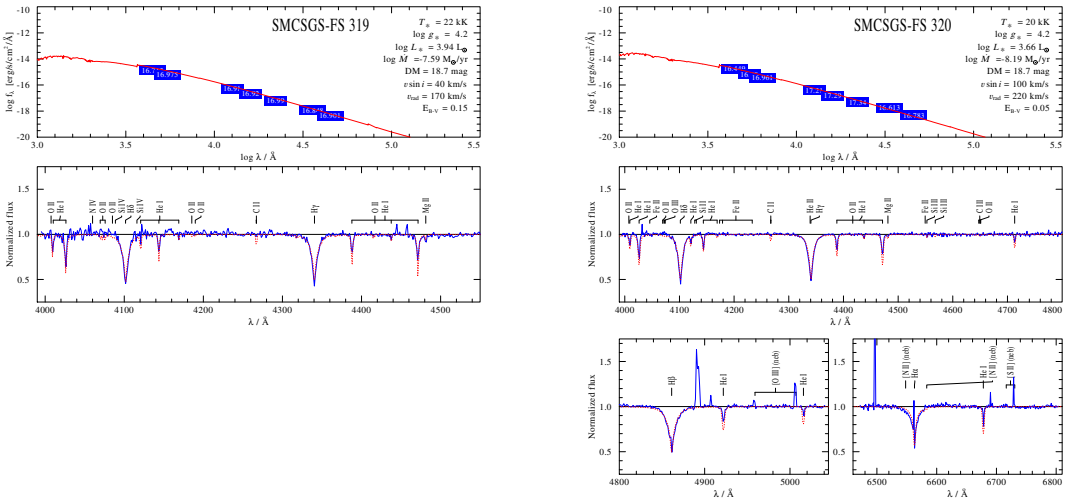

Figure C.107.: Spectral fit for SMCSGS-FS 319 and SMCSGS-FS 320